# DIRADICALOIDS

edited by **Jishan Wu**

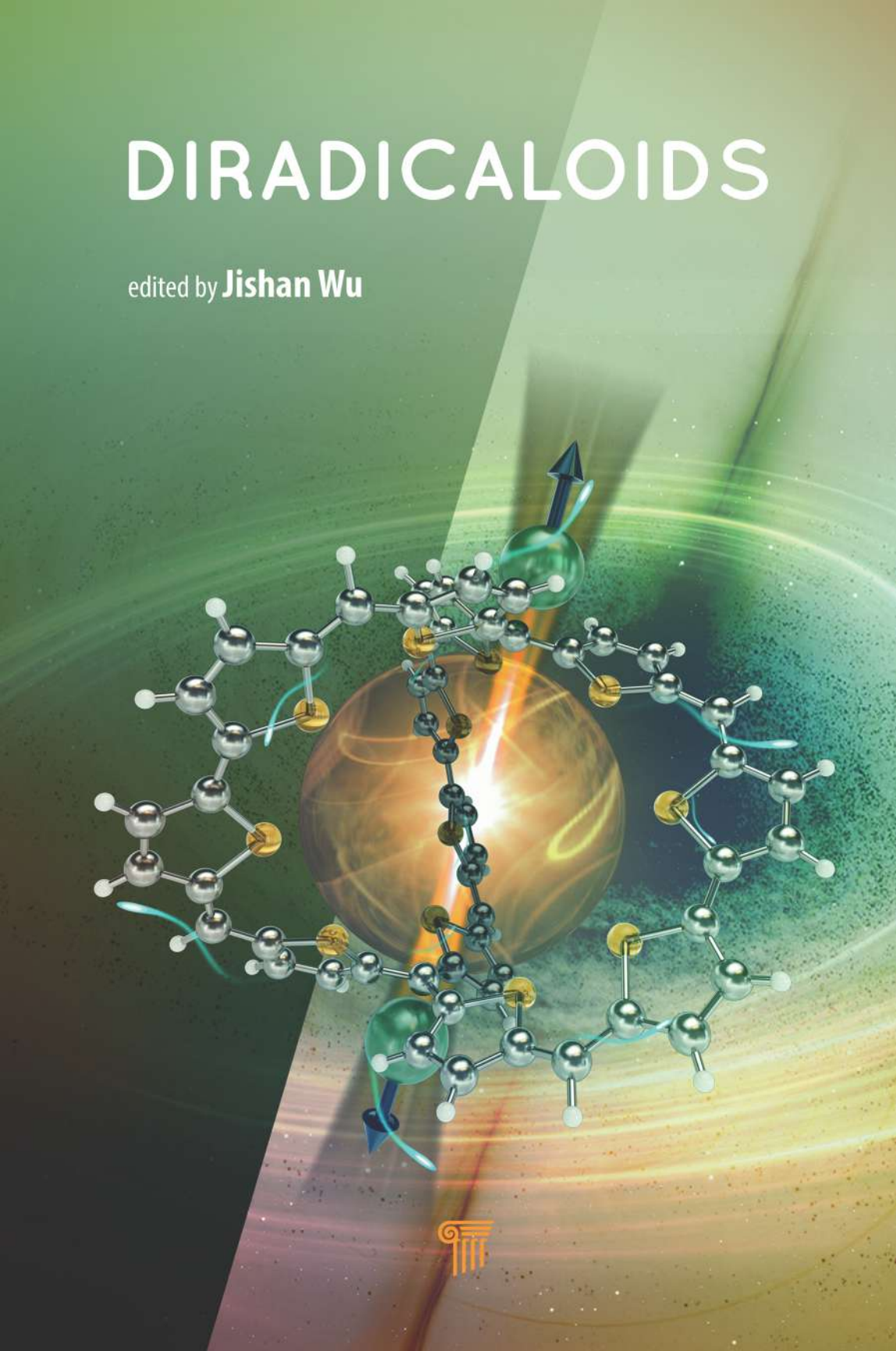

# DIRADICALOIDS

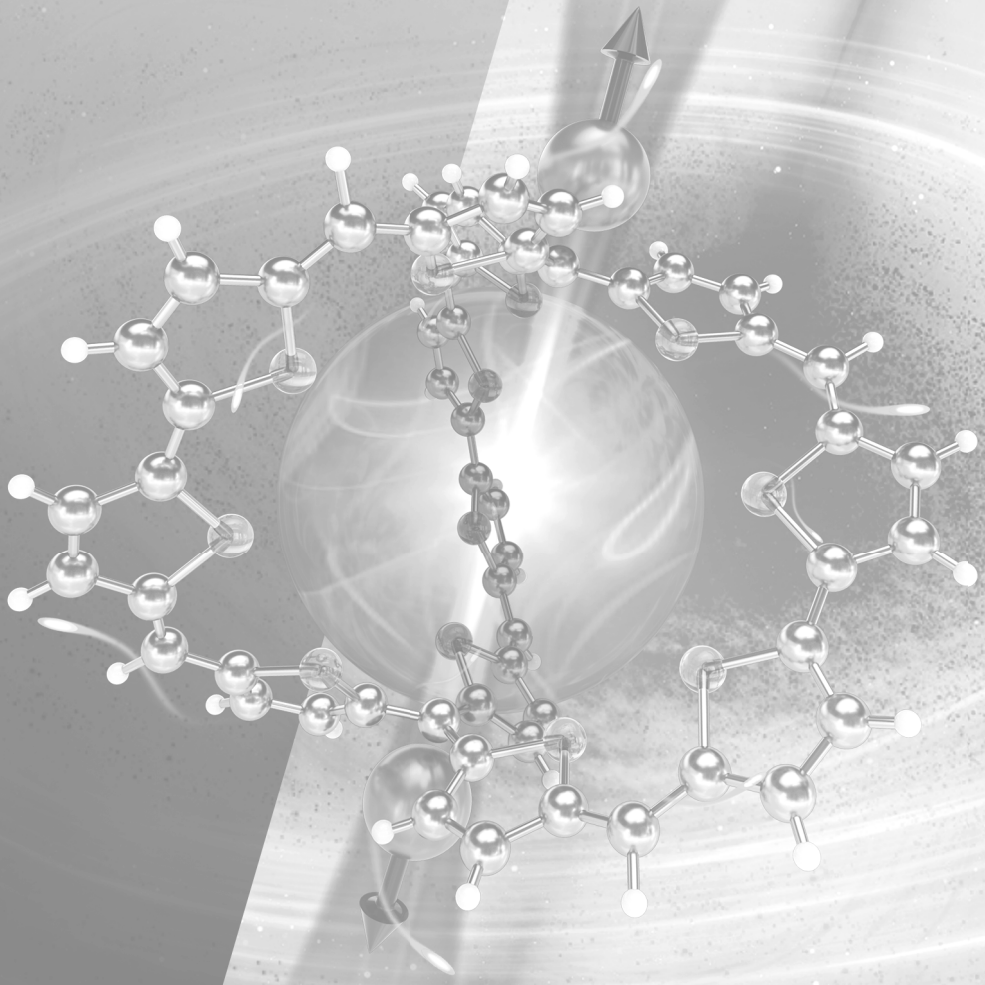

# DIRADICALOIDS

Edited by
**Jishan Wu**

JENNY STANFORD
PUBLISHING

*Published by*

Jenny Stanford Publishing Pte. Ltd.
Level 34, Centennial Tower
3 Temasek Avenue
Singapore 039190

Email: editorial@jennystanford.com
Web: www.jennystanford.com

**British Library Cataloguing-in-Publication Data**
A catalogue record for this book is available from the British Library.

**Diradicaloids**



ISBN 978-981-4968-08-9 (Hardcover)
ISBN 978-1-003-27724-8 (eBook)

# Contents

# Preface

In 1900, Gomberg reported the first-ever organic radical, the triphenylmethyl radical. Seven years later, Tschitschibabin synthesized a dimer of the triphenylmethyl radical, a quinoidal hydrocarbon showing high reactivity. Tschitschibabin's hydrocarbon can be regarded as the first open-shell singlet diradicaloid. Later on, more extended quinoidal hydrocarbons or quinones were prepared, which exhibited thermally populated paramagnetic property. Meanwhile, an *ortho*-quinodimethane-embedded hydrocarbon, pleiadene, was generated in situ and found to show diradical-like chemical reactivity. Notably, Michl et al. first correlated the experimentally observed absorption band to a doubly excited configuration, which is unique for diradicaloids. Since 1998, Nakasuji and Kubo's teams have reported a series of quinodimethane-bridged bis(phenalenyl) compounds and experimentally demonstrated their open-shell diradical character and interesting intermolecular multicentre covalent bonding interaction. In 2005, Otsubo et al. observed paramagnetic activity in extended quinoidal oligothiophenes, and the evolution from the closed-shell singlet state to the open-shell singlet state with extension of chain length was nicely revealed by Raman spectroscopy by Casado and López Navarrete's team. In 2006, Osuka et al. discovered the unusual diradical character in a doubly linked antiaromatic corrole dimer. In 2010 and 2013, Kubo et al. reported the challenging synthesis of two open-shell graphene-like molecules, teranthene and quateranthene, which can be used as model compounds to understand the edge states of zigzag-edged nanographenes and graphene nanoribbons. In 2011, our group occasionally found that a heptazethrene bis(dicarboximide) derivative, originally designed as an organic near-infrared dye, also exhibited open-shell singlet diradical character. This interesting discovery provoked us to explore various open-shell singlet diradicaloids in the following years. The past decade has witnessed a rapid growth of this research area. Owing

to the synergetic efforts between chemists and physicists, many relatively stable diradicaloids have been synthesized and we now have a much better understanding of the electronic properties of this type of unusual molecules. Diradicaloids exhibit remarkable optical properties (e.g., strong two-photon absorption), ambipolar charge transport, thermally populated magnetic activity, and even quantum properties and thus are promising molecular materials for electronics, photonics, spintronics, and quantum information processing.

Diradicaloids are diradical-like molecules with open-shell singlet ground state. Their electronic structure is in between typical open-shell diradicals and closed-shell molecules. Their unique electronic properties come from weakened π-bonds. Theoretical treatment of diradicaloids is a challenging task for computational chemists. In the first three chapters of this book, Nakano, Casanova, and Negri et al. introduce different ways to describe the electronic structure and optical property of diradicaloids. Particularly, "diradical character" is now a widely accepted term to describe the physical quantities. Vibrational spectroscopy such as Raman spectroscopy provides a qualitative measure of chemical bonding, which can be correlated to the diradical character, and this part has been introduced by Casado et al. in Chapter 4. One of the most challenging parts for the synthesis of diradicaloids is their radical-like high reactivity. Over the years, chemists have developed various synthetic methods and stabilizing strategies to access stable diradicaloids, which not only validated the theoretical predictions but also provided useful materials. These experimental works have been thoroughly summarized in Chapters 5–9, 11, and 12 by Kubo, Chi, Osuka, Feng, Wang, and Wu et al. In addition, diradical species are also involved in some photochemical reactions and show photochromic behavior, and this part has been described by Abe et al. in Chapter 10. Very recently, unusual aromaticity was observed in macrocyclic polyradicaloids. Owing to the intermediate intramolecular radical-radical coupling, the molecules could show global aromaticity by following both Hückel's rule in the singlet state and Baird's rule in the triplet state. Notably, 3D global aromaticity was attained in fully conjugated molecular cages. This latest progress has been discussed in Chapter 13.

Overall, this book provides a comprehensive overview of the progress in this emerging topic during the past decade. I would like to take this opportunity to thank all authors for their elegant

contribution and hard work during the COVID-19 pandemic. During the finalization of the editorial work for this book, we received very sad news that Professor Masayoshi Nakano passed away on November 1, 2021. He was one of the pioneers on the theory of diradicaloids and contributed the first chapter of this book. This is big loss for the field and we will remember him forever. With our collective efforts, I hope readers will find that this book indeed provides new insights and is helpful for their own research.

**Jishan Wu**

November 2021

Singapore

## Chapter 1

# Excitation Energies and Optical Properties of Open-Shell Singlet Diradicaloids

**Masayoshi Nakano**
*Department of Materials Engineering Science,*
*Graduate School of Engineering Science,*
*Osaka University, Machikaneyamacho 1-3,*
*Toyonaka, Osaka 560-8531, Japan*
mnaka@cheng.es.osaka-u.ac.jp

This chapter provides theoretical basis for the electronic states and optical properties of singlet diradicaloids using the valence configuration interaction (VCI) model and high-precision quantum chemical calculations. The physical quantities are described by "diradical character", which is a quantum chemically well-defined index for "bond weakness" in chemical sense or "electron correlation" in physical sense. Since the diradical character has a high affinity with chemical intuition, the description of physical quantities based on the diradical character has the advantage of facilitating the understanding of the structure, properties, and reactivity of singlet

*Diradicaloids*
Edited by Jishan Wu

ISBN 978-981-4968-08-9 (Hardcover), 978-1-003-27724-8 (eBook)
www.jennystanford.com

diradicaloids, and the construction of their design guidelines based on conventional chemical concepts such as resonance structure, aromaticity, and MO description.

## 1.1 Introduction

The concept of a singlet diradicaloid was proposed nearly 50 years ago and is characterized by "two weakly interacting electrons with similar energy" [1–3]. In general, the "bonding" is one of the most important fundamental concepts in chemistry that governs the structure, properties, and reactions of molecules and their aggregate systems. As it is well known, chemical bonding is a phenomenon first understood by quantum mechanics and has its origin in quantum mechanical superposition. For the simplest two-atom molecule like $H_2$, the bond is formed by the superposition of the orbitals of each atom in the valence bond (VB) picture, while in the molecular orbital (MO) picture, that is done by the MO delocalized over both atoms. The strength of the chemical bonds is described by the superposition of plural wavefunctions beyond a single configuration (in the present case, two configurations) in each picture. Namely, in the VB picture, it is described by constructive superposition between singly occupied atomic orbitals (AOs), giving the neutral (covalent) and ionic configurations, while in the MO picture, it is by superposition between a configuration composed of doubly occupied bonding MO (referred to as G configuration) and that composed of doubly occupied anti-bonding MO (referred to as doubly excited (D) configuration). The change in these superposition ratios changes the bond strength. For example, bond dissociation (i.e. a decrease in bond strength) qualitatively corresponds to a variation in the proportion of neutral and ionic configurations from 1:1 to 1:0 in the VB picture, and a variation in the proportion of G and D configurations from 1:0 to 1:1 in the MO picture. Thus, even though the VB and MO pictures give the same results, their interpretations are quite different, but they are useful for understanding the nature of bonds as they give us different chemical intuitions. As an alternative MO picture connecting these two pictures, there is a broken-symmetry (BS) (spin-unrestricted) MO picture [4]. Although this is not a correct symmetry-adapted (SA) wavefunction and is an approximate

picture involving spin contamination [4], the qualitative variation of wavefunction in the VB picture in the bond dissociation (splitting from a molecule to two atoms) is seen in MO (splitting a bonding MO delocalized over two atoms into an AO), so that the dissociation is easy to understand intuitively in the BS MO picture.

Figure 1.1 gives a schematic diagram showing the variations in potential energy and MOs with their energy levels in the SA and BS MO pictures, in the dissociation process of a two-atom molecule. In the SA MO picture, as increasing the bond distance, the energy levels of the bonding and anti-bonding MOs approach each other, indicating that the two electrons become more likely to cause doubly excitation from the bonding MO to the anti-bonding MO. On the other hand, in the BS MO picture, the dissociation is described by the change from the doubly occupied bonding MO to a spin-polarized MO with up and down spins localized respectively on the two atoms. Such changes in bond strength associated with bond dissociation can be classified into three categories: (I) stable bond region near the equilibrium atomic distance, (II) intermediate bond region, and (III) dissociation limit region. In the stable bond region, the G configuration is a good approximation, while the D configuration gradually mixes with the G configuration as dissociation proceeds. Thus, we can define the diradical character $y$ (which changes from 0 to 1 with dissociation) as twice the mixing ratio of the D configuration (which changes from 0 to 0.5) [5, 6]. This can be regarded as a quantitative measure of "bond weakness", where $y = 0$ indicates the closed-shell, 1 indicates the pure open-shell (diradical), and the intermediate $y$ between 0 and 1 indicates the intermediate open-shell. The system with an intermediate $y$ value is referred to as a "diradicaloid" (diradical-like system) [1]. Also, $1 - y$ can be defined as the "effective bonding order" since that value changes from 1 to 0 with dissociation. In contrast to this classification into three categories of electronic states based on changes in the bond strength in chemistry; in physics, it is possible to classify them according to the strength of the electron correlation (originating in the Coulomb interaction between electrons). Namely, the stable bond region corresponds to the weakly correlated region (1:1 superposition of neutral and ionic configurations in the VB picture); the intermediate bond region corresponds to the intermediate-correlated region (more mixing in the neutral configuration than in the ionic configuration), where the

localization of electrons on each atom becomes stronger; and the dissociation region corresponds to the strongly correlated region (described by a neutral configuration only), where electrons are localized on each atom. In other words, the diradical character *y* is a measure of the "strength of the electron correlation" in the physical sense. Thus, the diradical character *y* is a fundamental indicator that connects the concepts of chemistry (bond) and physics (electron correlation) about the electronic state [7, 8].

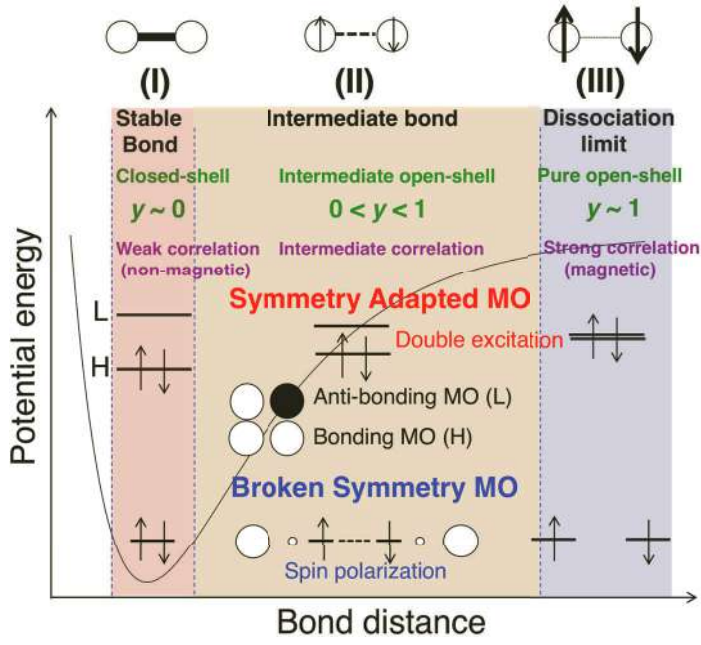


**Figure 1.1** Bond dissociation process of a homodinuclear molecule. Variations in the HOMO and LUMO in the SA method and magnetic orbitals in the BS method are also shown with a classification of electronic states (I)–(III) in the chemical (bond) and physical (correlation) pictures.

## 1.2 Electronic Structures of Singlet Diradicaloids

### 1.2.1 VCI Model of Symmetric Diradicaloids

We consider the simplest symmetric two-site diradical model A$^{\cdot}$–B$^{\cdot}$ with two electrons in two orbitals. The SA bonding ($g$) and anti-

bonding ($u$) MOs, e.g. the natural orbitals (NOs) obtained from the BS solutions, like the spin-projected unrestricted Hartree–Fock (UHF) solution, are described using the AO, $\chi_A$ and $\chi_B$:

$$g(x)=\frac{1}{\sqrt{2(1+S_{AB})}}\left[\chi_A(x)+\chi_B(x)\right], \text{ and}$$

$$u(x)=\frac{1}{\sqrt{2(1-S_{AB})}}\left[\chi_A(x)-\chi_B(x)\right] \tag{1.1}$$

Where $x$ indicates the coordinate in the bond direction, and $S_{AB}$ is the overlap integral between $\chi_A$ and $\chi_B$. Using these SA NOs, we define the localized natural orbital (LNO) as [7–10]

$$a(x)\equiv\frac{1}{\sqrt{2}}\left[g(x)+u(x)\right]\approx\chi_A(x), \text{ and } b(x)=\frac{1}{\sqrt{2}}\left[g(x)-u(x)\right]\approx\chi_B(x), \tag{1.2}$$

which satisfy the orthogonal condition, $\langle a|b\rangle=0$, and are well localized on one site (A or B). For the $z$-component of spin angular momentum $M_s=0$, there are two neutral $\{|a\bar{b}\rangle, |b\bar{a}\rangle\}$ and ionic $\{|a\bar{a}\rangle, |b\bar{b}\rangle\}$ determinants. The VCI matrix of the electronic Hamiltonian $H$ is represented by using the LNO basis [7–10]:

$$\begin{pmatrix} \langle a\bar{b}|H|a\bar{b}\rangle & \langle a\bar{b}|H|b\bar{a}\rangle & \langle a\bar{b}|H|a\bar{a}\rangle & \langle a\bar{b}|H|b\bar{b}\rangle \\ \langle b\bar{a}|H|a\bar{b}\rangle & \langle b\bar{a}|H|b\bar{a}\rangle & \langle b\bar{a}|H|a\bar{a}\rangle & \langle b\bar{a}|H|b\bar{b}\rangle \\ \langle a\bar{a}|H|a\bar{b}\rangle & \langle a\bar{a}|H|b\bar{a}\rangle & \langle a\bar{a}|H|a\bar{a}\rangle & \langle a\bar{a}|H|b\bar{b}\rangle \\ \langle b\bar{b}|H|a\bar{b}\rangle & \langle b\bar{b}|H|b\bar{a}\rangle & \langle b\bar{b}|H|a\bar{a}\rangle & \langle b\bar{b}|H|b\bar{b}\rangle \end{pmatrix} \tag{1.3}$$

$$=\begin{pmatrix} 0 & K_{ab} & t_{ab} & t_{ab} \\ K_{ab} & 0 & t_{ab} & t_{ab} \\ t_{ab} & t_{ab} & U & K_{ab} \\ t_{ab} & t_{ab} & K_{ab} & U \end{pmatrix}.$$

Here, the energy of the neutral determinant, $\langle a\bar{b}|H|a\bar{b}\rangle=\langle b\bar{a}|H|b\bar{a}\rangle$, is taken as the energy origin (0). $U$ represents the difference between on-site[$U_{aa}$ (=$U_{bb}$)] and neighbor-site ($U_{ab}$) Coulomb repulsions, referred to as effective Coulomb repulsion. $K_{ab}$ is a direct exchange integral [$K_{ab}$ = ($ab|ba$) ≥ 0], and $t_{ab}$ is a transfer integral [$t_{ab}=\langle a\bar{b}|H|b\bar{b}\rangle=\langle a|f|b\rangle \le 0$], where $f$ is the Fock operator in the LNO representation [11].

By diagonalizing the VCI matrix (Eq. (1.3)), the following four solutions are obtained [7, 8, 10].

(i) Neutral triplet state (u symmetry)

$$\left|T_{1u}\right\rangle = \frac{1}{\sqrt{2}}\left(\left|a\bar{b}\right\rangle - \left|b\bar{a}\right\rangle\right) \text{ with energy } {}^3E_{1u} = -K_{ab}. \qquad (1.4)$$

(ii) Ionic singlet state (u symmetry)

$$\left|S_{1u}\right\rangle = \frac{1}{\sqrt{2}}\left(\left|a\bar{a}\right\rangle - \left|b\bar{b}\right\rangle\right) \text{ with energy } {}^1E_{1u} = U - K_{ab}. \qquad (1.5)$$

(iii) Lower singlet state (with g symmetry)

$$\left|S_{1g}\right\rangle = \kappa\left(\left|a\bar{b}\right\rangle + \left|b\bar{a}\right\rangle\right) + \eta\left(\left|a\bar{a}\right\rangle + \left|b\bar{b}\right\rangle\right)$$

$$\text{with energy } {}^1E_{1g} = K_{ab} + \frac{U - \sqrt{U^2 + 16t_{ab}^2}}{2}. \qquad (1.6)$$

Here, $2(\kappa^2 + \eta^2) = 1$ and $\kappa > \eta > 0$, which indicates that state $S_{1g}$ has a larger weight of neutral determinant (the first term with coefficient κ) than that of ionic one (the second term with coefficient η). ${}^3E_{1u}$, ${}^1E_{1u}$, and ${}^1E_{1g}$ indicate the energies of triplet $T_{1u}$, singlet $S_{1u}$, and singlet $S_{1g}$ states, respectively.

(iv) Higher singlet state (g symmetry)

$$\left|S_{2g}\right\rangle = -\eta\left(\left|a\bar{b}\right\rangle + \left|b\bar{a}\right\rangle\right) + \kappa\left(\left|a\bar{a}\right\rangle + \left|b\bar{b}\right\rangle\right)$$

$$\text{with energy } {}^1E_{2g} = K_{ab} + \frac{U + \sqrt{U^2 + 16t_{ab}^2}}{2}. \qquad (1.7)$$

Here, $2(\kappa^2 + \eta^2) = 1$ and $\kappa > \eta > 0$. In contrast to $S_{1g}$, state $S_{2g}$ has a larger weight of ionic determinant (the second term with coefficient κ) than that of neutral one (the first term with coefficient η). ${}^1E_{2g}$ indicates the energy of singlet $S_{2g}$ state.

Here, $\kappa$ and $\eta$ are functions of $|t_{ab}/U|$ (= $r_t$) [7, 8, 10], which indicates the ease of the electron transfer (the degree of delocalization) between atoms A and B. Figure 1.2 shows that as $r_t$ is decreasing, the $\kappa$ increases toward $1/\sqrt{2}$ at $r_t = 0$, while the $\eta$ decreases toward 0 at $r_t = 0$. This indicates that the neutral (ionic) component increases (decreases) with decreasing $r_t$. It turns out from this behavior that the electron mobility between sites A and B, i.e. the delocalization nature over sites A and B governs the relative

neutral (covalent) and ionic natures of the state, i.e. the diradical character.

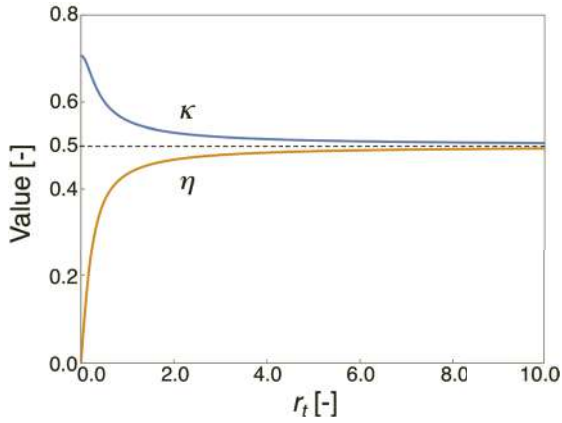


**Figure 1.2** Variations of $\kappa$ and $\eta$ as a function of $r_t$.

We here consider the expression of diradical character $y$ using the physical parameters $t_{ab}$ and $U$. Using the relationship between BS orbitals $\{a, b\}$ and SA MOs $\{g, u\}$ (Eq. (1.2)), state $S_{1g}$ (Eq. (1.6)) is expressed by

$$\left|S_{1g}\right\rangle = (\kappa+\eta)\left|g\bar{g}\right\rangle + (\kappa-\eta)\left|u\bar{u}\right\rangle . \tag{1.8}$$

As mentioned in Section 1.1, since the diradical character $y$ is defined as twice the weight of the doubly excitation configuration, $2\zeta^2 = 2(\kappa-\eta)^2 = 1 - 4\kappa\eta$, $y$ is represented by

$$y = 1 - \frac{1}{\sqrt{1+\left(U/(4t_{ab})\right)^2}} = 1 - \frac{1}{\sqrt{1+(4r_t)^{-2}}} \tag{1.9}$$

This is also found to be the occupation number of NOs, i.e. $n_{\mathrm{LUNO}} = 1 - n_{\mathrm{HONO}}$, within single determinant theory, where HONO (LUNO) represents the highest occupied (the lowest unoccupied) NO [6–8].

Figure 1.3 shows the variation of $y$ as a function of $\left|U/t_{ab}\right| (= 1/r_t)$. With increasing $r_t$, $y$ value exhibits an increase from 0 to 1, which corresponds to $r_t \leq \sim 1$ and $r_t \to 0$, respectively. From the physical meaning of the transfer integral $t_{ab}$ and the effective Coulomb repulsion $U$, $y \to 1$ at $r_t \to 0$ represents the localization of electrons on each site, i.e. a pure diradical state; while $y \to 0$ at $r_t \geq \sim 1$ represents

the delocalization of electrons over two sites, i.e. a closed-shell stable bond state. Namely, the diradical character $y$ indicates the degree of electron correlation $|U/t_{ab}|$ in the physical sense. On the other hand, from Eq. (1.9), we obtain

$$1 - y = \frac{n_{\mathrm{HONO}} - n_{\mathrm{LUNO}}}{2}, \tag{1.10}$$

which implies that $1 - y$ indicates the effective bond order concerned with bonding (HONO) and anti-bonding (LUNO) orbitals [7, 12]. Indeed, $1 - y$ shows a change from 1 (stable bond region) to 0 (bond breaking region) with increasing the electron correlation $U/t_{ab}$ (Figure 1.3), which implies that $y$ indicates the bond weakness in chemical sense. To summarize, the diradical character $y$ is a fundamental factor for describing electronic states and can bridge the physical (electron correlation) and chemical (effective chemical bond) pictures for electronic states [7, 8].

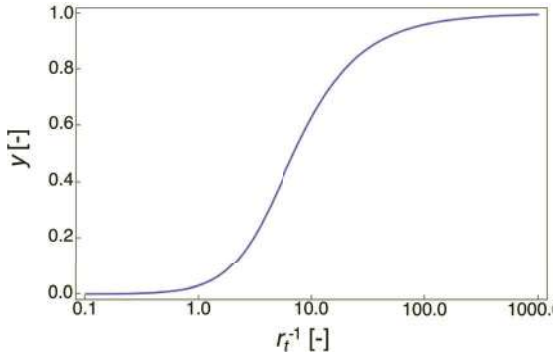


**Figure 1.3** Diradical character $y$ versus $|U/t_{ab}|$ (= $1/r_t$).

### 1.2.2 Diradical Character Dependences of Excitation Energies and Properties of Symmetric Diradicaloids by VCI Model

Figure 1.4 shows the four-state model constructed from the singlet and triplet states for a symmetric two-site diradical model, where $|S_{1g}\rangle$ and $|S_{2g}\rangle$ have the same symmetry (g symmetry), and the transition moment between these states vanishes. The analytical expressions of the singlet excitation energies and transition

moments squared using the dimensionless physical quantities ($r_t$ = $|t_{ab}/U|$, $r_K = 2K_{ab}/U$) and diradical character $y$ are given by [7, 8, 10]

$$\Delta E_{S_{1u},S_{1g}} = U\left(1 - r_K - \frac{1-\sqrt{1+(4r_t)^2}}{2}\right) = \frac{U}{2}\left[1 - 2r_K + \frac{1}{\sqrt{1-(1-y)^2}}\right], \tag{1.11}$$

$$\Delta E_{S_{2g},S_{1g}} = U\sqrt{1+(4r_t)^2} = \frac{U}{\sqrt{1-(1-y)^2}}, \tag{1.12}$$

$$(\mu_{S_{1g},S_{1u}})^2 = 2\eta^2(R_{BA})^2 = \frac{(R_{BA})^2}{2}\left[1 - \sqrt{1-(1-y)^2}\right] \tag{1.13}$$

$$(\mu_{S_{1u},S_{2g}})^2 = 2\kappa^2(R_{BA})^2 = \frac{(R_{BA})^2}{2}\left[1 + \sqrt{1-(1-y)^2}\right], \tag{1.14}$$

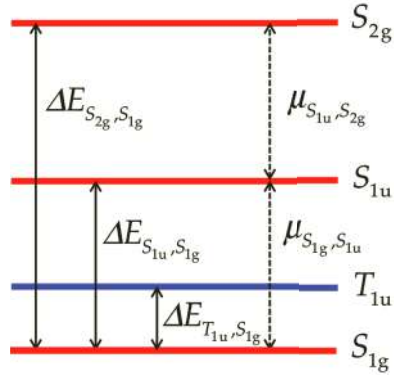


**Figure 1.4** Singlet ($S_{1g}$, $S_{1u}$, $S_{2g}$) and triplet ($T_{1u}$) states in a two-site diradical model. The excitation energies ($\Delta E_{S_{2g},S_{1g}}$, $\Delta E_{S_{1u},S_{1g}}$, $\Delta E_{T_{1u},S_{1g}}$) and transition moments ($\mu_{S_{1u},S_{2g}}$, $\mu_{S_{1g},S_{1u}}$) are shown.

where $R_{BA}$ is defined by the expectation values of the bond-axis component of the position $r$ of electrons using the LNOs $a$ and $b$, i.e. $(b|r|b) - (a|r|a)$, which indicates an effective distance between the two radicals. As seen from Eq. (1.13), the transition moment amplitude ($|\mu_{S_{1g},S_{1u}}|$) between $S_{1g}$ and $S_{1u}$ is proportional to the coefficient ($\eta$) of the ionic term in the singlet ground state $S_{1g}$, while that ($|\mu_{S_{1u},S_{2g}}|$) between $S_{1u}$ and $S_{2g}$ is to the coefficient ($\kappa$) of the neutral term in $S_{1g}$, which is also that of the ionic term in the excited

singlet state $S_{2g}$. The increase in diradical character (the increase in weight of the neutral component) of the singlet ground state $S_{1g}$ is found to cause the decrease in $|\mu_{S_{1g},S_{1u}}|$ and the increase in $|\mu_{S_{1u},S_{2g}}|$. This is understood by the fact that the ionic component of $S_{1g}$ ($S_{2g}$) decreases (increases) with the increase in the diradical character of $S_{1g}$ (Eqs. (1.6) and (1.7)), while $S_{1u}$ keeps the pure ionic nature (Eq. (1.5)). Note here that the transition moment between the ionic and neutral terms becomes 0, while that between the ionic terms has a finite value. Thus, larger ionic components in $S_{1g}$ and $S_{2g}$ cause larger amplitudes of the transition moments $\mu_{S_{1g},S_{1u}}$ and $\mu_{S_{1u},S_{2g}}$.

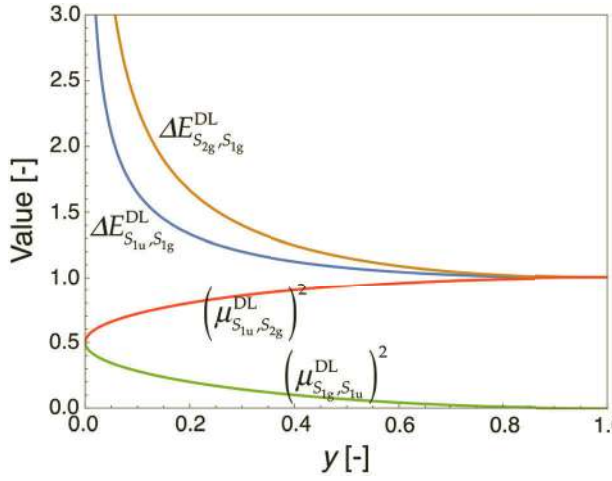


**Figure 1.5** Diradical character dependences ($y$) of dimensionless excitation energies ( $\Delta E^{DL}_{S_{1u},S_{1g}}$ , $\Delta E^{DL}_{S_{2g},S_{1g}}$ ) and dimensionless transition moments squared ( $(\mu^{DL}_{S_{1g},S_{1u}})^2$ , $(\mu^{DL}_{S_{1u},S_{2g}})^2$ ) for $r_K = 0$.

Figure 1.5 shows the evolution with $y$ of the dimensionless (DL) excitation energies ( $\Delta E^{DL}_{S_{1u},S_{1g}} \equiv \Delta E_{S_{1u},S_{1g}}/U$, $\Delta E^{DL}_{S_{2g},S_{1g}} \equiv \Delta E_{S_{2g},S_{1g}}/U$) and dimensionless transition moments squared ( $\left(\mu^{DL}_{S_{1g},S_{1u}}\right)^2 \equiv \left(\mu_{S_{1g},S_{1u}}/R_{BA}\right)^2$, $\left(\mu^{DL}_{S_{1u},S_{2g}}\right)^2 \equiv \left(\mu_{S_{1u},S_{2g}}/R_{BA}\right)^2$ ) for $r_K = 0$, which is a nonmagnetic case. It is found that both excitation energies decrease rapidly with $y$ and tend toward 1, while in the small $y$ region, $\Delta E^{DL}_{S_{1u},S_{1g}}$ decreases faster than $\Delta E^{DL}_{S_{2g},S_{1g}}$. $\left(\mu^{DL}_{S_{1u},S_{2g}}\right)^2$ displays a monotonic increase from 0.5 to 1, while $\left(\mu^{DL}_{S_{1g},S_{1u}}\right)^2$ exhibits the

opposite behavior and goes from 0.5 to 0. These mutually opposite behaviors result from the fact that the characters of the ground ($S_{1g}$) and the second ($S_{2g}$) excited states evolve toward neutral and ionic states, respectively. Therefore, when increasing $y$, the transition density $|S_{1g}\rangle \times |S_{1u}\rangle$ decreases, while $|S_{1u}\rangle \times |S_{2g}\rangle$ increases.

Next, we consider the first excitation energy $\Delta E_{S_{2g},S_{1g}}$ as a function of $y$ and other physical parameters [7, 11]. From Eq. (1.11), $\Delta E_{S_{1u},S_{1g}}$ is rewritten as

$$\Delta E_{S_{1u},S_{1g}} = \frac{U}{2} f_E(y) - 2K_{ab}, \text{ with } f_E(y) = 1 + \frac{1}{\sqrt{1-(1-y)^2}}. \quad (1.15)$$

Starting from Eq. (1.9), the diradical character $y$ can be rewritten as

$$y = 1 - \frac{1}{\sqrt{1+\left(U/(4t_{ab})^2\right)}} = 1 - \frac{1}{\sqrt{1+(K_{gu}^{M}/\varepsilon_{ug})}}, \quad (1.16)$$

where the second equality is obtained from the relations: $U = 2K_{gu}^{M}$ and $2t_{ab} = \varepsilon_{ug}$, where $2K_{gu}^{M}$ and $\varepsilon_{ug}$ represent the exchange integral and the HOMO($g$)–LUMO($u$) gap ($\varepsilon_u - \varepsilon_g$) in the SA MO basis representation (Eq. (1.1)) [7, 8, 10]. Using Eq. (1.1), the following relationship is also obtained [13]:

$$K_{ab} = \frac{1}{4}\left(J_{gg}^{M} + J_{uu}^{M} - 2J_{gu}^{M}\right), \quad (1.17)$$

where $J_{ij}^{M}$ is the Coulomb repulsion between MOs $i$ and $j$. Note that since $K_{ab}$ is definitely positive, larger $K_{ab}$ leads to decrease the energy $\Delta E_{S_{1u},S_{1g}}$ (Eq. (1.15)). First, let us consider nearly closed-shell systems ($y \sim 0$), where $U << 4|t_{ab}|$ (Eq. (1.16)). Thus, although $f_E(y)$ (Eq. (1.15)) becomes very large, the $U/2$ prefactor is negligible, resulting in a finite value for the first term $(U/2)f_E(y)$ in Eq. (1.15). Note that if $U$ and $|t_{ab}|$ decrease, while keeping $|t_{ab}|/U$ and $y$ constant, the first excitation energy $\Delta E_{S_{1u},S_{1g}}$ decreases. In addition, a decrease of $U$ ($K_{gu}^{M}$ which is proportional to the overlap between $g$ and $u$) leads to an increase in $K_{ab}$ since $g$ and $u$ tend to be distributed in different spatial regions, so that $J_{gg}^{M} > J_{gu}^{M}$ and $J_{uu}^{M} > J_{gu}^{M}$ (Eq. (1.17)). In summary, for small $y$ values, a decrease of $|t_{ab}|$ (HOMO–LUMO gap) and a decrease of $K_{gu}^{M}$ (overlap between $g$ and $u$) constitute ways for reducing the first excitation energy $\Delta E_{S_{1u},S_{1g}}$ (Eq. (1.15)).

On the other hand, Eq. (1.15) shows that increasing $y$ could be another way of decreasing $\Delta E_{S_{1u},S_{1g}}$ [13], in the case where $U(K_{gu}^{M})$ increases and $|t_{ab}|$ (HOMO–LUMO gap) decreases. In this case, $K_{ab}$ tends to decrease since $U$ ($K_{gu}^{M} \propto$ overlap between $g$ and $u$) becomes large, i.e. both $g$ and $u$ span over similar regions ($J_{gg}^{M} \sim J_{uu}^{M} \sim J_{gu}^{M}$) (Eq. (1.17)). As a result, the first excitation energy is governed by the first term (a function of $U$ and $y$) in Eq. (1.15): $\Delta E_{S_{1u},S_{1g}}$ decreases with increasing $y$ up to the intermediate diradical character region following the $y$-dependence of $f_E(y)$ (Figure 1.5). However, further increase of $y$ has the possibility of increasing $\Delta E_{S_{1u},S_{1g}}$. Indeed, an increase of $y$ is related to the increase of $U$ (Eq. (1.9)) while $f_E(y)$ in Eq. (1.15) rapidly decreases in the relatively small $y$ region ($y < \sim 0.2$), and subsequently reaches a stationary value. Thus, for larger $y$ values, $\Delta E_{S_{1u},S_{1g}}$ (the product of $U/2$ and $f_E(y)$) could increase again when $U$ is large and $f_E(y)$ stationary. Usually, π-delocalization extension tends to increase $y$ due to the decrease of $|t_{ab}|$ and the increase of $U$, so that this has a possibility of increasing the first excitation energy, which is contrary to the conventional feature of closed-shell π-conjugated molecules. This unusual behavior is observed in non-alternant anti-aromatic molecules, a fluoreno[2,3-*b*]fluorene derivative (24π-electron hydrocarbon) and the smaller congener indeno[2,1-*b*]fluorene derivative (20π-electron hydrocarbon) [13]. Although the former is found to have a larger diradical character $y_0$ (0.772) than the latter (0.645), the excitation energy of the former (0.959 eV) is found to be larger than that of the latter (0.729 eV). This trend is contrary for the well-known feature for common, alternant aromatic hydrocarbons.

Finally, the singlet-triplet (ST) energy gap is investigated in the two-site diradical VCI model. The dimensionless effective exchange $r_J$ reads as [7, 8, 10, 15]

$$r_J = r_K + \frac{1}{2}\left(1 - \sqrt{1 + (4r_t)^2}\right), \tag{1.18}$$

where $r_J$ is defined as

$$r_J \equiv \frac{2J}{U} = \frac{\Delta E_{ST}(\equiv E_S - E_T)}{U}. \tag{1.19}$$

So, within Heisenberg model [14], the effective exchange interaction describes the ground state magnetic interaction,

where negative (anti-ferromagnetic) and positive (ferromagnetic) $J$ correspond to singlet and triplet ground states, respectively. As seen from Eqs. (1.4)–(1.7), the dimensionless state energies depend linearly on $r_K$ (≥ 0 and proportional to the overlap between LNOs $a$ and $b$), which stabilizes the $S_{1u}$ and $T_{1u}$ states, but destabilizes the $S_{1g}$ and $S_{2g}$ states by $r_k/2$, so that the dimensionless first singlet excitation energy $\Delta E_{S_{1u},S_{1g}}/U$ and ST gap $\Delta E_{T_{1u},S_{1g}}/U$ decrease when $r_K$ increases. These stabilization and destabilization effects originate from the relative phase between the LNOs in the neutral $\{|a\bar{b}\rangle, |b\bar{a}\rangle\}$ and ionic $\{|a\bar{a}\rangle, |b\bar{b}\rangle\}$ determinants. From Eqs. (1.16) and (1.18), we obtain [7, 8, 10]

$$r_J = r_K + \frac{1}{2}\left(1 - \sqrt{\frac{1}{y(2-y)}}\right), \tag{1.20}$$

where the first term is definitely positive, but the second term takes a value ranging from 0 ($y$ = 1) and -∞ ($y$ = 0). Figure 1.6 shows the variation of $r_J$ as a function of $y$ and $r_K$. Although $r_J$ increases from a large negative value in the small $y$ region toward zero at $y$ ~ 1 for $r_K$ = 0, where the singlet and triplet states are degenerated, and $r_J$ becomes positive for large $y$ if the system possesses a finite $r_K$ (positive) value, larger than the second term in Eq. (1.20). Such triplet ground state defines the molecular magnet region. The $y$ value giving $r_J$ = 0, referred to as, $y_{\Delta E_{ST}=0}$ reads [16]

$$y_{\Delta E_{ST}=0} = 1 - \sqrt{1 - \frac{1}{(2r_K+1)^2}}\,. \tag{1.21}$$

This indicates that $y_{\Delta E_{ST}=0}$ decreases with increasing $r_K$ as shown in Figure 1.6. For instance, diradicaloids with relatively large $r_K$ have the possibility to display a triplet ground state associated with a singlet excited state having small or intermediate $y$ value. These systems are expected to attract much interest, owing to their gigantic nonlinear optical (NLO) responses in their first singlet excited state [10], though real compounds that have not been found yet. Still, candidates are conjectured among Baird triplet aromatic systems [17].

From Eqs. (1.18) and (1.19), one can derive its full expression:

$$\Delta E_{ST} = 2K_{ab} + \frac{U}{2}\left(1 - \sqrt{\frac{1}{y(2-y)}}\right) = 2K_{ab} + \frac{U}{2} f_{ST}(y)\,. \tag{1.22}$$

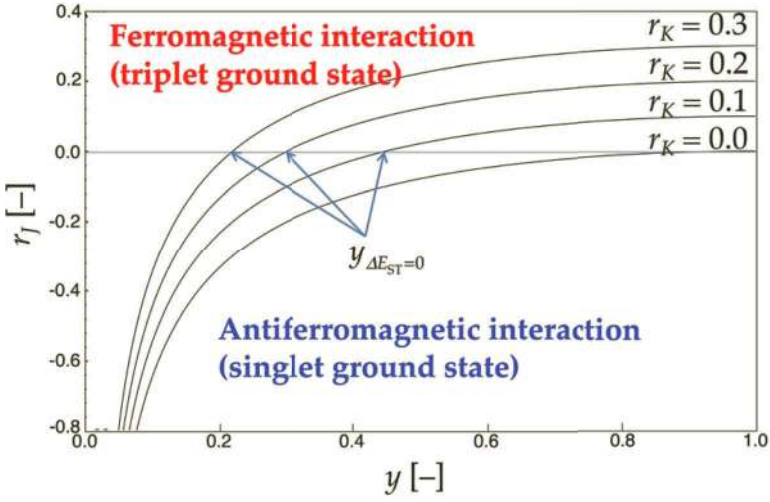


**Figure 1.6** Diradical character dependence of $r_J$ for the two-site diradical VCI model with $r_K$ = 0.0, 0.1, 0.2, and 0.3.

Thus, for nonmagnetic systems, with negligible $K_{ab}$ (positive) values, the ST gap is determined by the second term, which indicates that in addition to the $y$ dependence $f_{ST}(y)$, the ST gap also depends on $U$. This implies that even if two systems have similar $y$ values, their $\Delta E_{ST}$ values can be much different. From Eq. (1.22), since $y$ is a function of $|t_{ab}|/U$, systems, where $U$ increases but $y$ is constant, are achieved provided $|t_{ab}|$ also increases. These systems are predicted to have larger ST gap than those with smaller $U$ and $|t_{ab}|$, though their $y$ values are the same. This is in contrast to the conventional qualitative tendency: large diradical character reduces the ST gap. Such an example has been obtained for diindenoanthracene (DIAn) derivative and indenoindenodi(benzothiophene) (IIDBT) derivative [15]. It is found that the former and the latter have similar $y_0$ values (0.62 and 0.61, respectively), while the latter has larger amplitude of experimental ST gap (−8.0 kcal mol$^{-1}$) than the former (−4.18 kcal mol$^{-1}$).

Using the above relationships, design guidelines for tuning the ST gap and $y$, and thus controlling various physicochemical properties and reactivity could be elaborated. In summary, from Eq. (1.22), for a fixed $U$ value, a nonmagnetic molecule has a singlet ground state ($\Delta E_{ST} < 0$) and $|\Delta E_{ST}|$ gets smaller with increasing $y$, while for a non-

negligible $K_{ab}$, the ground state will become triplet at an intermediate $y$ value, of which the amplitude gets smaller with increasing $K_{ab}$.

### 1.2.3 VCI Model of Asymmetric Diradicaloids

We here investigate the asymmetric diradicaloids, where the asymmetric zwitterionic components are not negligible and the neutral (diradical) components play a complementary role in the ground state. As explained in Section 1.2.1, although the asymmetric charge distribution, referred to as asymmetry, tends to reduce the diradical character, "asymmetry" and primary "ionic" are not necessarily the same concept. In order to clarify these features, let us consider the ground and excited states based on an asymmetric two-site model A$^{\bullet}$–B$^{\bullet}$ with two electrons in two orbitals [18].

The asymmetric two-site model A$^{\bullet}$–B$^{\bullet}$ is located along the bond ($x$-axis). Using the AOs for A and B, i.e. $\chi_A$ and $\chi_B$, with overlap $S_{AB}$, bonding and anti-bonding MOs, $g$ and $u$ can be defined as in the symmetric system Eq. (1.1). Note here that these are not the canonical MOs of the asymmetric systems when A ≠ B. Using these MOs, we can define the LNOs $a$ and $b$, by Eq. (1.2), which become the corresponding AOs, $\chi_A$ and $\chi_B$, at the dissociation limit. Using the LNOs, the VCI matrix for zero $z$-component of spin angular momentum ($M_S = 0$, singlet, and triplet) is expressed by [18]

$$\begin{pmatrix} \langle a\bar{b}|H|a\bar{b}\rangle & \langle a\bar{b}|H|b\bar{a}\rangle & \langle a\bar{b}|H|a\bar{a}\rangle & \langle a\bar{b}|H|b\bar{b}\rangle \\ \langle b\bar{a}|H|a\bar{b}\rangle & \langle b\bar{a}|H|b\bar{a}\rangle & \langle b\bar{a}|H|a\bar{a}\rangle & \langle b\bar{a}|H|b\bar{b}\rangle \\ \langle a\bar{a}|H|a\bar{b}\rangle & \langle a\bar{a}|H|b\bar{a}\rangle & \langle a\bar{a}|H|a\bar{a}\rangle & \langle a\bar{a}|H|b\bar{b}\rangle \\ \langle b\bar{b}|H|a\bar{b}\rangle & \langle b\bar{b}|H|b\bar{a}\rangle & \langle b\bar{b}|H|a\bar{a}\rangle & \langle b\bar{b}|H|b\bar{b}\rangle \end{pmatrix} = \begin{pmatrix} 0 & K_{ab} & t_{ab(aa)} & t_{ab(bb)} \\ K_{ab} & 0 & t_{ab(aa)} & t_{ab(bb)} \\ t_{ab(aa)} & t_{ab(aa)} & -h+U_a & K_{ab} \\ t_{ab(bb)} & t_{ab(bb)} & K_{ab} & h+U_b \end{pmatrix} \quad (1.23)$$

Here, the matrix elements are similar to those of the symmetric case in Eq. (1.3). On the other hand, some additional and modified physical parameters are introduced to describe the asymmetric two-site system. For example, $h$ represents the

one-electron core Hamiltonian difference, $h \equiv h_{bb} - h_{aa}$, where $h_{pp} \equiv \langle p|h(1)|p\rangle = \langle \bar{p}|h(1)|\bar{p}\rangle \le 0$ and $h \ge 0$ ($h_{aa} \le h_{bb}$). Since the transfer integrals include the two-electron integral between the neutral and ionic determinants, there are two types of transfer integrals, e.g. $t_{ab(aa)} \equiv \langle a\bar{b}|\hat{H}|a\bar{a}\rangle$ and $t_{ab(bb)} \equiv \langle a\bar{b}|\hat{H}|b\bar{b}\rangle$, which are different since $(ab|aa) \neq (ab|bb)$. Thus, the average transfer integral, $t_{ab} \equiv (t_{ab(aa)} + t_{ab(bb)})/2$, is introduced. Since $U_a$ and $U_b$ represent effective Coulomb repulsions, $U_a \equiv U_{aa} - U_{ab}$ and $U_b \equiv U_{bb} - U_{ab}$, we define the average effective Coulomb repulsion $U[\equiv(U_a + U_b)/2]$ [18]. Similar to the symmetric diradical system in Section 1.2.2, the following dimensionless quantities are introduced [18],

$$\frac{|t_{ab}|}{U} \equiv r_t (\ge 0), \ \frac{2K_{ab}}{U} \equiv r_K (\ge 0), \ \frac{h}{U} \equiv r_h (\ge 0), \ \frac{U_a}{U_b} \equiv r_U (\ge 0),$$

$$\text{and } \frac{|t_{ab(aa)}|}{|t_{ab(bb)}|} \equiv r_{tab} (\ge 0). \tag{1.24}$$

We here introduce a parameter,

$$y_S = 1 - \frac{4r_t}{\sqrt{1+(4r_t)^2}}, \tag{1.25}$$

which indicates the diradical character before introducing the asymmetry, i.e. $(r_h, r_U, r_{tab}) = (0, 1, 1)$ [18]. Note here that this is not the diradical character for the asymmetric two-site model (referred to as $y_A$) and is referred to as "pseudo diradical character". The diradical character of the asymmetric two-site model is represented by $y_A$, which is a function of $(r_t, r_K, r_h, r_U, r_{tab})$. For simplicity, we consider the case that the asymmetry is caused by changing $r_h$ between 0 and 2 with keeping $(r_U, r_{tab}) = (1, 1)$, which means that the asymmetry is governed by the difference of ionization potentials of the constitutive atoms A and B. The dimensionless Hamiltonian matrix, $\boldsymbol{H}_{DL}(\equiv \boldsymbol{H}/U)$, in the case of $(r_U, r_{tab}) = (1, 1)$ is expressed by [18]

$$\mathbf{H}_{DL} = \begin{pmatrix} 0 & r_k/2 & -r_t & -r_t \\ r_k/2 & 0 & -r_t & -r_t \\ -r_t & -r_t & 1-r_h & r_k/2 \\ -r_t & -r_t & r_k/2 & 1+r_h \end{pmatrix}. \tag{1.26}$$

In this case, the eigenvalues and eigenvectors of $\boldsymbol{H}_{DL}$ are found to depend on the dimensionless quantities $(r_t, r_K, r_h)$, i.e. $(y_S, r_K, r_h)$. By

diagonalizing $\boldsymbol{H}_{\mathrm{DL}}$, the eigenvectors for state $\{j\} = \{\mathrm{T}, \mathrm{g}, \mathrm{k}, \mathrm{f}\}$ (T: triplet state, and g, k, f: singlet states) are obtained as

$$|j\rangle = C_{a\bar{b},j}|a\bar{b}\rangle + C_{b\bar{a},j}|b\bar{a}\rangle + C_{a\bar{a},j}|a\bar{a}\rangle + C_{b\bar{b},j}|b\bar{b}\rangle . \tag{1.27}$$

It is also noted that $C_{a\bar{b},j} = C_{b\bar{a},j}$ and $|C_{a\bar{a},j}| \neq |C_{b\bar{b},j}|$ for the asymmetric singlet states, while $C_{a\bar{b},\mathrm{T}} = -C_{b\bar{a},\mathrm{T}} = 1/\sqrt{2}$ or $-1/\sqrt{2}$, and $C_{a\bar{a},\mathrm{T}} = C_{b\bar{b},\mathrm{T}} = 0$ for the triplet state. Using the MOs ($g$ and $u$) (Eq. (1.1)), an alternative basis set $\{|\mathrm{G}\rangle, |\mathrm{S}\rangle, |\mathrm{D}\rangle\} = \{|g\bar{g}\rangle, (|g\bar{u}\rangle + |u\bar{g}\rangle)/\sqrt{2}, |u\bar{u}\rangle\}$ is constructed for the singlet states. Using this basis set, the singlet ground state is expressed as

$$|\mathrm{g}\rangle = \xi|\mathrm{G}\rangle + \eta|\mathrm{S}\rangle - \zeta|\mathrm{D}\rangle , \tag{1.28}$$

where the normalization condition, $\xi^2 + \eta^2 + \zeta^2 = 1$, is satisfied. From the comparison of Eqs. (1.27) and (1.28), we obtain

$$\xi = C_{a\bar{b},\mathrm{g}} + \frac{1}{2}(C_{a\bar{a},\mathrm{g}} + C_{b\bar{b},\mathrm{g}}) , \ \eta = \frac{1}{\sqrt{2}}(C_{a\bar{a},\mathrm{g}} - C_{b\bar{b},\mathrm{g}}) ,$$

$$\text{and } \zeta = C_{a\bar{b},\mathrm{g}} - \frac{1}{2}(C_{a\bar{a},\mathrm{g}} + C_{b\bar{b},\mathrm{g}}) \tag{1.29}$$

Let us consider the diradical character $y_{\mathrm{A}}$ of the two-site asymmetric model, which is defined as the occupation number ($n_{\mathrm{LUNO}}$) of the LUNO of the singlet ground state $|\mathrm{g}\rangle$. The diradical character $y_{\mathrm{A}}$ is expressed as

$$\begin{aligned} y_{\mathrm{A}} \equiv n_{\mathrm{LUNO}} &= 1 - |\xi - \zeta|\sqrt{2 - (\xi - \zeta)^2} \\ &= 1 - |C_{a\bar{a},\mathrm{g}} + C_{b\bar{b},\mathrm{g}}|\sqrt{2 - (C_{a\bar{a},\mathrm{g}} + C_{b\bar{b},\mathrm{g}})^2} \end{aligned} \tag{1.30}$$

which becomes the usual definition of $y$ for symmetric systems (Eq. (1.9)):

$$y_{\mathrm{A}} = y_{\mathrm{S}} = 2\zeta^2. \tag{1.31}$$

Figure 1.7 shows the $y_{\mathrm{S}}$ and $y_{\mathrm{A}}$ relationship, which indicates that $y_{\mathrm{A}}$ is smaller than $y_{\mathrm{S}}$; in particular for $y_{\mathrm{S}} \sim 0.5$, the asymmetry $r_h$ is increasing. As seen from Figure 1.7a, if $y_{\mathrm{S}} = 1$ then $y_{\mathrm{A}} = 1$ for $r_h < 1$, but $y_{\mathrm{A}} = 0$ for $r_h > 1$, while $y_{\mathrm{A}}$ is close to $\sim 0.134$ for $r_h = 1$ ($r_K = 0$). This behavior corresponds to the exchange of the dominant configurations (neutral/ionic) in state g, i.e. $P_{\mathrm{N}} = |C_{a\bar{b},\mathrm{g}}|^2 + |C_{b\bar{a},\mathrm{g}}|^2$ and $P_{\mathrm{I}} = |C_{a\bar{a},\mathrm{g}}|^2 + |C_{b\bar{b},\mathrm{g}}|^2$, between $r_h < 1$ and $r_h > 1$ for $y_{\mathrm{S}} > 0$ and $r_K = 0$ (Figure 1.8a).

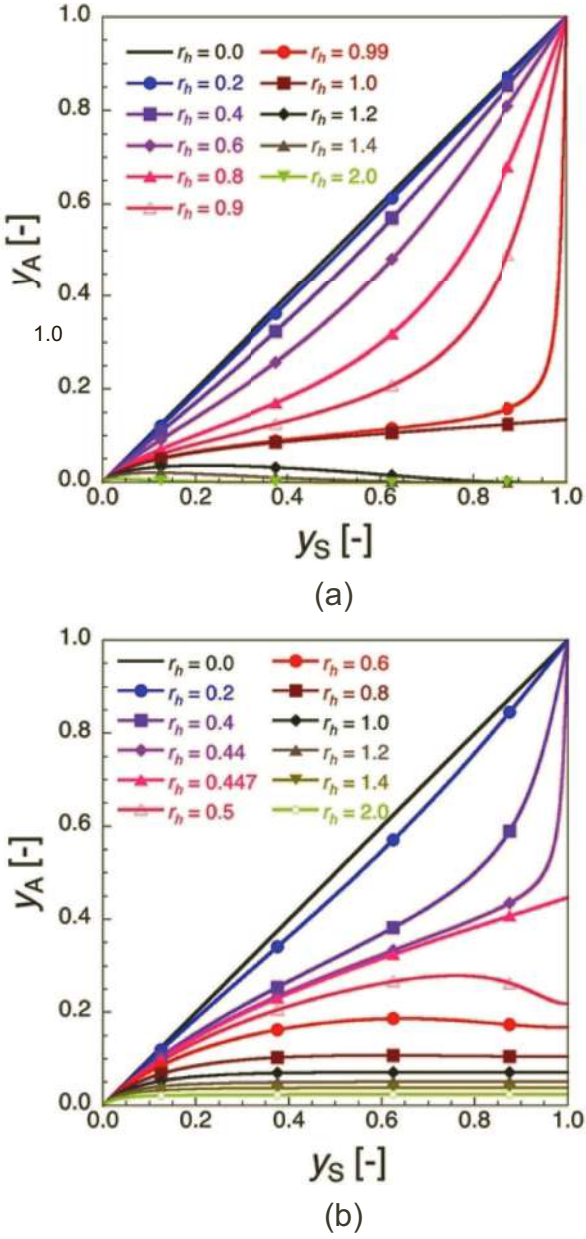


**Figure 1.7** $y_S$ versus $y_A$ plots with $r_h$ = 0.0 – 2.0 for $r_K$ = 0.0 (a) and 0.8 (b). Reprinted with permission from Ref. [19]. Copyright @ 2016 American Chemical Society.

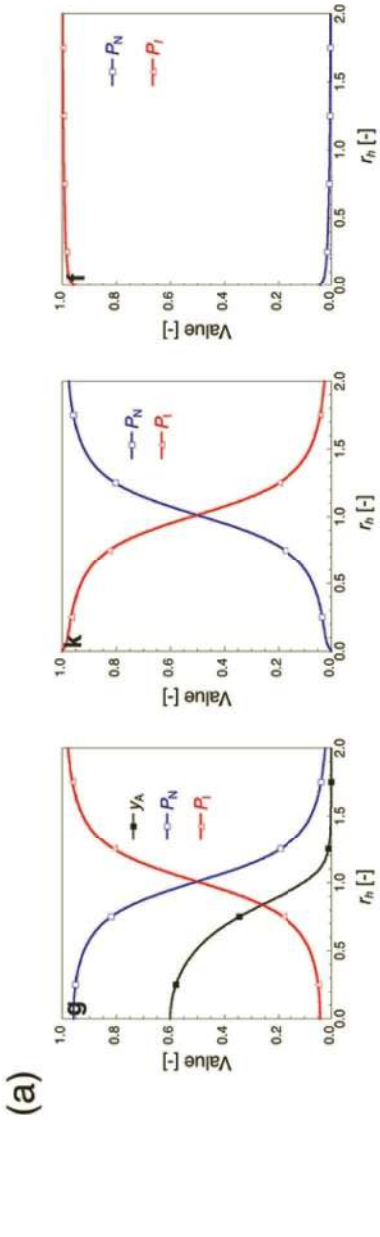


**Figure 1.8** $r_h$ dependences of $P_N$ and $P_I$ for states g, k, and f at $y_S = 0.6$ for $r_K = 0.0$ (a), and 0.8 (b). The variations in $y_A$ for state g are also shown. Reprinted with permission from Ref. [19]. Copyright @ 2016 American Chemical Society.

### 1.2.4 Diradical Character Dependences of Excitation Energies and Properties of Asymmetric Diradicaloids by VCI Model

Figure 1.8 shows asymmetry ($r_h$) dependences of $P_N$ and $P_I$ for states g, k, and f at $y_S$ = 0.6 for $r_K$ = 0 (a) and 0.8 (b). The asymmetry $r_h$ is found to cause the exchange between the dominant configurations (neutral/ionic) in each state and the variation in the diradical character $y_A$. In order to reveal the feature of $r_K$ effect, we investigate the analytical expressions of energies and wavefunctions of each state {g, k, f} in the case of ($y_S$, $r_U$, $r_{tab}$) = (1, 1, 1) ($r_h$ > 0), which are classified in the following three regions based on the amplitude relationship between $r_h^2$ and 1 – $r_K$ [19].

For $r_h^2 < 1 - r_K$ ,

$$|\mathrm{g}\rangle = \frac{1}{\sqrt{2}}|G\rangle - \frac{1}{\sqrt{2}}|D\rangle = \frac{1}{\sqrt{2}}|a\bar{b}\rangle + \frac{1}{\sqrt{2}}|b\bar{a}\rangle \text{ with } E_g = \frac{r_K}{2} \ (y_A = 1) \tag{1.32a}$$

$$|\mathrm{k}\rangle = \frac{1}{\sqrt{2(1+A^2)}}\left(|G\rangle + \sqrt{2}A|S\rangle + |D\rangle\right)$$
$$= \frac{1}{\sqrt{2(1+A^2)}}\left\{(1+A)|a\bar{a}\rangle + (1-A)|b\bar{b}\rangle\right\}$$

with
$$E_k = 1 - \sqrt{r_h^2 + \left(\frac{r_K}{2}\right)^2} \tag{1.32b}$$

$$|\mathrm{f}\rangle = \frac{1}{\sqrt{2(1+B^2)}}\left(|G\rangle + \sqrt{2}B|S\rangle + |D\rangle\right)$$
$$= \frac{1}{\sqrt{2(1+B^2)}}\left\{(1+B)|a\bar{a}\rangle + (1-B)|b\bar{b}\rangle\right\}$$

with
$$E_f = 1 + \sqrt{r_h^2 + \left(\frac{r_K}{2}\right)^2} \tag{1.32c}$$

For
$$r_h^2 = 1 - r_K ,$$

$$E_g = E_k = \frac{r_K}{2},\ E_f = 2 - \frac{r_K}{2} \tag{1.32d}$$

For $r_h^2 > 1 - r_K$,

$$|g\rangle = \frac{1}{\sqrt{2(1+A^2)}}\left(|G\rangle + \sqrt{2}A|S\rangle + |D\rangle\right)$$
$$= \frac{1}{\sqrt{2(1+A^2)}}\left\{(1+A)|a\bar{a}\rangle + (1-A)|b\bar{b}\rangle\right\}$$

with $E_g = 1 - \sqrt{r_h^2 + \left(\frac{r_K}{2}\right)^2}$ $\left(y_A = 1 - \frac{2A}{1+A^2}\right)$ (1.32e)

$$|k\rangle = \frac{1}{\sqrt{2}}|G\rangle - \frac{1}{\sqrt{2}}|D\rangle = \frac{1}{\sqrt{2}}|a\bar{b}\rangle + \frac{1}{\sqrt{2}}|b\bar{a}\rangle \text{ with } E_k = \frac{r_K}{2} \tag{1.32f}$$

$$|f\rangle = \frac{1}{\sqrt{2(1+B^2)}}\left(|G\rangle + \sqrt{2}B|S\rangle + |D\rangle\right)$$
$$= \frac{1}{\sqrt{2(1+B^2)}}\left\{(1+B)|a\bar{a}\rangle + (1-B)|b\bar{b}\rangle\right\}$$

with $E_f = 1 + \sqrt{r_h^2 + \left(\frac{r_K}{2}\right)^2}$ (1.32g)

Here,

$$A \equiv \frac{r_K + \sqrt{4r_h^2 + r_K^2}}{2r_h}\ (>0) \text{ and } B \equiv \frac{r_K - \sqrt{4r_h^2 + r_K^2}}{2r_h}\ (<0) \tag{1.32h}$$

For $r_h^2 < 1 - r_K$, states g and k are pure neutral (diradical) and ionic, while for $r_h^2 > 1 - r_K$, they are pure ionic and neutral (diradical), respectively. For $y_S$ = 1, the diradical character $y_A$ is abruptly reduced from 1 to $1 - 2A/(1+A^2)$ when changing from $r_h^2 < 1 - r_K$ to $r_h^2 > 1 - r_K$. In the case of $r_h^2 = 1 - r_K$ at $y_S \to 1$ (where $E_g = E_k$), $y_A$ asymptotically approaches $1 - \sqrt{1+2A^2}/(1+A^2)$ since the

neutral (Eq. (1.32a)) and ionic (Eq. (1.32e)) components contribute to the wavefunction equivalently. At the same $r_h$ value, $y_A$ is shown to decrease in the intermediate $y_S$ region with increasing $r_K$ up to $1-r_h^2$ ($\geq 0$), while further increase of $r_K$ is found to increase $y_A$ again as seen from Eqs. (1.32e) and (1.32h). The increase in $r_K$ operates similarly to asymmetry $r_h$ for $r_h^2 < 1-r_K$. This is also exemplified by the decrease of critical $r_h$ value ($r_{h\,c}$), at which the exchange of the dominant configurations (neutral/ionic) in states g and k occurs, with increasing $r_K$ until $1-r_{h\,c}^2$ ($\geq 0$) (Eq. (1.32d)), which is shown in $r_K$ dependences of $P_N$ and $P_I$ for g and k states (Figure 1.8).

Figure 1.9 shows the $r_h$ dependences of the dimensionless excitation energies and transition properties (for a fixed $y_S = 0.6$) for $r_K = 0.0$ and 0.8. It is found that $\Delta E_{kg}$ and $\Delta E_{fg}$ decrease and increase, respectively, with increasing $r_K$ for $r_h^2 < 1-r_K$, while that they increase with increasing $r_K$ for $r_h^2 > 1-r_K$. The increase of $r_K$ is found to move the behaviors around $r_h = 1.0$ of the excitation energies and transition moments to the lower $r_h$ region, due to the displacement of the critical point $r_{h\,c}$ as shown in Figure 1.8. Also, the increase of $r_K$ is shown to decrease $\Delta E_{kg}$ and $|\Delta\mu_{ii}|$ ($i$ = k, f), but increase $|\mu_{kf}|$ before $\sim r_{h\,c}$ as predicted from the analytical expressions of excitation energies and wavefunctions for $y_S = 1$ (Eqs. (1.32a–c)). Indeed, the asymmetric distributions represented by the relative contributions of $|a\bar{a}\rangle$ and $|b\bar{b}\rangle$ are shown to decrease with increasing $r_K$ at the same $r_h$, e.g. $|a\bar{a}\rangle : |b\bar{b}\rangle = 1 : 0$ for $r_K = 0$ vs. 1 + A : 1 – A for $r_K \neq 0$ (see Eqs. (1.32a–c), the feature of which decreases $|\Delta\mu_{ii}|$ ($i$ = k, f) and increases $|\mu_{kf}|$.

It is found for the ground-state singlet–triplet energy gap, $\Delta E_{gT}$($\equiv E_g - E_T$) (Figure 1.10), that (i) the increase of $y_S$ causes the decrease of $\Delta E_{gT}$ for $r_K = 0$, (ii) the increase in $r_K$ stabilizes the triplet state, and (iii) for a given $y_S$, the increase of $r_h$ leads to the increase of the $r_K$ giving a triplet ground state. As seen from Figure 1.10, the singlet ground state (antiferromagnetic) region is broad in small $y_S$ region and further broadens to larger $y_S$ values with increasing $r_h$. For $r_h > 1$, the singlet ground state region is found to be widely extended over the whole $y_S$–$r_K$ region.

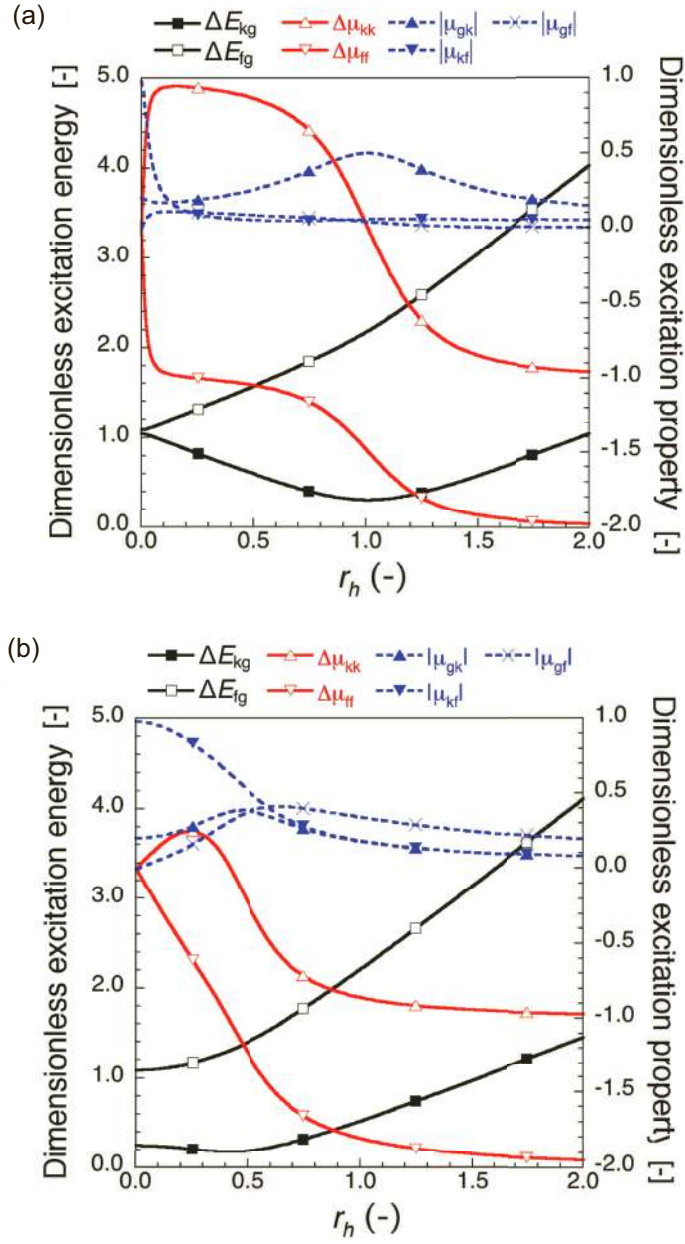


**Figure 1.9** $r_h$ dependences of the dimensionless excitation energies ($\Delta E_{ij}$), dimensionless dipole moment differences ($\Delta\mu_{ii}$) and dimensionless transition moment amplitudes ($|\mu_{ij}|$) at $y_S = 0.6$ for $r_K = 0.0$ (a) and 0.8 (b). Reprinted with permission from Ref. [19]. Copyright @ 2016 American Chemical Society.

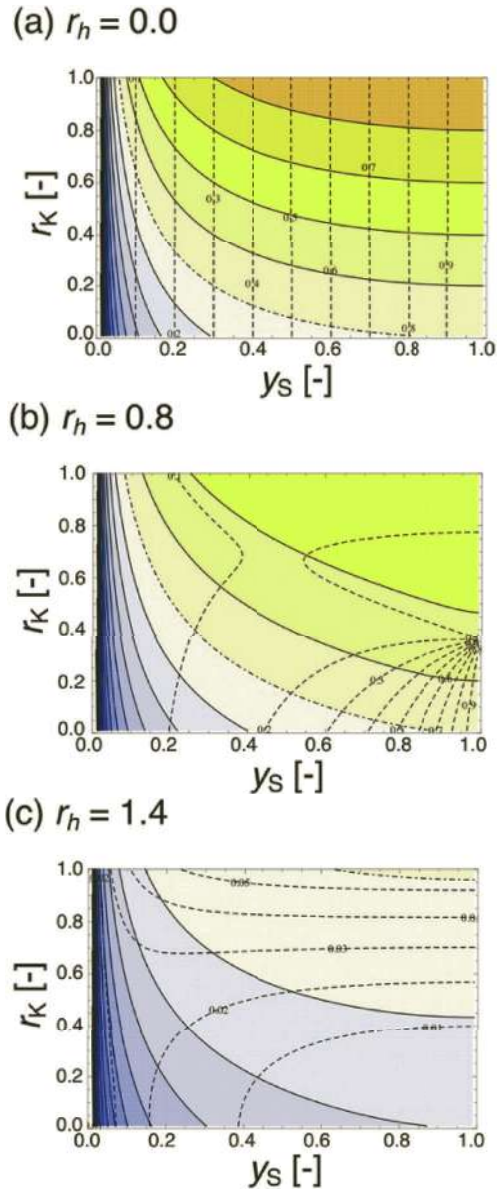


**Figure 1.10** Dimensionless $\Delta E_{gT}$ contours on the $y_S$-$r_K$ plane for $r_h$ = 0.0 (a), 0.8 (b), and 1.4 (c). The variation from cold to warm color indicates that from negative to positive $\Delta E_{gT}$ values. The black solid line $\Delta E_{gT}$ contours range from −3.0 to 3.0 with division 0.2 and 0.0 contour is shown by a black dashed-dotted line. The black dashed lines represent the iso-$y_A$ lines. Reprinted with permission from Ref. [19]. Copyright @ 2016 American Chemical Society.

### 1.2.5 Novel Definition of Diradical and Ionic Characters

As mentioned in previous sections, the diradical character has a chemical concept of "instability of chemical bonds" [12] proposed by Yamaguchi, and it is easily estimated by an approximate spin-projected UHF method [6]. The spatial contribution of diradical character can be understood by the odd (unpaired) electron density with the number of odd (unpaired) electrons, which were presented by Takatsuka et al. [20] and Head-Gordon [21]. The diradical characters have been employed to describe the electronic structures of a broad range of open-shell singlet systems, e.g. polycyclic aromatic hydrocarbons, including diphenalenyl compounds [22–25], transition-metal–metal bonded systems [26, 27], heavy main group compounds [28], and pancake bonded systems [29, 30]. Although these theoretical expressions are useful for description of radical and diradical characters in open-shell systems, their applicability is limited to open-shell singlet systems with a dominating covalent (neutral) component rather than an ionic one. Indeed, there are arbitrary electronic states, including excited states displaying large ionic components. We thus propose a novel definition of the ionic as well as of the diradical character, both of which can be straightforwardly connected to each other [31]. In this new definition, diradical and ionic characters with their densities are derived on the basis of a two-site model with two electrons in two active orbitals. The present indices are also related to the effective neutral and ionic chemical bond orders, and they describe the degree of electron correlation for arbitrary electronic states, including ground and excited states, and thus for any superposition of electronic states. These indices will not only provide a useful tool for describing the effective chemical bond nature and the electron correlation, but they will also contribute to constructing structure-property relationships for diradical/ionic-component dominant systems.

#### 1.2.5.1 Diradical and ionic characters and their densities for arbitrary states within the two-site model

An arbitrary state $j$ (Eq. (1.27)) is rewritten as

$$\left|\Psi_j\right\rangle = \sqrt{P_{\mathrm{N},j}}\left|\mathrm{N}_j\right\rangle + \sqrt{P_{\mathrm{I},j}}\left|\mathrm{I}_j\right\rangle = \left|\Psi_{\mathrm{N},j}\right\rangle + \left|\Psi_{\mathrm{I},j}\right\rangle, \qquad (1.33)$$

where the neutral (covalent or diradical) ($P_{\mathrm{N},j}$) and ionic ($P_{\mathrm{I},j}$) populations are defined as

$$P_{\mathrm{N},j} = \left|C_{a\bar{b},j}\right|^2 + \left|C_{b\bar{a},j}\right|^2, \text{ and } P_{\mathrm{I},j} = \left|C_{a\bar{a},j}\right|^2 + \left|C_{b\bar{b},j}\right|^2, \qquad (1.34)$$

and the orthonormalized neutral and ionic states are described, respectively, by

$$\left|\mathrm{N}_j\right\rangle = \frac{1}{\sqrt{P_{\mathrm{N},j}}}\left(C_{a\bar{b},j}\left|a\bar{b}\right\rangle + C_{b\bar{a},j}\left|b\bar{a}\right\rangle\right),$$

and

$$\left|\mathrm{I}_j\right\rangle = \frac{1}{\sqrt{P_{\mathrm{I},j}}}\left(C_{a\bar{a},j}\left|a\bar{a}\right\rangle + C_{b\bar{b},j}\left|b\bar{b}\right\rangle\right). \qquad (1.35)$$

The neutral two-electron density is defined using the neutral two-electron density operator $\hat{\rho}_{\mathrm{N},j}\left(\equiv\left|\Psi_{\mathrm{N},j}\right\rangle\left\langle\Psi_{\mathrm{N},j}\right|\right)$:

$$\begin{aligned}\rho_{\mathrm{N},j}(\mathbf{r}_1,\mathbf{r}_2;\mathbf{r}_1,\mathbf{r}_2) &= \left\langle\mathbf{r}_1,\mathbf{r}_2\right|\hat{\rho}_{\mathrm{N},j}\left|\mathbf{r}_1,\mathbf{r}_2\right\rangle = \Psi_{\mathrm{N},j}(\mathbf{r}_1,\mathbf{r}_2)\Psi^*_{\mathrm{N},j}(\mathbf{r}_1,\mathbf{r}_2)\\ &= P_{\mathrm{N},j}\left\langle\mathbf{r}_1,\mathbf{r}_2\right|\left|\mathrm{N}_j\right\rangle\left\langle\mathrm{N}_j\right|\left|\mathbf{r}_1,\mathbf{r}_2\right\rangle\\ &= \left\langle\mathbf{r}_1,\mathbf{r}_2\right|\left(C_{a\bar{b},j}\left|a\bar{b}\right\rangle + C_{b\bar{a},j}\left|b\bar{a}\right\rangle\right)\\ &\quad\left(C_{a\bar{b},j}\left|a\bar{b}\right\rangle + C_{b\bar{a},j}\left|b\bar{a}\right\rangle\right)^*\left|\mathbf{r}_1,\mathbf{r}_2\right\rangle, \end{aligned} \qquad (1.36)$$

where Eqs. (1.33) and (1.35) are used. Similarly, the ionic two-electron density is represented using the ionic two-electron density operator $\hat{\rho}_{\mathrm{I},j}\left(\equiv\left|\Psi_{\mathrm{I},j}\right\rangle\left\langle\Psi_{\mathrm{I},j}\right|\right)$, as

$$\begin{aligned}\rho_{\mathrm{I},j}(\mathbf{r}_1,\mathbf{r}_2;\mathbf{r}_1,\mathbf{r}_2) &= \left\langle\mathbf{r}_1,\mathbf{r}_2\right|\hat{\rho}_{\mathrm{I},j}\left|\mathbf{r}_1,\mathbf{r}_2\right\rangle = \Psi_{\mathrm{I},j}(\mathbf{r}_1,\mathbf{r}_2)\Psi^*_{\mathrm{I},j}(\mathbf{r}_1,\mathbf{r}_2)\\ &= P_{\mathrm{I},j}\left\langle\mathbf{r}_1,\mathbf{r}_2\right|\left|\mathrm{I}_j\right\rangle\left\langle\mathrm{I}_j\right|\left|\mathbf{r}_1,\mathbf{r}_2\right\rangle\\ &= \left\langle\mathbf{r}_1,\mathbf{r}_2\right|\left(C_{a\bar{a},j}\left|a\bar{a}\right\rangle + C_{b\bar{b},j}\left|b\bar{b}\right\rangle\right)\\ &\quad\left(C_{a\bar{a},j}\left|a\bar{a}\right\rangle + C_{b\bar{b},j}\left|b\bar{b}\right\rangle\right)^*\left|\mathbf{r}_1,\mathbf{r}_2\right\rangle. \end{aligned} \qquad (1.37)$$

Here, $\rho_j(\mathbf{r}_1,\mathbf{r}_2;\mathbf{r}_1,\mathbf{r}_2) \neq \rho_{\mathrm{N},j}(\mathbf{r}_1,\mathbf{r}_2;\mathbf{r}_1,\mathbf{r}_2) + \rho_{\mathrm{I},j}(\mathbf{r}_1,\mathbf{r}_2;\mathbf{r}_1,\mathbf{r}_2)$ in general because the total two-electron density operator is defined as $\hat{\rho}_j \equiv \left(\left|\Psi_{\mathrm{N},j}\right\rangle + \left|\Psi_{\mathrm{I},j}\right\rangle\right)\left(\left\langle\Psi_{\mathrm{N},j}\right| + \left\langle\Psi_{\mathrm{I},j}\right|\right) \neq \hat{\rho}_{\mathrm{N},j} + \hat{\rho}_{\mathrm{I},j}$.

Next, the neutral and ionic one-electron densities of state *j* are represented as

$$\begin{aligned}\rho_{\mathrm{N},j}(\mathbf{r}_1;\mathbf{r}_1) &= \int d\mathbf{r}_2 \rho_{\mathrm{N},j}(\mathbf{r}_1,\mathbf{r}_2;\mathbf{r}_1,\mathbf{r}_2) \\ &= \int d\mathbf{r}_2 \left\{ \left|C_{a\bar{b},j}\right|^2 \rho_{a\bar{b},a\bar{b}}(\mathbf{r}_1,\mathbf{r}_2;\mathbf{r}_1,\mathbf{r}_2) + \left|C_{b\bar{a},j}\right|^2 \rho_{b\bar{a},b\bar{a}}(\mathbf{r}_1,\mathbf{r}_2;\mathbf{r}_1,\mathbf{r}_2) \right. \\ &\left. + C_{a\bar{b},j} C^*_{b\bar{a},j} \rho_{a\bar{b},b\bar{a}}(\mathbf{r}_1,\mathbf{r}_2;\mathbf{r}_1,\mathbf{r}_2) + C_{b\bar{a},j} C^*_{a\bar{b},j} \rho_{b\bar{a},a\bar{b}}(\mathbf{r}_1,\mathbf{r}_2;\mathbf{r}_1,\mathbf{r}_2) \right\} \\ &= \left|C_{a\bar{b},j}\right|^2 \rho_{a\bar{b},a\bar{b}}(\mathbf{r}_1;\mathbf{r}_1) + \left|C_{b\bar{a},j}\right|^2 \rho_{b\bar{a},b\bar{a}}(\mathbf{r}_1;\mathbf{r}_1), \end{aligned} \tag{1.38}$$

and

$$\begin{aligned}\rho_{\mathrm{I},j}(\mathbf{r}_1;\mathbf{r}_1) &= \int d\mathbf{r}_2 \rho_{\mathrm{I},j}(\mathbf{r}_1,\mathbf{r}_2;\mathbf{r}_1,\mathbf{r}_2) \\ &= \int d\mathbf{r}_2 \left\{ \left|C_{a\bar{a},j}\right|^2 \rho_{a\bar{a},a\bar{a}}(\mathbf{r}_1,\mathbf{r}_2;\mathbf{r}_1,\mathbf{r}_2) + \left|C_{b\bar{b},j}\right|^2 \rho_{b\bar{b},b\bar{b}}(\mathbf{r}_1,\mathbf{r}_2;\mathbf{r}_1,\mathbf{r}_2) \right. \\ &\left. + C_{a\bar{a},j} C^*_{b\bar{b},j} \rho_{a\bar{a},b\bar{b}}(\mathbf{r}_1,\mathbf{r}_2;\mathbf{r}_1,\mathbf{r}_2) + C_{b\bar{b},j} C^*_{a\bar{a},j} \rho_{b\bar{b},a\bar{a}}(\mathbf{r}_1,\mathbf{r}_2;\mathbf{r}_1,\mathbf{r}_2) \right\} \\ &= \left|C_{a\bar{a},j}\right|^2 \rho_{a\bar{a},a\bar{a}}(\mathbf{r}_1;\mathbf{r}_1) + \left|C_{b\bar{b},j}\right|^2 \rho_{b\bar{b},b\bar{b}}(\mathbf{r}_1;\mathbf{r}_1). \end{aligned} \tag{1.39}$$

In these transformations, the one-electron reduced densities are expressed from the corresponding two-electron ones in the LNO basis representation, e.g.

$$\rho_{a\bar{b},a\bar{b}}(\mathbf{r}_1;\mathbf{r}_1) = \int d\mathbf{r}_2 \left\langle \mathbf{r}_1,\mathbf{r}_2 \middle| a\bar{b} \right\rangle \left\langle a\bar{b} \middle| \mathbf{r}_1,\mathbf{r}_2 \right\rangle = \int d\mathbf{r}_2 \rho_{a\bar{b},a\bar{b}}(\mathbf{r}_1,\mathbf{r}_2;\mathbf{r}_1,\mathbf{r}_2). \tag{1.40}$$

These one-electron reduced densities satisfy the following relations, due to the orthonormalization condition of LNOs.

$$\int d\mathbf{r}_1 \rho_{a\bar{b},a\bar{b}}(\mathbf{r}_1;\mathbf{r}_1) = \int d\mathbf{r}_1 d\mathbf{r}_2 \left\langle \mathbf{r}_1,\mathbf{r}_2 \middle| a\bar{b} \right\rangle \left\langle a\bar{b} \middle| \mathbf{r}_1,\mathbf{r}_2 \right\rangle = \left\langle a\bar{b} \middle| a\bar{b} \right\rangle = 1. \tag{1.41}$$

Similar relationships are also satisfied for other one-electron reduced densities. Using these relationships, integrals of the neutral and ionic one-electron reduced densities provide the neutral and ionic populations, respectively:

$$\int d\mathbf{r}_1 \rho_{\mathrm{N},j}(\mathbf{r}_1;\mathbf{r}_1) = \left|C_{a\bar{b},j}\right|^2 + \left|C_{b\bar{a},j}\right|^2 = P_{\mathrm{N},j},$$

and $$\int d\mathbf{r}_1 \rho_{\mathrm{I},j}(\mathbf{r}_1;\mathbf{r}_1) = \left|C_{a\bar{a},j}\right|^2 + \left|C_{b\bar{b},j}\right|^2 = P_{\mathrm{I},j}. \tag{1.42}$$

The neutral and ionic characters of the wavefunction of state *j* are then defined as the deviations from the neutral/ionic components in the non-correlated, e.g. Hartree–Fock, ground state of a symmetric system. In the non-correlated limit, the two-electron densities are given by

$$\begin{aligned}\rho_{\mathrm{N\,nc}}(\mathbf{r}_1,\mathbf{r}_2;\mathbf{r}_1,\mathbf{r}_2) &= P_{\mathrm{N\,nc}}\langle \mathbf{r}_1,\mathbf{r}_2|\mathrm{N_{nc}}\rangle\langle \mathrm{N_{nc}}|\mathbf{r}_1,\mathbf{r}_2\rangle \\ &= \frac{1}{2}\langle \mathbf{r}_1,\mathbf{r}_2|\mathrm{N_{nc}}\rangle\langle \mathrm{N_{nc}}|\mathbf{r}_1,\mathbf{r}_2\rangle,\end{aligned} \tag{1.43a}$$

and

$$\rho_{\mathrm{I\,nc}}(\mathbf{r}_1,\mathbf{r}_2;\mathbf{r}_1,\mathbf{r}_2) = P_{\mathrm{I\,nc}}\langle \mathbf{r}_1,\mathbf{r}_2|\mathrm{I_{nc}}\rangle\langle \mathrm{I_{nc}}|\mathbf{r}_1,\mathbf{r}_2\rangle = \frac{1}{2}\langle \mathbf{r}_1,\mathbf{r}_2|\mathrm{I_{nc}}\rangle\langle \mathrm{I_{nc}}|\mathbf{r}_1,\mathbf{r}_2\rangle, \tag{1.43b}$$

where

$$|\mathrm{N_{nc}}\rangle = \frac{1}{\sqrt{2}}\left(|a\bar{b}\rangle + |b\bar{a}\rangle\right), \text{ and } |\mathrm{I_{nc}}\rangle = \frac{1}{\sqrt{2}}\left(|a\bar{a}\rangle + |b\bar{b}\rangle\right). \tag{1.44}$$

The corresponding one-electron reduced densities are expressed by

$$\rho_{\mathrm{N\,nc}}(\mathbf{r}_1;\mathbf{r}_1) = \int d\mathbf{r}_2 \frac{1}{2}\langle \mathbf{r}_1,\mathbf{r}_2|\mathrm{N_{nc}}\rangle\langle \mathrm{N_{nc}}|\mathbf{r}_1,\mathbf{r}_2\rangle, \tag{1.45a}$$

and

$$\rho_{\mathrm{I\,nc}}(\mathbf{r}_1;\mathbf{r}_1) = \int d\mathbf{r}_2 \frac{1}{2}\langle \mathbf{r}_1,\mathbf{r}_2|\mathrm{I_{nc}}\rangle\langle \mathrm{I_{nc}}|\mathbf{r}_1,\mathbf{r}_2\rangle, \tag{1.45b}$$

which satisfy the relationships:

$$\int d\mathbf{r}_1 \rho_{\mathrm{N\,nc}}(\mathbf{r}_1;\mathbf{r}_1) = \frac{1}{2}\langle \mathrm{N_{nc}}|\mathrm{N_{nc}}\rangle = \frac{1}{2},$$

and $$\int d\mathbf{r}_1 \rho_{\mathrm{I\,nc}}(\mathbf{r}_1;\mathbf{r}_1) = \frac{1}{2}\langle \mathrm{I_{nc}}|\mathrm{I_{nc}}\rangle = \frac{1}{2}. \tag{1.46}$$

This indicates that the non-correlated ground-state wavefunction is composed of neutral and ionic components with equal weight. Thus, the degrees of neutral and ionic characters, which correspond to a weight of electron correlation, can be quantified by using the population deviations from the non-correlated populations (1/2).

Based on these quantities, new diradical and ionic characters as well as their densities are defined (referred to as "Nakano's definition"). For, $P_{N,j} \geq P_{I,j}$ (where $P_{N,j} + P_{I,j} = 1$ and thus $1 \geq P_{N,j} \geq 1/2$), the new diradical character $y^{N,j}$ of state $j$ is expressed by [31]

$$y^{N,j} = \int d\mathbf{r}_1 \rho_{y^{N,j}}(\mathbf{r}_1;\mathbf{r}_1) = 2P_{N,j} - 1 , \tag{1.47}$$

and the diradical character density is defined as

$$\rho_{y^{N,j}}(\mathbf{r}_1;\mathbf{r}_1) \equiv 2\left[\rho_{N,j}(\mathbf{r}_1;\mathbf{r}_1) - \rho_{N\,nc}(\mathbf{r}_1;\mathbf{r}_1)\right]. \tag{1.48}$$

From this definition, $y^{N,j}$ takes a value between 0 and 1, where $y^{N,j} = 0$ implies the non-correlated state (composed of equal-weighted neutral and ionic components), while $y^{N,j} = 1$ corresponds to a pure diradical state. On the other hand, for $P_{I,j} \geq P_{N,j}$ (where $P_{N,j} + P_{I,j} = 1$ and thus $1 \geq P_{I,j} \geq 1/2$), the ionic character of state $j$ is expressed as [31]

$$y^{I,j} = \int d\mathbf{r}_1 \rho_{y^{I,j}}(\mathbf{r}_1;\mathbf{r}_1) = 1 - 2P_{I,j} , \tag{1.49}$$

and the ionic character density is defined as

$$\rho_{y^{I,j}}(\mathbf{r}_1,\mathbf{r}_1) \equiv 2\left[\rho_{I\,nc}(\mathbf{r}_1;\mathbf{r}_1) - \rho_{I,j}(\mathbf{r}_1;\mathbf{r}_1)\right]. \tag{1.50}$$

Here, $y^{I,j}$ takes a value between 0 and −1, where $y^{I,j} = 0$ indicates the non-correlated limit (composed of equal-weighted neutral and ionic components) and $y^{I,j} = -1$ indicates the pure ionic limit. Thus, the "diradical character density" $\rho_{y^{N,j}}(\mathbf{r}_1;\mathbf{r}_1)$ of state $j$ describes the deviation of the neutral density in the diradical system ($P_{N,j} \geq P_{I,j}$) from that in the non-correlated symmetric system ($P_{N\,nc,j} \geq P_{I\,nc,j} = 1/2$): A positive (negative) diradical character density indicates the spatial distribution of the positive (negative) diradical correlation, where a positive value implies that the density increases upon correlation, and vice versa. On the other hand, the "ionic character density" $\rho_{y^{I,j}}(\mathbf{r}_1;\mathbf{r}_1)$ of state $j$ describes the deviation of ionic component density in the ionic system ($P_{I,j} \geq P_{N,j}$) from that in the non-correlated symmetric state ($P_{N\,nc,j} = P_{I\,nc,j} = 1/2$): A negative (positive) ionic character density indicates the spatial distribution of the positive (negative) pair-electron correlation relative to the case of a non-correlated symmetric state. The diradical and ionic characters are obtained by the spatial integration of these densities. The amplitudes of diradical ($0 \leq y^{N,j} \leq 1$) and ionic ($-1 \leq y^{I,j} \leq 0$)

characters represent the degree of localization of odd- and pair-electron densities on each site, respectively. Thus, the effective neutral (diradical or covalent) and ionic bond orders are defined, respectively, by [31]

$$q^{\mathrm{N},j} = 1 - y^{\mathrm{N},j} \text{ for } P_{\mathrm{N},j} \geq P_{\mathrm{I},j} \text{ and } q^{\mathrm{I},j} = 1 - |y^{\mathrm{I},j}| \text{ for } P_{\mathrm{I},j} \geq P_{\mathrm{N},j}, \quad (1.51)$$

where $0 \leq q^{\mathrm{N(I)},j} \leq 1$ is satisfied. For $P_{\mathrm{N},j} = P_{\mathrm{I},j}$, we obtain $q^{\mathrm{N},j} = q^{\mathrm{I},j} = 1$, which implies that, in the non-correlated or mean-field level of approximation, the chemical bond is composed of a superposition of equal-weighted covalent and ionic bond components, which take the maximum bond strength of 1. Note here that the present definitions of the diradical and ionic characters and their densities are applicable to arbitrary electronic states, including ionic-dominant states and time-dependent superposition states, in contrast to the conventional diradical character, which is only applicable to the electronic state with dominant covalent (diradical) character, i.e. small ionic bond nature.

Finally, it is worthy to address the relationships between this new diradical character (Nakano's definition) and conventional ones. For the ground state of the two-site model (Eq. (1.28)), Eq. (1.34) can be rewritten by taking advantage of Eq. (1.29) and the symmetry relationship ( $C_{a\bar{b}} = C_{b\bar{a}}$ ) for singlet states:

$$P_{\mathrm{N,g}} = \left|C_{a\bar{b},\mathrm{g}}\right|^2 + \left|C_{b\bar{a},\mathrm{g}}\right|^2 = \frac{1}{2}(\xi + \zeta)^2 ,$$

and

$$P_{\mathrm{I,g}} = \left|C_{a\bar{a},\mathrm{g}}\right|^2 + \left|C_{b\bar{b},\mathrm{g}}\right|^2 = \frac{1}{2}(\xi - \zeta)^2 + \eta^2 . \quad (1.52)$$

Using Eq. (1.47), the present diradical character $y^{\mathrm{N},j}$ is expressed by

$$y^{\mathrm{N,g}} = 2P_{\mathrm{N,g}} - 1 = 2\xi\zeta - \eta^2. \quad (1.53)$$

This can be compared with the conventional one ($y$), which is defined by the LUNO occupation number ($n_{\mathrm{LUNO}}$) (Eq. (1.30)):

$$(1 - y)^2 = (\xi - \zeta)^2 [2 - (\xi - \zeta)^2] \quad (1.54)$$

From Eqs. (1.53) and (1.54), and considering symmetric diradical system ($\eta = 0$), we obtain [31]

$$y^{\mathrm{N,g}} = \sqrt{y(2-y)} = \sqrt{n_{\mathrm{LUNO}}(2 - n_{\mathrm{LUNO}})} . \quad (1.55)$$

In general, there are plural definitions of the number and density of odd (unpaired) electrons as well as of the diradical character based on the one-electron reduced density. For example, the conventional

$y$ ($\equiv \min(n_{\mathrm{LUNO}}, 1 - n_{\mathrm{LUNO}}) = n_{\mathrm{LUNO}}$) together with the odd electron density and odd electron number were defined by Head-Gordon [21], while $y^{\mathrm{T}} \equiv n_{\mathrm{LUNO}}\,(2 - n_{\mathrm{LUNO}})$ was defined originally by Takatsuka and coworkers [20]. Figure 1.11 shows the deviations of $y^{\mathrm{T}}$ and $y^{\mathrm{N,g}}$ from the conventional $y$, which increase from 0 to a maximum and then decrease to 0, with a difference maximum for large and intermediate $y$ regions, respectively. Although the Nakano's and Takatsuka's definitions have disadvantages of yielding unpaired electron numbers larger than the total electron numbers, which are useful for comparing the diradical characters of open-shell frontier orbitals such as magnetic orbitals. In addition, the present definition has advantages of being applicable to arbitrary electronic states of symmetric/asymmetric systems as well as of providing the ionic character, which can be used for describing ionic dominant states.

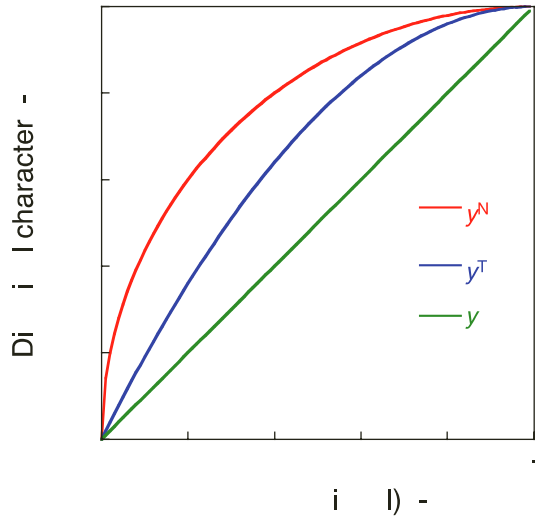


**Figure 1.11** Diradical characters [Nakano's definition ($y^{\mathrm{N}}$), Takatsuka's definition ($y^{\mathrm{T}}$)] versus conventional $y$. Reprinted with permission from Ref. [31]. Copyright @ 2017 American Chemical Society.

### 1.2.5.2 Application to π-stacked dimer of phenalenyl-derivatives with varying intermonomer distance

We apply the new definition of diradical/ionic character to clarify the variation of electronic structure of a π-stacked phenalenyl-

derivative dimer model as a function of the intermonomer distance $R$ (Figure 1.12). In this dimer model, the central carbon (C) atoms of the phenalenyl rings are replaced by boron (B) [Phn(B)] and nitrogen (N) [Phn(N)] atoms, respectively. This dimer (B, N) is isoelectronic to the neutral phenalenyl radical dimer (C, C), which is found to exhibit a gradual increase of the diradical character with increasing $R$ [32]. This indicates that the dimer with covalent-like (pancake bonding) interactions at $R$ = 3.0 Å ($y$ = 0.540 at $R$ = 3.0 Å) undergoes a homolytic dissociation to two phenalenyl radicals as increasing $R$, e.g. $y$ = 0.999 at $R$ = 5.0 Å. Considering the fact that B-/N-doped phenalenyl has zero (two) electron(s) in the central p orbital, the (B, N) system is predicted to present a somewhat covalent-like interaction between the monomers, which allows partial electron transfer from N to B around the equilibrium position, while it undergoes a heterolytic dissociation to B-/N-doped phenalenyls as increasing $R$. To confirm this prediction, the diradical/ionic character analysis is conducted. The dimer model is constructed by π-π stacking of B-/N-doped phenalenyls, where the monomer geometries are optimized at UB3LYP/6-311G* level of theory. The diradical and ionic characters are calculated by the CASCI(2,2)/6-31G* method using the localized MOs, which are obtained from localization of the SOMOs calculated at ROHF/6-31G* level of approximation.

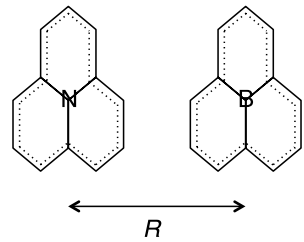


**Figure 1.12** π-stacked B-/N-doped phenalenyl dimer model with intermonomer distance $R$.

First, the variation in the electronic charge difference (using the Hirshfeld charges) between the monomers, $\Delta\rho = \rho^{ele}_{Phn(B)} - \rho^{ele}_{Phn(N)}$, are examined as a function of $R$ (Figure 1.13a). $\Delta\rho$ spans the [0, 2] interval, where $\Delta\rho$ = 0 and 2 correspond to homolytic [Phn($N^{\bullet+}$) and Phn($B^{\bullet-}$)] and heterolytic [Phn(N) and Phn(B), $\Delta\rho$ = 2] dissociation limits, respectively. The asymmetry of the electronic distribution

between the monomers increases with the increase in $\Delta\rho$. At 3.0 Å, $\Delta\rho$ = 1.35 implies that ~0.675 electrons are transferred from Phn($B^{\bullet-}$) to Phn($N^{\bullet+}$) (or ~0.325 electrons are transferred from Phn(N) to Phn(B)), which indicates a weak ionic-like interaction. Then, as increasing $R$, $\Delta\rho$ increases toward 2, which corresponds to a heterolytic dissociation. Figure 1.13b shows the variation in diradical/ionic character, which decreases from a slightly positive value (~0.18, nearly closed-shell) at 3.0 Å to negative values (which reaches −1 around $R$ = 5.0 Å) through zero value around $R$ = 3.5 Å. This implies that in the (B, N) dimer, the neutral component is slightly larger than the ionic component with nearly closed–shell for $R$ < 3.5 Å, while the ionic character increases with $R$ and the ionic component becomes dominant for $R$ > 3.5 Å. Note here that although this is not in agreement with the weak ionic-like interaction at $R$ = 3.0 Å, the increase behavior of ionic character with increasing $R$ from the nearly closed-shell state at $R$ = 3.0 Å is well described by the variation in the diradical/ionic character. It is also found that the first excited state k shows the inversed feature, i.e. it varies from a slightly ionic to a neutral diradical nature as increasing $R$, while the second excited state f remains nearly purely ionic as increasing $R$. Figure 1.13c shows the diradical/ionic character densities for the g, k, and f states at $R$ = 3.0, 4.0 and 5.0 Å. It is found that the ground state exhibits a small positive diradical character density (odd electron density) on each monomer at $R$ = 3.0 Å, which is consistent with a nearly closed-shell system, while at $R$ = 4.0 Å, positive and negative densities are shown to be well separated on the Phn(B) and Phn(N) monomers, respectively, which indicates that the pair-electron density distribution is increased in the negative ionic character domain on the Phn(N) monomer. The amplitudes of ionic character densities at $R$ = 5.0 Å are shown to be slightly larger than those at $R$ = 4.0 Å. The diradical/ionic character density distributions are also shown for the other excited states to reflect the distribution of the π electron pair between the monomers and the diradical/ionic character amplitude of each state. In summary, the (B, N) dimer is found to vary from a covalent-like bonding (pancake) dimer with slight diradical character and slight electron transfer from Phn($B^{\bullet-}$) to Phn($N^{\bullet+}$) at $R$ = 3.0 Å to a dimer with pure ionic character, which means that an electron is completely transferred from Phn($B^{\bullet-}$) to

Phn(N$^{\bullet+}$), resulting in Phn(B)–Phn(N) dimer at the dissociation limit.

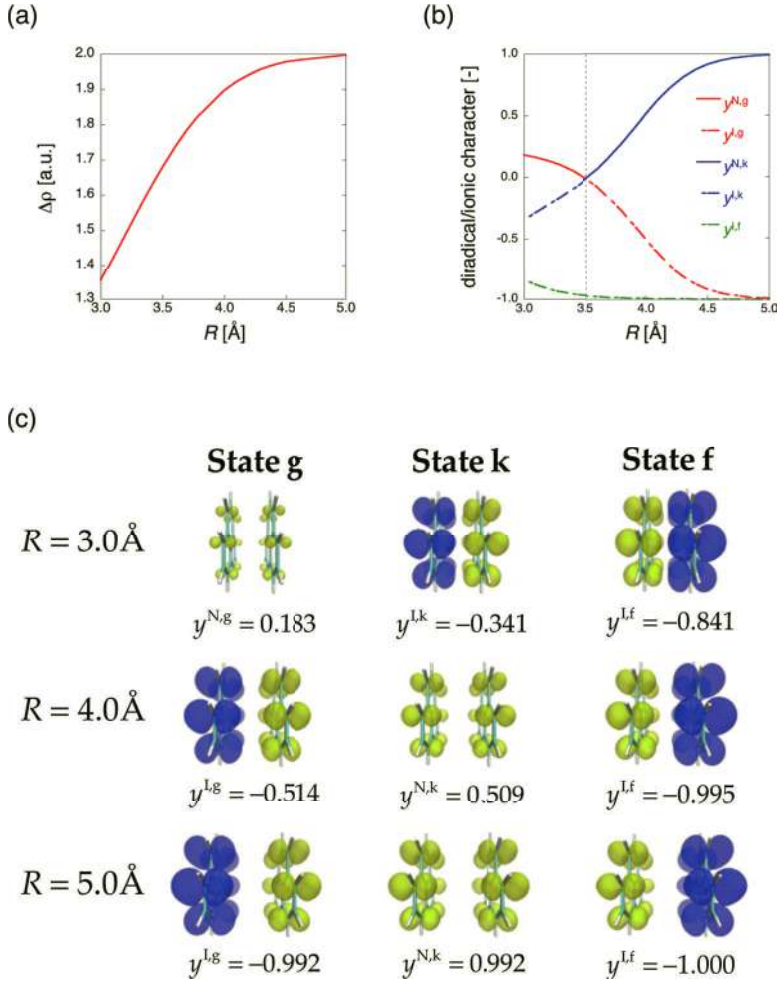


**Figure 1.13** Variations of the electronic charge difference $\Delta\rho = \rho^{\mathrm{ele}}_{\mathrm{Phn(B)}} - \rho^{\mathrm{ele}}_{\mathrm{Phn(N)}}$ for the ground state (g) (a) and diradical and ionic characters ($y^{\mathrm{N},j}$ and $y^{\mathrm{I},j}$, respectively) for the ground (g) and excited (k, f) states (b) as a function of intermonomer distance $R$. The diradical/ionic character densities of each electronic state are also shown at $R$ = 3.0, 4.0 and 5.0 Å (c). The vertical dotted line in (b) indicates the $R$ satisfying $y^{\mathrm{N/I},g} = y^{\mathrm{N/I},k} = 0$. In (c), the yellow and blue surfaces represent positive and negative diradical/ionic character densities with iso-surfaces of ±0.001 a.u., respectively.

### 1.2.6 Experimental Estimation of Diradical Character

As shown in previous sections, the diradical character is not an observable, but a chemical/physical index for bond nature and electron correlation. Therefore, the diradical nature is qualitatively estimated in experiments by using the molecular structure, e.g. quinoid vs. benzenoid forms in resonance structures, low-frequency optical absorption spectrum, small ST energy gap, and so on [23–25, 33–37]. The quantitative evaluation of the diradical character by the experimental measurements has not been conducted yet. In this regard, Nakano and coworkers have firstly proposed an approximate evaluation scheme of the diradical character $y$ using the relationships between the excitation energies and $y$ value for two-site VCI diradical model, Eqs. (1.11), (1.12), and (1.20) [10]. The diradical character $y$ can be expressed as [38]

$$y = 1 - \sqrt{1 - \left( \frac{{}^1E_{1u} - {}^3E_{1u}}{{}^1E_{2g} - {}^1E_{1g}} \right)^2} = 1 - \sqrt{1 - \left( \frac{\Delta E_{S(u)} - \Delta E_T}{\Delta E_{S(g)}} \right)^2} \quad (1.56)$$

Here, the energies in the first right-hand side (RHS) are concerned with the four electronic states (as shown in Figure 1.4). $\Delta E_{S(g)}$ ($\equiv {}^1E_{2g} - {}^1E_{1g}$), $\Delta E_{S(u)}$ ($\equiv {}^1E_{1u} - {}^1E_{1g}$), and $\Delta E_T$ ($\equiv {}^3E_{1u} - {}^1E_{1g}$) in the second RHS represent the excitation energies of the higher singlet state of g symmetry (two-photon allowed excited state), of the lower singlet state with u symmetry (one-photon allowed excited state), and of the triplet state with u symmetry, respectively. Namely, $\Delta E_{S(u)}$ and $\Delta E_{S(g)}$ are obtained from the lowest-energy peaks of the one- and two-photon absorption spectra, respectively, while $\Delta E_T$ is obtained from phosphorescence and Electron Spin Resonance (ESR) measurement. The experimental $y$ ($y^{exp}$) values and theoretically calculated ones ($y^{theor}$) are shown in Figure 1.14, which indicates a strong correlation between the experimental and theoretical results for all compounds though $y^{theor}$ values substantially and systematically overestimate $y^{exp}$. This difference in the scales is predicted to originate from several factors, including the effects of the environment (solvation or crystal packing), inconsistencies among different experimental methods, and approximate nature of the VCI model [10]. As a result, the theoretical correlation between the diradical character and measurable quantities (Eq. (1.56))

is found to provide semiquantitative estimates for the diradical character.

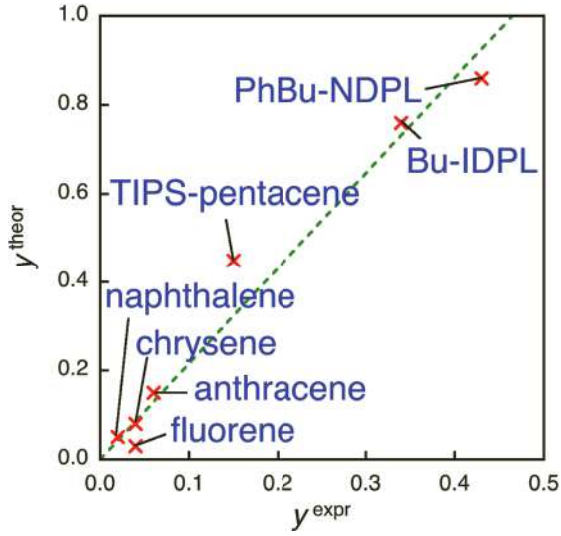


**Figure 1.14** Diradical character ($y^{expr}$) deduced from experimental results (Eq. (1.56)) versus that theoretical one ($y^{theor}$) obtained from PUHF/6-31G** calculations for several compounds [38].

## 1.3 BS Approach to Diradicaloids

### 1.3.1 Spin-Projected BS Approach to Diradical Character

In this section, the feature of spin-unrestricted (BS) ground state wavefunction is clarified using the SA wavefunctions. Using the BS HOMOs $\chi$ and $\eta$, the BS ground state wavefunction is expressed as

$$\left|\Psi^{BS}(\chi\bar{\eta})\right\rangle = \frac{1}{\sqrt{2}}\begin{vmatrix}\chi(1)\alpha(1) & \chi(2)\alpha(2)\\ \eta(1)\beta(1) & \eta(2)\beta(2)\end{vmatrix}$$
$$= \frac{1}{\sqrt{2}}\left(\chi(1)\eta(2)\alpha(1)\beta(2) - \eta(1)\chi(2)\beta(1)\alpha(2)\right). \quad (1.57)$$

Here, the BS orbitals $\chi$ and $\eta$ are represented by SA MOs $\phi_H$ and $\phi_L$ as [4]

$$\chi = \cos\frac{\theta}{2}\phi_H + \sin\frac{\theta}{2}\phi_L \text{ and } \eta = \cos\frac{\theta}{2}\phi_H - \sin\frac{\theta}{2}\phi_L, \qquad (1.58)$$

where $\theta$ is a mixing parameter ranging from 0 to π/2. For θ = 0, $\chi$ = $\eta$ = $\phi_H$, while θ = π/2, $\chi = (\phi_H + \phi_L)/\sqrt{2} \equiv a$ and $\eta = (\phi_H - \phi_L)/\sqrt{2} \equiv b$, where $a$ and $b$ are referred to as magnetic orbitals (LNOs) and are nearly equal to AO $\varphi_A$ and $\varphi_B$, respectively. This implies that the BS orbitals can represent the variation from the MO limit to the AO limit by changing θ from 0 to π/2. Using Eq. (1.58), the ground state BS wavefunction $\Psi^{BS}(\chi\bar{\eta})$ is expressed as [6]

$$\left|\Psi^{BS}(\chi\bar{\eta})\right\rangle = \cos^2\frac{\theta}{2}\left|\phi_H\bar{\phi}_H\right\rangle - \sqrt{2}\sin\frac{\theta}{2}\cos\frac{\theta}{2}\left[\frac{1}{\sqrt{2}}\left(\left|\phi_H\bar{\phi}_L\right\rangle - \left|\phi_L\bar{\phi}_H\right\rangle\right)\right] - \sin^2\frac{\theta}{2}\left|\phi_L\bar{\phi}_L\right\rangle \qquad (1.59)$$

where the first, the second, and the third terms involve the singlet closed-shell determinant $|G\rangle (= \left|\phi_H\bar{\phi}_H\right\rangle)$, the triplet determinant $|T\rangle = \left(\left|\phi_H\bar{\phi}_L\right\rangle - \left|\phi_L\bar{\phi}_H\right\rangle\right)/\sqrt{2}$, and singlet double excited determinant $|D\rangle = \left|\phi_L\bar{\phi}_L\right\rangle$, respectively. Since the correct spatial distribution of the singlet ground state wavefunction is built from superposition of $|G\rangle$ and $|D\rangle$, the BS wavefunction involves an incorrect spin component (triplet) $|T\rangle$. This triplet component, which is anti-symmetric with respect to the exchange of the real coordinate between electron 1 and 2, is shown to asymmetrize the neutral components. This is the reason why this wavefunction is called "BS" (neither symmetric nor anti-symmetric with respect to the exchange between electron 1 and 2), and is found to be made of BS HOMOs $\chi$ and $\eta$. Thus, the BS wavefunction suffers from a spin contamination, which is sometimes known to give improper relative energies for different spin states and cannot correctly reproduce physicochemical properties [12, 39, 40], whereas the BS method has an advantage of including partial electron-correlation by using a single determinant calculation scheme instead of high-cost multi-reference calculation schemes. To remove the spin contamination, Yamaguchi applied the perfect-pairing type spin-projection scheme to the BS solution and developed an easy evaluation method of diradical character $y$ [6, 12]. Using the overlap between $\chi$ and $\eta$, i.e. $T \equiv \langle\chi|\eta\rangle = \cos\theta$, we rewrite Eq. (1.59) as

$$\left|\Psi^{\mathrm{BS}}\right\rangle = \frac{1+T}{2}\left|\mathrm{G}\right\rangle - \sqrt{\frac{1-T^2}{2}}\left|\mathrm{T}\right\rangle - \frac{1-T}{2}\left|\mathrm{D}\right\rangle . \tag{1.60}$$

The perfect-pairing type spin-projection implies the removal of the second term from the BS wavefunction with keeping the weight ratio of the first and third terms,$(1 + T/1 - T)^2$. Thus, the spin-projected wavefunction is expressed as

$$\left|\Psi^{\mathrm{PU}}\right\rangle = \frac{1+T}{\sqrt{2(1+T^2)}}\left|\mathrm{G}\right\rangle - \frac{1-T}{\sqrt{2(1+T^2)}}\left|\mathrm{D}\right\rangle . \tag{1.61}$$

Since the diradical character $y$ is defined as twice the weight of the doubly excitation configuration, the diradical character in the PUHF formalism is expressed as [6, 12]

$$y^{\mathrm{PU}} = 1 - \frac{2T}{1+T^2} . \tag{1.62}$$

The one-electron reduced density using the BS wavefunction Eq. (1.57),

$$\begin{aligned}\rho(\mathbf{r}) &= \left|\chi(\mathbf{r})\right|^2 + \left|\eta(\mathbf{r})\right|^2 = 2\cos^2\frac{\theta}{2}\left|\phi_{\mathrm{H}}(\mathbf{r})\right|^2 + 2\sin^2\frac{\theta}{2}\left|\phi_{\mathrm{L}}(\mathbf{r})\right|^2 \\ &= (1+T)\left|\phi_{\mathrm{H}}(\mathbf{r})\right|^2 + (1-T)\left|\phi_{\mathrm{L}}(\mathbf{r})\right|^2 .\end{aligned} \tag{1.63}$$

This equation indicates that $\phi_{\mathrm{H}}(\mathbf{r})$ and $\phi_{\mathrm{L}}(\mathbf{r})$ are the HONO and LUNO of the BS solution with the occupation numbers of $1 + T$ ($\equiv n_{\mathrm{HONO}}$) and $1 - T$ ($\equiv n_{\mathrm{LUNO}}$), respectively. The occupation numbers of the HONO and LUNO of the spin-projected wavefunction Eq. (1.61) are given by

$$n_{\mathrm{HONO}}^{\mathrm{PU}} = \frac{(1+T)^2}{1+T^2} = \frac{n_{\mathrm{HONO}}^2}{1+T^2} = 2 - y^{\mathrm{PU}} \tag{1.64}$$

and

$$n_{\mathrm{LUNO}}^{\mathrm{PU}} = \frac{(1-T)^2}{1+T^2} = \frac{n_{\mathrm{LUNO}}^2}{1+T^2} = y^{\mathrm{PU}} , \tag{1.65}$$

where $n_{\mathrm{HONO}} = 1 + T$ and $n_{\mathrm{LUNO}} = 1 - T$ are employed (Eq. (1.63)). This expression can be straightforwardly extended to a $2n$-radical system, the perfect-pairing type (i.e. considering a doubly excitation from HONO$-i$ to LUNO$+i$) spin-projected diradical characters and occupation numbers are defined as [6, 12]

$$y_i^{\mathrm{PU}} = 1 - \frac{2T_i}{1+T_i^2}, \tag{1.66}$$

and

$$n_{\mathrm{HONO}\text{-}i}^{\mathrm{PU}} = 2 - y_i^{\mathrm{PU}}, \text{ and } n_{\mathrm{LUNO}+i}^{\mathrm{PU}} = y_i^{\mathrm{PU}}, \tag{1.67}$$

where $T_i$ is the overlap between the corresponding orbitals $\chi_i$ and $\eta_i$, and the occupation number of LUNO+$i$ ($n_{\mathrm{LUNO}+i}$) is given by $1 - T_i$.

We here address the functional dependence of diradical character in DFT calculations for typical open-shell singlet systems, i.e. polycyclic hydrocarbons. The diradical character $y$ defined by the occupation number of LUNO can be usually applied to the highly correlated method like spin-unrestricted coupled-cluster with single, double, and perturbative triple excitations (UCCSD(T)), multi-reference Møller-Plesset perturbation (MRMP) and full CI methods. As mentioned above, in the case of applying to BS methods, spin contamination effects must be considered for reproducing the highly correlated diradical character, e.g. UCCSD(T) $y$ value. The spin contamination effect on the diradical character is explicitly defined at UHF level of theory, so that approximate spin-projection schemes, e.g. perfect-pairing type PUHF (Eq. (1.66)), are applied to obtain semi-quantitatively correct diradical character. Indeed, the PUHF $y_0$ values are known to reproduce those at full CI level of theory. On the other hand, for BS DFT (UDFT) case, it is known that spin contamination effects are smaller than those at UHF level of theory, and depend on the exchange-correlation (xc)-functional. Figure 1.15 shows the diradical character $y$ at the UCCSD, LC-UBLYP, CAM-UBLYP, UBH and HLYP, and UB3LYP levels of approximation versus $y$ at PUHF level of approximation for dicyclopenta-fused acenes, DPA[$N$] ($N$ = 0, 1, 2, 3) [41]. It turns out that the UCCSD and LCUBLYP (μ = 0.47) methods give slightly larger $y$ values at each size of DPA[$N$] than PUHF $y$ value, while that the UBH and HLYP give a slightly smaller $y$ value than PUHF $y$ value at each $N$. The LC-UBLYP (μ = 0.33) and CAM-UB3LYP methods are shown to reproduce the PUHF $y$ values at large $N$ values ($N$ = 3, 2), while they show smaller $y$ values than the PUHF $y$ values at small $N$ values ($N$ = 2, 0), e.g. about a half of the PUHF $y$ value at $N$ = 0. The B3LYP is shown to give significantly undershot $y$ values as compared to the PUHF $y$ values in the whole $y$(PUHF) region. In summary, the inclusion of the HF exchange is important

for well reproducing *y* values at PUHF and strong-correlated UCCSD levels of theory. The UBH and HLYP, LC-UBLYP, and CAM-UB3LYP methods are found to work well for evaluating diradical character of open-shell singlet systems.

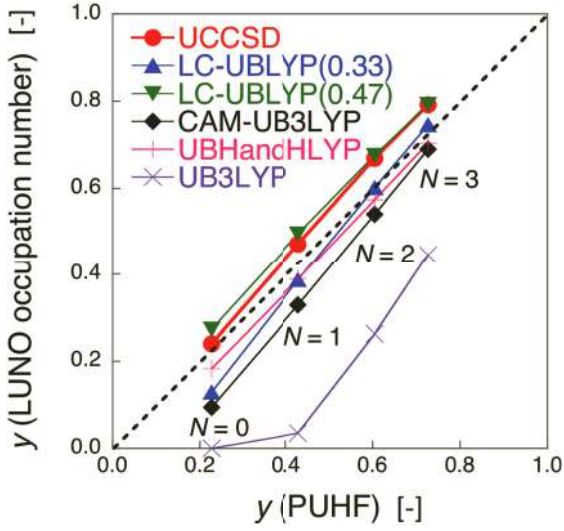


**Figure 1.15** Diradical character *y* at UCCSD and UDFT levels of approximation versus *y* at PUHF level of approximation for DPA[*N*] (*N* = 0, 1, 2, 3). The 6-31G basis set is used. Reprinted by permission from Ref. [41]. Copyright @ 2017 Springer.

### 1.3.2 Relationship between Diradical Character and Aromaticity

The spatial contribution to the open-shell character, i.e. bond weakness or electron correlation, is described by the odd electron density [20, 21, 42], which is expressed in the case of the HONO-*i*/LUNO+*i* pair:

$$\rho_i^{\mathrm{odd}}(\mathbf{r}) = n_{\mathrm{LUNO+i}}\left(\left|\phi_{\mathrm{HONO}-i}\right|^2 + \left|\phi_{\mathrm{LUNO}+i}\right|^2\right), \tag{1.68}$$

which satisfies the relation:

$$y_i = \frac{1}{2}\int d\mathbf{r}\rho_i^{\mathrm{odd}}(\mathbf{r}). \tag{1.69}$$

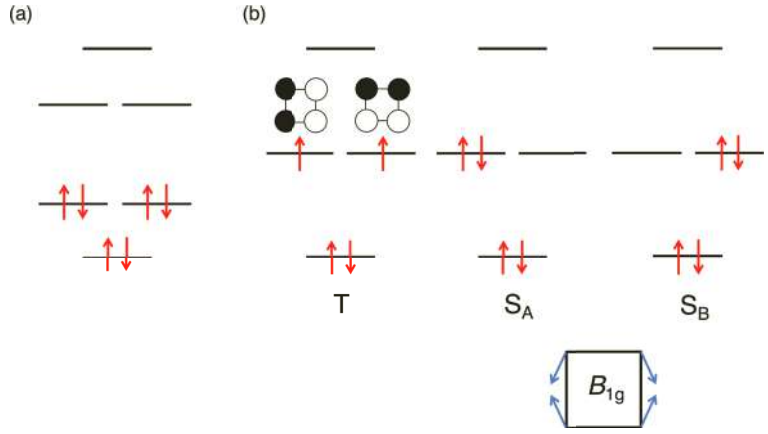


**Figure 1.16** MO energy levels of aromatic (benzene) (a) and antiaromatic (cyclobutadiene) (b) systems. For (b), triplet (T) and two singlet ($S_A$, $S_B$) configurations are shown as well as the vibrational normal mode ($B_{1g}$) which mixes two singlet states.

On the other hand, the aromaticity is a well-known chemical concept, associated with the electronic structure, property, and reactivity of condensed-ring π-conjugated systems [43–45]. So far, there have been many criteria of aromaticity based on the geometry (harmonic oscillator model of aromatic stability (HOMA) [46] and also the bond length alternation (BLA)), on the thermal stability, in relation with the Hückel $4n+2$ π rule, on the topological resonance energy (TRE) [47], as well as on magnetic properties, the nucleus-independent chemical shifts (NICS) [48], and the magnetically induced ring current (MIC) of π-electrons [49]. Among these, the Hückel rule is directly related to the orbital energy diagram, where $(4n+2)$ π-electron systems possess degenerate HOMOs and LUMOs with a finite energy gap, while $4n$ π-electron systems possess degenerate non-bonding orbitals, leading to a triplet ground state with high symmetry (Figure 1.16a,b). Usually, $4n$π systems adopt a lower symmetry due to the Jahn-Teller effect [50], which resolves the degeneracy of the non-bonding MOs and leads to a doubly occupied HOMO with a smaller HOMO-LUMO gap, as compared to similar-size aromatic systems. This small HOMO-LUMO gap causes the emergence of diradical character since the HOMO-to-LUMO double excitation configuration contributes to the ground state. Thus,

antiaromatic systems tend to be open-shell singlet or diradicaloid candidates.

The local aromaticity can be described by NICS and MIC [44, 49]. In fact, when an external magnetic field perpendicular to the π-conjugated ring system is applied, the diatropic and paratropic currents with mutually opposite flow directions are produced (Figure 1.17). In aromatic systems, the net current is dominated by diatropic currents that induce a magnetic field partially cancelling the external magnetic field; while in anti-aromatic systems, paratropic currents that reinforce the external field are induced. Thus, induced currents and their analysis have led to a number of aromaticity criteria. In particular, NICS (or its 3D maps) are widely used, albeit sometimes unreliable. NICS has been criticized for not being able to provide complete information about the MIC because it corresponds to an average value at some point in space (usually the ring center or a point above the ring center). For example, NICS depends on the size of the ring and is influenced by the induced magnetic field from adjacent rings of the molecule [43, 49, 51–53]. Despite similar deficiencies, another method consists in considering the out-of-plane diagonal element of the σ-tensor, called $NICS_{zz}$, $-\sigma_{zz}$ and its 3D map [54, 55].

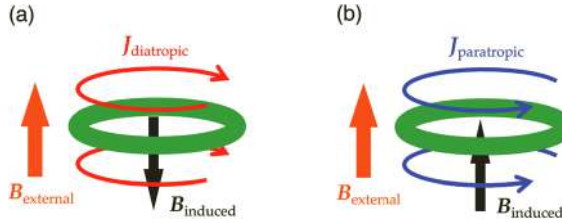


**Figure 1.17** MIC for ring molecules: diatropic (a) and paratropic (b) currents.

A more reliable measure of local aromaticity is the MIC density ($J_i^{B_j,\sigma}(\mathbf{r})$) with $B_j$ as the external magnetic field, $\mathbf{r}$ as the position in space, and $i$ and $j$ as the Cartesian coordinates, $\sigma = \alpha, \beta$. In the case of open-shell systems, the GIMIC method [56–59] can be used to calculate the MIC density from the unperturbed and magnetically perturbed density matrices of $\alpha$- and $\beta$-electrons. Then, the total MIC density is given by the sum of the contributions of $\alpha$ and $\beta$. In order to investigate the local aromaticity, the "bond" current strength ($J$) is

obtained by numerically integrating the MIC density of the bisected rectangular section of the chemical bonds:

$$J = \int J_i^{B_j,\sigma}(\mathbf{r}) \cdot d\mathbf{S} \tag{1.70}$$

The bond current patterns indicate the degree of aromaticity. By definition, diatropic and paratropic currents give positive and negative contributions to $J$, respectively. Therefore, net positive (negative) $J$ value implies that the contribution of the chemical bond to the ring is locally aromatic (antiaromatic).

Two one-dimensional condensed ring systems, dicyclopentacetonated acene (DPA) and polyacene (PA), are discussed in terms of their open-shell singlet natures and their interplay with (anti-) aromaticity [60]. In addition, the spin-restricted (R) and spin-unrestricted (U) DFT treatments are compared since the latter, with functional relevance, is known to be more suitable for describing the electronic structures of open-shell singlet molecules and their NLO response properties [61, 62]. The structures of DPA($N$) and PA($N$) ($3 \le N \le 9$) ($N$ is the number of fused rings) are shown in Figure 1.18. The GIMIC calculations were performed using the R/UBLYP ($\mu$ = 0.33 bohr$^{-1}$)/6–311+G* method, where a magnetic field is applied in the direction perpendicular to the molecular plane (along the $z$-axis).

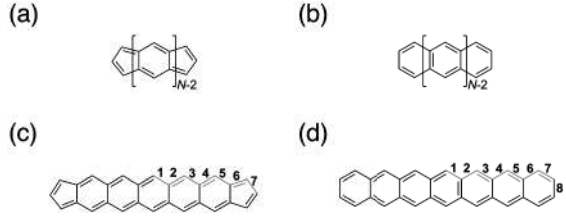


**Figure 1.18** Structures of DPA($N$) (a) and PA($N$) (b), where $N$ indicates the number of fused rings. The numbering of the C–C bonds are also shown for DPA(7) (c) and PA(7) (d). Reprinted with permission from Ref. [60]. Copyright © 2018 by John Wiley & Sons, Inc. or related companies.

Figure 1.19 plots the R and U MIC densities, $J^{B_z,\mathrm{R}}(\mathbf{r})$ and $J^{B_z,\mathrm{U}}(\mathbf{r})$, at 0.5 Å above the molecular plane for DPA(7) ($y$ = 0.860) and PA(7) ($y$ = 0.447), belonging to the intermediate diradical character region (Table 1.1). In DPA(7), diatropic (clockwise) and paratropic (anticlockwise) currents occur outside and inside the

rings, respectively. In the R solution (Figure 1.19a), there is almost no ring position dependence of both current densities. Whereas, in the U solution (Figure 1.19b), the diatropic currents flowing outside the rings are stronger near the center of the ring and gradually decrease toward the end of the rings; while the paratropic currents flowing inside the rings show the opposite trend. The opposite results are observed for PA(7) (Figure 1.19c,d). The spatial pattern of the U diatropic currents is similar to that of the R ones of DPA(7) and vice versa. To further highlight the spin polarization effect on the MIC density, the differences in U versus R, $J^{B_z,\mathrm{diff}}(\mathbf{r}) \equiv J^{B_z,\mathrm{U}}(\mathbf{r}) - J^{B_z,\mathrm{R}}(\mathbf{r})$, are plotted in Figure 1.20. As can be seen from Figure 1.20a, $J^{B_z,\mathrm{diff}}(\mathbf{r})$ of DPA(7) is localized in the central and terminal regions, rotating clockwise (diatropic) in the central region and counterclockwise (paratropic) in the terminal five-membered rings. Therefore, the spin polarization effects increase the aromaticity in the central region of DPA(7) and decrease the aromaticity in the terminal five-membered ring regions. In contrast, as can be seen from Figure 1.20b, $J^{B_z,\mathrm{diff}}(\mathbf{r})$ in PA(7) shows counterclockwise currents in the central region, suggesting that spin polarization effect reduces the aromaticity in the central ring region. These results are consistent with the fact that spin polarization appears in the terminal five-membered ring regions of DPA, but in the central region of PA [54]. These features are further supported by the current strength plots of selected peripheral C–C bonds as shown in Figure 1.20c,d.

**Table 1.1** Diradical character *y* for DPA(*N*) and PA(*N*) at LC-UBLYP/6-311+G** level

| N | DPA(*N*) | PA(*N*) |
|---|---|---|
| 3 | 0.357 | 0.000 |
| 4 | 0.548 | 0.000 |
| 5 | 0.689 | 0.098 |
| 6 | 0.790 | 0.301 |
| 7 | 0.860 | 0.447 |
| 8 | 0.908 | 0.563 |
| 9 | 0.940 | 0.650 |

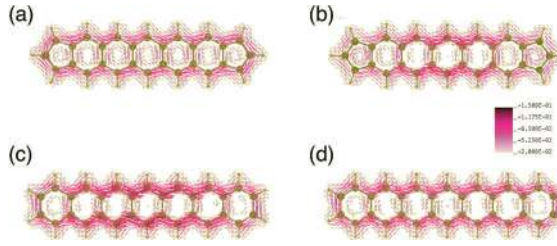


**Figure 1.19** Magnetically induced current density vector plots of DPA(7) and PA(7) on the plane located 0.5 Å above the molecular plane for the R (a, c) and U (b, d) solutions. Diatropic currents rotate clockwise, while the paratropic ones anticlockwise. The values in the color bar are given in a.u. The current vectors are scaled with a factor of 10 Å a.u. $^{-1}$, where 1 a.u. = 100.63 nA $T^{-1}$ $Å^{-2}$. Reprinted with permission from Ref. [60]. Copyright © 2018 by John Wiley & Sons, Inc., or related companies.

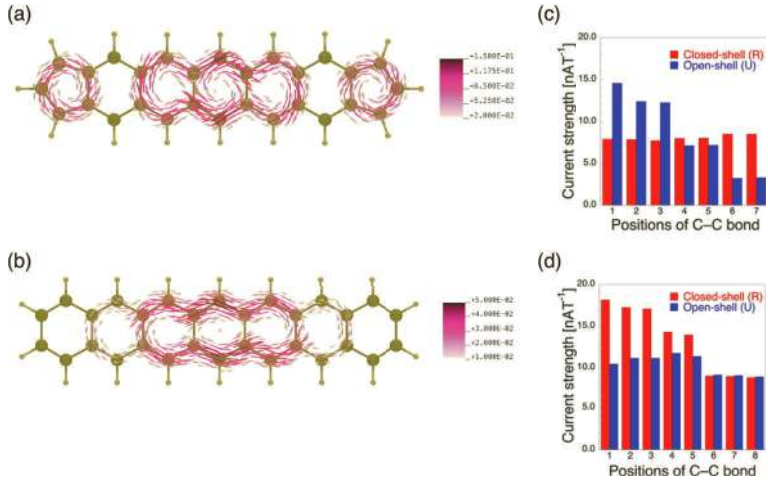


**Figure 1.20** Vector plots of MIC density differences between the U and R solutions for DPA(7) (a) and PA(7) (b). Current strength for selected peripheral C–C bonds of DPA(7) (c) and PA(7) (d). The C–C bond numbering refers to Figure 1.18c and d. See the caption of Figure 8 for more details. Reprinted with permission from Ref. [60]. Copyright © 2018 by John Wiley & Sons, Inc. or related companies.

It is noteworthy to compare these MIC results with the NICS(1) and $-\sigma(1)_{zz}$ values (Figure 21a,b). First, they are all negative, indicating an aromatic character, consistently with the MIC maps and

with the bond currents (Figure 1.20). Indeed, in DPA(7), the NICS(1) values at the center and at the extremity indicate −5.27 (−11.38) ppm and −7.25 (−2.43) ppm for the R (U) solutions, respectively, and the corresponding current strengths for the R (U) solutions are 7.9 (14.5) nA $T^{-1}$ and 8.5 (3.2) nA $T^{-1}$, respectively. However, this consistency between MIC and magnetic shielding criteria is not always observed since NICS suffers from geometry-dependence and it does not always reflect the local/bond character of diatropicity/paratropicity.

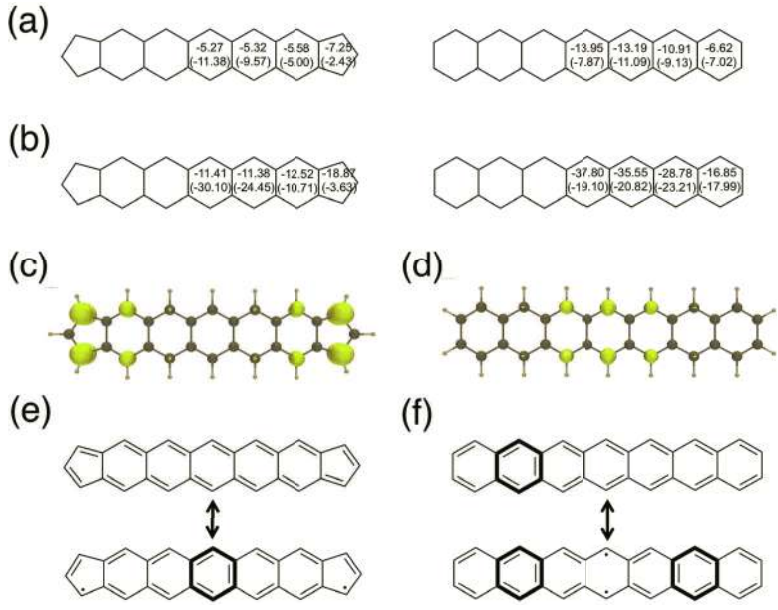


**Figure 1.21** NICS(1) (a) and $-\sigma_{zz}(1)$ (b) for DPA(7) (left) and PA(7) (right), where the values [ppm] obtained from the R and U solutions are shown in each ring, where the U values are given in parentheses. Odd-electron density distributions (isosurface with 0.005 a.u.) of DPA(7) (c) and PA(7) (d) at LC-UBLYP/6-311+G** level of approximation. The resonance structures for DPA(7) (e) and PA(7) (f) are also shown. Reprinted with permission from Ref. [60]. Copyright © 2018 by John Wiley & Sons, Inc. or related companies.

On the other hand, the $y$ values for both DPA and PA increase with the number of fused rings ($N$) and, for any given $N$, $y$ is larger for DPA than for PA (Table 1.1). For DPA(7), the odd-electron density appears alternately on the carbon atoms at the zigzag edges

of both extremities, while of the central region for PA(7) (Figure 21c,d). Similar distributions are observed in DPA($N$) ($3 \leq N \leq 9$) and PA($N$) ($5 \leq N \leq 9$) systems [60]. Those features are understood by their resonance structures (Figure 21e,f), which show the local aromaticity and match the smaller π-electron currents in the regions with larger odd-electron densities (Figures 1.20 and 1.21). In summary, the appearance of open-shell singlet character or localized odd electron reduces the delocalization of π-electrons related to the ring currents. Since $y$ increases with $N$ for both DPA($N$) and PA($N$), we can now correlate its evolution with the MIC-based aromaticity (evaluated at the unrestricted DFT level except for PA(3) and PA(4), where the U solutions reduce to the R ones). We consider the central and terminal regions because they characterize the open-shell character in those systems (Figure 1.22a). The bond current strengths are evaluated at each C–C bond (Figure 1.18). For DPA(3), the current strengths of all rings are negative, indicating clearly antiaromaticity, which agrees with the prediction of Hückel theory, i.e. DPA(3) has 12 π electrons and is classified as an antiaromatic system. Then, the bond current strengths increase with $N$, and the gap between the central 6-membered and terminal 5-membered rings increases as well. DPA(4) provides positive currents in the center, but negative ones at the terminals. It is also found that these positive currents in the central ring region continue to increase, from 3.6 nA $T^{-1}$ ($N = 4$) to 16.8 nA $T^{-1}$ ($N = 9$). On the other hand, for the terminal 6-membered ring, the variations are smaller, from 3.8 nA $T^{-1}$ ($N = 4$) to a maximum of 7.2 nA $T^{-1}$ ($N = 6$) and then a gradual decrease to 6.6 nA $T^{-1}$ ($N = 9$), where these values are smaller than that of benzene (11.9 nA $T^{-1}$). For the 5-membered ring, the bond current starts from a weak antiaromatic character for $N = 4$ ($J = -1.2$ nA $T^{-1}$) and increases up to a weak aromatic character for larger systems, that converges to the value of 3.4 nA $T^{-1}$ ($N = 9$). The 5-membered ring can be classified either as weakly antiaromatic or weakly aromatic depending on the molecular size, where its current strength is much smaller than that of aromatic benzene. In contrast to DPAs, it is found that the bond current strength of PA($N$) ($N \geq 5$) in the central region significantly decreases with increasing $N$, and the bond current strength finally becomes smaller than that of the terminal one at $N = 9$. This indicates that with the increasing size of the molecule, the open-shell singlet nature increases and the local

aromaticity decreases drastically in the central region in parallel with the accumulation of odd-electron density. Furthermore, longer PA(*N*)s ($N \geq 7$) are found to be less aromatic than benzene (11.9 nA $T^{-1}$) both at the central and the terminal rings.

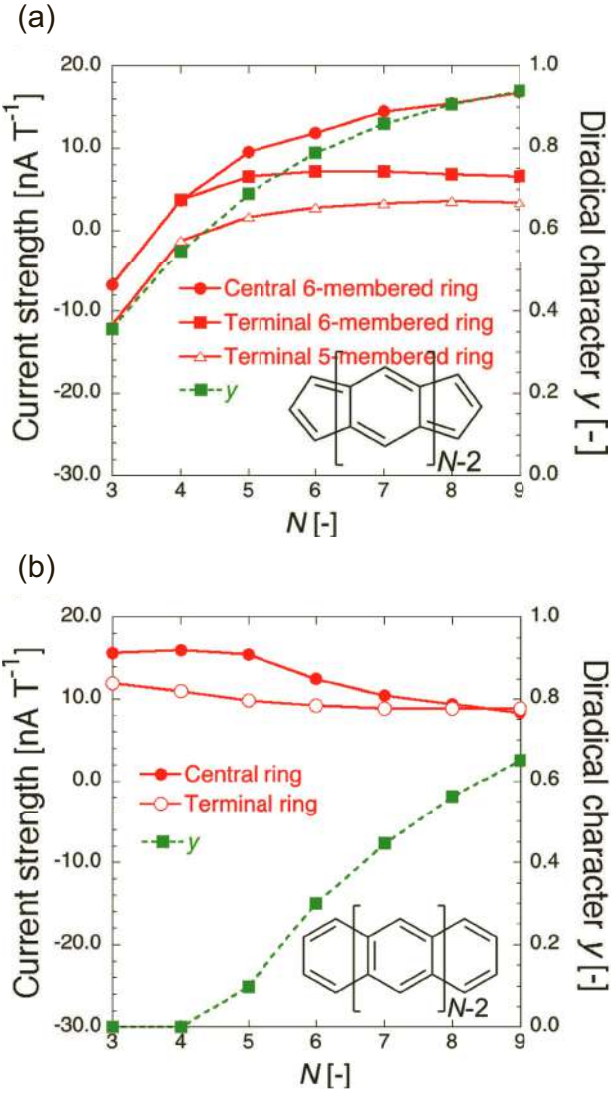


**Figure 1.22** Size dependences of current strengths (red) for the U solutions and diradical character *y* (green) for DPA(*N*) (a) and PA(*N*) (b).

### 1.3.3 Estimation of Singlet Excitation Energies and ST Energy Gap for Diradicaloids

First, the first excitation energy $\Delta E_{S_{1u},S_{1g}} = \Delta E_{\mathrm{kg}}$ of indenofluorenes **1** and **2** (Figure 1.23) is examined. These are diradicaloids involving an *m*-quinodimethane (QDM) unit ($y$ = 0.645 for **1** and 0.772 for **2** at LC-UB3LYP/6-311+G** level) [13]. Contrary to usual expectations, the UV/NearIR absorption spectroscopy of their dimesityl derivatives (**1b**, **2b**) shows that the lowest-energy transition peak at 1293 nm (0.96 eV) for the larger system **2b** (24π), whereas it appears at 1700 nm (0.73 eV) for the smaller compound **1b** (20π) [13]. In order to clarify the origin of this unusual feature, we investigate the physical parameters in Eqs. (1.15) and (1.16) by employing a complete-active-space configuration-interaction method with two electrons in two orbitals [CASCI(2,2)], where the $g$ and $u$ SA MOs were obtained using the IP-tuned (LC)-BLYP method and a range-separating parameter $\mu$ of 0.202 bohr$^{-1}$ for **1** and of 0.187 bohr$^{-1}$ for **2**. Table 1.2 lists the calculated $\Delta E_{\mathrm{kg}}$ and electronic/optical quantities. It is found that (i) $y$ value is smaller for **1** than for **2**, which originates from the combined effect of a larger $|t_{ab}|$ and a smaller $U$ in **1** than in **2**, (ii) for both molecules, $(U/2)f_E(y)$ is the primary contribution to $\Delta E_{\mathrm{kg}}$ since $|-2K_{ab}|$ is much smaller, (iii) larger $y$ values lead to smaller $K_{ab}$, (iv) $(U/2)f_E(y)$ is larger in **2** though $f_E(y)$ is smaller, and (v) $\Delta E_{\mathrm{kg}}$ is larger in **2** than in **1**.

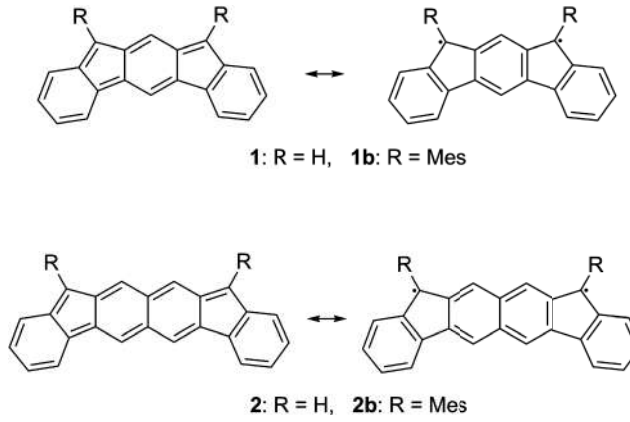


**Figure 1.23** Chemical structure of indenofluorenes (1, 2) and their resonance structures.

**Table 1.2** First optically allowed excitation energy ($\Delta E_{kg}$)[a] and associated electronic/optical parameters[a] for indenofluorenes **1** and **2** (Figure 1.23) as calculated at the CASCI(2,2) level using tuned-LC-RBLYP/6-31G* NOs

| | **1** | **2** |
|---|---|---|
| $\Delta E_{kg}$ | 2.6449 | 3.2191 |
| y | 0.1797 | 0.3121 |
| $\|t_{ab}\|$ | 0.8327 | 0.7075 |
| $f_E(y)$ | 2.7483 | 2.3777 |
| $U/2=K^M_{gu}$ | 1.1592 | 1.4966 |
| $(U/2)f_E(y)$ | 3.1892 | 3.5565 |
| $J^M_{gg}$ | 5.3498 | 4.6531 |
| $J^M_{uu}$ | 5.4178 | 4.8654 |
| $J^M_{gu}$ | 4.8409 | 4.4219 |
| $-2K_{ab}$ | −0.5442 | −0.3374 |

[a] All values are given in eV, with the exception of $y$ and $f_E(y)$, which are pure numbers.

Second, we consider the ST gap by examining compounds **3** and **4** (Figure 1.24), which involve the same dicyclopenta-fused acene unit in their center [15]. The CASCI(2,2) method is also employed together with the IP-tuned (LC)-BLYP method to obtain the NOs, where the tuned range-separating parameter $\mu$ for compound **3** (**4**) amounts to 0.1546 (0.1444) bohr$^{-1}$. It turns out that compound **4** presents a larger $y$ value and a smaller $|\Delta E_{ST}|$ than **3**. This difference originates obviously from the introduction of thiophene rings, but the detailed mechanism has to be disclosed. Table 1.3 lists the corresponding electronic and optical parameters, which shows that (i) the CASCI(2,2) parameters well reproduce the relationship between $y$ and $|\Delta E_{ST}|$ for the compounds **3** and **4**, (ii) the $y$ value of **3** is indeed smaller than that of **4**, which originates from a larger $|t_{ab}|$ and a smaller $U$ in **3** than in **4**, (iii) as a result, $|f_{ST}(y)|$ of **3** is 36% larger than in **4**, leading to a larger magnitude for $(U/2)f_{ST}(y)$ in **3** than in **4**, and (iv) $2K_{ab}$ is again much smaller than $|(U/2)f_{ST}(y)|$, so that these compounds present a singlet ground state. The differences between the physical parameters of **3** and **4** are analyzed by comparing the HOMO ($g$) and LUMO ($u$) distributions

(Figure 1.25a). In the molecular center, their relative amplitude and phase are similar, with large overlap between $g$ and $u$, due to the alternant hydrocarbon structure. Still, $U$ (= $2K_{gu}^{\mathrm{M}}$, the overlap between $g$ and $u$) is slightly larger in **4** than in **3**. This is qualitatively understood by the fact that the distribution region of $g$ and $u$ in **3** is more extended than in **4,** since the thiophene rings seem to hinder the π-electron delocalization to the terminal benzene rings (Figure 1.25a). Then, as a consequence of the large overlap between $g$ and $u$ in both compounds, $J_{gg}^{\mathrm{M}} \sim J_{uu}^{\mathrm{M}} \sim J_{gu}^{\mathrm{M}}$, which results in small $2K_{ab}$ values. Finally, the larger transfer integral $|t_{ab}|$ in **3** than in **4** correlates with the larger HOMO–LUMO gap and indicates more spin polarization in **4** than in **3**, which is also understood by the more diradical forms in **4** than in **3** (Figure 1.24). Such smaller spin polarization in **3** is associated with the delocalized odd electron densities with smaller amplitudes, since they extend to the terminal benzene rings in **3** (Figure 1.25b). In summary, the introduction of thiophene rings reduces slightly the π-electron delocalization and localizes the odd electron density to the middle region, leading to an increase in $U$ and decrease in $|t_{ab}|$, and therefore an increase in $y$, resulting in a decrease of $|\Delta E_{\mathrm{ST}}|$.

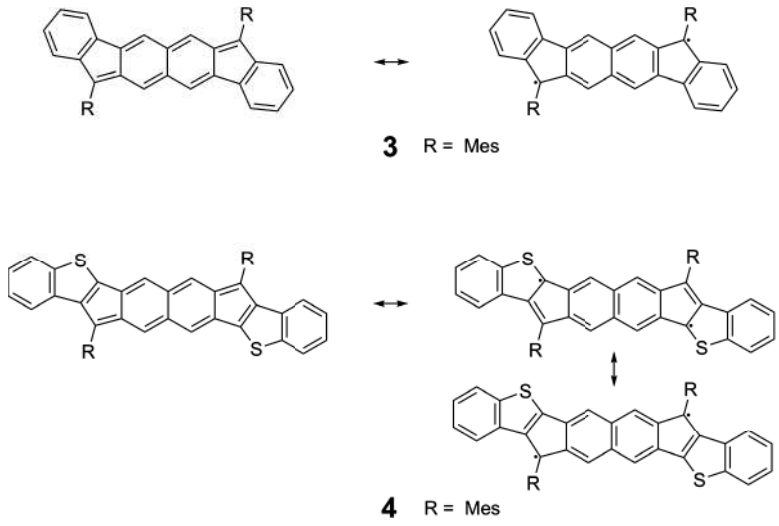


**Figure 1.24** Closed-shell and open-shell resonance forms of **3** and **4**.

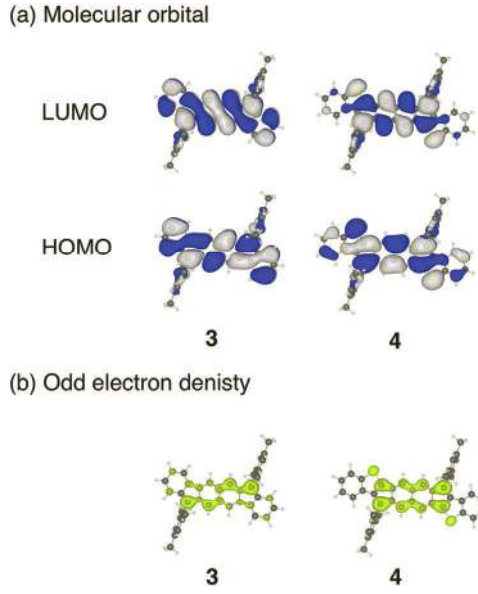


**Figure 1.25** (a) Spatial distributions of HOMO and LUMO of **3** and **4** at tuned-LC-RBLYP/6-311G(d) level of approximation (isosurface value of ±0.01 a.u.). (b) Odd-electron density distributions for **3** and **4** at LC-UBLYP/6-311G(d) level of approximation. Yellow mesh represents the isosurface of odd-electron density with the contour value of 0.001 a.u.

## 1.4 Functionalities of Singlet Diradicaloids

### 1.4.1 NLO Property

NLO materials have attracted much attention both experimentally and theoretically because of their potential applications in future optoelectronics and photonics, e.g. optical power limiting, ultrafast NLO switching, ultra-high capacity memory, three-dimensional nanofabrication, and photodynamic therapy [63–71]. In particular, organic NLO materials have many advantages, i.e. their large NLO susceptibilities and their ultrafast response times, which originate from the responses of the π-conjugated electrons [63–66], as well as their easy chemical modifications. A variety of organic π-conjugated NLO systems, e.g. donor–acceptor substituted molecules and polymers, polyaromatic hydrocarbons, and their molecular crystals,

have been so far investigated [63–66]. In 2005, Nakano et al. theoretically proposed a novel class of highly efficient NLO systems based on open-shell singlet molecules with intermediate diradical characters [72]. This new class of molecules was predicted to exhibit significantly larger $\gamma$ values than conventional closed-shell systems of similar π-conjugation size [1, 7, 8, 10, 36, 61, 62]. Subsequently, this prediction was verified by the measurement of extraordinarily large two-photon absorption (TPA), a typical third-order NLO property, in diphenalenyl diradicaloids [22], e.g. *s*-indaceno[1,2,3-*cd*;5,6,7-*c'd'*]diphenalene (IDPL) [73], and other NLO properties in other types of diradicaloids [74–76].

The NLO properties at the molecular scale, i.e. hyperpolarizabilities, are explained briefly. The induced polarization $\boldsymbol{p}$ (= $\mu - \mu_0$, where $\mu$ is the dipole moment and $\mu_0$ is the permanent dipole moment) is expanded as a power series of the external electric field [63–65]:

$$p^i = \sum_j \alpha_{ij} F^j(\omega_1) + \sum_{jk} \beta_{ijk} F^j(\omega_1) F^k(\omega_2) + \sum_{jkl} \gamma_{ijkl} F^j(\omega_1) F^k(\omega_2) F^l(\omega_3) + \cdots \tag{1.71}$$

where $F^i(\omega_l)$ denotes the $i$th component ($i = x, y, z$) of the electric field with frequency $\omega_l$. The polarizability $\alpha_{ij}$, the first ($\beta_{ijk}$), and the second ($\gamma_{ijki}$) hyperpolarizability tensor components represent the first, second, and third-order optical responses. Both the phase and the amplitude of the hyperpolarizabilities determine the characteristics of the NLO properties. For example, the real and imaginary parts of $\gamma$ describe off-resonant (e.g. third-harmonic generation, THG) and resonant (e.g. TPA) NLO properties, respectively. Equation (1.71) also shows that even-order responses, like $\beta$, vanish in centrosymmetric systems, while odd-order properties, like $\gamma$, have in principle non-zero values regardless of the symmetry. The macroscopic NLO susceptibilities are then obtained from a tensor sum of the molecular responses by including the intermolecular interactions effects. Using time-dependent perturbation theory, these NLO responses are expressed in terms of summations over states involving the excitation energies, transition moments, and dipole moment differences. As seen in Section 1.2.2, since these properties exhibit unique $y$-dependences, strong correlations are expected between the NLO responses of open-shell singlet systems

and their diradical character, which contribute to constructing new design guidelines for efficient open-shell NLO systems. In the static limit ($\omega_l = 0$), any diagonal (generally, one of these is dominant) $\gamma_{iiii}$ component is expressed by [7, 61]:

$$\gamma_{iiii} = 4\sum_{m\neq 0}\frac{(\mu^i_{0m})^2(\Delta\mu^i_{m0})^2}{\Delta E^3_{m0}} - 4\sum_{n,m\neq 0}\frac{(\mu^i_{0m})^2(\mu^i_{n0})^2}{\Delta E^2_{m0}\Delta E_{n0}} + 8\sum_{\substack{n,m\neq 0\\ m\neq n}}\frac{\mu^i_{0m}\Delta\mu^i_{m0}\mu^i_{mn}\mu^i_{n0}}{\Delta E^2_{m0}\Delta E_{n0}} + 4\sum_{\substack{m,n,m'\neq 0\\ m\neq n,m'\neq n}}\frac{\mu^i_{0m}\mu^i_{mn}\mu^i_{nm'}\mu^i_{m'0}}{\Delta E_{m0}\Delta E_{n0}\Delta E_{m'0}} \quad (1.72a)$$

where $\Delta E_{m0}$ represents the excitation energy from the ground to the $m$th excited state, $\mu^i_{0m}$ is the $i$th component ($i = x, y, z$) of the transition moment between the $m$th and $n$th states, and $\Delta\mu^i_{m0}$ is the $i$th component ($i = x, y, z$) of the dipole moment difference between the $m$th excited state and the ground state. In the case of symmetric two-site diradical models (Figure 1.4), only the three singlet states {g, k, f} = {$S_{1g}$, $S_{1u}$, $S_{2g}$} have to be considered while the dipole moments of the ground and excited states are always zero, by symmetry. Equation (1.72a) reduces therefore to [10]:

$$\gamma = -4\frac{(\mu_{gk})^4}{\Delta E^3_{kg}} + 4\frac{(\mu_{gk})^2(\mu_{kf})^2}{\Delta E^2_{kg}\Delta E_{fg}} \quad (1.72b)$$

where the component index "$i$" is omitted for simplicity. By substituting Eqs. (1.11–14) into Eq. (1.72b), we obtain the dimensionless $\gamma(\gamma^{DL})$ [10]:

$$\gamma^{DL} \equiv \frac{\gamma}{(R^4_{BA}/U^3)} = -\frac{8q^4}{\left(1+\sqrt{1-q^2}\right)^2\left(1-2r_K+1/\sqrt{1-q^2}\right)^3} + \frac{4q^2}{\left(1-2r_K+1/\sqrt{1-q^2}\right)^2\left(1/\sqrt{1-q^2}\right)} \quad (1.73)$$

which is a function of the effective bond order $q = 1 - y$ and of the dimensionless direct exchange $r_K$. The first term of the RHS corresponds to type II virtual excitation processes and is negative, while the second one is positive and is associated with virtual excitation processes of type III-2 [77].

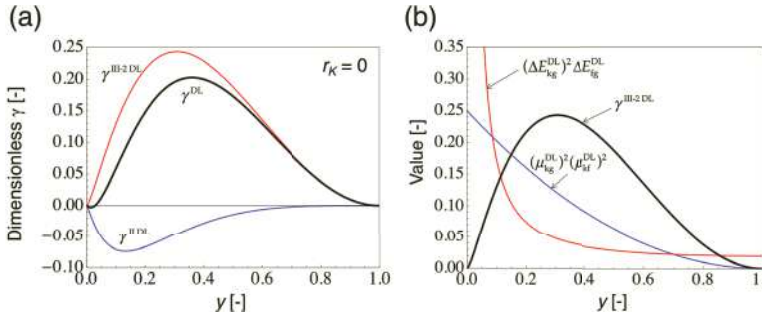


**Figure 1.26** Diradical character dependences of $\gamma^{DL}$, $\gamma^{II\,DL}$, and $\gamma^{III\text{-}2\,DL}$ for $r_K = 0$ (a) and of $\gamma^{III\text{-}2\,DL}$, $(\Delta E_{kg}^{DL})^2 \Delta E_{fg}^{DL}$ and $(\mu_{kg}^{DL})^2 (\mu_{kf}^{DL})^2$ (b).

Figure 1.26a shows the variations of $\gamma^{DL}$ and of its type II/III contributions ($\gamma^{II/III\,DL}$) as a function of $y$ for $r_K = 0$. The $\gamma^{II\,DL}$ exhibits a negative minimum ($\gamma^{II\,DL}{}_{min}$) in the small $y$ region, while $\gamma^{III\text{-}2\,DL}$ exhibits a positive maximum ($\gamma^{III\text{-}2\,DL}{}_{max}$) in the intermediate $y$ region. Since $|\gamma^{II\,DL}{}_{max}|$ is much smaller than $|\gamma^{III\text{-}2\,DL}{}_{max}|$, the $\gamma^{DL}$ variation with $y$ is governed by the second term. Note first that for both $y \to 0$ and $\to 1$, $\gamma^{III\text{–}2\,DL}$ tends to zero (Figure 1.26a). As increasing $y$ from 0 to 1, since the denominator decreases more rapidly in the small $y$ region than the numerator, $\gamma^{III\text{–}2\,DL}$ increases and it attains a maximum ($\gamma^{III\text{–}2\,DL} \sim 0.243$) in the intermediate $y$ region ($y \sim 0.306$). Thus, this behavior is caused by the combined evolution of their numerator $(\mu_{gk}^{DL})^2 (\mu_{kf}^{DL})^2$ and denominator $(\Delta E^{DL}{}_{kg})^2 (E^{DL}{}_{fg})$. The larger value of $|\gamma^{III\text{–}2\,DL}|$ with respect to $|\gamma^{II\,DL}|$ (except for $y \sim 0$) is caused by the fact that the numerator of the first term, $(\mu_{gk}^{DL})^4$, decreases more rapidly than that in the second term, $(\mu_{gk}^{DL})^2 (\mu_{kf}^{DL})^2$ (Figure 1.26b). As a result, open-shell singlet systems with intermediate diradical character are predicted to show significantly larger $\gamma$ values than closed-shell and pure diradical systems. For asymmetric systems, $\beta$ and $\gamma$ are also significantly enhanced in the intermediate diradical/ionic character region [18, 19], and furthermore dynamical NLO properties, like THG and TPA, exhibit similar enhancements of their properties [78, 79]. Some of these relationships have been confirmed by TPA measurements on diphenalenyl diradicaloids [73] and bis(acridine) dimers [76] and by THG measurements on 1,4-bis-(4,5-diphenylimidazole-2-ylidene)-cyclohexa-2,5-diene [74]. Thus, the experimental verification of these theoretical predictions has

helped pioneering a novel class of highly efficient NLO compounds [7, 8, 61].

For singlet diradicaloids, let us consider diphenalenyl diradical molecules (**1**, **3**–**7**) together with a corresponding closed-shell analog composed of pyrene moieties (Figure 1.27a and Table 1.3). It is found from these results that a guideline for realizing diradicaloids is given as follows: For condensed-ring systems bearing both benzenoid and quinoid resonance structures in the ground state, increasing the benzenoid (quinoid) contribution increases the diradical (closed-shell) character. This is verified by a computational study on *p*-quinodimethane model (Figure 1.27b), where the increase of diradical character and a bell-shape $\gamma$ variation with diradical character are observed with increasing the both-end C-C bond lengths in association with the increase of the contribution of benzenoid form in the resonance structure. The relative benzenoid/quinoid character can be controlled by tuning the molecular architecture based on the resonance structures with Clar's sextet rule [80]. For instance, for diphenalenyl diradicaloids **1**(*n*), the increase of the aromaticity of the central fused-ring linker causes the increase of the diradical character (see **1**(1) – **1**(3)), where the monotonous increase of longitudinal $\gamma$ with the size of **3** is understood by the size enhancement effect ($\gamma \propto R_{\mathrm{BA}}^4$) in addition to the $y$ dependence of dimensionless $\gamma$ (Eq. (1.73)). It is found that according to our $y$–$\gamma$ correlation, the $\gamma$ of IDPL [**1**(1)] with an intermediate $y$ value is enhanced by about one-order as compared to the closed-shell (**2**) and pure open-shell [*as*-IDPL (**3**)] analogs [81]. It also turns out that the heterosubstitution of the central ring changes aromaticity and leads to a slight [**4** (X = O) and **5** (X = S)] or significant [**6** (X = BH) and **7** (X = CS)] decrease of $y$ [81]. Similar relationship between the benzenoid/quinoid resonance structures in the middle benzene rings and diradical characters is also found in zethrenes [82]. Other types of diradicaloid structures are observed in a variety of π-conjugated molecules, e.g. acetylene-linked diphenalenyl compounds [83], graphene nanoflakes [84–87], and fullerenes [88, 89], where the differences in geometry and topology significantly affect the diradical character. For these compounds, the $\gamma$ values in the intermediate diradical character region are found to be more than one-order larger than their closed-shell or pure open-shell counterparts.

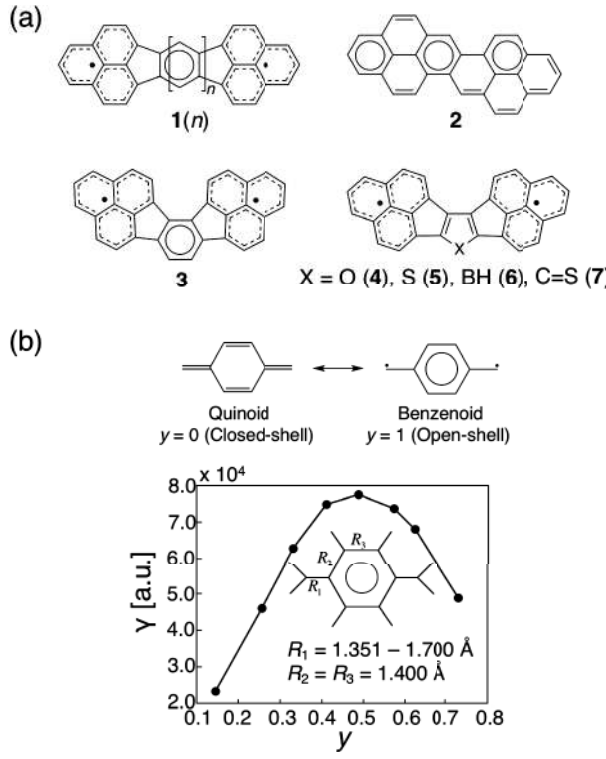


**Figure 1.27** (a) Diphenalenyl diradical molecules (1, 3–7) together with a corresponding closed-shell analog (2). (b) Diradical character dependence of longitudinal $\gamma$ for *p*-quinodimethane model.

**Table 1.3** Diradical characters $y$ and longitudinal $\gamma$ values calculated for compounds 1–7

| Compound | $y$ | $\gamma$ [x10$^3$ a.u.] |
|---|---|---|
| 1(1) | 0.770 [a] | 2284 [c] |
| 1(2) | 0.854 [a] | 3342 [c] |
| 1(3) | 0.901 [a] | 5143 [c] |
| 2 | 0.0 [b] | 194 [c] |
| 3 | 0.923 [b] | 472 [c] |
| 4 | 0.731 [a] | 1934 [c] |
| 5 | 0.768 [a] | 1349 [c] |
| 6 | 0.374 [a] | 415 [c] |
| 7 | 0.0 [a] | 98 [c] |

[a]Calculated using the PUHF/6-31G*. [b]Calculated using the PUHF/6-31G*+*p*.
[c]Calculated using the UBHHLYP/6-31G*.

### 1.4.2 Singlet Fission (SF)

SF is a photophysical phenomenon, where a singlet exciton splits into two triplet excitons having long lifetimes in crystal phase of organic molecular aggregates or in molecules. Although its mechanism was proposed in the 1960s, in order to interpret the significant reduction of fluorescence yields observed for anthracene and tetracene crystals [90, 91], it has started receiving attention again since Nozik and co-workers emphasized its importance in the application to photovoltaics in 2004 [92, 93], where they proposed a possibility of improving photoelectric conversion efficiency from the Shockley–Queisser limit ~33% to ~47% through multi-exciton generation due to SF [94]. Subsequently, a series of theoretical and experimental studies by Michl and co-workers suggested a promising potential of well-designed materials for an application in SF [95, 96]. There have been lots of studies on the detailed mechanism of SF, design for highly efficient SF molecules and aggregates, together with measurements of the SF of novel molecules and crystals. Recent experimental and theoretical investigations have been conducted particularly by focusing on the relationships between electronic structures, electronic couplings (intermolecular interactions), exciton-phonon (vibronic) couplings, and SF dynamics [95–101]. These results would contribute to clarify the comprehensive mechanisms of the SF as well as to construct novel design guidelines for efficient SF molecular systems, while the fact that there is still a small number of efficient SF molecules/aggregates prevents further progress in the SF study.

The SF process is approximately described by [95, 96]

$$S_1 + S_0 \underset{k_2}{\overset{k_{-2}}{\rightleftarrows}} {}^1(T_1T_1) \underset{k_1}{\overset{k_{-1}}{\rightleftarrows}} T_1 + T_1 \tag{1.74}$$

Here, we consider two molecules in a crystal, and assume that one is in the first singlet excited state ($S_1$), while the other is in the ground state ($S_0$). $T_1$ is the lowest triplet state, and $^1(T_1T_1)$ (also referred to as TT or $^1$(TT), hereafter) indicates the singlet state composed of two triplet excitons on adjacent molecules, referred to as “correlated triplet pair” or “double triplet”. Due to this singlet nature of correlated triplet pair, SF is considered as spin-conserving process. Therefore, spin–orbit interaction is not required for SF, which is distinguished from traditional triplet generation by

intersystem crossing. From the viewpoint of energy level matching in SF process, Michl et al. proposed the following conditions of excitation energies of a single molecule for SF [95, 96]:

$$2E(T_1) \sim E(S_1) \text{ or } 2E(T_1) < E(S_1), \tag{1.75a}$$

$$2E(T_1) < E(T_2) \tag{1.75b}$$

Equation (1.75a) indicates the condition required for split of a singlet exciton (with energy $E(S_1)$) to two triplet excitons (with energy $E(T_1)$), while Eq. (1.75b) is required to suppress the recombination of the split two triplet excitons into another triplet exciton (with energy $E(T_2)$) represented by $T_1 + T_1 \rightarrow T_2 + S_0$. From the viewpoint of decreasing the energy loss in the photoelectric conversion process, molecules satisfying $2E(T_1) \sim E(S_1)$ are expected to be appropriate for efficient SF. For exothermic SF, $2E(T_1) - E(S_1) < 0$, the process is expected to undergo efficiently from the energetic viewpoint. For endothermic SF, $2E(T_1) - E(S_1) > 0$, there may be an energy barrier to be overcome by thermal excitation. We here focus on molecular design for efficient SF from the viewpoint of energetically favorable (isothermic or exothermic) SF. In general, most thermally stable closed-shell molecules do not tend to satisfy the energy level matching condition because they have large $E(T_1)$ values near to $E(S_1)$ [95]. Michl et al. proposed two types of molecular species, "alternant hydrocarbon" and "biradicaloid" (diradicaloid), as potential candidates for SF [95, 96]. This is based on the consideration of exchange interactions between frontier orbitals in a molecule. On the other hand, there are also many exceptions, e.g. naphthalene and phenanthrene, which are typical alternant hydrocarbons, but are not known to exhibit SF. Diradical molecules tend to have small $S_0$–$T_1$ gap, which leads to relatively lower $T_1$ state than $S_1$ state so as to satisfy the first condition (Eq. (1.75a)). However, the systems with too small $S_0$–$T_1$ gaps and those with triplet ground states are not suitable for efficient SF because they have large deviation from $2E(T_1) \sim E(S_1)$, leading to high energy loss and slow SF rate.

Thus, although design guidelines presented so far are useful to roughly determine the searching area and to find similar systems to existing SF molecules, they are still insufficient to quest for unknown SF molecules. In order to improve these deficiencies as well as to obtain more reliable (quantitative) design guidelines for efficient SF molecules, Nakano and coworkers have constructed a

new design principle based on the multiple diradical characters ($y_0$ and $y_1$) since tetraradical model is, at least, necessary for describing the SF process [102, 103]. For such tetraradical model, we apply the full configuration interaction (full-CI) method to obtain excitation energies and diradical characters for a hydrogen chain ($H_4$) model, which is one of the minimum models of tetraradical systems [102, 103]. We examine a wide range variation of interatomic distances, i.e. two kinds of distances corresponding to the inner and outer H–H moieties, which cause the variation in $y_0$ and $y_1$.

To examine the energy level matching conditions, we need to consider three excitation energies of $E(S_1)$, $E(T_1)$, and $E(T_2)$, where $T_1$ state is usually described by the HOMO → LUMO singly excited configuration, and $T_2$ state is described by the other excited configurations except for the HOMO and/or LUMO. In a tetraradical model, the singly excited configurations of HOMO → LUMO, HOMO−1 → LUMO, and/or HOMO → LUMO+1 contribute to the description of the singlet excited state $S_1$ (from which SF starts), which are referred to as class I and II [95]. There is also the case that $S_1$ is a tetraradical excited state composed of two triplet excitons, which is described by plural doubly excited configurations among HOMO−1, HOMO, LUMO, and LUMO+1. This case is referred to as class III, which needs four electrons for the description and is found to be the lowest singlet excited state for polyenes. Thus, we examine the excited states of the symmetric linear $H_4$ model using the full-CI method with STO-3G basis set [102], where the singlet diradical ($y_0$) and tetraradical ($y_1$) characters can be controlled by changing the interatomic distances, $R_1$ and $R_2$. This model is shown to well reproduce the qualitative features, e.g. relative excitation energies and response properties as a function of diradical/tetraradical character obtained using more extended basis sets [104]. The $R_1$ and $R_2$ ranging from 0.5 to 4.0 Å are found to span a whole range of multiple diradical characters ($0.0 < y_0, y_1 < 1.0$). The closed-shell, pure diradical, and pure tetraradical ground states, i.e. ($y_0$, $y_1$) ~ (0, 0), (1, 0), and (1, 1), are shown to correspond to ($R_1$, $R_2$) ~ (0.5 Å, 0.5 Å), (4.0 Å, 0.5 Å), and (4.0 Å, 4.0 Å), respectively (Figure 1.28). In the symmetric linear $H_4$ model, the ground state is the lowest singlet state with $A_g$ symmetry ($S_0 = 1^1A_g$), while $T_1$ and $T_2$ states are identified by the $1^3B_u$ and $1^3A_g$ states, respectively. There are two candidates for the first singlet excited state $S_1$, i.e. $1^1B_u$ or $2^1A_g$, where $1^1B_u$ is the lowest singlet state

including the HOMO → LUMO singly excited configuration, and $2^1A_g$ is the second lowest singlet state including the HOMO−1 (HOMO) → LUMO (LUMO+1) singly excited configuration together with several doubly excited configurations. According to the classification of SF [95], $S_1 = 1^1Bu$ belongs to class I, and $S_1 = 2^1A_g$ to class II and/or III in the present model. For simplicity, class III was redefined to include class II, i.e. the case of $S_1 = 2^1A_g$ belongs to class III. The order of the $1^1B_u$ and $2^1A_g$ states is shown to depend on the interatomic distances ($R_1$ and $R_2$) as well as on the multiple diradical characters ($y_0$ and $y_1$). In summary, the $1^1A_g$ ground state and the four excited states ($1^1B_u$, $2^1A_g$, $1^3B_u$, and $1^3A_g$) can be used for the evaluation of the energy level matching conditions as well as for the classification of SF molecules in the present model.

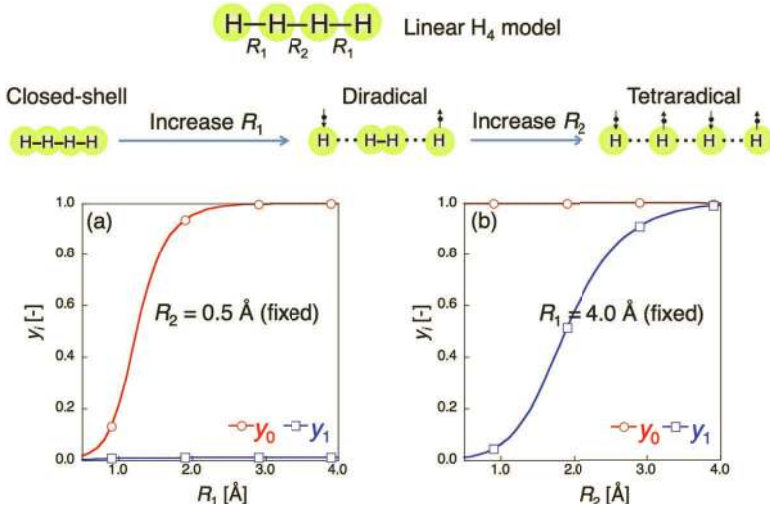


**Figure 1.28** Linear $H_4$ model. Variations of multiple diradical characters, $y_0$ and $y_1$, are also shown as a function of $R_1$ with fixed $R_1$ = 0.5 Å (a), and of $R_2$ with fixed $R_1$ = 4.0 Å (b). Reprinted with permission from Ref. [8]. Copyright © 2017 by John Wiley & Sons, Inc. or related companies.

To clarify the variation in the energies of these excited states, the two limit cases, i.e. $y_1 \sim 0$ and $y_0 \sim 1$, are examined. Figure 1.29 shows variations in excitation energies, $E(2^1A_g)$, $E(1^1B_u)$, $E(1^3B_u)$, and $E(1^3A_g)$ as a function of $y_0$ for $y_1 \sim 0$, and of $y_1$ for $y_0 \sim 1$. As seen from Figure 1.29a, as increasing $y_0$, $E(1^3B_u)$ decreases toward

0 at $y_0 = 1$, while $E(1^1B_u)$, $E(2^1A_g)$ and $E(1^3A_g)$ rapidly decrease for $y_0 < \sim 0.2$ and then reach similar stationary values. The behavior of $E(1^3B_u)$ is explained as follows: The $1^1A_g$ state is shown to be destabilized with increasing $y_0$ from the closed-shell ($y_0 = 0$) to diradical ($y_0 = 1$), which corresponds to the increase in the weight of doubly excited configuration (HOMO, HOMO $\rightarrow$ LUMO, LUMO) at ($R_1$, $R_2$) = (4.0 Å, 0.5 Å), while the $1^3B_u$ state is shown to remain a pure diradical state for $0 < y_0 < 1$, resulting in the decrease in $E(1^3B_u)$. As a result, the triplet excitation energy $E(1^3B_u)$ is turned out to be strongly correlated with ground-state diradical character ($y_0$). Similarly, with increasing $y_1$, it is found from Figure 1.29b that $E(2^1A_g)$ and $E(1^3A_g)$ decrease toward zero at $y_1 \sim 1$ because these behaviors originate in tetraradical characters of $1^1A_g$, $2^1A_g$, and $1^3A_g$ states at $y_1 \sim 1$, while that the ground state ($1^1A_g$) with a stable bond has a lower energy than the others in the region with small $y_1$. As a result, the $E(2^1A_g)$ and $E(1^3A_g)$ are shown to be strongly correlated with the ground-state tetraradical character ($y_1$). It is also found that $E(1^1B_u)$ is insensitive to the variation of $y_0$ and $y_1$, and has non-zero excitation energies in the whole $y_1$ region, which are similar to the case of $2^1A_g$ for $y_0 > \sim 0.2$ at $y_1 \sim 0$ (Figure 1.29a). This stationary behavior of $E(1^1B_u)$ comes from the ionic character of the HOMO $\rightarrow$ LUMO singly excited configuration, which increases the electron repulsion as compared to the ground state.

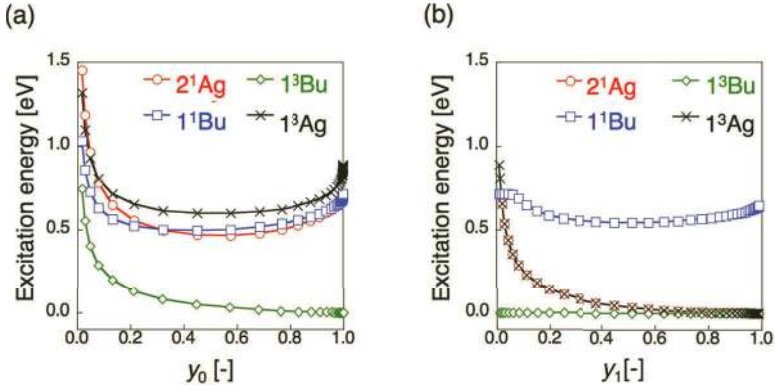


**Figure 1.29** Variations of excitation energies of the $2^1Ag$, $1^1Bu$, $1^3B_u$, and $1^1Ag$ states as a function of $y_0$ for $y_1 \sim 0$ (by increasing $R_1$ with keeping $R_2$ = 0.5 Å) (a) and of $y_1$ for $y_0 \sim 1$ (by increasing $R_2$ with keeping $R_1$ = 4.0 Å) (b). Reprinted with permission from Ref. [8]. 

Figure 1.30 shows the feasibility map of SF (often referred to as "Nakano map") based on the energy level matching conditions Eqs. (1.75a,b) [102]. The darker density region indicates higher energy efficiency of SF from the absorption of light by the $1^1B_u$ state (the lowest optically allowed state), where the highest efficiency is obtained at $\eta = [2E(1^3B_u) - E(1^1B_u)]/E(1^1B_u) \sim 0$. The class I and III regions of SF molecules are shown by the auxiliary lines, $[E(2^1A_g) - E(1^1B_u)] / E(1^1B_u) = 0$ (solid) and −0.3 (dashed), which imply that the doubly excited state ($2^1A_g$) tends to be the lowest singlet excited state in high $y_1$ region, i.e. class III is realized in the region with large tetraradical nature. From these analyzes, it is found that the (i) energy level matching conditions are satisfied except for the closed-shell ($y_0 < 0.1$) and tetraradical ($y_0 \sim y_1$) systems, and (ii) SF energy efficiency becomes worse with increasing $y_0$, due to the increase in the gap between the optically allowed singlet excitation energy ($E(1^1B_u)$) and twice the lowest triplet excitation energy, $E(1^3B_u)$.

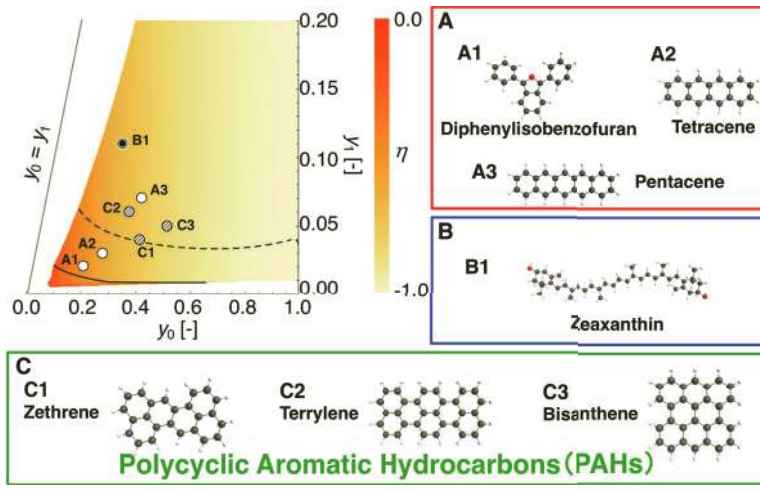


**Figure 1.30** Feasibility map of SF on $y_0$-$y_1$ plane based on the energy level matching conditions for the linear $H_4$ model. Several examples of SF molecules (A–C) are also plotted on the map. The density plot indicates the energy efficiency with a function of $\eta = [2E(1^3B_u) - E(1^1B_u)/E(1^1B_u)]$, where the darker region has higher efficiency. The solid and dashed lines show $[E(2^1A_g) - E(1^1B_u)/E(1^1B_u)] = 0$ and −0.3, respectively. The $y_0$ and $y_1$ are calculated at the PUHF/6-31G* level of approximation. Reprinted with permission from Ref. [8]. 

We here plot the several SF molecules on the $y_0$–$y_1$ map for screening molecules satisfying the energy level matching conditions. First, we consider 1,3-diphenylisobenzofuran (**A1**), tetracene (**A2**), pentacene (**A3**), and zeaxanthin (**B1**), which are known to undergo efficient SF and **A*n*** and **B*n*** belong to class I and III, respectively. These systems are shown to lie in the colored open-shell region with $y_0 >$ 0.2, and **B*n*** indicates higher $y_1$ value than **A*n***, indicating that the $S_1$ state of **A*n*** (**B*n***) is described primarily by the HOMO→LUMO singly excited configuration (the doubly excited configurations). Although **A*n*** lies slightly outside the region with $E(2^1A_g) - E(1^1B_u) > 0$ in the present model, the relative features between class I (**A1**, **A2, A3**) and III (**B1**) are distinguished on the $y_0$–$y_1$ plane. As a result, the multiple diradical character $y_0$–$y_1$ map is useful for the semi-quantitative prediction of the feasibility region of SF. Next, we examine a new type of SF candidates, polycyclic aromatic hydrocarbons, e.g. zethrene (**C1**), terrylene (**C2**), and bisanthene (**C3**), which lie in the feasibility region of SF. Obviously, these PAHs belong to the boundary region between class I and III, due to their intermediate $y_0$ and non-negligible $y_1$ values. Note here that since it is known that as the size of PAHs is increasing, the $y_0$ and $y_1$ values increase and then $E(1^3B_u)$ significantly decreases, larger-size PAHs tend to belong to class III, but will be inefficient SF systems with large energy loss.

The usefulness of the $y_0$-$y_1$ map was demonstrated by the theoretical prediction of oligorylenes as a new class of SF candidates, which preceded the experiments [105]. The excitation energies and transition properties of a series of oligorylenes at time-dependent tuned long-range corrected density functional theory, TD-Tuned-LC-BLYP/6-31+G* level of approximation, are shown in Figure 1.31 [105]. These quantities obtained by this method were known to well reproduce the experimental ones for describing the optically allowed excited states of relatively small-size oligorylenes [105]. The diradical characters $y_0$ and $y_1$ for oligorylenes are given in Figure 1.31. The increase in values of the $y_0$ and $y_1$ is found to correspond to the decrease in the orbital energy gaps of the HOMO–LUMO and (HOMO−1)–(LUMO+1), respectively [102, 103]. It is found that all the oligorylenes examined here present the intermediate $y_0$ and small $y_1$ values, so that these systems are possible candidates for SF. In order to understand the spatial distribution of diradicals, we examine the resonance structure and odd electron density of

perylene (Figure 1.32). As seen from the closed-shell resonance form in Figure 1.32a, the two benzenoid forms (B) and the four pairs of double bonds except for benzenoid forms (D) are found at most, in which all the π-electrons make the pairs, resulting in the closed-shell form. On the other hand, several diradical resonance forms, which possess two B forms and three D forms together with two unpaired electrons, could contribute to the ground state (Figure 1.32a). These resonance forms are in good agreement with the spatial distribution of the unpaired α and β spin densities and odd electron densities (Figure 1.32a, b).

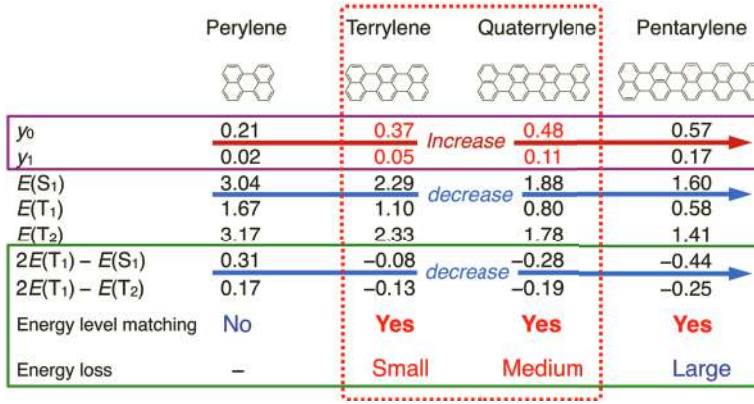


**Figure 1.31** Diradical characters ($y_0$ and $y_1$ at PUHF/6-31G* level of approximation), excitation energies (at TD-tuned-LC-RBLYP/6-31+G* level of approximation), energy level matching conditions ($2E(T_1) - E(S_1)$, $2E(T_1) - E(T_2)$) and energy loss ($|2E(T_1) - E(S_1)|$) for oligorylenes, i.e. perylene, terrylene, quaterrylene, and pentarylene.

The multiple diradical characters ($y_0$ and $y_1$), vertical excitation energies ($E(S_1)$, $E(T_1)$, and $E(T_2)$), and energy differences concerned with the energy level matching conditions are shown in Figure 1.31. For perylene, judging from a relatively small diradical character ($y_0$ = 0.21), which leads to positive $2E(T_1) - E(S_1)$, SF is predicted to be difficult to occur from the $S_1$ state, and even if SF occurs from high-lying singlet excited states, the split triplet excitons will be recombined easily due to the positive value of $2E(T_1) - E(T_2)$. On the other hand, for pentarylene, which exhibits a relatively large diradical character ($y_0$ = 0.57), the large energy loss ($|2E(T_1) - E(S_1)|$) is observed and then is not predicted to be suitable for

energetically efficient SF. In contrast, terrylene and quaterrylene, which have intermediate diradical ($y_0$) characters together with much less tetraradical character ($y_1$), are turned out to satisfy the energy level matching conditions as well as the relatively small energy loss. As a result, terrylene and quaterrylene are expected to be the promising candidates of energetically efficient SF. Recently, the former prediction has been verified experimentally using crystals of terrylene derivatives [106].

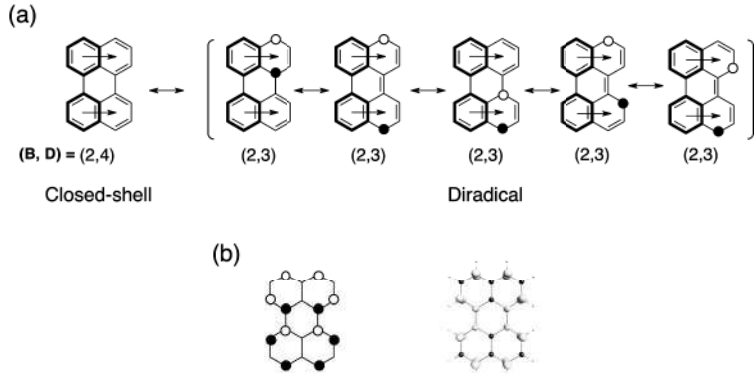


**Figure 1.32** (a) Resonance structure of perylene. "B" and "D" indicates the number of benzenoid form and that of double bond except for the benzenoid form. It represents the resonance of benzenoid form. White and black filled circles represent the two unpaired electrons with mutually opposite spins. (b) Spatial distribution of unpaired electrons derived from the resonance structure (left), and that of odd electron density at PUHF/6-31+G* level of theory with iso-contour value of 0.0003 a.u. (right) for perylene. Reprinted with permission from Ref. [8]. Copyright © 2017 by John Wiley & Sons, Inc. or related companies.

It is important to mention that the energy level matching is a condition to be satisfied for SF molecule and thus is only a part of conditions for realizing SF, the efficiency of which is also influenced by intermolecular electronic coupling (intermolecular configuration) and intra-/inter-molecular vibronic coupling and exciton relaxation dynamics [107–109, 110, 111, 112–115]. However, the energy level matching condition is expected to be useful for prescreening SF candidate molecules. Thus, the diradical character based design guideline using SF feasibility map (Figure 1.30) can present a simple way of prescreening efficient SF candidates because of using easily

calculated diradical character in the ground state at PUHF level of approximation as compared to using more demanding accurate quantum chemical calculations or difficult measurements of the excitation energies concerning energy level matching conditions.

Finally, we present an analytical expression of energy level matching condition (Eq. (1.75a)) $2E(\mathrm{T}_1) \leq E(\mathrm{S}_1)$ in terms of $y_0$ and exchange integral $K_{ab}$ in two-site diradical model. From Eqs. (1.19), (1.20), and (1.11), we obtain

$$f \equiv \frac{2E(\mathrm{T}_1) - E(\mathrm{S}_1)}{U} = -\frac{3}{2} + \frac{1}{2\sqrt{1-(1-y_0)^2}} - \frac{2K_{ab}}{U} \qquad (f \geq -1) \quad (1.76)$$

where $f \geq -1$ due to assuming a singlet ground state [$E(\mathrm{T}_1) \geq 0$] in Eq. (1.18). From this equation, $f$ decreases with increasing $y_0$, and thus, a molecule with a large $y_0$ value has the possibility to satisfy $2E(\mathrm{T}_1) \sim E(\mathrm{S}_1)$ or $2E(\mathrm{T}_1) < E(\mathrm{S}_1)$. The third term of Eq. (1.76) ($2K_{ab}/U$) is predicted to be small in most diradical molecules because $K_{ab}$ [= $(ab|ab)$] depends on the spatial overlap between the unpaired electrons (short-range interaction) though $U$ [= $(aa|aa)$ – $(aa|bb)$] does on the Coulomb interaction between them (long-range interaction). This prediction – small $2K_{ab}/U$ – seems to be satisfied for alternant hydrocarbons since $K_{ab}$ is expected to be quite small, due to the pairing theorem in the HOMO and LUMO, which leads to the negligible overlap between the corresponding LNOs (in other words, a large $K_{gu}^{\mathrm{M}}$ and small $J_{gg}^{\mathrm{M}} + J_{uu}^{\mathrm{M}} - 2J_{gu}^{\mathrm{M}}$ (Eqs. (1.16) and (1.17)). In fact, $U$ and $K_{ab}$ of anthracene are estimated to be 2.07 eV and 0.03 eV, respectively, at the CASCI/6-31G* level of theory with two-active electrons in two active orbitals by using Eqs. (1.16) and (1.17). In such cases, $y_0$ is found to be the controlling factor of one of the energy level matching conditions, $2E(\mathrm{T}_1) \sim E(\mathrm{S}_1)$ or $2E(\mathrm{T}_1) < E(\mathrm{S}_1)$. By assuming one of the energy level matching conditions ($f \sim 0$ or $f < 0$), we obtain

$$E(\mathrm{S}_1) \sim 2U \text{ and } E(\mathrm{T}_1) \sim U \text{ or } E(\mathrm{S}_1) \sim 2U \text{ and } E(\mathrm{T}_1) < U, \quad (1.77)$$

which is derived from the functional forms of $U$ [= $E(\mathrm{S}_1) - E(\mathrm{T}_1)$] and the energy level matching condition [= $2E(\mathrm{T}_1) - E(\mathrm{S}_1) \sim 0$ or $< 0$]. This implies that $U$ is the maximum limit of $E(\mathrm{S}_1)$ and $E(\mathrm{T}_1)$ for a SF molecule. Thus, for typical SF molecules possessing appropriate $E(\mathrm{T}_1)$ of ~1 eV [95, 96], the third term of Eq. (1.76) ($2K_{ab}/U$) should be small, due to the relatively large $U$ value. As a result, in such

systems, $y_0$ is expected to be an essential factor for tuning $f$ to satisfy the energy level matching condition, $f \sim 0$ or $f < 0$. Nevertheless, more recently, a breaking of the pairing theorem is presented as a novel path of satisfying the energy level matching condition ($2E(T_1) \sim E(S_1)$ or $2E(T_1) < E(S_1)$) by increasing the amplitude of third term ($2K_{ab}/U$). For example, it is found that anthracene, which is known not to satisfy the energy level matching condition, becomes a candidate for efficient SF by relevant multiple heteroatom (N and B atoms) substitution [116]. Such novel guidelines based on increasing exchange integral ($K_{ab}$) is expected to open a novel path to designing efficient SF molecules, which have relatively high $E(T_1)$ energies resulting in large open circuit voltage.

## 1.5 Summary

In this section, we explained the electronic structures of diradicaloids based on the diradical character, which is a key factor for describing the ground and excited states. By the VCI method using a two-site diradical model with two electrons in two orbitals, the excitation energies and properties (transition moment and dipole moment) are found to be described as a function of diradical character in the ground state. The diradical character is not an observable, but a well-defined index in quantum chemistry, and has a meaning of "bond weakness" in chemistry and "electron correlation" in physics. Therefore, systems can be classified by the diradical character, i.e. $y_0 \sim 0$ (closed-shell), $0 < y_0 < 1$ (intermediate diradical (diradicaloid)), and $y_0 \sim 1$ (pure diradical), and the diradical character is closely related to the structure, reactivity and property of the system as shown in Figure 1.33. Such diradical-character-based description of chemical/physical quantities for diradicaloids has the advantage of easy intuitive understanding of the electronic structures of the systems and affinity with conventional chemical concepts, e.g. resonance structures, aromaticity, and MO pictures. This also implies that such description is useful for constructing rational design principles for efficient functional molecular systems, since experimentalists can easily understand and employ the design principles based on the chemical concepts.

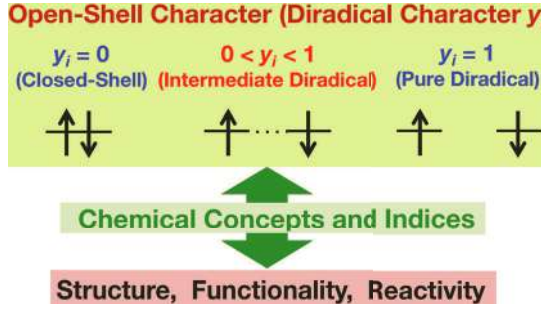


**Figure 1.33** Open-shell-character-based design for structure, reactivity, and property of molecular systems.

Indeed, we pioneered a novel class of NLO systems with open-shell singlet nature, which is referred to as "open-shell NLO systems" and could be superior to conventional closed-shell NLO systems. Further, we found that systems with intermediate open-shell character exhibit larger NLO properties than closed-shell and pure open-shell systems. This new principle is applied to designing realistic molecules, e.g. using the resonance structures with quinoid and benzenoid forms, and such designed molecules are experimentally found to exhibit extraordinary NLO properties. The principle has a wide range of applicability, i.e. from organic to inorganic molecular systems, e.g. polycyclic hydrocarbons including graphenes and fullerenes, the heavier main group compounds and transition-metal–metal bonded systems. A variety of design guidelines for enhancing/controlling NLO properties of these systems have been presented by modifying architectures and size, chemical substitutions, application of external electric field, and solvation.

Another example is a molecular design of efficient SF. Using the full-CI linear $H_4$ model, we have elucidated the SF feasibility region on the $y_0$-$y_1$ map and have classified SF molecules into class I–III. From the analysis of plotting known SF molecules and other possible candidates on the $y_0$-$y_1$ map, it is found that molecules having small diradical character ($0 < y_0 < \sim 0.5$) and much smaller tetraradical character ($y_1/y_0 < \sim 0.2$) tend to satisfy the energy level matching conditions ($E(S_1) \sim$ or $> 2E(T_1)$ and $E(T_2) > 2E(T_1)$). From this guideline, several novel SF candidate molecules have been proposed

and furthermore a novel design principle for efficient SF systems with higher triplet energies has been presented based on the analytical expressions of the energy level matching condition as a function of diradical character and dimensionless exchange integral. These principles are employed for designing practical molecules with the aid of conventional chemical concepts and indices such as resonance structures, including closed-shell and open-shell resonance forms with Clar's sextet rule, aromaticity/antiaromaticity, pairing theorem in alternant hydrocarbons, captodative effects by heteroatom substitution, etc.

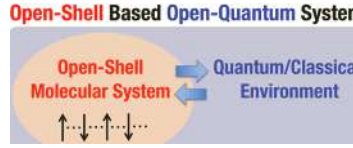


**Figure 1.34** Open-shell-based open-quantum system as a novel class of systems with dynamic high functionalities.

As seen from the above two examples, the diradical-character-based design principles can be used for physicochemical phenomena concerning the energies and properties of the ground and excited states. For example, open-shell-character-based analysis and design scheme will be useful for constructing triplet-triplet annihilation (TTA) materials, the process of which is an opposite to SF process, single molecule conductors, molecular magnets, magnetooptical materials, and so on. As mentioned before, the advantage of using diradical-character-based schemes exist in obtaining the pictures based on conventional chemical concepts and chemical indices that most of chemists are familiar with. Furthermore, the diradical/ionic-character-based analysis scheme presented in Section 1.2.5 is expected to be extended to dynamical behaviors, as it is applicable to any quantum superposition of the ground and plural excited states. As a result, this could contribute to analysis and construction of design principles of dynamical functionalities and time evolution of coherency and/or relaxation process of the open quantum system composed of open-shell molecular units interacting with environments (Figure 1.34). Thus, the open-shell-character-based analysis and design principles will provide novel chemical concepts

and indices, which chemists can easily understand and utilize, not only for static quantum functional materials, but also for future quantum information materials and their dynamical quantum processes.

## Acknowledgments

This work is supported by JSPS KAKENHI Grant Number JP18H01943 in Scientific Research (B), Grant Number JP20K21173 for Challenging Research (Exploratory), Center for Spintronics Research Network (CSRN), Center for Quantum Information and Quantum Biology (QIQB), and Innovative Catalysis Science (ICS) Division, Institute for Open and Transdisciplinary Research Initiatives (OTRI), Osaka University. Theoretical calculations are partly performed using the Research Center for Computational Science, Okazaki, Japan.

## References

1. Salem, L. and Rowland, C. (1972). The electronic properties of diradicals, *Angew. Chem., Int. Ed.,* **11**, pp. 92–111.
2. Borden, W. T. (ed.) (1982) *Diradicals*, Wiley, New York.
3. Bonačić-Koutecký, V., Koutecký, J., and Michl, J. (1987). Neutral and charged biradicals, zwitterions, funnels in $S_1$, and proton translocation: Their role in photochemistry, photophysics, and vision, *Angew. Chem. Int. Ed.,* **26**, pp. 170–189.
4. Szabo, A. and Ostlund, N. S. (1996). Modern quantum chemistry: Introduction to advanced electronic structure theory, Dover Publications, New York.
5. Hayes, E. F. and Siu, A. K. Q. (1971). Electronic structure of the open forms of three-membered rings, *J. Am. Chem. Soc.*, **93**, pp. 2090–2091.
6. Yamaguchi, K. (1975). The electronic structures of biradicals in the unrestricted Hartree–Fock approximation, *Chem. Phys. Lett.*, **33**, pp. 330–335.
7. Nakano, M. (2014). Excitation energies and properties of open-shell singlet molecules, Springer International Publishing.
8. Nakano, M. (2017). Open-shell-character-based molecular design principles: Applications to nonlinear optics and singlet fission, *Chem. Rec.,* **17**, pp. 27–62.

9. Calzado, C. J., Cabrero, J., Malrieu, J. P., and Caballol, R. (2002). Analysis of the magnetic coupling in binuclear complexes. I. Physics of the coupling, *J. Chem. Phys.*, **116**, pp. 2728–2747.
10. Nakano, M., Kishi, R., Ohta, S., Takahashi, H., Kubo, T., Kamada, K., Ohta, K., Botek, E., and Champagne, B. (2007). Relationship between third-order nonlinear optical properties and magnetic interactions in open-shell systems: A new paradigm for nonlinear optics, *Phys. Rev. Lett.*, **99**, 033001–1–4.
11. Minami, T., Ito, S., and Nakano, M. (2013). Signature of singlet open-shell character on the optically allowed singlet excitation energy and singlet–triplet energy gap, *J. Phys. Chem. A*, **117**, 2000–2006.
12. Yamaguchi, K. (1990), Self-consistent field: Theory and application, Carbo, R. and Klobukowski, M. (ed.), "Instability of chemical bonding", Elsevier, Amsterdam, pp. 727–823.
13. Miyoshi, H., Miki, M., Hirano, S., Shimizu, A., Kishi, R., Fukuda, K., Shiomi, D., Sato, K., Takui, T., Hisaki, I., Nakano, M., and Tobe, Y. (2017). Fluoreno[2,3-*b*]fluorene vs indeno[2,1-*b*]fluorene: Unusual relationship between the number of π electrons and excitation energy in *m*-quinodimethane-type singlet diradicaloids, *J. Org. Chem.,* **82**, pp. 1380–1388.
14. Heisenberg, W. (1928). Zur theorie des ferromagnetismus, *Z. Phys.*, **49**, pp. 619–636.
15. Dressler, J., Teraoka, M., Espejo, G. L., Kishi, R., Takamuku, S., Gómez-García, C., Zakharov, L., Nakano, M., Cordon, J. C., and Haley, M. (2018). Thiophene and its sulfur inhibit indenoindenodibenzothiophene diradicals from low-energy lying thermal triplets, *Nat. Chem.,* **10**, pp. 1134–1140.
16. Rudebusch, G. E., Zafra, J. L., Jorner, K., Fukuda, K., Marshall, J. L., Arrechea-Marcos, I., Espejo, G. L., Ponce Ortiz, R., Gómez-García, C. J., Zakharov, L. N., Nakano, M., Ottosson, H., Casado, J., and Haley, M. M. (2016). Diindeno-fusion of an anthracene as a design strategy for stable organic biradicals, *Nat. Chem.,* **8**, pp. 753–759.
17. Baird, N. C. (1972). Quantum organic photochemistry. II. Resonance and aromaticity in the lowest 3ππ* state of cyclic hydrocarbons, *J. Am. Chem. Soc.*, **94**, pp. 4941–4948.
18. Nakano, M. and Champagne, B. (2013). Diradical character dependences of the first and second hyperpolarizabilities of asymmetric open-shell singlet systems, *J. Chem. Phys.*, **138**, pp. 244306–1–13.
19. Nakano, M., Fukuda, K., and Champagne, B. (2016). Third-order nonlinear optical properties of asymmetric non-alternant open-

shell condensed-ring hydrocarbons: Effects of diradical character, asymmetricity, and exchange interaction, *J. Phys. Chem. C*, **120**, pp. 1193–1207.

20. Takatsuka, K., Fueno, T., and Yamaguchi, K. (1978). Distribution of odd electrons in ground-state molecules, *Theor. Chim. Acta.*, **48**, pp. 175–183.
21. Head-Gordon, M. (2003). Characterizing unpaired electrons from the one-particle density matrix, *Chem. Phys. Lett.*, **372**, pp. 508–511.
22. Kubo, T., Shimizu, A., Sakamoto, M., Uruichi, M., Yakushi, K., Nakano, M., Shiomi, D., Sato, K., Takui, T., Morita, Y., and Nakasuji, K. (2005). Synthesis, intermolecular interaction, and semiconductive behavior of a delocalized singlet biradical hydrocarbon, *Angew. Chem. Int. Ed.*, **44**, pp. 6564–6568.
23. Sun, Z., Ye, Q., Chi, C., and Wu, J. (2012). Low band gap polycyclic hydrocarbons: From closed-shell near infrared dyes and semiconductors to open-shell radicals, *Chem. Soc. Rev.*, **41**, pp. 7857–7889.
24. Abe, M. (2013). Diradicals, *Chem. Rev.*, **113**, pp. 7011–7088.
25. Cotton, F. A., Murillo, C. A., and Walton, R. A. (2005). Multiple bonds between metal atoms, 3rd Ed., Springer, New York, USA.
26. Sun, Z., Zeng, Z., and Wu, J. (2014). Zethrenes, extended *p*-quinodimethanes, and periacenes with a singlet biradical ground state, *Acc. Chem. Res.*, **47**, pp. 2582–2591.
27. Parkin, G. (ed.) (2010). Metal-metal bonding, Springer, Heidelberg.
28. Breher, F. (2007). Stretching bonds in main group element compounds–borderlines between biradicals and closed-shell species, *Coord. Chem. Rev.*, **251**, pp. 1007–1043.
29. Huang, J. and Kertesz, M. (2007). Intermolecular covalent π-π bonding interaction indicated by bond distances, energy bands, and magnetism in biphenalenyl biradicaloid molecular crystal, *J. Am. Chem. Soc.*, **129**, pp. 1634–1643.
30. Kertesz, M. (2018). Pancake bonding: An unusual π–stacking interaction, **25**, pp. 400–416.
31. Nakano, M., Fukuda, K., Ito, S., Matsui, H., Nagami, T., Takamuku, S., Kitagawa, Y., and Champagne, B. (2017). Diradical and ionic characters of open-shell singlet molecular systems, *J. Phys. Chem. A*, **121**, pp. 861–873.
32. Yoneda, K., Nakano, M., Fukuda, K., Matsui, H., Takamuku, S., Hirosaki, Y., Kubo, T., Kamada, K., and Champagne, B. (2014). Third-order

nonlinear optical properties of one-dimensional open-shell molecular aggregates composed of phenalenyl radicals, *Chem.-Eur. J.,* **20**, pp. 11129–11136.

33. Lambert, C. (2011). Towards polycyclic aromatic hydrocarbons with a singlet open-shell ground state, *Angew. Chem., Int. Ed.*, **50**, pp. 1756–1758.
34. Sun, Z. and Wu, J. (2012). Open-shell polycyclic aromatic hydrocarbons, *J. Mater. Chem.,* **22**, pp. 4151–4160.
35. Sun, Z., Zeng, Z., and Wu, J. (2013). Benzenoid polycyclic hydrocarbons with an open–shell biradical ground state, *Chem.–Asian J.*, **8**, pp. 2894–2904.
36. Kubo, T. (2015). Recent progress in quinoidal singlet biradical molecules, *Chem. Lett.*, **44**, pp. 111–122.
37. Tobe, Y. and Kubo, T. (eds.) (2018). Physical organic chemistry of quinodimethanes, Springer International Publishing.
38. Kamada, K., Ohta, K., Shimizu, A., Kubo, T., Kishi, R., Takahashi, H., Botek, E., Champagne, B., and Nakano, M. (2010). Singlet diradical character from experiment, *J. Phys. Chem. Lett.*, **1**, pp. 937–940.
39. Yamanaka, S., Okumura, M., Nakano, M., and Yamaguchi, K. (1994). EHF theory of chemical reactions Part 4. UNO CASSCF, UNO CASPT2 and R(U)HF coupled-cluster (CC) wavefunctions, *J. Mol. Structure (Theochem)*, **310**, pp. 205–218.
40. Kitagawa, Y., Saito, T., Nakanishi, Y., Kataoka, Y., Matsui, T., Kawakami, T., Okumura, M., and Yamaguchi, K. (2009). Spin contamination error in optimized geometry of singlet carbene ($^1A_1$) by broken-symmetry method, *J. Phys. Chem. A*, **113**, pp. 15041–15046.
41. Nakano, M. (2017). Electronic structure of open-shell singlet molecules: Diradical character viewpoint, *Top. Curr. Chem.,* **375**, pp. 47.
42. Nakano, M., Fukui, H., Minami, T., Yoneda, K., Shigeta, Y., Kishi, R., Champagne, B., Botek, E., Kubo, T., Ohta, K., and Kamada, K. (2011). (Hyper)polarizability density analysis for open-shell molecular systems based on natural orbitals and occupation numbers, *Theoret. Chem. Acc.*, **130**, pp. 711–724; *erratum,* **130**, pp. 725.
43. Minkin, V. I., Glukhovtsev, M. N., and Simkin, B. Y. (1994). Aromaticity and antiaromaticity, John Wiley & Sons, New York.
44. Schleyer, P. v. R. (guest ed.) (2001). Special issue on aromaticity, *Chem. Rev.,* **101**, pp. 1115–1566.

45. Kertesz, M., Choi, C. H., and Yang, S. (2005). Conjugated polymers and aromaticity, *Chem. Rev.*, **105**, pp. 3448–3481.
46. Kruszewski, J. and Krygowski, T. M. (1972). Definition of aromaticity basing on the harmonic oscillator model, *Tetrahedron Lett.*, **13**, pp. 3839–3842.
47. Aihara, J. (1976). A new definition of dewar-type resonance energies, *J. Am. Chem. Soc.*, **98**, pp. 2750–2758.
48. Chen, Z., Wannere, C. S., Corminboeuf, C., Puchta, R., and Schleyer, P. v. R. (2005). Nucleus-independent chemical shifts (NICS) as an aromaticity criterion, *Chem. Rev.*, **105**, pp. 3842–3888.
49. Lazzeretti, P. (2004). Assessment of aromaticity via molecular response properties, *Phys. Chem. Chem. Phys.,* **6**, pp. 217–223.
50. Jahn, H. A. and Teller, E. (1937). Stability of polyatomic molecules in degenerate electronic states - I–Orbital degeneracy, *Proc. R. Soc. (London)*, **A161**, pp. 220–235.
51. Lazzeretti, P. (2000). Ring currents, *Prog. Nucl. Magn. Reson. Spectrosc.*, **36**, pp. 1–88.
52. Feixas, F., Matto, E., Poater, J., and Solà, M. (2008). On the performance of some aromaticity indices: A critical assessment using a test set, *J. Comput. Chem.*, **29**, pp. 1543–1554.
53. Monaco, G., Zanasi, R., Pelloni, S., and Lazzeretti, P. (2010). Relative weights of σ and π ring currents in a few simple monocycles, *J. Chem. Theory Comput.***, 6**, pp. 3343–3351.
54. Motomura, S., Nakano, M., Fukui, H., Yoneda, K., Kubo, T., Carion, R., and Champagne, B. (2011). Size dependences of the diradical character and the second hyperpolarizabilities in dicyclopenta-fused acenes: Relationships with their aromaticity/antiaromaticity, *Phys. Chem. Chem. Phys.*, **13**, pp. 20575–20583.
55. Fukuda, K., Nagami, T., Fujiyoshi, J., and Nakano, M. (2015). Interplay between open-shell character, aromaticity, and second hyperpolarizabilities in indenofluorenes, *J. Phys. Chem. A*, **119**, pp. 10620–10627.
56. Jonas, J., Sundholm, D., and Jürgen, G. (2004). Calculation of current densities using gauge-including atomic orbitals, *J. Chem. Phys.*, **121**, pp. 3952–3963.
57. Taubert, S., Sundholm, D., and Jusélius, J. (2011). Calculation of spin-current densities using gauge-including atomic orbitals, *J. Chem. Phys.*, **134**, 054123.

58. Fliegl, H., Taubert, S., Lehtonen, O., and Sundholm, D. (2011). The gauge including magnetically induced current method, *Phys. Chem. Chem. Phys.*, **13**, pp. 20500–20518.

59. Rauhalahti, M., Taubert, S., Sundholm, D., and Liégeois, V. (2017). Calculations of current densities for neutral and doubly charged persubstituted benzenes using effective core potentials, *Phys. Chem. Chem. Phys.*, **19**, pp. 7124–7131.

60. Nagami, T., Fujiyoshi, J., Tonami, T., Watanabe, K., Okada, K., Kishi, R., Nakano, M., Champagne, B., and Liégeois, V. (2018). Evaluation of aromaticity for open-shell singlet dicyclopenta-fused acenes and polyacenes based on magnetically induced current, *Chem, Eur. J.,* **24**, pp. 13457–13466.

61. Nakano, M. and Champagne, B. (2015). Theoretical design of open-shell singlet molecular systems for nonlinear optics, *J. Phys. Chem. Lett.,* **6**, pp. 3236–3256.

62. Nakano, M. and Champagne, B. (2016). Nonlinear optical properties in open-shell molecular systems, *WIREs Comput. Mol. Sci.*, **6**, pp. 198–210.

63. Burland, D. (ed.) (1994). Special issue on optical nonlinearities in chemistry, *Chem. Rev*., **94**, pp. 1–278.

64. Nalwa, H. S. and Miyata, S. (eds.) (1997). Nonlinear optics of organic molecules and polymers, CRC, Boca Raton, FL.

65. Nalwa, H. S. (ed.) (2001). Handbook of advanced electronic and photonic materials and devices 9, Academic Press, New York.

66. Pathenopoulos, D. A. and Rentzepis, P. M. (1989). Three-dimensional optical storage memory, *Science*, **245**, pp. 843–845.

67. Albota, M. A., Beljonne, D., Brédas, J. L., Ehrlich, J. E., Fu, J. Y., Heikal, A. A., Hess, S., Kogej, T., Levin, M. D., Marder, S. R., McCord-Maughon, D., Perry, J. W., Röckel, H., Rumi, M., Subramaniam, G., Webb, W. W., Wu, X.-L., and Xu, C. (1998). Design of organic molecules with large two-photon absorption cross sections, *Science*, **281**, pp. 1653–1656.

68. Spangler, C. W. (1999). Recent development in the design of organic materials for optical power limiting, *J. Mater. Chem.*, **9**, pp. 2013–2020.

69. 69. Cumpston, B. H., Ananthavel, S. P., Barlow, S., Dyer, D. L., Ehrlich, J. E., Erskine, L. L., Heikal, A. A., Kuebler, S. M., Lee, I.-Y. S., McCord-Maughon, D. J., Qin, J., Röckel, H., Rumi, M., Wu, X.-L., Marder, S. R., and Perry, J. W. (1999). Two-photon polymerization initiators for three-dimensional optical data storage and microfabrication, *Nature*, **398**, pp. 51–54.

70. Kawata, S., Sun, H.-B., Tanaka, T., and Takada, K. (2001). Finer features for functional microdevices, *Nature*, **412**, pp. 697–698.

71. Zhou, W., Kuebler S. M., Braun, K. L., Yu, T., Cammack, J. K., Ober, C. K., Perry, J. W., and Marder, S. R. (2002). An efficient two-photon-generated photoacid applied to positive-tone 3D microfabrication, *Science*, **296**, pp. 1106–1109.

72. Nakano, M., Kishi, R., Nitta, T., Kubo, T., Nakasuji, K., Kamada, K., Ohta, K., Champagne, B., Botek, E., and Yamaguchi, K. (2005). Second hyperpolarizability (γ) of singlet diradical system: Dependence of γ on the diradical character, *J. Phys. Chem. A*, **109**, pp. 885–891.

73. Kamada, K., Ohta, K., Kubo, T., Shimizu, A., Morita, Y., Nakasuji, K., Kishi, R., Ohta, S., Furukawa, S., Takahashi, H., and Nakano, M. (2007). Strong two-photon absorption of singlet diradical hydrocarbons, *Angew. Chem. Int. Ed.*, **46**, pp. 3544–3546.

74. Kishida, H., Hibino, K., Nakamura, A., Kato, D., and Abe, J. (2010). Third-order nonlinear optical properties of a pi-conjugated biradical molecule investigated by third-harmonic generation spectroscopy, *Thin Solid Films*, **519**, pp. 1028–1030.

75. Ishida, M., Shin, J.-Y., Lim, J. M., Lee, B. S., Yoon, M.-C., Koide, T., Sessler, J. L., Osuka, A., and Kim, D. (2011). Neutral radical and singlet biradical forms of meso-free, -keto, and -diketo hexaphyrins(1.1.1.1.1.1): Effects on aromaticity and photophysical properties, *J. Am. Chem. Soc.*, **133**, pp. 15533–15544.

76. Kamada, K., Fuku-en, S.-I., Minamide, S., Ohta, K., Kishi, R., Nakano, M., Matsuzaki, M., Okamoto, H., Higashikawa, H., Inoue, K., Kojima, S., and Yamamoto, Y. (2013). Impact of diradical character on two-photon absorption: Bis(acridine) dimers synthesized from an allenic precursor, *J. Am. Chem. Soc.*, **135**, pp. 232–241.

77. Nakano, M. and Yamaguchi, K. (1993). A proposal of new organic third-order nonlinear optical compounds, Centrosymmetric systems with large negative third-order hyperpolarizabilities, *Chem. Phys. Lett.*, **206**, pp. 285–292.

78. Nakano, M., Yoneda, K., Kishi, R., Takahashi, H., Kubo, T., Kamada, K., Ohta, K., Botek, E., and Champagne, B. (2009). Remarkable two-photon absorption in open-shell singlet systems, *J. Chem. Phys.*, **131**, pp. 114316–1–7.

79. Nakano, M. and Champagne, B. (2015). Diradical character dependence of third-harmonic generation spectra in open-shell singlet systems, *Theoret. Chem. Acc.*, **134**, pp. 23–1–9.

80. Clar, E. (1972). The aromatic sextet, Wiley, New York.

81. Nakano, M., Nakagawa, N., Kishi, R., Ohta, S., Nate, M., Takahashi, H., Kubo, T., Kamada, K., Ohta, K., Champagne, B., Botek, E., Morita, Y., Nakasuji, K., and Yamaguchi, K. (2007). Second hyperpolarizabilities of singlet polycyclic diphenalenyl radicals: Effects of the nature of the central heterocyclic ring and substitution to diphenalenyl rings, *J. Phys. Chem. A*, **111**, pp. 9102–9110.

82. Nakano, M., Kishi, R., Takebe, A., Nate, M., Takahashi, H., Kubo, T., Kamada, K., Ohta, K., Champagne, B., and Botek, E. (2007). Second hyperpolarizability of zethrenes, *Computing Letters*, **3**, pp. 333–338.

83. Ohta, S., Nakano, M., Kubo, T., Kamada, K., Ohta, K., Kishi, R., Nakagawa, N., Champagne, B., Botek, E., Takebe, A., Umezaki, S., Nate, M. Takahashi, H., Furukawa, S., Morita, Y., Nakasuji, K., and Yamaguchi, K. (2007). Theoretical study on the second hyperpolarizabilities of phenalenyl radical systems involving acetylene and vinylene linkers: Diradical character and spin multiplicity dependences, *J. Phys. Chem. A*, **111**, pp. 3633–3641.

84. Nakano, M., Nagai, H., Fukui, H., Yoneda, K., Kishi, R., Takahashi, H., Shimizu, A., Kubo, T., Kamada, K., Ohta, K., Champagne, B., and Botek, E. (2008). Theoretical study of third-order nonlinear optical properties in square nanographenes with open-shell singlet ground states, *Chem. Phys. Lett.*, **467**, pp. 120–125.

85. Nagai, H., Nakano, M., Yoneda, K., Fukui, H., Minami, T., Bonness, S., Kishi, R., Takahashi, H., Kubo, T., and Kamada, K. (2009), Theoretical study on third-order nonlinear optical properties in hexagonal graphene nanoflakes: Edge shape effect, *Chem. Phys. Lett.*, **477**, pp. 355–359.

86. Yoneda, K., Nakano, M., Kishi, R., Takahashi, H., Shimizu, A., Kubo, T., Kamada, K., Ohta, K., Champagne, B., and Botek, E. (2009). Third-order nonlinear optical properties of trigonal, rhombic and bow-tie graphene nanoflakes with strong structural dependence of diradical character, *Chem. Phys. Lett.*, **480**, pp. 278–283.

87. Yoneda, K., Nakano, M., Inoue, Y., Inui, T., Fukuda, K., Shigeta, Y., Kubo, T., and Champagne, B. (2012). Impact of antidot structure on the multiradical characters, aromaticities and third-order nonlinear optical properties of hexagonal graphene nanoflakes, *J. Phys. Chem. C*, **116**, pp. 17787–17795.

88. Muhammad, S., Fukuda, K., Minami, T., Kishi, R., Shigeta, Y., and Nakano, M. (2013). Interplay between diradical characters and third-order nonlinear optical properties in fullerene systems, *Chem.–Eur. J.*, **19**, pp. 1677–1685.

89. Muhammad, S., Ito, S., Nakano, M., Kishi, R., Yoneda, K., Kitagawa, Y., Shkir, M., Irfan, A., Chaudhry, A. R., AlFaify, S., Kalamd, A., and Al-Sehemi, A. G. (2015). Diradical character and nonlinear optical properties of buckyferrocenes: Focusing on the use of suitably modified fullerene fragments, *Phys. Chem. Chem. Phys.*, **17**, pp. 5805–5816.

90. Singh, S., Jones, W. J., Siebrand, W., Stoicheff, B. P., and Schneider, W. G. (1965). Laser generation of excitons and fluorescence in anthracene crystals, *J. Chem. Phys.*, **42**, pp. 330–342.

91. Swenberg, C. E. and Stacy, W. T. (1968). Bimolecular radiationless transitions in crystalline tetracene, *Chem. Phys. Lett.*, **2**, pp. 327–328.

92. Nozik, A. J., Ellingson, R. J., Mićić, O. I., Blackburn, J. L., Yu, P., Murphy, J. E., Beard, M. C., and Rumbles, G. (2004). Unique approaches to solar photon conversion based on semiconductor nanostructures and novel molecular chromophores, dynamics of electron relaxation, interfacial charge transfer, and carrier multiplication, *Proc. 27th DOE Solar Photochem. Res. Conf.,* pp. 63–66, Washington, DC, US Dep. Energy.

93. Hanna, M. C. and Nozik, A. J. J. (2006). Solar conversion efficiency of photovoltaic and photoelectrolysis cells with carrier multiplication absorbers, *Appl. Phys.*, **100**, pp. 074510–1–8.

94. Shockley, W. and Queisser, H. J. (1961). Detailed balance limit of efficiency of p-n junction solar cells, *J. Appl. Phys.*, **32**, pp. 510–519.

95. Smith, M. B. and Michl, J. (2010). Singlet fission, *Chem. Rev.*, **110**, pp. 6891–6936.

96. Smith, M. B. and Michl, J. (2013). Recent advances in singlet fission, *Annu. Rev. Phys. Chem.*, **64**, pp. 361–386.

97. Piland, G. B., Burdett, J. J., Dillon, R. J., and Bardeen, C. J. (2014). Singlet fission: From coherences to kinetics, *J. Phys. Chem. Lett.*, **5**, pp. 2312–2319.

98. Casanova, D. (2018). Theoretical modeling of singlet fission, *Chem. Rev.*, **118**, pp. 7164–7207.

99. Ito, S., Nagami, T., and Nakano, M. (2018). Molecular design for efficient singlet fission, *J. Photochem. Photobiol. C Photochem. Rev.*, **34**, pp. 85–120.

100. Japahuge, A. and Zeng, T. (2018). Theoretical studies of singlet fission: Searching for materials and exploring mechanisms, *ChemPlusChem*, **83**, pp. 146–182.

101. Miyata, K., Conrad-Burton, F. S., Geyer, F. L., and Zhu, X. Y. (2019). Triplet pair states in singlet fission, *Chem. Rev.*, **119**, pp. 4261–4292.

102. Minami, T. and Nakano, M. (2012). Diradical character view of singlet fission, *J. Phys. Chem. Lett.*, **3**, pp. 145–150.

103. Minami, T., Ito, S., and Nakano, M. (2013). Fundamental of diradical-character-based molecular design for singlet fission, *J. Phys. Chem. Lett.*, **4**, pp. 2133–2137.

104. Nakano, M., Minami, T., Fukui, H., Kishi, R., Shigeta, Y., and Champagne, B. (2012). Full configuration interaction calculations of the second hyperpolarizabilities of the $H_4$ model compound: summation-over-states analysis and interplay with diradical characters, *J. Chem. Phys.*, **136**, pp. 0243151–1–7.

105. Minami, T., Ito, S., and Nakano, M. (2012). Theoretical study of singlet fission in oligorylenes, *J. Phys. Chem. Lett.,* **3**, pp. 2719–2723.

106. Eaton, S. W., Miller, S. A., Margulies, E. A., Shoer, L. E., Schaller, R. D., and Wasielewski, M. R. (2015). Singlet exciton fission in thin films of *tert*-butyl-substituted terrylenes, *J. Phys. Chem. A*, **119**, pp. 4151–4161.

107. Berkelbach, T. C., Hybertsen, M. S., and Reichman, D. R. (2013). Microscopic theory of singlet exciton fission. I. General formulation, *J. Chem. Phys.*, **138**, pp. 114102–1–16.

108. Berkelbach, T. C., Hybertsen, M. S., and Reichman, D. R. (2013). Microscopic theory of singlet exciton fission. II. Application to pentacene dimers and the role of superexchange, *J. Chem. Phys.*, **138**, pp. 114103–1–12.

109. Berkelbach, T. C., Hybertsen, M. S., and Reichman, D. R. (2014). Microscopic theory of singlet exciton fission. III. Crystalline pentacene, *J. Chem. Phys.*, **141**, pp. 074705–1–12.

110. Tao, G. (2018). Bath effect in singlet fission dynamics, *J. Phys. Chem. C*, **118**, pp. 27258–27264.

111. Renaud, N. and Grozema, F. C. (2015). Intermolecular vibrational modes speed up singlet fission in perylenediimide crystals, *J. Phys. Chem. Lett.*, **6**, pp. 360–365.

112. Miyata, K., Kurashige, Y., Watanabe, K., Sugimoto, T., Takahashi, S., Tanaka, S., Takeya, J., Yanai, T., and Matsumoto, Y. (2017). Coherent singlet fission activated by symmetry breaking, *Nat. Chem.*, **9**, pp. 983–989.

113. Nakano, M., Ito, S., Nagami, T., Kitagawa, Y., and Kubo, T. (2016). Quantum master equation approach to singlet fission dynamics of realistic/artificial pentacene dimer models: Relative relaxation factor analysis, *J. Phys. Chem. C*, **120**, pp. 22803–22815.

114. Nakano, M., Nagami, T., Tonami, T., Okada, K., Ito, S., Kishi, R., Kitagawa, Y., and Kubo, T. (2019). Quantum master equation approach to singlet fission dynamics in pentacene linear aggregate models: Size dependences of excitonic coupling effects, *J. Comput. Chem.*, **40**, pp. 89–104.

115. Nakano, M. (2019). Quantum master equation approach to singlet fission dynamics in pentacene ring-shaped aggregate models, *J. Chem. Phys.*, **150**, pp. 234305–1–18.

116. Nagami, T., Okada, K., Miyamoto, H., Yoshida, W., Tonami, T., and Nakano, M. (2020). Molecular design principle for efficient singlet fission based on diradical characters and exchange integrals: Multiple heteroatom substitution effect on anthracenes, *J. Phys. Chem. C*, **124**, pp. 11800–11809.

Chapter 2

# Electronic Structure Characterization of Diradicaloids with Spin-Flip (SF) Methods

**David Casanova**
*Donostia International Physics Center (DIPC),*
*Manuel de Lardizabal Pasealekua 4, 20018 Donostia,*
*Euskadi, Spain*
david.casanova@ehu.eus

## 2.1 Introduction

Diradicals are atomic or molecular species with two unpaired electrons [1] populating the degenerated (or near-degenerated) highest occupied molecular orbital (HOMO) and lowest unoccupied molecular orbital (LUMO). If the two radical centers significantly interact, the molecule is referred as a diradical-like or diradicaloid. For diradicaloids, the two frontier orbitals are energetically close, but not degenerated, with an electronic structure in between a diradical and a closed-shell molecule, i.e., with intermediate diradical character (Figure 2.1).

*Diradicaloids*
Edited by Jishan Wu

ISBN 978-981-4968-08-9 (Hardcover), 978-1-003-27724-8 (eBook)
www.jennystanford.com

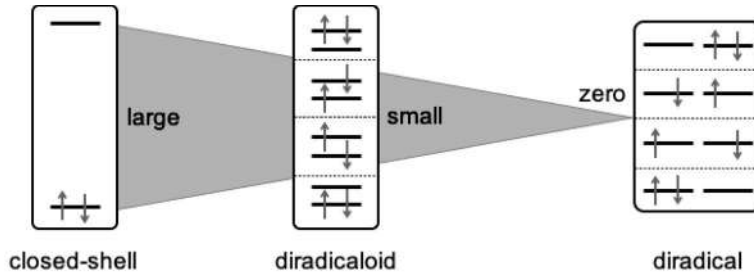


**Figure 2.1** Schematic representation of the transition between a closed-shell (left), diradicaloid (center), and diradical (right), with large, small, and zero HOMO-LUMO gaps, respectively, as represented by the gray triangular area. Low-energy configurations for the description of singlet states are indicated in each case.

As the present book highlights, diradicaloids are intriguing systems with fascinating properties. Their intricate electronic structure, small relative energies between the triplet and singlet states, tunable chemical stability, and rich reactivity pose great challenges to their theoretical and experimental characterization. Besides, lately there has been a revamping interest for the design of novel diradicaloids due to their potential applications in a variety of research fields, such as in molecular electronics [2, 3] and optoelectronics [4], nonlinear optics [5], magnetism [6], singlet fission [7–9], and activation of molecular hydrogen [10, 11].

The theoretical description and computational characterization of the electronic wave function and its properties in diradicals and diradicaloids are much more involved than for closed-shell systems. Near-degeneracies between occupied and virtual orbitals require more than one configuration to describe, even qualitatively, the wave functions of the lowest singlet states (static or non-dynamic correlation). As a consequence, the non-correlated (mean-field) Hartree-Fock (HF) model, resulting in a single determinant wave function (Slater determinant), is ill-qualified for the characterization of diradicals and diradicaloids. Moreover, traditional HF-based methods such as Møller-Plessed (MP) perturbation theory or truncated configuration interaction (CI) and coupled-cluster (CC) expansions, e.g., CC singles and doubles (CCSD), are not able to properly recover the strong electron correlation effects between unpaired electrons. The multi-configurational character of diradicaloids can be attained by multi-reference approaches [12,

13], that is wave function methods built from two or more Slater determinants, in which the important configurations are determined and chosen by the idiosyncrasy of the system under study. These methods typically belong to the multi-configurational self-consistent field (MCSCF) family, with the complete active space SCF (CASSCF) method [13–15] being one of the most relevant examples. The MCSCF wave functions accounting for non-dynamic correlations can be used as reference states for their posterior refinement through CI schemes, like in multi-reference CI (MRCI) [16, 17], or via multi-reference perturbation theory [18–20], like in complete active space second-order perturbation theory (CASPT2) [21–23], to include the missing (dynamic) electron correlation. The main limitation for the application of these methods is their computational demands, limiting their application to rather small molecules.

In principle, density functional theory (DFT) [24] provides an exact solution for the ground state of any given molecule. In practice, while available approximations to the energy functional within the Kohn-Sham (KS) formulation [25] are extremely efficient to deal with dynamic correlations between electrons, inexorably produce unphysical results in the case of strongly correlated electrons, e.g., diradicals and diradicaloids.

In this chapter, an alternative strategy is described to obtain multi-configurational wave functions, in particular in the description of diradicaloids, within the single-reference formalism combining a high-spin Slater determinant with a SF excitation operator, i.e., spin-α to spin-β electronic excitations. Also, the theoretical foundations of SF methods within wave function theories (WFTs) and DFT are presented. The performance of the SF methods, in particular the restricted active space CI SF (RASCI-SF or RAS-SF in short), will be illustrated by their application to the characterization of diradicals, diradicaloids, and polyradicaloids.

## 2.2 Theory of SF Methods

### 2.2.1 SF Methods to Describe Diradicals

The suitability of the (single-reference) SF ansatz in the characterization of diradicals and diradicaloids is based on two main aspects:

(i) high-spin states are properly described by a single determinant even in the presence of orbital near-degeneracies;
(ii) the SF excitation operator is very efficient in order to reach important configurations with two or more excited electrons.

These two points constitute the basis of the SF idea and its suitability to deal with strongly correlated systems, such as in diradicals and diradicaloids. Moreover, these two central elements will be rationalized through the electronic structure characterization of ethylene along its molecular torsion.

From a formal point of view, a diradical (two unpaired electrons) can be seen as the opposite extreme of the chemical bond (two paired electrons). Hence, bond-breaking processes, such as the stretching of a single bond or the torsion of a double bond, can be used to model the transition from a closed-shell system to a perfect diradical through a continuously increasing range of diradical character (diradicaloid region). The torsion of ethylene around the C=C central bond is the simplest example of the dissociation of a π-bond while preserving the σ-interaction.

At the planar ground state equilibrium geometry of ethylene the two frontier π-orbitals, that is, the HOMO and the LUMO, are respectively obtained as the in-phase (bonding) and out-of-phase (anti-bonding) combinations of the $2p_z$ atomic orbitals of the two $sp^2$ carbons (Figure 2.2). As a result of the strong π-interaction at the planar structure, the two orbitals are well separated in energy and the ground state is well described with a single (closed-shell) electronic configuration, i.e., the double occupancy of the HOMO (Figure 2.3a). The molecular torsion around the double bound weakens the strength of the π-interaction, and the gap between π and π* orbitals decreases. For dihedral angles approaching orthogonality, the two orbitals become close in energy, i.e., a situation depicted by strong electron correlation that can be associated to a system with a partial diradical character (diradicaloid). In this region, the small HOMO-to-LUMO gap facilitates the partial occupation of the LUMO, and the ground state singlet is no longer properly described by a single Slater determinant. As a consequence, the HF solution departs from the energy profile depicted by the exact ground state energy (full CI, FCI). At 90° torsion, the two frontier orbitals are degenerated and the ground state features a perfect diradical nature. Here, the

ground state singlet accommodates one electron on each of the two degenerated orbitals, and the exact wave function acquires two-configurational character. This situation cannot be described by a single Slater determinant and the HF energy explodes, exceeding the FCI isomerization barrier by several electron-volts.

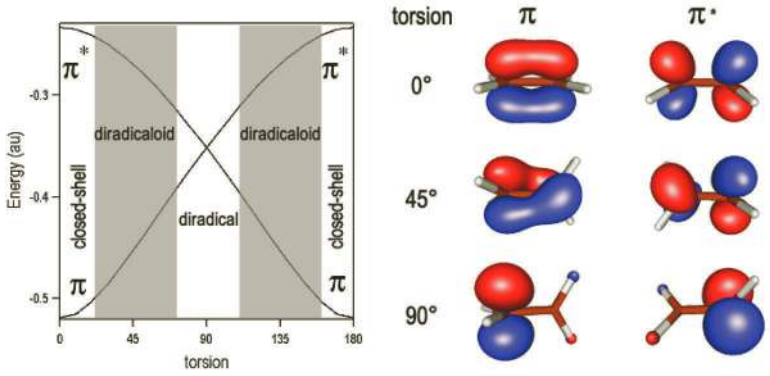


**Figure 2.2** Left: energy diagram of the frontier π-orbitals along the molecular torsion for the ethylene molecule. Right: representation of the π and π* at different torsion angles (0°, 45°, and 90°).

On the other hand, the orbital occupancy of the $M_S$ = 1 ($\alpha\alpha$) component of the triplet state $^3[(\pi)^1(\pi^*)^1]$ is not affected by the energy difference between the two orbitals. The high-spin triplet holds a single configuration character along the entire molecular torsion, and the quality of the HF wave function does not deteriorate, producing an almost perfectly parallel energy profile with respect to FCI (Figure 2.3b).

The SF methods take advantage of the well-behaved high-spin determinant in the presence of near-degeneracies and use it as the starting (reference) configuration to compute ground and excited electronic states by applying an excitation operator, i.e., excitations of spin-$\alpha$ electrons to empty spin-$\beta$ orbitals. Interestingly, the action of the SF operator on the high-spin configuration is able to generate all the low-energy configurations necessary for the description of the ground and low-lying states. Mean-field theories, such as HF, are not only unable to describe the ground state of a diradicaloid, as in the distorted ethylene molecule, but also fail in the characterization of the low-lying electronic transitions. Single electron excitations

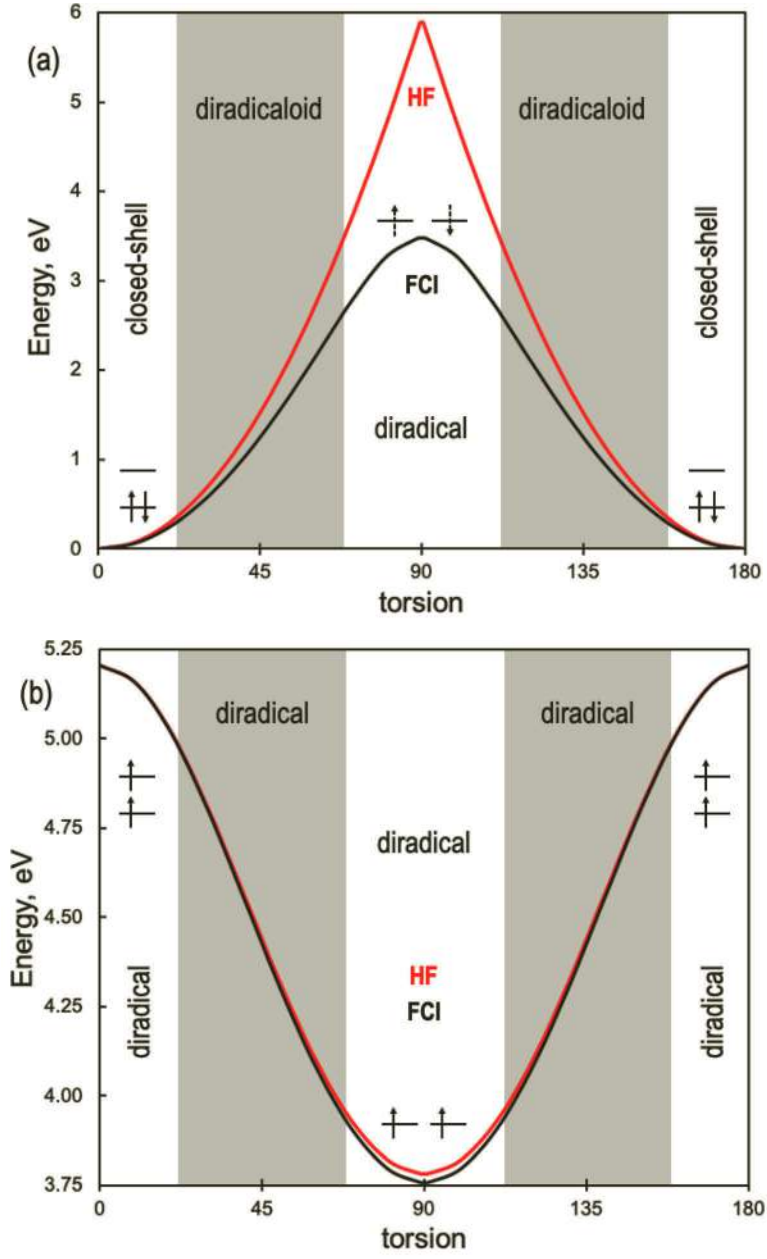


**Figure 2.3** Ground state singlet (a) and triplet (b) energy profiles along the molecular torsion for the ethylene molecule computed with FCI (black) and HF (red) with the STO-3G basis set. HF energy curves have been displaced to match the FCI energy at the planar geometry.

produce the two open-shell configurations in ethylene, i.e., $(\pi)^1(\pi^*)^1$, but miss the $(\pi^*)^2$ configuration (Figure 2.4a), which strongly mixes with $(\pi)^2$ for small HOMO-LUMO gaps. On the contrary, the SF flavor of the single excitation operator generates all four configurations within the two-electron in two-orbital space to properly describe the ground and low-lying excitations, corresponding to three singlets (two closed-shell states and one open-shell state) and one triplet state (Figure 2.4b).

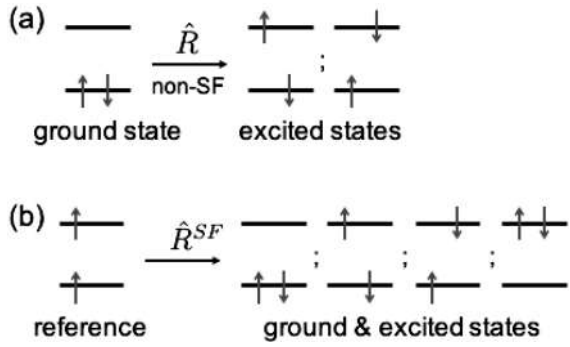


**Figure 2.4** Schematic orbital diagram of the (a) singles (non-SF) excitation operator acting on the ground state determinant, and (b) SF operator applied to the high-spin triplet (reference) configuration.

### 2.2.2 SF in CC and CI

The SF formalism for the characterization of electronic states in atomic and molecular systems was initially introduced within the equation-of-motion coupled-cluster (EOM-CC) ansatz [26, 27], and almost simultaneously for CI wave functions [28]. In EOM-CC electronic states are defined as the eigenstates of the non-Hermitian similarity transformed Hamiltonian ($\bar{\hat{H}} \equiv e^{-\hat{T}} \hat{H} e^{\hat{T}}$):

$$\bar{\hat{H}} \hat{R} |\Phi_0\rangle = \omega \hat{R} |\Phi_0\rangle, \tag{2.1}$$

where $\omega$ is the excitation energy with respect to the CC reference energy, $\Phi_0$ is the reference configuration, $\hat{T}$ is the cluster excitation operator, and $\hat{R}$ is an excitation operator connecting the Slater determinant $\Phi_0$ to the target states. In practice, operators $\hat{T}$ and $\hat{R}$ are truncated to a certain excitation level, e.g., singles and

doubles: $\hat{T} \approx \hat{T}_1 + \hat{T}_2, \hat{R} \approx \hat{R}_1 + \hat{R}_2$. Typically, the terms in the EOM excitation operator ($\hat{R}$) contain the same number of creation and annihilation spin-orbital operators, hence conserving the number of electrons and the spin projection of the reference. In that case, the operator is classified as electronically excited (EOM-EE-CC). The EOM-CC formalism can be easily generalized to the description of different classes of target states by combining a particular reference configuration $\Phi_0$ with a certain type of excitation operator (Figure 2.5), which might not conserve the number of electrons, like ionization potential (EOM-IP-CC) or electron attachment (EOM-EA-CC) [29–31], or the spin projection such as in SF methods (EOM-SF-CC) [32].

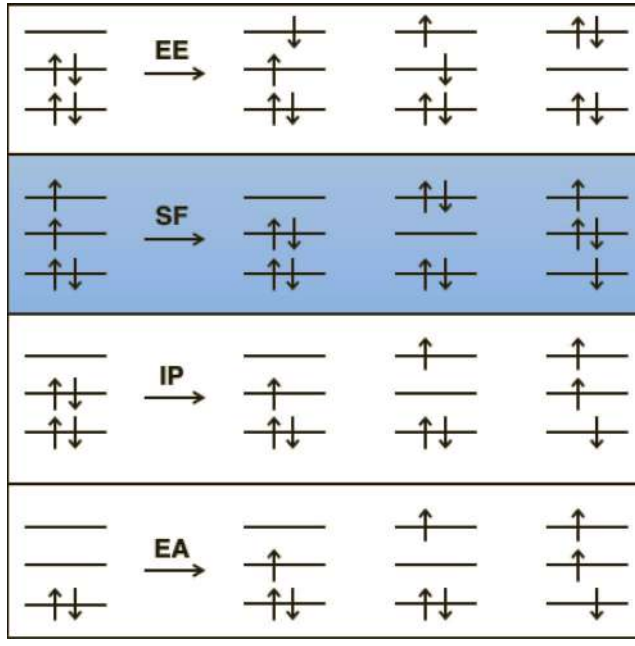


**Figure 2.5** Possible combination of reference and target states, and excitation operators within the EOM-CC formalism. EE: electronically excited, SF: spin-flip (highlighted in blue), EA: electron attachment, IP: ionization potential.

In particular, the SF variant of EOM-CC is defined by the action of an $\Delta M_S = -1$ (SF) excitation operator ($\hat{R}^{SF}$) that renders promotions of spin-$\alpha$ electrons into empty spin-$\beta$ orbitals. For example, for an

$M_S = 1$ triplet reference, it yields a set of $M_S = 0$ configurations for the description of low-spin target singlet and triplet states. Similarly, $M_S = 1/2$ doublet and quartet states can be obtained as SF excitations from an $M_S = 3/2$ quartet reference. In addition to EOM-CC, the SF operator has been also exploited in other CC-related approaches, like the optimized orbitals CCD (SF-OO-CCD or SF-OD for short) [33], EOM-MP2 [34], and the algebraic diagrammatic construction (ADC) method [35, 36].

In the absence of the cluster operator, $\hat{T} = 0$, Eq. (2.1) converges to the CI methodology and to its SF flavor (SF-CI) [27, 28] in the case of $\Delta M_S = -1$ excitation operators. Like in the non-SF case, SF-CI treatments are variational and potentially size-extensive [28, 37, 38], and many different versions of SF-CI methods have been introduced depending on the particularities of the SF configurational space [27, 28, 37–41].

### 2.2.3 SF in TDDFT

The use of the SF excitation operator within the time-dependent density functional theory (TDDFT) framework was introduced by Shao and collaborators in 2003 [42] and its theoretical foundations and implementation were expanded in a series of works by different authors [43–46]. The SF-TDDFT method is defined through $\alpha \rightarrow \beta$ spin non-conserving excitations in the linear response TDDFT. Excitation energies within the SF-TDDFT approach are obtained via the SF version of the Casida's equation:

$$\begin{bmatrix} \mathbf{A} & \mathbf{B} \\ \mathbf{B}^* & \mathbf{A}^* \end{bmatrix} \begin{bmatrix} \mathbf{X} \\ \mathbf{Y} \end{bmatrix} = \omega \begin{bmatrix} \mathbf{1} & \mathbf{0} \\ \mathbf{0} & -\mathbf{1} \end{bmatrix} \begin{bmatrix} \mathbf{X} \\ \mathbf{Y} \end{bmatrix}, \tag{2.2}$$

where $\omega$ is the excitation energy, and $\mathbf{X}$ and $\mathbf{Y}$ vectors contain the transition amplitudes. The elements of the $\mathbf{A}$ and $\mathbf{B}$ matrices for the general case of hybrid exchange-correlation (xc) functionals and within the adiabatic approximation are defined as:

$$\mathrm{A}_{i\bar{a},j\bar{b}} = \delta_{ij}\delta_{\bar{a}\bar{b}}(\epsilon_{\bar{a}} - \epsilon_i) - c_{HF}(ij|f_H|\bar{a}\bar{b}); \mathrm{B}_{i\bar{a},\bar{j}b} = -c_{HF}(ib|f_H|\bar{a}\bar{j}), \tag{2.3}$$

where the upper bars indicate $\beta$ spin-orbitals, $c_{HF}$ determines the amount of exact exchange (in hybrid functionals), $\varepsilon_p$ is the energy associated with the KS orbital $\phi_p$, $f_H$ is the Hartree kernel, and the two-electron integrals are given in Mulliken's notation:

$$(pq \mid f_H \mid st) = \int \phi_p^*(\mathbf{x})\phi_q(\mathbf{x})\frac{1}{|\mathbf{r}-\mathbf{r}'|}\phi_t^*(\mathbf{x}')\phi_s(\mathbf{x}')d\mathbf{x}d\mathbf{x}', \qquad (2.4)$$

with $\mathbf{x} = (\mathbf{r}, \sigma)$ and $\sigma = \alpha, \beta$ spin projections.

Similarly to the behavior of spin-conserving TDDFT, the performance of SF-TDDFT is largely dependent on the chosen xc-functional. It is important to notice that in the case of pure xc-functionals ($c_{HF} = 0$), Eq. (2.3) reduces to:

$$\mathrm{A}_{i\bar{a},j\bar{b}} = \delta_{ij}\delta_{\bar{a}\bar{b}}(\epsilon_{\bar{a}} - \epsilon_i); \mathrm{B}_{i\bar{a},\bar{j}b} = 0, \qquad (2.5)$$

and the computed excitation energies ($\omega$) simply correspond to the KS spectrum, that is, energy differences between the non-interacting single-electron states. Hence, exact exchange is crucial in order to capture state interaction effects in SF-TDDFT, and the best performance is achieved with functionals containing about 50% HF exchange, such as BHHLYP, 50-50, or PBE50 [45, 47]. In particular, HF exchange allows recovering the degeneracy between spin-multiplet components [44, 48].

The matrix terms in Eq. (2.3) correspond to the case of non-relativistic (collinear) xc kernels, in which the first order change in the $\alpha\beta$ block of the density matrix induces a second order change of the collinear xc potential. On the other hand, it can cause a linear response in relativistic (non-collinear) xc potentials, resulting in non-vanishing couplings between SF excitations even with pure functionals [43, 49, 50]. Non-collinear xc kernels emerge from relativistic DFT [51, 52] functionals, and have been implemented for the TDA [53, 54] and full TDDFT [55]. Comparison of properties and performance of collinear and non-collinear approaches can be found somewhere else [56].

Finally, it is also worth mentioning that a simplified version of SF-TDDFT, labeled as SF-sTDDFT, has been proposed for the fast calculation of electronic states and transition energies, which allows the computational characterization of very large diradicals [57].

### 2.2.4 SF with Active Space

The restricted active space configuration interaction (RASCI) methodology [39] is defined through the division of the molecular

orbital set of a reference configuration, commonly a HF determinant, in three orbital spaces: RAS1, RAS2, and RAS3. Typically, the three RAS subspaces expand the entire set of molecular orbitals, although it can be reduced by freezing low energy occupied and/or high energy virtual orbitals. The RASCI electronic wave function is obtained as the action of an excitation operator (Eq. (2.6)) including all possible electronic promotions within RAS2 ($\hat{r}_0$), i.e., reduced FCI, and expanded in terms of hole and particle excitations, that is, configurations with vacancies (holes) and electrons (particles) in RAS1 and RAS3, respectively.

$$\hat{R} = \hat{r}_0 + \hat{r}_h + \hat{r}_p + \hat{r}_{hp} + \hat{r}_{2h} + \hat{r}_{2p} + \hat{r}_{2hp} + \ldots \tag{2.6}$$

The right hand side of Eq. (2.6) converges to the exact (non-relativistic) FCI solution, while truncations to it establish a hierarchy of correlated methods with an increasing complexity and computational cost.

The excitation operator connects the reference configuration $\Phi_0$ with the target states $\{\Psi_I\}$:

$$|\Psi_I\rangle = \hat{R}\,|\Phi_0\rangle \tag{2.7}$$

Like in the EOM-CC framework, several flavors of $\hat{R}$ can be used to generate RASCI electronic states, i.e., EE, SF operators performing single or multiple excitations of spin-$\alpha$ electrons to empty spin-$\beta$ orbitals (or the other way around), and IP and EA operators connecting the reference configuration with states with fewer and more electrons, respectively (Figure 2.5). In particular, the action of a SF operator with $\Delta M_S < 0$ to a high-spin reference within the hole and particle approximation ($\hat{R} = \hat{r}_0 + \hat{r}_h + \hat{r}_p$, Figure 2.6) has been successfully applied to a variety of strongly correlated systems, such in the characterization of diradicals [58, 59] and polyradicals [60–62], the analysis of multiexcitons in multichromophoric systems [63, 64], and to the computational study of singlet fission [9, 65–69].

The RASCI family of methods have been implemented for the analytical integral evaluation [70, 71] and within the use of the resolution of the identity (RI) approximation [72] in the Q-Chem program [73].

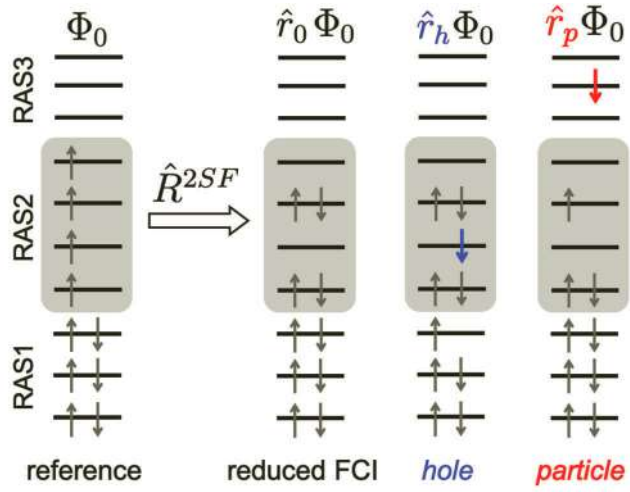


**Figure 2.6** Schematic representation of the restricted active space orbitals: RAS1, RAS2 and RAS3, in RAS-SF for the case of a high-spin quintet state reference and a (double) SF excitation operator ($\hat{R}^{2SF}$) within the hole and particle approximation.

### 2.2.5 Characterization of Diradical Character

Computational characterization and quantification of the diradical character is a standard and useful procedure in the study of diradicaloids that might assist to rationalize relative molecular stabilities, establish correlations with electronic properties, and design new systems with increased diradicaloid character. Like other useful concepts in Chemistry, such as conjugation or aromaticity, the diradical character in molecules is not well-defined since it is not a physical observable and, hence, there is no unequivocal quantum mechanical operator corresponding to it. Several techniques have been designed to measure the diradical strength of the system from electronic structure calculations, e.g., with SF methods. The following sections shortly describe several computational tools for the characterization of diradicaloids, namely, singlet–triplet energy gaps, diradical index, natural orbitals, fractional occupation densities, and effective number of unpaired electrons. Although this list does not pretend to be complete, these are some of the most typically employed quantities and representations for the

quantification of the diradical character available from electronic structure calculations, in particular with SF methods.

#### 2.2.5.1 Singlet–triplet energy gap

Since diradicaloids are defined by a small energy difference between occupied and virtual orbitals, they exhibit energy gaps between the lowest singlet and triplet states ($\Delta E_{ST}$) considerably smaller than in closed-shell systems. Following such rationale, it is normal practice to associate the strength of the diradical character to $\Delta E_{ST}$, with smaller energy gaps related to larger diradical nature of the ground state singlet. Accurate computation of $\Delta E_{ST}$ in diradicaloids constitute a real challenge for electronic structure methods since differential correlation effects are necessary for the precise estimation of the relative energy between the two states, as discussed in Section 2.2.1. On the other hand, the SF scheme is able to easily recover the main configurations describing the singlet and triplet states in diradicaloids, and has shown to produce accurate energies for a large variety of systems, which will be shown in Section 2.3 of this chapter.

The computational evaluation of singlet–triplet gaps in molecular species, and in diradicaloids in particular, can be done at a fixed molecular structure (typically the ground state optimized geometry), i.e., vertical energies, or they might refer to adiabatic energies, i.e., energy differences between the singlet and triplet state minima. In some systems, the optimal geometry of the triplet state is rather different from that of the singlet state, hence, it is important to distinguish between vertical and adiabatic quantities. Moreover, comparison with experiment needs to be done with care, since in some cases singlet–triplet splitting should be compared to vertical value, e.g., phosphorescent emission, whereas typical experimental singlet–triplet measurements in diradicaloids are obtained from the thermal equilibrium distributions between the singlet and triplet, and should be related to adiabatic gaps.

Most of the SF methods introduced in the previous section can be used to find local minima on the potential energy surface of ground and excited states (geometry optimization), allowing to compute both vertical and adiabatic singlet–triplet energy gaps of diradicaloids. On the other hand, analytical gradients have not been implemented yet for the RAS-SF method.

### 2.2.5.2 Diradical index

The spin-singlet ground state of a diradicaloid can be obtained, to a very good approximation, as the linear combination of the HF-like term ($\psi_0$) and the HOMO-to-LUMO doubly excited configuration ($\psi_D$):

$$|^1\Psi_0\rangle = c_0\,|\psi_0\rangle + c_D\,|\psi_D\rangle. \tag{2.8}$$

From Eq. (2.8), deviation of the ground state electronic structure with respect to the closed-shell configuration ($\psi_0$) can be directly related to the relative contribution of $\psi_D$. This rationale motivated the definition of the diradical index ($y$) [74, 75] as twice the weight of the doubly excited configuration: $y \equiv 2c_D^2$. By definition, $y$ takes values between 0 (closed-shell) and 1 (perfect diradical), while intermediate values quantify different degrees of diradical character in diradicaloids. Moreover, the diradical character can be linked to the occupancy of the lowest unoccupied natural orbital (LUNO) of spin-projected unrestricted HF (PUHF). Such connection can be extended to the definition of $y$ in correlated electronic structure methods, e.g., SF approaches. This approach allows the definition of higher radical characters $y_i$ through the occupancies of LUNO+$i$: $y_i = n_{\mathrm{LUNO}+i}$, i.e., $y_0 \equiv y$ (diradical), $y_1$ (tetraradical), $y_2$ (hexaradical), etc. Since SF methods explicitly generate the two-electron excited configuration (Figure 2.4b), the diradical degree $y$ can be estimated either as the LUNO's occupation or as twice the square of $c_D$. If the ground state wave function can be described by Eq. (2.8) to a good approximation, both approaches should provide similar results.

### 2.2.5.3 Natural orbitals and occupation numbers

Natural orbitals [76] are the eigenfunctions of the spinless reduced density matrix $\rho(\mathbf{r}, \mathbf{r}')$:

$$\rho(\mathbf{r}, \mathbf{r}') = N \int \psi^*(\mathbf{r}, \mathbf{r}_2, \ldots \mathbf{r}_N)\,\psi(\mathbf{r}', \mathbf{r}_2, \ldots \mathbf{r}_N) d\mathbf{r}_2 \ldots d\mathbf{r}_N, \tag{2.9}$$

where $N$ is the number of electrons and $\psi$ is the normalized electronic wave function. In the natural orbital basis, the density matrix is directly obtained as a sum of the squared natural orbitals ($\{\phi_i\}$) weighted by their eigenvalues, i.e., occupation numbers ($\{n_i\}$):

$$\rho(\mathbf{r}, \mathbf{r}') = \sum_i n_i \phi_i^*(\mathbf{r}')\phi_i(\mathbf{r}), \tag{2.10}$$

where $\Sigma_i n_i = N$ and $0 \le n_i \le 2$, $\forall i$. For closed-shell systems, natural orbitals converge to the mean-field canonical MOs with occupation

numbers of 2 (occupied orbital) or 0 (virtual orbital), while correlated systems generate natural orbitals with fractional occupancies. Hence, the presence of natural orbitals with intermediate occupancies might be related to the multi-configurational nature of the system and in particular can be used as a measure of the diradical (or polyradical) character, with the wave function of an ideal spin-singlet diradical exhibiting N/2 – 1 doubly occupied orbitals and two natural orbitals with one electron. Therefore, the use of $\{n_i\}$ is rather convenient for the quantification of the diradical and polyradical character in general, as it has been described in Section 2.2.5.2 in relation to the indices $y_i$. Moreover, the representation of the frontier natural orbitals with fractional occupancies inform of the spatial distribution of correlated electrons.

### 2.2.5.4 Density of unpaired electrons

The density of unpaired electrons, also named as the fractional occupation density (FOD) [77, 78], is described as:

$$\rho^{\mathrm{FOD}}(\mathbf{r}) = \sum_i f(n_i)\phi_i^*(\mathbf{r})\phi_i(\mathbf{r}) \tag{2.11}$$

where $f(n_i)$ is the unpaired electron distribution number expressed as a function of the electronic occupation number. The FOD is a real space distribution of the strongly correlated electrons that gathers the information contained in the $\{n_i, \phi_i\}$ pairs in a compact representation. Since the metric for the quantification of the number of unpaired electrons is ambiguously defined, the $\{n_i\}$ to $f(n_i)$ mapping can be done in infinite possible manners, and several forms of $f(n_i)$ have been introduced [79–81]:

$$f_D(n_i) = 2n_i - n_i^2 \tag{2.12}$$

$$f_U(n_i) = \min(n_i, 2 - n_i) \tag{2.13}$$

$$f_S(n_i) = n_i^2\ (2 - n_i)^2 \tag{2.14}$$

The three metrics defined in Eqs. (2.12–2.14) ($f_D$, $f_U$, and $f_S$) have the same distribution number for occupations of 0, 1, and 2 electrons, but differ at intermediate values (Figure 2.7). As discussed by several authors [80, 82], $f_U$ and $f_S$ mappings have some advantages over $f_D$, since the latter tends to overestimate the number of unpaired electrons. Near closed-shell occupations ($n_i < 0.4$ and $n_i > 1.6$), the

linear $f_U$ distribution is larger than the quadratic $f_S$, while at $0.4 < n_i < 1.6$ the $f_S$ distribution is larger than $f_U$. The largest deviation between $f_U$ and $f_S$ metrics occurs around the natural orbital occupation numbers of 0.15 and 1.85 electrons.

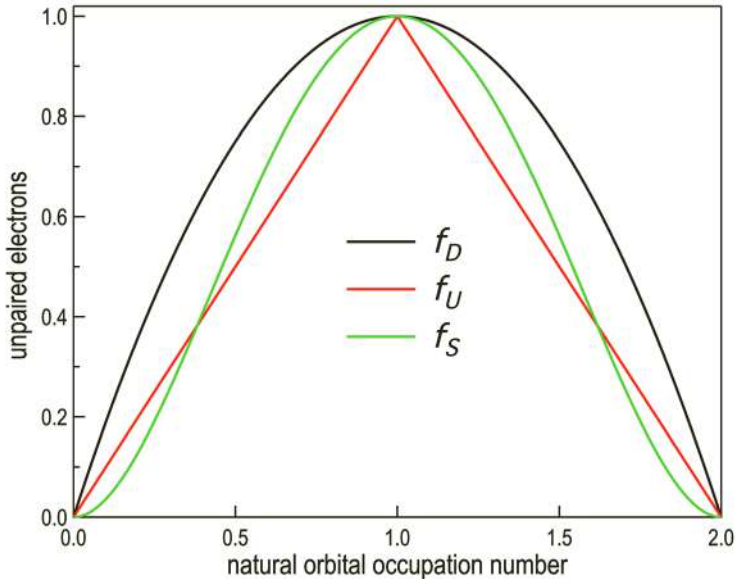


**Figure 2.7** Plot of three possible mappings for the number of unpaired electrons $f_D$ (black), $f_U$ (red), and $f_S$ (green), as defined in Eqs. (2.12–2.14).

### 2.2.5.5 Number of unpaired electrons

The total number of unpaired electrons of the system can be defined as the spatial integration of the FOD:

$$N_{\mathrm{FOD}} = \int \rho^{\mathrm{FOD}}(\mathbf{r}) d\mathbf{r} = \sum_i f(n_i). \tag{2.15}$$

The general definition of the effective number of unpaired electrons in Eq. (2.15) takes a specific mathematical form upon choosing a concrete expression for the unpaired electron distribution number. Therefore $f_D$, $f_U$, and $f_S$ univocally define three possible measures for $N_{\mathrm{FOD}}$, namely $N_D$, $N_U$, and $N_S$, respectively. By definition, $N_D$ is always larger than $N_U$ and $N_S$. On the other hand, one might expect $N_U < N_S$ for strongly correlated systems, that is, with several

natural orbitals with occupancies around 1 electron, while the linear $N_U$ will be larger for systems with mild diradical (and polyradical) character.

## 2.3 Application of SF Methods to the Study of Diradicaloids

### 2.3.1 Ethylene Torsion with SF-TDDFT

The molecular torsion of a C=C double bond, discussed in Section 2.2.1, can be used as a model to explore the performance of (collinear) SF-TDDFT approaches in the description of the ground state singlet of diradicaloids. The impact of HF exchange in SF-TDDFT is evaluated by considering a range of energy functionals. Moreover, SF-TDDFT results are compared to (non-SF) KS-DFT and to the two-configurational self-consistent field augmented by CI including single and double excitations (TCSFC-CISD) as a reference, since it is flexible enough to treat different mixings of $(\pi)^2$ and $(\pi^*)^2$ configurations in a balanced way [27]. Calculations have been done with the double-$\zeta$ with polarization basis set of Dunning (DZP) [83].

Like in the (restricted) HF solution (Figure 2.3a), B3LYP is unable to reproduce the energy profile for molecular torsions with large dihedral angles, i.e., in the diradicaloid-diradical region, and largely overestimates the energy of the singlet ground state relative to the planar structure, with a cusp at 90° (Figure 2.8). On the other hand, UB3LYP energy is rather close to TCSCF-CISD, but this result is obtained at the expense of triplet state mixing in the UB3LYP determinant, as manifested by large $\hat{S}^2$ expectation values near orthogonality ($\langle \hat{S}^2 \rangle \approx 1$). In general, despite the improved relative energies along potential energy surfaces, UKS solutions present several problems derived from the ill-defined electronic structure, such as the computation of electronic properties or the evaluation of energy gaps to excited states. Despite, it is worth noticing that some reports have shown that UKS-based TDDFT calculations with relevant functionals and/or spin projection techniques are able to reproduce excitation energies and hyperpolarizabilites of systems with intermediate-large diradical characters [84–87].

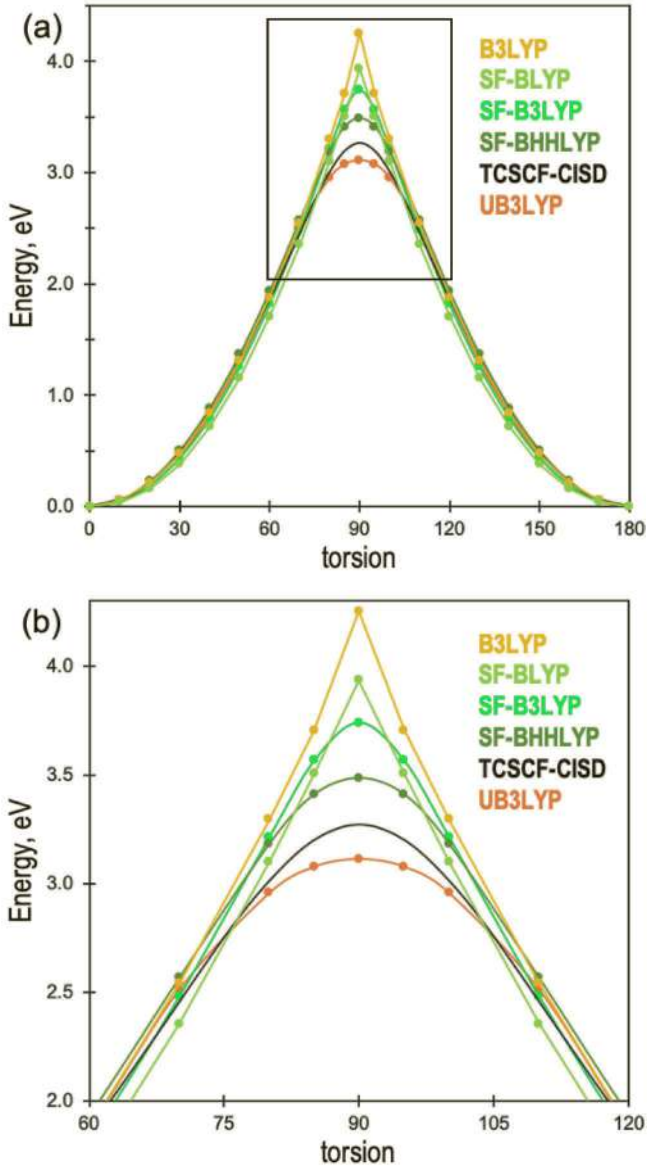


**Figure 2.8** Ground state singlet energy profiles (in eV) along the molecular torsion for the ethylene molecule computed with restricted and unrestricted KS-DFT with the B3LYP functional (B3LYP and UB3LYP, respectively), SF-TDDFT with the BLYP, B3LYP, and BHHLYP xc-functionals, and TCSCF-CISD from Ref. [27]. All calculations have been done with the DZP basis set. All curves are shifted such that the energy at 0° is zero. (b) Zoom of the energy profiles within 60–120° torsion range, indicated with a rectangle in (a).

As discussed in Section 2.2.3, the performance of SF-TDDFT is strongly dependent on the amount of exact exchange in the energy functional. The use of a non-hybrid functional disregards CI effects and the energy profile is considerably overestimated and exhibits an unphysical energy cusp at the orthogonal torsion. Inclusion of HF exchange removes the energy cusp and systematically improves the energy profile of SF-TDDFT, with SF-B3LYP (20% HF exchange) and SF-BHHLYP (50% HF exchange) approaching to TCSCF-CISD as the exact exchange increases.

### 2.3.2 Radical Character of Triangulenes

Two-dimensional nanosized materials arising from the fusion of benzene rings constitute a fascinating family of organic compounds. Their electronic and magnetic properties make them a very promising alternative in applications for molecular electronics [88] and spintronic devices [89]. These systems can be understood as fragments of graphene or graphene nanofragments (GNFs) [90, 91], in which quantum confinement breaks the degeneracy between valence and conduction bands of graphene. The countless possible combinations of polycyclic aromatic hydrocarbon (PAH) units allow for a wide range of diverse electronic properties dictated by their size, shape, and topology. While many of these PAHs possess a closed-shell electronic structure, others feature an open-shell high-spin ground state [92]. This is the case of non-Kekuké triangular GNFs (TGNFs) [93], such as phenalenyl [94] and triangulene [93, 95–97] (Figure 2.9), in which open-shell character emerges due to the topology of the system with unpaired electrons showing great spatial delocalization facilitating long-range interactions.

Phenalenyl is the smallest member of the TGNF family. It has an odd number of $sp^2$ carbon atoms and π-electrons, which makes it a radical. On the other hand, triangulene holds nine fused benzenoid rings and an even number of π-electrons. Both systems are perfectly planar with a $D_{3h}$ symmetry. The ground state spin multiplicity of phenalenyl and triangulene, and of GNFs in general, can be predicted by the simple Ovchinnikov's rule [98] established by the Lieb's theorem [99]:

$$S = \frac{|N_A - N_B|}{2}, \tag{2.16}$$

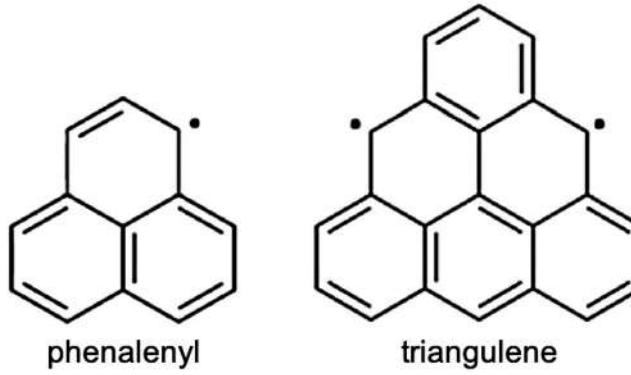


**Figure 2.9** Phenalenyl (left) and triangulene (right) structures.

where $S$ is the ground state spin quantum number, and $N_A$ and $N_B$ are the number of carbon atoms in each of the two alternant sublattices ($A$ and $B$). Application of Eq. (2.16) predicts spin doublet and triplet ground states for phenalenyl and triangulene, respectively, in agreement with the electronic structure assignment derived by the Hückel model (Figure 2.10).

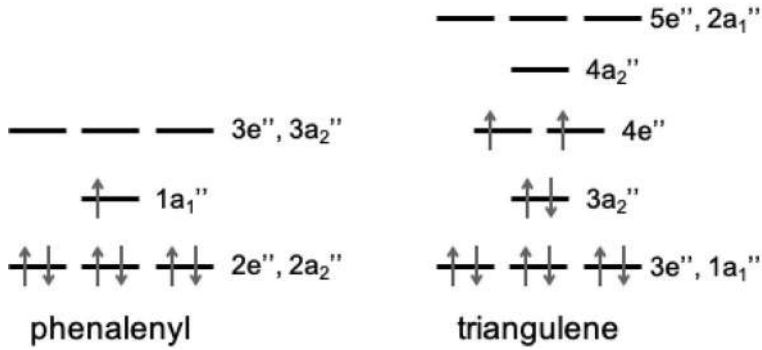


**Figure 2.10** Hückel molecular orbital diagram of phenalenyl (left) and triangulene (right).

The lowest state of phenalenyl corresponds to the single electronic occupancy of the $1a_1''$ orbital, i.e., the $1^2A_1''$ state. Electronic structure calculations at the RAS-SF level (see Appendix A.1 for details) confirm the radical nature of phenalenyl. The $1^2A_1''$ state exhibits a density of unpaired electrons coming from a singly

occupied natural orbital (SONO in Figure 2.11, left). Representation of the ground state FOD shows that the unpaired electron equally spreads over the six carbon atoms at the molecular edges. Notice that the participation of the central atom in the density of unpaired electrons is symmetry forbidden, since the $2p_z$ orbital at the molecular center belongs to the $A_2''$ irreducible representation.

Electronic transitions to the lowest excited states of phenalenyl are obtained as ($\pi \rightarrow \pi^*$) excitations to the singly occupied $1a_1''$ orbital: $2e'' \rightarrow 1a_1''$ ($1^2E''$) and $2a_2'' \rightarrow 1a_1''$ ($1^2A_2''$). Natural orbital analysis identifies the lowest doublet-doublet twofold transition to $1^2E''$ as the excitation of edge electrons, while $1^2A_1'' \rightarrow 1^2A_2''$ involves a partial displacement of central electrons to the molecular border. RAS-SF vertical energy gaps to the two excited doublets are computed at 2.76 eV and 3.04 eV (Table 2.1), in very good agreement with other highly correlated results [100].

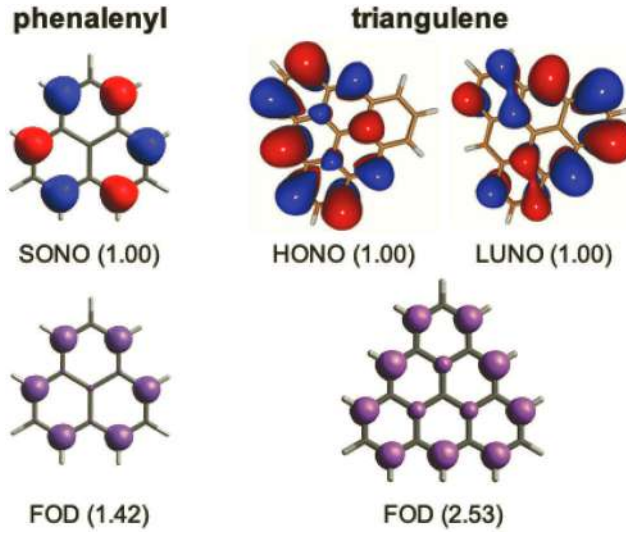


**Figure 2.11** Ground state frontier natural orbitals and their occupation numbers (in parenthesis), and the FOD ($N_U$ in parenthesis) for phenalenyl (left) and triangulene (right) computed with RAS-SF.

The ground and the lowest excited electronic states of triangulene are obtained as the different possible distributions of two electrons in the two degenerated $4e''$ frontier molecular orbitals, generating

three singlet states and one triplet state. The direct product $E'' \otimes E''$ is a four-dimensional space that can be expressed by the $A_1'$, $A_2'$, and $E'$ representations. Since $A_2'$ is spatially anti-symmetric, it corresponds to the spin-triplet state, while $A_1'$ and $E'$ must be associated to spin-singlet states. RAS-SF calculations support the spin-triplet $1^3A_1'$ character of the ground state, in agreement with ESR spectroscopical characterization [93, 94]. Like in phenalenyl, the electron in the central $2p_z$ orbital can only contribute to π-orbitals with that symmetry, i.e., $a_2''$ orbitals, banning unpaired electron density on the central atom (Figure 2.11). For the most part, the density of unpaired electrons in the ground state of triangulene concentrates at the three edges of the triangle.

Excitation to the doubly degenerated excited singlet ($1^1E'$) is manly obtained as the spin-adapted state corresponding to single electron occupation of $4e''$ orbitals. The $1^1E'$ state is energetically close to the ground state, with a computed energy gap of 0.57 eV, and also exhibits a FOD mainly on the molecular edges. Finally, the first triplet-triplet transition in triangulene corresponds to the degenerated excitation to $1^3E'$, with a computed energy gap of 2.82 eV. The $1^3E'$ state is mainly characterized by electronic configurations with the partial occupation of the $4e''$ and $3a_2''$ or $4a_2''$ orbitals.

**Table 2.1** Vertical transition energies ($\Delta E$ in eV) to the lowest excited state of phenalenyl and triangulene computed at the RAS-SF level

| **Molecule** | **State** | $\Delta E$ |
|---|---|---|
| Phenalenyl | $1^2\,E''$ | 2.76 |
| | $1^2\,A_2''$ | 3.04 |
| Triangulene | $1^1E'$ | 0.57 |
| | $1^3\,E'$ | 2.82 |

In summary, the RAS-SF calculations on phenalenyl and triangulene describe in great detail their radical character, with unpaired electrons localized on the molecular edges. This behavior appears to be a general feature in the TGNF family, and might be extendable to larger triangular PAHs.

### 2.3.3 Diradical Character of Linear Acenes and Zethrenes

Linearly fused benzene rings, i.e., linear acenes (Figure 2.12, left), have attracted much attention due to their potential technological applications [101, 102] motivated by their electronic and magnetic properties [103–106]. A large number of theoretical works have described the electronic structure of acenes [39, 107–111]. Many of these efforts have focussed on the ground state spin multiplicity, and in the accurate quantification of the relative energy gap between the lowest singlet and triplet states. Clar's sextet rule [112] predicts an increase of the diradical character of linear acenes with the number of fused rings, since resonance structures with no unpaired electrons only contain one aromatic sexted ring independently of the molecular length. This behavior has been largely supported by electronic structure calculations performed with many different methodologies.

The chemical instability derived from strong open-shell nature of long acenes has prevented the synthesis of pristine linear acenes beyond hexacene [113] and heptacene [114, 115]. Proper chemical substitution hinders the interaction of radical centers with the environment [116–120], and has allowed the synthesis and characterization of a nonacene derivative [121].

Extended zethrenes (Figure 2.12, right), also regarded as dibenzo-acenes, are π-conjugated polycyclic hydrocarbons closely related to acenes [122–140]. Zethrene (dibenzo [de, mn]naphthacene) is the smallest member of the family, consisting of two phenalene fused units, i.e., featuring six fused benzene rings. Longer zethrenes with seven or more fused hexagon rings are consecutively named as: heptazethrene, octazethrene, nonazethrene, etc. Zethrene has a closed-shell electronic structure, which can be rationalized due to the stabilization of the quinoidal form with two aromatic sextet rings. On the other hand, experimental characterizations of derivatives of heptazethrene [127], octazethrene [122], and nonazethere [123] have identified them as open-shell singlet diradicaloids. Similar to higher order acenes, the more extended zethrenes are supposed to be extremely reactive due to the increased diradical character.

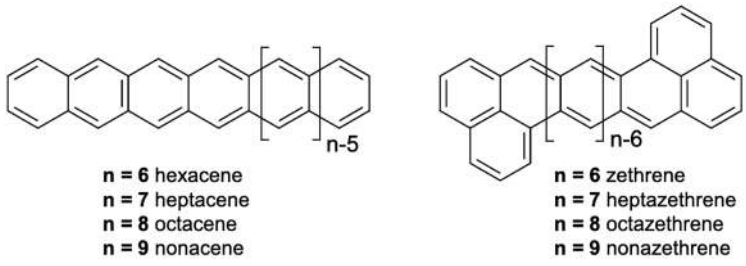


**Figure 2.12** Molecular structure of linear acenes (left) and zethrenes (right).

This section investigates and rationalizes the diradicaloid nature of extended zethrenes with respect to the linear acenes by means of SF electronic structure calculations. Concretely, most of the results were obtained with the RAS-SF method.

**Table 2.2** Vertical singlet–triplet energy difference ($\Delta E_{ST} = E(T_1) - E(S_0)$, in kcal/mol) and diradical index ($y_0$) computed at the SF-BHHLYP and RAS-SF levels[a]. Diradical character values obtained as: $y_0 = 2c^2{}_D$ (SF-BHHLYP) and $y_0 = n_{LUNO}$ (RAS-SF) for the linear acenes and zethrenes series from six to nine fused benzene rings ($n$)

| | Acenes | | | | Zethrenes | | | |
|---|---|---|---|---|---|---|---|---|
| | SF-BHHLYP | | RAS-SF | | SF-BHHLYP | | RAS-SF | |
| $n$ | $\Delta E_{ST}$ | $y_0$ | $\Delta E_{ST}$ | $y_0$ | $\Delta E_{ST}$ | $y_0$ | $\Delta E_{ST}$ | $y_0$ |
| 6 | 18.7 | 0.10 | 17.0 | 0.25 | 35.7 | 0.14 | 37.8 | 0.10 |
| 7 | 12.2 | 0.17 | 11.3 | 0.35 | 18.7 | 0.25 | 18.3 | 0.25 |
| 8 | 8.5 | 0.25 | 7.5 | 0.45 | 12.2 | 0.31 | 9.2 | 0.42 |
| 9 | 6.5 | 0.35 | 5.7 | 0.52 | 9.6 | 0.34 | 5.2 | 0.56 |

[a]Values from Ref. [123].

Table 2.2 shows SF-BHHLYP and RAS-SF calculated values for the vertical singlet–triplet energy gaps and the estimated ground state singlet diradical character index ($y_0$) along the linear acene and zethrene series with six to nine fused benzene rings (see Appendix A.2 for details). Energy difference between the ground state singlet and the lowest triplet in linear acenes decreases with the number of fused rings. The SF-BHHLYP and RAS-SF energies are in good agreement to each other with a gap of 17–19 kcal/mol for hexacene, and about three times smaller (~ 6 kcal/mol) in nonacene. Natural

orbital occupancies of hexacene computed with RAS-SF mildly depart from the closed-shell values of two and zero electrons for the occupied and virtual orbitals. Fractional electron occupation of the LUNO ($y_0$ index) systematically increases with the number of fused rings, in agreement with a diradical character gain.

It is important to notice that the singlet–triplet gap for zethrene ($n$ = 6) is rather large, much larger than in hexacene, suggesting nearly no diradical character (closed-shell structure), in agreement with experimental measurements [126]. Like in the linear acene series, the energy gap to the lowest triplet decreases with the size of the molecule, in accordance with an increase in the ground state open-shell character as quantified by $y_0$. The simultaneous decrease of the singlet–triplet gap and increase of the diradical character within the extended zethrene family with the number of fused rings is considerably faster than in linear acenes (Figure 2.13). As a result, nonazethrene exhibits a smaller singlet–triplet energy gap and larger diradical character ($y_0$) than nonacene (at the RAS-SF level).

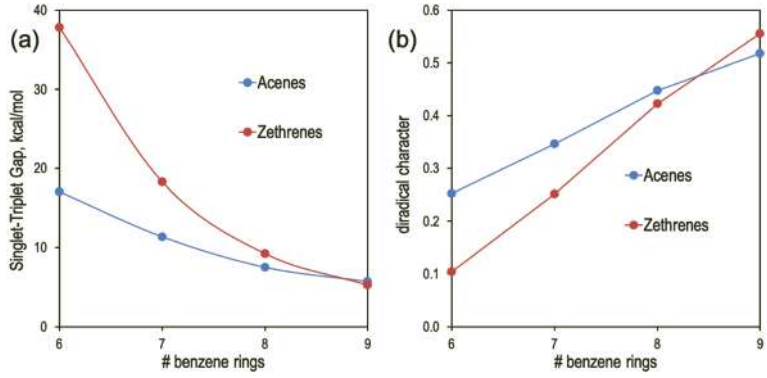


**Figure 2.13** (a) Singlet–triplet energy gaps (in kcal/mol) and (b) diradical character ($y_0$) of linear acenes (blue) and extended zethrenes (red) with $6 \leq n \leq 9$ computed at the RAS-SF level. Values from Ref. [123].

The rapid increase of the diradical character in zethrenes compared to the computed diradical gain in linear acenes can be analyzed and rationalized in terms of the interaction between radical centers. To that aim, the RAS-SF ground state singlet wave function in the linear acenes and zethrenes has been decomposed in different contributions based on the localization of molecular orbitals [63, 64].

The use of fragment localized orbitals on two radical centers allows expressing the electronic wave function of these systems in terms of neutral contributions, those corresponding to one electron on each radical center, and charge resonances, in which two electrons coexist on one center:

$$|\Psi_{GS}\rangle = c_{NE}\,|\psi_{NE}\rangle + c_{CR}\,|\psi_{CR}\rangle, \tag{2.17}$$

where NE and CR terms correspond to neutral configurations and charge resonances, respectively, described as:

$$|\psi_{NE}\rangle = \frac{1}{\sqrt{2}}\left[|\phi_A^\alpha \phi_B^\beta\rangle + |\phi_B^\alpha \phi_A^\beta\rangle\right] \tag{2.18}$$

$$|\psi_{CR}\rangle = \frac{1}{\sqrt{2}}\left[|\phi_A^\alpha \phi_A^\beta\rangle + |\phi_B^\alpha \phi_B^\beta\rangle\right], \tag{2.19}$$

where $\phi_X$ represent the fragment orbital localized on the radical center $X$ ($X$ = $A$, $B$), and superindex $\alpha(\beta)$ indicates spin-up (spin-down).

The amplitude $c_{CR}$ in Eq. (2.17) weights the magnitude of the (symmetric) charge transfer contributions (charge resonances) between the two radical centers, which can be interpreted as a measure of the inter-radical interaction strength. The localized frontier orbitals obtained for acenes and zethrenes, associated here as fragment orbitals on each radical center, present some important differences (Figure 2.14a and b). In acenes, the two unpaired electrons are localized at the middle of the two zigzag edges, respectively. Increasing the number of rings in the acene series does not severely change the radical-radical interaction, since the two radicals remain at the center of the molecule with the same inter-radical distance and with only slightly larger delocalization along the molecular zigzag edges for longer molecules, which might explain the moderate decrease in the CR contributions with the number of rings. On the other hand, the unpaired electrons in zethrenes are located on each of the two phenalene units. Hence, increasing the number of benzene rings enforces an important spatial separation between the two radicals. As a consequence, in zethrenes, the interaction between the two radicals drops quite rapidly with the molecular length, and the decrease in weight of CR between the two radicals is faster than in acenes (Figure 2.14c). CR contributions in nonacene are larger than those in nonazethrene, suggesting larger

diradical character in the latter in agreement with the $y_0$ index and computed singlet–triplet gaps.

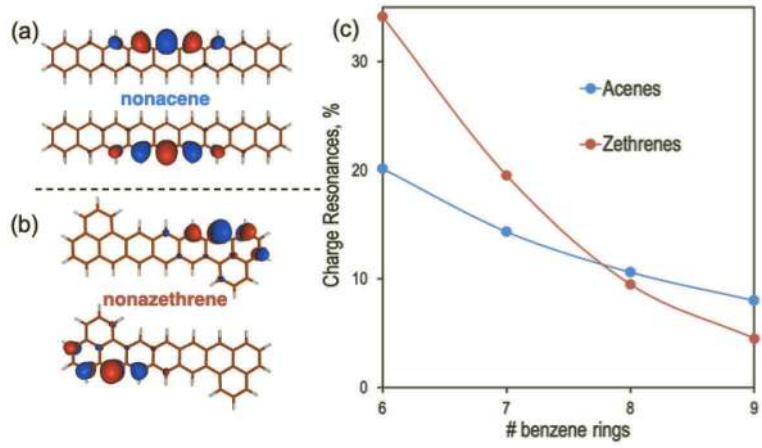


**Figure 2.14** Localized fractional natural orbitals representing radical centers in linear acenes and zethrenes for the case with nine fused rings, nonacene (a) and nonazethrene (b). (c) Charge resonances between radical centers (in %) of linear acenes (blue) and extended zethrenes (red) with $6 \leq n \leq 9$.

Therefore, it might be concluded that the different spatial localizations of the unpaired electrons in the molecular scaffold determine the interaction between the radical centers in linear acenes and zethrenes, and have a huge impact on the singlet–triplet gaps and diradical character of these two families of compounds.

### 2.3.4 Diradical Character of Fluorenofluorenes

Antiaromatic extended polycyclic conjugated hydrocarbons based on *s*-indacene have recently received significant attention. This is the case of the indenofluorene family of compounds, for which all possible isomers have been synthesized and characterized [141–144]. Indenofluorenes can be modified by expanding the central six-membered conjugated ring to naphthalene, generating fluorenofluorene (FF) compounds, and anthracene, resulting in diindenoanthracenes [145].

Molecules within the FF family can present closed-shell *ortho-*, *meta-*, or *para*-quinoidal patterns. So far, four members of the FF

family have been experimentally realized: three *para*-substituted molecules (FF-1 [146], FF-2 [147], and FF-3 [148, 149]) and FF-4 [150] with an *ortho*-quinoidal scaffold (Figure 2.15). Notice that FF-3 exhibits a *meta*-substitution pattern in the diradical form. The substitution pattern of FF-*n* molecules determines their electronic properties such as the open-shell character, which can be rationalized as the result of two competing effects: (i) conjugation, which promotes the bonding of unpaired electrons toward the closed-shell form, and (ii) the formation of aromatic benzene rings favoring the Kekuké diradical form.

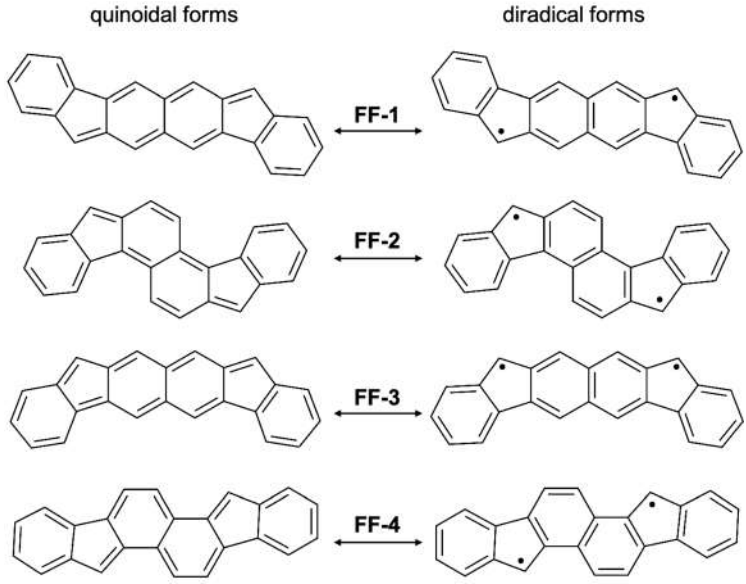


**Figure 2.15** Chemical structures of the closed-shell quinoidal (left) and diradical aromatic (right) forms of FF-1, FF-2, FF-3, and FF-4.

Diradical structures of all four molecules, FF-1–4, are stabilized with respect to the quinoidal forms by the development of the aromatic naphthalene unit. Besides, FF-3 gains a third Clar aromatic sextet in the diradical canonical form, providing an additional stabilization driving force to the open-shell form with respect to the other three FFs. As a result, while FF-1 and FF-2 can be characterized as closed-shell molecules, FF-3 and FF-4 are ground state singlet

diradicaloids, with FF-3 holding stronger diradical character than FF-4. This section explores the diradical character of the four members of the FF family by means of quantum chemistry calculations based on the RAS-SF approach.

RAS-SF calculations produce large singlet–triplet energy differences for FF-1 and FF-2, indicating a markedly closed-shell character (Table 2.3). On the other hand, the theoretically predicted singlet–triplet gap for FF-3 is quite small (2.4 kcal/mol), and nearly three times smaller than in FF-4 (7.0 kcal/mol). These values are in very good agreement with the singlet–triplet gaps experimentally determined through superconducting quantum interfering device (SQUID) measurements [148, 150]. The relative energies to the lowest triplet identify FF-3 having a larger diradical character degree than FF-4. This trend is well recovered by the $y_0$ indices evaluated as the occupation number of the LUNO. Overall, these results are in line with an important diradical character of the ground state of FF-3 and a moderate open-shell character in FF-4.

**Table 2.3** Vertical singlet–triplet energy gaps ($\Delta E_{ST}$ in kcal/mol) and diradical index $y_0$ of FFs computed at the RAS-SF level. Experimental singlet–triplet gaps (in kcal/mol) indicated as $\Delta E_{ST}^{exp}$

| **Molecule** | $\boldsymbol{\Delta E_{ST}^{exp}}$ | $\boldsymbol{\Delta E_{ST}}$ | $\boldsymbol{y_0}$ |
|---|---|---|---|
| FF-1 | - | 16.8 | 0.31 |
| FF-2 | - | 19.7 | 0.28 |
| FF-3 | 2.5[a] | 2.4 | 0.60 |
| FF-4 | 6.5[b] | 7.0 | 0.50 |

[a]From Ref. [148]. [b]From Ref. [150].

Representation of the frontier natural orbitals (HONO and LUNO) and the FOD for the ground state of FF-3 and FF-4 shows a sizable delocalization of the unpaired electrons with larger density on the radical carbons of the canonical aromatic forms (Figure 2.16). In FF-3, the unpaired density located at the carbon atoms of the naphthalene core bonded to the radical centers (indicated with arrows in Figure 2.16) is rather small. The density of unpaired electrons connecting the two radical centers is slightly larger in FF-4,

justifying a stronger coupling between the two unpaired electrons, which results in a weaker diradical character and larger $\Delta E_{ST}$ with respect to FF-3.

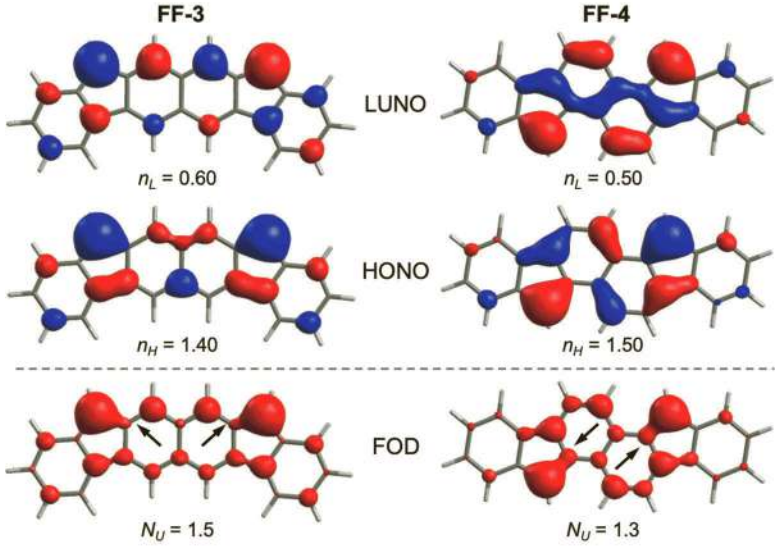


**Figure 2.16** Representation of the HONO and LUNO with their occupation numbers ($n_H$ and $n_L$), and the FOD with $N_U$, corresponding to the singlet ground state of FF-3 (left) and FF-4 (right) computed at the RAS-SF level. Arrows denote the key positions discussed in the text.

These results clearly indicate that while *meta*-substitution of the aromatic naphthalene moiety (diradical form) produces large diradical character, *para*-naphtho substitution provides stable closed-shell molecules. The *ortho*-naphtho pattern represents an intermediate situation with a moderate diradical character.

### 2.3.5 Diradical Character of Cyclic Acenes and Carbon Nanobelts

Cyclic organic molecules built as *n* benzene units either fused, i.e., sharing a carbon-carbon bond, or connected through a single bond in a ring-shaped structure are very interesting compounds that have attracted the efforts of both experimental and theoretical researchers

in the last decade [151–159]. In addition to their intrinsic properties, these systems can be potentially used for the growth of size-specific single-walled carbon nanotubes (SWCNT) [160]. This is the case of cycloparaphenylene (CPP) leading to SWCNT with armchair edges. While CPPs are easy to synthesize and chemically stable, other cyclic organic families have not been experimentally obtained yet. This is the case of cyclic acenes (Figure 2.17), also termed as cyclacenes (CC or [*n*]CC where *n* is the number of benzene rings) [161], which correspond to hoop-like structures formed by fused aromatic rings, and can be seen as the cyclic version of linear acenes. Clar's rule predicts CCs to be more reactive than their linear counterparts, since closed-shell resonance structures in linear oligoacenes can be drawn with one aromatic sextet ring, while in CCs, it is not possible to form a Clar's sextet without unpaired electrons. Accordingly, electronic structure calculations at different levels of theory predict strong diradical character of CCs [60, 162], even for the smallest members of the family ($n$ = 5, 6). The open-shell nature of these systems impairs their chemical stability and, so far, has made their experimental realization elusive [161].

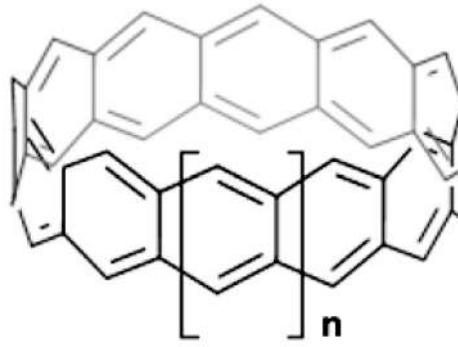


**Figure 2.17** Molecular structure of cyclic acenes (CC or [*n*]CC).

In the following, to describe in detail the electronic characteristics of CC compounds and, in particular, the physical origin of their diradicaloid nature, the computational results obtained for [*n*]CC with five to twelve fused rings, i.e., $5 \leq n \leq 12$, are discussed.

Contour conditions in CC compounds impose strong molecular symmetry, with [*n*]CC members belonging to the $D_{nh}$ point groups, that is, with all *n* six-membered rings being structurally identical. Ground state optimized geometries recover the predicted molecular symmetries. Obtained C–C bond distances along the zigzag edges are close to the bond length in benzene (1.41–1.42 Å), while the length of the bonds between the two edges is considerably larger (1.45–1.47 Å) and in the range of a typical single bond between two $sp^2$ carbon atoms (Table 2.4).

**Table 2.4** Ground state C–C bond distances (in Å) along the zigzag (edge) and connecting the two zigzag chains (bridge) for [*n*]CC with $5 \leq n \leq 12$ optimized at the M06-2X/6-31+G(d) level

| *n* | Edge | Bridge |
|---|---|---|
| 5 | 1.416 | 1.473 |
| 6 | 1.416 | 1.450 |
| 7 | 1.413 | 1.456 |
| 8 | 1.410 | 1.456 |
| 9 | 1.410 | 1.454 |
| 10 | 1.407 | 1.457 |
| 11 | 1.408 | 1.455 |
| 12 | 1.407 | 1.457 |

Molecular symmetry has an important impact on the electronic properties of [*n*]CC. Hückel molecular orbitals around the Fermi level (HOMO and LUMO) for even *n* are degenerated (Figure 2.18a). The HOMO/LUMO degeneracy is broken if the Hückel model is expanded beyond the first neighbor interactions by considering an additional (weaker) interaction between non-bonded carbons at the edges in *para*-position within each benzene ring ($\gamma \neq 0$ in Figure 2.18a). On the other hand, for systems with an odd number of six-membered rings, the two HOMOs and two LUMOs are degenerated with an occupied-virtual finite gap that decreases with the number of rings (*n*). In this case, the $\gamma$-interaction destabilizes and stabilizes the two HOMOs and LUMOs, respectively, shrinking their energy gap.

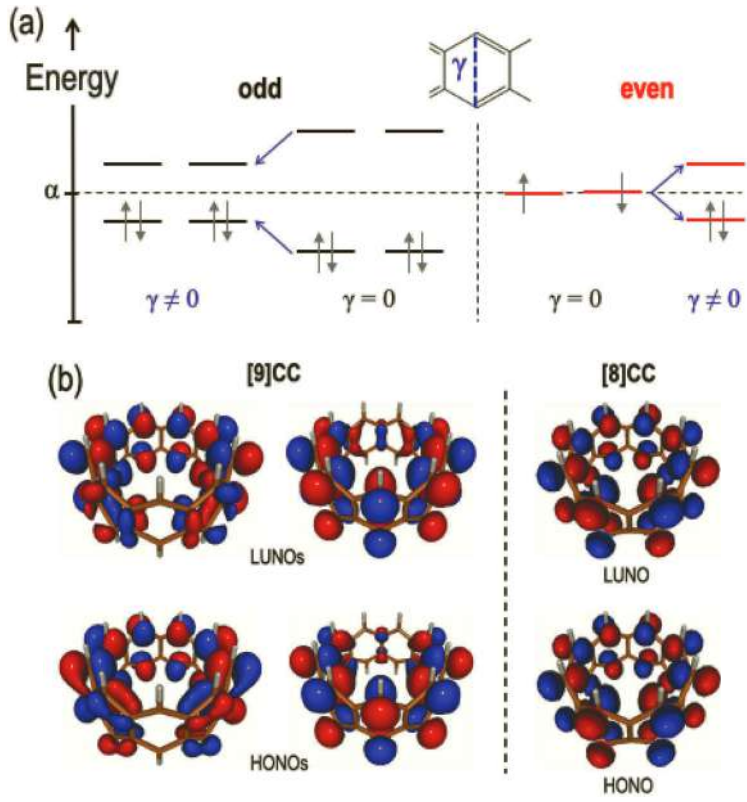


**Figure 2.18** (a) Hückel molecular orbital energy diagram around the Fermi level ($E = \alpha$) of odd (left) and even (right) [*n*]CC. Orbital energy change due to radical center interaction ($\gamma$) with respect to first neighbors ($\gamma = 0$) indicated with blue arrows. (b) Frontier natural orbitals of [9]CC (left) and [8]CC (right) computed at the RAS-SF level. Figure adapted from Ref. [60].

Electronic structure calculations at the RAS-SF level confirm the qualitative description of the Hückel model, with partially occupied frontier natural orbitals. Molecules with an odd number of rings have four natural orbitals with occupancies strongly departing from the closed-shell electronic distribution (0 or 2 electrons). Unpaired electrons are located on the non-bridge zigzag edge carbon atoms, as exemplified by [9]CC in Figure 2.18b. Interestingly, the two highest occupied natural orbitals (HONO and HONO-1) show anti-bonding interaction between the radical centers on different molecular

edges ($\gamma$-interaction in the Huckel model), whereas this interaction stabilizes, i.e., in-phase interaction, the LUNO and LUNO+1. Electron occupation numbers for the LUNO and LUNO+1 (HONO and HONO-1) systematically increase (decrease) with the number of benzene rings ($n$ = 5, 7, 9, and 11). Each of the odd-$n$ molecules show nearly identical diradical ($y_0$) and tetraradical ($y_1$) characters that increase with the size of the molecule (Table 2.5). The effective number of unpaired electrons ($N_U$) rapidly grows with $n$, largely exceeding two unpaired electrons for $n$ = 9 and 11. Therefore, these systems can be classified as singlet tetraradicaloids. The radical center interactions in the even-$n$ cyclic oligoacenes (Figure 2.18b) stabilize the HONO with respect to the LUNO, in good agreement with the energy gap obtained within the Hückel model with $\gamma \neq 0$. The diradical index for $n$ = 6, 8, 10, and 12 is sensibly larger than $y_1$ in each molecule, with large and rather constant $y_0$ values ($0.54 \leq y_0 \leq 0.66$), while $1.6 \leq N_U \leq 2.2$. Hence, [$n$]CCs with even number of rings are better classified as singlet diradicaloids.

**Table 2.5** Ground state diradical ($y_0$) and tetraradical ($y_1$) character indices and $N_U$ for cyclic oligoacenes [$n$]CC of increasing size computed at the RAS-SF/6-31G(d) level. Values from Ref. [60]

| | **[5]CC** | **[6]CC** | **[7]CC** | **[8]CC** | **[9]CC** | **[10]CC** | **[11]CC** | **[12]CC** |
|---|---|---|---|---|---|---|---|---|
| $y_0$ | 0.266 | 0.542 | 0.369 | 0.542 | 0.549 | 0.570 | 0.689 | 0.664 |
| $y_1$ | 0.216 | 0.102 | 0.368 | 0.119 | 0.549 | 0.158 | 0.682 | 0.186 |
| $N_U$ | 1.22 | 1.60 | 1.79 | 1.66 | 2.57 | 1.82 | 3.19 | 2.15 |

Computed vertical singlet–triplet energy gaps of [$n$]CC for $5 \leq n \leq 12$ are rather small, with $\Delta E_{ST}$ = 0.85 eV in [5]CC and $\Delta E_{ST} < 0.4$ eV for $n \geq 6$, in accordance with their strong diradical and tetradiradical characters. Importantly, cyclic oligoacenes with odd and even number of rings follow different $\Delta E_{ST}$ vs. $n$ trends (Figure 2.19). The tetraradicaloid odd-$n$ systems exhibit a fast decrease of $\Delta E_{ST}$ as $n$ increases, with $\Delta E_{ST}$ = 0.11 eV for $n$ = 11. Moreover, the singlet-quintet gap decreases from 2.07 eV in $n$ = 5 to 0.84 eV ($n$ = 7), 0.40 eV ($n$ = 9), and a very small value for $n$ = 11 (0.28 eV). On the other hand, $\Delta E_{ST}$ is obtained within the 0.2–0.3 eV range for $n$ = 6, 8, 10, and 12, in agreement with the trend of $y_0$ in Table 2.5. Hence, the computation of singlet–triplet and singlet–quintet gaps reinforces

the characterization of odd and even cyclic acenes as tetraradicaloids and diradicaloids, respectively.

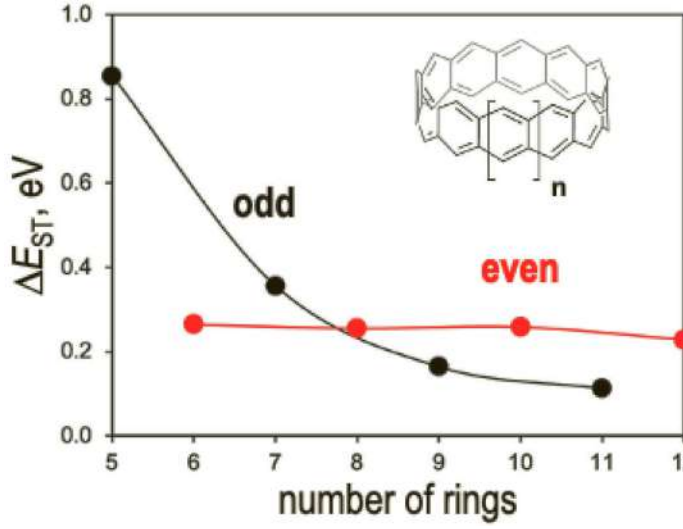


**Figure 2.19** Vertical singlet–triplet energy gap (in eV) of [*n*]CC for $5 \leq n \leq 12$ computed at the RAS-SF level.

Cyclic organic molecules formed as fused benzene rings, such as CCs, constitute the smallest segment of carbon nanotubes and could potentially be used as templates for the controlled generation of SWCNT. Concretely, the growth of [*n*]CC along the molecular $C_n$ axis would give rise to zigzag SWCNT. The family of short size nanobelt structures generated from [*n*]CC can be labeled as [*n*, *L*]CC, where *n* is the number of fused benzene rings in a single nanoring and *L* is the length of the nanobelt, that is, the number of fused nanorings. In the following, the [*n*, *L*]CC series of nanobelts with $1 \leq L \leq 6$ generated from the [12]CC ($L = 1$) singlet diradicaloid is considered.

The FOD along the [*n*, *L*]CC series mainly localizes at the zigzag edges with spurious delocalization toward the carbon atoms that would correspond to the atomic edges of the $L - 1$ system (Figure 2.20). The effective number of unpaired electrons ($N_U$) increases with the length of the nanobelt, that is, from about two unpaired electrons in [12, 1]CC to six unpaired electrons in [12, 6]CC, suggesting important polyradical character. Since the FOD localizes at the two ends of the nanobelt, increasing *L* pulls the radical centers

far apart from each other, sensibly diminishing their interaction. As a consequence, the singlet–triplet energy gap decays from ~ 6 kcal/mol for $L = 1$ to below 1 kcal/mol for $L \geq 3$.

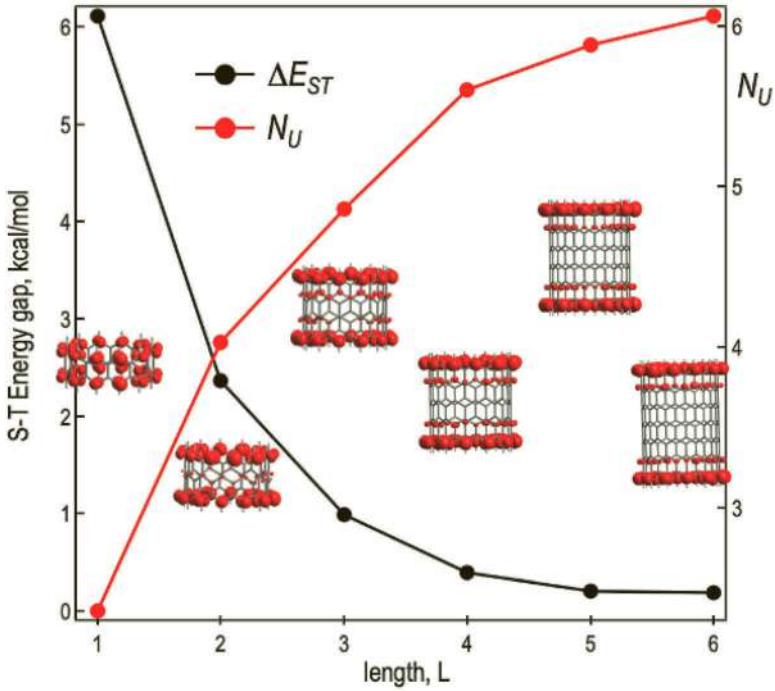


**Figure 2.20** Vertical singlet–triplet energy gap (in kcal/mol) and number of unpaired electrons ($N_U$) of [12, $L$]CC for $1 \leq L \leq 6$ computed at the RAS-SF level. Inset: representation of the density of unpaired electrons (FOD) for each nanobelt.

In conclusion, pristine zigzag nanobelt structures obtained as the fusion of CCs are expected to have large poliradical characters (stronger than their [$n$]CC building blocks), with unpaired electrons concentrated at the two molecular edges.

### 2.3.6 Diradical Character in Nanographene Induced by Pressure

In the last example of this chapter, it is showed how combining DFT and RAS-SF calculations might be used in the computational

characterization of the diradical character of a substituted nanographene. Concretely, this section focuses on the study of stable polycyclic frameworks synthesized by Morin and collaborators (**M1** and **M2** in Figure 2.21) [59].

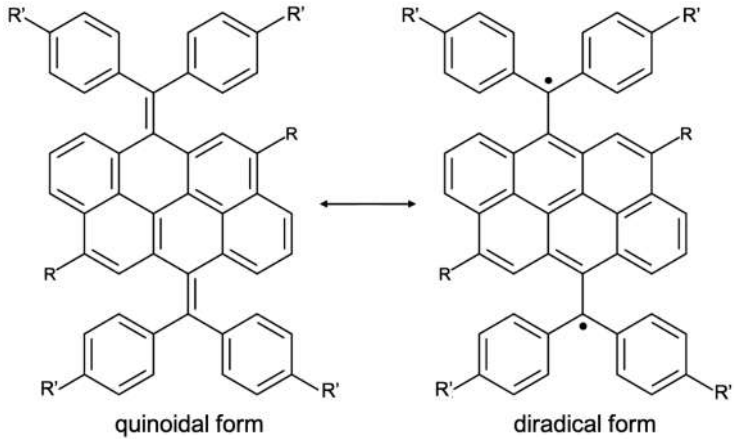


**Figure 2.21** Closed-shell quinoidal (left) and diradical canonical (right) forms of compounds **M1** (R' = tBu) and **M2** (R' = CN). In the present computational study R = H.

Molecules **M1** and **M2** present a laterally functionalized anthanthrone core, and exhibit remarkable stability because of extended delocalization of the π-conjugation, like other anthanthrone derivatives [163, 164]. But, in contrast to other chemically substituted anthanthrones, steric congestion in **M1** and **M2** is expected to promote diradical character upon planarization of the polycyclic core. Therefore, this type of system provides a unique opportunity in which a close relationship between structural strain and relative stability of closed-shell and open-shell electronic structures can be established. Molecules **M1** and **M2** have two main electronic structures, namely, the quinoidal and diradical forms, as shown in Figure 2.21. The driving force for their relative stability cannot be related to the formation of Clar's sextets, since both forms (closed-shell and open-shell) hold two aromatic six-membered rings, and was assigned to the release of steric interactions at the *peri* position of anthanthrone. Steric hindrance between the protons at the *peri* position of the anthanthrone core and the protons from the

peripheral phenyl groups impose an energy penalty to the quinoidal forms of **M1** and **M2** with respect to the planar anthranone core. In the crystalline solid, **M2** adopts a bent molecular structure, labeled in the following as butterfly geometry, in which the anthanthrone core is highly contorted along the transversal aromatic axis and the angle of the terminal methylene groups is twisted by 27°, in good agreement with the optimized ground state geometry (see Appendix A.5). Hence, both X-ray diffraction measurements and electronic structure calculations suggest a closed-shell singlet ground state for **M2**. On the other hand, variable-temperature $^1$H NMR experiments of **M1** and **M2** in solution show that the diradical form is thermally accessible. Moreover, the transition between closed and open-shell forms is reversible, since the closed-shell signals are fully recovered by lowering the temperature (0 °C). In the solid state, the formation of the diradical species can be achieved by applying a moderate pressure (0.3 GPA). The mechano-induced closed-shell to open-shell transition was observed by a change in color of the crystalline powder of **M2**, which is orange at atmospheric pressure, while it turns dark brown upon grinding and reverses back to orange by solvent vapor annealing with dichloromethane. Changes in the experimental and simulated Raman bands associated to the stretching modes of the central naphtoquinoid moiety and the peripheral benzenoid groups also support the formation of the planar-diradical form and the posterior recovery of the initial quinoidal species upon release of pressure [59].

DFT geometry optimization of **M2** with the B3LYP xc functional identifies the butterfly structure as the global minimum in the ground state potential energy surface (Figure 2.22). RAS-SF calculations on the ground state butterfly structure confirm its strong closed-shell character, with a large singlet–triplet vertical gap of 58.9 kcal/mol, and HONO and LUNO occupancies very close to the perfect closed-shell situation, i.e., 1.96 and 0.04 electrons, respectively (Figure 2.23). At the B3LYP level, the optimized diradical structure of **M2** is computed at $\Delta G$ = 1.3 kcal/mol with respect to the butterfly overall minimum (Figure 2.22). At the metastable planar conformation, the singlet state has a strong diradical character, with the lowest triplet state nearly degenerated. The computed RAS-SF electronic vertical gap is only 0.3 kcal/mol, in very good agreement with the experimental

value extracted from the adjustment of $\chi_m T$ to the Bleaney-Bowers model [165] (0.8 kcal/mol). The two frontier natural orbitals of the singlet at the planar minimum have electron occupancies close to one with two unpaired electrons overall (Figure 2.23). The two unpaired electrons are located at the two *exo*-acene carbon atoms with vanishing delocalization at the polycyclic core. Such decoupling of the two radical centers at the planar conformation explains the small singlet–triplet gap and the strong diradical character of the local (metastable) minimum.

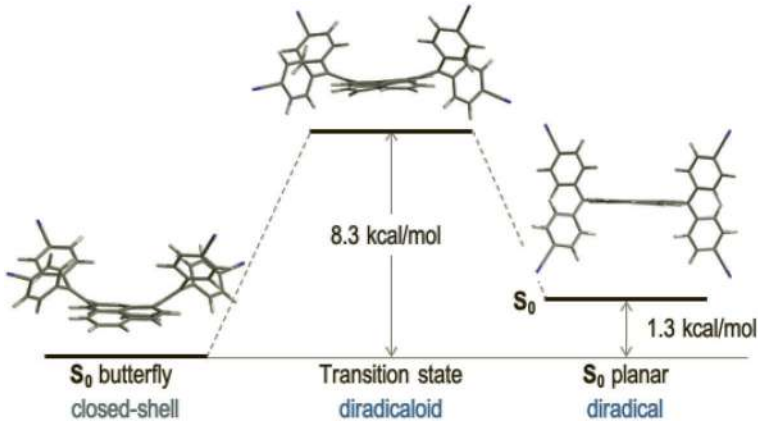


**Figure 2.22** Butterfly and planar ground state minima and the transition state for their interconversion of **M2** with relative Gibbs free energies at 298.15 K (B3LYP). Adapted from Ref. [59].

Interestingly, the conversion between the two conformers of **M2**, i.e., from the quinoidal butterfly form to the diradical planar structure, has to overcome a quite small energy barrier of 8.3 kcal/mol. This explains the changes in the $^1$H resonances of the aromatic region at high temperature and the transition induced by a mild pressure in the solid state. The transition state along quinoidal to diradical pathway presents an intermediate structure between the two forms, with a quite planar anthranone core. The transition state singlet can be regarded as a mild diradicaloid, with an energy gap to the first excited triplet state of 26.6 kcal/mol and an increased density of unpaired electrons with respect to the butterfly singlet (Figure 2.23).

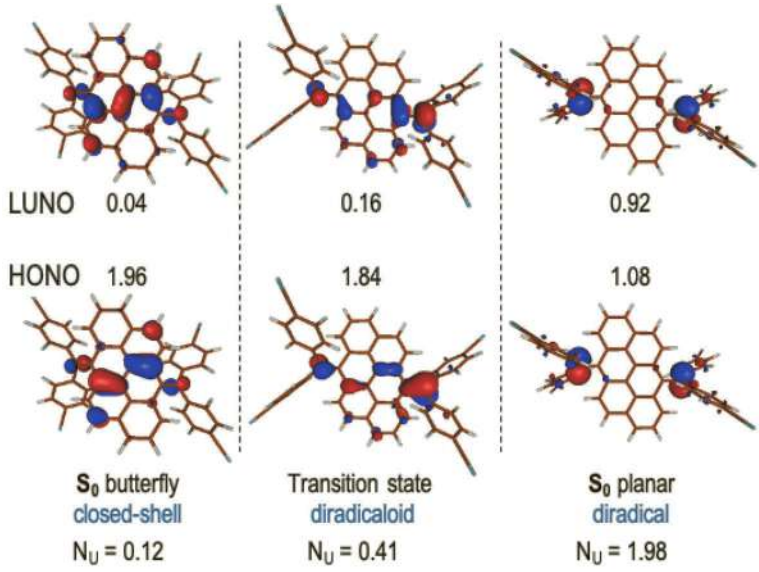


**Figure 2.23** Closed-shell quinoidal (left), transition state diradicaloid (center), and diradical canonical (right) forms of compound **M2**. Adapted from Ref. [59].

To summarize, the studied anthanthrone-based quinodimethane compounds present a contorted ground state geometry with a closed-shell character that can be easily flatten in the solid state upon application of mild mechanical stress. The applied pressure allows the system to overcome a diradicaloid transition state and forms a kinetically trapped diradical with a planar anthanthrone core in which the break of a π-bond is compensated by the release of steric strain.

## 2.4 Summary

This chapter discusses the use of SF methods in the study of molecular diradicaloids. The theoretical foundations of SF approaches have been presented and their applicability has been illustrated by several examples.

The SF ansatz has demonstrated to be a suitable approach in the computational study of molecules with strongly correlated electrons, like in diradicals or diradicaloids. The SF excitation operator has

been introduced for different quantum chemistry models (CI, CC, or DFT), all with their advantages and limitations. Amongst them, the SF version of (linear-response) TDDFT has shown to provide excellent results in the study of molecules with two or three correlated electrons, i.e., diradicals and triradicals, but it is not able to properly describe low-lying electronic states when electron correlation extends to four or more electrons. On the other hand, the definition of an active orbital space in conjunction with a SF excitation operator in RAS-SF (or RASCI-SF) has proven to be an excellent approach for the study of diradicaloids and polyradicaloids in general. The flexibility and relatively low computational cost of RAS-SF within the hole and electron approximation make it applicable to the study of medium to large size molecules with multiple unpaired electrons. Moreover, this methodology has been complemented by a variety of computational tools extremely useful in the characterization of strongly correlated molecular systems, e.g., natural orbitals or the density of unpaired electrons, and in particular in organic diradicaloids.

SF methods have experienced great progress in the recent years [56] and have become a rather standard approach, regularly employed by many computational chemists. Moreover, current developments trying to improve the accuracy of SF approaches, e.g., adding dynamic correlation to the RAS-SF method [166] and new implementations for the calculation of molecular properties [167] will shortly expand even more the range of applicability of the methods.

For all of the above, I am convinced that in the years to come SF methods will continue to be used in the computational characterization of novel systems with unique electronic structure properties, and will help to design new interesting molecules with partial diradical (or polyradical) character.

## Acknowledgements

The author acknowledges financial support from the Spanish Government MINECO/FEDER (project PID2019-109555GB-I00) and the Eusko Jaurlaritza (Basque Government, project PIBA19-0004).

# Appendix A

# Computational Details

## A.1 Computational Details for Section 2.3.2

Molecular geometries of phenalenyl and triangulene where optimized at the M06-2X/6-311G(d,p) level. RAS-SF calculations of phenalenyl were done by using the lowest restricted open-shell HF (ROHF) spin-doublet state as the reference configuration, with a RAS2 subspace formed by 7 electrons in the $2e''$, $2a_2''$, $1a_1''$, $3e'$, and $3a_2''$ orbitals. In triangulene, RAS2 included 10 electrons in the $3e''$, $1a_1''$, $3a_2''$, $4e''$, $4a_2''$, $5e''$, and $2a_1''$ orbitals. All doubly occupied and virtual orbitals were included in RAS1 and RAS3 subspaces, respectively. RAS-SF calculations were done with the 6-311G(d,p) basis set. Most of these results have been published in Ref. [58].

## A.2 Computational Details for Section 2.3.3

Molecular geometries of linear acenes and zethrenes were optimized with the spin unrestricted version of the Coulomb Attenuated Method version of B3LYP energy functional (CAM-B3LYP) [168]. Singlet–triplet energy gaps were computed at the SF-TDDFT level with the TDA and the BHHLYP functionals [169] (SF-BHHLYP), and with the RAS-SF method [42]. RAS-SF calculations were performed with the presence of hole and particle contributions using the lowest triplet state as the reference configuration and with four electrons in four orbitals in the RAS2 space. All doubly occupied and virtual orbitals were included in RAS1 and RAS3 subspaces, respectively. Carbon 1s core orbitals were frozen in the CI expansion of the wave function. All calculations were done with the 6-31G(d,p) basis set. Charge resonance contributions were obtained at the RAS-SF method with two electrons in two orbitals in the RAS2 space. Most of these results have been published in [123].

## A.3 Computational Details for Section 2.3.4

Molecular geometries of FF-1, FF-2, FF-3, and FF-4 were optimized at the UB3LYP level with the 6-311G(d,p) basis set. Calculation of vertical singlet–triplet energy gaps, diradical indices ($y_0$), and effective number of unpaired electrons ($N_U$), and spatial representation of natural orbitals and density of unpaired electrons (FOD) were done at the RAS-SF/6-31G(d) level. The reference configuration employed in all RAS-SF calculations corresponds to the lowest triplet ROHF state; RAS2 contains eight electrons in eight orbitals, while RAS1 (RAS3) contains the entire set of doubly occupied (virtual) molecular orbitals. Most of these results have been published in Ref. [150].

## A.4 Computational Details for Section 2.3.5

Molecular orbital energy diagrams of cyclic acenes within the Hückel model were obtained with $\beta = \alpha/10$ and $\gamma = \beta/5$ for the Coulomb and resonance integrals. Ground state geometries were optimized with the M06-2X functional [170] and the 6-31+G(d) basis set. RAS-SF calculations used the lowest ROHF triplet state as the reference Slater determinant in all cyclic acenes with an even number of benzene rings, whereas the lowest ROHF quintet was employed as the reference configuration for [*n*]CC molecules with *n*-odd. The restricted orbital space considered eight electrons in eight π-orbitals for the RAS2 subspace. All virtual and doubly occupied π-orbitals were included in the RAS1 and RAS3 subspaces, respectively. Excitations from core electrons (1s carbon orbitals) were disregarded. RAS-SF calculations were done with the 6-31G(d) basis set.

## A.5 Computational Details for Section 2.3.6

Molecular geometries of **M2** were optimized at the (unrestricted) B3LYP level with the 6-31G(d) basis set. The character of the critical points on the ground state potential energy surface (minima or transition states) was characterized by their harmonic vibrational frequencies. Relative Gibbs free energies between the two minima

and the transition state were obtained with the harmonic oscillator approximation. Electronic energies were further refined by single-point calculations at the optimized geometries by using the triple-zeta quality 6-311++G(2df,2p) basis set. RAS-SF calculations were performed with the 6-31G(d) basis set and by considering four electrons in four orbitals in the RAS2 space. All occupied and virtual orbitals were included in the RAS1 and RAS2 subspaces, respectively.

## References


1. Moss, G. P., Smith, P. A. S., and Tavernier, D. (1995). Glossary of class names of organic compounds and reactivity intermediates based on structure (IUPAC recommendations 1995), *Pure Appl. Chem.* **67**, 8–9, pp. 1307–1375, doi:https://doi.org/10.1351/pac199567081307, URL https://www.degruyter.com/view/journals/pac/67/8-9/article-p1307.xml.
2. Stuyver, T., Zeng, T., Tsuji, Y., Geerlings, P., and De Proft, F. (2018). Diradical character as a guiding principle for the insightful design of molecular nanowires with an increasing conductance with length, *Nano Lett.* **18**, 11, pp. 7298–7304, doi:10.1021/acs.nanolett.8b03503, URL https://doi.org/10.1021/ acs.nanolett.8b03503.
3. Tsuji, Y., Hoffmann, R., Strange, M., and Solomon, G. C. (2016). Close relation between quantum interference in molecular conductance and diradical existence, *Proc. Nat. Acad. Sci.* **113**, 4, p. E413, doi:10.1073/pnas.1518206113, URL http://www.pnas. org/content/113/4/E413.abstract.
4. Nagai, H., Nakano, M., Yoneda, K., Kishi, R., Takahashi, H., Shimizu, A., Kubo, T., Kamada, K., Ohta, K., Botek, E., and Champagne, B. (2010). Signature of multiradical character in second hyperpolarizabilities of rectangular graphene nanoflakes, *Chem. Phys. Lett.* **489**, 4, pp. 212–218, doi:https://doi.org/10.1016/j.cplett.2010.03.013, URL http://www.sciencedirect.com/science/article/pii/S0009261410003787.
5. Nakano, M. and Champagne, B. (2016). Nonlinear optical properties in open-shell molecular systems, *WIREs: Comput. Mol. Sci.* **6**, 2, pp. 198–210.
6. Lahti, P. M. (1999). *Magnetic Properties of Organic Materials* (Taylor & Francis), ISBN 9780824719760, URL https://books. google.es/books?id=YqIz4vdt14MC.
7. Smith, M. and Michl, J. (2013). Recent advances in singlet fission, *Annu. Rev. Phys. Chem.* **64**, pp. 361–368.

8. Smith, M. B. and Michl, J. (2010). Singlet fission, *Chem. Rev.* **110**, pp. 6891–6936.
9. Casanova, D. (2018). Theoretical modeling of singlet fission, *Chem. Rev.* **118**, pp. 7164–7207.
10. Zhivonitko, V. V., Bresien, J., Schulz, A., and Koptyug, I. V. (2019). Parahydrogen-induced polarization with a metal-free pp biradicaloid, *Phys. Chem. Chem. Phys.* **21**, 11, pp. 5890–5893, doi:10.1039/C8CP07625A, URL http://dx.doi.org/10.1039/C8CP07625A.
11. Mendez-Vega, E., Maehara, M., Raut, A. H., Mieres-Perez, J., Tsuge, M., Lee, Y.-P., and Sander, W. (2018). Activation of molecular hydrogen by arylcarbenes, *Chemistry –A European Journal* **24**, 70, pp. 18801–18808, doi:https://doi.org/10.1002/chem.201804657.
12. Hinze, J. (1973). MC-SCF. I. the multi-configuration self–consistent–field method, *J. Chem. Phys.* **59**, 12, pp. 6424–6432, doi:10.1063/1.1680022, URL http://dx.doi.org/10.1063/1.1680022.
13. Roos, B. O., Taylor, P. R., and Siegbahn, P. E. M. (1980). A complete active space SCF method (CASSCF) using a density matrix formulated super-CI approach, *Chem. Phys.* **48**, pp. 157–173.
14. Siegbahn, P., Heiberg, A., Roos, B., and Levy, B. (1980). A comparison of the super-CI and the Newton-Raphson scheme in the complete active space SCF method, *Phys. Scr.* **21**, 3–4, pp. 323–327, doi:10.1088/0031-8949/21/3-4/014, URL http://dx.doi.org/10.1088/0031-8949/21/3-4/014.
15. Siegbahn, P. E. M., Almlöf, J., Heiberg, A., and Roos, B. O. (1981). The complete active space SCF (CASSCF) method in a Newton-Raphson formulation with application to the HNO molecule, *J. Chem. Phys.* **74**, 4, pp. 2384–2396, doi:10.1063/1.441359, URL https://doi.org/10.1063/L441359.
16. Buenker, R. J. and Peyerimhoff, S. D. (1974). Individualized configuration selection in CI calculations with subsequent energy extrapolation, *Theor. Chim. Acta* **35**, 1, pp. 33–58, doi:10.1007/ BF02394557, URL https://doi.org/10.1007/BF02394557.
17. Buenker, R. J., Peyerimhoff, S. D., and Butscher, W. (1978). Applicability of the multi-reference double-excitation CI (MRD-CI) method to the calculation of electronic wavefunctions and comparison with related techniques, *Mol. Phys.* **35**, 3, p. 771791, doi:10.1080/00268977800100581, URL https://doi.org/10.1080/00268977800100581.
18. Davidson, E. R. and Bender, C. F. (1978). Perturbation theory for multiconfiguration reference states, *Chem. Phys. Lett.* **59**, 3, pp. 369–374,

doi:https://doi.org/10.1016/ 0009-2614(78)85001-5, URL http://www.sciencedirect.com/science/article/pii/0009261478850015.

19. Kirtman, B. (1981). Simultaneous calculation of several interacting electronic states by generalized Van Vleck perturbation theory, *J. Chem. Phys.* **75**, 2, pp. 798–808, doi:10.1063/1.442123, URL https://doi.org/10.1063/1.442123.
20. Roos, B. O., Linse, P., Siegbahn, P. E. M., and Blomberg, M. R. A. (1982). A simple method for the evaluation of the second-order-perturbation energy from external double-excitations with a CASSCF reference wavefunction, *Chem. Phys.* **66**, 1, pp. 197–207, doi:https://doi.org/10.1016/0301-0104(82)88019-1, URL http://www.sciencedirect.com/science/article/pii/0301010482880191.
21. Andersson, K. (1995). Different forms of the zeroth-order hamiltonian in second-order perturbation theory with a complete active space self-consistent field reference function, *Theor. Chim. Acta* **91,** 1, pp. 31–46, doi:10.1007/BF01113860, URL https://doi.org/10.1007/BF01113860.
22. Andersson, K., Malmqvist, P.-Å., Roos, B. O., Sadlej, A., and Wolinski, K. (1990). 2nd order perturbation theory with a CASSCF reference function, *J. Phys. Chem.* **94**, pp. 5483–5488.
23. Andersson, K., Malmqvist, P.-Å., and Roos, B. O. (1992). Second-order perturbation theory with a complete active space self-consistent field reference function, *J. Chem. Phys.* **96**, p. 1218.
24. Parr, R. and Yang, W. (1989). *Density functional theory of atoms and molecules, International Series of Monographs on Chemistry,* Vol. 16 (Oxford, New-York).
25. Kohn, W. and Sham, L. (1965). Self-consistent equations including exchange and correlation effects, *Phys. Rev.* **140**, pp. A1133–A1138.
26. Krylov, A. I. (2001). Size-consistent wave functions for bond-breaking: The equation-of-motion spin-flip model, *Chem. Phys. Lett.* **338**, pp. 375–384.
27. Krylov, A. I. and Sherrill, C. D. (2002). Perturbative corrections to the equation-of-motion spin-flip SCF model: Application to bond-breaking and equilibrium properties of diradicals, *J. Chem. Phys.* **116**, pp. 3194–3203.
28. Krylov, A. I. (2001). Spin-flip configuration interaction: An electronic structure model that is both variational and size-consistent, *Chem. Phys. Lett.* **350**, pp. 522–530.

29. Stanton, J. F. and Bartlett, R. J. (1993). The equation of motion coupled-cluster method: A systematic biorthogonal approach to molecular excitation energies, transition probabilities, and excited state properties, *J. Chem. Phys.* **98**, pp. 7029–7039.
30. Krylov, A. I. (2008). Equation-of-motion coupled-cluster methods for open-shell and electronically excited species: The hitchhiker's guide to Fock space, *Annu. Rev. Phys. Chem.* **59**, pp. 433–462.
31. Nooijen, M. and Snijders, J. G. (1993). Coupled-cluster green's function method: Working equations and applications, *Int. J. Quant. Chem.* **48**, 1, pp. 15–48, doi:https://doi.org/10.1002/qua.560480103.
32. Krylov, A. I. (2006). The spin-flip equation-of-motion coupled-cluster electronic structure method for a description of excited states, bond-breaking, diradicals, and triradicals, *Acc. Chem. Res.* **39**, pp. 83–91.
33. Krylov, A. I., Sherrill, C. D., and Head-Gordon, M. (2000). Excited states theory for optimized orbitals and valence optimized orbitals coupled-cluster doubles models, *J. Chem. Phys.* **113**, pp. 6509–6527.
34. Ghosh, D. (2013). Perturbative approximations to single and double spin-flip equation-of-motion coupled-cluster singles doubles methods, *J. Chem. Phys.* **139**, p. 124116.
35. Lefrancois, D., Wormit, M., and Dreuw, A. (2015). Adapting algebraic diagrammatic construction schemes for the polarization propagator to problems with multi-reference electronic ground states exploiting the spin-flip ansatz, *J. Chem. Phys.* **143**, p. 124107.
36. Dreuw, A. and Wormit, M. (2015). The algebraic diagrammatic construction scheme for the polarization propagator for the calculation of excited states, *WIREs: Comput. Mol. Sci.* **5**, pp. 82–95.
37. Casanova, D. and Head-Gordon, M. (2008). The spin-flip extended single excitation configuration interaction method, *J. Chem. Phys.* **129**, p. 064104.
38. Sears, J. S., Sherrill, C. D., and Krylov, A. I. (2003). A spin-complete version of the spin-flip approach to bond breaking: What is the impact of obtaining spin eigenfunctions?, *J. Chem. Phys.* **118**, pp. 9084–9094.
39. Casanova, D. and Head-Gordon, M. (2009). Restricted active space spin-flip configuration interaction approach: Theory, implementation and examples, *Phys. Chem. Chem. Phys.* **11**, pp. 9779–9790.
40. Mayhall, N. J., Horn, P. R., Sundstrom, E. J., and Head-Gordon, M. (2014). Spin-flip non-orthogonal configuration interaction: A variational and almost black-box method for describing strongly correlated molecules, *Phys. Chem. Chem. Phys.* **16**, 41, pp. 22694–22705.

41. Mato, J. and Gordon, M. S. (2018). A general spin-complete spin-flip configuration interaction method, *Phys. Chem. Chem. Phys.* **20**, 4, pp. 2615–2626, doi:10.1039/c7cp06837a, URL http://dx.doi.org/10.1039/C7CP06837A.

42. Shao, Y., Head-Gordon, M., and Krylov, A. I. (2003). The spin-flip approach within time-dependent density functional theory: Theory and applications to diradicals, *J. Chem. Phys.* **118**, pp. 4807–4818.

43. Wang, F. and Ziegler, T. (2004). Time-dependent density functional theory based on a noncollinear formulation of the exchange-correlation poential, *J. Chem. Phys.* **121**, p. 12191.

44. Li, Z. D., Liu, W. J., Zhang, Y., and Suo, B. B. (2011). Spin-adapted open-shell time-dependent density functional theory. II. Theory and pilot application, *J. Chem. Phys.* **134**, p. 134101.

45. Bernard, Y. A., Shao, Y., and Krylov, A. I. (2012). General formulation of spin-flip time-dependent density functional theory using non-collinear kernels: Theory, implementation, and benchmarks, *J. Chem. Phys.* **136**, p. 204103.

46. Zhang, X. and Herbert, J. M. (2015). Spin-flip, tensor equation-of-motion configuration interaction with a density-functional correction: A spin-complete method for exploring excited-state potential energy surfaces, *J. Chem. Phys.* **143**, p. 234107.

47. Orms, N. and Krylov, A. I. (2018). Singlet–triplet energy gaps and the degree of diradical character in binuclear copper molecular magnets characterized by spin-flip density functional theory, *Phys. Chem. Chem. Phys.* **20**, pp. 13127–13144.

48. Li, Z. D. and Liu, W. J. (2010). Spin-adapted open-shell random phase approximation and time-dependent density functional theory. I. Theory, *J. Chem. Phys.* **133**, p. 064106.

49. Wang, F. and Ziegler, T. (2005). The performance of time-dependent density functional theory based on a noncollinear exchange-correlation potential in the calculations of excitation energies, *J. Chem. Phys.* **122**, p. 074109.

50. Wang, F. and Ziegler, T. (2006). Use of noncollinear exchange-correlation potential in multiplet resolutions by time-dependent density functional theory, *Int. J. Quant. Chem.* **106**, pp. 2545–2550.

51. Yamanaka, S., Yamaki, D., Shigeta, Y., Nagao, H., Yoshioka, Y., Suzuki, N., and Yamaguchi, K. (2000). Generalized spin density functional theory for noncollinear molecular magnetism, *Int. J. Quant. Chem.* **80**, 4–5, pp. 664–671, doi:10.1002/1097-461X(2000) 80:4/5(664::AID-

QUA15}3.0. CO;2-C, URL https://doi.org/10.1002/1097-461X(2000)80: 4/5<664::AID-QUA15>3.0.CO;2-C.

52. Yamanaka, S., Yamaki, D., Shigeta, Y., Nagao, H., and Yamaguchi, K. (2001). Noncollinear spin density functional theory for spin-frustrated and spin-degenerate systems, *Int. J. Quant. Chem.* **84**, 6, pp. 670–676, doi:10.1002/qua.1422, URL https://doi.org/10.1002/qua.1422.
53. Rinkevicius, Z., Vahtras, O., and Ågren, H. (2010). Spin-flip time dependent density functional theory applied to excited states with single, double, or mixed electron excitaion character, *J. Chem. Phys.* **133**, p. 114104.
54. Rinkevicius, Z. and Argen, H. (2010). Spin-flip time dependent density functional theory for singlet–triplet splittings in $\sigma,\sigma$-biradicals, *Chem. Phys. Lett.* **491**, pp. 132–135.
55. Li, Z. and Liu, W. (2012). Theoretical and numerical assessments of spin-flip time-dependent density functional theory, *J. Chem. Phys.* **136**, p. 024107.
56. Casanova, D. and Krylov, A. I. (2020). Spin-flip methods in quantum chemistry, *Phys. Chem. Chem. Phys.* **22**, 8, pp. 4326–4342, doi:10.1039/C9CP06507E, URL http://dx.doi.org/10. 1039/C9CP06507E.
57. de~Wergifosse, M., Bannwarth, C., and Grimme, S. (2019). A simplified spin-flip time-dependent density functional theory approach for the electronic excitation spectra of very large diradicals, *J. Phys. Chem. A* **123**, pp. 5815–5825.
58. Sandoval-Salinas, M. E., Carreras, A., and Casanova, D. (2019). Triangular graphene nanofragments: Open-shell character and doping, *Phys. Chem. Chem. Phys.* **21**, 18, pp. 9069–9076, doi:10.1039/c9cp00641a, URL http://dx.doi.org/10.1039/C9CP00641A.
59. Desroches, M., Burrezo, P. M., Boismenu-Lavoie, J., Alvarez, M. P., Gomez-Garcia, C. J., Matxain, J. M., Casanova, D., Morin, J.-F., and Casado, J. (2017). Breaking bonds and forming nanographene diradicals with pressure, *Angew. Chem. Int. Ed.* **56**, 51, pp. 16212–16217, doi:10.1002/anie.201708740, URL https: //doi.org/10.1002/anie.201708740.
60. Pérez-Guardiola, A., Sandoval-Salinas, M. E., Casanova, D., San-Fabián, E., Pérez-Jiménez, A. J., and Sancho-García, J.C. (2018). The role of topology in organic molecules: Origin and comparison of the radical character in linear and cyclic oligoacenes and related oligomers, *Phys. Chem. Chem. Phys.* **20**, 10, pp. 7112–7124, doi:10.1039/c8cp00135a, URL http://dx.doi.org/10.1039/C8CP00135A.

61. Li, Z., Gopalakrishna, T. Y., Han, Y., Gu, Y., Yuan, L., Zeng, W., Casanova, D., and Wu, J. (2019). [6]cyclo-para-phenylmethine: An analog of benzene showing global aromaticity and open-shell diradical character, *J. Am. Chem. Soc.* **141**, 41, pp. 16266–16270, doi:10.1021/jacs.9b09780, URL http://dx.doi.org/10. 1021/jacs.9b09780.

62. Chunchen, L., Sandoval-Salinas, M. E., Hong, Y., Gopalakrishna, T. Y., Phan, H., Aratani, N., Herng, T. S., Ding, J., Yamada, H., Kim, D., Casanova, D., and Wu, J. (2018). Macrocyclic polyradicaloids with unusual super-ring structure and global aromaticity, *Chem* **4**, 7, pp. 1586–1595, doi:https://doi.org/10.1016/j.chempr.2018.03.020, URL http://www.sciencedirect. com/science/article/pii/S2451929418301335.

63. Luzanov, A. V., Casanova, D., Feng, X., and Krylov, A. I. (2015). Quantifying charge resonance and multiexciton character in coupled chromophores by charge and spin cumulant analysis, *J. Chem. Phys.* **142**, p. 224104.

64. Casanova, D. and Krylov, A. I. (2016). Quantifying local excitation, charge resonance, and multiexciton character in correlated wave functions of multichromophoric systems, *J. Chem. Phys.* **144**, p. 014102.

65. Zimmerman, P., Bell, F., Casanova, D., and Head-Gordon, M. (2011). Mechanism for singlet fission in pentacene and tetracene: From single exciton to two triplets, *J. Am. Chem. Soc.* **133**, pp. 19944–19952.

66. Casanova, D. (2014). Electronic structure study of singlet-fission in tetracene derivatives, *J. Chem. Theory Comput.* **10**, pp. 324–334.

67. Feng, X., Casanova, D., and Krylov, A. I. (2016). Intra- and inter-molecular singlet fission in covalently linked dimers, *J. Phys. Chem. C* **120**, pp. 19070–19077.

68. Sandoval-Salinas, M. E., Carreras, A., Casado, J., and Casanova, D. (2019). Singlet fission in spiroconjugated dimers, *J. Chem. Phys.* **150**, 20, p. 204306, doi:10.1063/1.5097048, URL http:// dx.doi.org/10.1063/1.5097048.

69. Matsika, S., Feng, X., Luzanov, A. V., and Krylov, A. I. (2014). What we can learn from the norms of one-particle density matrices, and what we can't: Some results for interstate properties in model singlet fission systems, *J. Phys. Chem. A* **118**, pp. 11943–11955.

70. Casanova, D. (2013). Efficient implementation of restricted active space configuration interaction with the hole and particle approximation, *J. Comput. Chem.* **34**, 9, pp. 720–730, doi:10.1002/jcc.23188, URL https://doi.org/10.1002/jcc.23188.

71. Casanova, D. (2012). Avoided crossings, conical intersections, and low-lying excited states with a single reference method: The restricted

active space spin-flip configuration interaction approach, *J. Chem. Phys.* **137**, 8, p. 084105, doi:10.1063/1.4747341, URL http://dx.doi.org/10.1063/1.4747341.

72. Zimmerman, P. M., Bell, F., Goldey, M., Bell, A. T., and Head-Gordon, M. (2012). Restricted active space spin-flip configuration interaction: Theory and examples for multiple spin flips with odd numbers of electrons, *J. Chem. Phys.* **137**, 16, p. 164110.
73. Shao, Y., Gan, Z., et al. (2015). Advances in molecular quantum chemistry contained in the Q-Chem 4 program package, *Mol. Phys.* **113**, pp. 184–215.
74. Hayes, E. F. and Siu, A. K. Q. (1971). Electronic structure of the open forms of three-membered rings, *J. Am. Chem. Soc.* **93**, 8, pp. 2090–2091, doi:10.1021/ja00737a064, URL https://doi.org/ 10.1021/ja00737a064.
75. Yamaguchi, K. (1975). The electronic structures of biradicals in the unrestricted Hartree-Fock approximation, *Chem. Phys. Lett.* **33**, 2, pp. 330–335, doi:https://doi.org/10.1016/0009-2614(75)80169-2, URL http://www.sciencedirect.com/ science/article/pii/0009261475801692.
76. Davidson, E.R. and Löwdin, P.-O. (1972). *Natural Orbitals,* Vol. 6 (Academic Press), ISBN 0065-3276, pp. 235–266, doi:https://doi.org/10.1016/S0065-3276(08)60547-X, URL http://www.sciencedirect.com/science/article/pii/S006532760860547X.
77. Grimme, S. and Hansen, A. (2015). A practicable real-space measure and visualization of static electron-correlation effects, *Angew. Chem. Int. Ed.* **54**, 42, pp. 12308–12313, doi:https://doi.org/10.1002/anie.201501887.
78. Bauer, C. A., Hansen, A., and Grimme, S. (2017). The fractional occupation number weighted density as a versatile analysis tool for molecules with a complicated electronic structure, *Chem. Eur. J.* **23**, 25, pp. 6150–6164, doi:https://doi.org/10.1002/chem.201604682.
79. Takatsuka, K., Fueno, T., and Yamaguchi, K. (1978). Distribution of odd electrons in ground-state molecules, *Theor. Chim. Acta* **48**, pp. 175–183.
80. Head-Gordon, M. (2003). Characterizing unpaired electrons from the one-particle density matrix, *Chem. Phys. Lett.* **372**, pp. 508–511.
81. Head-Gordon, M. (2003). Reply to comment on 'characterizing unpaired electrons from the one-particle density matrix', *Chem. Phys. Lett.* **380**, 3, pp. 488–489, doi:https://doi.org/10.1016/j.

cplett.2003.09.036, URL http://www.sciencedirect. com/science/article/pii/S0009261403015951.

82. Orms, N., Rehn, D. R., Dreuw, A., and Krylov, A. I. (2017). Characterizing bonding patterns in diradicals and triradicals by density-based wave function analysis: A uniform approach, *J. Chem. Theory Comput.* **14**, pp. 638–648.

83. Dunning Jr., T. (1970). Gaussian basis functions for use in molecular calculations. I. Contraction of (9s5p) atomic basis sets for the first-row atoms, *J. Chem. Phys.* **53**, p. 2823.

84. Canola, S., Casado, J., and Negri, F. (2018). The double exciton state of conjugated chromophores with strong diradical character: Insights from TDDFT calculations, *Phys. Chem. Chem. Phys.* **20**, pp. 24227–24238, doi:10.1039/C8CP04008G, URL http://dx.doi.org/10.1039/C8CP04008G.

85. Nakano, M., Kishi, R., Nitta, T., Kubo, T., Nakasuji, K., Kamada, K., Ohta, K., Champagne, B., Botek, E., and Yamaguchi, K. (2005). Second hyperpolarizability (γ) of singlet diradical system: Dependence of γ on the diradical character, *J. Phys. Chem. A* **109**, 5, pp. 885–891.

86. Nakano, M., Minami, T., Fukui, H., Yoneda, K., Shigeta, Y., Kishi, R., Champagne, B., and Botek, E. (2010). Approximate spin-projected spin-unrestricted density functional theory method: Application to the diradical character dependences of the (hyper)polarizabilities in p-quinodimethane models, *Chem. Phys. Lett.* **501**, 1, pp. 140–145, doi:https://doi.org/ 10.1016/j.cplett.2010.10.057, URL http://www.sciencedirect. com/science/article/pii/S0009261410014387.

87. Kishi, R., Bonness, S., Yoneda, K., Takahashi, H., Nakano, M., Botek, E., Champagne, B., Kubo, T., Kamada, K., Ohta, K., and Tsuneda, T. (2010). Long-range corrected density functional theory study on static second hyperpolarizabilities of singlet diradical systems, *J. Chem. Phys.* **132**, 9, p. 094107, doi:10.1063/ 1.3332707, URL https://doi.org/10.1063/1.3332707.

88. Feringa, B. L. and Browne, W. R. (2011). *Molecular Switches, 2 Volume Set* (Wiley), ISBN 9783527313655, URL https://books.google.es/books?id=ajpjvQEACAAJ.

89. Han, W., Kawakami, R. K., Gmitra, M., and Fabian, J. (2014). Graphene spintronics, *Nat. Nanotechnol.* **9**, 10, pp. 794–807, doi:10.1038/nnano.2014.214, URL https://doi.org/10.1038/nnano.2014.214.

90. Geim, A. K. and Novoselov, K. S. (2007). The rise of graphene, *Nat. Materials* **6**, 3, pp. 183–191, doi:10.1038/nmat1849, URL https://doi.org/10.1038/nmat1849.

91. Wang, W. L., Meng, S., and Kaxiras, E. (2008). Graphene nanoflakes with large spin, *Nano Lett.* **8**, 1, pp. 241–245, doi:10.1021/nl072548a, URL https://doi.org/10.1021/nl072548a.
92. Haddon, R. C. (1975). Design of organic metals and superconductors, *Nature* **256**, 5516, pp. 394–396, doi:10.1038/256394a0, URL https://doi.org/10.1038/256394a0.
93. Inoue, J., Fukui, K., Kubo, T., Nakazawa, S., Sato, K., Shiomi, D., Morita, Y., Yamamoto, K., Takui, T., and Nakasuji, K. (2001). The first detection of a Clar's hydrocarbon, 2,6,10-tri-tert-butyltriangulene: A ground-state triplet of non-kekulepolynuclear benzenoid hydrocarbon, *J. Am. Chem. Soc.* **123**, 50, pp. 12702–12703, doi:10.1021/ja016751y, URL https://doi.org/10.1021/ja016751y.
94. Morita, Y., Suzuki, S., Sato, K., and Takui, T. (2011). Synthetic organic spin chemistry for structurally well-defined open-shell graphene fragments, *Nat. Chem.* **3**, 3, pp. 197–204, doi:10.1038/ nchem.985, URL https://doi.org/10.1038/nchem.985.
95. Clar, E. (1964). *Polycyclic Hydrocarbons*, Parts I and II (Academic Press), URL https://books.google.es/books?id= aJwhAQAAMAAJ.
96. Fukui, K., Inoue, J., Kubo, T., Nakazawa, S., Aoki, T., Morita, Y., Yamamoto, K., Sato, K., Shiomi, D., Nakasuji, K., and Takui, T. (2001). The first non-kekulepolynuclear aromatic high-spin hydrocarbon: Generation of a triangulene derivative and band structure calculation of triangulene-based high-spin hydrocarbons, *Synth. Met* **121**, 1, pp. 1824–1825, doi:https://doi.org/10. 1016/S0379-6779(00)01023-7, URL http://www.sciencedirect. com/science/article/pii/S0379677900010237.
97. Allinson, G., Bushby, R. J., Paillaud, J. L., Oduwole, D., and Sales, K. (1993). Esr spectrum of a stable triplet.pi. biradical: Trioxytriangulene, *J. Am. Chem. Soc.* **115**, 5, pp. 2062–2064, doi:10.1021/ja00058a076, URL https://doi.org/10.1021/ ja00058a076.
98. Ovchinnikov, A. (1978). Multiplicity of the ground state of large alternant organic molecules with conjugated bonds, *Theor. Chim. Acta* **47**, pp. 297–304.
99. Lieb, E. H. (1989). Two theorems on the Hubbard model, *Phys. Rev. Lett.* **62**, 10, pp. 1201–1204, doi:10.1103/PhysRevLett.62. 1201, URL https://link.aps.org/doi/10.1103/PhysRevLett. 62.1201.
100. Das, A., Muller, T., Plasser, F., and Lischka, H. (2016). Polyradical character of triangular non-kekuléstructures, zethrenes, p-quinodimethane-linked bisphenalenyl, and the clar goblet in comparison: An extended multireference study, *J. Phys. Chem. A* **120**, 9, pp. 1625–1636,

doi:10.1021/acs.jpca.5b12393, URL https://doi.org/10.1021/acs.jpca.5b12393.

101. Pitkethly, M. J. (2004). Nanomaterials – The driving force, *Mater. Today* **7**, 12, pp. 20–29, doi:https://doi.org/10.1016/ S1369-7021(04)00627-3, URL http://www.sciencedirect.com/ science/article/pii/S1369702104006273.

102. Müllen, K. and Wegner, G. (2008). *Electronic Materials: The Oligomer Approach* (Wiley), ISBN 9783527612055, URL https: //books.google.es/books?id=eMLQrD20pj4C.

103. Bendikov, M., Wudl, F., and Perepichka, D. F. (2004). Tetrathiafulvalenes, oligoacenenes, and their buckminsterfullerene derivatives: The brick and mortar of organic electronics, *Chem. Rev.* **104**, 11, pp. 4891–4946, doi:10.1021/cr030666m, URL https://doi.org/10.1021/cr030666m.

104. Kivelson, S. and Chapman, O. L. (1983). Polyacene and a new class of quasi-one-dimensional conductors, *Phys. Rev. B* **28**, 12, pp. 7236–7243, doi:10.1103/PhysRevB.28.7236, URL https:// link.aps.org/doi/10.1103/PhysRevB.28.7236.

105. dos Santos, M. C. (2006). Electronic properties of acenes: Oligomer to polymer structure, *Phys. Rev. B* **74**, 4, pp. 045426–, doi:10.1103/PhysRevB.74.045426, URL https://link.aps.org/ doi/10.1103/PhysRevB.74.045426.

106. Dimitrakopoulos, C. D. and Malenfant, P. R. L. (2002). Organic thin film transistors for large area electronics, *Advanced Materials* **14**, 2, pp. 99–117, doi:https://doi.org/10.1002/1521-4095(20020116)14:2(99::AID-ADMA99)3.0.CO;2-9.

107. Hachmann, J., Dorando, J. J., Aviloés, M., and Chan, G. K. L. (2007). The radical character of the acenes: A density matrix renormalization group study, *J. Chem. Phys.* **127**, 13, p. 134309, doi:10.1063/1.2768362, URL https://doi.org/10.1063/ 1.2768362.

108. Houk, K. N., Lee, P. S., and Nendel, M. (2001). Polyacene and cyclacene geometries and electronic structures: Bond equalization, vanishing band gaps, and triplet ground states contrast with polyacetylene, *J. Org. Chem.* **66**, 16, pp. 5517–5521, doi:10.1021/jo010391f, URL https://doi.org/10.1021/jo010391f.

109. Gao, Y., Liu, C.-G., and Jiang, Y.-S. (2002). The valence bond study for benzenoid hydrocarbons of medium to infinite sizes, *J. Phys. Chem. A* **106**, 11, pp. 2592–2597, doi:10.1021/jp012057t, URL https://doi.org/10.1021/jp012057t.

110. Bendikov, M., Duong, H. M., Starkey, K., Houk, K. N., Carter, E. A., and Wudl, F. (2004). Oligoacenes: Theoretical prediction of open-shell

singlet diradical ground states, *J. Am. Chem. Soc.* **126**, 24, pp. 7416–7417, doi:10.1021/ja048919w, URL https://doi.org/10.1021/ja048919w.

111. Jiang, D.-E. and Dai, S. (2008). Electronic ground state of higher acenes, *J. Phys. Chem. A* **112**, 2, pp. 332–335, doi:10.1021/ jp0765087, URL https://doi.org/10.1021/jp0765087.
112. Clar, E. and Clar, E. J. (1972). *The Aromatic Sextet* (J. Wiley), ISBN 9780471158400, URL https://books.google.es/books?id=IXRIAAAAMAAJ.
113. Watanabe, M., Chang., Y., Liu, S., Chao, T., Goto, K., Islam, M., Yuan, C., Tao, Y., Shinmyozu, T., and Chow, T. (2012). The synthesis, crystal structure and chargetransport properties of hexacene, *Nat. Chem.* **4**, pp. 574–578.
114. Mondal, R., Shah, B. K., and Neckers, D. C. (2006). Photo-generation of heptacene in a polymer matrix, *J. Am. Chem. Soc.* **128**, 30, pp. 9612–9613, doi:10.1021/ja063823i, URL https://doi.org/10.1021/ja063823i.
115. Einholz, R., Fang, T., Berger, R., Gruninger, P., Früh, A., Chassoe, T., Fink, R. F., and Bettinger, H. F. (2017). Heptacene: Characterization in solution, in the solid state, and in films, *J. Am. Chem. Soc.* **139**, 12, pp. 4435–4442, doi:10.1021/jacs.6b13212, URL https://doi.org/10.1021/jacs.6b13212.
116. Qu, H. and Chi, C. (2010). A stable heptacene derivative substituted with electron-deficient trifluoromethylphenyl and triisopropylsilylethynyl groups, *Org. Lett.* **12**, 15, pp. 3360–3363, doi:10.1021/ol101158y, URL https://doi.org/10.1021/ ol101158y.
117. Chun, D., Cheng, Y., and Wudl, F. (2008). The most stable and fully characterized functionalized heptacene, *Angew. Chem. Int. Ed.* **47**, 44, pp. 8380–8385, doi:https://doi.org/10.1002/anie.200803345.
118. Payne, M. M., Parkin, S. R., and Anthony, J. E. (2005). Functionalized higher acenes: Hexacene and heptacene, *J. Am. Chem. Soc.* **127**, 22, pp. 8028–8029, doi:10.1021/ja051798v, URL https://doi.org/10.1021/ja051798v.
119. Kaur, I., Stein, N. N., Kopreski, R. P., and Miller, G. P. (2009). Exploiting substituent effects for the synthesis of a photooxidatively resistant heptacene derivative, *J. Am. Chem. Soc.* **131**, 10, pp. 3424–3425, doi:10.1021/ja808881x, URL https://doi.org/10.1021/ja808881x.
120. Kaur, I., Jazdzyk, M., Stein, N. N., Prusevich, P., and Miller, G. P. (2010). Design, synthesis, and characterization of a persistent nonacene

derivative, *J. Am. Chem. Soc.* **132**, 4, pp. 1261–1263, doi:10.1021/ja9095472, URL https://doi.org/10.1021/ja9095472.

121. Purushothaman, B., Bruzek, M., Parkin, S. R., Miller, A.-F., and Anthony, J. E. (2011). Synthesis and structural characterization of crystalline nonacenes, *Angew. Chem. Int. Ed.* **50**, 31, pp. 7013–7017, doi:https://doi.org/10.1002/anie.201102671.

122. Li, Y., Heng, W., Lee, B., Aratani, N., Zafra, J., Bao, N., Lee, R., Sung, Y., Sun, Z., Huang, K., Webster, R., Navarrete, J. L., Kim, D., Osuka, A., Casado, J., Ding, J., and Wu, J. (2012). Kinetically blocked stable heptazethrene and octazethrene: Closed-shell or open-shell in the ground state? *J. Am. Chem. Soc.* **134**, 36, pp. 14913–14922.

123. Huang, R., Phan, H., Herng, T. S., Hu, P., Zeng, W., Dong, S.-q., Das, S., Shen, Y., Ding, J., Casanova, D., and Wu, J. (2016). Higher order π-conjugated polycyclic hydrocarbons with open-shell singlet ground state: Nonazethrene versus nonacene, *J. Am.Chem. Soc.* **138**, 32, pp. 10323–10330, doi:10.1021/jacs.6b06188, URL https://doi.org/10.1021/jacs.6b06188.

124. Hu, P., Lee, S., Park, K. H., Das, S., Herng, T. S., Goncalves, T. P., Huang, K.-W., Ding, J., Kim, D., and Wu, J. (2016). Octazethrene and its isomer with different diradical characters and chemical reactivity: The role of the bridge structure, *J. Org. Chem.* **81**, 7, pp. 2911–2919, doi:10.1021/acs.joc.6b00172, URL https://doi.org/10.1021/acs.joc.6b00172.

125. Yadav, P., Das, S., Phan, H., Herng, T. S., Ding, J., and Wu, J. (2016). Kinetically blocked stable 5,6:12,13-dibenzozethrene: A laterally π-extended zethrene with enhanced diradical character, *Org. Lett.* **18**, 12, pp. 2886–2889, doi:10.1021/acs.orglett.6b01196, URL https://doi.org/10.1021/acs.orglett.6b01196.

126. Zafra, J., Gonziález Cano, R. C., Ruiz Delgado, M. C., Sun, Z., Li, Y., Lóipez Navarrete, J. T., Wu, J., and Casado, J. (2014). Zethrene biradicals: How pro-aromaticity is expressed in the ground electronic state and in the lowest energy singlet, triplet, and ionic states?, *J. Chem. Phys.* **140**, 5, p. 054706, doi:10.1063/1.4863557, URL https://doi.org/10.1063/1.4863557.

127. Sun, Z., Huang, K.-W., and Wu, J. (2011). Soluble and stable heptazethrenebis(dicarboximide) with a singlet open-shell ground state, *J. Am. Chem. Soc.* **133**, 31, pp. 11896–11899, doi:10.1021/ja204501m, URL https://pubs.acs.org/doi/abs/10. 1021/ja204501m.

128. Sun, Z., Lee, S., Park, K. H., Zhu, X., Zhang, W., Zheng, B., Hu, P., Zeng, Z., Das, S., Li, Y., Chi, C., Li, R.-W., Huang, K.-W., Ding, J., Kim, D., and Wu, J. (2013). Dibenzoheptazethrene isomers with different biradical characters: An

exercise of Clar's aromatic sextet rule in singlet biradicaloids, *J. Am. Chem. Soc.* **135**, 48, pp. 18229–18236, doi:10.1021/ja410279j, URL https:// doi.org/10.1021/ja410279j.

129. Hu, P., Lee, S., Herng, T. S., Aratani, N., Goncalves, T. P., Qi, Q., Shi, X., Yamada, H., Huang, K.-W., Ding, J., Kim, D., and Wu, J. (2016). Toward tetraradicaloid: The effect of fusion mode on radical character and chemical reactivity, *J. Am. Chem. Soc.* **138**, 3, pp. 1065–1077, doi:10.1021/jacs.5b12532, URL https:// doi.org/10.1021/jacs.5b12532.
130. Sun, Z. and Wu, J. (2013). 7,14-diaryl-substituted zethrene diimides as stable far-red dyes with tunable photophysical properties, *J. Org. Chem.* **78**, 18, pp. 9032–9040, doi:10.1021/jo401061g, URL https:// doi.org/10.1021/jo401061g.
131. Sun, Z., Huang, K.-W., and Wu, J. (2010). Soluble and stable zethrenebis(dicarboximide) and its quinone, *Org. Lett.* **12**, 20, pp. 4690–4693, doi:10.1021/ol102088j, URL https://doi.org/10.1021/ol102088j.
132. Umeda, R., Hibi, D., Miki, K., and Tobe, Y. (2009). Tetradehydrodinaphtho [10]annulene: A hitherto unknown dehy-droannulene and a viable precursor to stable zethrene derivatives, *Org. Lett.* **11**, 18, pp. 4104–4106, doi:10.1021/ol9015942, URL https://doi.org/10.1021/ol9015942.
133. Das, S., Lee, S., Son, M., Zhu, X., Zhang, W., Zheng, B., Hu, P., Zeng, Z., Sun, Z., Zeng, W., Li, R.-W., Huang, K.-W., Ding, J., Kim, D., and Wu, J. (2014). Para-quinodimethane-bridged perylene dimers and pericondensed quaterrylenes: The effect of the fusion mode on the ground states and physical properties, *Chem. Eur. J.* **20**, 36, pp. 11410–11420, doi:https:// doi.org/10.1002/chem.201402831.
134. Wu, T.-C., Chen, C.-H., Hibi, D., Shimizu, A., Tobe, Y., and Wu, Y.-T. (2010). Synthesis, structure, and photophysical properties of dibenzo [de,mn]naphthacenes, *Angew. Chem. Int. Ed.* **49**, 39, pp. 7059–7062, doi:https://doi.org/10.1002/anie.201001929.
135. Hsieh, Y. C., Fang, H. Y., Chen, Y. T., Yang, R., Yang, C. I., Chou, P. T., Kuo, M. Y., and Wu, Y. T. (2015). Zethrene and dibenzozethrene: Masked biradical molecules, *Angew. Chem. Int. Ed.* **54**, 10, pp. 3069–3073, doi:https://doi.org/10.1002/anie.201410316.
136. Zeng, W., Sun, Z., Herng, T. S., Goncalves, T. P., Gopalakrishna, T. Y., Huang, K.-W., Ding, J., and Wu, J. (2016). Super-heptazethrene, *Angew. Chem. Int. Ed.* **55**, 30, pp. 8615–8619, doi:https://doi.org/10.1002/anie.201602997.

137. Sun, Z., Zheng, B., Hu, P., Huang, K.-W., and Wu, J. (2014). Highly twisted 1,2:8,9-dibenzozethrenes: Synthesis, ground state, and physical properties, *ChemPlusChem* **79**, 11, pp. 1549–1553, doi:https://doi.org/10.1002/cplu.201402127.

138. Shan, L., Liang, Z., Xu, X., Tang, Q., and Miao, Q. (2013). Revisiting zethrene: Synthesis, reactivity and semiconductor properties, *Chem. Sci.* **4**, 8, pp. 3294–3297, doi:10.1039/ C3SC51158H, URL http://dx.doi.org/10.1039/C3SC51158H.

139. Li, Y., Huang, K.-W., Sun, Z., Webster, R. D., Zeng, Z., Zeng, W., Chi, C., Furukawa, K., and Wu, J. (2014). A kinetically blocked 1,14:11,12-dibenzopentacene: A persistent triplet diradical of a non-kekulepolycyclic benzenoid hydrocarbon, *Chem. Sci.* **5**, 5, pp. 1908–1914, doi:10.1039/C3SC53015A, URL http://dx.doi.org/ 10.1039/C3SC53015A.

140. Nakano, M., Kishi, R., Takebe, A., Nate, M., Takahashi, H., Kubo, T., Kamada, K., Ohta, K., Champagne, B., and Botek, E. (2007). Second hyperpolarizability of zethrenes, *Comput. Lett.* **3**, 2–4, pp. 333–338.

141. Chase, D. T., Rose, B. D., McClintock, S. P., Zakharov, L. N., and Haley, M. M. (2011). Indeno [1,2-b]fluorenes: Fully conjugated antiaromatic analogs of acenes, *Angew. Chem. Int. Ed.* **50**, 5, pp. 1127–1130, doi:https://doi.org/10.1002/anie.201006312.

142. Shimizu, A. and Tobe, Y. (2011). Indeno [2,1-a]fluorene: An air-stable ortho-quinodimethane derivative, *Angew. Chem. Int. Ed.* **50**, 30, pp. 6906–6910, doi:https://doi.org/10.1002/anie.201101950.

143. Shimizu, A., Kishi, R., Nakano, M., Shiomi, D., Sato, K., Takui, T., Hisaki, I., Miyata, M., and Tobe, Y. (2013). Indeno [2,1-b]fluorene: A 20-π-electron hydrocarbon with very low-energy light absorption, *Angew. Chem. Int. Ed.* **52**, 23, pp. 6076–6079, doi:https://doi.org/10.1002/anie.201302091, URL https://doi. org/10.1002/anie.201302091.

144. Miyoshi, H., Nobusue, S., Shimizu, A., Hisaki, I., Miyata, M., and Tobe, Y. (2014). Benz [c]indeno [2,1-a]fluorene: A 2,3-naphthoquinodimethane incorporated into an indenofluorene frame, *Chem. Sci.* **5**, 1, pp. 163–168, doi:10.1039/C3SC52622D, URL http://dx.doi.org/10.1039/C3SC52622D.

145. Rudebusch, G. E., Zafra, J., Jorner, K., Fukuda, K., Marshall, J. L., Arrechea-Marcos, I., Espejo, G. L., Ponce Ortiz, R., Gómez-García, C. J., Zakharov, L. N., Nakano, M., Ottosson, H., Casado, J., and Haley, M. M. (2016). Diindeno-fusion of an anthracene as a design strategy for stable organic biradicals, *Nat. Chem.* **8**, 8, pp. 753–759, doi:10.1038/nchem.2518, URL https://doi.org/10.1038/nchem.2518.

146. Barker, J. E., Frederickson, C. K., Jones, M.H., Zakharov, L. N., and Haley, M. M. (2017). Synthesis and properties of quinoidal fluorenofluorenes, *Org. Lett.* **19**, 19, pp. 5312–5315, doi:10.1021/acs.orglett.7b02605, URL https://doi.org/10.1021/acs.orglett.7b02605.

147. Rose, B. D., Vonnegut, C. L., Zakharov, L. N., and Haley, M. M. (2012). Fluoreno [4,3-c]fluorene: A closed-shell, fully conjugated hydrocarbon, *Org. Lett.* **14**, 9, pp. 2426–2429, doi:10.1021/ ol300942z, URL https://doi.org/10.1021/ol300942z.

148. Miyoshi, H., Miki, M., Hirano, S., Shimizu, A., Kishi, R., Fukuda, K., Shiomi, D., Sato, K., Takui, T., Hisaki, I., Nakano, M., and Tobe, Y. (2017). Fluoreno [2,3-b]fluorene vs indeno [2,1-b]fluorene: Unusual relationship between the number of π-electrons and excitation energy in m-quinodimethane-type singlet diradicaloids, *J. Org. Chem.* **82**, 3, pp. 1380–1388, doi:10.1021/acs.joc.6b02500, URL https://doi.org/10.1021/acs.joc.6b02500.

149. Tobe, Y. (2015). Non-alternant non-benzenoid aromatic compounds: Past, present, and future, *Chem. Rec.* **15**, 1, pp. 86–96, doi:https://doi.org/10.1002/tcr.201402077.

150. Hacker, A. S., Pavano, M., Wood, J. E., Hashimoto, H., D'Ambrosio, K. M., Frederickson, C. K., Zafra, J., Gomez-Garcia, C. J., Postils, V., Ringer McDonald, A., Casanova, D., Frantz, D. K., and Casado, J. (2019). Fluoreno [2,1-a]fluorene: An ortho- naphthoquinodimethane-based system with partial diradical character, *Chem. Commun.* **55**, 94, pp. 14186–14189, doi:10.1039/C9CC07474K, URL http://dx.doi.org/10.1039/C9CC07474K.

151. Omachi, H., Segawa, Y., and Itami, K. (2012). Synthesis of cycloparaphenylenes and related carbon nanorings: A step toward the controlled synthesis of carbon nanotubes, *Acc. Chem. Res.* **45**, 8, pp. 1378–1389, doi:10.1021/ar300055x, URL https://doi.org/ 10.1021/ar300055x.

152. Golder, M. R. and Jasti, R. (2015). Syntheses of the smallest carbon nanohoops and the emergence of unique physical phenomena, *Acc. Chem. Res.* **48**, 3, pp. 557–566, doi:10.1021/ar5004253, URL https://doi.org/10.1021/ar5004253.

153. Kayahara, E., Patel, V. K., Xia, J., Jasti, R., and Ya-mago, S. (2015). Selective and gram-scale synthesis of [6]cycloparaphenylene, *Synlett* **26**, 11, pp. 1615–1619, doi:10.1055/s-0034-1380714.

154. Hirst, E. S. and Jasti, R. (2012). Bending benzene: Syntheses of [n]cycloparaphenylenes, *J. Org. Chem.* **77**, 23, pp. 10473–10478, doi:10.1021/jo302186h, URL https://doi.org/10.1021/ jo302186h.

155. Segawa, Y., Yagi, A., Matsui, K., and Itami, K. (2016). Design and synthesis of carbon nanotube segments, *Angew. Chem. Int. Ed.* **55**, 17, pp. 5136–5158, doi:https://doi.org/10.1002/anie.201508384.

156. Yamago, S., Kayahara, E., and Iwamoto, T. (2014). Organoplatinum-mediated synthesis of cyclic π-conjugated molecules: Towards a new era of three-dimensional aromatic compounds, *Chem. Rec.* **14**, 1, pp. 84–100, doi:https://doi.org/10.1002/tcr.201300035.

157. Segawa, Y., Fukazawa, A., Matsuura, S., Omachi, H., Yamaguchi, S., Irle, S., and Itami, K. (2012). Combined experimental and theoretical studies on the photophysical properties of cycloparaphenylenes, *Org. Biomol. Chem.* **10**, 30, pp. 5979–5984, doi:10.1039/C2OB25199J, URL http://dx.doi.org/10.1039/C2OB25199J.

158. Darzi, E. R. and Jasti, R. (2015). The dynamic, size-dependent properties of [5]–[12]cycloparaphenylenes, *Chem. Soc. Rev.* **44**, 18, pp. 6401–6410, doi:10.1039/C5CS00143A, URL http://dx.doi. org/10.1039/C5CS00143A.

159. Muhammad, S., Minami, T., Fukui, H., Yoneda, K., Minamide, S., Kishi, R., Shigeta, Y., and Nakano, M. (2013). Comparative study of diradical characters and third-order nonlinear optical properties of linear/cyclic acenes versus phenylenes, *Int. J. Quant. Chem.* **113**, 4, pp. 592–598, doi:https://doi.org/10.1002/qua.24032.

160. Omachi, H., Nakayama, T., Takahashi, E., Segawa, Y., and Itami, K. (2013). Initiation of carbon nanotube growth by well-defined carbon nanorings, *Nat. Chem.* **5**, 7, pp. 572–576, doi:10.1038/ nchem.1655, URL https://doi.org/10.1038/nchem.1655.

161. Lu, X. and Wu, J. (2017). After 60 years of efforts: The chemical synthesis of a carbon nanobelt, *Chem* **2**, 5, pp. 619–620, doi:https://doi.org/10.1016/j.chempr.2017.04.012, URL http://www.sciencedirect.com/science/article/pii/S245192941730178X.

162. Wu, C.-S., Lee, P.-Y., and Chai, J.-D. (2016). Electronic properties of cyclacenes from TAO-DFT, *Sci. Rep.* **6**, 1, p. 37249, doi:10.1038/srep37249, URL https://doi.org/10.1038/srep37249.

163. Giguère, J.-B. and Morin, J.-F. (2013). Synthesis and optoelectronic properties of 6,12-bis(amino)anthanthrene derivatives, *J. Org. Chem.* **78**, 24, pp. 12769–12778, doi:10.1021/jo402313c, URL https://doi.org/10.1021/jo402313c.

164. Giguère, J.-B., Boismenu-Lavoie, J., and Morin, J.-F. (2014). Cruciform alkynylated anthanthrene derivatives: A structure-properties relationship case study, *J. Org. Chem.* **79**, 6, pp. 2404–2418, doi:10.1021/jo402674m, URL https://doi.org/10.1021/ jo402674m.

165. Bleaney, B. and Bowers, K. D. (1952). Anomalous paramagnetism of copper acetate, *Proc. R. Soc. London A* **214**, 1119, pp. 451–465, doi:10.1098/rspa.1952.0181, URL https://doi.org/10.1098/rspa.1952.0181.

166. Casanova, D. (2018). Short-range density functional correlation within the restricted active space CI method, *J. Chem. Phys.* **148**, 12, p. 124118, doi:10.1063/1.5018895.

167. Carreras, A., Jiang, H., Pokhilko, P., Krylov, A., Zimmerman, P., and Casanova, D. (2020). Calculation of spin-orbit couplings using RASCI spinless one-particle density matrices: Theory and applications, doi:10.26434/chemrxiv.12951407.v1, URL https://doi.org/10.26434/chemrxiv.12951407.v1.

168. Yanai, T., Tew, D. P., and Handy, N. C. (2004). A new hybrid exchange-correlation functional using the coulomb-attenuating method (CAM-B3LYP), *Chem. Phys. Lett.* **393**, 1, pp. 51–57, doi:https://doi.org/10.1016/j.cplett.2004.06.011, URL http://www.sciencedirect.com/science/article/pii/S0009261404008620.

169. Lee, C., Yang, W., and Parr, R. G. (1988). Development of the Colle-Salvetti correlation-energy formula into a functional of the electron density, *Phys. Rev. B* **37**, 2, pp. 785–789, doi:10.1103/PhysRevB.37.785, URL https://link.aps.org/doi/10.1103/PhysRevB.37.785.

170. Zhao, Y. and Truhlar, D. G. (2008). The M06 suite of density functionals for main group thermochemistry, thermochemical kinetics, noncovalent interactions, excited states, and transition elements: Two new functionals and systematic testing of four M06-class functionals and 12 other functionals, *Theor. Chem. Acc.* **120**, 1, pp. 215–241, doi:10.1007/s00214-007-0310-x, URL https://doi.org/10.1007/s00214-007-0310-x.

## Chapter 3

# Spectroscopy of Open-Shell Singlet Ground-State Diradicaloids: A Computational Perspective

**Fabrizia Negri, Sofia Canola, and Yasi Dai**
*Department of Chemistry "Giacomo Ciamician," University of Bologna, Via F. Selmi 2, 40126 Bologna, Italy*
fabrizia.negri@unibo.it

Recently there has been an increased effort to design stable conjugated diradicaloids with a singlet ground state and variable diradical character. These species have several potential technological applications and are characterized by distinctive photophysical properties, among which a low-lying excited state dominated by a doubly excited configuration. Starting from the simple description provided by the two electrons in two orbitals model, we introduce the two lowest energy excited singlet states determining the low-energy portion of the absorption spectra of most conjugated diradicaloids. We summarize recent high-level computational investigations that have identified the low-lying weak bands, in the red-side region of the absorption spectrum of several diradicaloids,

*Diradicaloids*
Edited by Jishan Wu

ISBN 978-981-4968-08-9 (Hardcover), 978-1-003-27724-8 (eBook)
www.jennystanford.com

as due to the double-exciton (DE) state. Because of the large molecular dimension of several recently synthesized diradicaloids, it is desirable to predict their photophysical properties relying on cheaper computational tools. We therefore discuss cost-effective density functional theory (DFT)-based computational approaches that can capture, with suitable accuracy, the excitation energies of these low-lying electronic states.

## 3.1 Introduction

Over the past decades, there has been growing interest in studying and synthesizing open-shell di- and multi-radical molecules. Diradicaloids have been proposed as candidates for a variety of applications in materials science, such as ambipolar organic field effect transistors, singlet fission in organic photovoltaics, near infrared absorption, large two-photon absorption, and thermally convertible spin states [1–4].

A large number of conjugated chromophores with open-shell singlet ground state have been rationally designed and synthesized recently [5–6], displaying varying diradical characters, such as quinoidal oligothiophenes [7–9], tetracyano quinodimethane derivatives of phenylene-vinylenes [10], diphenalenyl compounds [11], several different flavors of polycyclic aromatic hydrocarbons [5, 12–17], heteroacenes [18–20], indeno-derivatives [21–24], rylene ribbons [25], and their tetracyano derivatives [26, 27]. Most of these systems have become accessible by incorporating bulky groups and thanks to significant improvement of current research into stabilization via different strategies [28, 29]. Among these, cross-conjugation has enabled thermodynamic stabilization of the diradical system [24, 30].

A typical character of these systems is a small HOMO-LUMO (H-L) gap, which, in turn, is associated with their ambipolar conduction properties, their possible application in singlet fission [2, 31, 32], and their electronic absorption toward the near infrared region.

The simplest model to describe the low-lying electronic absorption features of a diradical is based on two electrons in two orbitals (2e-2o) from which four electronic states can be constructed:

three singlets and one triplet state [33–35]. In a delocalized orbital basis, the lowest singlet electronic state is described by the ground configuration corrected with the doubly excited (H,H→L,L) configuration [34, 35]. The second singlet state is a singly excited (H→L) or single-exciton (SE) state (generally a strongly dipole-allowed electronic transition) and the third is dominated by the doubly excited (H,H→L,L) configuration, and is thereafter, labeled the DE state.

According to the 2e-2o model, the DE state is found at higher energy than the SE state [31, 34]. However, the 2e-2o model is useful for the description of electronic structure of diradical molecules, but it is generally an approximation. Diradicals of real interest normally contain more than two electrons and orbitals and the energetic order of closely spaced states that can be incorrect, owing to the lack of electron correlation. Indeed, some of us have computationally demonstrated [36] that for a series of quinoidal oligothiophenes, the DE state becomes the lowest-energy-excited singlet state. This is a distinctive character, which is well known for the class of polyenes [37], whose diradical character has been indeed recognized [38]. Similarly to oligoenes and polyenes, the DE state of open-shell singlet diradicaloids is generally one-photon forbidden or only weakly allowed and it appears in the optical spectra as a weak progression of bands, often on the red-side of the main strong absorption band, due to the strongly allowed SE state [36, 39]. The energy location of the DE state can strongly influence the photophysical properties such as linear and non-linear optical (NLO) properties (since the DE state can be active in two-photon absorption) or fluorescence lifetimes, owing to its generally dipole-forbidden character.

The purpose of this chapter is twofold: first, we summarize the outcomes of the 2e-2o model focusing especially on the evidence of a low-lying DE state and we review previous studies in which the distinctive features appearing in the absorption spectra of singlet ground-state diradicaloids were analyzed with high level quantum-chemical calculations. Second, in view of the large molecular dimension of several recently designed diradicaloids, we discuss the suitability of computationally less demanding approaches, and investigate the low-energy side of the absorption spectra of different

diradicaloid systems, using DFT-based methods. More specifically, because intermediate diradical character of diradicaloids is both desirable to maximize NLO response and to act as intermediates in singlet fission applications [31, 32, 40, 41], it is urgent to validate cost-effective methods suitable for the prediction of the SE and DE states of extended conjugated systems over the entire range of diradical character.

Therefore, we consider the set of conjugated diradicaloids investigated in previous studies [36, 39, 42, 43] (Figure 3.1a) [9–12, 14, 15, 17, 18, 44–47] and extend the investigation, including the three tetracyano oligorylene derivatives [26, 27] as shown in Figure 3.1b, featuring small-to-medium diradical character. The excitation energies of low-lying excited states (both SE and DE) are determined with several DFT-based computational schemes, encompassing standard time dependent DFT (TDDFT) based on a closed-shell (CS) reference configuration, and other flavors of the TD approach either based on an unrestricted spin paired reference configuration (TDUDFT), or on spin-flip (SF)-TDDFT [48]. In addition, we also employ the DFT multi-reference configuration interaction (MRCI) method [49, 50], a promising approach combining dynamic and static electron correlations. Computed results are compared with the experimental data which, for most of the systems investigated, display weak features on the red-side of the main strong absorption band that can be assigned to the DE state.

## 3.2 Cost-Effective Computational Approaches for Description of SE and DE States of Diradicaloids

Although the quantum-chemical description of open-shell singlet ground state of conjugated diradicals requires multi-reference methods to include static correlation effects, a very common approach is the use of DFT in its unrestricted formulation (UDFT) which, for significant diradical character, leads to broken symmetry (BS) localized molecular orbitals, in contrast with the delocalized orbitals obtained from CS DFT calculations in the spin-restricted approach.

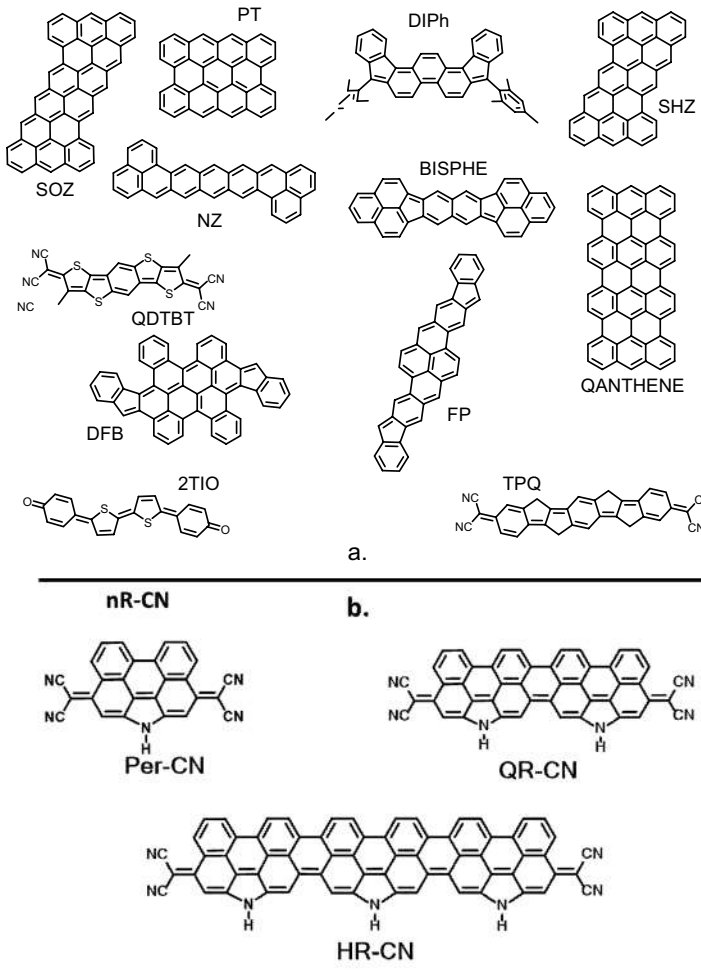


**Figure 3.1** Chemical structures of the molecular systems investigated, displaying varying diradical character. Each compound is assigned a label, which in most cases, is a shorthand of the full name of the investigated molecule: QANTHENE for quateranthene [12], BISPHE for bisphenalenyl [11], SHZ for superheptazethrene [15], SOZ for superoctazethrene [45], NZ for nonazethrene [44], PT for peritetracene [46], DFB for diindeno-fused-bischrysene [14], DIPh for dimesityl-diindenophenanthrene [47], QDTBT for quinoidal dithienobenzo-dithiophene [18], 2TIO for quinoidal phenyl end-capped dithiophene [9, 36], FP for bis-fluoreno-pyrene [17], TPQ for tri-p-quinodimethane [10], and nR-CN for tetracyano oligorylene derivatives [26–27].

The equilibrium structures of the molecules shown in Figure 3.1 were determined with DFT calculations employing the B3LYP functional and the 6-31G* basis set. The geometry optimization was first carried out with the restricted approach to determine a CS equilibrium structure. When a more stable open-shell BS solution was found, the equilibrium structure corresponding to the BS solution was also determined. The overall CS-BS stability (ΔE(CS-BS)) was determined as the energy difference between the energy of the CS structure computed with restricted DFT and the energy of the BS structure computed with UDFT. All these calculations were carried out with the Gaussian16 suite of programs [51].

### 3.2.1 Descriptors of Diradical Character

To characterize the diradicaloids, we employed two different descriptors of the diradical character. The first is the $y_0$ parameter which, in the spin-unrestricted single-determinant formalism, can be determined in the spin-projection scheme as [2, 52]:

$$y_0^{\text{PUnrestricted}} = 1 - \frac{2T_0}{1+T_0^2}, \tag{3.1}$$

where $T_0$ is calculated as:

$$T_0 = \frac{n_{\text{HONO}} - n_{\text{LUNO}}}{2} \tag{3.2}$$

and $n$ is the occupation number of the frontier natural orbitals.

We employed this formulation to determine both the $y_0$ (PUHF) and the $y_0$ (PUB3LYP) values, the latter required to correlate in a consistent way the value of the diradical descriptor with the orbital localization (i.e. rotation, see below) determined at the BS level with the B3LYP functional.

The second descriptor considered is based on finite-temperature DFT (FT-DFT) and is the $N_{\text{FOD}}$ value, which is the integral of the fractional orbital density (FOD) $\rho^{\text{FOD}}(r)$, over all space.

$$N_{\text{FOD}} = \int \rho^{\text{FOD}}(r)dr \tag{3.3}$$

The $\rho^{\text{FOD}}(r)$ is defined as [53, 54]:

$$\rho^{\text{FOD}}(r) = \sum_i^N (\delta_1 - \delta_2 f_i)|\varphi_i(r)|^2, \tag{3.4}$$

where $\delta_1$ and $\delta_2$ are two constants set such that only fractionally occupied orbitals are taken into account; $\varphi_i$ are molecular spin orbitals, and $f_i$ are the fractional orbital occupancies ($0 \leq f_i \leq 1$) determined by the Fermi-Dirac distribution. In other words, FOD yields for each point in real space, only the contribution of 'hot' or strongly correlated electrons and is therefore an analysis tool of static correlation that can monitor not only the diradical, but also the multi-radical character.

The $y_0$ and $N_{FOD}$ parameters were computed at the lowest energy B3LYP geometry for the entire set of diradicals as shown in Figure 3.1. The $N_{FOD}$ parameter was computed with the ORCA 4.0.1.2 package [55] with the default setting (TPSS/def2-TZVP level with $T_{el}$ = 5000 K).

### 3.2.2 2e-2o Model

From a full configuration interaction (CI) within the 2e-2o model, for a perfect symmetric diradical, the four electronic states shown in Figure 3.2 are determined. The DE state emerges as one of the two singlet excited states. In the pioneering work of Michl [34], two limiting cases were considered: A delocalized basis set labeled *a*, *b* and a localized basis set labeled *A*, *B*. Using the same notation as in Ref. [34], we can write, for the two sets of orbitals, the following configurations with paired spins: $a(1)a(2) = a^2$; $b(1)b(2) = b^2$; $a(1)b(2) = ab$; $b(1)a(2) = ba$ in the delocalized basis, and $A(1)A(2) = A^2$; $B(1)B(2) = B^2$; $A(1)B(2) = AB$; $B(1)A(2) = BA$, in the localized basis.

Assuming the energy $E(b) < E(a)$, these configurations mix to form one triplet state, and three singlet states whose spatial wavefunctions for perfect homosymmetric diradicals are expressed as follows [34]:

$$\begin{aligned} S_0 &= \psi_0 = b^2 - a^2 = AB + BA \\ S_1 &= \psi_1 = ab + ba = A^2 - B^2 \\ S_2 &= \psi_2 = a^2 + b^2 = A^2 + B^2 \end{aligned} \tag{3.5}$$

Note that the $S_2$ state is the DE state in which the (H,H→L,L) excitation or $a^2$ in the delocalized basis, strongly contributes to the wavefunction. Within the 2e-2o model, this state is predicted to be always above $S_1$, the (H→L) or $ab + ba$ state in the delocalized basis.

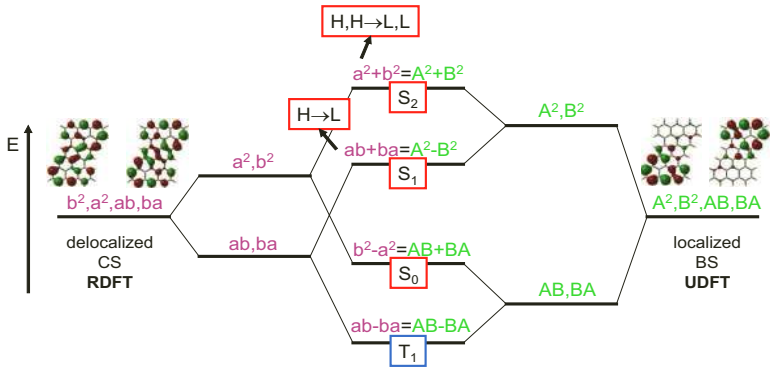


**Figure 3.2** A schematic representation of the four electronic states resulting from the 2e-2o model applied to a perfect diradical and their construction starting from a delocalized set of orbitals (left side of the scheme) or a localized set of orbitals (right side of the scheme). As an example, we include the delocalized (left) and localized (right) orbitals of SHZ computed with restricted and unrestricted DFT calculations, respectively.

Moving to DFT-based computational approaches, we note that the ground state of open-shell singlet diradical systems, displaying medium to large diradical character, whose nature is intrinsically multi-configurational, can be described in a one determinant approach, by the spin-unrestricted BS solution. Owing to the relaxed constraint, molecular orbitals (MOs) of the BS solution are localized on opposite moieties of the molecule, in contrast with the delocalized orbitals determined for the CS solution (Figure 3.2).

In the light of the 2e-2o model described above, we note that CS and BS solutions obtained from standard DFT calculations correspond, in several cases, to the two limiting cases of a set of delocalized (the CS solution) or localized (the BS solution) MOs. In the following section, therefore, we explore the suitability of the TD approach based on an unrestricted reference configuration (thereafter indicated as TDUDFT) to describe the low-lying singlet excited states of conjugated diradicaloids.

### 3.2.3 TDUDFT

As stated above, we refer in this case to TD calculations using a spin-paired open-shell reference configuration characterized by BS

frontier orbitals. Within the 2e-2o model, the BS HOMO and LUMO orbitals of the unrestricted wavefunction can be described as linear combinations of the delocalized $H_{CS}$ and $L_{CS}$ orbitals obtained from the CS solution. Following previous work [2, 52], we can write:

$$\begin{aligned} H_\alpha &= \varphi^\alpha_{\mathrm{HOMO}} = \cos\theta \cdot H_{CS} + \sin\theta \cdot L_{CS} \\ H_\beta &= \varphi^\beta_{\mathrm{HOMO}} = \cos\theta \cdot H_{CS} - \sin\theta \cdot L_{CS} \\ L_\alpha &= \varphi^\alpha_{\mathrm{LUMO}} = \sin\theta \cdot H_{CS} - \cos\theta \cdot L_{CS} \\ L_\beta &= \varphi^\beta_{\mathrm{LUMO}} = \sin\theta \cdot H_{CS} + \cos\theta \cdot L_{CS} \end{aligned} \tag{3.6}$$

where $\theta$ is the rotation angle of the BS set with respect to the CS set of orbitals. By substituting the expressions of Eq. (3.6) in the Slater determinant corresponding to the unrestricted ground state wavefunction:

$$\begin{aligned} \psi^{\mathrm{UGround}} &= \left|\varphi^\alpha_{\mathrm{HOMO}}\varphi^\beta_{\mathrm{HOMO}}\right\rangle \\ &= \frac{1}{\sqrt{2}}\left[\varphi^\alpha_{\mathrm{HOMO}}(1)\varphi^\beta_{\mathrm{HOMO}}(2) - \varphi^\beta_{\mathrm{HOMO}}(1)\varphi^\alpha_{\mathrm{HOMO}}(2)\right] \end{aligned} \tag{3.7}$$

the wavefunction describing the singlet open-shell ground state can be recast in terms of combination coefficients $C_{GR}$, $C_D$, $C_T$:

$$\psi^{\mathrm{UGround}} = C_{GR}\left|H_{CS}\bar{H}_{CS}\right\rangle + C_D\left|L_{CS}\bar{L}_{CS}\right\rangle + C_T\frac{1}{\sqrt{2}}(|H_{CS}\bar{L}_{CS} - |L_{CS}\bar{H}_{CS}) \tag{3.8}$$

Where $C_{GR} = (\cos^2\theta)$, $C_D = -(\sin^2\theta)$, $C_T = -\sin\theta\cos\theta$, $|H_{CS}\bar{H}_{CS}\rangle$ is the CS ground state determinant, $|L_{CS}\bar{L}_{CS}\rangle$ is the doubly excited determinant and $\frac{1}{\sqrt{2}}(|H_{CS}\bar{L}_{CS}\rangle - |L_{CS}\bar{H}_{CS}\rangle)$ is the combination of singly excited determinants corresponding to a triplet spin multiplicity, which accounts for spin contamination. Interestingly, the $y_0$ diradical descriptor can also be expressed in terms of the coefficients appearing in Eq. (3.8) [2] and because of their dependence on the orbital rotation angle, the following expression results:

$$y_0 = 2(\sin^4\theta)/(1 - 2(\sin^2\theta)(\cos^2\theta)). \tag{3.9}$$

The above relation defines a direct correspondence between the diradical character $y_0$ and the orbital rotation angle $\theta$. The latter can be readily obtained from the BS frontier orbitals expressed as linear combinations of the CS frontier orbitals. For all the molecules investigated featuring a BS solution, these linear combinations were determined by projecting each BS frontier orbital over the set of CS orbitals.

We now derive an expression of the wavefunction describing the DE state within the TDUDFT approach and discuss when the method can capture this low-lying excited state. We start from the limiting case when the BS orbitals are strongly localized and disjoint (which is associated with a large diradical character). In this situation the HOMO orbital holding the α electron is almost identical to the LUMO orbital computed for the β electrons and vice versa. This corresponds to setting $\theta$ = 45° in Eq. (3.6). In this case, there is a clear correspondence between the computed UDFT frontier MOs for α and β electrons and the localized *A, B* pair of the 2e-2o model. The four configurations of the model can be identified with the four configurations based on UDFT frontier MOs, and more specifically, the singly excited configurations $[H_\alpha \rightarrow L_\alpha]$ and $[H_\beta \rightarrow L_\beta]$, generated from the unrestricted reference configuration and shown in Figure 3.3, correspond to the $A^2$ and $B^2$ configurations in Eq. (3.5).

The DE state is, therefore, identified by the positive combination of the two single excitations $[H_\alpha \rightarrow L_\alpha]$ + $[H_\beta \rightarrow L_\beta]$ [42] or, in terms of the corresponding Slater determinants, as:

$$\begin{aligned}\psi^{\mathrm{DE}} &= \frac{1}{\sqrt{2}}\left\{\left|\varphi^{\alpha}_{\mathrm{LUMO}}\varphi^{\beta}_{\mathrm{HOMO}}\right\rangle + \left|\varphi^{\alpha}_{\mathrm{HOMO}}\varphi^{\beta}_{\mathrm{LUMO}}\right\rangle\right\} \\ &= \frac{1}{2}\left[\varphi^{\alpha}_{\mathrm{LUMO}}(1)\varphi^{\beta}_{\mathrm{HOMO}}(2) - \varphi^{\beta}_{\mathrm{HOMO}}(1)\varphi^{\alpha}_{\mathrm{LUMO}}(2)\right] \\ &\quad + \frac{1}{2}\left[\varphi^{\alpha}_{\mathrm{HOMO}}(1)\varphi^{\beta}_{\mathrm{LUMO}}(2) - \varphi^{\beta}_{\mathrm{LUMO}}(1)\varphi^{\alpha}_{\mathrm{HOMO}}(2)\right] \end{aligned} \quad (3.10)$$

Substituting the expressions of Eq. (3.6) into Eq. (3.10), one gets:

$$\psi^{\mathrm{DE\ state}} = D_{\mathrm{GR}}\,|\,H_{\mathrm{CS}}\bar{H}_{\mathrm{CS}}\rangle + D_{\mathrm{D}}\,|\,L_{\mathrm{CS}}\bar{L}_{\mathrm{CS}}\rangle + D_{\mathrm{T}}\frac{1}{\sqrt{2}}(|\,H_{\mathrm{CS}}\bar{L}_{\mathrm{CS}}\rangle - |\,L_{\mathrm{CS}}\bar{H}_{\mathrm{CS}}\rangle) \quad (3.11)$$

where the combination coefficients are $D_{GR} = D_D = \sin(2\theta)/\sqrt{2}$ and $D_T = \cos(2\theta)$. Equation (3.11) shows that the wavefunction of the DE state, as in the case of the ground state, is composed by a combination of singlet and triplet spin contributions, which implies that spin contamination can be a relevant issue. For angles increasing from 0 to 45°, the square of the coefficient of the triplet spin multiplicity component $(D_T)^2$ decreases from 1 to 0, while the sum of the two singlet spin multiplicity components, $(D_{GR})^2 + (D_D)^2$, increases from 0 to 1. This implies that the DE state wavefunction is a pure singlet state only for fully localized BS orbitals ($\theta = 45°$); while decreasing the $\theta$ rotation angle, the triplet component becomes more and more important. For $\theta = 22.5°$, the triplet equates the singlet component (Figure 3.4) and for $\theta = 0$, the state becomes a pure triplet state. Because diradical character is a function of $\theta$ (Eq. (3.9)), the above results imply that for very small rotation angles (small diradical character), the triplet spin contribution dominates and the predicted TDUDFT result for the DE state is unreliable because of the mixed spin nature.

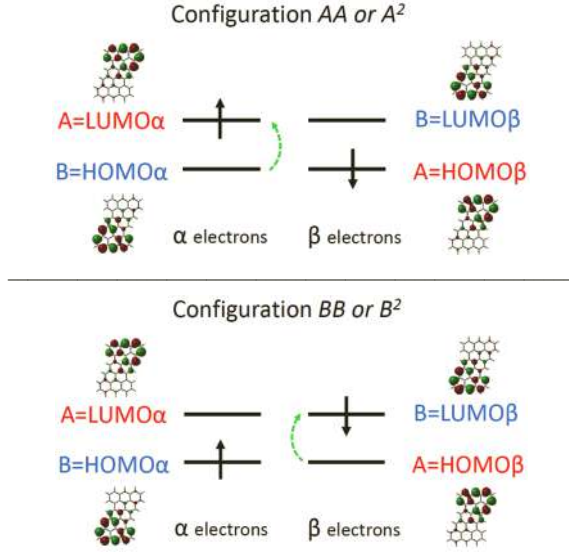


**Figure 3.3** Correspondence between the notation *A, B* of localized orbitals in the 2e-2o model and the localized HOMO α,β and LUMO α,β orbitals from UDFT calculations on diradical systems with large diradical character. The BS orbitals from SHZ are reported as an example.

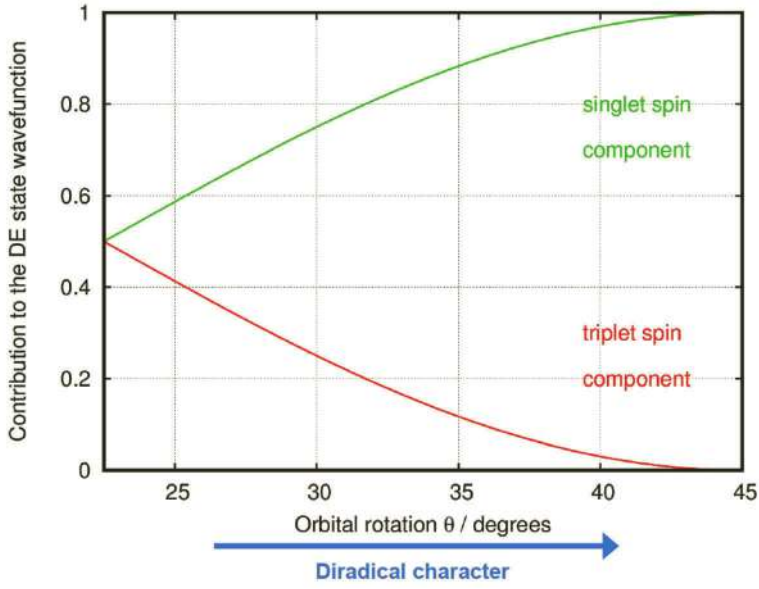


**Figure 3.4** A schematic representation of the contamination of the DE state by a triplet spin component in TDUDFT calculation, as a function of the diradical character, increasing with orbital rotation angle $\theta$.

### 3.2.4 SF-TDDFT

Double excitations can be recovered from TDDFT calculations also with the SF scheme [35, 48]. SF-TDDFT treats ground- and excited-state electron correlation on the same footing, while also incorporating some doubly excited configurations that are important for biradicals. Accordingly, this approach was employed to investigate the excitation energy of the low-lying DE state of the molecules shown in Figure 3.1. The SF-TDDFT calculations were carried out in the collinear approximation as implemented in the Gamess package [56].

### 3.2.5 DFT/MRCI

This method is a powerful tool that combines the dynamic and static electron correlations. It is a combination of DFT (which

gives information about dynamic correlation) and truncated MRCI expansions (to take the static correlation into account). It makes use of a semi-empirical Hamiltonian that has been parameterized in combination with the BHLYP functional. The methodological idea behind DFT/MRCI is to employ DFT orbitals for constructing configuration state functions (CSFs) and to dress the MRCI matrix elements by appropriate portions of Coulomb and exchange-like integrals [49, 50]. In the original work [49], different parameter sets were employed for singlet and triplet state calculations. More recently, a spin-invariant parameterization has been introduced [50], which incorporates less empiricism as compared to the original formulation, while preserving its computational efficiency.

The method has been shown to perform well in extended π-systems such as polyenes [57], where doubly excited configurations are essential for the proper discussion of the DE state. The method is, therefore, suitable to describe both SE and DE states of singlet ground state diradicaloids. We have carried out DFT/MRCI calculations using both sets of parameters, hereafter labeled as original [49] and R2018 [50].

## 3.3 Results

In this section, we discuss separately the results of DFT-based calculations for the SE and DE states of conjugated diradicaloids. For the systems shown in Figure 3.1, we have carried out the following sets of calculations to estimate the vertical excitation energy of the SE state: (i) TDB3LYP/6-31G* using a CS reference configuration, at the CS optimized geometry and at the BS optimized geometry; (ii) TDUB3LYP/6-31G* calculations using a BS reference configuration at the BS optimized geometry; and (iii) DFT/MRCI calculations carried out with two sets of parameters, the original [49] and the R2018 set [50]. We selected the B3LYP functional because of its generally reliable performance for large conjugated systems [60–62] in conjunction with its generally smaller spin contamination compared to hybrid functionals with larger contributions of HF exchange [63].

To determine the excitation energy of the DE state, we have carried out the following sets of calculations: (i) TDUB3LYP/6-31G*

using a BS reference configuration at the BS optimized geometry; (ii) SF-TDBHHLYP/6-31G* calculations using the BS optimized geometry; and (iii) DFT/MRCI calculations carried out with two sets of parameters, the original [49] and the R2018 set [50].

Before discussing excitation energies predicted from DFT-based approaches, we analyze the computed values of the diradical character descriptors, and briefly review previous investigations of the absorption spectra of diradicaloids, carried out with highly correlated levels of theory that paved the way to the assignment of the DE state.

### 3.3.1 Diradical Character from $y_0$ and $N_{FOD}$ Descriptors

It is interesting to explore the correlation between computed descriptors of diradical character and the set of conjugated molecular systems investigated. The $y_0$ values computed with the PUB3LYP method are always much smaller than those computed at PUHF values. Nevertheless, for the set of molecules investigated, the trend is very similar at all levels of theory considered, as shown in Figure 3.5. It should be noted that the diradical character is generally remarkably dependent on the chosen geometry and increases, as expected, when moving from CS to BS geometries [42]. As expected, the molecules displaying the larger $y_0$ are also displaying the larger CS–BS stabilization energy, and generally, an approximately linear correlation between the diradical character and computed BS stabilization is found (Figure 3.5).

In summary, the absolute magnitude of $y_0$ is strongly dependent on geometrical parameters and strongly dependent on the level of theory employed to evaluate the descriptor. It is, therefore, important to refer precisely to the method and geometry employed to calculate the diradical character, when reporting its value. To clarify this point, we present in Figure 3.6, the correlation between $y_0$ (PUB3LYP) and the $\theta$ angle determined from the BS orbitals computed at the same level of the theory. It can be seen that the agreement with the analytical expression of Eq. (3.9) is very close only because the $y_0$ (PUB3LYP) is used.

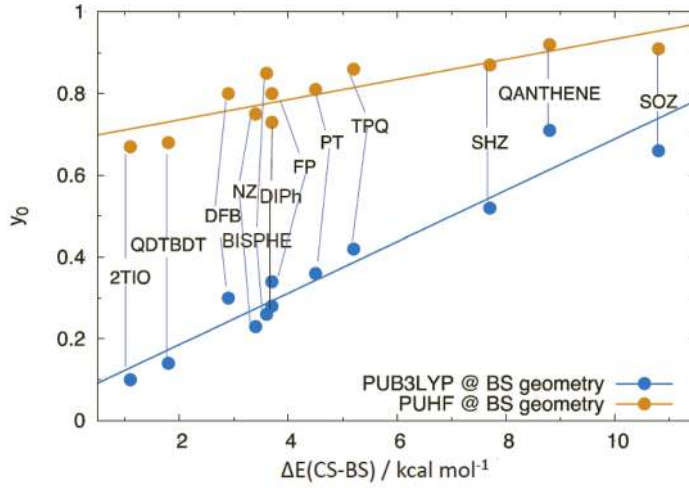


**Figure 3.5** Correlation between the $y_0$ values computed at PUHF (yellow circles) or PUB3LYP (blue circles) level and the computed stabilization of the BS structure with respect to the CS structure, both optimized at B3LYP/6-31G* level.

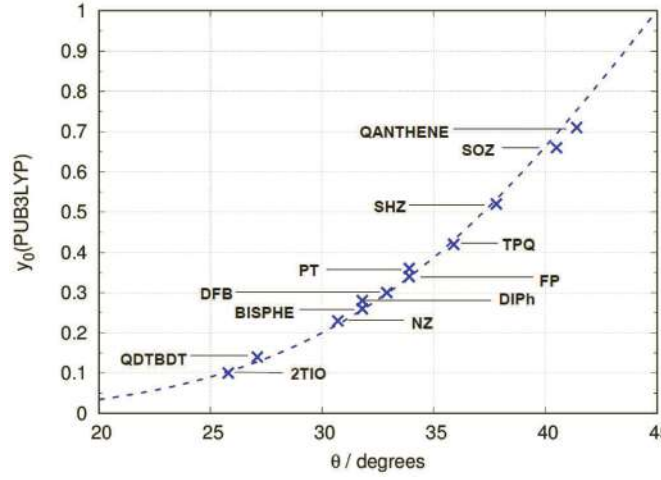


**Figure 3.6** Correlation between computed diradical character $y_0$ UB3LYP) and orbital rotation angle θ for the diradicaloids investigated. (dashed line) Analytic expression from Eq. (3.9); (blue crosses) angle θ determined for the computed LUMO BS orbitals at UB3LYP/6-31G* level of theory.

The values of the $N_{FOD}$ descriptor have been determined for a variety of chemical systems, including small-size linear and cyclic oligoacenes, and have been used to demonstrate the poly-radical character of cyclacenes [58]. For the set of diradicals investigated here, it can be seen that the $N_{FOD}$ value remains below 2 in most cases, indicating that the 2e-2o model should be suitable, but in some cases, it exceeds 2, such as for DFB, SHZ, SOZ, and QANTHENE (Figure 3.7). In these cases, it is expected that more than two electrons should be correlated for a proper description of ground and excited states.

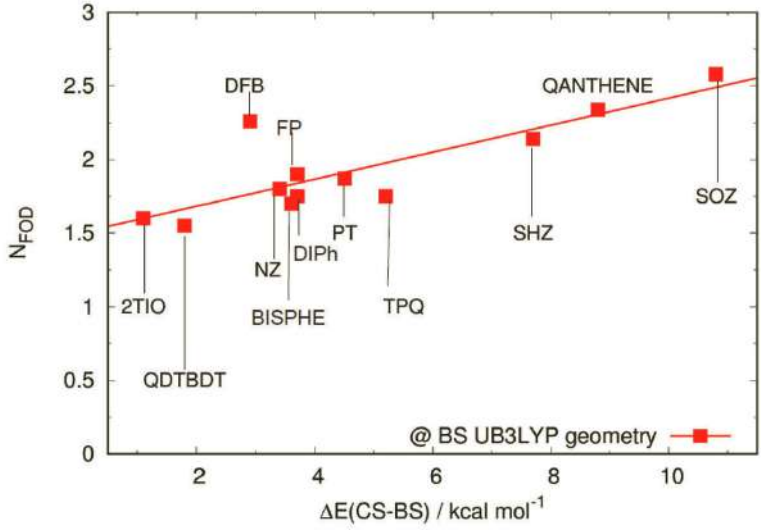


**Figure 3.7** Correlation between the $N_{FOD}$ computed values and the stabilization of the BS structure with respect to the CS structure (E(CS)-E(BS)), both optimized at B3LYP/6-31G* level.

The previous discussion indicates that the $N_{FOD}$ parameter offers the advantage of collecting in a single descriptor, all the effects originated by the multi-reference nature of the chromophore. Although most of the systems investigated here have a dominant diradical character, some display a non-negligible multiradical character. For this reason, in the following discussion, we generally use the $N_{FOD}$ descriptor for correlating the computed results, since it captures the contributions of all the 'hot' or strongly correlated electrons of the investigated chromophore.

### 3.3.2 DE State from High-Level Computational Studies

A reliable prediction of the excited states and excitation energies of conjugated diradicaloids is challenging because of correlation effects and multi-reference methods that ensure the appropriate level of electron correlation.

In previous studies, complete active space self-consistent field (CASSCF) followed by CASPT2 calculation was chosen to account for static and dynamic electron correlations in these systems. In a study on the low-lying excited electronic states of quinoidal oligothiophenes, seeking more explicit signatures of their biradicaloid character, it was showed that the pattern of low-lying singlet excited states resembles closely that of polyenes, with a DE state becoming the lowest excited singlet state as the length of the oligomer increases. Indeed, despite the correct extension of the simulated Franck-Condon progression associated with the dipole-allowed transition in absorption (i.e. the transition to the SE state), well described by TDDFT calculations, some bands remained unassigned in the experimental spectrum of 2TIO and of its smaller oligomer. These are the additional bands at lower excitation energies as shown in Figure 3.8 with arrows. Thanks to the use of CASPT2//CASSCF calculations, it was possible to prove that the DE state becomes the lowest energy excited singlet state in these cases (Figure 3.8) [36]. The CASPT2 corrected adiabatic excitation energies compared well with the experimentally determined low-energy features in the n-hexane absorption spectra and allowed to assign, for the first time, the weak transition on the red-side of the main absorption band, to the DE state of quinoidal oligothiophenes displaying increasingly large diradical character with the length of the conjugated chain.

More recently, a similar agreement via CASPT2//CASSCF calculations has been demonstrated for tetracyano quinodimethane derivatives of phenylene-vinylenes [39]. Similar calculations, at CASSCF level followed by NEVPT2 perturbative correction, were recently carried out for quateranthene [12] and demonstrated the presence of a low-lying DE state.

Oligoacenes, especially longer members, display some degree of diradical character and recent computations at the

multiconfiguration coupled electron pair approximation (MCCEPA) level of theory using CASSCF reference wavefunctions showed that for heptacene the $2A_g$ state drops below the $1B_{2u}$ state (dominated by the H-L excitation) by 0.17 eV. These computational results offer an explanation for the weak feature observed at 768 nm in the absorption spectrum of heptacene, in terms of a transition to a state that is forbidden in the Franck–Condon approximation, but gains intensity, for instance, due to an intensity borrowing mechanism via vibronic coupling [59]. Interestingly a DFT/MRCI study of Marian [57] reported the $2A_g$ state of octacene to be significantly lower in energy than the $1B_{2u}$ state, in keeping with the suggestion provided by the calculations [59] on heptacene.

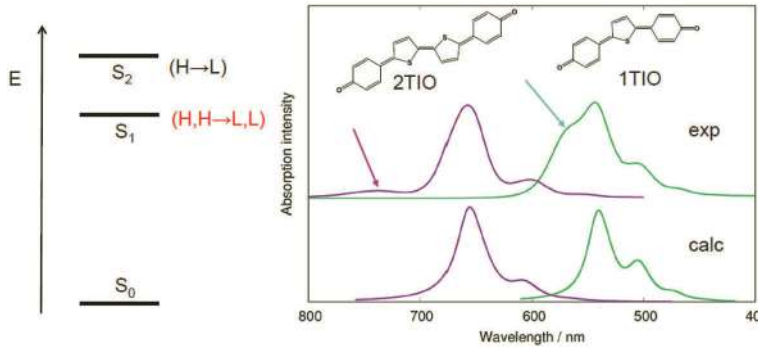


**Figure 3.8** (Left) Schematic representation of the excited state's order for the two quinoidal oligothiophenes on the right. (Right) Experimental evidence for the presence of a low-lying DE state in quinoidal oligothiophenes. (Top) Experimental absorption spectra obtained in n-hexane. (Bottom) The TDB3LYP/6-31G* computed spectra (including also the simulated vibronic structures) reproduce most of the observed features, but fail to account for the low-energy bands indicated by arrows.

All these previously reported high level calculations on conjugated diradicaloids demonstrate that correlated quantum-chemical approaches can support the assignment of low-lying excited states bearing DE contributions. Seeking computational tools of suitable quality to correctly predict the low-lying excited states of large diradicaloids, in the following we discuss the performance of cost-effective approaches, demanding much lower computational resources.

### 3.3.3 Bright SE Excited State from DFT-Based Approaches

The difference between vertical excitation energies observed and computed from TDB3LYP calculations for two sets of geometries (CS B3LYP and BS B3LYP) (Table 3.1) is plotted against the $N_{FOD}$ descriptor as shown in Figure 3.9. To visually capture the trend and compare computed results with experimental data, we fitted them linearly, keeping in mind that the computed data may be affected by systematic errors, due to the simplifications of the models compared to the real systems and the absence of solvent effects.

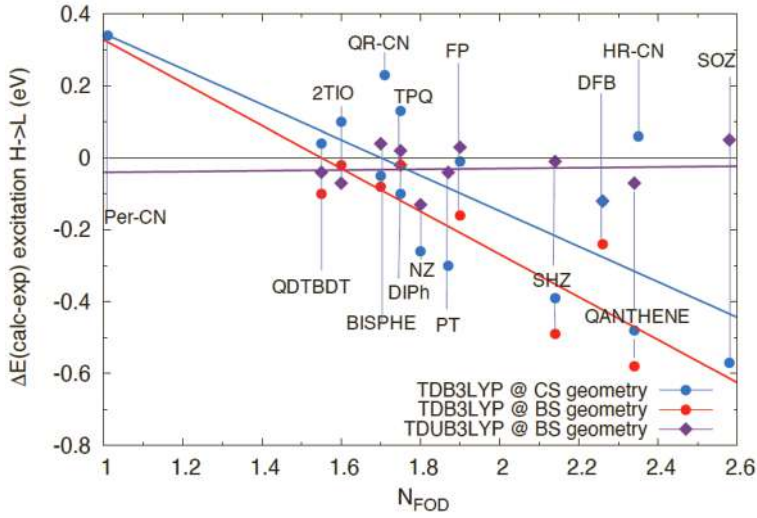


**Figure 3.9** The quality of different DFT-based computational approaches employed to predict the excitation energy of the SE state (i.e. the state dominated by the H→L excitation). The graph collects the difference between computed and observed excitation energy of the SE state versus the computed $N_{FOD}$ descriptor of di/multi-radical character: (blue circles) TDB3LYP at CS B3LYP geometry; (red circles) TDB3LYP at BS B3LYP geometry; and (violet diamonds) TDUB3LYP at BS B3LYP geometry. The lines in the same colors are linear fittings of the computed data to visualize the trends in computed values. Vertical bars indicate the compound to which computed data correspond.

It can be seen that the linear fittings of the two sets of computed excitation energies obtained from TDDFT calculations based on CS

reference configurations (blue and red circles) are almost parallel, which indicates a similar average quality of the results, with an energy difference increasing with the $N_{FOD}$ value, as a result of an increased geometry difference between the two sets, of CS and BS geometries. It emerges clearly from the figure that TDDFT calculations based on a CS reference configuration underestimate the excitation energy of the dipole-allowed SE state for increasingly large diradical character (larger $N_{FOD}$ values). This originates from the lack of static correlation in the ground state description, whose energy is therefore overestimated. Indeed, the data showing a stronger deviation from the experimental values are those computed for molecules with larger $N_{FOD}$ values (diradical character) and consequently those more affected by static correlation that is missing for a CS reference configuration, which is used in the reported TDB3LYP calculations.

In contrast, the violet diamonds and the violet fitting line in Figure 3.9 (TDUB3LYP predictions, Table 3.1) indicate minor average deviations from the experimental data. The quality is good for all the systems investigated and independent of the $N_{FOD}$ value. We attribute the better agreement with experiment of TDUB3LYP calculations, to use an unrestricted reference configuration, which is able to recover static correlation effects in the ground state, in spite of some degree of spin contamination.

In Figure 3.10, we collect the difference between observed excitation energies of the SE state and computed data from two parameterizations of the DFT/MRCI approach. We include results from the old parameterization, since previously published data for the oligoacene diradicaloids was determined with this set of parameters [57]. The quality of the two sets is similar, almost independent on the $N_{FOD}$ descriptor, but the new R2018 parameterization (which is recommended because it is not dependent on the spin state) underestimates more markedly the excitation energies of the SE state. Comparing Figures 3.9 and 3.10, we can conclude that the TDUB3LYP approach predicts excitation energies on average closer to observed values than the DFT/MRCI method. However, as discussed in detail in Section 3.3.2 and as it will be seen in the next section, the TDUDFT approach is suitable to predict the DE state only for large diradical character.

**Table 3.1** Computed vertical excitation energies (eV) of the dipole-allowed excited state SE (H→L) from TDDFT and DFT/MRCI approaches and comparison with the available experimental data for the diradicaloids shown in Figure 3.1

| Molecule | DFT/MRCI original | DFT/MRCI R2018 | Exp. | TDUB3LYP | TDB3LYP | TDB3LYP |
|---|---|---|---|---|---|---|
| geometry | | | | BS B3LYP | BS B3LYP | CS B3LYP |
| 2TIO | 1.95 | 1.74 | 1.88[a] | 1.81 | 1.86 | 1.98 |
| QDTBDT | 1.91 | 1.64 | 1.85[b] | 1.81 | 1.75 | 1.89 |
| NZ | 1.84 | 1.67 | 1.85[c] | 1.72 | - | 1.59 |
| BISPHE | 1.66 | 1.39 | 1.43[d] | 1.47 | 1.35 | 1.38 |
| DIPh | 1.39 | 1.32 | 1.46[e] | 1.44 | - | 1.36 |
| DFB | 1.19 | 1.05 | 1.25[f] | 1.13 | 1.01 | 1.13 |
| FP | 1.62 | 1.39 | 1.48[g] | 1.51 | 1.32 | 1.47 |
| PT | 1.55 | 1.27 | 1.42[h] | 1.38 | - | 1.12 |
| TPQ | 1.57 | 1.41 | 1.46[i] | 1.48 | 1.44 | 1.59 |
| SHZ | 1.65 | 1.38 | 1.50[j] | 1.49 | 1.01 | 1.11 |
| SOZ | 1.40 | 1.35 | 1.51[k] | 1.56 | - | 0.94 |
| QANTHENE | 1.58 | 1.15 | 1.35[l] | 1.28 | 0.77 | 0.87 |
| Per-CN | 2.12 | 2.03 | 1.98[m] | - | - | 2.32 |
| QR-CN | 1.49 | 1.38 | 1.41[n] | - | - | 1.64 |
| HR-CN | 1.34 | 1.13 | 1.27[n] | - | - | 1.33 |

*absorption spectra registered: [a]in n-hexane [36]; [b]in $CHCl_3$ [18]; [c]in $CH_2Cl_2$ [44]; [d]in $CHCl_3$ [11]; [e]in $CH_2Cl_2$ [47]; [f]in $CH_2Cl_2$ [14]; [g]in $CH_2Cl_2$ [17]; [h]in $CH_2Cl_2$ [46]; [i]in $CH_2Cl_2$ [10]; [j]in $CH_2Cl_2$ [15]; [k]in $CCl_4$ [45]; [l]in $CH_2Cl_2$ [12]; [m]in $CHCl_3$ [26]; [n]in toluene [27].

### 3.3.4 DE Excited State from DFT-Based Approaches

In Table 3.2, we collect the computed excitation energies of the DE state (i.e. whose character is generally dominated by the (H,H→L,L) double excitation) obtained from TDUB3LYP, SF-TDBHHLYP, and DFT/MRCI calculations and compare them with available experimental data. The computed SF-TDBHHLYP (yellow squares) and TDUB3LYP (violet diamonds) excitation energies are plotted against experimental values in Figure 3.11.

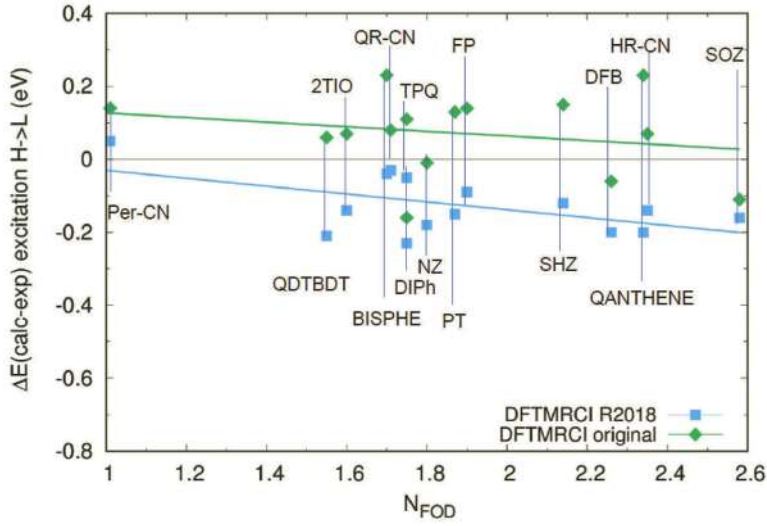


**Figure 3.10** The quality of DFT/MRCI computed excitation energies of the SE state (i.e. the state dominated by the H→L excitation) for the diradicaloids in Figure 3.1. The graph collects the difference between computed and observed excitation energy of the SE state versus the computed $N_{FOD}$ descriptor of di/multi-radical character: (green diamonds) DFT/MRCI results employing the original parameterization; and (blue squares) DFT/MRCI results employing the most recent R2018 parameterization. The lines in the same colors are linear fittings of the computed data to visualize the trends. Vertical bars indicate the compound to which computed data correspond.

**Table 3.2** Computed vertical excitation energies (eV) of the dipole-forbidden DE state *(*H,H→L,L*)* from TDDFT and DFT/MRCI approaches and comparison with the available experimental data for the diradicaloids shown in Figure 3.1

| Molecule | DFT/MRCI original | DFT/MRCI R2018 | Exp*. | TDUB3LYP | SF-TDBHHLYP |
|---|---|---|---|---|---|
| 2TIO | 1.37 | 1.54 | 1.68[a] | 0.98 | 1.35 |
| QDTBDT | 1.59 | 1.72 | 1.57[b] | 1.07 | 1.56 |
| NZ | 1.38 | 1.43 | 1.39[c] | 1.22 | 1.16 |
| BISPHE | 1.58 | 1.68 | 1.54[d] | 1.03 | 1.57 |
| DIPh | 1.33 | 1.50 | 1.18[e] | 1.21 | 1.23 |
| DFB | 0.98 | 1.03 | 0.92[f] | 0.91 | 0.88 |
| FP | 1.22 | 1.23 | 1.13[g] | 1.13 | 0.93 |

| Molecule | DFT/MRCI original | DFT/ MRCI R2018 | Exp*. | TDUB3LYP | SF-TDBHHLYP |
|---|---|---|---|---|---|
| PT | 1.36 | 1.48 | 1.23[h] | 1.13 | 1.56 |
| TPQ | 1.31 | 1.28 | 1.13[i] | 1.16 | 1.01 |
| SHZ | 1.50 | 1.38 | 1.19[j] | 1.32 | 1.12 |
| SOZ | 1.34 | 1.14 | 1.07[k] | 1.41 | 0.79 |
| QANTHENE | 1.47 | 1.26 | 1.08[l] | 1.17 | 0.94 |
| Per-CN | 2.05 | 2.23 | 2.06[m] | - | - |
| QR-CN | 1.25 | 1.37 | 1.23[n] | - | - |
| HR-CN | 0.97 | 1.08 | 1.12[o] | - | - |

*absorption spectra registered: [a]in n-hexane [36]; [b]in $CHCl_3$ [18]; [c]in $CH_2Cl_2$ [44]; [d]in $CHCl_3$ [11]; [e]in $CH_2Cl_2$ [47]; [f]in $CH_2Cl_2$ [14]; [g]in $CH_2Cl_2$ [17]; [h]in $CH_2Cl_2$ [46]; [i]in $CH_2Cl_2$ [10]; [j]in $CH_2Cl_2$ [15]; [k]in $CCl_4$ [45]; [l]in $CH_2Cl_2$ [12]; [m]two-photon absorption spectrum in THF [26]; [n]spectrum measured at low temperature [64]; [o]in toluene [27].

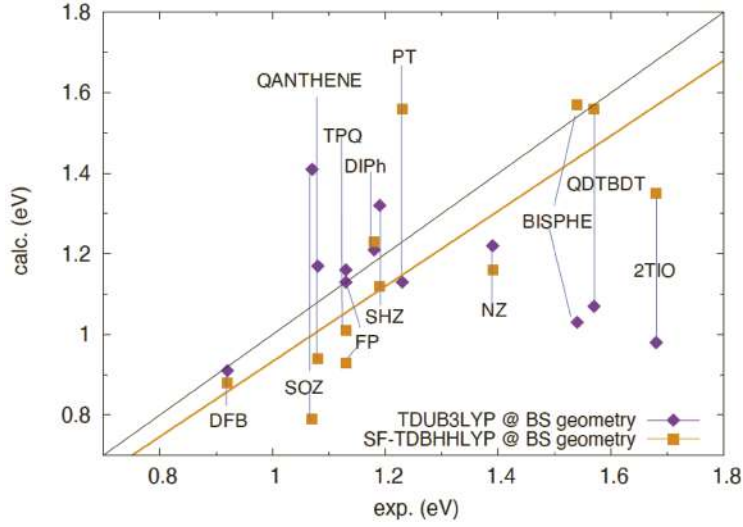


**Figure 3.11** TDUDFT and SF-TDDFT computed excitation energies of the DE state (i.e. the state dominated by the H,H→L,L excitation) versus experimental excitation energy: (yellow squares) SF-TDBHHLYP/6-31G* calculations; and (violet diamonds) TDUB3LYP/6-31G* results. The lines in the same colors are linear fittings of the computed data. The TDUB3LYP data was not fitted due to their lower quality when the diradical character is not large (see the text for the discussion). The black line is the bisector of the graph and corresponds to perfect agreement with experimental data. Vertical bars indicate the compound to which computed and experimental data correspond.

The TDUB3LYP computed excitation energies of the DE state were identified by inspecting the wavefunction in which the singly excited configurations $A^2$ and $B^2$ appear with the same sign and as the dominant contribution (see the discussion in Section 3.2.3 and the schemes in Figures 3.2 and 3.3). Figure 3.11 shows that for some of the systems investigated, the TDUB3LYP results are in very good agreement with experimental data; while for others, the computed excitation energies display unacceptable deviations from the experiment.

This behavior can be easily accounted for by considering the mixing of singlet and triplet spin components in the DE state wavefunction within a TDUDFT approach, given by Eq. (3.11) and shown in Figure 3.4. More specifically, the TDUDFT approach can be used to describe the DE state when (i) the 2e-2o model is valid to a good extent and (ii) when the diradical character is large, namely when the rotation angle of BS orbitals is close to 45°, otherwise mixing with the triplet spin component and spin contamination make the results unreliable. In these favorable cases, the BS reference configuration recovers via localization, the static correlation that is missing in the CS reference configuration and, on the other hand, the appropriate combination of singly excited configurations between localized orbitals, $A^2$+$B^2$, (Figures 3.1. and 3.3 and Eq. (3.5)) corresponds to the DE state. Indeed, the $S^2$ value of the DE state in these cases remains always acceptably close to the value for a pure singlet spin state, which implies a moderate triplet spin contamination.

There is, however, an additional limit in the TDUDFT representation of the DE state, which is the identical contribution of ground $|H_{CS}\overline{H}_{CS}\rangle$ and doubly excited $|L_{CS}\overline{L}_{CS}\rangle$ configurations to the singlet spin component emerging from Eq. (3.11). This restriction may not be optimal and may lead to inconsistencies also for systems displaying marked diradical character.

Finally, additional inaccuracies may be originated by the presence of a multiradical character, which can be monitored by considering the $N_{FOD}$ descriptor. As noted above, if $N_{FOD}$ is greater than 2, this indicates that more than two electrons need to be correlated and this may be the case for some of the systems investigated (Figure 3.7) such as SHZ, SOZ, and QANTHENE. In summary, the TDUB3LYP may

provide a good estimate of the energy location of the DE state only for large diradical, but modest multiradical character.

Because the TDUDFT approach is suitable to describe the DE state only under the specific conditions limiting the triplet spin contamination (in turn related with the amount of diradical character), the results in Figure 3.11 were not linearly fitted in this case. In contrast, the SF-TDDFT method is not formally limited by the diradical character of the system investigated. The trend shown by the linear fit of SF-TDBHHLYP predictions in Figure 3.11 goes almost parallel with the experimental values (black bisector line), indicating an average similar accuracy for the set of diradicals considered and a general underestimate of excitation energies. One advantage of the SF approach is that it is suitable to describe systems displaying also some degree of multiradical character because double excitations are not limited to the 2e-2o space. The SF wavefunction does not suffer from the contamination with the triplet component typical of the TDUDFT approach; however, in SF-TDDFT, only those excitations within the open-shell space are able to generate spin-pure solutions, whereas all other configurations are missing their "spin complements," leading to spin-contaminated solutions [48]. Therefore, spin contamination may affect the quality of the results, owing to the spin incomplete expansion of the wavefunction beyond the 2e-2o orbital space. In this regard, recent implementations of the spin-adapted SF approach [64] will be able to overcome this limit and will be tested in the future.

The DFT/MRCI computed excitation energies, for the two sets of parameters (original and R2018), are collected in Figures 3.12 and 3.13. In Figure 3.12, the computed excitation energies are reported against the observed data. The original parameterization, used in previous investigations on oligoacenes and oligoenes [57], shows an acceptable trend for the set of diradicaloids investigated here with excitation energies slightly overestimated in some regions and slightly underestimated for others. Indeed, the fitted line of computed results is not parallel to the bisector of the graph. In contrast, the fitting of excitation energies computed with the new R2018 parameterization, is almost parallel with the bisector and just a little bit above it, indicating a very similar performance for all the molecules investigated, with a systematic tendence to slightly overestimate the excitation energy of the DE state.

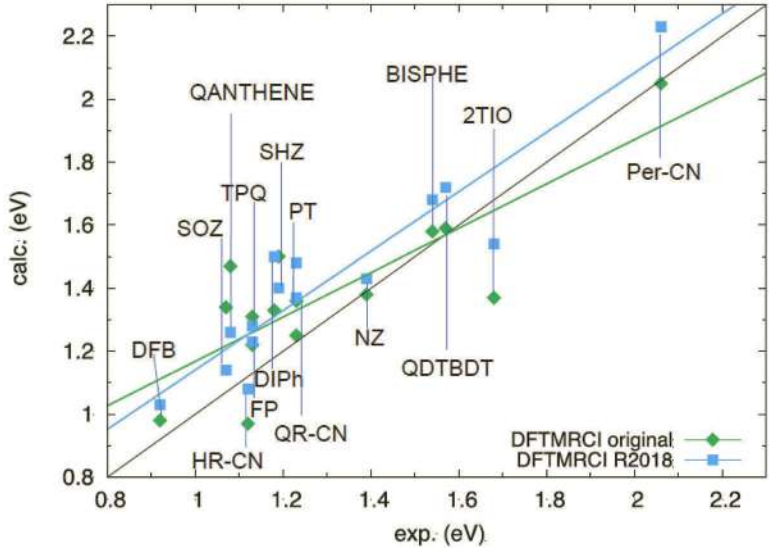


**Figure 3.12** DFT/MRCI computed excitation energies of the DE state (i.e. the state dominated by the H,H→L,L excitation) versus experimental excitation energy: (green diamonds) DFT/MRCI calculations with the original parameterization [49]; and (blue squares) DFT/MRCI calculations with the most recent parameterization R2018 [50]. The lines in the same colors are linear fittings of the computed data. The black line is the bisector of the graph and corresponds to perfect agreement with experimental data. Vertical bars indicate the compound to which computed and experimental data correspond.

A similar trend is documented in Figure 3.13, where the difference between computed and observed excitation energies is plotted against the $N_{FOD}$ descriptor. The trend shown by the new R2018 parameterization is of superior quality compared to the original parameterization. The computed excitation energies tend to be slightly overestimated compared to the experiment, but the deviation is almost independent on the $N_{FOD}$ value, and the DFT/MRCI method with the R2018 parameterization is therefore suitable to predict the location of the DE state for the entire range of diradical or multiradical character. Because the diradical character increases for increasingly longer oligomers of diradical molecules and the DE state tends to decrease its energy much faster along the series compared to the SE state, a crossing between the DE and SE states may occur at a given oligomer length. Based on the slight

deviations from experimental data discussed here, this crossing may be predicted by DFT/MRCI calculations for longer oligomers than observed. This is the case for the three tetracyano oligorylene derivatives investigated here.

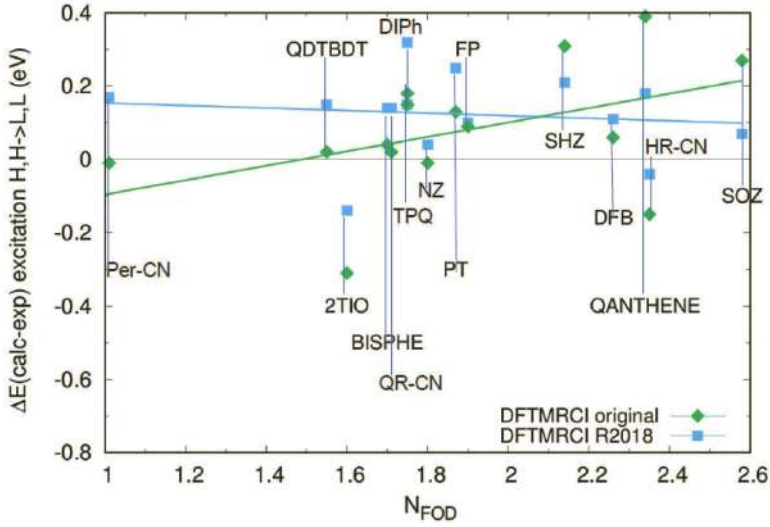


**Figure 3.13** The quality of DFT/MRCI computed excitation energies for the DE state. The graph collects the difference between computed and observed excitation energy of the DE state versus the computed $N_{FOD}$ descriptor of di/multi-radical character: (green diamonds) DFT/MRCI results employing the original (old) parameterization [49]; and (blue squares) DFT/MRCI results employing the most recent R2018 parameterization [50]. The lines in the same colors are linear fittings of the computed data. Vertical bars indicate the compound to which computed data correspond.

## 3.4 Concluding Remarks

The photophysical properties of diradicaloids and their potential applications are strongly influenced by their electronic structure and by the sequence of low-lying excited electronic states. For singlet ground-state diradicaloids, there are two low-lying excited states, one is generally one-photon active and dominated by the H→L excitation (the SE state), while the other is weakly active in one-photon spectroscopy, it may be active in two-photon spectroscopy,

and is dominated by the H,H→L,L double excitation (the DE state). The occurrence of a low-lying DE state is predicted by the very simple 2e-2o model; however, within this model, it is located above the SE state. More extended computational investigations, carried out with large orbital spaces and highly correlated methods, have shown that the DE state can become the lowest excited singlet state and this has been thereafter documented for several diradicaloids. Since the DE state may influence the NLO properties and possibly the efficiency of singlet fission, its correct energy prediction is relevant.

In this chapter, we focused on cost-effective DFT-based computational approaches, since recent efforts in the design of new stable diradicaloids have led to molecular systems of very large dimension. We discussed the results of different computational methods, encompassing TDDFT, TDUDFT, SF-TDDFT, and DFT/MRCI, and critically evaluated their suitability to describe the SE and DE states. The TDDFT method can describe the SE state, but for large diradical characters, the TDUDFT approach provides excitation energies closer to experimental values.

While TDDFT method cannot capture the DE state because only single excitations are included, we have shown that single excitations between frontier orbitals in TDUDFT may describe the DE state provided that specific conditions are fulfilled, which can be summarized by the requirement of a very large diradical character combined with a negligible multiradical character. The TDUDFT method is therefore suitable only for a restrict range of diradical character. When these conditions are not fulfilled, the computed results are unreliable because of a large triplet spin component entering into the DE state wavefunction.

The SF-TDDFT approach is widely applicable in this regard, since its quality is almost independent of the diradical character. Furthermore, it can describe systems with multiradical character because double excitations are not limited to the 2e-2o space. However, unless the spin-adapted SF approach is used, the quality of predicted excited states may be affected by spin-contamination. We can conclude that SF-TDDFT is suitable to describe the DE state for a more extended range of diradical systems compared to TDUDFT.

Finally, we have investigated two parameterizations of the DFT/MRCI approach. The method describes satisfactorily both the SE and DE excitation energies. The spin-invariant R2018 parameterization

tends to slightly underestimate the excitation energy of the SE state and slightly overestimate the excitation energy of the DE state. Most importantly, however, the trend in computed excitation energies for both SE and DE states is independent on the diradical character, a highly desirable feature for a cost-effective computational approach.

In conclusion, a careful choice of the appropriate DFT-based computational approach can provide reliable information on the low-lying excited states of diradicaloids with varying diradical characters and large molecular dimension, including the energy location of an unusual excited state like the DE state.

## Acknowledgments

We gratefully acknowledge the financial support from University of Bologna (RFO) and computational resources from CINECA through an Italian Super Computing Resource Allocation (ISCRA) C project. Yasi Dai acknowledges MIUR for her Ph.D. fellowship.

## References

1. Muhammad, S., Nakano, M., Al-Sehemi, A. G., Kitagawa, Y., Irfan, A., Chaudhry, A. R., Kishi, R., Ito, S., Yoneda, K., and Fukuda, K. (2016). Role of a singlet diradical character in carbon nanomaterials: A novel hot spot for efficient nonlinear optical materials, *Nanoscale*, **8**, pp. 17998–18020.
2. Nakano, M. (2017). Open-shell-character-based molecular design principles: Applications to nonlinear optics and singlet fission, *Chem. Rec.*, **17**, pp. 27–62.
3. Huang, Y. and Egap, E. (2018). Open-shell organic semiconductors: An emerging class of materials with novel properties, *Polym. J.*, **50**, pp. 603–614.
4. Hu, X., Wang, W., Wang, D., and Zheng, Y. (2018). The electronic applications of stable diradicaloids: Present and future, *J. Mater. Chem. C*, **6**, pp. 11232–11242.
5. Sun, Z. and Wu, J. (2012). Open-shell polycyclic aromatic hydrocarbons, *J. Mater. Chem.,* **22**, pp. 4151–4160.
6. Gopalakrishna, T. Y., Zeng, W., Lu, X., and Wu, J. (2018). From open-shell singlet diradicaloids to polyradicaloids, *Chem. Commun.,* **54**, pp. 2186–2199.

7. Takahashi, T., Matsuoka, K., Takimiya, K., Otsubo, T., and Aso, Y. (2005). Extensive quinoidal oligothiophenes with dicyanomethylene groups at terminal positions as highly amphoteric redox molecules, *J. Am. Chem. Soc.,* **127**, pp. 8928–8929.
8. Ortiz, R. P., Casado, J., González, S. R., Hernández, V., López Navarrete, J. T., Viruela, P. M., Ortí, E.; Takimiya, K., and Otsubo, T. (2010). Quinoidal oligotiophenes: Towards biradical ground-state species, *Chem. Eur. J.,* **16**, pp. 470–484.
9. Fazzi, D., Canesi, E. V., Negri, F., Bertarelli, C., and Castiglioni, C. (2010). Biradicaloid character of thiophene-based heterophenoquinones: The role of electron-phonon coupling, *ChemPhysChem*, **11**, pp. 3685–3695.
10. Zhu, X., Tsuji, H., Nakabayashi, K., Ohkoshi, S. I., and Nakamura, E. (2011). Air- and heat-stable planar tri-p-quinodimethane with distinct biradical characteristics, *J. Am. Chem. Soc*., **133**, pp. 16342–16345.
11. Kamada, K., Ohta, K., Shimizu, A., Kubo, T., Kishi, R., Takahashi, H., Botek, E., Champagne, B., and Nakano, M. (2010). Singlet diradical character from experiment, *J. Phys. Chem. Lett*., **1**, pp. 937–940.
12. Konishi, A., Hirao, Y., Matsumoto, K., Kurata, H., Kishi, R., Shigeta, Y., Nakano, M., Tokunaga, K., Kamada, K., and Kubo, T. (2013). Synthesis and characterization of quarteranthene: Elucidating the characteristics of the edge state of graphene nanoribbons at the molecular level, *J. Am. Chem. Soc*., **135**, pp. 1430–1437.
13. Liu, J., Ravat, P., Wagner, M., Baumgarten, M., Feng, X., and Müllen, K. (2015). Tetrabenzo[a,f,j,o]perylene: A polycyclic aromatic hydrocarbon with an open-shell singlet biradical ground state, *Angew. Chem. Int. Ed.,* **54**, pp. 12442–12446.
14. Ma, J., Liu, J., Baumgarten, M., Fu, Y., Tan, Y. Z., Schellhammer, K. S., Ortmann, F., Cuniberti, G., Komber, H., Berger, R., Müllen, K., and Feng, X. (2017). A stable saddle-shaped polycyclic hydrocarbon with an open-shell singlet ground state, *Angew. Chem. Int. Ed.*, **56**, pp. 3280–3284.
15. Zeng, W., Sun, Z., Herng, T. S., Gonçalves, T. P., Gopalakrishna, T. Y., Huang, K. W., Ding, J., and Wu, J. (2016). Super-heptazethrene, *Angew. Chem. Int. Ed.*, **55**, pp. 8615–8619.
16. Ravat, P., Šolomek, T., Rickhaus, M., Häussinger, D., Neuburger, M., Baumgarten, M., and Juríček, M. (2016). Cethrene: A helically chiral biradicaloid isomer of heptazethrene, *Angew. Chem. Int. Ed.,* **55**, pp. 1183–1186.
17. Hu, P., Lee, S., Herng, T. S., Aratani, N., Gonçalves, T. P., Qi, Q., Shi, X., Yamada, H., Huang, K.-W., Ding, J., Kim, D., and Wu, J. (2016). Toward

tetraradicaloid: The effect of fusion mode on radical character and chemical reactivity, *J. Am. Chem. Soc.,* **138**, pp. 1065–1077.

18. Li, J., Qiao, X., Xiong, Y., Li, H., and Zhu, D. (2014). Five-ring fused tetracyanothienoquinoids as high-performance and solution-processable n-channel organic semiconductors: Effect of the branching position of alkyl chains, *Chem. Mater.*, **26**, pp. 5782–5788.
19. Xia, D., Keerthi, A., An, C., and Baumgarten, M. (2017). Synthesis of a quinoidal dithieno[2,3-d;2',3'-d]benzo[2,1-b;3,4-b']-dithiophene based open-shell singlet biradicaloid, *Org. Chem. Front.*, **4**, pp. 18–21.
20. Lin, Z., Chen, L., Xu, Q., Shao, G., Zeng, Z., Wu, D., and Xia, J. (2020). Tuning biradical character to enable high and balanced ambipolar charge transport in a quinoidal π-system, *Org. Lett.*, **22**, pp. 2553–2558.
21. Tobe, Y. (2018). Quinodimethanes incorporated in non-benzenoid aromatic or antiaromatic frameworks, *Top. Curr. Chem. (Z)*, **376**, 12.
22. Lu, R. Q., Wu, S., Yang, L. L., Gao, W. B., Qu, H., Wang, X. Y., Chen, J. B., Tang, C., Shi, H. Y., and Cao, X. Y. (2019). Stable diindeno-fused corannulene regioisomers with open-shell singlet ground states and large diradical characters, *Angew. Chem. Int. Ed.*, **58**, pp. 7600–7605.
23. Rudebusch, G. E., Zafra, J. L., Jorner, K., Fukuda, K., Marshall, J. L., Arrechea-Marcos, I., Espejo, G. L., Ponce Ortiz, R., Gómez-García, C. J., Zakharov, L. N., Nakano, M., Ottosson, H., Casado, J., and Haley, M. M. (2016). Diindeno-fusion of an anthracene as a design strategy for stable organic biradicals, *Nat. Chem*., **8**, pp. 753–759.
24. Barker, J. E., Dressler, J. J., Cárdenas Valdivia, A., Kishi, R., Strand, E. T., Zakharov, L. N., Macmillan, S. N., Gómez-García, C. J., Nakano, M., Casado, J., and Haley, M. M. (2020). Molecule isomerism modulates the diradical properties of stable singlet diradicaloids, *J. Am. Chem. Soc.*, **142**, pp. 1548–1555.
25. Zeng, W., Phan, H., Herng, T. S., Gopalakrishna, T. Y., Aratani, N., Zeng, Z., Yamada, H., Ding, J., and Wu, J. (2017). Rylene ribbons with unusual diradical character, *Chem*, **2**, pp. 81–92.
26. Zeng, Z., Ishida, M., Zafra, J. L., Zhu, X., Sung, Y. M., Bao, N., Webster, R. D., Lee, B. S., Li, R. W., Zeng, W., Li, Y., Chi, C., López Navarrete, J. T., Ding, J., Casado, J., Kim, D., and Wu, J. (2013). Pushing extended *p*-quinodimethanes to the limit: Stable tetracyano-oligo(*N*-annulated perylene)quinodimethanes with tunable ground states, *J. Am. Chem. Soc.*, **135**, pp. 6363–6371.
27. Zeng, Z., Lee, S., Zafra, J. L., Ishida, M., Zhu, X., Sun, Z., Ni, Y., Webster, R. D., Li, R. W., López Navarrete, J. T., Chi, C., Ding, J.,

Casado, J., Kim, D., and Wu, J. (2013). Tetracyanoquaterrylene and tetracyanohexarylenequinodimethanes with tunable ground states and strong near-infrared absorption, *Angew. Chem. Int. Ed*., **52**, pp. 8561–8565.

28. Wen, J., Havlas, Z., and Michl, J. (2015). Captodatively stabilized biradicaloids as chromophores for singlet fission, *J. Am. Chem. Soc.,* **137**, pp. 165–172.
29. Zeng, T., Ananth, N., and Hoffmann, R. (2014). Seeking small molecules for singlet fission: A heteroatom substitution strategy, *J. Am. Chem. Soc.,* **136**, pp. 12638–12647.
30. Zhang, C., Medina Rivero, S., Liu, W., Casanova, D., Zhu, X., and Casado, J. (2019). Stable cross-conjugated tetrathiophene diradical, *Angew. Chem. Int. Ed.*, **58**, pp. 11291–11295.
31. Nakano, M. (2014). Excitation energies and properties of open-shell singlet molecules, Springer, Germany.
32. Ito, S., Nagami, T., and Nakano, M. (2018). Molecular design for efficient singlet fission, *J. Photochem. Photobiol. C Photochem. Rev.*, **34**, pp. 85–120.
33. Salem, L. and Rowland, C. (1972). The electronic properties of diradicals, *Angew. Chem. Int. Ed. Engl*., **11**, pp. 92–111.
34. Bonačić-Koutecký, V., Koutecký, J., and Michl, J. (1987). Neutral and charged biradicals, zwitterions, funnels in S1, and proton translocation: Their role in photochemistry, photophysics, and vision, *Angew. Chem. Int. Ed. Engl.,* **26**, pp. 170–189.
35. Slipchenko, L. V. and Krylov, A. I. (2002). Singlet-triplet gaps in diradicals by the spin-flip approach: A benchmark study, *J. Chem. Phys.*, **117**, pp. 4694–4708.
36. Di Motta, S., Negri, F., Fazzi, D., Castiglioni, C., and Canesi, E. V. (2010). Biradicaloid and polyenic character of quinoidal oligothiophenes revealed by the presence of a low-lying double-exciton state, *J. Phys. Chem. Lett.*, **1**, pp. 3334–3339.
37. Schulten, K. and Karplus, M. (1972). On the origin of a low-lying forbidden transition in polyenes and related molecules, *Chem. Phys. Lett.,* **14**, pp. 305–309.
38. Gu, J., Wu, W., Danovich, D., Hoffmann, R., Tsuji, Y., and Shaik, S. (2017). Valence bond theory reveals hidden delocalized diradical character of polyenes, *J. Am. Chem. Soc.,* **139**, pp. 9302–9316.
39. González-Cano, R. C., Di Motta, S., Zhu, X., López Navarrete, J. T., Tsuji, H., Nakamura, E., Negri, F., and Casado, J. (2017). Carbon-

bridged phenylene-vinylenes: On the common diradicaloid origin of their photonic and chemical properties, *J. Phys. Chem. C*, **121**, pp. 23141–23148.

40. Omar, Ö. H., Padula, D., and Troisi, A. (2020). Elucidating the relationship between multiradical character and predicted singlet fission activity, *ChemPhotoChem*, **4**, pp. 5223–5229.
41. Ullrich, T., Pinter, P., Messelberger, J., Haines, P., Kaur, R., Hansmann, M. M., Munz, D., and Guldi, D. M. (2020). Singlet fission in carbene-derived diradicaloids, *Angew. Chem. Int. Ed.,* **59**, pp. 7906–7914.
42. Canola, S., Casado, J., and Negri, F. (2018). The double exciton state of conjugated chromophores with strong diradical character: Insights from TDDFT calculations, *Phys. Chem. Chem. Phys.,* **20**, pp. 24227–24238.
43. Canola, S., Dai, Y., and Negri, F. (2019). The low lying double-exciton state of conjugated diradicals: Assessment of TDUDFT and spin-flip TDDFT predictions, *Computation*, **7**, pp. 68.
44. Huang, R., Phan, H., Herng, T. S., Hu, P., Zeng, W., Dong, S. Q., Das, S., Shen, Y., Ding, J., Casanova, D., and Wu, J. (2016). Higher order π-conjugated polycyclic hydrocarbons with open-shell singlet ground state: Nonazethrene versus nonacene, *J. Am. Chem. Soc.*, **138**, pp. 10323–10330.
45. Zeng, W., Gopalakrishna, T. Y., Phan, H., Tanaka, T., Herng, T. S., Ding, J., Osuka, A., and Wu, J. (2018). Superoctazethrene: An open-shell graphene-like molecule possessing large diradical character but still with reasonable stability, *J. Am. Chem. Soc.*, **140**, pp. 14054–14058.
46. Ni, Y., Gopalakrishna, T. Y., Phan, H., Herng, T. S., Wu, S., Han, Y., Ding, J., and Wu, J. (2018). A peri-tetracene diradicaloid: Synthesis and properties, *Angew. Chem. Int. Ed.*, **57**, pp. 9697–9701.
47. Majewski, M. A., Chmielewski, P. J., Chien, A., Hong, Y., Lis, T., Witwicki, M., Kim, D., Zimmerman, P. M., and Stępień, M. (2019). 5,10-Dimesityldiindeno[1,2-a:2',1'-i]phenanthrene: A stable biradicaloid derived from Chichibabin's hydrocarbon, *Chem. Sci.*, **10**, pp. 3413–3420.
48. Shao, Y., Head-Gordon, M., and Krylov, A. I. (2003). The spin-flip approach within time-dependent density functional theory: Theory and applications to diradicals, *J. Chem. Phys.,* **118**, pp. 4807–4818.
49. Grimme, S. and Waletzke, M. (1999). A combination of Kohn-Sham density functional theory and multi-reference configuration interaction methods, *J. Chem. Phys.*, **111**, pp. 5645–5655.

50. Marian, C. M., Heil, A., and Kleinschmidt, M. (2019). The DFT/MRCI Method, *WIREs Comput. Mol. Sci.,* **9**, e1394.
51. Gaussian 16, Revision A.03, Frisch, M. J., Trucks, G. W., Schlegel, H. B., Scuseria, G. E., Robb, M. A., Cheeseman, J. R., Scalmani, G., Barone, V., Petersson, G. A., Nakatsuji, H., Li, X., Caricato, M., Marenich, A. V., Bloino, J., Janesko, B. G., Gomperts, R., Mennucci, B., Hratchian, H. P., Ortiz, J. V., Izmaylov, A. F., Sonnenberg, J. L., Williams-Young, D., Ding, F., Lipparini, F., Egidi, F., Goings, J., Peng, B., Petrone, A., Henderson, T., Ranasinghe, D., Zakrzewski, V. G., Gao, J., Rega, N., Zheng, G., Liang, W., Hada, M., Ehara, M., Toyota, K., Fukuda, R., Hasegawa, J., Ishida, M., Nakajima, T., Honda, Y., Kitao, O., Nakai, H., Vreven, T., Throssell, K., Montgomery, J. A., Jr., Peralta, J. E., Ogliaro, F., Bearpark, M. J., Heyd, J. J., Brothers, E. N., Kudin, K. N., Staroverov, V. N., Keith, T. A., Kobayashi, R., Normand, J., Raghavachari, K., Rendell, A. P., Burant, J. C., Iyengar, S. S., Tomasi, J., Cossi, M., Millam, J. M., Klene, M., Adamo, C., Cammi, R., Ochterski, J. W., Martin, R. L., Morokuma, K., Farkas, O., Foresman, J. B., and Fox, D. J. (2016). Gaussian Inc., Wallingford CT.
52. Yamaguchi, K. (1975). The electronic structures of biradicals in the unrestricted Hartree-Fock approximation, *Chem. Phys. Lett.*, **33**, pp. 330–335.
53. Grimme, S. and Hansen, A. (2015). A practicable real-space measure and visualization of static electron-correlation effects, *Angew. Chem. Int. Ed.,* **54**, pp. 12308–12313.
54. Bauer, C. A., Hansen, A., and Grimme, S. (2017). The fractional occupation number weighted density as a versatile analysis tool for molecules with a complicated electronic structure, *Chem. - A Eur. J.*, **23**, pp. 6150–6164.
55. Neese, F. (2012). The ORCA program system, *WIREs Comput. Mol. Sci.*, **2**, pp. 73–78.
56. Schmidt, M. W., Baldridge, K. K., Boatz, J. A., Elbert, S. T., Gordon, M. S., Jensen, J. H., Koseki, S., Matsunaga, N., Nguyen, K. A., Su, S. J., Windus, T. L., Dupuis, M., and Montgomery, J. A. (1993). General atomic and molecular electronic structure system, *J. Comput. Chem.*, **14**, pp. 1347–1363.
57. Marian, C. M. and Gilka, N. (2008). Performance of the density functional theory/multireference configuration interaction method on electronic excitation of extended π-systems, *J. Chem. Theory Comput,* **4**, pp. 1501–1515.
58. Pérez-Guardiola, A., Sandoval-Salinas, M. E., Casanova, D., San Fabián, E., Pérez-Jiménez, A., and Sancho-García, J. C. (2018). The role of

topology in organic molecules: Origin and comparison of the radical character in linear and cyclic oligoacenes and related oligomers, *Phys. Chem. Chem. Phys.,* **20**, pp. 7112–7124.

59. Einholz, R., Fang, T., Berger, R., Grüninger, P., Früh, A., Chassé, T., Fink, R. F., and Bettinger, H. F. (2017). Heptacene: Characterization in solution, in the solid state, and in films*, J. Am. Chem. Soc.,* **139**, pp. 4435–4442.
60. Qian, H., Negri, F., Wang, C., and Wang, Z. (2008). Fully conjugated tri(perylene bisimides): An approach to the construction of n-type graphene nanoribbons, *J. Am. Chem. Soc.,* **130**, pp. 17970–17976.
61. Li, Y., Gao, J., Di Motta, S., Negri, F., and Wang, Z. (2010). Tri-*N*-annulated hexarylene: An approach to well-defined graphene nanoribbons with large dipoles, *J. Am. Chem. Soc.,* **132**, pp. 4208–4213.
62. Yue, W., Lv, A., Gao, J., Jiang, W., Hao, L., Li, C., Li, Y., Polander, L. E., Barlow, S., Hu, W., Di Motta, S., Negri, F., Marder, S. R., and Wang, Z. (2012). Hybrid rylene arrays via combination of Stille coupling and C−H transformation as high-performance electron transport materials, *J. Am. Chem. Soc*., **134,** pp. 5770–5773.
63. Menon, A. S. and Radom, L. (2008). Consequences of spin contamination in unrestricted calculations on open-shell species: Effect of Hartree-Fock and Møller-Plesset contributions in hybrid and double-hybrid density functional theory approaches, *J. Phys. Chem. A*, **112,** pp. 13225–13230.
64. Zhang, X. and Herbert, J. M. (2015). Spin-flip, tensor equation-of-motion configuration interaction with a density-functional correction: A spin-complete method for exploring excited-state potential energy surfaces, *J. Chem. Phys.,* **143**, pp. 234107.
65. Casado J., personal communications on unpublished results.

## Chapter 4

# Vibrational Raman Spectroscopy of Diradicaloids: Revealing Their Physical Origin

**Samara Medina Rivero, José Luis Zafra, and Juan Casado**
*Department of Physical Chemistry, University of Málaga, Campus de Teatinos s/n, Málaga, Spain*
casado@uma.es

This chapter summarizes the Raman spectra of the main families of diradicaloids studied in the context of the oligomer approach. It takes the variation of the wavenumbers of selected/main bands of the Raman spectra as the experimental observable and their chain length dependences are related with the appearance of diradical character. Diradicaloids that develop in one- and two-dimensions have been addressed and the changes of their electronic structures were discussed in terms of Peierls distortion, pro-aromaticity, planar/distortion effects, graphene nanoribbon (GNR) electronic structure, etc. The Raman spectra of singlet diradicaloids and triplets of the same molecules have been also described and discussed. We realize that the Raman spectral property and the diradical character

*Diradicaloids*
Edited by Jishan Wu

ISBN 978-981-4968-08-9 (Hardcover), 978-1-003-27724-8 (eBook)
www.jennystanford.com

have the same physical origin thus highlighting how the vibrational Raman characterizations of open-shell molecules are very useful to assess comparative analysis of the degree of diradical character in series of homologue molecules.

## 4.1 Introduction to Vibrational Spectroscopy of Hydrocarbon Molecules

Vibrational spectroscopy has two main faces, infrared and Raman, which are based on rather different vibrational excitation processes and subjected to different selection rules. From a classical standpoint, spectroscopic bands are observed in the infrared spectrum when the normal modes carry out a net variation of the molecular dipole momentum, whereas the Raman bands are visible in the vibrational spectrum when net changes of the overall molecular polarizability are produced alongside the vibrational normal mode. Quantum assessment [1, 2] of these two vibrational processes needs to invoke perturbation theory of the matter-radiation interaction: (i) first-order approach leads to the appearance of vibrational excited states produced by the radiation and that are coupled to the ground (unperturbed state) by an electric dipole transition moment in the case of infrared spectroscopy; and (ii) within a second order perturbative approach, scattering processes merged are articulated by intermediate virtual states appearing between the unperturbed ground and the excited states in the case of the multiphoton Raman spectroscopy.

The classical view of the Raman spectroscopy allows to easily understand that normal modes involving the motion of the π-conjugated hydrocarbon skeletons, and particularly carbon-carbon stretching modes [abbreviated as ν(CC)] are those promoting large variations of molecular polarizability. Consequently, their associated Raman bands become intense and easily detectable [3–5]. The semiclassical view of the Raman process allows to easily assuming the role of intermediate virtual electronic states in the whole scattering effect and the joint action of electronic and vibrational transitions in the final Raman result. The role of the electronic states in the Raman spectroscopy will account for the interesting Raman spectra of poly-conjugated molecules in terms

of electron-phonon coupling [6, 7]. The Raman spectroscopy, thus, represents a unique tool for the elucidation of electronic properties of π-conjugated oligomers and polymers [8–12] though its use to explore poly-conjugated open-shell molecules is much scarce. In this chapter, it will be shown some of the unique insights that vibrational spectroscopy, particularly vibrational Raman, has provided to the understanding of diradicaloid molecules.

The Raman spectroscopy was used in the characterization of π-conjugated molecules from the very beginning of the research of conducting polymers at the end of the 70's of the past century [13, 14]. Nowadays, investigation in π-conjugated compounds is encompassed in current area of organic electronics. On the first studies on polyconjugated polymers, and polyacetylene [6–12] in particular, the Raman spectroscopy had a relevant role since it evidenced experimentally the existence of Peierls distortion in these one-dimensional systems as this displayed the vibrational wavenumber associated to the dimerization mode of the distorted structure [6, 7]. Though this chapter is mainly devoted to the Raman spectroscopy, it can be cited that infrared spectroscopy also played a role on the development of these π-conjugated organic systems; for instance, it was used in the pioneering works in the 70's dealing with charge transfer salts in the search of metal organic solids [15, 16]. In the case of the Raman spectroscopy, it was not only considered in the study of polyconjugated molecules, π-conjugated polymers and oligomers, but also actively participated in the knowledge of the electronic properties of fullerenes [17], carbon nanotubes [18], and more recently graphene [19].

## 4.2 Fundamental Physics on the Raman Spectra of Poly-Conjugated Molecules and Diradicaloids

Peierls distortion [20, 21] deserves particular attention, not only because of its impact on the vibrational Raman spectra, but also due to its importance to fundamentally understand the electronic structure of one-dimensional π-conjugated systems. Peierls distortion results from the competition between two opposite effects, the stabilization of electron pairs by dimerization and their

destabilization by the decrease of elastic energy (Scheme 4.1). One-dimensional π-conjugated systems such as polyacetylene and its oligomers, and oligoenes in Scheme 4.1, might be considered as examples of the competition between these two forces: full pairing and largest dimerization favor a low-spin state, while bond length equalization (minimal elastic energy) fuels a high-spin state against bonding. In this dimerization effect, the tendency of fermions to get paired under a potential (the attraction of nuclei) is revealed, which is the ultimate essence of the chemical bond, a bonding effect that is limited by the elastic energy term. The nature of the elastic term is related in π-conjugated molecules with the array of the sigma (single) bonds, which are compressed/elongated from their equilibrium positions by π–dimerization (i.e. responding against the deformation). For the benefit of the reader, the case of a linear chain of hydrogen atoms (with one 1s electron each) also undergoes Peierls distortion which, in the absence of sigma bonds, leads to full dimerization in the form of gaseous $H_2$. Or even more similar, the case of benzene, which attains a structure of bond length equalization to minimize elastic energy by sacrificing dimerization energy (Kekulé forms) in favor of a multicenter 6 electrons-6 carbons bonding form (this highlights the view that aromaticity stabilization in benzene is mainly caused by the σ-electrons bonds not by the π-electrons).

Going from small oligoenes to polyacetylene, the elastic/kinetic energy term gains weight, resulting in a progressive reduction of the bond length alternation (BLA) toward non-bonding states. This is what one observes in series of oligoenes of increasing size, an evolution toward reduced BLA (i.e. increment of π-electron). This trend is not continuous with chain lengthening since the reduction of bonding marks a limit that cannot be overpassed. This, overall, results in a saturation of this structural evolution and of the spectral properties in the vicinity of BLA = 0, a consequence of Peierls distortion of one-dimensional π-conjugated systems.

So far, the situation deals with oligoenes of even number of carbons, but it can be extended to their analog compounds with an odd number of carbons, oligomethines and polymethines [22]. Their structures can be viewed as those of even oligoenes plus one carbon atom (containing one $p_z$ electron). Here, the “odd” electron cannot dimerize by which the only way to minimize its energy is by minimizing its elastic term by delocalization among all existing

C–C bonds. This full delocalization produces bond equalization in polymethines and cyanines, a situation that progresses up to the so-called cyanine limit from which the systems evolve by getting asymmetric through localization of the unpaired electron in one of the terminal sites (i.e. the remaining part discloses electron pairing mimicking the oligoene parent).

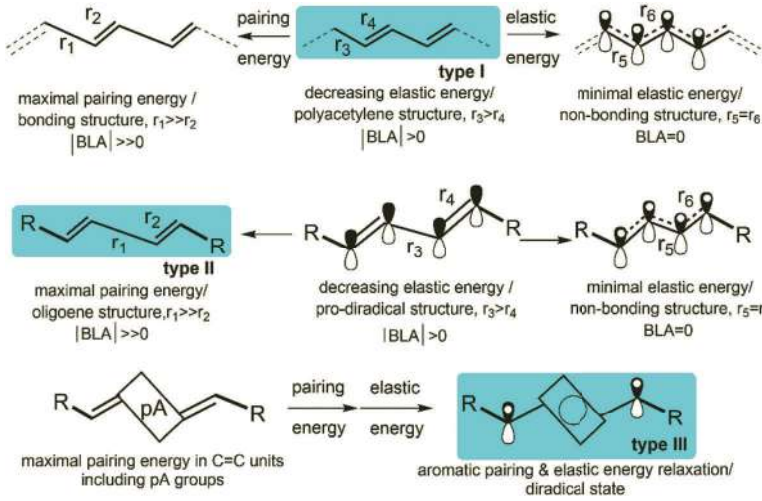


**Scheme 4.1** Representation of the bonding/elastic energy balance leading to a Peierls dimerized structures in polyacetylene (top, type I); in oligoenes (middle, type II) with the diradical and multiradical characters being formed by increasing elastic energy relaxation. Oligoene-like structures (bottom, type III) with pro-aromatic (pA) groups help develop the diradical structure inaccessible in oligoenes, due to the small effect of elastic energy. Note that most of the structures described in this chapter are those having pA moieties. $r_1$, $r_2$, $r_3$, $r_4$, $r_5$, and $r_6$ are the bond distances from which the BLA is calculated.

In this scenario, we have already set the discussion to address the formation of diradical species [23–28]: (i) the situation of large BLA, or strong bonding, stabilizes the closed-shell low-spin state, and (ii) smaller BLA or larger π–delocalization acts toward high spin diradicaloid states. Diradical states in oligoenes, however, cannot be reached since its elastic driving force, before reaching the Peierls limit, is insufficient. Additional driving forces have to be incorporated in the π-conjugated system in order to promote the diradical stabilization. This is attained by the inclusion of pro-aromatic moieties that, by aromaticity recovery, reduce the

overall pairing/bonding contribution allowing to emerge the diradical state.

This chapter will demonstrate the use of the Raman spectroscopy in the characterization of π-conjugated organic diradicaloid systems made of oligomers including pro-aromatic groups, but not restricted to. More than an exhaustive overview of all research reported so far, we will focus on the main results by the Raman spectroscopy in the knowledge that there are other relevant international research teams that have also made key contributions to the field. All systems that now follows constitute different families of oligomers in which the variation or dependence of the Raman spectra, mainly wavenumbers of selected bands, with the oligomer size or number of repeating units (i.e. oligomer approach), will be considered in the analysis. The main characteristic of these oligomeric families of diradicals is that the open-shell species is formed at some point in the series. In these cases, singular changes in the Raman spectra will provide valuable insights on the physical and chemical reasons behind their formation and structure.

## 4.3 Tetracyano Quinoidal Oligothiophenes: The Oligomer Approach to Diradicaloid Molecules by Raman Spectroscopy

The Raman spectra of aromatic oligothiophenes [29, 30] in Figure 4.1, up to the hexamer, such as many other aromatic oligomers, display an intense and dominant Raman band, which is assigned to the collective symmetric C=C/C–C stretching mode along the whole conjugated π–path [i.e. usually designed as thiophene-ring based ν(C=C)].

This ν(C=C) band shows a concomitant wavenumber decreases with increasing oligomer size that is directly ascribed to the reduction of the BLA pattern as a result of the overall weakening of the pairing/bonding of the C=C units, due to the increasing dominance of the overall elastic energy. This wavenumber downshift with increasing length of the oligomer, according to the Peierls instability, has a saturation effect, which is attained in the hexamer or similar. So, our aromatic oligothiophenes, no matter their sizes, will always display dominant aromatic/bonded electronic structures with

characteristic Raman wavenumbers for their most intense bands in the interval of 1500–1450 $cm^{-1}$. These Raman wavenumber bands represent the vibrational marks of the electronic structures of aromatic oligothiophenes.

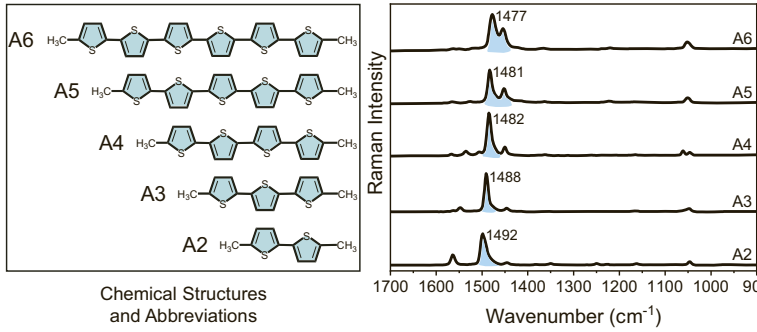


**Figure 4.1** Chemical structures of the aromatic oligothiophenes (**An**) encapsulated by methyl groups, from a dimer to a hexamer, together with their solid-state Raman spectra where the wavenumber values correspond to the ν(C=C) bands.

In contrast with the monotonous behavior of the Raman bands in aromatic oligothiophenes, quinoidal oligothiophenes (**Qn**, with n the number of thiophene rings) such as those represented in Figure 4.2, made by dicyanomethylene encapsulation of the oligothiophene cores [31], and from a dimmer to a hexamer, show a different wavenumber behavior for their most intense Raman bands [32]. From the dimer (**Q2**) to the tetramer (**Q4**), the Raman behavior is essentially the same as that described in the aromatic oligothiophenes, which consist of a continuous wavenumber downshift in the three compounds when the chain length is increased. A distinctive feature of the decreased wavenumber in **Qn** is that it is much larger than that observed in aromatic oligothiophenes. This larger change in the Raman wavenumbers can be ascribed to a larger variation of the BLA pattern, highlighting the increasing role of the elastic energy term in these quinoids relative to the aromatic oligomers. Another aspect, playing a secondary effect here though deserving mention, is the role of inter-ring distortions in the aromatic oligothiophenes, which favor the paired dimerized structure or disfavor the elastic energy relaxation that is thus maximal in the planar forms, such as in the quinoidals.

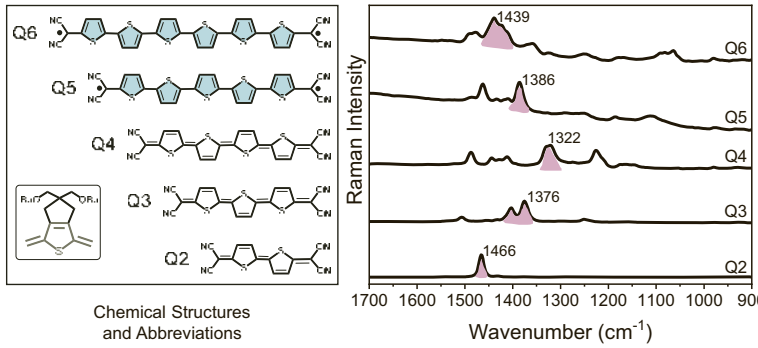


**Figure 4.2** Chemical structures of the quinoidal oligothiophenes encapsulated by dicyanomethylene groups, from a dimer to a hexamer (note the substitution at the lateral positions of each thiophene such as in the box), together with their solid state Raman spectra where the wavenumber values correspond to the ν(C=C) bands.

Conversely, the spectra of the quinoidal pentamer and hexamer, **Q5** and **Q6**, display the most intense ν(C=C) Raman bands upshifted in wavenumbers regarding the tetramer, and further upshifted from the pentamer to the hexamer. In the case of the latter, the wavenumber of the dominant Raman bands is at 1439 $cm^{-1}$ very close to the 1480–1450 $cm^{-1}$ range of aromatic oligothiophenes. Overall, these spectroscopic Raman data indicate that for the shorter quinoidal oligomers (dimer to tetramer), the BLA, in absolute terms, is decreased thus approaching toward bond length equalization. Going to the quinoidal pentamer and hexamer, if these would follow the behavior of their aromatic congeners, the BLA variation would collapse or saturate such as imposed by the Peierls prohibited region. However, the strong elastic relaxation of the π-conjugated structure in the tetramer occurs at the expenses of the weakening of the electron pairing in the C=C units, thus leading to a situation in which the reorganization of the bonding pattern in the thiophene rings adopting an aromatic structure produces an additional stabilization of the system relative to the quinoidal array. This process of aromatization takes place by the rupture of one double bond and the formation of an aromatic diradical structure. Despite the apparent elastic energy gaining upon formation of the two unpaired electrons, the overall result is a neat stabilization of the

bonded structure, which passes from C=C dimerization to aromatic-thiophene dimerization. In more chemical terms, the energy gaining by aromatization is greater than the energy required to break a double bond. Therefore, the quinoidal pentamer and hexamer have to be represented by diradical structures, as shown in Scheme 4.2. According to this interpretation, the aromatic structure should be more developed in the hexamer since it has more pro-aromatic rings and the C=C unit to break is also more weakened. Dimerization (aromatization) mode is more marked in the hexamer such as reflected by the increase of the Raman wavenumber of the collective ν(C=C) Raman band.

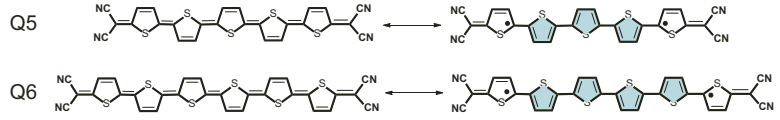


**Scheme 4.2** Formation of diradical structures in the **Q5** and **Q6** molecules by aromatization of the thiophene rings.

This description of the vibrational Raman behavior associated with the ν(C=C) bands explained in the context of the Peierls distortion and of the balance between elastic and dimerization energies of one dimensional π-conjugated structures represented the first piece of evidence from the vibrational spectra, corroborating the formation of a diradical species. Nicely, whereas on going from **Q2** to **Q4**, the elastic energy is reduced at the expenses of the dimerization energy, passing to **Q5** and **Q6**, the elastic energy would further decrease because of the formation of two quasi-non-bonded electrons, but also the pairing energy is decreased by the formation of aromatic alternating units. It is fascinating to reveal how the electronic structure of these molecules explores all possibilities of stabilization. Whereas aromatic oligomers subscribe a collapse or saturation of the electronic changes in the vicinity of the Peierls limit, in the quinoidal family, the possibility of aromatization of the thiophene rings adds a new degree of freedom to the electronic structure to evolve, dodging the region of bond length equalization. This is another nice example of the physics of the Peierls instability in one-dimensional systems intimately linked to strongly interacting fermions, where a "competition" between localization (minimizing

potential energy) and itinerancy (minimizing kinetic energy) dictates all emerging electronic properties. The new aspect in this discussion is the dual way the quinoidal oligomers have to account for the pairing, either in the form of localization in C=C units or localization in aromatic units.

According to this description, the quinoidal hexamer represents a diradicaloid with a clear "localized" or "dimerized" aromatic structure in which two electrons are weakly bonded, forming a singlet ground electronic state by occupying two separated regions of the space. This singlet diradical can evolve by modifying its overall elastic energy in its first triplet excited state. The absorption of a quantum of kinetic energy in a photon of electromagnetic radiation increases the kinetic energy term of the molecule, which thus promotes to an excited state. In our case, the absorption of heat excites the molecule from the singlet to the triplet state.

In the triplet state, the bonding interaction of the two electrons of the diradical is removed by aligning the two spins in a situation of increased kinetic energy as both electrons cannot occupy the same spatial region. The Raman experiment with variable temperature on **Q6** reveals little spectral changes, owing to the rather small singlet-triplet energy gap due to the large separation of the two radical centers in the largest molecule [32]. This vanishing gap makes both singlet and triplet states to be similarly populated at room temperature, a fact that helps detect the triplet by the resonance Raman spectroscopy as shown in Figure 4.3. In this case, by properly adjusting the laser energy in the Raman experiment with the energy of the electronic absorption of the triplet state, its resonant Raman spectrum is taken.

Another Raman spectrum of a triplet excited state was reported for a viologen-like molecule as shown in Figure 4.3 [33]. In this case, the triplet is recorded by heating the sample and registering the vibrational spectrum with the same laser excitation Raman line at 1064 nm [34]. The spectrum at low temperature corresponds to the singlet diradical state, whereas that at high temperature belongs to the triplet species populated by heating through a moderate singlet-triplet gap of −2.98 kcal/mol. The Raman spectra of these triplet states, obtained in different ways, for **Q6** and for the viologen system represent the first Raman spectra of triplet states of organic π-conjugated diradicaloid molecules.

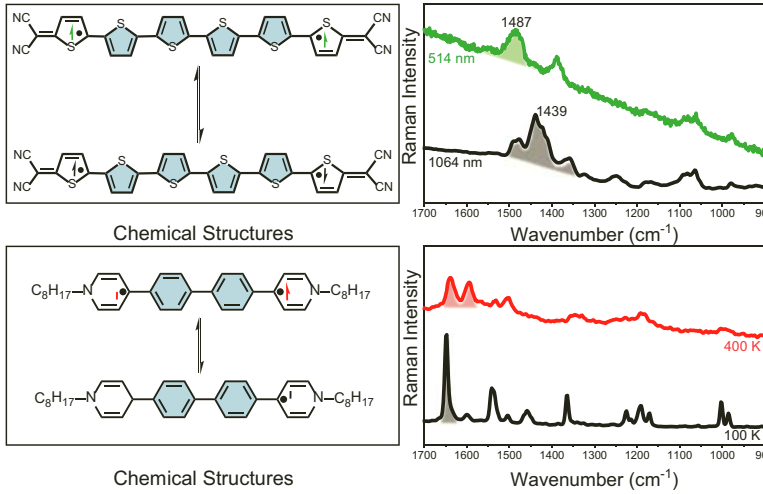


**Figure 4.3** Top: Solid-state Raman spectra of **Q6** taken with the excitation laser Raman lines at 1064 nm (black line, in resonance with the singlet diradical absorption at 1000 nm) and at 514 nm (green line, in resonance with the absorption of the triplet at 530 nm) where the wavenumber values correspond to the ν(C=C) bands. Bottom: Solid state Raman spectra of an extended viologen compound taken with the 1064 nm excitation laser Raman line at 100 K (black line) and 400 K (red line).

## 4.4 Tetracyano Oligoperylenes: Ground Electronic State Triplets Detected by Raman Spectroscopy

The Raman spectra of quinoidal oligoperylenes formed by terminal dicyanomethylene encapsulation [35], from a monomer to a hexamer (i.e. **nPerCN** in Figure 4.4), were also studied by vibrational Raman spectroscopy. We now wish to describe their main features in comparison with those of the quinoidal oligothiophenes.

The Raman spectra of the **nPerCN** are displayed in Figure 4.4. From the monomer up to the trimer, we observe a continuous wavenumber downshift of the main Raman bands associated to the collective vibrational modes along the quinoidal π-conjugated path between the dicyanomethylene groups, or benzene based ν(C=C) modes. This part of the behavior is interpreted in equivalent terms

as that previously described for the quinoidal oligothiophenes going from the dimer to the tetramer. Passing, however, to the larger quinoidal tetramer, pentamer, and hexamer oligoperylenes, the whole Raman spectra (not only the ν(C=C) modes) keep invariant with the lengthening of the oligomer chain.

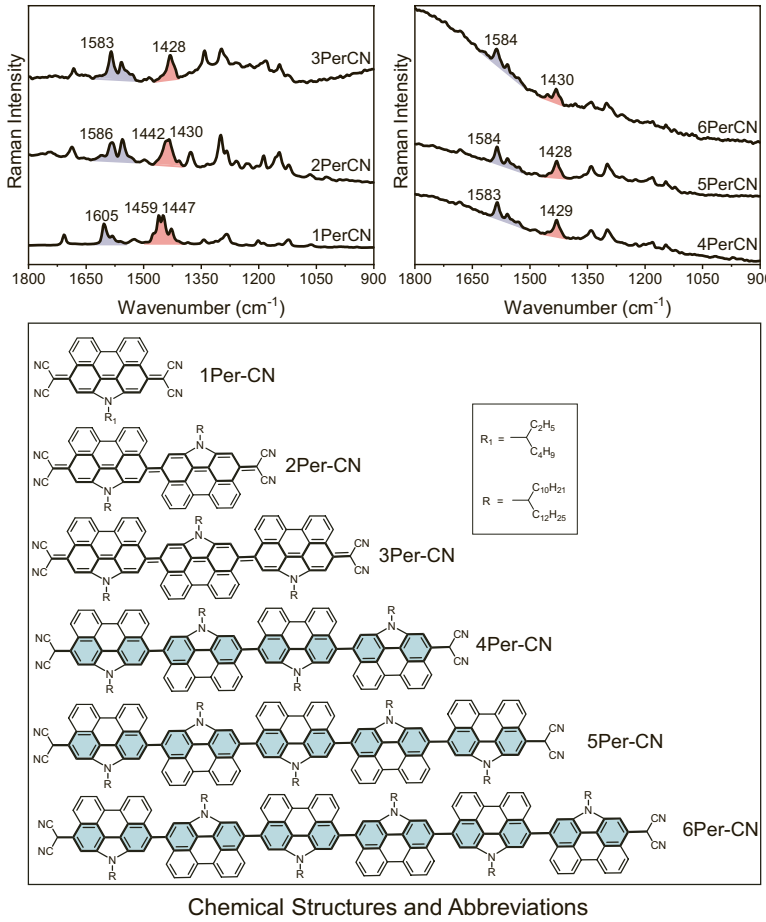


**Figure 4.4** Top: Solid state 1064 nm Raman spectra of **nPerCN** with n=1−6 recorded at 100 K. Bottom: Chemical structures of the **nPerCN** with n=1−6.

This wavenumber behavior on the **nPerCN** contrasts with that of the thienoquinoidal oligomers in which for the longer compounds the evolution reversed that found in the shorter elements; now, the

observation is that the Raman spectra do not further change from the trimer to the longer analogs. Hence, in the shorter elements of the series, the relevant dimerized units are the C=C ones and the elastic energy relaxation on lengthening decreases the bonding on them, a relaxation that is very effective in the planar disposition of all perylene units.

At the level of the trimer/tetramer, such as in the thienoquinoids, the system reorganizes the dimerized unit in favor of aromatic perylenes at the expenses of the generation of a diradical structure (Scheme 4.3). Simultaneously, the CC distances between repeating units are enlarged in the multi-perylene array and, contrarily to the quinoidal oligothiophenes, the connected units get distorted in between maximizing the decrease of the dimerization energy and cancelling any further effect of elastic energy relaxation. This overall results in the spectral invariance in the longer oligomers (i.e. in the thienoquinoidal compounds distortions are not produced among the thiophene units, so dimerization in the form of aromatic thiophenes is progressive and, in all cases, competing with elastic relaxation). The collapse of the delocalization effect acting against dimerization by conformational distortions is a new piece of knowledge provided by the analysis in the **nPerCN** series.

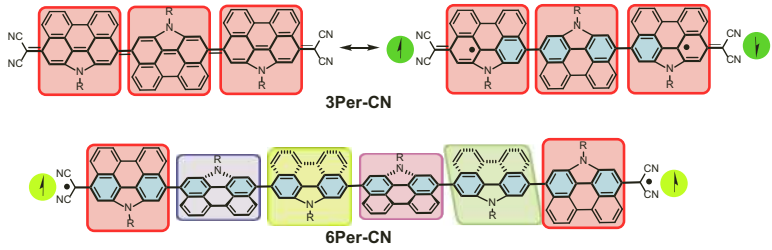


**Scheme 4.3** Formation of singlet diradical ground electronic state structures in planar **3PerCN** and of a fully aromatic/distorted triplet in **6PerCN**.

Another consequence of the blockade of the elastic relaxation is the loss of wavefunction overlap between the unpaired electrons which get electronically disconnected, thus favoring the high-spin configuration and alignment of the two spins, or triplet. Whereas, in the thienoquinoidal compounds, the triplet state was always an excited state, now in the quinoidal oligoperylenes, the triplet becomes isoenergetic with the singlet, thus turning into the ground

electronic state. This indicates that the Raman spectra taken for the longer oligoperylenes own to the triplet states. These ground state triplets in **nPerCN** contrast with the "hot" triplets in the quinoidal oligothiophenes.

The intramolecular distortions, relative to the full planar structure, are the driving force for the full localization of the electronic wavefunction ("perylene aromatic" dimerizing unit) blocking the elastic energy effects. We can mention here the so-called double spin-polarization (DSP) [36]. For this to be understood, we should look at the diradical structure as two radical centers interacting through a π-conjugated bridge with all its bridge electrons being paired. The DSP (spin polarization of two radicals) consists and produces a delocalization (kinetic energy effect) of these bridge-paired electrons into the semi-occupied radical sites, thus minimizing the kinetic energy term and contributing positively to the stabilization of the system. Since we are dealing with correlated fermions, this effect is doubly favored in the singlet configuration than in the triplet, resulting that a low-spin ground electronic state is always preferred by DSP. Assuming that the delocalization effect is maximal in the planar conformation, distortions of it always decrease DSP efficiency and in the limit of maximal distortion disappears, resulting in a vanishing singlet-triplet gap or even a triplet ground electronic state, such as observed in the **nPerCN** compounds.

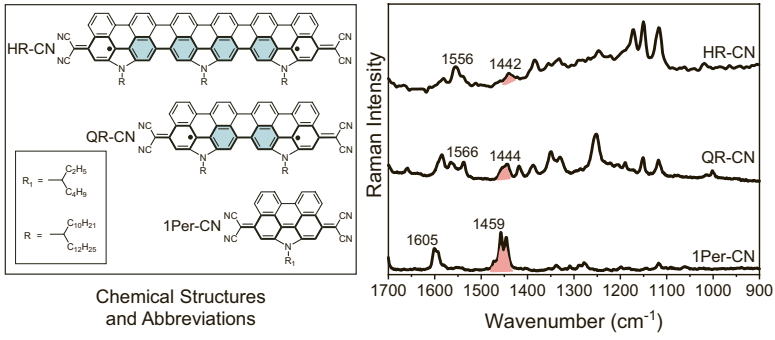


**Figure 4.5** Chemical structures of the quinoidal oligorylenes together with their solid state 1064 nm Raman spectra at 100 K.

In line with the effect of planarization/distortion in pairing/elastic energy balance, similar compounds to the **nPerCN,** but

with the contiguous perylene units fixed in oligorylenes planar conformations or bis(dicyano) encapsulated quinoidal oligorylenes (Figure 4.5) can be mentioned [37]. We observed that for the Raman wavenumbers of the analog benzene based ν(C=C) modes, the shift to lower values is continuous and greater than in the **nPer-CN** series, in line with the effective delocalization or elastic/kinetic energy relaxation that progressively weakens bonding and pairing of the C=C units, but in this case, being more effective, owing to the uniform planar structure along which delocalization is always maximal.

## 4.5 Planar Aromatic Oligorylenes Diradicaloids: Raman Spectra beyond Peierls Restrictions

The attempt to account for the electronic structure of molecular diradicals in physical terms facilitates and opens the interpretation of the vibrational Raman spectra to graphenoid systems with two-dimensional electronic structures. Graphene-based compounds currently have attracted great attention by the realization of systems with topological structures, twisted graphene bilayers, and others [38, 39].

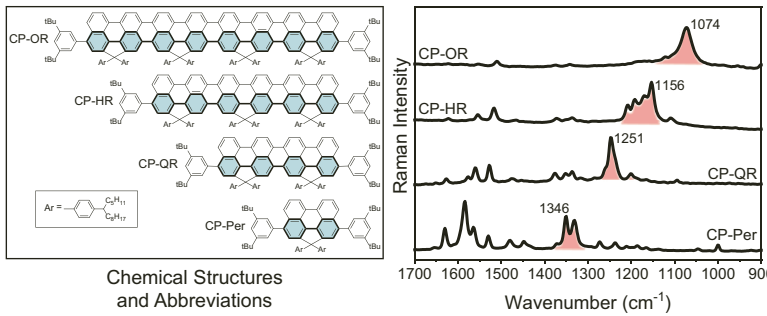


**Figure 4.6** Chemical structures of the aromatic oligorylenes (**CP-nR**), from a monomer to an octamer, together with their solid state 1064 nm Raman spectra at 100 K.

In this regard, the series of compounds that will be addressed now consist of linear oligomers of rylene [40] from a dimer to a tetramer, as depicted in Figure 4.6 (i.e. **CP-nR**). The whole series of reported compound expands up to a hexamer, but their Raman

spectra could be studied only for the members up to the tetramer, as shown in Figure 4.6 [41]. These spectra, such as those previously discussed in linearly conjugated aromatic and quinoidal compounds, are characterized by only a few very intense bands that contrast with a large number of vibrational 3N-6 modes. However, the distinctive feature in these molecules compared to the previous linearly conjugated cases is that the dominant Raman bands display a progressive and continuous Raman wavenumber downshift from compound to compound with the increase of the chain length.

In addition, the UV-Vis-NIR electronic absorption spectra, which could be recorded for the whole series up to the hexamer, display the same continuous wavelength redshift of the lowest energy lying absorption (typically due to the excitation from the highest occupied molecular orbital to the lowest unoccupied molecular orbital). In consequence, within the studied compounds, it is not observed an apparent or appreciable saturation neither of the electronic absorption wavelengths nor of the Raman wavenumbers in the largest members.

This behavior represents another twist in the understanding of the electronic structure of π-conjugated molecules, presenting a different scenario than those discussed for the aromatic oligothiophenes (i.e. quick saturation of the wavenumber downshift behavior in only five oligomers), and for the quinoidal oligothiophenes and quinoidal rylenes, double behaviors are observed in the chain length evolution of the Raman wavenumbers (i.e. downshift-upshift in **Q2**/**Q4**-**Q5**/**Q6** and downshift-constancy in **1PerCN**-**3PerCN**/**4PerCN**-**6PerCN**). These effects have been accounted by the role of Peierls distortion underpinned by aromatic stabilization and steric destabilization. None of these three circumstances seem to apply in the case of the aromatic **CP-nR** oligorylenes. Hence, is Peierls instability no longer applying in these molecules?

The distinctive situation in regard of the electronic structure of these aromatic oligorylenes is that these cannot be longer considered one-dimensional or linearly π-conjugated molecules (Scheme 4.4). The similarity of the two arrays of oligophenylene moieties fused in parallel, or poly-*peri*-naphthalene (polyrylene) [42], makes the whole structure to behave as a two-dimensional π-conjugated system, thus evading the Peierls instability, or at least in the terms it operates in one-dimensional arrangements.

The different π-conjugated shapes and distinctive two-dimensional delocalization in oligorylenes are reflected in the non-saturation behavior described for the wavenumber of Raman spectra.

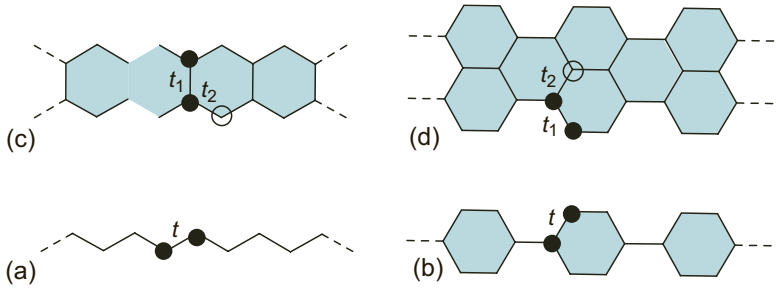


**Scheme 4.4** Neighbor-neighbor couplings (black filled and empty circles denote different coupling and transfer integrals, *t*) in one-dimensional: (a) polyacetylene-like and (b) polyphenylene-like structures; and in two-dimensional π-conjugated systems: (c) polyacene-like and (d) poly-*peri*-naphthalene-like structures, this latter formed by fusing two polyphenyl ribbons.

These **CP-nR**, therefore, are better conceptualized in the framework of the electronic structure of GNR [43, 44]. Their significance of being composed of parallelly coupled/fused oligophenylenes is that the interaction mode changes from one-dimensional character, with only 'one interaction mode' of one given atom with its vicinal ones in oligophenylene/polyphenylene in Scheme 4.4, to a two-dimensional character in oligorylenes/poly-*peri*-naphthalenes with 'two coupling modes' of one given atom with those surrounding (Scheme 4.4). It is convenient now to clarify the case of quinoidal oligorylenes (Figure 4.5) formed by dicyanomethylene encapsulation, which might also have, in analogy with these aromatic oligorylene parents, a two-dimensional π-electron delocalization. However, in the latter, the formation of a quinoidal structure in one of the two oligophenylene arrays electronically segregates both ribbons and, as a consequence, the overall system behaves as a one-dimensional system, as it has been described in the previous section.

Invoking a solid-state physical perspective, polyacetylene, quinoidal, and aromatic oligothiophenes can be described according to the existence of only one transfer integral parameter (*t*) between vicinal atoms. Conversely, in two-dimensional electron conjugated

systems, such as aromatic oligorylene, each atom is surrounded by two different classes of atoms, and therefore, two different interaction modes (anticipating the description of two different unit cells in graphene) require two different transfer integral parameters ($t_1$ and $t_2$) at the origin of the alteration of the conditions for π-electron delocalization in 2D systems.

Aromatic oligorylenes can be viewed as a particular case of GNR [45]. The GNR, briefly, can be divided into arm-chair and zig-zag types. While zig-zag GNR are all metallic, arm-chair GNRs can be either metallic or semiconductors [46]. Aromatic **CP-nR** oligorylenes are of the arm-chair GNR family with polyrylene (poly-*peri*-naphthalene) being the GNR obeying $N = 3p + 2$, with $p = 1$ and width $N = 5$, thus featuring metallic conductivity (i.e. the narrowest metallic arm-chair GNR). The electronic structure of metallic arm-chair GNRs and polyrylene consists of featuring edge states with non-bonding characteristics or gapless states (responsible of the unique metallicity). These states are described as having contribution from one-type of atom and with nodes in the vicinal atoms revealing the non-bonding property. The aromatic oligorylenes and particularly the longer members of the series already tend to form such non-bonding states by developing, at the molecular level, diradicaloid states.

Another consequence of the establishment of non-bonding structures in metallic arm-chair GNR is that these cohabitate with bulk gapped forms, a duality of states that starts to appear in long aromatic oligorylenes and it is here where the Raman spectroscopy gives a fundamental experimental evidence of this situation. In the long aromatic oligorylenes, the non-bonding states appear in the mid-gap region and are placed in the short zig-zag edges of the system. Simultaneously, the gapped states get developed in the 'trans-cissoid' structures. A profound difference between the vibrational dynamics of these two states is that while those in the zig-zag edge do not undergo electron-phonon coupling, those in the arm-chair edges are effectively affected by such coupling providing intense Raman signals. This is the case of the band at 1074 $cm^{-1}$ of **CP-OR**, a band that resembles very much to the typical Raman ν(CC) mode of polyacetylene.

Another interesting Raman fingerprint of the particular structure of long aromatic oligorylenes is the detection of a

vibrational overtone band, in our case for **CP-OR**, of the fundamental vibration at 1074 $cm^{-1}$, appearing at $2 \times 1074 \approx 2144$ $cm^{-1}$ (Figure 4.7), which is another analogy with the vibrational Raman spectrum of polyacetylene [47] and that vibrationally characterizes the progression of these amazing types of electronic states in oligorylenes. It is interesting to note here that the Raman spectra of graphene are characterized by the existence of double and triple resonance bands, which are vibrational excitations equivalent to the overtone bands described in **CP-OR**. These vibrational description highlights an electronic structure of long **CP-nR** composed of segmented polyacetylene-like ribbons in contraposition to the benzenoid polycyclic structure characteristic of the smaller **CP-nR** aromatic oligorylenes.

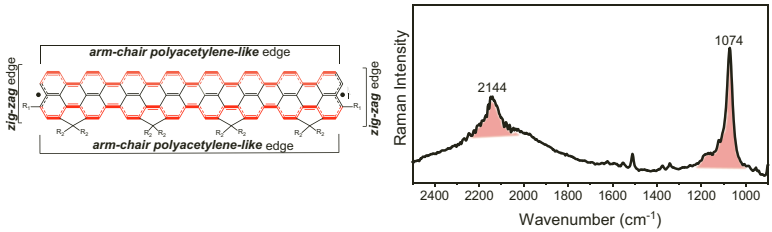


**Figure 4.7** Structure of the diradical state of **CP-OR** in agreement with a double *trans-cissoid* polyacetylene-like structure in the arm-chair edges, together with its Raman spectrum displaying the fundamental and overtone bands.

As already mentioned, the main ν(C=C) Raman band of the spectra of the aromatic oligorylenes displays a continuous wavenumber downshift in the series of compounds without appreciable size saturation. In contrast with the one-dimensional π-conjugated molecules discussed in previous sections, in the case of the aromatic oligorylenes, two-dimensional π–delocalization is only driven by minimization of elastic energy, which eventually reverses dimerization pattern from benzenoid (smaller **CP-nR**) to polyacetylene-like in favor of the diradical state. Thus, in these oligomers, the structural evolution is from benzenoid-like to polyacetylene-like in contrast with the case of the quinoidal homologues that evolve from polyacetylene-like to benzenoid-like. These distinctive trends are nicely reflected in the behavior of the Raman spectra.

## 4.6 Planar Zethrenes and Indenoacene Diradicaloids

Oligoacenes and polyacene [48] depicted in Scheme 4.4 represent the molecular and polymer versions of zig-zag GNRs. Of these, the long versions of the former and polyacene are inaccessible to Raman characterization, since their high chemical reactivity. In fact, it is from hexacene onward that the diradical character and chemical instability start to be noticeable and increasingly marked for all its higher analogs [49]. Alternatively, the analogs of oligoacenes, such as zethrenes [50–53] and indenoacenes [54–59], have been developed and prepared, showing enough stability to be addressed by spectroscopic methods, including vibrational Raman.

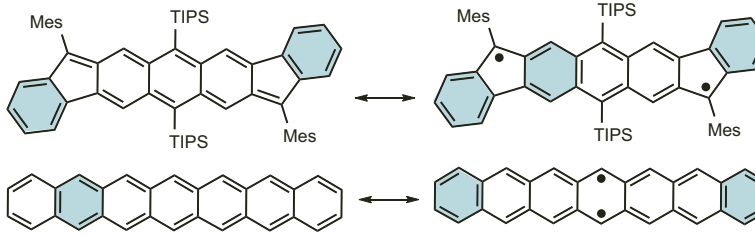


**Scheme 4.5** Chemical structures of the diradical forms of heptacene and of the diindenoanthracene (**DIAn**) as examples of the oligoacene and indenoacene families. Mes: mesityl; TIPS: triisopropylsilylethynyl.

Indenoacenes and zethrenes conceptually take advantage of the quinoidal approach (such as those previously discussed) in order to imprint to the acenoid cores with diradical character. Oligoacenes, *per se*, develop open-shell character by stabilizing non-bonding states on the zig-zag edge peripheries (Scheme 4.5, as discussed for long oligorylenes) helped by the gaining of one more Clar's sextet. However, the inclusion of quinoidal units, for instance in the case of **DIAn** in Scheme 4.5 [60], increases the diradical character by the formation of an anthracene aromatic open-shell structure. Aside of the chemical blocking of the reactive sites in **DIAn** with bulky groups, either the large inter-radical separation on it or the larger aromatic stabilization, are factors that justify the distinctive behavior of **DIAn** regarding related oligoacenes. On the other hand, the lengthening of the size in the zethrene and indenoacene families minimizes the

elastic energy term along the alternant C=C/C–C ribbons at the expenses of a reduction of the C=C dimer/π–pairing energy. This trend is reversed by the aromatization of the anthracene group in which the system recovers stability by aromatic π-electron pairing though sacrificing part of the bonding stabilization, due to the formation of unpaired electrons.

Figures 4.8–4.10 show the Raman spectra of the available indenoacenes and zethrenes. Such as in the case of previous compounds in this chapter, the important bands to follow the effect of the diradical character in the vibrational spectra are the ν(CC) bands of the benzenoid rings, which appear as medium-weak Raman features in the spectra of all these compounds in the interval 1550–1630 $cm^{-1}$.

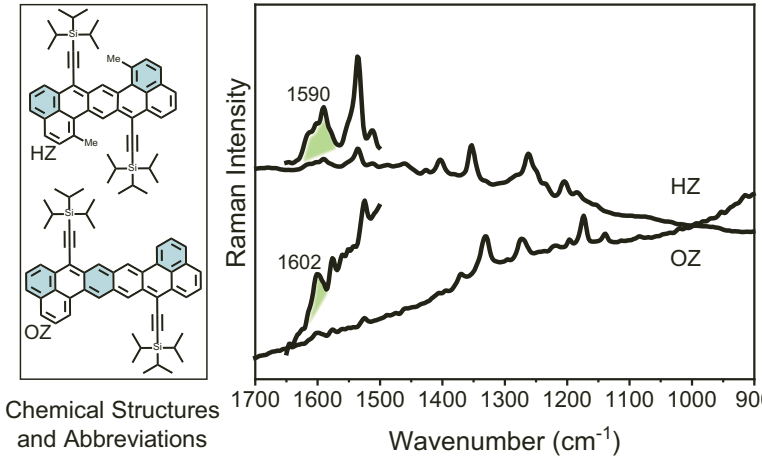


**Figure 4.8** Chemical structures of the heptazethrene (**HZ**) and octazethrene (**OZ**), together with their Raman spectra taken with the 1064 nm laser line.

Figure 4.8 displays the Raman spectra of the two zethrene compounds [51]. The compound with an internal quinoidal benzene core, **HZ**, shows the benzenoid ν(CC) band at 1590 $cm^{-1}$, whereas the analog band in **OZ**, with a naphthalene quinoidal core, is upshifted up to 1602 $cm^{-1}$. The relevant 1590→1602 $cm^{-1}$ Raman upshift behavior gives account for the overall aromatization process in the pro-aromatic cores on passing from benzo to naphtho fragments and is the vibrational fingerprint of the increasing diradical character.

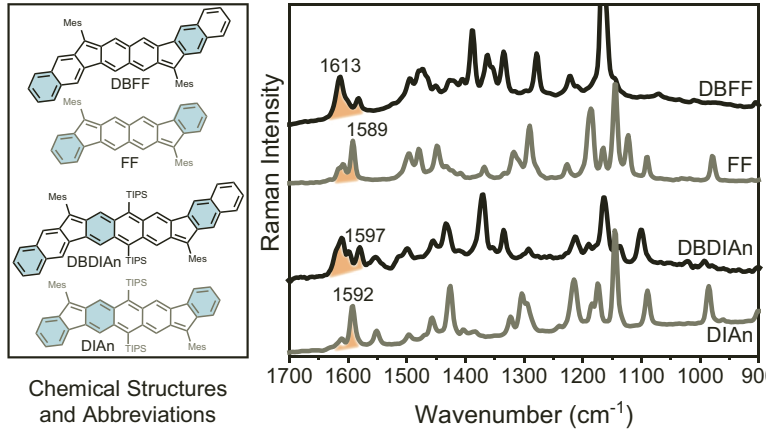


**Figure 4.9** Chemical structures of the **DIAn**, **FF**, linear dibenzo **DIAn** (**DBDIAn**), and linear dibenzo **FF** (**DBFF**) together with their 1064 nm Raman spectra.

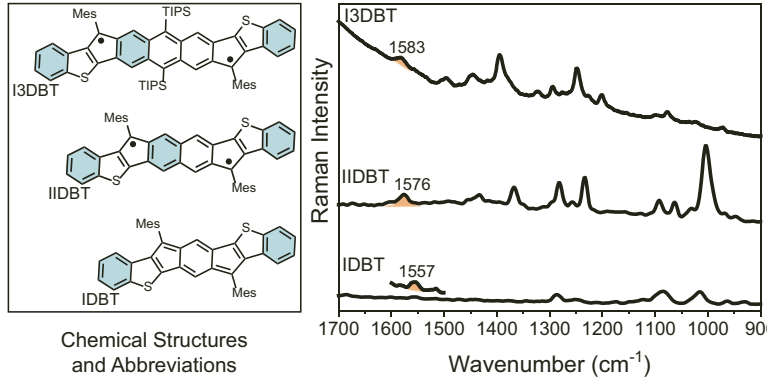


**Figure 4.10** Chemical structures of the dibenzothiophene-indenoacene compounds (**IDBT**, **IIDBT,** and **I3DBT**) together with their 1064 nm Raman spectra.

Figure 4.9 displays the Raman spectra of four indenoacenes compounds [61, 62]. From fluoreno-fluorene (**FF**) to **DIAn**, in which the quinoidal core is enlarged from naphtho- to anthraceno-quinoidal, the relevant ν(CC) Raman band experiences a moderate 1589→1592 $cm^{-1}$ wavenumber upshift. This is in agreement with the overall increasing aromatization in the central anthracene of **DIAn** compared to the naphthalene segment in **FF**, such as in the zethrene

family of compounds, further in agreement with the increment of diradical character reported for **FF** and **DIAn** (as discussed below). Dibenzo-substitution of the terminal benzenes of the **FF** and **DIAn** [61] molecules produces an increase in the wavenumber values of the ν(CC) Raman bands revealing the impact of the electronic effects in the terminal positions on the internal cores. The 1589→1613 $cm^{-1}$ and 1592→1597 $cm^{-1}$ upshifts in the **FF** and **DIAn** derivatives, respectively, upon dibenzo-substitution, are in agreement with an increase of the aromatic character in these central cores, further in line with the increment of diradical character in the dibenzo extended compounds.

Figure 4.10 shows the Raman spectra of three dithiophene substituted indenoacenes [61–64]. These encompass from a central benzo-, to a naphtho- and to an anthraceno-quinoid core. The behavior of the ν(CC) Raman band is similar to the cases above, i.e. an upshift on enlarging the central core. This is the only family of compound with three members and it is interesting to see how the evolution of the increments in diradical character, 0.41→0.61→0.74 in **IDBT**→**IIDBT**→**I3DBT**, and the wavenumber shifts, 1557→1576→1583 $cm^{-1}$ in **IDBT**→**IIDBT**→**I3DBT** are very similar by which the experimental wavenumbers certainly represent an experimental guide of the diradical character in this series, a quantitative assessment that cannot be generalized for the other compounds (i.e. though they all have a qualitative validity). A reason for this divergence is that in the band wavenumbers, not only electronic effects influence the resulting values, but others, such as mechanical effects further imparted by the type of substitution, also play an important role.

In Figure 4.11, an attempt to correlate the variation of the diradical character, $y_0$, with the Raman ν(CC) band wavenumber values is done. The diradical character, designed as $y_0$ [65, 66], is a theoretical parameter that defines the degree of open-shell character of families of diradicaloids. It takes a value of $y_0 = 0$ for the closed-shell analog and continuously varies to $y_0 = 1$ for the parent system with full open-shell character. It can be estimated in different ways and is strongly dependent on the theoretical method used [67] by which its validity is controversial. Nonetheless, for a given family of compounds and calculated by the same method, it might give both a qualitative and quantitative insights of the degree of diradical

character and its evolution in the series. Calculated at the PUHF/6-311G(d) level, the values of $y_0$ for the compounds discussed in this section are represented against the ν(CC) Raman band values in Figure 4.11.

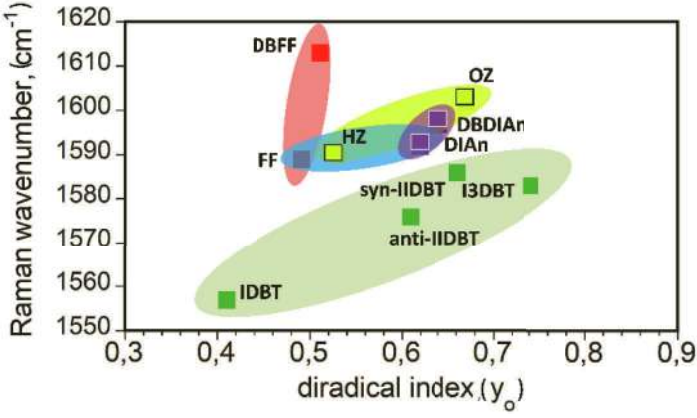


**Figure 4.11** Representation of the $y_0$ values calculated at the PUHF/6-311G(d) level for the acenoid quinoidal compounds versus the wavenumbers of the ν(CC) Raman bands.

It is observed that compounds of a same family are clustered in separated regions of the $y_0$/ν(CC) representation. In all cases, increments of $y_0$ produce increments of ν(CC), which is in agreement with the understanding that the driving force for the increment of diradical character is the gaining of aromaticity in the pro-aromatic cores, the same effect that produces and increments of the wavenumber of the benzenoid ν(CC) Raman bands. The degree of evolution of both quantities is variable from family to family; for instance, it is small from **FF** to **DIAn** and moderate from **HZ** to **OZ** and similarly on the thiophene-derivatives.

Finally, the validity of the $y_0$/ν(CC) fitting is also checked in the case of isomeric diradicals [64], such as the case of **IIDBT** discussed above which is termed as **anti-IIDBT** with its isomer, **syn-IIDBT**, as shown in Figure 4.12. The Raman spectra displays the ν(CC) Raman band at 1576 $cm^{-1}$ for **anti-IIDBT** (Figure 4.11) and at 1585 $cm^{-1}$ for **syn-IIDBT,** whereas their $y_0$ values are 0.61 for **anti-IIDBT** and 0.66 for **syn-IIDBT**.

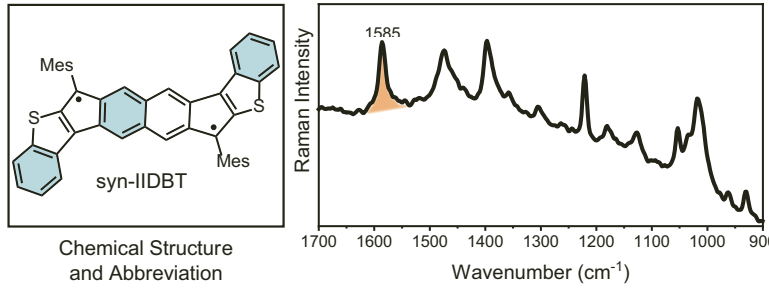


**Figure 4.12** Chemical structure of **syn-IIDBT** and its Raman 1064 nm spectrum.

## 4.7 Conclusions

In this chapter, a summary of the Raman spectra of the main families of diradicals studied in our group has been presented. The first Raman spectrum of a singlet diradicaloid molecule discussed in the context of the oligomer approach was reported by us in 2007. Since then, an increasing number of diradicaloid families has been studied, in which the Raman behavior has been connected with the degree of diradical character. On the other hand, the evolution of the Raman spectra has been also connected with the main electronic factors shaping the electronic structure of π-conjugated molecules, in general, and diradicaloids, in particular.

In linear π-conjugated oligomers, the effect of the Peierls distortion (i.e. resulting from a balance between dimerization and elastic energy) in the formation of diradical species has been underlined in the context of the evolution of the Raman spectra. The modification of the dimerization/elastic balance by including pro-aromatic units produces a change on the alternation pattern from polyacetylene/oligoene-like to aromatic-like at the expenses of the formation of a diradical. The Raman behavior in diradical molecules constituted by two-dimensionally π-electron delocalized structures has been also described, which represented a profound modification regarding that described in linear, one-dimensional, systems.

The Raman spectra of some of the triplet species associated with the discussed singlet diradicaloids have been also reviewed and their vibrational pattern explained in the contexts of the parent singlets. Finally, a correlation between the diradical index, $y_0$, and

the relevant ν(CC) Raman wavenumber bands has been made with emphasis in the mutual connections when the central pro-aromatic core varies from benzo- to naphtho-quinoid, when the lateral parts of the molecules are extended either with dithiophenes or with dibenzo-substitution as well as with the isomerization.

Overall, this chapter attempts to unify all these Raman spectra in a common diradical context and in connection with their structures. On the other hand, these changes in the spectra in these diradicaloids are addressed from the basic electronic structure factors that shape the form of π-conjugated molecules.

## Acknowledgments

We wish to thank the collaborators for their gratitude in providing us with all the samples discussed here. We also thank MINECO/FEDER of the Spanish Government (project reference PGC2018-098533-B-100) and the Junta de Andalucía, Spain (UMA18FEDERJA057). We also thank the vibrational spectroscopy unit of the Research Central Services (SCAI) of the University of Málaga.

## References

1. Long, D. A. (2002). The Raman Effect: A unified treatment of the theory of Raman scattering by molecules, 1st. Ed., John Wiley & Sons Ltd., USA.
2. Albrecht, A. C. (1961). On the theory of Raman intensities, *J. Chem. Phys.*, **34**, pp. 1476–1484.
3. Castiglioni, C., Tommasini, M., and Zerbi, G. (2004). Raman spectroscopy of polyconjugated molecules and materials: Confinement effect in one and two dimensions, *Phil. Trans. R. Soc. Lond. A*, **362**, 2425–2459.
4. Castiglioni, C., Gussoni, M., Lopez Navarrete, J. T., and Zerbi, G. (1988). A simple interpretation of the vibrational spectra of undoped, doped and photoexcited polyacetylene: Amplitude mode theory in the GF formalism, *Solid State Commun.*, **65**, 625–630.
5. Mayorga Burrezo, P., Zafra, J. L., López Navarrete, J. T., and Casado, J. (2017). Quinoidal/Aromatic transformations in π–conjugated oligomers: Vibrational Raman studies on the limits of rupture for π–bonds, *Angew. Chem. Int. Ed.*, **56**, 2250–2259.

6. Ehrenfreund, E., Vardeny, Z., Brafman, O., and Horovitz, B. (1987). Amplitude and phase modes in trans-polyacetylene: Resonant Raman scattering and induced infrared activity, *Phys. Rev. B*, **36**, 1533–1553.
7. Horovitz, B. (1982). Infrared activity of Peierls systems and application to polyacetylene, *Solid State Commun.*, **41**, 729–734.
8. Schaffer, H. E., Chance, R. R., Silbey, R. J., Knoll, K., and Schrock, R. R. (1991). Conjugation length dependence of Raman scattering in a series of linear polyenes: Implications for polyacetylene, *J. Chem. Phys.*, **94**, 4161–4170.
9. Mayorga Burrezo, P., Zhu, X., Zhu, S.-F., Yan, Q., López Navarrete, J. T., Tsuji, H., Nakamura, E., and Casado, J. (2015). Planarization, fusion, and strain of carbon-bridged phenylenevinylene oligomers enhance π-electron and charge conjugation: A dissectional vibrational Raman study, *J. Am. Chem. Soc.*, **137**, 3834–3843.
10. Casado, J., Hernández, V., Ruiz Delgado, M. C., Ponce Ortiz, R., López Navarrete, J. T., Facchetti, A., and Marks, T. J. (2005). Incisive structure–spectroscopic correlation in oligothiophenes functionalized with (±) inductive/mesomeric fluorine groups: Joint Raman and DFT study, *J. Am. Chem. Soc.*, **127**, 13364–13372.
11. Liu, F., Espejo, G. L., Qiu, S., Moreno Oliva, M., Pina, J., Seixas de Melo, J. S., Casado, J., and Zhu, X. (2015). Multifaceted regioregular oligo(thieno[3,4-b]thiophene)s enabled by tunable quinoidization and reduced energy band gap, *J. Am. Chem. Soc.*, **137**, 10357–10366.
12. Casado, J., Ponce Ortiz, R., Ruiz Delgado, M. C., Azumi, R., Oakley, R. T., Hernández, V., and López Navarrete, J. T. (2005). Multidisciplinary physicochemical analysis of oligothiophenes end-capped by nitriles: Electrochemistry, UV–Vis–Near-IR, IR, and Raman spectroscopies and quantum chemistry, *J. Phys. Chem. B*, **109**, 10115–10125.
13. Shirakawa, H., Ito, T., and Ikeda, S. (1973). Raman scattering and electronic spectra of poly(acetylene), *Polymer J.*, **4**, 460–462.
14. Kuzmany, H. (1980). Resonance Raman scattering from neutral and doped polyacetylene, *Phys. Stat. Sol.*, **97**, 521–531.
15. Chappell, J. S., Bloch, A. N., Bryden, W. A., Maxfield, M., Poehler, T. O., and Cowan, D. O. (1981). Degree of charge transfer in organic conductors by infrared absorption spectroscopy, *J. Am. Chem. Soc.*, **103**, 2443–2446.
16. Bozio, R., Zanon, I., Girlando, A., and Pecile, C. (1979). Vibrational spectroscopy of molecular constituents of one-dimensional organic conductors. Tetrathiofulvalene (TTF), TTF+, and (TTF+)2 dimer, *J. Chem. Phys.*, **71**, 2282–2293.

17. Dresselhaus, M. S., Dresselhaus, G., and Eklund, P. C. (1996). Raman scattering in fullerenes, *J. Raman Spectrosc*., **27**, 351–371.
18. Dresselhaus, M. S., Dresselhaus, G., Saito, R., and Jorio, A. (2005). Raman spectroscopy of carbon nanotubes, *Phys. Rep.*, **409**, 47–99.
19. Ferrari, A. C. and Basko, D. M. (2013). Raman spectroscopy as a versatile tool for studying the properties of graphene, *Nat. Nanotechnol.*, **8**, 235–246.
20. Peierls, R. E. (1955). Quantum theory of solids, Oxford, Clarendon Press, London.
21. Su, W. P., Schrieffer, J. R., and Heeger, A. J. (1979). Solitons in polyacetylene, *Phys. Rev. Lett.*, **42**, 1698–1701.
22. Tolbert, L. M. and Zhao, X. (1997). Beyond the cyanine limit: Peierls distortion and symmetry collapse in a polymethine dye, *J. Am. Chem. Soc.*, **119**, 3253–3258.
23. Moss, G. P., Smith, P. A. S., and Tavernier, D. (1995). Glossary of class names of organic compounds and reactivity intermediates based on structure (IUPAC Recommendations 1995), *Pure Appl. Chem.*, **67**, 1307–1375. According to the IUPAC Golden Book, a diradical is defined as "Molecular species having two unpaired electrons, in which at least two different electronic states with different multiplicities [electron-paired (singlet state) or electron-unpaired (triplet state)] can be identified".
24. For a review, see Abe, M. (2013). Diradicals, *Chem. Rev.*, **113**, 7011–7088.
25. Gopalakrishna, T. Y., Zeng, W., Xuefeng, L., and Wu, J. (2018). From open–shell singlet diradicaloids to polyradicaloids, *Chem. Commun.*, **54**, 2186–2199.
26. Breher, F. (2007). Stretching bonds in main group element compounds—Borderlines between biradicals and closed-shell species, *Coor. Chem. Rev*., **251**, 1007–1043.
27. Casado, J., Ponce Ortiz, R., and López Navarrete, J. T. (2012). Quinoidal oligothiophenes: New properties behind an unconventional electronic structure, *Chem. Soc. Rev*, **41**, 5672–5686.
28. Sun, Z., Zeng, Z., and Wu, J. (2014). Zethrenes, extended *p*-quinodimethanes, and periacenes with a singlet biradical ground state, *Acc. Chem. Res*., **47**, 2582–2591.
29. Hotta, S. and Waragai, K. (1993). Solid-state absorption spectroscopy of alkyl-substituted oligothiophenes, *J. Phys. Chem*., **97**, 7427–7434.

30. Hernández, V., Casado, J., Ramírez, F. J., Zotti, G., Hotta, S., and López Navarrete, J. T. (1996). Efficient π electrons delocalization in α,α′-dimethyl end-capped oligothiophenes: A vibrational spectroscopic study, *J. Chem. Phys*., **104**, 9271–9282.

31. Takahashi, T., Matsuoka, K.-i., Takimiya, K., Otsubo, T., and Aso, Y. (2005). Extensive quinoidal oligothiophenes with dicyanomethylene groups at terminal positions as highly amphoteric redox molecules, *J. Am. Chem. Soc*., **127**, 8928–8929.

32. Ponce Ortiz, R., Casado, J., Hernandez, V., Lopez Navarrete, J. T., Viruela, P. M., Orti, E., Takimiya, K., and Otsubo, T. (2007). On the biradicaloid nature of long quinoidal oligothiophenes: Experimental evidence guided by theoretical studies, *Angew. Chem. Int. Ed. Engl*., **46**, 9057–9061.

33. Porter, W. W., Vaid, T. P., and Rheingold, A. L. (2005). Synthesis and characterization of a highly reducing neutral "extended viologen" and the isostructural hydrocarbon 4,4‘ ‘ ‘-di-*n*-octyl-*p*-quaterphenyl, *J. Am. Chem. Soc.,* **127**, 16559–16566.

34. Casado, J., Patchkovskii, S., Zgierski, M. Z., Hermosilla, L., Sieiro, C., Moreno Oliva, M., and López Navarrete, J. T. (2008). Raman detection of "ambiguous" conjugated biradicals: Rapid thermal singlet-to-triplet intersystem crossing in an extended viologen, *Ang. Chem. Int. Ed*., **47**, 1443–1446.

35. Zeng, Z., Ishida, M., Zafra, J. L., Zhu, X., Sung, Y. M., Bao, N., Webster, R. D., Lee, B. S., Li, R.-W., Zeng, W., Li, Y., Chi, C., López Navarrete, J. T., Ding, J., Casado, J., Kim, D., and Wu, J. (2013). Pushing extended *p*-quinodimethanes to the limit: Stable tetracyano-oligo(*N*-annulated perylene)quinodimethanes with tunable ground states, *J. Am. Chem. Soc.*, **135**, 6363–6371.

36. Borden, W.T. (1982). Diradicals, Wiley, New York.

37. Zeng, Z., Lee, S., Zafra, J. L., Ishida, M., Zhu, X., Sun, Z., Ni, Y., Webster, R. D., Li, R.-W., López Navarrete, J. T., Chi, C., Ding, J., Casado, J., Kim, D., and Wu, J. (2013). Tetracyanoquaterrylene and tetracyanohexarylenequinodimethanes with tunable ground states and strong near-infrared absorption, *Angew. Chem. Int. Ed*., **52**, 8561–8565.

38. Cao, T., Zhao, F., and Louie, S.G., (2017). Topological phases in graphene nanoribbons: Junction states, spin centers, and quantum spin chains, *Phys. Rev. Lett.*, **119**, 076401.

39. Stepanov, P., Das, I., Lu, X., Fahimniya, A., Watanabe, K., Taniguchi, T., Koppens, F. H. L., Lischner, J., Levitov, L., and Efetov, D. K. (2020).

Untying the insulating and superconducting orders in magic-angle graphene, *Nature*, **583**, 375–378.

40. Zeng, W., Phan, H., Herng, T. S., Gopalakrishna, T. Y., Aratani, N., Zeng, Z., Yamada, H., Ding, J., and Wu, J. (2017). Rylene ribbons with unusual diradical character, *Chem*, **2**, 81–92.
41. Medina Rivero, S., Canola, S., Zeng, W., Ramírez, F. J., Zafra, J. L., Wu, J., Negri, F., and Casado, J. (2019). Long rylene nanoribbons express polyacetylene-like signatures on their edges, *Phys. Chem. Chem. Phys*., **21**, 7281–7287.
42. Swager, T. M. (2017). Conducting/Semiconducting conjugated polymers: A personal perspective on the past and the future, *Macromolecules*, **50**, 4867–4886.
43. Cai, J., Ruffieux, P., Jaafar, R., Bieri, R., Braun, T., Blankenburg, S., Muoth, M., Seitsonen, A. P., Saleh, M., Feng, X., Müllen, K., and Fasel, R. (2010). Atomically precise bottom-up fabrication of graphene nanoribbons, *Nature*, **466**, 470–473.
44. Narita, A., Wang, X-Y., Feng, X., and Müllen, K. (2015). New advances in nanographene chemistry, *Chem. Soc. Rev*., **44**, 6616–6643.
45. Fujii, S. and Enoki, T. (2013). Nanographene and graphene edges: Electronic structure and nanofabrication, *Acc. Chem. Res.,* **46**, 2202–2210.
46. Son, Y.-W., Cohen, M. L., and Louie, S. G. (2006). Energy gaps in graphene nanoribbons, *Phys. Rev. Lett.*, **97**, 216803.
47. Harada, I., Furukawa, Y., Tasumi, M., Shirakawa, H., and Ikeda, S. (1980). Spectroscopic studies on doped polyacetylene and β-carotene, *J. Chem. Phys*., **73**, 4746–4757.
48. Kertesz, M. and Hoffmann. R. (1983). Higher order Peierls distortion of one-dimensional carbon skeletons, *Solid State Commun.*, **47**, 97–102.
49. Bendikov, M., Duong, H. M., Starkey, K., Houk, K. N., Carter, E. A., and Wudl, F. (2004). Oligoacenes: Theoretical prediction of open-shell singlet diradical ground states, *J. Am. Chem. Soc*., **126**, 7416–7417.
50. Sun, Z., Huang, K.-W., and Wu, J. (2011). Soluble and stable heptazethrenebis(dicarboximide) with a singlet open-shell ground state, *J. Am. Chem. Soc.*, **133**, 11896–11899.
51. Li, Y., Heng, W.-K., Lee, B. S., Aratani, N., Zafra, J. L., Bao, N., Lee, R., Sung, Y. M., Sun, Z., Huang, K.-W., Webster, R. D., López Navarrete, J. T., Kim, D., Osuka, A., Casado, J., Ding, J., and Wu, J. (2012). Kinetically blocked stable heptazethrene and octazethrene: Closed-shell or open-shell in the ground state?, *J. Am. Chem. Soc.*, **134**, 14913–14922.

52. Sun, Z., Lee, S., Park, K., Zhu, X., Zhang, W., Zheng, B., Hu, P., Zeng, Z., Das, S., Li, Y., Chi, C., Li, R., Huang, K., Ding, J., Kim, D., and Wu, J. (2013). Dibenzoheptazethrene isomers with different biradical characters: An exercise of Clar's aromatic sextet rule in singlet biradicaloids, *J. Am. Chem. Soc.*, **135**, 18229–18236.

53. Zafra, J. L., Gonzalez Cano, R. C., Ruiz Delgado, M. C., Sun, Z., Li,'Y., López Navarrete, J. T., Wu, J., and Casado, J. (2014). Zethrene biradicals: How pro-aromaticity is expressed in the ground electronic state and in the lowest energy singlet, triplet, and ionic states?, *J. Chem. Phys.*, **140**, 054706.

54. Shimizu, A., Kishi, R., Nakano, M., Shiomi, D., Sato, K., Takui, T., Hisaki, I., Miyata, M., and Tobe, Y. (2013). Indeno[2,1-b]fluorene: A 20-π-electron hydrocarbon with very low-energy light absorption, *Angew. Chem. Int. Ed*., **52**, 6076–6079.

55. Shimizu, A. and Tobe, Y. (2011). Indeno[2,1-a]fluorene: An air-stable *ortho*-quinodimethane derivative, *Angew. Chem. Int. Ed.*, **50**, 6906–6910.

56. Chase, D. T., Rose, B. D., McClintock, S. P., Zakharov, L. N., and Haley, M. M. (2011). Indeno[1,2-b]fluorenes: Fully conjugated antiaromatic analogues of acenes, *Angew. Chem. Int. Ed*., **50**, 1127–1130.

57. Chase, D. T., Fix, A. G., Kang, S. J., Rose, B. D., Weber, C. D., Zhong, Y., Zakharov, L. N., Lonergan, M. C., Nuckolls, C., and Haley, M. M. (2012). 6,12-Diarylindeno[1,2-b]fluorenes: Syntheses, photophysics, and ambipolar OFETs, *J. Am. Chem. Soc*., **134**, 10349–10352.

58. Fix, A. G., Deal, P. E., Vonnegut, C. L., Rose, B. D., Zakharov, L. N., and Haley, M. M. (2013). Indeno[2,1-c]fluorene: A new electron-accepting scaffold for organic electronics, *Org. Lett.*, **15**, 1362–1365.

59. Rudebusch, G. E., Fix, A. G., Henthorn, H. A., Vonnegut, C. L., Zakharov, L. N., and Haley, M. M. (2014). Quinoidal diindenothienoacenes: Synthesis and properties of new functional organic materials, *Chem. Sci*., **5**, 3627–3633.

60. Rudebusch, G.E., Zafra, J. L., Jorner, K., Fukuda, K., Marshall, J. L., Gómez-García, C. J., Zakharov, L. N., Nakano, M., Ottosson, H., Casado, J., and Haley, M. M. (2016). Diindeno-fusion of an anthracene as a design strategy for stable organic biradicals, *Nat. Chem*., **8**, 753–759.

61. Dressler, J. J., Valdivia, A. C., Kishi, R., Rudebusch, G. E., Ventura, A. M., Chastain, B. E., Gómez-García, C. J., Zakharov, L. N., Nakano, M., Casado, J., and Haley, M. M. (2020). Diindenoanthracene diradicaloids enable rational, incremental tuning of their singlet-triplet energy gaps, *Chem*, **6**, 1353–1368.

62. Hayashi, H., Barker, J. E., Valdivia, A. C., Kishi, R., MacMillan, S. N., Gómez-García, C. J., Miyauchi, H., Nakamura, Y., Nakano, M., Kato, S.-i., Haley, M. M., and Casado, J. (2020). Monoradicals and diradicals of dibenzofluoreno[3,2-b]fluorene isomers: Mechanisms of electronic delocalization, *J. Am. Chem. Soc*, doi: 10.1021/jacs.0c09588.

63. Dressler, J. J., Teraoka, M., Espejo, G., Kishi, R., Takamuku, S., Gómez-García, C. J., Zakharov, L. N., Nakano, M., Casado, J., and Haley, M. M. (2018). Thiophene and its sulfur inhibit indenoindenodibenzothiophene diradicals from low-energy lying thermal triplets, *Nat. Chem.*, **10**, 1134–1140.

64. Barker, J. E., Dressler, J. J., Valdivia, A. C., Kishi, R., Strand, E. T., Zakharov, L. N., MacMillan, S. N., Gómez-García, C. J., Nakano, M., Casado, J., and Haley, M. M. (2020). Molecule isomerism modulates the diradical properties of stable singlet diradicaloids, *J. Am. Chem. Soc.*, **142**, 1548–1555.

65. Döhnert, D. and Koutecky, J. (1980). Occupation numbers of natural orbitals as a criterion for biradical character: Different kinds of biradicals, *J. Am. Chem. Soc*., **102**, 1789–1796.

66. Yamaguchi, K. (1975). The electronic structures of biradicals in the unrestricted Hartree-Fock approximation, *Chem. Phys. Lett.*, **33**, 330–335.

67. Nakano, M., Fukui, H., Minami, T., Yoneda, K., Shigeta, Y., Kishi, R., Champagne, B., Botek, E., Kubo, T., Ohta, K., and Kamada, K. (2011). (Hyper)polarizability density analysis for open-shell molecular systems based on natural orbitals and occupation numbers, *Theor. Chem. Acc.*, **130**, 711–724.

## Chapter 5

# Phenalenyl- and Anthene-Based Diradicaloids

**Takashi Kubo**
*Graduate School of Science, Osaka University, 1-1 Machikaneyama, Toyonaka, Osaka 560-0043, Japan*
kubo@chem.sci.osaka-u.ac.jp

In recent years, structure of diradicaloids has become increasingly diverse and many unique phenomena, which originate from a resonance hybrid of closed-shell and open-shell electronic structures, have been revealed by experimental and theoretical studies. This chapter focuses on behaviors of phenalenyl-based and anthene-based diradicaloids. The phenalenyl-based diradicaloids are characterized by appreciable inter-molecular spin–spin interactions. Short π–π contacts, a lower-energy shift in HOMO–LUMO absorption bands, dual nature in pericyclic reactions, and a fluxional σ-bond shift are prominent features experimentally observed. Interests on anthene-based diradicaloids arise from the structure–property relationship for understanding the mechanism of electron localizations at zigzag-edges of graphene nanoribbons

*Diradicaloids*
Edited by Jishan Wu

ISBN 978-981-4968-08-9 (Hardcover), 978-1-003-27724-8 (eBook)
www.jennystanford.com

(GNRs). Systematic studies reveal that aromatic stabilization energy plays a crucial role in the appearance of unpaired electrons at zigzag-edges.

## 5.1 Introduction

Diradicaloids are compounds in which a covalent bonding interaction between two unpaired electrons is much weaker than normal covalent bonds. Generally, covalent bonds are weakened by decoupling an electron pair through stretching σ-bonds or twisting π-bonds. However, covalent bonds can also be weakened by a special conjugation manner in π-conjugated systems, where aromaticity plays an important role. Homolytic cleavage of a π-bond makes a compound energetically unstable, but if aromatic rings appear with the cleavage, part of the destabilization energy can be compensated by aromatic stabilization energy. The delocalization of unpaired electrons, which are generated by the homolytic cleavage, also contributes to weakening of a π-bond. The electronic state of diradicaloids is appropriately expressed in terms of the resonance hybrid of closed-shell and open-shell canonical structures. With increasing the relative stability of the open-shell structure, diradical character of a compound becomes larger. This chapter focuses on diradicaloids, where phenalenyl and cumulative quinoid scaffolds play a crucial role in open-shell character.

## 5.2 Phenalenyl-Based Diradicaloids

### 5.2.1 Thermodynamic Stability of Phenalenyl Radical

The phenalenyl radical **1** is a tricyclic π-conjugated hydrocarbon radical. Because **1** has a symmetric skeleton of $D_{3h}$, an unpaired electron is equally delocalized on six equivalent carbon atoms called α-position (1, 3, 4, 6, 7, and 9-position in Figure 5.1). The singly occupied molecular orbital (SOMO) of **1** has a coefficient of $\pm 1/\sqrt{6}$ (black and white circles) on α-carbons, and otherwise zero. Due to high delocalization manner of an unpaired electron, **1** is thermodynamically stabilized. The thermodynamic stability of **1** can be estimated from the bond dissociation energy of the methylene

C–H bond of phenalene **2** (270 kJ/mol) [1], which is much smaller than that of normal benzylic C–H bonds (~370 kJ/mol). Small bond dissociation enthalpy of an σ-dimer **3** (41 kJ/mol in toluene and 47.5 kJ/mol in $CCl_4$) also supports thermodynamically stabilized nature of **1** [2].

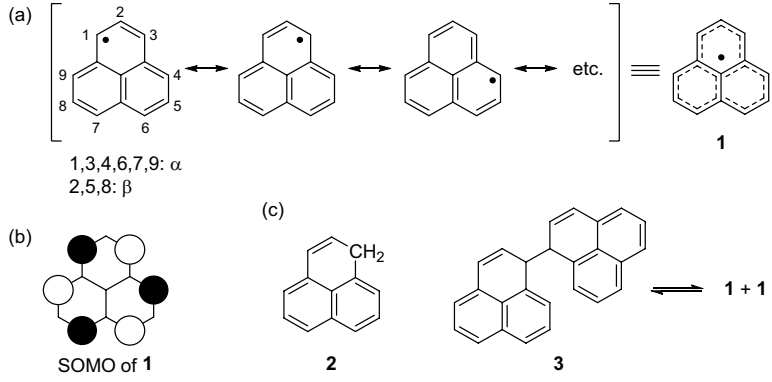


**Figure 5.1** (a) Delocalization of an unpaired electron of **1**; (b) SOMO of **1**; (c) Structures of **2** and **3**.

## 5.2.2 Design and Synthesis of Bisphenalenyl Diradicaloid

*p*-Quinodimethane (*p*-QDM) is the simplest and best studied diradicaloid hydrocarbon. The parent *p*-QDM is long-lived in gas phase [3] or in dilute solution state [4]; whereas, in condensed phase, the *p*-QDM undergoes bimolecular reactions to afford poly(*p*-xylylene) [3] and [2.2]paracyclophane [5]. Although the *p*-QDM can be described by a quinoidal Kekulé structure, its reactivity implies non-negligible diradical contribution to the ground state electronic structure. Combination of spin-delocalizing units (i.e., phenalenyl) and a diradicaloid scaffold (i.e., *p*-QDM) would lead to a thermodynamically stabilized diradicaloid. Following this concept, a bisphenalenyl diradicaloid compound **4** was designed and synthesized. As shown in Figure 5.2, the quinoidal Kekulé form **4** resonates well with the diradical form **4'** as a result of gaining aromatization energy of the central six-membered ring, and then unpaired electrons emerging on the terminal carbons of the *p*-QDM moiety can delocalize on the phenalenyl rings (**4''**). The

diradical index ($y_0$) of **4a**, which is estimated from the natural orbital occupation number (NOON) of the lowest unoccupied natural orbital (LUNO) [6], is 37% within the broken-symmetry formalism at the UB3LYP/6-31G** level of theory. Unpaired electrons mostly reside on the phenalenyl moieties with the same distribution pattern as the phenalenyl radical **1**.

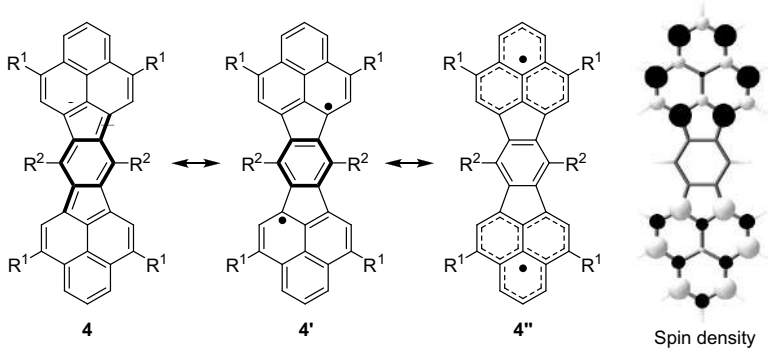


**4a**, $R^1 = R^2 = H$
**4b**, $R^1$ = *tert*-Bu, $R^2 = H$
**4c**, $R^1 = H$, $R^2$ = Ph

**Figure 5.2** Resonance structure and spin density map (UB3LYP/6-31G**) of bisphenalenyl diradicaloid **4**.

Non-substituted bisphenalenyl diradicaloid **4a** is insoluble in most organic solvents. Substituent groups are necessary for improving the solubility of **4a**. *tert*-Butyl and phenyl derivatives (**4b** and **4c**, respectively) were initially prepared by very long multi-step syntheses (Figure 5.3) [7, 8]. However, the synthetic route to **4c** is considerably improved by fragment coupling synthetic strategy (Figure 5.4) [9]. The key reaction is the catalytic Rh(II)-carbenoid cyclization of phenalenyl rings.

### 5.2.3 Physical Properties of Bisphenalenyl Diradicaloid

Diradicaloids have common phenomenological features, such as high reactivity, a low-energy absorption band, a small difference between oxidation and reduction potentials, broadening of NMR signals, thermally induced electron spin resonance (ESR) signals, and a weak absorption band derived from HOMO,HOMO → LUMO,LUMO double excitation.

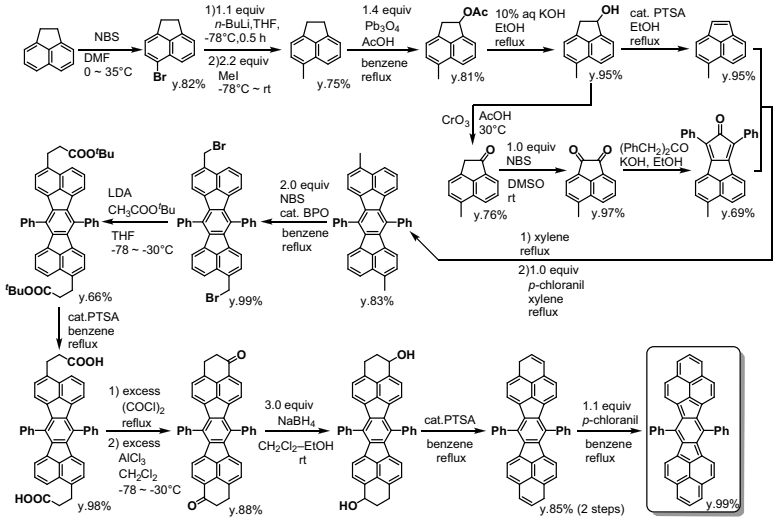


**Figure 5.3** Long-synthetic route to **4c**.

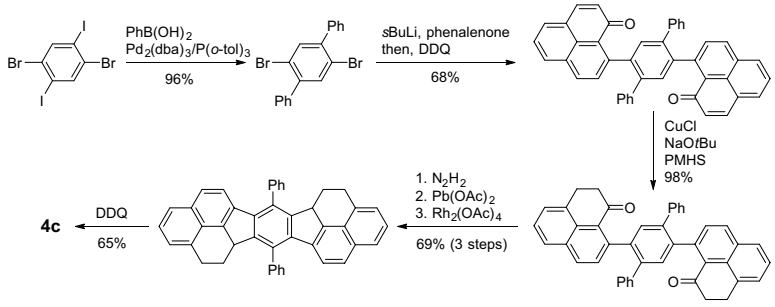


**Figure 5.4** Chen's improved seven steps synthesis of **4c**.

A solution $^1$H NMR spectrum of a tetra-*tert*-butyl derivative **4b** at room temperature shows broad signals for aromatic protons [7]. These broad signals become sharp upon cooling, as shown in Figure 5.5a. This behavior can be explained by thermal excitation to the triplet state. The thermally populated triplet species is indeed detected by a solid-state ESR measurement, which shows signals with a zero-field parameter of $D$ = 9.6 mT and $E \leq 0.2$ mT (Figure 5.5b). Least-square curve fitting of signal intensities at various temperatures reveals the energy gap between singlet and triplet ($\Delta E_{S-T}$) of –20.4 kJ/mol (singlet is the ground state).

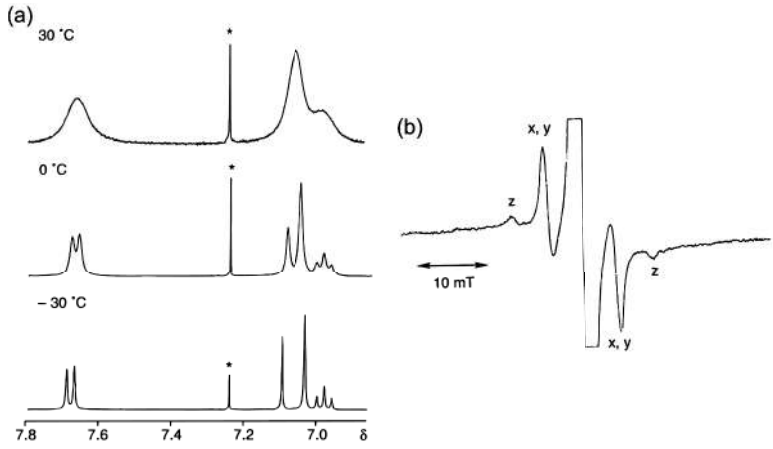


**Figure 5.5** (a) Variable temperature $^1$H NMR spectra of **4b**; (b) ESR spectrum of **4b** in solid state measured at 130 °C [7].

The small $\Delta E_{S\text{-}T}$ implies a weak covalent bonding interaction between two unpaired electrons within the molecule. These two unpaired electrons are spatially separated from each other, but are still demanding electron–electron pairing. When two diradicaloids are close together, the molecules demand an inter-molecular covalent bonding interaction, eventually forming a dimer. Actually, a diphenyl derivative **4c** forms a one-dimensional (1D) chain in solid state, with a dimeric pair of the spin-bearing phenalenyl ring (Figure 5.6a) [8]. The π–π separation distance in the overlapping phenalenyl dimer is only 3.137 Å, which is substantially shorter than the sum of the van der Waals radius of a carbon atom (3.4 Å). The overlap pattern is identical to that of a phenalenyl radical dimer [10, 11], in which a covalent bonding interaction operates very effectively due to a maximized SOMO–SOMO overlap [12]. A strong inter-molecular covalent bonding interaction is responsible for the short π–π contact of **4b**. The electronic absorption band (1470 nm) of the 1D chain showed a drastic red-shift with respect to the band of a monomer (746 nm), as shown in Figure 5.6b, due to a long-range π-conjugation through the intra- and inter-molecular covalent bonding interactions. The strength of the covalent bonding interactions is quantum-chemically estimated. According to the calculation, the inter-molecular interaction (3400 K, 28 kJ/mol) is stronger than the intra-molecular one (2300 K, 19 kJ/mol) [13].

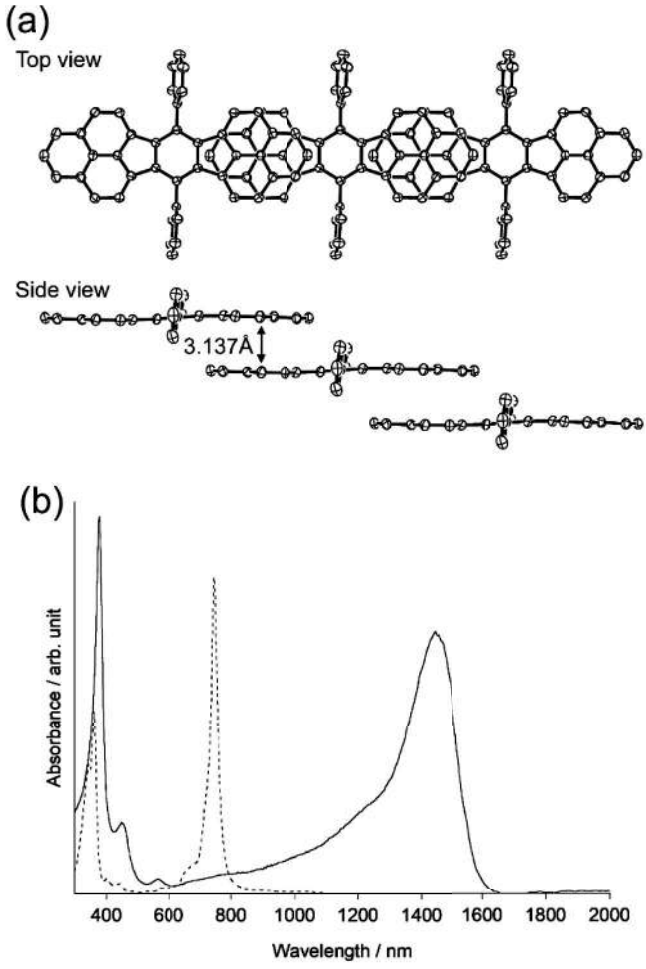


**Figure 5.6** (a) 1D stack of **4c**; (b) Electronic absorption spectra in solution (dashed line) and solid (solid line) states of **4c**.

The sequence of the alternating interactions in the 1D chain is implicated in an electroconductive property. The electroconductivity of a compressed pellet of **4c** at room temperature is $1.0 \times 10^{-5}$ S/cm with an activation energy of 0.3 eV [8]. This single component semiconductive behavior is supported by an extended Hückel molecular orbital (HMO) calculation that shows a very large dispersion in the valence and conduction bands and a small gap between them, along the stacking direction (Figure 5.7a). Thin-film properties and

ambipolar transport have also been investigated. The organic field-effect transistors (OFETs) based on **4c** exhibit ambipolar transport with balanced hole and electron mobilities in the order of $10^{-3}$ $cm^2/(V•s)$ (Figure 5.7b) [14].

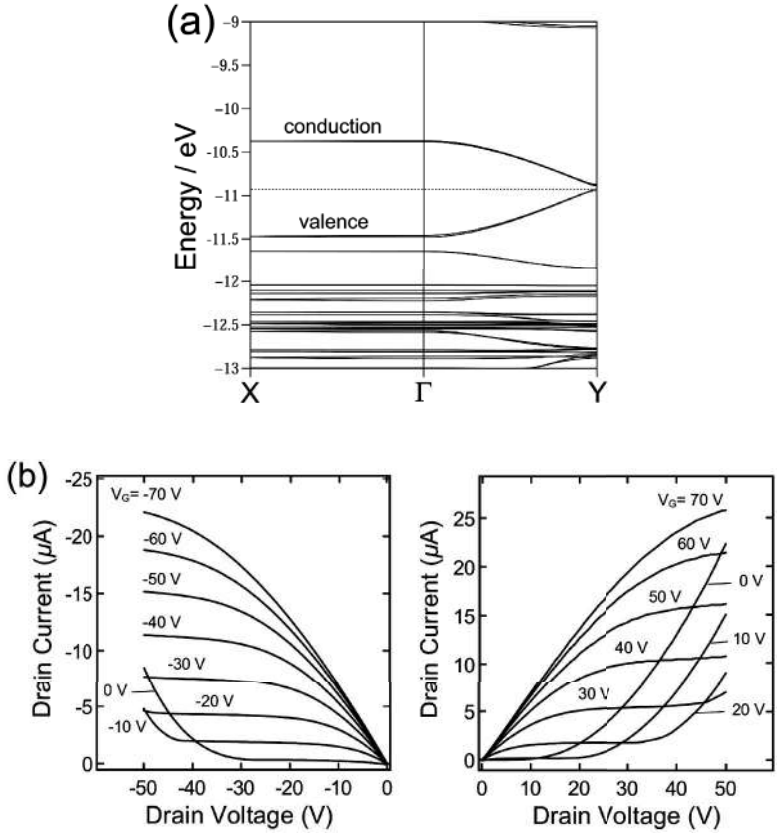


**Figure 5.7** (a) Band structure of **4c** near the Fermi level, the stacking direction is labeled with Y [8]; (b) Output characteristics of an ambipolar OFET based on **4c** [14].

### 5.2.4 Tuning of Diradical Character of Bisphenalenyl Diradicaloids

The stabilization of the diradical contributor in the resonance formula leads to larger diradical character. Replacement of the

central benzene ring in **4** with naphthalene or anthracene rings enhances diradical character because naphthalene and anthracene have larger aromatic stabilization energies than benzene (Figure 5.8). According to UB3LYP/6-31G** calculations, naphthalene- and anthracene-embedded bisphenalenyl, **5a** and **6a**, possess 56% and 62% of singlet diradical index ($y_0$) in the ground state, respectively. Table 5.1 summarizes the data related to diradical character of **4b**, **5b**, and **6b** [15, 16].

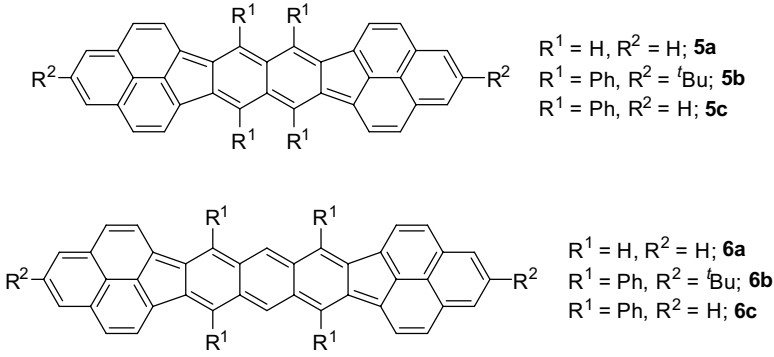


**Figure 5.8** Naphthalene- and anthracene-embedded bisphenalenyl diradicaloids.

**Table 5.1** Data of **4b**, **5b**, and **6b** related to diradical character

| | **4b** | **5b** | **6b** |
|---|---|---|---|
| Diradical index, $y_0$[a] | 37% | 56% | 62% |
| $\Delta E_{S-T}$ (kJ/mol) [b] | –20.4 | –16 | ~–8 |
| $\Delta E_{HOMO-LUMO,\ elec.}$ (eV)[c] | 1.16 | 1.04 | 0.98 |
| $\Delta E_{HOMO-LUMO,\ opt.}$ (eV)[d] | 1.65 | 1.43 | 1.26 |

[a]Estimated by UB3LYP/6-31G** calculations for **4a**, **5a**, and **6a**. [b]Singlet–triplet energy gaps determined by ESR for **4b** and by SQUID for **5b** and **6b**. [c]HOMO–LUMO energy gaps estimated from the difference between the first oxidation and the first reduction potentials in cyclic voltammograms. [d]HOMO–LUMO energy gaps estimated from the lowest-energy bands in electronic absorption spectra.

**5c** and **6c**, which have no substituent on the phenalenyl rings, form 1D chains in slipped stacking arrangement with superimposed phenalenyl overlapping. The stacking motifs are almost the same as

that of **4c**. The very short π–π contacts (3.16 Å for **5c** [17], 3.15 Å for **6c** [16]) indicate appreciable covalent bonding interaction between molecules. Interestingly, as shown in Figure 5.9, the lowest-energy absorption bands in solid state shift to higher energy region with increasing diradical character, which is in contrast to the solution behavior (Table 5.1). This strange phenomenon can be explained in terms of how largely the intra- and inter-molecular covalent bonding interactions are unbalanced in the 1D chains. A 1D chain with more unbalanced interactions is equivalent to a linear π-conjugation system (like polyene) with more enhanced bond alternation. Actually, polarized reflection measurements on a crystal of **6c** reveals that a covalent bonding interaction in the 1D chain of **6c** is substantially strong between molecules compared to within a molecule.

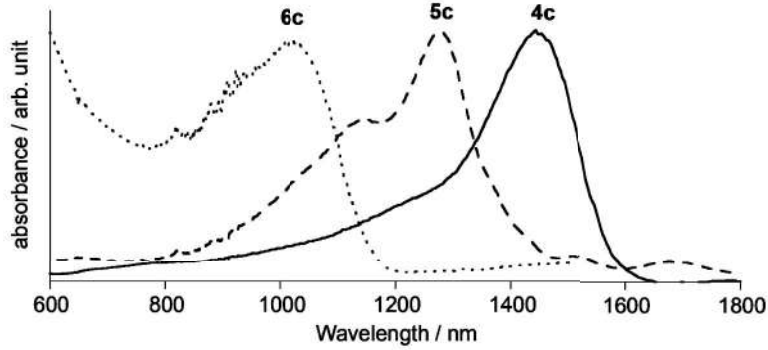


**Figure 5.9** The lowest-energy absorption bands of solid **4c** (solid line), **5c** (dashed line), and **6c** (dotted line); the peak tops are at 1440 nm, 1280 nm, and 1025 nm, respectively.

### 5.2.5 Non-linear Optical Property of Bisphenalenyl Diradicaloids

According to Nakano's theoretical studies, molecules with an intermediate singlet diradical nature have an enhanced third-order nonlinear optical response including two-photon absorption (TPA) activity. Diradicaloids possess a weakly coupled electron pair, which allows the electronic distribution in a π-conjugated system to distort easily. The TPA cross-section measurements of **4b**, **4c**, and **5b** in solution state show TPA peaks at 1300, 1425, and 1500 nm

with cross-sectional values of $\sigma^{(2)}$ = 330, 424, and 850 GM (1 GM = $10^{-50}$ $cm^4$•s /(photon•molecule)), respectively (Figure 5.10). These values of TPA activity are much stronger than those of closed-shell π-conjugated hydrocarbons with similar molecular size [18].

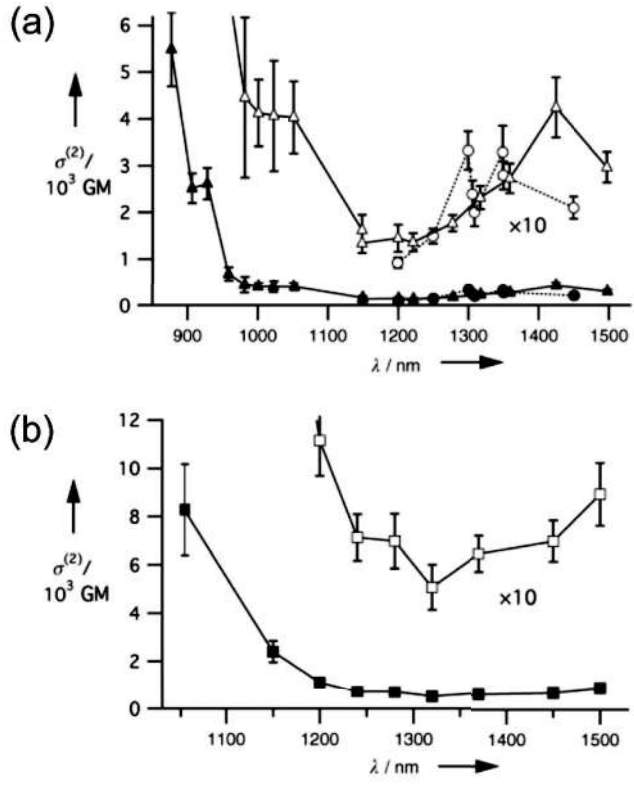


**Figure 5.10** TPA spectra of (a) **4b** (circles) and **4c** (triangles), and (b) **5c**. The vertical scales for the open symbols are magnified by 10 [18].

### 5.2.6 Cycloaddition Reactions of Bisphenalenyl Diradicaloid having o-Quinodimethane Scaffold

*o*-Quinodimethane (*o*-QDM) is another well studied diradicaloid hydrocarbon. Similar to *p*-QDM, *o*-QDM also shows high reactivity, a rapid self-dimerization in the solution state even at −150 °C [19–21] and a valence tautomerization into benzocyclobutene in the gas phase [22].

*o*-QDM-embedded bisphenalenyl diradicaloid, sigmarene **7**, has appreciable diradical character ($y_0$ = 44%) as predicted from the resonance formula shown in Figure 5.11. Spin density calculation of **7a** indicates that unpaired electrons widely distribute on the phenalenyl moieties, but the highest spin density resides on the exo-methylene carbon atoms of the *o*-QDM scaffold.

A tetra-substituted derivative **7b** has been prepared by a straightforward stepwise synthesis and isolated as a doubly σ-bonded dimer **7b-dimer**. Two sigmarene subunits are connected with two σ-bonds at the carbon atoms that bear the highest spin density (Figure 5.12). The length of the σ-bond is 1.614(7) Å, which is longer than the typical C($sp^3$)–C($sp^3$) σ-bond length (1.54 Å).

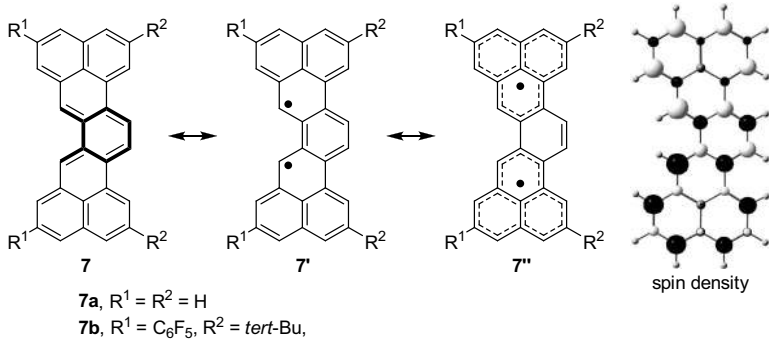


**Figure 5.11** Resonance structure of sigmarene **7**.

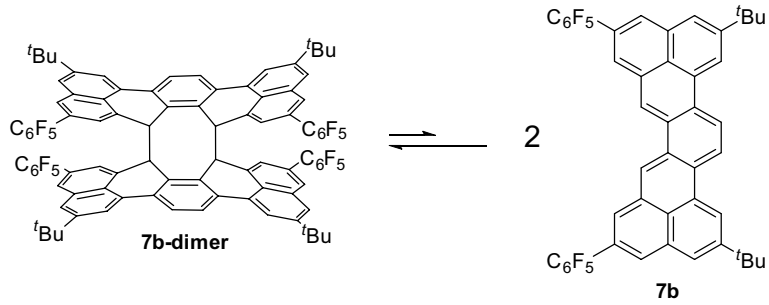


**Figure 5.12** Equilibrium between **7b-dimer** and **7b**.

**7b-dimer** slightly dissociates into monomeric **7b** in a dilute solution at room temperature (Figure 5.12). The equilibrium

between **7b-dimer** and **7b** is confirmed by variable temperature UV-vis spectroscopic measurements, which appreciably show an intense absorption band at 707 nm, that is, assignable to a HOMO → LUMO transition. From the temperature dependence of the dissociation constant ($K_d$), the changes in enthalpy and entropy for the dissociation of **7b-dimer** are determined to be 84 ± 1 kJ/mol and 147 ± 3 J/(mol•K), respectively. The rate constant of the dimerization of **7b** is determined to be 17,600 ± 300 1/(M•s) at 21 °C by laser-flash photolysis (LFP) measurements. The activation enthalpy and entropy of the dimerization are only 26 ± 1 kJ/mol and –78 ± 5 J/(mol•K), respectively. Interestingly, the self-dimerization reaction occurs very rapidly even at room temperature under dark condition although a [4+4] cycloaddition reaction is considered to be thermally forbidden. Although the time–dependence of the transient absorption peak of **7b** in the LFP experiment follows single-exponential decay, quantum chemical calculation reveals that the dimerization reaction proceeds in a stepwise manner, not by a concerted mechanism. On the other hand, **7b** undergoes a concerted [4+2] cycloaddition reaction with fumaronitrile at room temperature under dark condition. These reactivities represent the dual nature of the closed-shell and open-shell electronic structures of **7b** (Figure 5.13).

### 5.2.7 Electrocyclization of Bisphenalenyl Diradicaloid

The phenalenyl radical **1** is in equilibrium with a σ-dimer **3** in solution state. In the presence of oxidizing reagents, **3** affords dihydroperopyrene **8** through intermediates of *E*- and *Z*-biphenalenylidene, *E*-**9** and *Z*-**9** (Figure 5.14). The UV irradiation (365 nm) of **8** in a glassy 2-methyltetrahydrofuran (MTHF) matrix at 98 K results in *retro*-electrocyclization to yield *Z*-**9**, and upon melting the matrix, *Z*-**9** transforms into *E*-**9**, which is energetically more stable than *Z*-**9** by 5.9 kJ/mol (UB3LYP/6-31G**). A kinetic study reveals the activation barrier for the thermal isomerization from *Z*-**9** to *E*-**9** is only 18 kJ/mol. This extraordinary low barrier for the double bond rotation can be attributed to large singlet diradical character of *Z*-**9** ($y_0$ = 94%, UB3LYP/6-31G*) in the ground state. *E*-**9** rapidly undergoes electrocyclization to afford **8**, through *Z*-**9** intermediate, at room temperature under dark condition. According

to time-dependent UV-vis absorption measurements, the activation barrier for the ring-closure reaction is 66 kJ/mol. It is noted that this reaction occurs in conrotatory fashion under a thermal condition although this reaction mode is kinetically unfavorable according to the Woodward–Hoffmann rule. The low barriers for the double bond rotation and for the symmetry-forbidden electrocyclization can be rationalized by appreciable singlet diradical character of *E,Z*-**9**. Similar reactions, which are facilitated due to singlet diradical character, are also found in a dimethyl derivative of the cethrene, **10** [23, 24]. The cethrene will be described in more detail in Chapter 6.

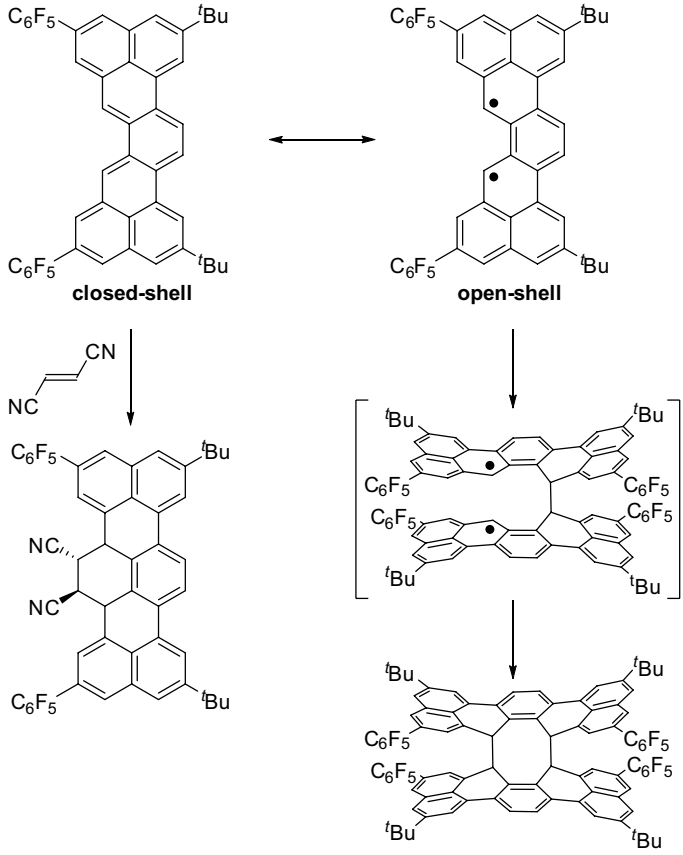


**Figure 5.13** Dual nature of the reactivity of **7b**.

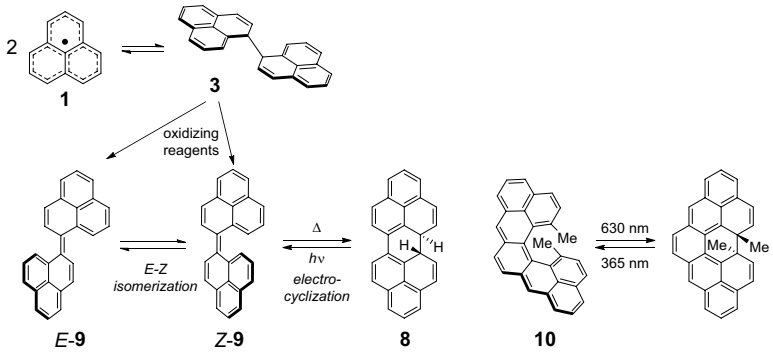


**Figure 5.14** Reactions of biphenalenylidenes *E*,*Z*-**9** facilitated by diradical nature. Similar facilitated electrocyclizations found in **10** is also shown.

## 5.2.8 Through-Space Conjugated Bisphenalenyl Diradicaloids

As mentioned above, it is believed that **1** forms σ-dimer **3** in solution state by spectroscopic [25] and product analyzes [26]. However, the introduction of bulky *tert*-butyl groups on the β-position of **1** leads to another dimerization form. 2,5,8-Tri-*tert*-butylphenalenyl radical **11** was prepared in nine steps from naphthalene. In the crystalline state, **11** forms a face-to-face π-dimer $\mathbf{11}_2$-π, in which the α-positions of phenalenyl radicals are superimposed at a separation distance of 3.306 Å (averaged) at 300 K (Figure 5.15). It is revealed that this π-dimerization also occurs in solution [27] and in the gas phase [28]. The π-dimer $\mathbf{11}_2$-π shows deep blue color, which originates from an intense broad absorption band at 612 nm. From the polarized reflection spectra of a single crystal of $\mathbf{11}_2$-π, the intense band can be assigned to an electronic transition between the HOMO and LUMO, newly formed by the orbital interaction of a pair of SOMO in the π-dimer. The strength of the interaction between the two SOMOs, that is, the covalent bonding interaction of two unpaired electrons, has been determined to be 2000 K (= 17 kJ $mol^{-1}$) by SQUID measurements of powdered $\mathbf{11}_2$-π [29]. This new mode of dimerization invokes the term "multicenter/two-electron (mc/2e) bonding"[30] or "pancake bonding"[31] to describe the structure, and is characterized by attractive interactions derived from a covalent

bonding interaction between two unpaired electrons, as well as a dispersion force [27]. The sizable covalent bonding interaction of 2000 K makes $\mathbf{11}_2$-π diamagnetic. However, quantum chemical broken-symmetry [32] or multi-reference [27] approaches suggest appreciable diradical character for $\mathbf{11}_2$-π ($y_0$ = 32% estimated by a CP-MRMP2 method).

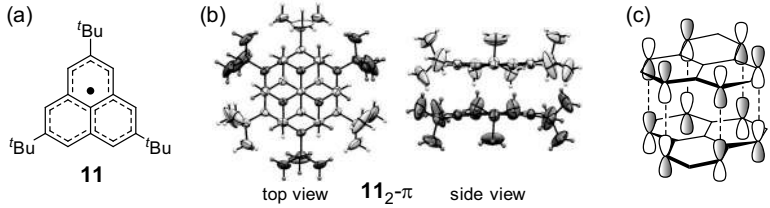


**Figure 5.15** (a) Tri-*tert*-butylphenalenyl radical **11**; (b) X-ray crystal structure of the π-dimer $\mathbf{11}_2$-π; and (c) 12-center/2-electron bonding (SOMO–SOMO overlap).

The dimerization mode of phenalenyl radical depends on substituent groups. As shown in Figure 5.16, a pentafluorophenyl ($C_6F_5$) substituted derivative **12** prefers an σ-dimer over a π-dimer [33], whereas a phenyl derivative **13** a π-dimer [34]. The π-dimer of **13** shows very short C(α)–C(α) separation of 3.067 Å at 300 K, which is much shorter than that of $\mathbf{11}_2$-π (3.306 Å). The smaller interplanar separation leads to a stronger covalent bonding interaction of two unpaired electrons because of the larger overlap between the two SOMOs of adjacent phenalenyl rings. Indeed, the $\chi T$ values in the SQUID measurements does not increase even at high temperatures up to 380 K. The electronic absorption measurement of the π-dimer of **13** in a KBr pellet shows an intense broad band centered at 574 nm, which is blue-shifted with respect to the band of $\mathbf{11}_2$-π (612 nm). As mentioned above, those intense low-energy bands are assignable to the HOMO→LUMO transitions of the π-dimers. A larger SOMO–SOMO overlap in the π-dimer of **13** causes the larger HOMO–LUMO gap. According to the reference [27], the diradical character $y_0$ of the π-dimer should be smaller than 25%. The toluene solution of **13** shows a well-resolved multiline ESR spectrum at room temperature, and the ESR signal decreases in intensity with decreasing temperature and almost disappears at 170 K, due to the formation of the diamagnetic π-dimer. $^1$H NMR measurements of **13**

in $CD_2Cl_2$ shows no signal at 273 K, whereas at 203 K, two broad signals are observed at $\delta$ = 7.5 ppm (phenyl protons) and 6.8 ppm (phenalenyl protons).

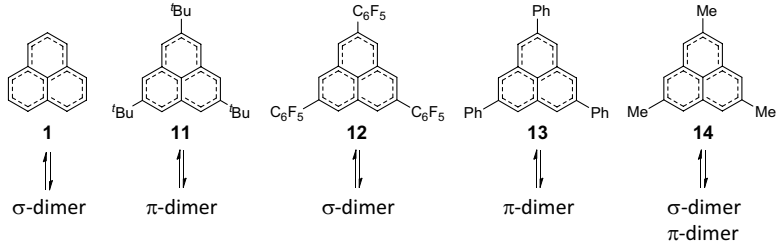


**Figure 5.16** Dimerization mode of phenalenyl radicals.

From the preferential dimerization mode of **11**, **12**, and **13**, it can be concluded that steric bulkiness is not a major factor for phenalenyl radical to adopt σ-dimer or π-dimer forms as the most stable state. The intrinsic dimerization behavior of phenalenyl radical was investigated with a derivative **14** having small methyl groups at 2,5,8-positions. The low temperature solution $^1$H NMR study of **14** reveals the presence of three stable structural isomers for the dimers of **14**: σ-dimer chiral form (**14**$_2$-σ-chiral), σ-dimer meso form (**14**$_2$-σ-meso), and π-dimer (**14**$_2$-π) form (Figure 5.17a) [35]. From the integration ratio of the 1D $^1$H NMR signals, the most stable isomer is found to be the σ-dimer chiral form (**14**$_2$-σ-chiral) and the other two (**14**$_2$-σ-meso and **14**$_2$-π) are metastable forms. However, the energy differences, estimated from the ratio of the NMR signal intensities and Boltzmann distribution, between the metastable forms relative to the most stable **14**$_2$-σ-chiral are very small: 0.33 kJ mol$^{-1}$ for **14**$_2$-σ-meso and 2.8 kJ mol$^{-1}$ for **14**$_2$-π. The structures of **14**$_2$-σ-chiral and **14**$_2$-π are also confirmed by X-ray crystallographic analysis [34]. **14**$_2$-π shows a superimposed structure, similar to the π-dimers of **10** and **13**, with a short contact of α-carbons (av. 3.054 Å at 100 K).

The three isomeric dimer forms of **14** are in equilibrium with each other in solution state [35]. The most striking feature related to the equilibrium is that six-fold σ-bond shift occurs in **14**$_2$-σ-chiral in equal probabilities among the six sets of α-carbon pairs, as shown in Figure 5.17b. The nonselective σ-bond shift is explained by a

stepwise mechanism through $\mathbf{14}_2$-π. Thus, the consecutive σ-dimer ↔ π-dimer transformation, that is, 2c/2e-bond ↔ 12c/2e-bond transformation, contributes to the unusual σ-bond fluxionality in $\mathbf{14}_2$-σ-chiral.

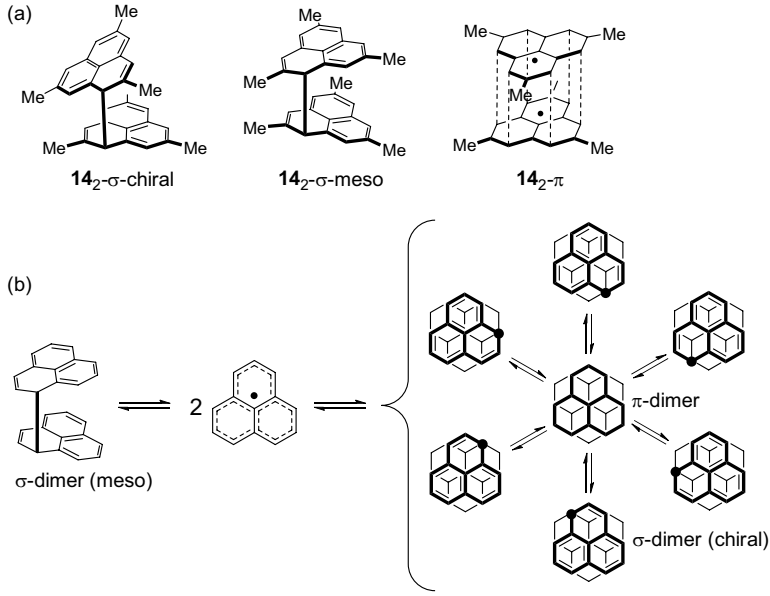


**Figure 5.17** (a) Three isomeric dimers formation of **14**; (b) Equilibrium relationship for the dimers of **14**. Methyl groups were omitted for clarity. The black circle in $\mathbf{14}_2$-σ-chiral denotes the σ-bond connecting two phenalenyl rings.

## 5.3 Anthene-Based Diradicaloids

### 5.3.1 Unique Electronic Properties of Graphene

Since the elucidation of graphene's unique electronic properties by Geim and Novoselov in 2004 [36], graphene has been recognized as a completely new carbon material and has attracted considerable attention in the fields of physics, chemistry, and electronic device applications. The electronic structure of graphene is characterized by two features. The one is a linear band dispersion near the Fermi level (Dirac cone), which is closely related to unusual electronic properties, such as high electron mobility, half-integer quantum Hall

effects, and giant diamagnetism. The other is a localized electronic state at zigzag-shaped open edges, which is related to magnetic properties such as ferromagnetism. Interestingly, only the zigzag edge bears localized unpaired electrons, whereas armchair edges not.

The existence of the special localized electronic state, called the "edge states", was predicted by Tanaka [37] and Fujita [38] in their theoretical calculations of GNRs, and indeed Enoki confirmed the high electron density on the zigzag edge near the Fermi level by STM/STS measurements [39]. This means that the edge states indeed exist and are closely related to the magnetic properties of graphene. When graphene is reduced down to nanosize, the ratio of edges to the whole would increase, and the properties of graphene would become more dependent on its shape and size. Accurate understanding of the correlation between the edge structure and the properties of graphene requires nanosized graphene with an atomically controlled structure.

### 5.3.2 Model System for Investigating Edge State

If relatively small model molecules can be used to investigate the edge state, it is possible to elucidate the structure–property relationships in detail using various spectroscopic and diffraction measurements. Model molecules, which are partly extracted from zigzag-edged GNR (ZGNR), have been used in the theoretical investigation of the edge state (Figure 5.18). Considering that the edge state is the localized electron state on zigzag edges, the unpaired electron density (spin density) on zigzag edges is a good indicator of the localization for small molecules. Furthermore, the localized state is the spin-polarized state caused by multi-electron correlation among unpaired electrons on the zigzag edges, and for small molecules, two-electron correlation is important. Therefore, singlet diradical character $y_0$ well represents the degree of the edge state for model systems.

Figure 5.19 shows a rectangular model system, which is referred to as periacenes, along with singlet diradical character $y_0$. The UBH and HLYP/6-31G** calculation using the broken symmetry method is used to estimate $y_0$. At $y_0$ = 0%, there is no electron localization, whereas at $y_0$ = 100%, electrons are fully localized on zigzag edges. For molecules of naphthalene connected vertically (a sequence of

$m$ = 2, called rylenes), the change in $y_0$ is very slow and essentially no edge state is observed. On the other hand, in the region where $m$ > 3, $y_0$ increases rapidly as the molecules are extended vertically. What is important here is that $y_0$ increases from an unexpectedly small molecule size, which means that the edge state is expected to be experimentally verifiable even with chemically synthesizable molecules.

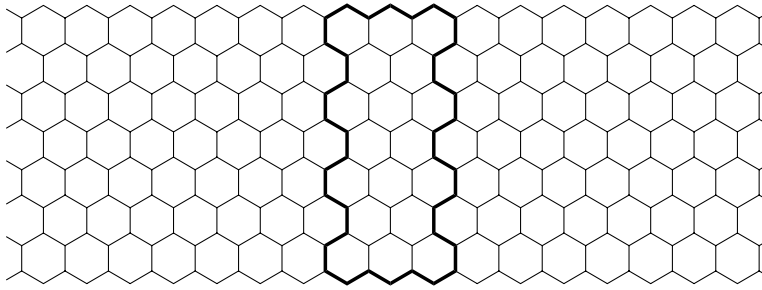

**Figure 5.18** ZGNR and a model system (bold lines) partly extracted from ZGNR.

### 5.3.3 Synthesis of Anthenes

Given the ease of synthesis of compounds, it is reasonable to choose the column with $m$ = 3 (the dashed box in Figure 5.19) as the actual study target. This group of compounds are called anthenes and the minimum one is bisanthene ($m$ = 3, $n$ = 3). Although the parent bisanthene is quite unstable in air, derivatives kinetically stabilized by bulky substituent groups can be isolated as stable crystalline forms (Figure 5.20a) [40–42]. Teranthene ($m$ = 3, $n$ = 5) and quateranthene ($m$ = 3, $n$ = 7) are also successfully isolated through multi-step straightforward syntheses [43, 44]. Figure 5.20b shows the synthetic procedure for derivatives of quateranthene. The key reactions for the syntheses are a partial cyclization with KOH/quinoline and a full cyclization with DDQ/$Sc(OTf)_3$.

Tetra-*tert*-butylbisanthene **15** is relatively stable with a half-life of 19 days in an air-saturated solution. On the other hand, the half-life of **16** is only two days under the same condition, and the half-life of **17a** at room temperature is only 15 h when exposed to air under room light.

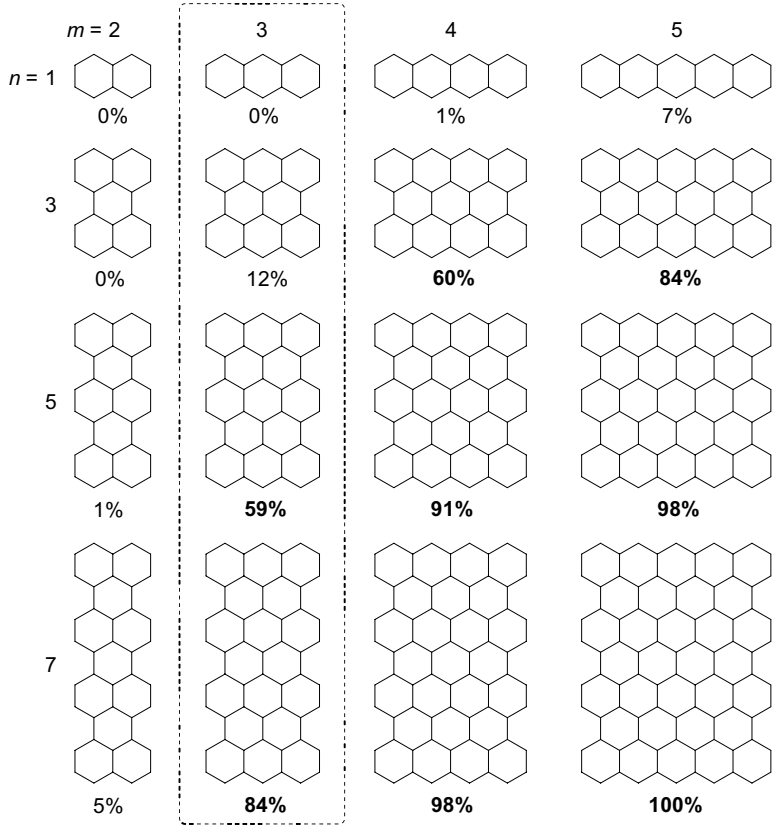


**Figure 5.19** Periacenes as a model system to investigate the edge state. The numericals below the molecules indicate singlet diradical character $y_0$. The dashed line encloses anthenes.

### 5.3.4 Molecular Structure of Anthenes

X-ray structures of **15**, **16**, and **17a** are shown in Figure 5.21. It is noteworthy that the bond length at the center of the molecule becomes shorter as the size of the compound increases. The ground state of anthenes can be described as a resonance hybrid of the Kekulé structure (closed-shell structure) and the diradical structure (open-shell structure), as shown in Figure 5.22. The increase of $y_0$ means larger contribution of the diradical structure in the ground state, and then, the central bonds (denoted with ***a*** in Figure 5.22) bears

larger double bond character. The experimentally observed changes in the bond lengths indicate an increase in $y_0$ with the elongation of the system. The harmonic oscillator model of aromaticity (HOMA) [45, 46], which is used as an indicator of aromaticity, shows that the hexagon rings at the periphery of the molecule are closer to 1 in **16** and **17a**, supporting larger diradical contribution in the ground state.

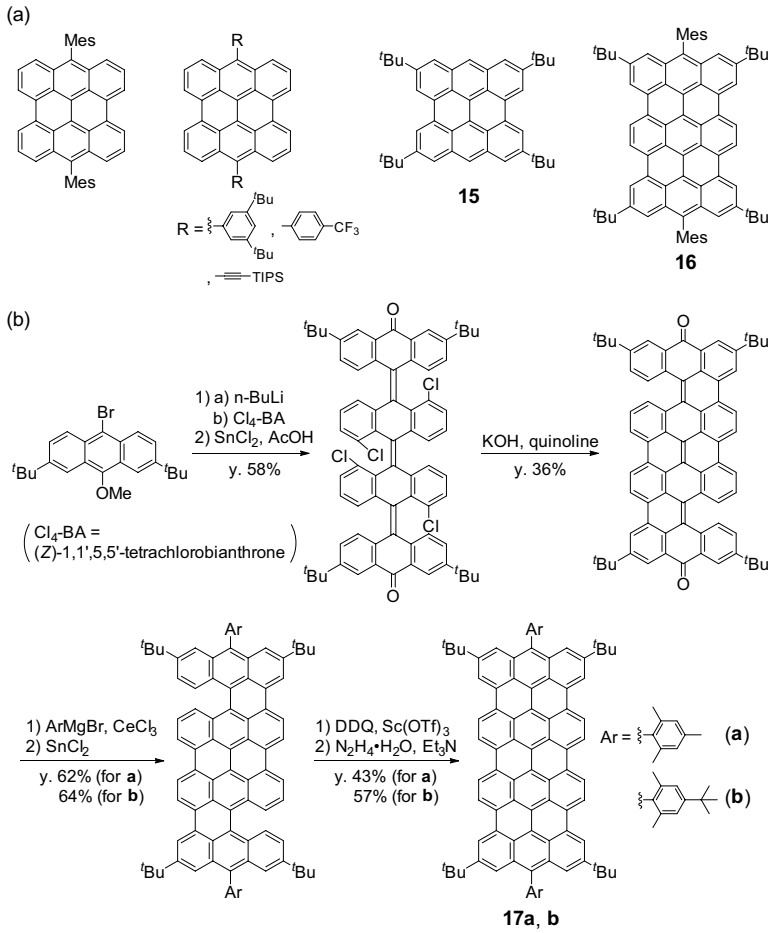


**Figure 5.20** (a) Bisanthenes and teranthene are isolated in crystalline forms; (b) Synthetic route to quateranthene.

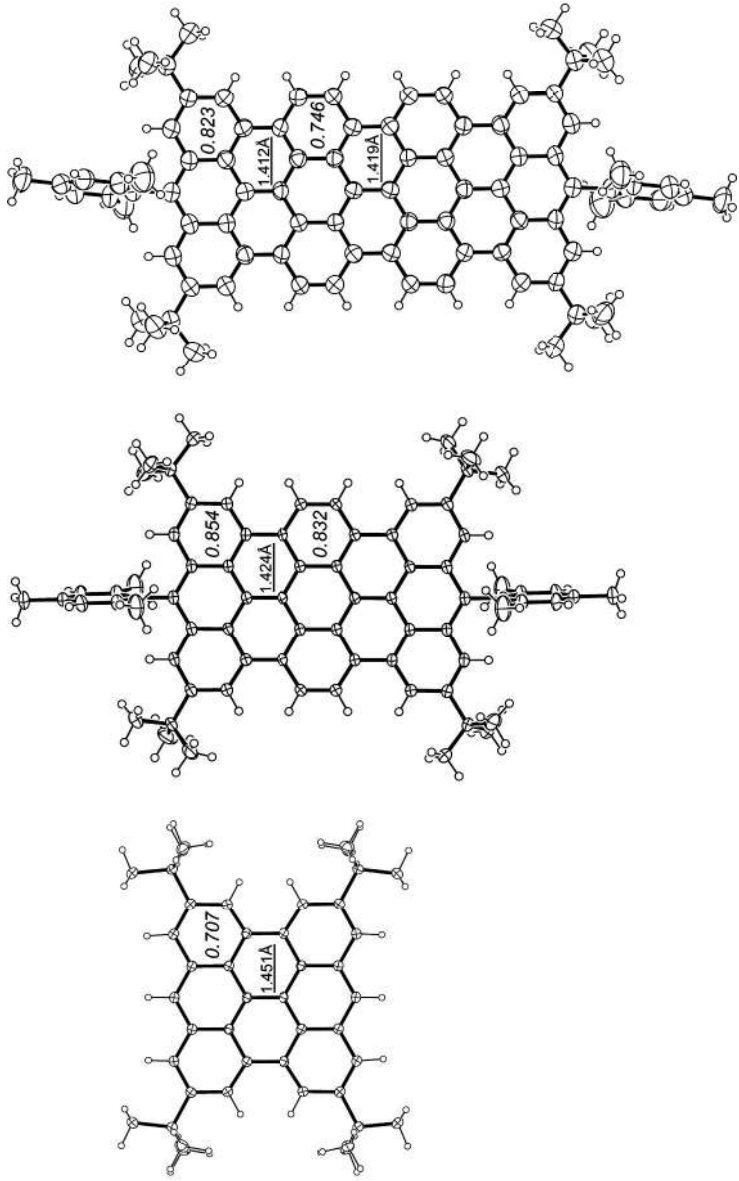


**Figure 5.21** ORTEP drawing of **15**, **16,** and **17a**. The numericals represent the length of the central bonds (underlined) and HOMA values (italic).

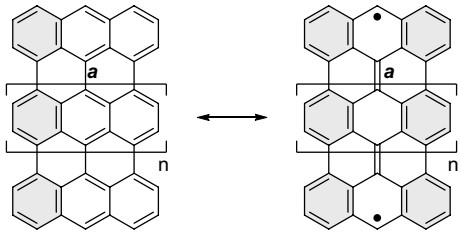


Bisanthene (n=0), $y_0$ = 12%
Teranthene (n=1), $y_0$ = 59%
Quateranthene (n=2), $y_0$ = 84%

**Figure 5.22** Resonance formula of anthenes. The diradical index $y_0$ is calculated at the UBHandHLYP/6-31G* level. The hexagons shaded in gray represent benzene rings that enjoy aromatic stabilization energy.

### 5.3.5 Magnetic Properties of Anthenes

Intrinsically, magnetic properties of singlet diradical molecules cannot be measured because of strong antiferromagnetic coupling of two unpaired electrons. Instead, the presence of thermally excited triplet species is a good criterion for a singlet diradical state. Because the $^1$H NMR signals of **15** does not broaden at 110 °C [42], no magnetic triplet species are generated even at high temperatures. Therefore, bisanthene can be considered to behave basically as a closed-shell species. Indeed, the electrochemically and optically estimated HOMO–LUMO gaps are relatively large, about 1.7–1.9 eV, supporting the small diradical character. On the other hand, the $^1$H NMR signals of teranthene **16** are severely broadened at room temperature (Figure 5.23) [43], suggesting the presence of thermally excited triplet species. The line sharpening of the signals at low temperatures confirms that the ground state of **16** is the singlet state. The energy difference between the ground singlet and excited triplet states ($\Delta E_{S\text{-}T}$) is found to be about −1920 K (= −16 kJ/mol) by SQUID measurements, which is much smaller than that of the usual closed-shell molecules. In quateranthene **17b**, the $^1$H NMR signals do not become sharper even at low temperatures and the $\Delta E_{S\text{-}T}$ is only −347 K (= −2.89 kJ/mol) from SQUID measurements (Figure 5.23) [44], indicating that two unpaired electrons behave almost independently. The substantially small $\Delta E_{S\text{-}T}$ of teranthene

and quateranthene, that is, very weak coupling of electrons, strongly support the edge localization of unpaired electrons in large anthenes.

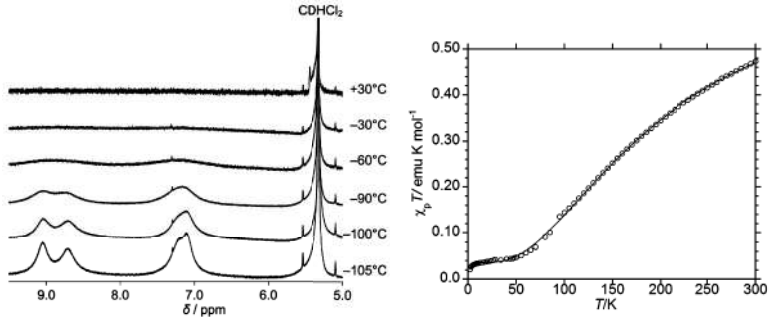


**Figure 5.23** (Left) Variable temperature $^1$H NMR spectra of **16** in $CD_2Cl_2$ in the aromatic region [43]; (Right) $\chi_pT$–$T$ plot for powdered **17a** [44].

### 5.3.6 Optical Properties of Anthenes

Figure 5.24 shows the electronic absorption spectra of **15**, **16**, and **17b**. The longest-wavelength absorption band of **15** is typical in profile for usual aromatic compounds. On the other hand, the spectra of **16** and **17b** show completely different aspects, and are characterized by very weak absorption bands (1054 nm for **16** and 1147 nm for **17b**) in the near-infrared (NIR) region. The weak NIR bands observed in **16** and **17b** are assignable to a HOMO,HOMO → LUMO,LUMO double excitation by a strongly contracted second-order *n*-electron valence state perturbation theory (NEVPT2) calculation that allows multi-electron excitation [47]. The presence of a low-lying excited singlet state dominated by the doubly excited configuration is characteristic feature of singlet diradical compounds [48]. Because the electronic state reached by double excitation is the $A_g$ state, absorptions related to the double excitation are one-photon-forbidden but two-photon-allowed process. TPA measurements show a broad band at around 2300 nm, which is the same excitation energy as that of the one-photon band at 1147 nm. Thus, the weak NIR bands observed in **16** and **17b** are associated with the simultaneous excitation of the edge-localized electrons.

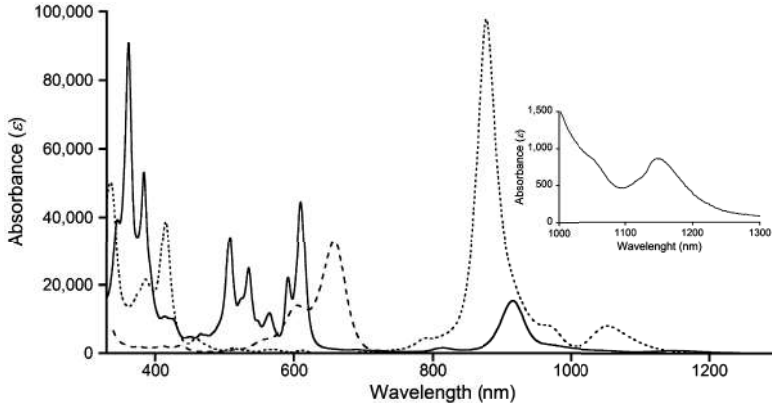


**Figure 5.24** One-photon electronic absorption spectra of **15** (hashed line), **16** (dotted line), and **17b** (solid line). The inset indicates the weak band of **17b** derived from the HOMO–LUMO double excitation.

### 5.3.7 Mechanism of Diradical Character in Anthenes

The ground state of anthenes is described by the resonance structure, as shown in Figure 5.22. With the transformation from the Kekulé structure (left-hand side of Figure 5.22) to the diradical structure (right-hand side), one π-bond is cleaved to produce two unpaired electrons. This cleavage results in destabilization energy of 270 kJ/mol [49]. On the other hand, because the number of benzene rings (the bold rings in Figure 5.22) increases, the stabilization energy is also increased by ensuring aromaticity. As the system enlarges (i.e., as *n* increases), the difference in the number of benzene rings in the Kekulé and diradical structures increases, and aromatic stabilization eventually exceeds destabilization by cleavage of a π-bond. Considering that the aromatic stabilization energy is about 90 kJ/mol (based on the homodesmic stabilization energy) [50], a balance between destabilization and stabilization is expected to be achieved when the difference is three, and the contribution of the Kekulé and diradical structures becomes equal. Teranthene is in exactly that situation, which is in good agreement with the experimental observations that indicate the onset of diradicaloid behavior. Because the contribution of the diradical structure is larger in quateranthene, it can be interpreted as a clear indication of the open-shell nature.

### 5.3.8 Lateral Extension from Anthenes

The mechanism of the energy balance is applicable to the diradical character of the system larger in the lateral direction (i.e., $m$ = 4 and 5, in Figure 5.19). For example, in peritetracene ($m$ = 4, $n$ = 3), the difference of the number of the aromatic hexagon rings between the Kekulé and diradical structures is three, leading to the open-shell singlet ground state. The diradical index $y_0$ of peritetracene is almost identical to that of teranthene. Recently peritetracene was synthesized by two independent groups at almost the same time (Figure 5.25) [51, 52]. Indeed, a tetra-substituted peritetracene **18** possesses characteristic features of diradicaloids, such as a small HOMO–LUMO gap (1.31 eV, from electrochemical measurement), a very weak NIR absorption band (1010 nm) derived from a HOMO,HOMO → LUMO,LUMO double excitation, signal broadening in $^1$H NMR spectrum, and small $\Delta E_{S\text{-}T}$ (–10.5 kJ/mol).

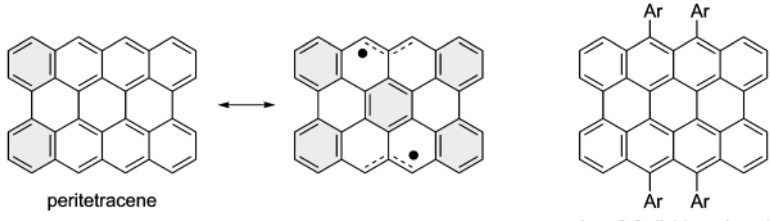


**Figure 5.25** Peritetracene. The hexagons shaded in gray represent benzene rings that enjoy aromatic stabilization energy.

Peritetracene is subjected to Diels-Alder reactions with dienophiles at the bay region [53] to yield mono-adducts **20** and bis-adducts **21** (Figure 5.26). The Diels-Alder adducts that are equipped with a dichloroquinoid ring show a feature of diradicaloids, that is, small $\Delta E_{S\text{-}T}$ values (–7.3 to –15 kJ/mol) and weak NIR absorption bands (approximately 1000 nm). Similar addition reactions have been observed in Diels-Alder reactions of the mesityl-substituted bisanthene (Figure 5.20a) with dienophiles [40, 54]. The bis-adducts **21**, which are called circumanthracenes, have been predicted to possess a larger HOMO–LUMO gap than peritetracene by a DFT calculation [55], which is consistent with theoretically estimated

diradical indices that decrease with increasing the number of ring annulation at the bay region of peritetracene [53].

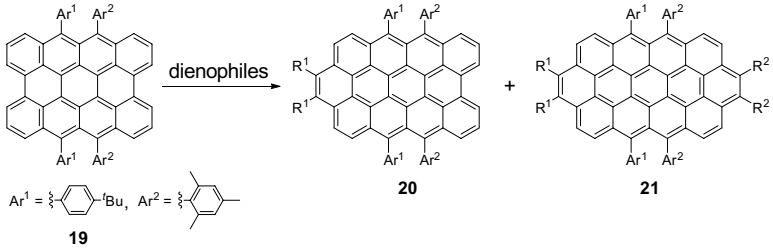


**Figure 5.26** Diels-Alder reactions of peritetracene **19**.

The isolation of peripentacene ($m$ = 5, $n$ = 3) in a crystalline form has not yet been successful although some attempts have been done by several research groups [56, 57]. Peripentacene **23** was first detected in a mass spectrometry through the ionization process of pentacene [58]. The generation mechanism of **23** has been investigated by DFT calculations [59]. **23** is also prepared by on-surface synthesis on a Au(111) surface and its structure is imaged by a non-contact atomic force microscopy (nc-AFM) [60], as shown in Figure 5.27.

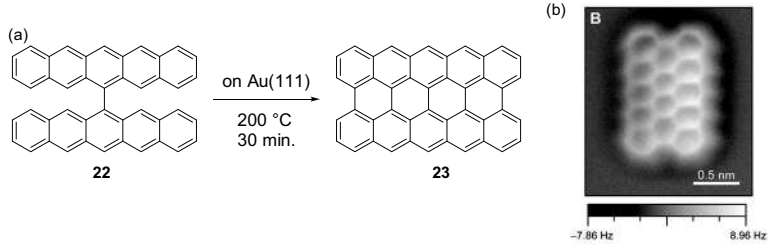


**Figure 5.27** (a) Generation of peripentacene **23** from the 6,6'-bipentacene precursor **22**; (b) nc-AFM image of **23**. After ref. [60].

## 5.3.9 Other Model Systems of Graphene

The rectangular models, such as periacenes, possess both zigzag and armchair edges. Recently, another type of graphene-like molecules, in which all the peripheries are zigzag-edged, have been synthesized and isolated in crystalline forms [61, 62]. These parallelogram-

shaped models are referred to as periacenoacenes (Figure 5.28). Periacenoacenes potentially behave as diradicaloids because there are several quinoid structures in the molecules. However, based on resonance structure consideration, periacenoacenes benefit from fewer aromatic hexagon rings (shaded rings in Figure 5.29) in the diradical form compared to periacenes with the same size.

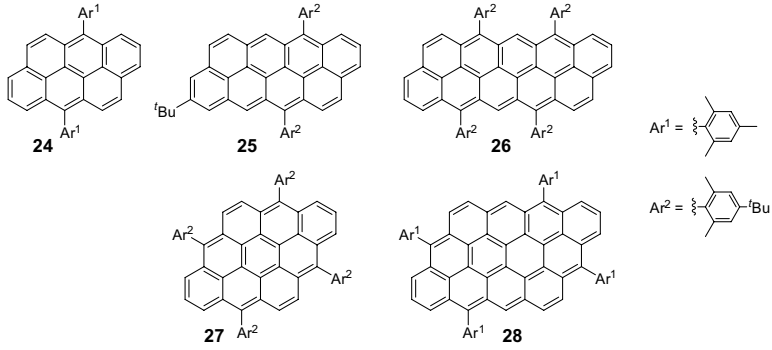


**Figure 5.28** Periacenoacenes.

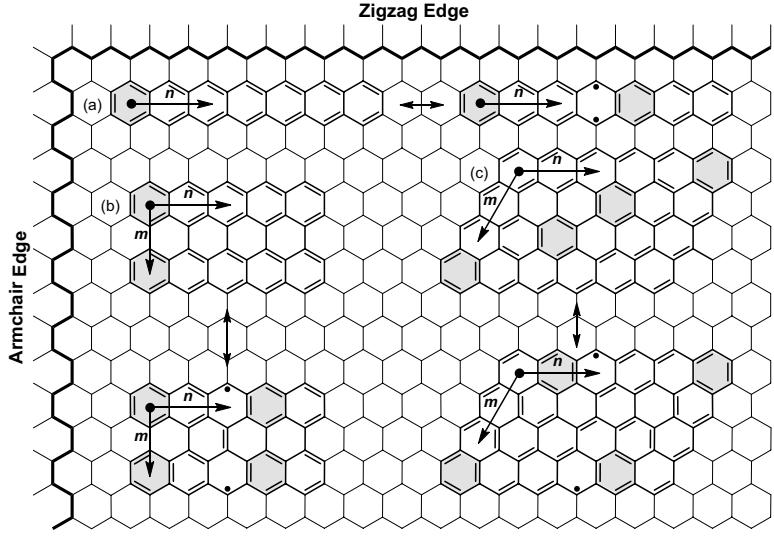


**Figure 5.29** Model systems for investigating the edge state: (a) Acenes, (b) periacenes, and (c) periacenoacenes [61].

A series of periacenoacenes, **24**–**28**, has been prepared and isolated in crystalline forms. As predicted by the resonance structure, all the periacenoacens isolated show non-diradicaloid behaviors like sharp $^1$H NMR signals even at high temperatures and relatively large HOMO–LUMO gaps. Absorption bands derived from the HOMO–LUMO transition of **24**–**28** resemble those of usual closed-shell polycyclic aromatic hydrocarbons (PAHs) in appearance. Further π-extension would be required to grasp diradical character experimentally for periacenoacenes. It is noteworthy that periacenoacenes exhibit a strong diamagnetic ring current in the periphery of the molecule, leading to global aromaticity.

In addition to zigzag and armchair edges, graphene has another edge structure, cove edge, as shown in Figure 5.30. Recently, cove-edged graphene-like molecules, **29** and **30**, have been prepared and investigated [63]. The cove-edged compounds, corresponding to a model system that some zigzag edges are removed from periacenes, possess a π-conjugated system consisted only with benzene rings and ethylene double bonds. Therefore, a cove-edged system intrinsically behaves as non-diradicaloids. Indeed, **29** and **30** show sharp $^1$H NMR signals and relatively large HOMO–LUMO gaps.

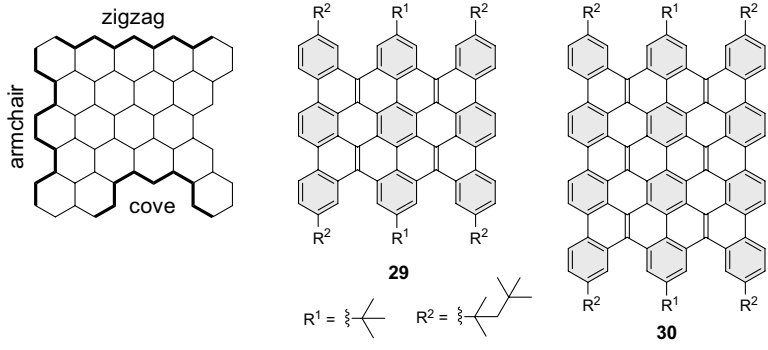


**Figure 5.30** Cove-edged graphene-like molecules. The hexagons shaded in gray represent benzene rings that enjoy aromatic stabilization energy.

Laterally extended cove-edged graphene-like molecules **31** have also been prepared (Figure 5.31) [64]. **31** ($n$ = 0, 1) possesses large HOMO–LUMO gaps (2.36 eV, 1.90 eV, respectively), indicating non-diradicaloid character. The structural feature of cove-edged graphene-like molecules is helical conformation (i.e., up and down)

at cove-edges because the those molecules contain a [4]helicene substructure. Therefore, cove-edged graphene-like molecules can potentially behave as chiral compounds.

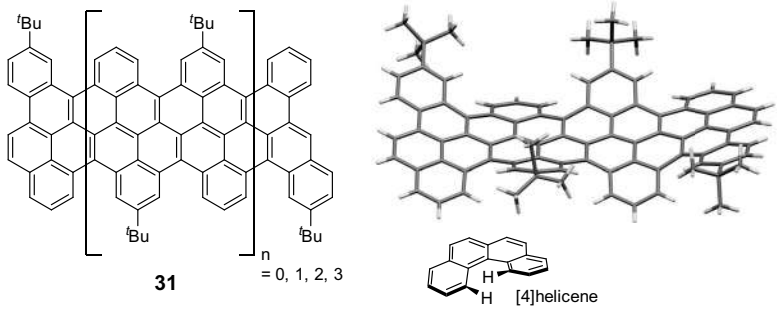


**Figure 5.31** Laterally extended cove-edged graphene-like molecules **31**. Right figure indicates crystal structure of **31** (*n* = 1).

## 5.4 Summary

In this chapter, phenomenological features of polycyclic aromatic hydrocarbons were summarized in terms of diradical character. Recent studies by various chemists have revealed that diradicaloid nature is a relatively universal property of π-conjugated quinoid compounds. At the same time, it is quite certain that fundamental issues still remain to be answered. For instance, how can we figure out what are novel and unique phenomena that derive from diradical character? A strong collaboration among synthetic organic chemists, physical chemists, and theoretical chemists is the key to the formidable challenges.

## References

1. Bausch, M. J., Gostowski, R., Jirka, G., Selmarten, D., and Winter, G. (1990). Dimethyl sulfoxide phase carbon-hydrogen bond dissociation energies for phenalene and benzanthrene, *J. Org. Chem.*, **55**, pp. 5805–5806.
2. Zheng, S., Lan, J., Khan, S. I., and Rubin, Y. (2003). Synthesis, characterization, and coordination chemistry of the 2-azaphenalenyl radical, *J. Am. Chem. Soc.*, **125**, pp. 5786–5791.

3. Szwarc, M. (1947). Some remarks on the $CH_2$[benzene]$CH_2$ molecule, *Discuss. Faraday Soc.*, **2**, pp. 46–49.
4. Trahanovsky, W. S. and Lorimor, S. P. (2006). Room temperature observation of *p*-xylylenes by $^1$H NMR and evidence for diradical intermediates in their oligomerization, *J. Org. Chem.*, **71**, pp. 1784–1794.
5. Brown, C. J. and Farthing, A. C. (1949). Preparation and sructure of di-*p*-xylylene, *Nature*, **164**, pp. 915–916.
6. Doehnert, D. and Koutecky, J. (1980). Occupation numbers of natural orbitals as a criterion for biradical character: Different kinds of biradicals, *J. Am. Chem. Soc.*, **102**, pp. 1789–1796.
7. Ohashi, K., Kubo, T., Masui, T., Yamamoto, K., Nakasuji, K., Takui, T., Kai, Y., and Murata, I. (1998). 4,8,12,16-Tetra-*tert*-butyl-*s*-indaceno[1,2,3-*cd*:5,6,7-*c'd'*]diphenalene: A four-stage amphoteric redox system, *J. Am. Chem. Soc.*, **120**, pp. 2018–2027.
8. Kubo, T., Shimizu, A., Sakamoto, M., Uruichi, M., Yakushi, K., Nakano, M., Shiomi, D., Sato, K., Takui, T., Morita, Y., and Nakasuji, K. (2005). Synthesis, intermolecular interaction, and semiconductive behavior of a delocalized singlet biradical hydrocarbon, *Angew. Chem. Int. Ed.*, **44**, pp. 6564–6568.
9. Wehrmann, C. M., Charlton, R. T., and Chen, M. S. (2019). A concise synthetic strategy for accessing ambient stable bisphenalenyls toward achieving electroactive open-shell π-conjugated materials, *J. Am. Chem. Soc.*, **141**, pp. 3240–3248.
10. Goto, K., Kubo, T., Yamamoto, K., Nakasuji, K., Sato, K., Shiomi, D., Takui, T., Kubota, M., Kobayashi, T., Yakusi, K., and Ouyang, J. (1999). A stable neutral hydrocarbon radical: Synthesis, crystal structure, and physical properties of 2,5,8-tri-*tert*-butyl-phenalenyl, *J. Am. Chem. Soc.*, **121**, pp. 1619–1620.
11. Mou, Z., Uchida, K., Kubo, T., and Kertesz, M. (2014). Evidence of σ- and π-dimerization in a series of phenalenyls, *J. Am. Chem. Soc.*, **136**, pp. 18009–18022.
12. Cui, Z. H., Lischka, H., Beneberu, H. Z., and Kertesz, M. (2014). Rotational barrier in phenalenyl neutral radical dimer: Separating pancake and van der Waals interactions, *J. Am. Chem. Soc.*, **136**, pp. 5539–5542.
13. Huang, J. and Kertesz, M. (2007). Intermolecular covalent π-π bonding interaction indicated by bond distances, energy bands, and magnetism in biphenalenyl biradicaloid molecular crystal, *J. Am. Chem. Soc.*, **129**, pp. 1634–1643.

14. Chikamatsu, M., Mikami, T., Chisaka, J., Yoshida, Y., Azumi, R., Yase, K., Shimizu, A., Kubo, T., Morita, Y., and Nakasuji, K. (2007). Ambipolar organic field-effect transistors based on a low band gap semiconductor with balanced hole and electron mobilities, *Appl. Phys. Lett.*, **91**, pp. 043506–1–3.
15. Kubo, T., Shimizu, A., Uruichi, M., Yakushi, K., Nakano, M., Shiomi, D., Sato, K., Takui, T., Morita, Y., and Nakasuji, K. (2007). Singlet biradical character of phenalenyl-based Kekulé hydrocarbon with naphthoquinoid structure, *Org. Lett.*, **9**, pp. 81–84.
16. Shimizu, A., Hirao, Y., Matsumoto, K., Kurata, H., Kubo, T., Uruichi, M., and Yakushi, K. (2012). Aromaticity and π-bond covalency: Prominent intermolecular covalent bonding interaction of a Kekulé hydrocarbon with very significant singlet biradical character, *Chem. Commun*., **48**, pp. 5629–5631.
17. Shimizu, A., Kubo, T., Uruichi, M., Yakushi, K., Nakano, M., Shiomi, D., Sato, K., Takui, T., Hirao, Y., Matsumoto, K., Kurata, H., Morita, Y., and Nakasuji, K. (2010). Alternating covalent bonding interactions in a one-dimensional chain of a phenalenyl-based singlet biradical molecule having Kekulé structures, *J. Am. Chem. Soc.*, **132**, pp. 14421–14428.
18. Kamada, K., Ohta, K., Kubo, T., Shimizu, A., Morita, Y., Nakasuji, K., Kishi, R., Ohta, S., Furukawa, S., Takahashi, H., and Nakano, M. (2007). Strong two-photon absorption of singlet diradical hydrocarbons, *Angew. Chem. Int. Ed*., **46**, pp. 3544–3546.
19. Errede, L. A. (1961). The chemistry of xylylenes, VIII: The formation of spiro-di-*o*-xylylene and related compounds 1, *J. Am. Chem. Soc.*, **83**, pp. 949–954.
20. Flynn, C. R. and Michl, J. (1973). Photochemical preparation of *o*-xylylene from 1,3-dihydrophthalazine in rigid glass, *J. Am. Chem. Soc.*, **95**, pp. 5802–5803.
21. Trahanovsky, W. S., Chou, C. H., Fischer, D. R., and Gerstein, B. C. (1988). Observation of reactive *o*-quinodimethanes by flow NMR, *J. Am. Chem. Soc.*, **110**, pp. 6579–6581.
22. Cava, M. P. and Deana, A. A. (1959). Condensed cyclobutane aromatic compounds, VI. The pyrolysis of 1,3-dihydroisothianaphthene-2,2-dioxide: A new synthesis of benzocyclobutene 1, *J. Am. Chem. Soc.*, **81**, pp. 4266–4268.
23. Ravat, P., Šolomek, T., Häussinger, D., Blacque, O., and Juríček, M. (2018). Dimethylcethrene: A chiroptical diradicaloid photoswitch, *J. Am. Chem. Soc.*, **140**, pp. 10839–10847.

24. Šolomek, T., Ravat, P., Mou, Z., Kertesz, M., and Juríček, M. (2018). Cethrene: The chameleon of Woodward–Hoffmann rules, *J. Org. Chem.*, **83**, pp. 4769–4774.

25. Zaitsev, V., Rosokha, S. V, Head-Gordon, M., and Kochi, J. K. (2006). Steric modulations in the reversible dimerizations of phenalenyl radicals via unusually weak carbon-centered π- and σ-bonds, *J. Org. Chem.*, **71**, 520–526.

26. Reid, D. H. (1965). The chemistry of the phenalenes, *Q. Rev. Chem. Soc.*, **19**, pp. 274–302.

27. Small, D., Zaitsev, V., Jung, Y., Rosokha, S. V., Head-Gordon, M., and Kochi, J. K. (2004). Intermolecular π-to-π bonding between stacked aromatic dyads: Experimental and theoretical binding energies and near-IR optical transitions for phenalenyl radical/radical versus radical/cation dimerizations, *J. Am. Chem. Soc.*, **126**, pp. 13850–13858.

28. Suzuki, S., Morita, Y., Fukui, K., Sato, K., Shiomi, D., Takui, T., and Nakasuji, K. (2006). Aromaticity on the pancake-bonded dimer of neutral phenalenyl radical as studied by MS and NMR spectroscopies and NICS analysis, *J. Am. Chem. Soc.*, **128**, pp. 2530–2531.

29. Fukui, K., Sato, K., Shiomi, D., Takui, T., Itoh, K., Gotoh, K., Kubo, T., Yamamoto, K., Nakasuji, K., and Naito, A. (1999). Electronic structure of a stable phenalenyl radical in crystalline state as studied by SQUID measurements, cw-ESR, and $^{13}C$ CP/MAS NMR spectroscopy, *Synth. Met.*, **103**, pp. 2257–2258.

30. Miller, J. S. (2007). Four-center carbon–carbon bonding, *Acc. Chem. Res.*, **40**, pp. 189–196.

31. Mulliken, R. S. and Person, W. B. (1969). Molecular complexes, John Wiley & Sons, New York.

32. Takano, Y., Taniguchi, T., Isobe, H., Kubo, T., Morita, Y., Yamamoto, K., Nakasuji, K., Takui, T., and Yamaguchi, K. (2002). Hybrid density functional theory studies on the magnetic interactions and the weak covalent bonding for the phenalenyl radical dimeric pair, *J. Am. Chem. Soc.*, **124**, pp. 11122–11130.

33. Uchida, K., Hirao, Y., Kurata, H., Kubo, T., Hatano, S., and Inoue, K. (2014). Dual association modes of the 2,5,8-tris(pentafluorophenyl) phenalenyl radical, *Chem. Asian J.*, **9**, pp. 1823–1829.

34. Mou, Z., Uchida, K., Kubo, T., and Kertesz, M. (2014). Evidence of σ- and π-dimerization in a series of phenalenyls, *J. Am. Chem. Soc.*, **136**, pp. 18009–18022.

35. Uchida, K., Mou, Z., Kertesz, M., and Kubo, T. (2016). Fluxional σ-bonds of the 2,5,8-trimethylphenalenyl dimer: Direct observation of the sixfold σ-bond shift via a π-dimer, *J. Am. Chem. Soc.*, **138**, pp. 4665–4672.

36. Novoselov, K. S., Geim, A. K., Morozov, S. V., Jiang, D., Zhang, Y., Dubonos, S. V., Grigorieva, I. V., and Firsov, A. A. (2004). Electric field in atomically thin carbon films, *Science*, **306**, pp. 666–669.

37. Tanaka, K., Yamashita, S., Yamabe, H., and Yamabe, T. (1987). Electronic properties of one-dimensional graphite family, *Synth. Met.*, **17**, pp. 143–148.

38. Fujita, M., Wakabayashi, K., Nakada, K., and Kusakabe, K. (1996). Peculiar localized state at zigzag graphite edge, *J. Phys. Soc. Japan*, **65**, pp. 1920–1923.

39. Kobayashi, Y., Fukui, K., Enoki, T., Kusakabe, K., and Kaburagi, Y. (2005). Observation of zigzag and armchair edges of graphite using scanning tunneling microscopy and spectroscopy, *Phys. Rev. B*, **71**, pp. 193406–1–4.

40. Fort, E. H., Donovan, P. M., and Scott, L. T. (2009). Diels-Alder reactivity of polycyclic aromatic hydrocarbon bay regions: Implications for metal-free growth of single-chirality carbon nanotubes, *J. Am. Chem. Soc.*, **131**, pp. 16006–16007.

41. Li, J., Zhang, K., Zhang, X., Huang, K.-W., Chi, C., and Wu, J. (2010). *Meso*-substituted bisanthenes as soluble and stable near-infrared dyes, *J. Org. Chem.*, **75**, pp. 856–863.

42. Hirao, Y., Konishi, A., Matsumoto, K., Kurata, H., and Kubo, T. (2012). Synthesis and electronic structure of bisanthene: A small molecular-sized graphene with zigzag edges, *AIP Conf. Proc.*, **1504**, pp. 863–866.

43. Konishi, A., Hirao, Y., Nakano, M., Shimizu, A., Botek, E., Champagne, B., Shiomi, D., Sato, K., Takui, T., Matsumoto, K., Kurata, H., and Kubo T. (2010). Synthesis and characterization of teranthene: A singlet biradical polycyclic aromatic hydrocarbon having Kekulé structures, *J. Am. Chem. Soc.*, **132**, pp. 11021–11023.

44. Konishi, A., Hirao, Y., Matsumoto, K., Kurata, H., Kishi, R., Shigeta, Y., Nakano, M., Tokunaga, K., Kamada, K., and Kubo, T. (2013). Synthesis and characterization of quarteranthene: elucidating the characteristics of the edge state of graphene nanoribbons at the molecular level, *J. Am. Chem. Soc.*, **135**, pp. 1430–1437.

45. Kruszewski, J. and Krygowski, T. M. (1972). Definition of aromaticity basing on the harmonic oscillator model, *Tetrahedron Lett.*, **13**, pp. 3839–3842.

46. Krygowski, T. M. (1993). Crystallographic studies of inter- and intramolecular interactions reflected in aromatic character of π-electron systems, *J. Chem. Inf. Model.*, **33**, pp. 70–78.
47. Angeli, C., Pastore, M., and Cimiraglia, R. (2007). New perspectives in multireference perturbation theory: The n-electron valence state approach, *Theor. Chem. Acc.*, **117**, pp. 743–754.
48. Di Motta, S., Negri, F., Fazzi, D., Castiglioni, C., and Canesi, E. V. (2010). Biradicaloid and polyenic character of quinoidal oligothiophenes revealed by the presence of a low-lying double-exciton state, *J. Phys. Chem. Lett.*, **1**, pp. 3334–3339.
49. Douglas, J. E., Rabinovitch, B. S., and Looney, F. S. (1955). Kinetics of the thermal cis-trans isomerization of dideuteroethylene, *J. Chem. Phys.*, **23**, pp. 315–323.
50. Slayden, S. W. and Liebman, J. F. (2001). The energetics of aromatic hydrocarbons: An experimental thermochemical perspective, *Chem. Rev.*, **101**, pp. 1541–1566.
51. Ni, Y., Gopalakrishna, T. Y., Phan, H., Herng, T. S., Wu, S., Han, Y., Ding, J., and Wu, J. (2018). A peri-tetracene diradicaloid: Synthesis and properties, *Angew. Chem. Int. Ed.*, **57**, pp. 9697–9701.
52. Ajayakumar, M. R., Fu, Y., Ma, J., Hennersdorf, F., Komber, H., Weigand, J. J., Alfonsov, A., Popov, A. A., Berger, R., Liu, J., Müllen, K., and Feng, X. (2018). Toward full zigzag-edged nanographenes: *peri*-tetracene and its corresponding circumanthracene, *J. Am. Chem. Soc.*, **140**, pp. 6240–6244.
53. Ajayakumar, M. R., Fu, Y., Liu, F., Komber, H., Tkachova, V., Xu, C., Zhou, S., Popov, A. A., Liu, J., and Feng, X. (2020). Tailoring magnetic features in zigzag-edged nanographenes by controlled Diels–Alder reactions, *Chem. Eur. J.*, **26**, pp. 7497–7503.
54. Konishi, A., Hirao, Y., Matsumoto, K., Kurata, H., and Kubo, T. (2013). Facile synthesis and lateral π-expansion of bisanthenes, *Chem. Lett.*, **42**, pp. 592–594.
55. Jiang, D. and Dai, S. (2008). Circumacenes versus periacenes: HOMO–LUMO gap and transition from nonmagnetic to magnetic ground state with size, *Chem. Phys. Lett.*, **466**, pp. 72–75.
56. Zhang, X., Li, J., Qu, H., Chi, C., and Wu, J. (2010). Fused bispentacenequinone and its unexpected Michael addition, *Org. Lett.*, **12**, pp. 3946–3949.
57. Zöphel, L., Berger, R., Gao, P., Enkelmann, V., Baumgarten, M., Wagner, M., and Müllen, K. (2013). Toward the *peri*-pentacene framework, *Chem. Eur. J.*, **19**, pp. 17821–17826.

58. Roberson, L. B., Kowalik, J., Tolbert, L. M., Kloc, C., Zeis, R., Chi, X., Fleming, R., and Wilkins, C. (2005). Pentacene disproportionation during sublimation for field-effect transistors, *J. Am. Chem. Soc.*, **127**, pp. 3069–3075.

59. Northrop, B. H., Norton, J. E., and Houk, K. N. (2007). On the mechanism of peripentacene formation from pentacene: Computational studies of a prototype for graphene formation from smaller acenes, *J. Am. Chem. Soc.*, **129**, pp. 6536–6546.

60. Rogers, C., Chen, C., Pedramrazi, Z., Omrani, A. A., Tsai, H. Z., Jung, H. S., Lin, S., Crommie, M. F., and Fischer, F. R. (2015). Closing the nanographene gap: Surface-assisted synthesis of peripentacene from 6,6′-bipentacene precursors, *Angew. Chem. Int. Ed.*, **54**, pp. 15143–15146.

61. Gu, Y., Tullimilli, Y. G., Feng, J., Phan, H., Zeng, W., and Wu, J. (2019). *peri*-Acenoacenes, *Chem. Commun.*, **55**, pp. 5567–5570.

62. Gu, Y., Wu, X., Gopalakrishna, T. Y., Phan, H., and Wu, J. (2018). Graphene-like molecules with four zigzag edges, *Angew. Chem. Int. Ed.,* **57**, pp. 6541–6545.

63. Gu, Y., Muñoz-Mármol, R., Wu, S., Han, Y., Ni, Y., Díaz-García, M.A., Casado, J., and Wu, J. (2020). Cove-edged nanographenes with localized double bonds, *Angew. Chem. Int. Ed.*, **59**, pp. 8113–8117.

64. Liu, J., Li, B.-W., Tan, Y.-Z., Giannakopoulos, A., Sanchez-Sanchez, C., Beljonne, D., Ruffieux, P., Fasel, R., Feng, X., and Müllen, K. (2015). Toward cove-edged low band gap graphene nanoribbons, *J. Am. Chem. Soc.*, **137**, pp. 6097–6103.

## Chapter 6

# Zethrenes and Related Molecules

**Wangdong Zeng and Jishan Wu**
*Department of Chemistry, National University of Singapore,*
*3 Science Drive 3, 117543, Singapore*
chmwuj@nus.edu.sg

This chapter provides a brief summary of zethrene-based diradicaloids. Zethrenes are a family of Z-shaped benzenoid polycyclic hydrocarbons, which contain isolated C–C double bonds or quinodimethane moieties. The vertically and laterally extended zethrenes show unusual open-shell diradical character and magnetic activity. They are synthesized by different methods and stabilized by both thermodynamic and kinetic strategies. The fundamental structure-diradical character-physical property relationships are investigated. The synthesis, chemical reactivities, and electronic properties of some zethrenes isomers are also discussed.

## 6.1 Pioneers of Zethrene Chemistry

Zethrene (**1**, Scheme 6.1a), which can be regarded as a Z-shaped polycyclic hydrocarbon with fusion of two phenalenyl moieties,

*Diradicaloids*
Edited by Jishan Wu

ISBN 978-981-4968-08-9 (Hardcover), 978-1-003-27724-8 (eBook)
www.jennystanford.com

was first reported by Clar et al. in 1955 [1]. The precursor **2** was synthesized by multiple condensation, cyclization, decarboxylation and reduction reactions, and subsequent dehydrogenation by Pd/C gave **1**. Zethrene crystallized as deep violet needles from xylene were decolorized in light and air. It showed absorption maximum at 550 nm in benzene solution and reacted with maleic anhydride to form colorless adduct moiety. In 1968, Mitchell and Sondheimer found that the 1,2,3:6,7,8-di(1′,8′-naphth)[10] annulene (**3**) was gradually converted into the zethrene (**1**) in the air (Scheme 6.1b) [2], which may involve an initial isomerization into 7, 14-dihydrozethrene, followed by further oxidative dehydrogenation. In the same year, Staab et al. reported that coupling of the copper compound **4** resulted in the formation of the zethrene (**1**), rather than the expected tetradehydrodinaphtho [10] annulene **5** (Scheme 6.1c) [3]. In 1970, Mitchell and Sondheimer demonstrated that coupling of the di-cuprous derivative **6** with 1,8-diiodonaphthalene (**7**), or the intramolecular coupling of mono-cuprous mono-iodo compound **8**, all gave identical product, zethrene (**1**) (Scheme 6.1d) [4]. Therefore, zethrene could possibly be formed from the intermediate **5**, which is unstable and can undergo spontaneous transannular cyclization.

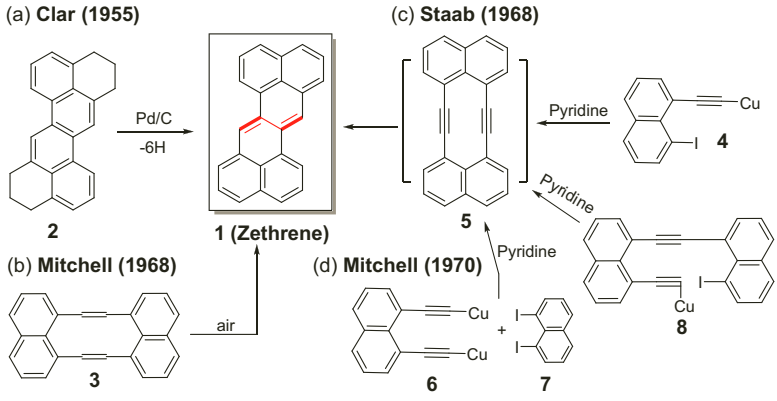


**Scheme 6.1** Pioneering syntheses of the parent zethrene.

Clar et al. then attempted the synthesis of extended zethrene, the heptazethrene **10** containing seven condensed benzenoid rings, by oxidative dehydrogenation of the 7,15-dihydro-heptzethene

precursor **9** with *p*-chloranil (Scheme 6.2a) [5]. The parent heptazethrene was obtained as a green solid, with an absorption maximum at 586 nm in solution. However, it is very reactive and can be easily protonated by hydrochloric acid and oxidized into heptazethrene-quinone. Clar et al. also attempted to synthesize the heptazethrene isomer **12** by oxidative dehydrogenation of the 5,7-dihydro-1,14:11,12-dibenzopentacene precursor **11** in boiling trichlorobenzene, but an insoluble, non-sublimable, chlorine-containing condensation product was formed, which could possibly be the polymers formed by a radical-radical coupling reaction of the in situ generated open-shell triplet diradicals. In 1963, Clar et al. reported the synthesis of a laterally extended 5,6-benzozethrene **14** via oxidative dehydrogenation of its tetrahydroderivative **15**

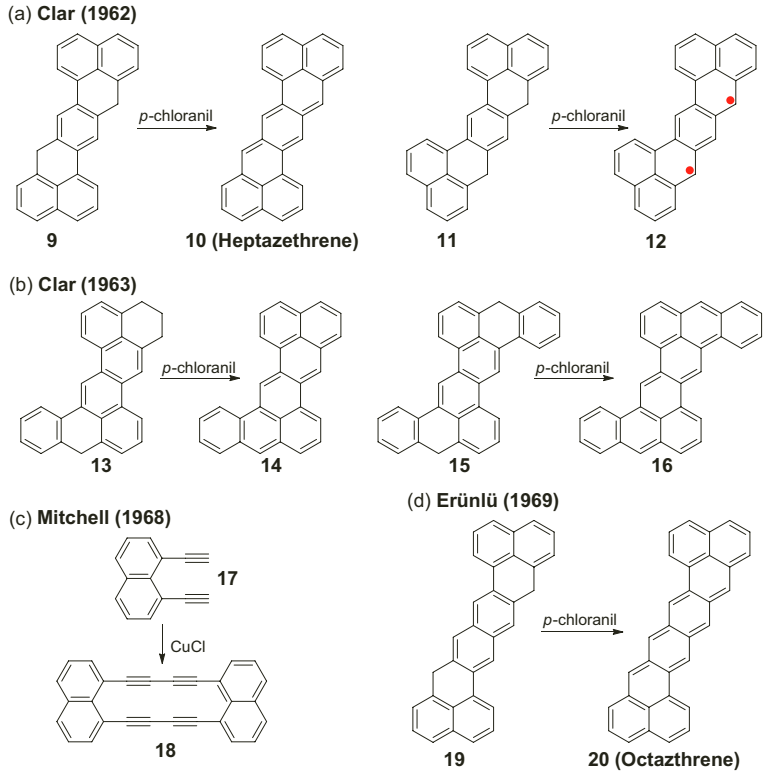


**Scheme 6.2** Early attempted syntheses of extended zethrenes and zethrene isomers.

(Scheme 6.2b) [6]. Compound **14** exhibits an absorption maximum at 611 nm, but it is highly sensitive to air. The attempted synthesis of the 5,6:12,13-dibenzozethrene **16** by dehydrogenation of the dihydro-precursor **15** failed, due to very high reactivity of **16**. In 1968, Mitchell et al. discovered that homo-coupling of the 1,8-diethynylnaphthalene **17** mediated by CuCl led to the formation of the red cyclic dimer **18** (Scheme 6.2c), which, unfortunately, was very unstable and could only exist in relatively dilute solution for less than one hour [7]. Similar to compound **5**, this cyclic dimer could undergo transannular cyclization to give the heptazethrene, which was demonstrated by us later (vide infra). In 1968, Erünlü et al. reported the attempted synthesis of even more extended zethrene, the octazethrene **20** containing eight fused benzenoid rings (Scheme 6.2d) [8]. Again, the dehydrogenation of the dihydro-precursor **19** failed due to the extremely high reactivity of the parent octazethrene.

## 6.2 Modern Syntheses of Zethrenes and Discovery of Open-Shell Diradical Character

Forty years later, several research groups independently revisited the zethrene chemistry. In 2009, Tobe's group isolated compound **5**, which was then treated by iodine to give the 7,14-diiodozethrene **21** (Scheme 6.3a) [9]. Compound **21** can undergo transition metal-catalyzed cross-coupling reactions and afford various 7,14-substituted zethrene derivatives **22**. In 2010, Y. T. Wu's group discovered that Pd-catalyzed cyclodimerization of 1-iodo-8-ethynylnaphthalenes **23** gave the zethrene derivatives **24** in good yields (Scheme 6.3b) [10]. In the same year, our group found that Stille coupling between the 1,8-dibromo-naphthalene monoimide **25** and bis(tributylstannyl)acetylene directly generated the zethrene diimide **27** in 20% yield (Scheme 6.3c) [11]. Similar to the early works from Sondheimer and Staab's teams, the tetradehydrodinaphtho[10]annulene diimde **26** was believed to be the intermediate, which can undergo thermally induced transannular cyclization reaction. Compound **27** exhibited much better stability as compared to the parent zethrene. Interestingly, attempted bromination of **27** with *N*-bromosuccinimide in DMF

did not produce the desirable brominated product, but instead a zethrenebis(dicarboximide)quinone. This unusual reaction could be explained by the central *trans*-1,3-butadiene character in zethrene, which favors an electrophilic addition rather than an electrophilic substitution reaction. In 2013, Miao's group reported a new synthetic route for the parent zethrene by intramolecular Heck coupling of a diene precursor **28** using stoichiometric amount of $Pd(OAc)_2$ (Scheme 6.3d) [12]. X-ray crystallographic analysis of the single crystals of zethrene clearly disclosed the fixed double bond character. In addition, zethrene was used as a semiconducting material in organic field effect transistors, with hole mobility up to 0.05 $cm^2\ V^{-1}\ s^{-1}$.

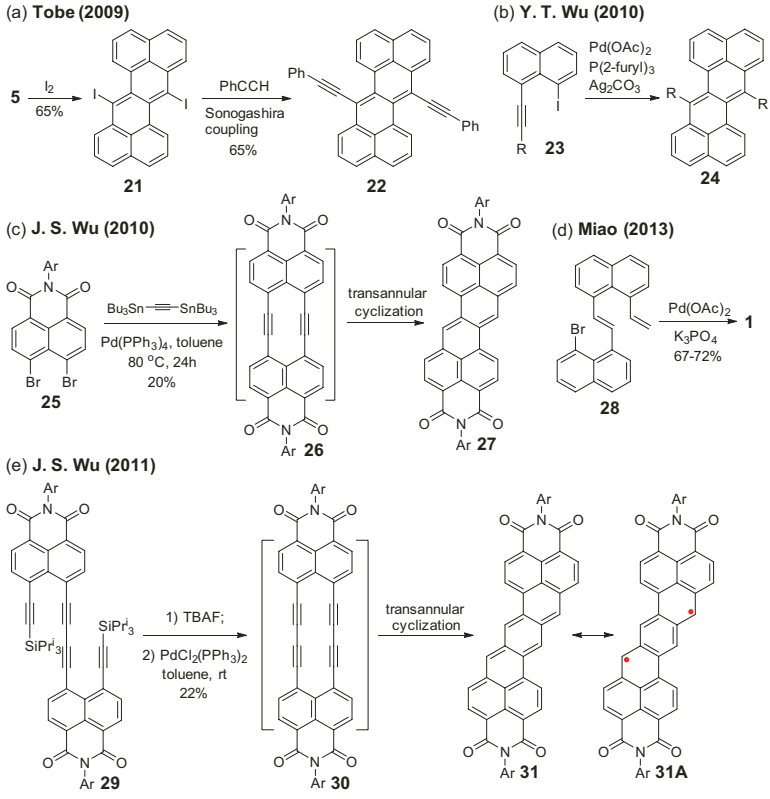


**Scheme 6.3** Modern syntheses of zethrene and heptazethrene derivatives. Ar: 2,6-diisopropylphenyl.

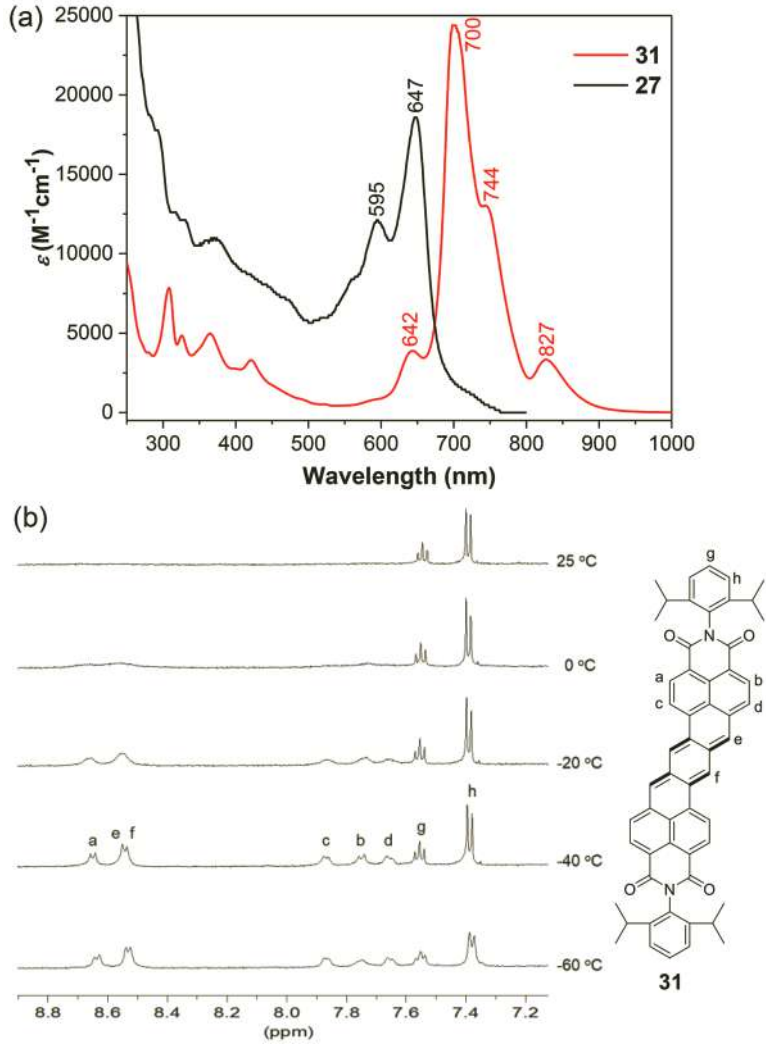


**Figure 6.1** (a) Absorption spectra of compounds **27** and **31** in DCM; (b) VT $^{1}$H NMR spectra of **31** in $CD_2Cl_2$ and the assignment.

Encouraged by the facile synthesis of the zethrene diimide **27** in a one-pot approach, we attempted the synthesis of the higher homolog heptazethrene diimide **31** by using the same strategy (Scheme 6.3e). To our delight, in situ desilylation of **29** followed by Pd-catalyzed homo-coupling directly gave the target compound

**31** in 22% yield [13]. Again, the cyclic dimer **30** was believed to be the intermediate, which can undergo transannular cyclization thermally. Due to the attachment of electron-withdrawing groups, compound **31** is reasonably stable and can be purified by routine silica gel column chromatography. The absorption spectrum of **31** in dichloromethane (DCM) is red-shifted as compared to that of **27,** due to extended conjugation (Figure 6.1a). Notably, two weak shoulders appear at 747 nm and 827 nm in the lower-energy side, indicating a different ground-state electronic structure. More interestingly, the $^{1}$H nuclear magnetic resonance (NMR) spectra of **31** in $CD_2Cl_2$ exhibited fully broadened signals for the heptazethrene core at room temperature, while the peaks began to emerge and sharpened upon cooling (Figure 6.1b). The appearance of weak shoulders at the low-energy end of the absorption spectrum (see Chapter 3) and the observed thermally induced broadening of the NMR spectrum strongly suggest an open-shell singlet ground state. Indeed, spin-unrestricted DFT calculations (UCAM-B3LYP) predicted that the open-shell singlet state of **31** was located to be 5.8 kcal/mol and 7.5 kcal/mol more stable than the closed-shell singlet and the triplet states, respectively. The small singlet-triplet energy gap allows us to experimentally probe the thermally populated triplet species. This is the first time that we revealed the unique open-shell diradical character for higher order zethrenes, and this breakthrough work led to development of a number of vertically and laterally extended zethrenes with open-shell singlet ground state.

## 6.3 Extended Zethrenes-Based Diradicaloids

According to similar calculations (UCAM-B3LYP/6-31G(d,p)), the vertically extended zethrene homologs, such as heptazethrene (**10**), octazethrene (**20**), and nonazethrene (**32**), are predicted to display open-shell diradical character ($y_0$) of 0.17, 0.37, and 0.50, respectively (Figure 6.2a). From closed-shell to the open-shell diradical forms, the central *p*-quinodimethane (*p*-QDM), 2,6-naphthoquinodimethane (2,6-NQDM), and 2,6-anthraquinodimethane (2,6-AQDM) moieties become aromatic, and the enhanced diradical characters with extension can be simply explained by increased aromatic stabilization energy. Lateral extension of zethrene, heptazethrene, and octazethrene gives a series of quinoidal hydrocarbons,

namely, superzethrene (**33**), superheptazethrene (**34**), and superoctazethrene (**35**), respectively (Figure 6.2b). In these molecules, two aromatic sextets (the hexagons shaded in blue color) are gained from closed-shell quinoidal forms to open-shell diradical forms, leading to further increased diradical characters. The intrinsic diradical characters also imply high reactivity of these open-shell singlet molecules. As a result, all the early attempts to prepare parent heptazethrene and octazethrene failed due to this reason.

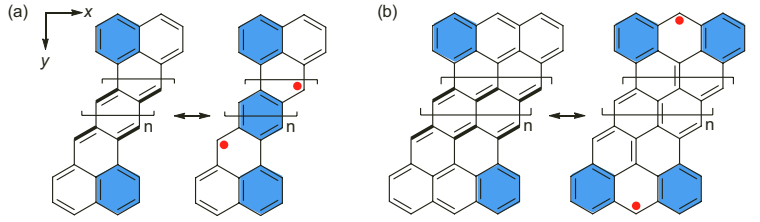


**Figure 6.2** Representative closed-shell and open-shell resonance structures of some extended zethrenes, and their calculated diradical characters.

### 6.3.1 Vertically Extended Zethrenes

To attain stable extended zethrenes, two general stabilizing strategies have been considered: (i) thermodynamically, efficient spin delocalization, and attachment of electron-withdrawing substituents can help to stabilize high-energy frontier π-electrons; and (ii) kinetically, introduction of bulky groups to the most reactive sites would prevent intermolecular reactions. In 2012, we reported the successful synthesis of bulky triisopropylsilyl (TIPS) ethynyl groups substituted heptazethrene derivative **38** and octazethrene derivative **39** by nucleophilic addition of the corresponding quinones (**36, 37**) followed by reduction with $SnCl_2$ (Scheme 6.4a) [14]. The kinetic blocking by TIPS group and the extended spin delocalization to the ethynyl unit render compounds **38** and **39** as stable materials. Interestingly, in contrast with heptazethrene diimide **31**, compound **38** was found to behave like a typical closed-shell compound. Such difference can be supported by the relatively

larger HOMO-LUMO energy gap of **38** (1.47 eV) as compared to that of **31** (0.99 eV), which renders the admixing of HOMO and LUMO in the ground state less efficient. The further extended octazethrene derivative **39** exhibited typical open-shell diradical character and thermally induced paramagnetic properties. The singlet-triplet energy gap ($\Delta E_{S\text{-}T}$) was estimated to be −3.87 kcal/mol, according to superconducting quantum interference device (SQUID) measurements. In addition, large two-photon absorption (TPA) cross sections ($\sigma^{(2)}$) were determined for **38** ($\sigma^{(2)}_{max}$ = 920 GM at 1250 nm) and **39** ($\sigma^{(2)}_{max}$ = 1200 GM at 1250 nm), in accordance with theoretical prediction by Nakano et al. (see Chapter 1). Alternatively, bulky aryl groups substituted heptazethrene and octazethrene derivatives (**38**, **39**), which can be synthesized by nucleophilic addition of the corresponding dialdehyde intermediates (**40**, **41**) followed by Friedel-Crafts alkylation and oxidative dehydrogenation (Scheme 6.4a) [15].

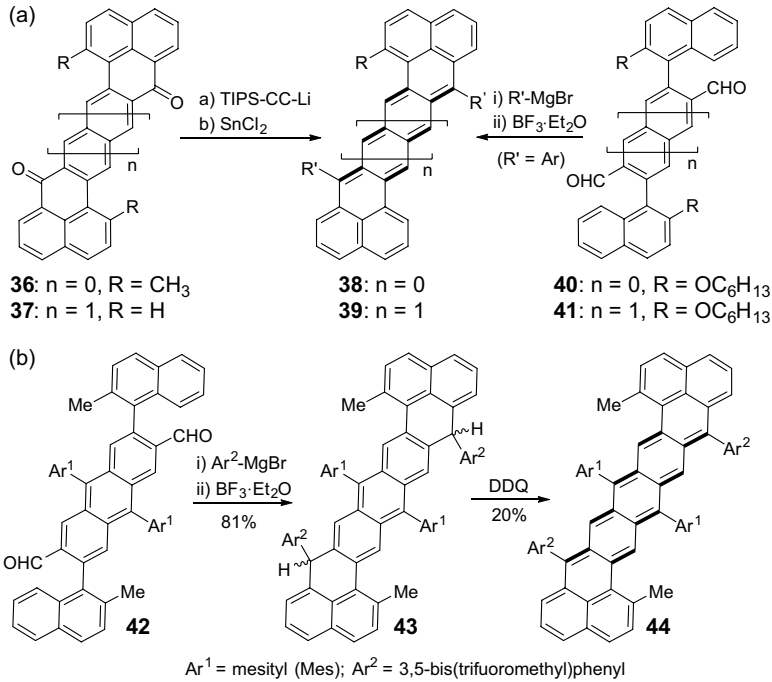


**Scheme 6.4** Syntheses of the kinetically blocked heptazethrene, octazethrene, and nonazethrene derivatives.

Similar strategy was employed to the synthesis of a further extended nonazethrene derivative **44** (Scheme 6.4b) [16]. To ensure sufficient stability, bulky mesityl (Mes), and electron-withdrawing 3,5-bis(trifluoromethyl) phenyl groups are attached onto the most reactive sites. Compound **44** exhibited typical open-shell diradical character, showing significant NMR broadening at room temperature and strong ESR signal. The $\Delta E_{S-T}$ value was estimated to be −5.2 kcal/mol by SQUID measurement, which is larger than that of **39**, presumably due to the electron-withdrawing substituents. In addition, its electronic structure and physical properties are compared with a nonacene derivative **JA-NA**. It was found that the unpaired electrons in **JA-NA** are localized at the center of the two zigzag edges, while in **39,** they are at the two terminal phenalenyl moieties (see Chapter 2). Such a difference in spatial localization of the unpaired electrons was generally observed between higher-order acenes and extended zethrenes. As a result, a faster decrease of singlet-triplet energy gap and increase of diradical character with extension of the skeleton were observed in zethrene series. Therefore, spatial localization of the frontier molecular orbitals plays an important role in the diradical character and excitation energies.

### 6.3.2 Laterally Extended Zethrenes

To further elaborate the fundamental structure–diradical character–physical property relationships in zethrene family, the derivatives (**46**, **48**) of two laterally extended dibenzozethrene isomers, 1,2:9,10-dibenzoheptazethrene (isomer 1) and 5,6:13,14-dibenzoheptazethrene (isomer 2), were synthesized (Scheme 6.5a) [17]. Compound **46** was prepared from the dialdehyde intermediate **45** by the above-mentioned nucleophilic addition/Friedel-Crafts alkylation/oxidative dehydrogenation protocol, while the compound **48** was synthesized from the corresponding quinone **47** via a nucleophilic addition/reduction method. The ground state and diradical characters of these molecules were carefully studied by both experimental and theoretical methods. The diradical characters were calculated (UCAM-B3LYP/6-31G(d,p)) to be 0.31 and 0.58 for **46** and **48**, respectively. The difference in the diradical character between the two isomers could be explained by the

different number of aromatic sextet rings gained from closed-shell to open-shell diradical resonance forms. Specifically, for isomer 1, one aromatic sextet is gained (**46A**), while for isomer 2, an additional three additional aromatic sextets can be obtained (**48A**). Therefore, the diradical form of isomer 2 gains more aromatic stabilization energy than that of isomer 1 and shows larger diradical character. Bond length analysis on the X-ray crystallographic structures of **46** and **48** revealed their different ground-state geometry that can be correlated to their different diradical character (Figure 6.3a). For **46**, there is an obvious bond length alternation in the central *p*-QDM subunit, indicating a dominant quinoidal structure. On the other hand, the bond *b* (1.376 Å) is longer than the typical double bond in olefins (1.33–1.34 Å), indicating a contribution of the open-shell diradical form. For **48**, the bond lengths in the central benzene ring (1.399 Å, 1.409 Å, and 1.411 Å) are almost uniform, indicating an aromatic character. The bond *c* (1.457 Å) and bond *d* (1.454 Å) are more like single bonds, in accordance with a large diradical character. The calculated nucleus independent chemical shift ($NICS(1)_{zz}$) values of the central benzene ring are −11.6 ppm and −19 ppm for **46** and **48**, respectively, further supporting a larger diradical character in the latter. The calculated spin densities at the specific carbon atoms (numbers in pink) also indicate the dominant contribution of the resonance forms **46A** and **48A**. In fact, this study is an extension of Clar's aromatic sextet rule in open-shell diradicaloids, which can be summarized as follows: *For benzenoid polycyclic hydrocarbons with the same chemical composition, the molecule that can be drawn with more aromatic sextet rings in the diradical resonance forms exhibits greater diradical character*. Their one-photon absorption (OPA) and TPA spectra are also significantly different (Figure 6.3b). Compound **46** in chloroform solution shows a *p*-band with maximum at 687 nm ($\varepsilon = 7.2 \times 10^4\ M^{-1}cm^{-1}$) with a weak absorption tail up to 850 nm, implying a small diradical character. Compound **48** in chloroform displays a typical absorption feature for open-shell singlet diradicaloids, with an intense absorption at 804 nm ($\varepsilon = 1.5 \times 10^5\ M^{-1}cm^{-1}$) and several small bands at lower energy region. In accordance with the enhanced diradical character, compound **48** exhibits five-fold larger TPA cross section maximum ($\sigma^{(2)}_{max}$ = 2800 GM at 1600 nm) as compared to that of **46** ($\sigma^{(2)}_{max}$ = 530 GM at 1400 nm).

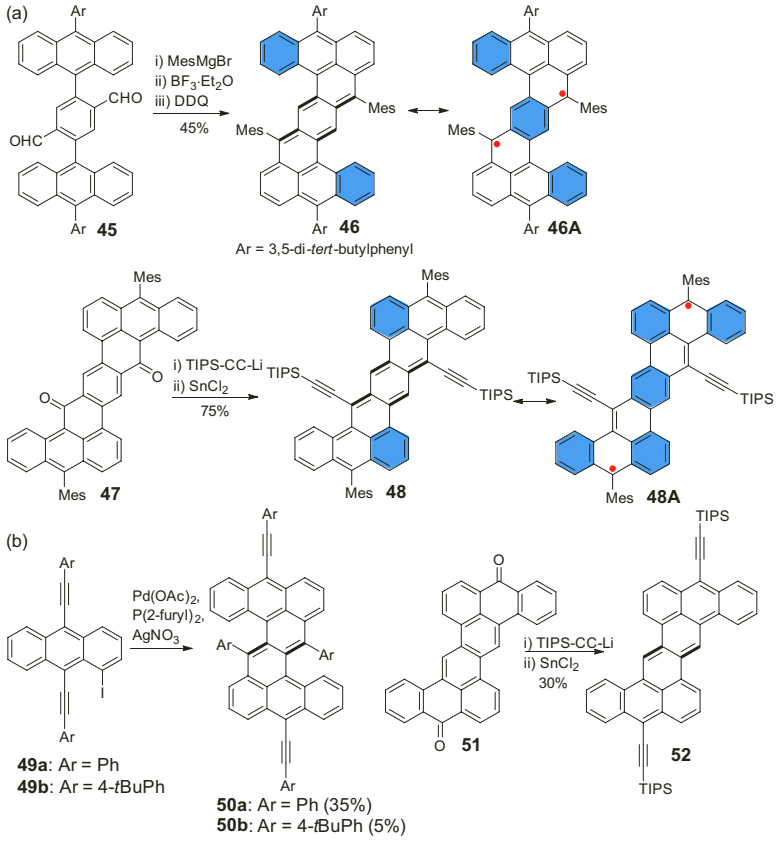


**Scheme 6.5** Syntheses of dibenzo-heptazethrene (a) and zethrene (b) isomers, showing different diradical characters.

Two laterally extended dibenzozethrene isomers, 1,2:8,9-dibenozethrene and 5,6:12,13-dibenzozethrene, were also investigated by our group. Their derivatives **50a/50b** [18] and **52** [19] were synthesized by Pd-catalyzed cyclodimerization of **49a/49b** and from the quinone **51**, respectively (Scheme 6.5b). The above discussed Clar's aromatic sextet rule can be applied to this system too, and the diradical character of compounds **50a** and **52** were calculated to be 0.210 and 0.414, respectively. Experimentally, compound **50a/50b** behaves more of a closed-shell structure, while **52** is a typical singlet diradicaloid with thermally populated paramagnetic activity.

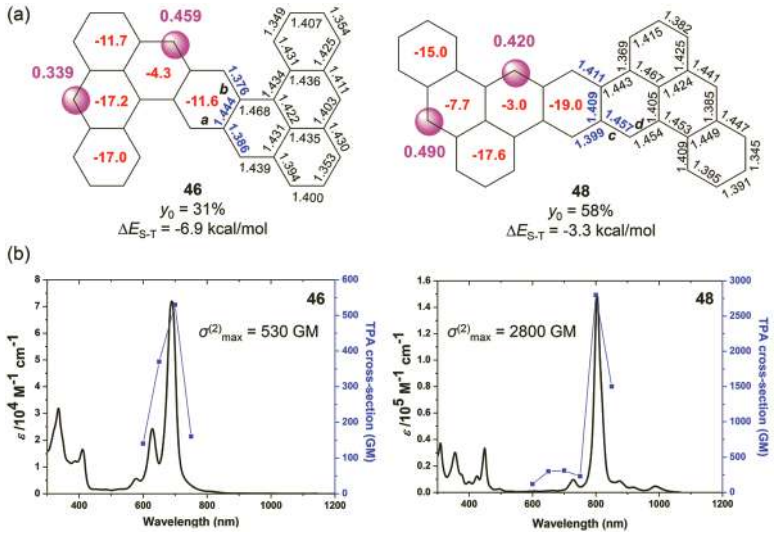


**Figure 6.3** (a) Mean values (black and blue numbers) of bond lengths (Å), calculated NICS(1)$_{zz}$ values (red numbers, in ppm), and spin density (pink numbers) at the specific sites for the core of the **46** and **48**. (b) OPA spectra and TPA spectra of **46** and **48** in toluene. TPA spectra are plotted at $\lambda_{ex}/2$.

The next challenging synthetic targets are the laterally extended superzethrenes, in view of expected high reactivity related to their large diradical characters (Figure 6.2b). After much effort, our group successfully synthesized two stable superheptazethrene (**56**) [20] and superoctazethrene (**60**) [21] derivatives (Scheme 6.6). The same synthetic strategy was adopted for both. The intermediate tetraaldehydes **55** and **59** were first synthesized via multi-step conversion starting from the dialdehydes **53** and **57**. Subsequent nucleophilic addition, Friedel-Crafts alkylation and oxidative dehydrogenation afforded the target compounds **56** and **60** in good yields. Bulky and electron-withdrawing 3,5-di(trifluoromethyl) phenyl or 2,6-dichlorophenyl groups are attached onto the most reactive sites, and thus, they are reasonably stable and can be isolated by deactivated silica gel column chromatography. Both compounds displayed typical behavior of open-shell diradicaloids, with significantly broadened NMR spectra and strong ESR signals at room temperature. The electrochemical energy gap was determined to be 0.66 eV and 1.01 eV for **56** and **60**, respectively. The singlet-

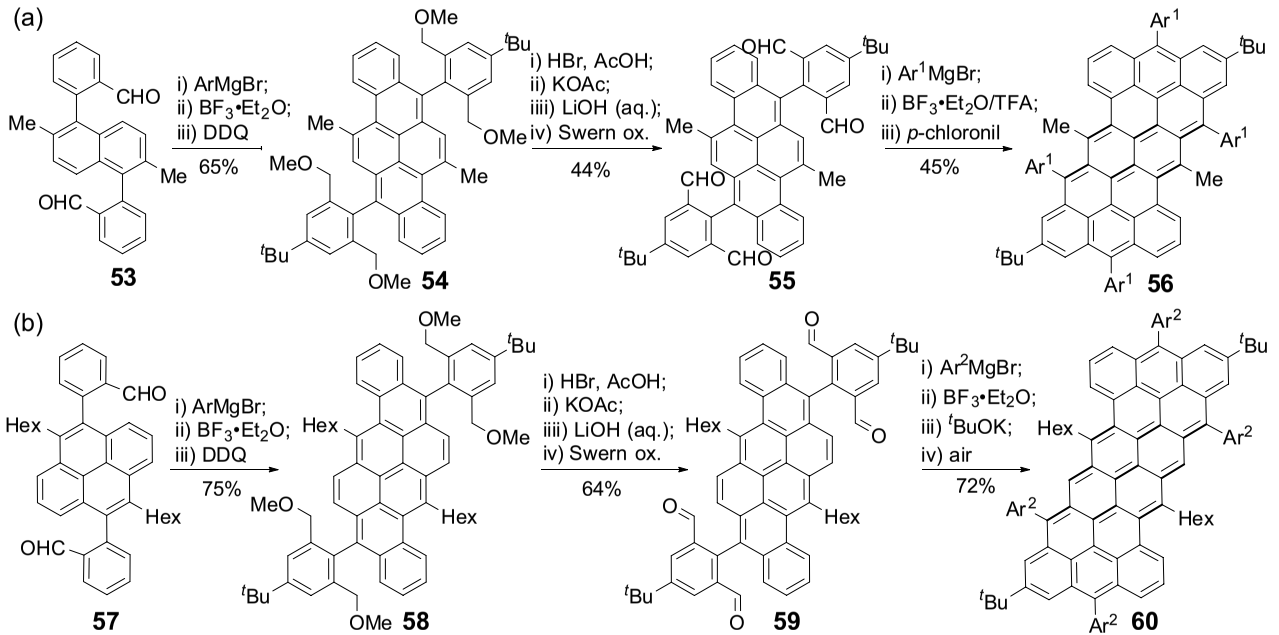


**Scheme 6.6** Synthesis of kinetically blocked superheptazethrene (a) and superoctazethrene (b). $Ar^1$ = 3,5-di(trifluoromethyl)phenyl, and $Ar^2$ = 2,6-dichlorophenyl.

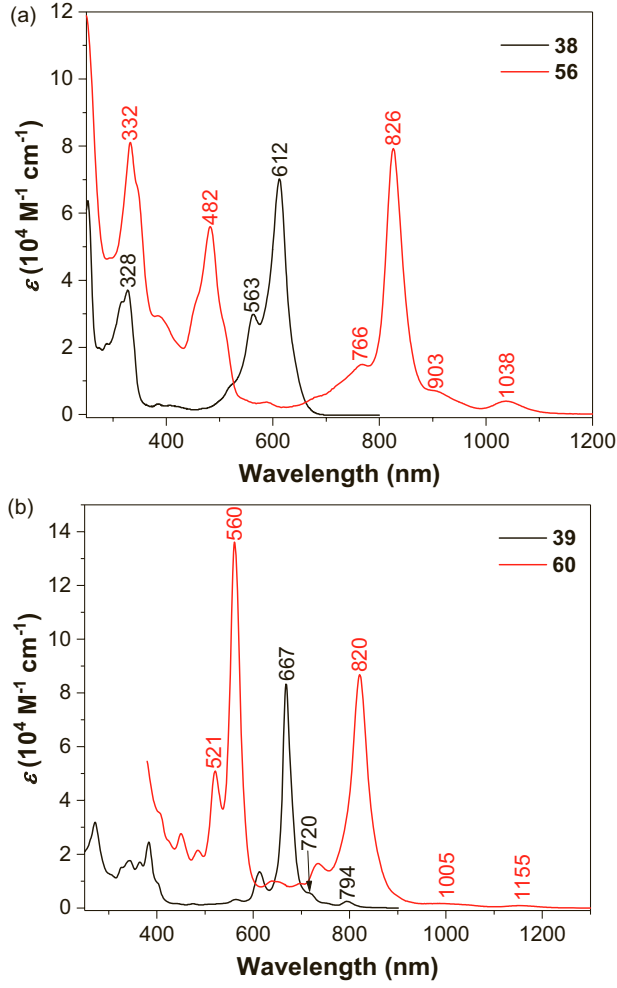


**Figure 6.4** A comparison of the electronic absorption spectra in solution: (a) heptazethrene **38** (R = hexyloxy, R′ = mesityl) vs superheptazethrene **56**; (b) octazethrene **39** (R = H, R′ = TIPSE) vs superoctazethrene **60**.

triplet energy gap was estimated to be −0.94 and −2.30 kcal/mol, respectively, by SQUID measurements. Considering of a larger diradical character of the superoctazethrene than superheptazethrene, the observed larger electrochemical energy gap and singlet-triplet energy gap in **60** could possibly be due to the strong electron-withdrawing effect of the 2,6-dichlorophenyl substituents. Compared to

the respective heptazethrene (**38**) and octazethrene (**39**) derivatives, the absorption spectra of **56** and **60** display 214 nm and 153 nm red shift, respectively (Figure 6.4). Both **56** and **60** show weak shoulder peaks in the long-wavelength near infrared (NIR) region, in accordance with their large diradical characters. Synthesis of a stable superzethrene derivative remains elusive.

## 6.4 Zethrene Isomers and Analogs

Chemical and physical properties of different zethrene isomers are also of interest. There are four structural isomers for the parent heptazethrene depending on the fusion mode of the phenalenyl units onto the central benzene ring (Figure 6.5). In the isomers **62** and **63**, the two electrons of each phenalenyl unit can couple with each other to give a closed-shell Kekulé structure, thus they are predicted to have a singlet ground state. However, the two isomers **61** and **64** are predicted to have a triplet biradical ground state, due to the existence of two unpaired electrons. Thus, derivatives of **61**–**63** have been successfully synthesized and characterized, but the derivative of **64** still remains a challenge to be tackled.

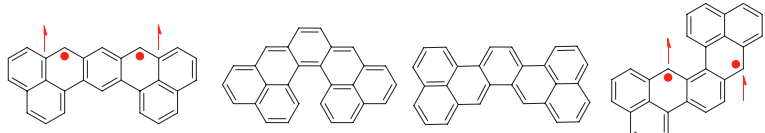


**Figure 6.5** Four possible structural isomers of heptazethrene.

In 2014, our group reported a kinetically blocked heptazethrene isomer **67** derived from **61** (Scheme 6.7) [22]. The precursor **66** was synthesized from the dialdehyde **65** by nucleophilic addition followed by Friedel-Crafts cyclization. Deprotonation of the **66** with 2.5 equiv. lithium diisopropylamide (LDA) and subsequent oxidation by 1.06 equiv. iodine in 2-methyl-THF gave compound **67**. Due to the attachment of bulky mesityl groups at the most reactive sites, the in situ generated diradical **67** was persistent at −78 °C under the protection of nitrogen. The singlet-triplet energy gap was calculated (UCAM-B3LYP/6-31G(d,p)) to be +5.3 kcal/mol, implying a triplet

ground state. The existence of triplet diradical was confirmed by low temperature ESR and 2D electron spin transient nutation (ESTN) measurements (Scheme 6.7b,c). Both experiments revealed a dominant triplet species ($S$=1, about 60%), together with significant amount of monoradical impurities ($S$=1/2, about 40%) due to the high reactivity of the high-spin diradical.

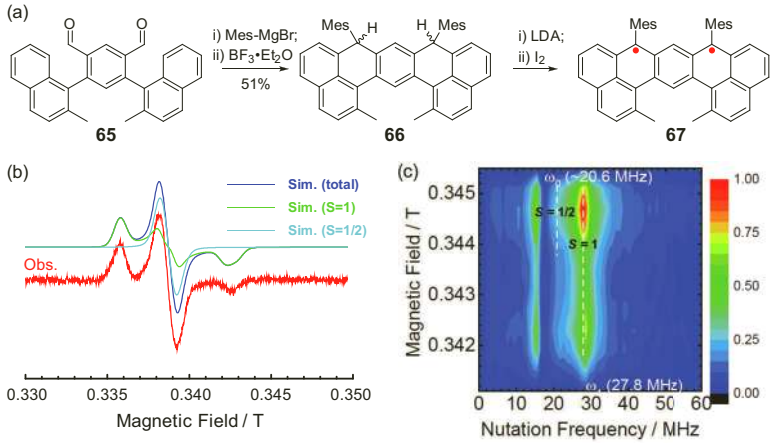


**Scheme 6.7** (a) Synthetic route of the triplet diradical **67**; (b) ESR spectrum of **67** together with the monoradical impurities recorded at 20 K and the simulated ESR spectra; (c) 2D ESTN spectrum for the solution of **67** (recorded at 5 K).

In 2016, Jurížek's group reported the formation and spectral characterization of a derivative (**73**) of the heptazethrene isomer **62**, which was coined "cethrene" due to its C-shape and chirality (Scheme 6.8a) [23]. The dihydro- precursor **72** was synthesized by multi-step reactions starting from the dibromo-compound **68**, through Heck coupling, hydrogenation, Friedel-Crafts acylation, and dehydration. Treatment of **72** with *p*-chloranil generated the cethrene **73**, which was characterized by NMR, electronic absorption, and ESR measurements. Calculations predicted cethrene to have a larger diradical character and a smaller singlet-triplet compared to the heptazethrene. Experimentally, its absorption maximum (665 nm) is significantly red-shifted compared with that of heptazethrene (586 nm), which can be explained by the through-space anti-bonding/bonding interactions within the HOMO/LUMO, due to its unique helical structure. Compound **73**, however, rapidly formed

intramolecular C–C linked dimer due to its diradical character (**73A**), and subsequent oxidative dehydrogenation gave the planar hydrocarbon **74**. The in situ generated intermediate **73** was fully converted into **74** in a few hours in toluene or benzene. In 2018, the same group reported a new cethrene molecule **76**, in which two methyl groups are installed at the Fjord position (Scheme 6.8b). It was synthesized by oxidative dehydrogenation of **75** by *p*-chloranil and can be isolated by routine column chromatography. Due to steric repulsion, its absorption maximum in toluene (627 nm) is blue-shifted as compared to that of **73**. Interestingly, it can be transformed reversibly via conrotatory electrocyclization to its more stable closed form **77** by light (630 nm) or heat and back to its open form by light (365 nm). The switching process was monitored by NMR, UV-vis, and circular dichroism, and distinct changes in the optical and chiroptical properties were observed. This represents a rare robust photo-switchable diradicaloid system.

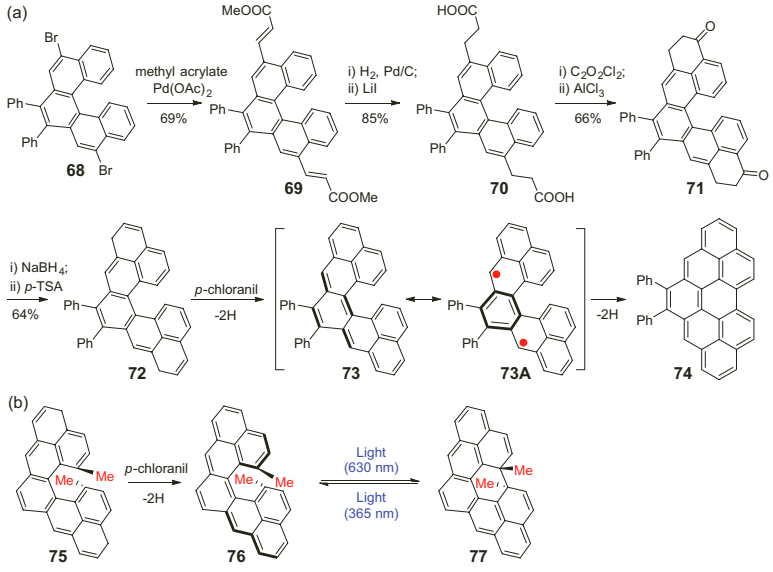


**Scheme 6.8** (a) Synthesis of a cethrene intermediate **73**/**73A** and its subsequent cyclization reaction; (b) a dimethylcethrene (**76**) based photoswitch.

In 2020, Kubo's group reported another heptazethrene isomer, so-called sigmarene **63**, due to its Σ-shape [24]. The derivative **85** was synthesized according to a similar strategy to the cethrene

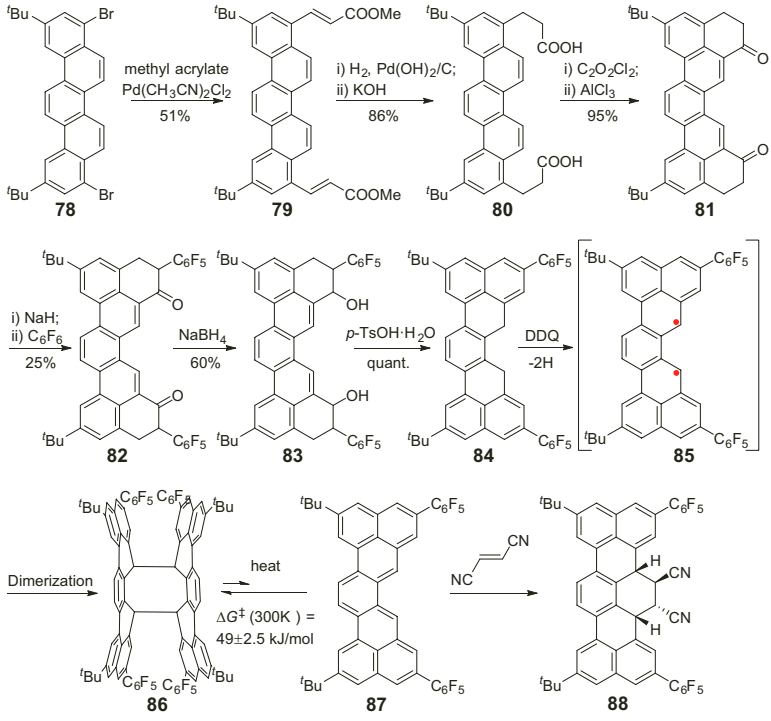


**Scheme 6.9** Synthesis of a sigmarene (**87**) and its dual reactivity.

(Scheme 6.9). Starting from the dibromo-compound **78**, a reaction sequence, including Heck coupling, hydrogenation, Friedel-Crafts acylation, nucleophilic substitution, reduction, and dehydration, gave the dihydro-precursor **84**. Treatment of **84** with one equivalent 2,3-dichloro-5,6-dicyanobenzoquinone (DDQ) in degassed toluene at 55 °C afforded an orange solution in the early stage of the reaction, which turned to light-green in a few minutes. Light yellow crystals were obtained by recrystallization of the reaction solution at room temperature and X-ray crystallographic analysis revealed a σ-dimer **86**, where two sigmarene subunits are connected with two σ-bonds at the carbon atoms that bear the highest spin density (**85**). Heating of the yellow solution in *o*-dichlorobenzene led to dissociation of the dimer to give the monomer **87**, which displayed light green color with an absorption maximum at 707 nm. After cooling the solution down to room temperature, the spectrum reverted to the initial state immediately. In addition, laser-flash photolysis ($\lambda_{exc}$: 355 nm) of the

dimer in toluene also resulted in similar dissociation. The half-life time of the generated monomer was measured to be about 0.8 s and the activation energy of the thermal dimerization was estimated to be 49 ± 2.5 kJ·mol$^{-1}$ at 300 K. Theoretical calculations suggest that the [4 + 4] dimerization goes through a radical stepwise pathway, rather than a concerted mechanism that is a formally forbidden in the framework of the orbital symmetry rule. Due to the existence of an *o*-quinodimethane scaffold, the monomer **87** can undergo thermally allowed [4 + 2] cycloaddition with fumaronitrile to give the enantiomer **88** as the only product. Detailed NMR analysis and theoretical calculations suggest a concerted mechanism. The reactivity of the sigmarene demonstrates the dual nature of the closed-shell and open-shell electronic structures of diradicaloid species.

The intrinsic open-shell diradical character and low energy gap of zethrenes indicate that they could be good candidates of organic NIR dyes and several stable zethrene analogs have been reported by our group (Figure 6.6a). A *p*-QDM bridged perylene monoimide dimer **89**, which can be regarded as an extended heptazethrene diimide, was prepared as a stable material due to the incorporation of electron-withdrawing imide group [25]. Similar to **31**, **89** has an open-shell singlet ground state and the diradical character was calculated to be 0.465. It shows very intense absorption in the NIR region, with absorption maximum at 915 nm ($\varepsilon$ = 2.49 × 10$^5$ M$^{-1}$ cm$^{-1}$). It also exhibits large TPA cross section ($\sigma^{(2)}_{max}$ = 1300 GM at 1800 nm). Similarly, a *p*-QDM bridged porphyrin dimer **90** was synthesized [26], which exhibits an intense absorption at 955 nm ($\varepsilon$ = 4.54 × 10$^4$ M$^{-1}$ cm$^{-1}$) (Figure 6.6b). However, it is proved to have a closed-shell ground state, presumably because resonance of the open-shell diradical forms destroys the aromaticity of the two porphyrin macrocycles. On the other hand, 2,6-NQDM and 1,5-NQDM bridged porphyrin dimers **91** and **92** both exhibit open-shell singlet ground state, according to variable temperature magnetic measurements as well as theoretical calculations [27]. The isomer **92** has a larger diradical character ($y_0$ = 0.772, based on the restricted active space-spin flip calculations) and smaller singlet-triplet energy gap ($\Delta E_{S\text{-}T}$ = −2.6 kcal/mol, based on SQUID measurements) compared to the isomer **91** ($y_0$ = 0.501, $\Delta E_{S\text{-}T}$ = −3.1 kcal/mol). In addition, **91** shows intense OPA ($\lambda_{max}$ = 976 nm, $\varepsilon$ = 72200 M$^{-1}$ cm$^{-1}$) and a large TPA

cross section ($\sigma^{(2)}_{max}$ = 3500 GM at 1400 nm) in the NIR region, while **92** with larger diradical character displays red-shifted but weaker OPA ($\lambda_{max}$ = 1147 nm, $\varepsilon$ = 18030 $M^{-1}$ $cm^{-1}$) and a smaller TPA cross section ($\sigma^{(2)}_{max}$ = 1750 GM at 1600 nm) (Figure 6.6b). Both compounds show four reversible redox waves and **92** has a smaller electrochemical energy gap (1.06 eV vs 1.16 eV for **91**). Therefore, the bridge structure has a significant impact on the diradical character, electronic properties, and magnetic behaviors of the obtained porphyrin-based diradicaloids. The diradical concept was also applied by our group for the design of BODIPY-based NIR dyes. The *para*- and *meta*-QDM bridged BODIPY dimers **93** and **94** with small diradical character ($y_0$ = 0.069 and 0.26, respectively) were synthesized as stable compounds [28]. These BODIPY-based diradicaloids exhibit very intense absorption at 1088 nm ($\varepsilon$ = 6.65 × $10^5$ $M^{-1}$ $cm^{-1}$) and 1136 nm ($\varepsilon$ = 6.44×$10^5$ $M^{-1}$ $cm^{-1}$), respectively (Figure 6.6c) in the NIR II region.

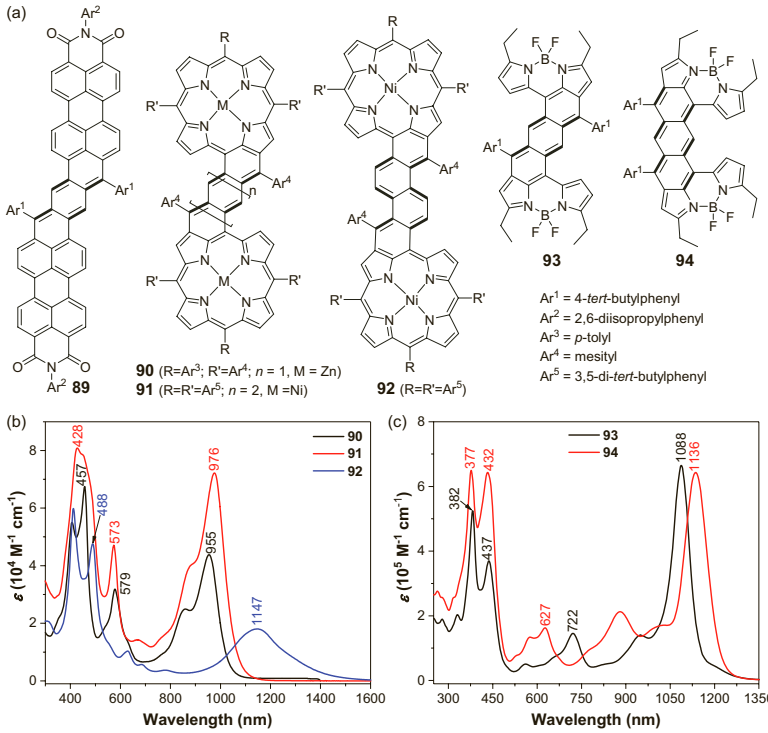


**Figure 6.6** (a) Structures of some zethrene analogues; and (b) and (c) UV-vis-NIR absorption spectra of representative compounds.

## 6.5 Conclusion

In summary, after the pioneering works by Clar et al., zethrene chemistry has received much attention in recent years. The discovery of the open-shell diradial character of extended zethrenes substantiated failures from previous synthetic attempts. Several efficient synthetic methods and stabilizing strategies have been developed. The diradical character and singlet-triplet gap are found to closely be related to the number of aromatic sextet rings gained in the diradical form, energy gap, fusion mode, and spatial distribution of the frontier molecular orbitals. In addition, the optical properties (OPA and TPA) have close relation to the diradical character, which is in agreement with theoretical calculations (see Chapters 1 and 2). It was also found that extended zethrenes and their analogs with small to moderate diradical characters exhibit long-wavelength absorption in the NIR region and large TPA cross sections, and thus, can be used as both organic NIR dyes and non-linear optical chromophores. These studies provoked us to investigate a wider range of open-shell singlet diradicaloids and even polyradicaloids (see Chapters 7, 8, and 13).

## References


1. Clar, E., Lang, K. F., and Kiesow, H. S. (1955). Aromatische kohlenwasserstoffe, LXX. Mitteil.[1)]: zethren (1.12; 6.7-dibenztetracen), *Chem. Ber*., **88**, pp. 1520–1527.
2. Mitchell, R. H. and Sondheimer, F. (1968). A dinaphth[10]annulene, *J. Am. Chem. Soc*., **90**, pp. 530–531.
3. Staab, H. A., Nissen, A., and Ipaktschi, J. (1968). Attempted preparation of 7,8,15,16-tetradehydrodinaphtho[1,8-*ab*; 1,8-*fg*]cyclodecene, *Angew. Chem. Int. Ed*., **7**, pp. 226–226.
4. Mitchell, R. H. and Sondheimer, F. (1970). The attempted synthesis of a dinaphth-1,6-bisdehydro[10]annulene, *Tetrahedron*, **26**, pp. 2141–2150.
5. Clar, E. and Macpherson, I. A. (1962). The significance of Kekulé structures for the stability of aromatic systems–II, *Tetrahedron,* **18**, pp. 1411–1416.
6. Clar, E., Macpherson, I. A., and Schulz-Kiesow, H. (1963). Benzozethren und dibenzozethren derivate, *Liebigs Ann.*, **44**, pp. 669–677.
7. Mitchell, R. H. and Sondheimer, F. (1968). Unsaturated macrocyclic compounds-LII: The synthesis of 1,8-diethynylnaphthalene and

it is oxidation to a conjugated fourteen-membered ring system, *Tetrahedron*, **24**, pp. 1397–1405.

8. Erünlü, R. K. (1969). Octazethren Ein aromatischer Kohlenwasserstoff mit sechs formal fixierten Doppelbindungen, *Justus Liebigs Ann. Chem.,* **721**, pp. 43–47.
9. Umeda, R., Hibi, D., Miki, L., and Tobe, Y. (2009). Tetradehydrodinaphtho[10]annulene: A hitherto unknown dehydroannulene and a viable precursor to stable zethrene derivatives, *Org. Lett*., **11**, pp. 4104–4106.
10. Wu, T. C., Chen, C.-H., Hibi, D., Shimizu, A., Tobe, Y., and Wu, Y. T. (2010). Synthesis, structure, and photophysical properties of dibenzo[de,mn] naphthacenes, *Angew. Chem. Int. Ed*., **49**, pp. 7059–7062.
11. Sun, Z., Huang, K.-W., and J. Wu (2010). Soluble and stable zethrenebis(dicarboximide) and its quinone, *Org. Lett.*, **12**, pp. 4690–4693.
12. Shan, L., Liang, Z., Xu, X., Tang, Q., and Miao, Q. (2013). Revisiting zethrene synthesis, reactivity and semiconductor properties, *Chem. Sci.,* **4**, pp. 3294–3297.
13. Sun, Z., Huang, K.-W., and Wu, J. (2011). Soluble and stable heptazethrenebis(dicarboximide) with a singlet open-shell ground state, *J. Am. Chem. Soc*., **133**, pp. 11896–11899.
14. Li, Y., Heng, W.-K., Lee, B. S., Aratani, N., Zafra, J. L., Bao, N., Lee, R., Sung, Y. M., Sun, Z., Huang, K.-W., Webster, R. D., López Navarrete, J. T., Kim, D., Osuka, A., Casado, J., Ding, J., and Wu, J. (2012). Kinetically blocked stable heptazethrene and octazethrene: Closed shell or open-shell in the ground State?, *J. Am. Chem. Soc*., **134**, pp. 14913–14922.
15. Hu, P., Lee, S., Herng, T. S., Aratani, N., Gonçalves, T. P., Qi, Q., Shi, X., Yamada, H., Huang, K.W., Ding, J., Kim, D., and Wu, J. (2016). Toward tetraradicaloid: The effect of fusion mode on radical character and chemical reactivity, *J. Am. Chem. Soc*., **138**, pp. 1065–1077.
16. Huang, R., Phan, H., Herng, T. S., Hu, P., Zeng, W., Dong, S., Das, S., Shen, Y., Ding, J., Casanova, D., and Wu, J. (2016). Higher order π-conjugated polycyclic hydrocarbons with open-shell singlet ground state: Nonazethrene versus nonacene, *J. Am. Chem. Soc*., **138**, pp. 10323–10330.
17. Sun, Z., Lee, S., Park, K., Zhu, X., Zhang, W., Zheng, B., Hu, P., Zeng, Z., Das, S., Li, Y., Chi, C., Li, R., Huang, K., Ding, J., Kim, D., and Wu, J. (2013). Dibenzoheptazethrene isomers with different biradical characters: An exercise of clar's aromatic sextet rule in singlet biradicaloids, *J. Am. Chem. Soc.,* **135**, pp. 18229–18236.

18. Sun, Z., Zheng, B., Hu, P., Huang, K.-W., and Wu, J. (2014). Highly twisted 1,2-8,9-dibenzozethrenes synthesis, ground state, and physical properties, *ChemPlusChem*, **79**, pp. 1549–1553.
19. Yadav, P., Das, S., Hu, P., Herng T. S., Ding, J., and Wu, J. (2016). Kinetically blocked stable 5,6:12,13-dibenzozethrene: A laterally π-extended zethrene with enhanced diradical character, *Org. Lett*., **18**, pp. 2886–2889.
20. Zeng, W. D., Sun, Z., Herng, T. S., Gonçalves, T. P., Gopalakrishna, T. Y., Huang, K.-W., Ding, J., and Wu, J. (2016). Super-heptazethrene, *Angew. Chem., Int. Ed*., **55**, pp. 8615–8619.
21. Zeng, W. D., Gopalakrishna, T. T., Phan, H., Tanaka, T., Herng, T. S., Ding, J., Osuka, A., and Wu, J. (2018). Superoctazethrene: An open-shell graphene-like molecule possessing large diradical character but still with reasonable stability, *J. Am. Chem. Soc.,* **140**, pp. 14054–14058.
22. Li, Y., Huang, K.-W., Sun, Z., Webster, R.D., Zeng, Z., Zeng, W., Chi, C., Furukawa, K., and Wu, J. (2014). A kinetically blocked 1,14:11,12-dibenzopentacene: A persistent triplet diradical of non-Kekulé polycyclic benzenoid hydrocarbons, *Chem. Sci*., **5**, pp. 1908–1914.
23. Ravat, P., Šolomek, T., Rickhaus, M., Häussinger, D., Neuburger, M., Baumgarten, M., and Juríček, M. (2016). Cethrene: A helically chiral biradicaloid isomer of heptazethrene, *Angew. Chem. Int. Ed.,* **55**, pp. 1183–1186.
24. Sahara, K., Abe, M., Zipse, H., and Kubo, T. (2020). Duality of reactivity of a biradicaloid compound with an *o*-quinodimethane scaffold, *J. Am. Chem. Soc.*, **142**, pp. 5408–5418.
25. Das, S., Lee, S., Son, M., Zhu, X., Zhang, W., Zheng, B., Hu, P., Zeng, Z., Sun, Z., Zeng, Z., Li, R.-W., Huang, K., Ding, J., Kim, D., and Wu, J. (2014). *para*-Quinodimethane-bridged perylene dimers and *peri*-condensed quaterrylenes: The effect of the fusion mode on the ground states and physical properties, *Chem. Eur. J*., **20**, pp. 11410–11420.
26. Zeng, W., Ishida, M., Lee, S., Sung, Y., Zeng, Z., Ni, Y., Chi, C., Kim, D., and Wu, J. (2013). A *p*-quinodimethane-bridged porphyrin dimer, *Chem. Eur. J.,* **19**, pp. 16814–16824.
27. Zhang, H. J., Kim, J., Phan, H., Herng, T. S. Gopalakrishnaa, T. Y., Zeng, W., Ding, J., Kim, D., and Wu, J. (2020). 2,6-/1,5-Naphthoquinodimethane bridged porphyrin dimer diradicaloids, *J. Porphyrins Phthalocyanines*, **24**, pp. 220–229.
28. Ni, Y., Lee, S., Son, M., Aratani, N., Ishida, M., Yamada, H., Chang, Y.-T., Furuta, H., Kim, D., and Wu, J. (2016). A diradical approach towards BODIPY-based dyes with intense near-infrared absorption around λ=1100 nm, *Angew. Chem. Int. Ed.,* **55**, pp. 2815–2819.

Chapter 7

# Extended *para*-Quinodimethanes and Quinones

**Guangwu Li and Jishan Wu**
*Department of Chemistry, National University of Singapore,*
*3 Science Drive 3, Singapore 117543*
chmwuj@nus.edu.sg

Quinoidal π-conjugated molecules have irresistible tendency to become open-shell diradicals through recovery of aromaticity of the quinoidal rings. In this chapter, we will mainly be discussing about extended *para*-quinodimethanes (*p*-QDMs) and quinone-based diradicaloids. The contents include synthesis, chain-length dependent electronic properties, their chemical reactivity, and their material applications in organic electronic devices.

## 7.1 Extended Para-Quinodimethanes

The quinoidal π-conjugated *p*-QDM (Figure 7.1) is a basic unit in diradical chemistry and it can be in situ generated by pyrolysis of *p*-xylene [1, 2] or (2,2)paracyclophane [3]. Although it has never

*Diradicaloids*
Edited by Jishan Wu

ISBN 978-981-4968-08-9 (Hardcover), 978-1-003-27724-8 (eBook)
www.jennystanford.com

been separated due to its labile properties and easy to polymerize at condensed phase, several spectroscopic studies of *p*-QDM had been reported to reveal its physical properties, including infrared spectroscopy (IR), UV-visible spectroscopy (UV), nuclear magnetic resonance spectroscopy (NMR), and X-ray, indicating a quinoidal structure along with diradical population in agreement with theoretical prediction [3–9]. The source of the high reactivity of *p*-QDM has been ascribed to kinetic instability rather than ground state destabilization [10].

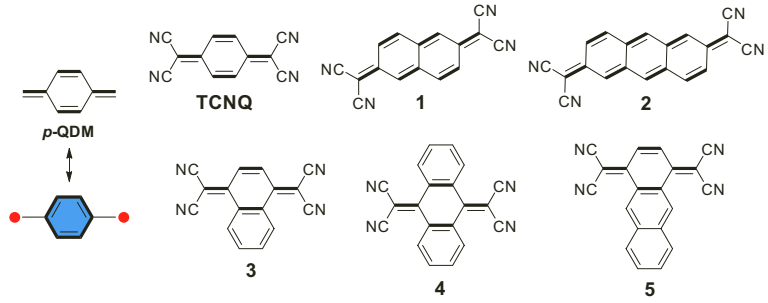


**Figure 7.1** Chemical structures of *p*-QDM, TCNQ, and its extended analogs.

Kinetic blocking of the terminal methylene sites is the main strategy to stabilize *p*-QDM. The well-known 7,7,8,8-tetracyanoquinodimethane (TCNQ) with strong electron-withdrawing cyano-groups exhibits good stability under ambient condition, and its strong electron-accepting property makes it a good candidate for donor-acceptor complex to achieve organic metals [11]. Later on, much effort had been made to develop its π-extended analogs whose structures would enhance the electrical conductivities of their charge transfer (CT) complexes. Compounds **1**–**5** were successfully prepared and all of them exhibit closed-shell ground states and high stability (Figure 7.1) [12, 13]. This mainly stems from the fact that the aromatic stabilizing energy is insufficient to compensate the energy required to break a π-bond.

The 13,13,14,14-tetracyanodiphenoquinodimethane (TCNDQ, **6**), where two dicyanomethylene groups are far apart compared to those in TCNQ (Figure 7.2), exhibited very high reactivity and tended to polymerize in solution [12]. Its high reactivity mainly derived from its much higher diradical character due to the recovery of two

aromatic sextet rings in the diradical form (for comparison, only one sextet can be recovered in the diradical form of TCNQ). Yamaguchi et al. reported the synthesis and crystallographic structure of **7**, which is a tetrabenzo- derivative of **6** [14]. X-ray analysis revealed that the central six-membered rings in each anthracene units adopt a boat-shaped conformation due to steric repulsion between hydrogen atoms at the *peri* positions. The lower diradical character and much higher stability can be explained by the remaining four aromatic sextet rings in its quinoidal form. Yamada et al. reported the synthesis of **8** and **9**, and both were stable electron-accepting materials with closed-shell ground state [15]. The crystal structure of **8** revealed a butterfly-shaped skeleton similar to that of **7.** Compound **9** exhibited one reversible single-wave reduction at −1.51 V, implying the electron storage ability.

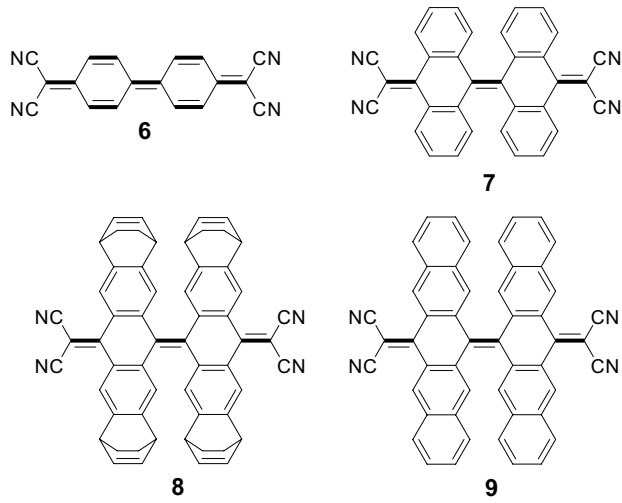


**Figure 7.2** Chemical structures of TCNDQ (**6**) and its extended benzo-annulated analogs.

Planarization of the backbone of **6** is another strategy to lower the radical character and enhance the stability. Compounds **10** and **11** with two additional ethyl or ethenyl groups, respectively, exhibit good stability with a typical closed-shell quinoidal structure in the ground state (Figure 7.3) [16, 17]. Yamashita et al. reported a novel electron acceptor **12**, in which the intramolecular [N…CH] hydrogen bond leads to a planar structure, and the intramolecular [N…CH]

hydrogen bond and [S...N] contacts afford a two-dimensional, coplanar sheet-like structure on the (101) plane [18]. The 1:1 CT complexes of **12** with tetrathiafulvalene (TTF), bis(ethylenedithio)-TTF, tetramethyltetraselenafulvalene and tetrathiatetracene exhibited high electrical conductivity of 7.9, 9.8, 18, and 9.9 S/cm, respectively. Wang et al. developed a carbazole-based diradicaloid **13** via Pd-catalyzed Takahashi coupling reaction followed by oxidative dehydrogenation [19]. The freshly prepared purple solution of monomer **13** can be fully converted to cyclophane tetramer **14** as a white powder simply by removing solvent, which can be considered as a σ-dimerization product of the reactive diradical intermediate **13A**. Further investigations revealed a dynamic and reversible cyclic transformation between monomer **13** and tetramer **14** upon external stimuli (light absorption, temperature, and moderate pressure). Nakamura et al. reported two thermally stable di- and tri-*p*-QDM compounds **15** and **16** [20]. The $^{1}$H NMR signals of **16** showed temperature-dependent broadening and the electron spin resonance (ESR) spectrum at 340 K in the solid state exhibited a signal with a fine structure, suggesting the presence of thermally populated triplet species. The energy gap between $S_0$ and $T_1$ states for **16** was determined to be 2.12 kcal/mol by superconducting quantum interference device (SQUID) measurements. Compound **15** gave well-resolved NMR spectrum at room temperature and it is ESR silent, indicating closed-shell ground state. Both **15** and **16** compounds exhibited a broad UV-vis absorption spectrum up to 800 nm and 1000 nm, respectively. Li et al. reported pyrrolo[3,2-*b*] pyrrole-based quinoidal compounds **17** and **18** [21]. Both the compounds have low-lying lowest unoccupied molecular orbital (LUMO) energy level and high thermal stability. The well-resolved NMR spectra indicate closed-shell nature. The compounds **17** and **18** exhibited nearly identical solution absorptions in $CH_2Cl_2$ solutions with a strong absorbance in the range of 550–850 nm. They both showed typical *n*-channel field-effect behaviors, and the electron mobility was measured to be 0.09 $cm^2V^{-1}s^{-1}$ and 0.75 $cm^2V^{-1}s^{-1}$ for the thin films of **17** and **18**, respectively. Both α-phase ribbons and β-phase flakes were observed in the micro-sized structures of **18**. Transistors based on single ribbons displayed gate voltage-dependent electron mobility with an average of 4.0 $cm^2V^{-1}s^{-1}$ and a peak over 6.0 $cm^2V^{-1}s^{-1}$.

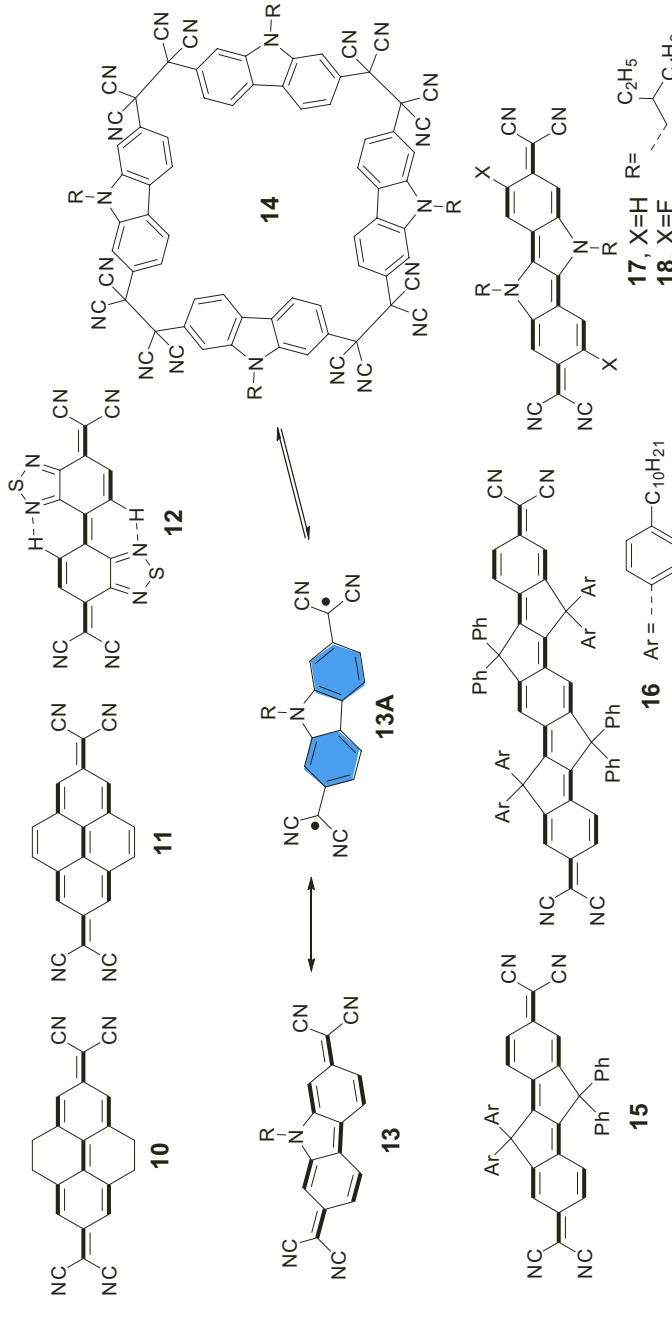


**Figure 7.3** Planar extended analogs of TCNDQ.

Our group synthesized a series of soluble and stable quinoidal oligomers **19**–**24** based on *N*-annulated perylene [22] (Figure 7.4). This series of molecules exhibited tunable ground-state structures, with **19** as a closed-shell hydrocarbon, **20**–**22** as open-shell singlet diradical species, and the higher order compounds **23** and **24** as triplet biradicals. The diradical character derived from the large strain induced by steric repulsion between the neighboring *N*-annulated perylene units. Raman spectra revealed that the vibrational bands for the (C=C) (benzenoid rings and the exo-C=C(CN)2) were shifted to lower frequency from the monomer to tetramer simultaneously, indicating the saturation of diradical character at tetramer (see Chapter 4). Finally, planarized quinoidal rylenes **25** and **26** for dimer and trimer were synthesized and characterized by our group [23]. In both molecules, the large strain was eliminated, leading to a much lower radical character. The planarized dimer has a closed-shell quinoidal structure in the ground state due to the strong anti-ferromagnetic coupling between the terminal radicals. The fused trimer retains an open-shell singlet ground state with a small diradical character ($y_0$ = 0.064), while the non-fused trimer exhibited more distinctive diradical character ($y_0$ = 0.99). In addition, two quinoidal rylenes **27** and **28** with two additional thiophene units showed enhanced diradical character as compared with the respective quinoidal rylenes **25** and **26** [24]. This can be explained by the recovery of two additional aromatic thiophene rings together with the conformational flexibility around the thiophene-rylene connections.

Substitution of the terminal methylene sites of *p*-QDM with phenyl groups affords the Thiele's hydrocarbon (**29**), which was firstly reported in 1904 (Figure 7.5) [25]. Thiele's hydrocarbon reacted with oxygen, but could be manipulated without elaborate precautions. Its inherent reactivity derived from its intrinsic diradical character. Uchiyama et al. reported a series of bridged tetra-aryl-*p*-quinodimethanes (**32**–**37**), which exhibit intense near-infrared (NIR) absorption and fluorescence up to 1000 nm [26]. Sharp and distinct $^1$H NMR signals were observed for all compounds, suggesting that they have closed-shell quinoidal structures in the ground state. Due to the strong donor/acceptor properties of the aryl groups, they exhibited good stability. Bottom-gate top-contact field-effect transistors (FETs) with a spin-coated film of **35** were fabricated and the hole mobility was determined to be 1.6 × $10^{-3}$ $cm^2V^{-1}s^{-1}$.

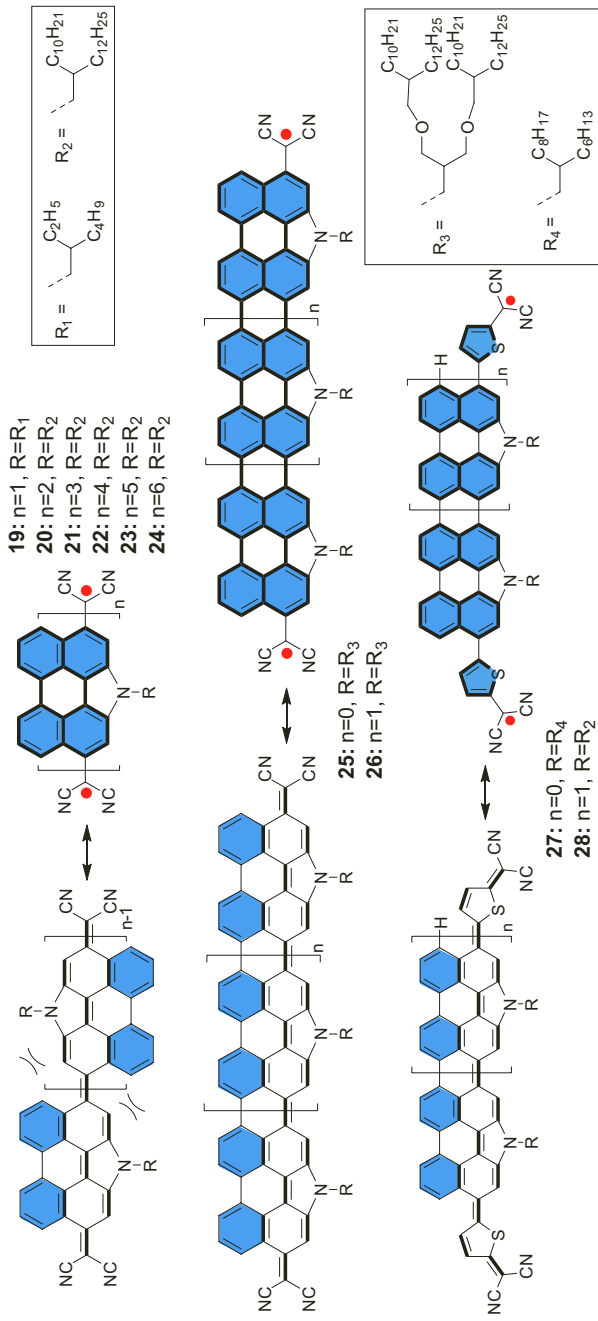


**Figure 7.4** Quinoidal oligomers based on the *N*-annulated perylene.

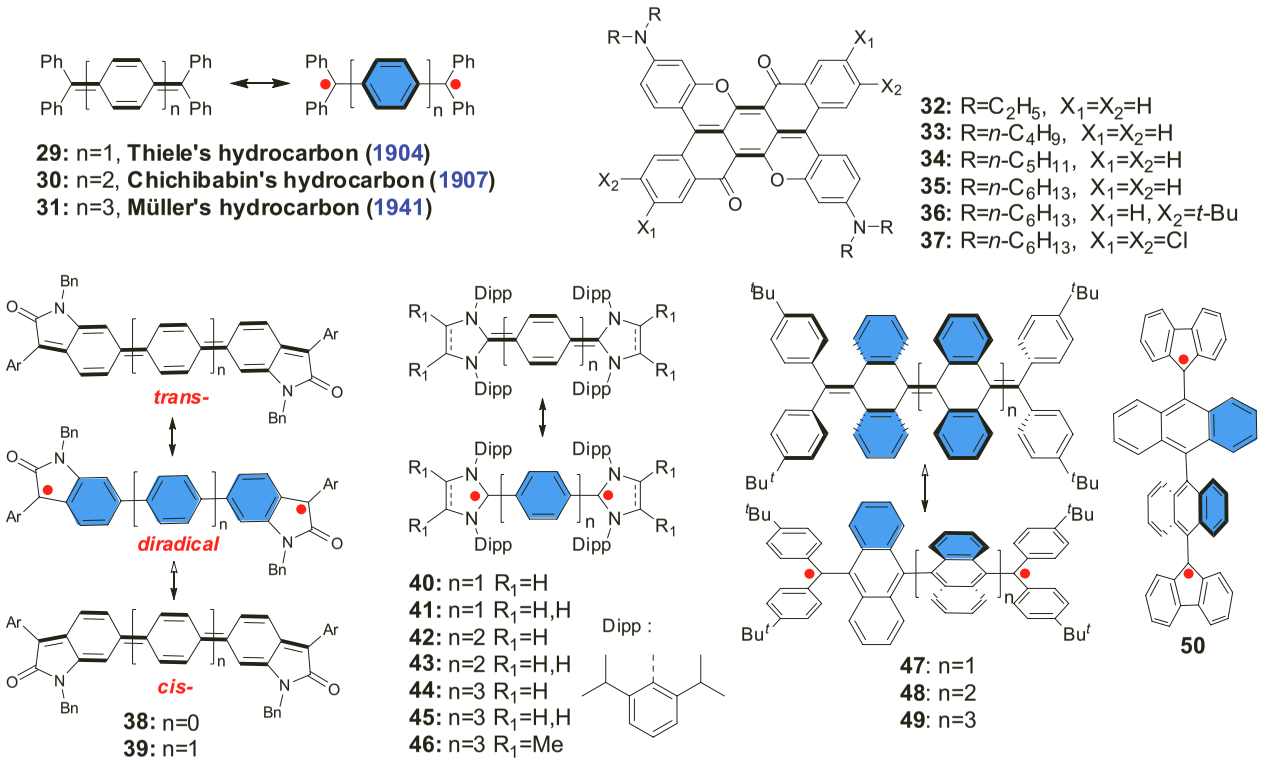


**Figure 7.5** Chemical structures of Thiele's hydrocarbon, Chichibabin's hydrocarbon, Müller's hydrocarbon, and their analogs.

The linearly extended analogs of Thiele's hydrocarbon to diphenoquinodimethane and triphenoquinodimethane were termed Chichibabin's hydrocarbon (**30**) [27] and Müller's hydrocarbon (**31**) [28], respectively (Figure 7.5), and both were unstable due to their large diradical character. Chichibabin's hydrocarbon revealed a singlet quinoidal structure with appreciable diradical character elucidated by X-ray crystallographic analysis obtained at low temperature [29]. Müller's hydrocarbon was even more reactive than Chichibabin's hydrocarbon, and thus, it was hard to obtain pure samples for reliable measurements [28]. Our group developed their stable analogs **38** and **39** based on the oxindolyl radicals [30]. X-ray crystallographic analysis of **38** revealed a *trans*-configuration with a nearly planar backbone. Large bond length alternation (BLA) was observed in diphenylquinodimethane unit similar to that of Chichibabin's hydrocarbon. Variable-temperature NMR studies on **38** revealed a slow *cis*-/*trans*-isomerization process in solution by going through a diradical transition state, with a moderate energy barrier ($\Delta G_{298K}$ = 15–16 kcal/mol). Density functional theory (DFT) calculations (UB3LYP/6-31G(d,p)) suggested that **38** had a smaller diradical character ($y_0$ = 11.1%) than Chichibabin's hydrocarbon ($y_0$ = 26.5%), and **39** also had a smaller diradical character ($y_0$ = 80.6%) than Müller's hydrocarbon ($y_0$ = 90.6%). A careful structural comparison clearly demonstrated that they indeed could be regarded as the stable analogs of Chichibabin's hydrocarbon and Müller's hydrocarbon, but with a slightly diminished diradical character. More importantly, their stability was largely improved due to thermodynamic stabilizing effect in the oxindolyl ring. Ghadwal et al. reported a series of stable *N*-heterocyclic carbene terminated analogs of Thiele's hydrocarbon (**40** and **41**), Chichibabin's hydrocarbon (**42** and **43**) and Müller's hydrocarbon (**44**–**46**), and the high stability derived from the bulky protecting groups [31]. The ground state for both **40** and **41** is a closed-shell singlet, and the calculated singlet-triplet energy gap is approximately 27 kcal/mol. The BLA for the phenyl rings in compounds **42** and **43** (0.08 Å) are smaller as compared to **40** and **41** (0.10 Å). The calculated diradical characters for **42** ($y_0$ = 0.41 at B3LYP/def2-SVP level of theory) and **43** ($y_0$ = 0.43 at B3LYP/def2-TZVPP level of theory) are higher than that of **40** and **41,** but lower as compared to that of Chichibabin's hydrocarbon ($y_0$ = 0.72). As expected, and according to Clar's aromatic sextet rule,

elongation of the spacer size leads to enhancement of the diradical characters of **44** ($y_0$ = 0.65), **45** ($y_0$ = 0.65), and **46** ($y_0$ = 0.64). The singlet-triplet energy gaps of **44** (−7.24 kcal/mol), **45** (−7.40 kcal/mol), and **46** (−7.60 kcal/mol) are significantly smaller compared to the related monophenylene **40** (−38.28 kcal/mol) and biphenylene **42** (−18.56 kcal/mol) derivatives at the same level of theory.

Our group reported a tetrabenzo-Chichibabin's hydrocarbon **47** with good stability [32]. Its closed-shell form **47-CS** and open-shell form **47-OS** were carefully investigated. X-ray crystallographic analysis revealed that **47-CS** existed in a highly contorted, quinoidal structure. A highly twisted butterfly-like geometry in the crystalline form was observed due to large steric repulsion between the two anthracene units and the four phenyl groups. The lengths of the *exo* methylene bond and the bond between the two anthracene units are 1.342 Å and 1.349 Å, which correspond closely to those in typical olefins. The observation of sharp NMR peaks and silence in ESR spectrum are evident of a closed-shell quinoidal structure for compound **47-CS**. Interestingly, the in situ generated diradical **47-OS** showed a slow decay toward the quinoidal ground state **47-CS**, with a half-lifetime of approximately 495 min as monitored by UV-vis absorption spectra. A large energy barrier (up to 22.7 kcal/mol at room temperature) with regards to the transition from the biradical form to the quinoidal form was determined, mainly due to large strain in the closed-shell quinoidal form. On the other hand, the fluorenyl-terminated analog **50** was characterized as an open-shell biradical, due to the thermodynamic stabilization of the spin by the fluorenyl unit. Then quinoidal 9,10-anthryl trimer **48** and tetramer **49** were synthesized and characterized [33]. DFT calculations and ESR measurements revealed triplet biradical (or two isolated radicals) ground state, due to the increased steric strain upon elongation of the chain length.

Some other protecting groups (i.e. **51** and **52**, Figure 7.6) were also developed. Compounds **51** and **52** underwent homopolymerization readily under thermal, radical, and anionic conditions [34, 35]. This phenomenon suggested the significant contribution of the singlet diradical resonance form to the ground electronic state. Their extended counterparts, therefore, were not investigated due to the poor stability. Zimmermann et al. first reported the air-persistent quinoidal bisimidazoly benzene **53** [36]. Later, Sakaino

et al. demonstrated that **53** existed predominantly in the quinoid structure at room temperature and reversibly isomerized to **54** (0.1% at 200 °C based on ESR) upon heating [37, 38]. Abe et al. provided a direct proof for the contribution of diradical form in bisimidazoly derivatives by the detection of an imidazole dimer **56** with X-ray crystallographic analysis (see Chapter 10) [39].

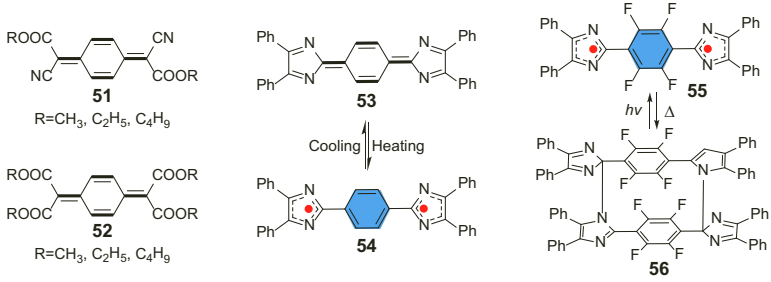


**Figure 7.6** Some analogs of the Thiele's hydrocarbon.

## 7.2 Extended Quinones

Besides the carbon-centered diradicaloids, oxygen-centered diradicaloids also gained wide interest and some examples are shown in Figure 7.7. Oxygen-centered quinoidal structures also coined as quinones, which were important dyes and pigments in industry production. *p*-Benzoquinone (**57**) and *p*-diphenoquinone (**58**) showed closed-shell ground state, whereas *p*-terphenoquinone exhibited either a closed-shell or an open-shell singlet ground state depending on the substituents [40–42]. The *tert*-butyl substituted terphenoquinone **59** displayed a closed-shell quinoidal structure, while the phenyl-substituted terphenoquinone **60** was reported as a paramagnetic substance with strong ESR signal, presumably due to extended spin delocalization to the phenyl rings. The *tert*-butyl substituted tetraphenoquinone **61** was also prepared as relatively stable compound with larger diradical character. These results demonstrated that the oxygen-centered diradicaloids exhibited much higher stability compared to the carbon analogs [43, 44]. Takahashi et al. prepared a series of extended quinones **62**–**65** with one or more dihydrothiophenediylidene moieties inserted between

the two rings of diphenoquinone. Their amphoteric redox properties were investigated, but their magnetic properties were not reported [45]. Later, computational and experimental studies indicated the closed-shell ground state of **62** and open-shell diradical nature of **63**–**65** [46, 47]. Oda et al. reported a stable dibenzoannulated *p*-terphenoquinone **66**, which showed sharp NMR signals without ESR signal, suggesting a closed-shell nature [48]. The longest absorption maximum in the UV-vis spectrum is 424 nm, which is largely blue-shifted compared to that of **66** at 631 nm, indicating less effective conjugation, due to the highly distorted conformation. Its reversible photochemical and thermal isomerization process between the quinoidal form and diradical form was reported via ESR spectroscopy. The ESR signals of diradical form decreased in the dark with a half-life of about 4 min at 298 K. The energy barrier ΔG was calculated to be about 21 kcal/mol referring to conformational change from the twisted structure of diradical form with a planar anthracene to the butterfly structure of quinoidal form. Extended compound **68** and partially fused **67** were developed by our group [49]. They exhibited sharp NMR signals in organic solvents even at elevated temperatures, indicating that both molecules existed in the form of quinone instead of diradicals.

The solution of **68** in concentrated sulfuric acid displays long-wavelength absorption bands with a maximum at 700 nm, which is largely red-shifted as compared with **66**. Würthner and Kim et al. reported a perylene bisimide quinone **69**, which exhibited an unusual sharp and intense NIR band at 783 nm [50]. Optical and magnetic spectroscopic measurements, as well as quantum chemical calculations, revealed an open-shell singlet diradical ground state for **69** with a relatively small singlet–triplet energy gap of 0.94 kcal/mol and a large diradical character ($y_0$ = 0.72). Osuka et al. presented a series of porphyrin- and hexaphyrin-based quinones **70**–**75** [51]. Compound **70** was shown to be a closed-shell quinonoid, while **71** exhibited as a diradical and was sensitive toward air and moisture. The energy gap between singlet and triplet states of **71** was estimated to be quite small of 0.13 kcal/mol by SQUID measurement, indicating the weak coupling between the two unpaired electrons. Compound **72** was not isolated due to its instability. Compounds **73** and **74** exhibited as closed-shell quinonoids without any appreciable diradical character, while **75** was a remarkably stable diradicaloid

displaying large diradical character ($y_0$ = 0.85). The energy gap between singlet and triplet states of **75** was estimated to be −3.72 kcal/mol, which was larger than **71**.

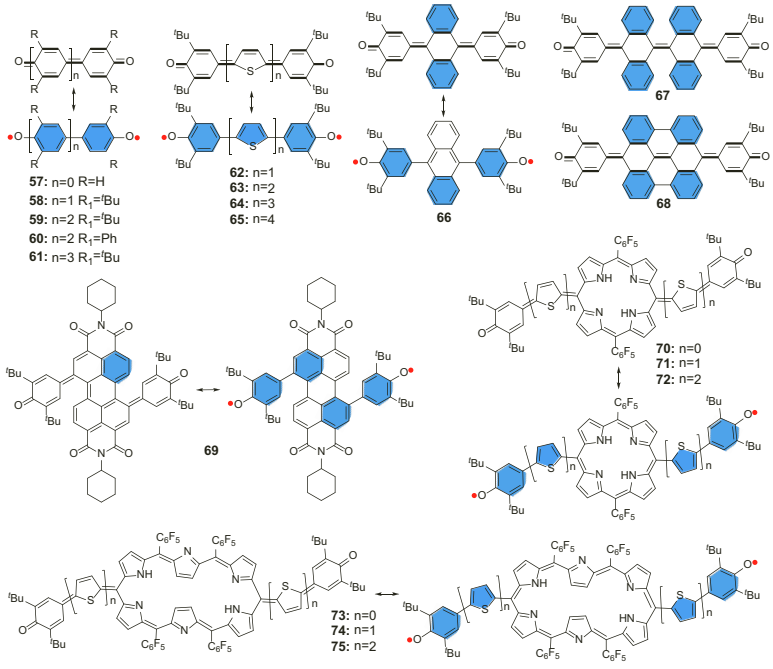


**Figure 7.7** Representative examples of linear extended quinones.

Star-shaped quinones **76** and **77** have been synthesized with closed-shell ground state (Figure 7.8), and they both showed interesting optical and redox properties [52–54]. Our group reported a star-shaped hexaquinocyclohexane molecule **79**, which turned out to be a closed-shell extended [6]radialene with a twisted-boat conformation according to X-ray crystallographic analysis [55]. It was formed by an unusually slow decay of its in situ generated open-shell valence isomer, the hexa-radical **78**, with a half-life time of about 156 min at room temperature. Reaction progress kinetic analysis revealed a large energy barrier of about 22.7 kcal/mol at room temperature from the hexa-radical form **78** to the more stable contorted [6]radialene form **79**. Hexa-*peri*-hexabenzocoronene (HBC) is one classic polycyclic aromatic hydrocarbon and can be considered as "superbenzene", owing to its benzene-like structure

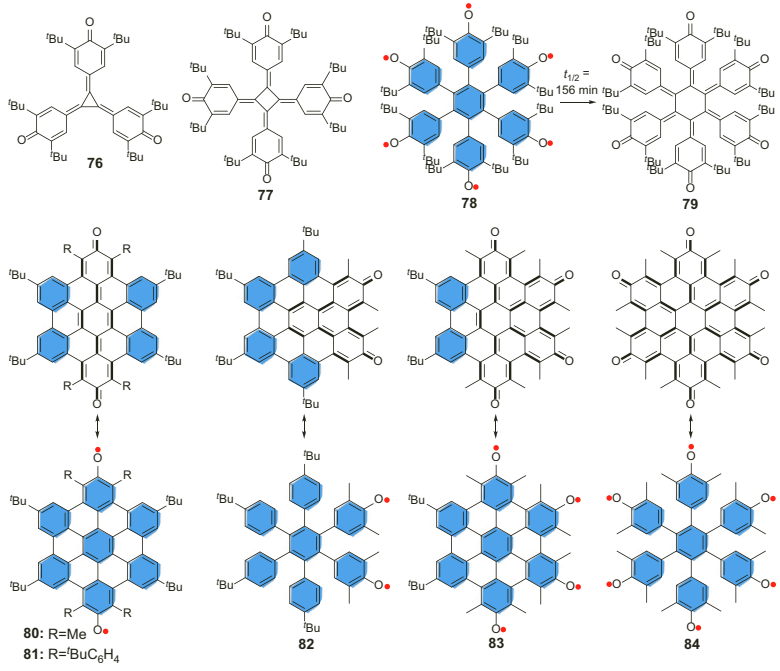


**Figure 7.8** Representative examples of star-shaped extended quinones.

with six-fold symmetry. Its quinone can thus be referred to as "superbenzoquinone" (SBQ). Shinokubo et al. attempted the synthesis of a SBQ derivative, however, the quinone product was not stable enough to be isolated, and the instability may derive from its radical species. Our group reported the first successful synthesis of SBQ (**80** and **81**) by incorporating bulky groups to kinetically block the reactive site [56]. Methyl-substituted **80** had a half-life of about 2.3 h when exposed to air and light under ambient conditions, while 4-*tert*-butylphenyl-substituted **81** demonstrated much better stability and could be isolated in crystalline form. X-ray chromatography revealed a butterfly-like geometry with four substituents bent to one side and the SBQ core bent to the other side, and bond length analysis indicated the large contribution of the quinoidal resonance form to the ground-state geometry of SBQ. Both compounds have an open-shell singlet ground state and showed thermally populated paramagnetic activity. Small diradical character ($y_0$ = 0.21) was calculated based on the X-ray structure,

and the singlet-triplet energy gap was estimated to be −2.77 kcal/mol by the SQUID measurements. Later, other SBQs **82**–**84** were reported by us through step-wise de-aromatization of HBC and these quinoidal compounds exhibit open-shell multiradical character due to the intrinsic tendency to recover aromaticity [57]. **84** has a high $S_6$ symmetry and large BLA, and small harmonic oscillator model of aromaticity values were observed for each outermost six-membered rings, consistent with a quinoidal structure. The bond length of the C=O bonds is 1.246 Å, which is slightly longer than that of the closed-shell **59**, indicating a major quinoidal structure with certain degree of open-shell radical character. The calculated anisotropy of induced current density (ACID) plot of **84** showed no obvious ring current circuit. Nuclear independent chemical shift (NICS) calculations revealed that there was no aromatic ring in **84**, indicating full de-aromatization of the HBC core.

The nitrogen analog of Thiele's hydrocarbon **85** is the construction block of polyaniline, and it can be easily doped with acid to form cations as conducting polymers (Figure 7.9) [58, 59]. The nitrogen analog of Chichibabin's hydrocarbon **86** readily undergoes a polymerization reaction, due to its intrinsic diradical character [60, 61]. Wudl et al. reported the nitrogen analogs of Chichibabin's hydrocarbon **87** based on stable 1,2,4-benzotriazinyl radicals [62]. VT $^1$H NMR spectra of **87** were recorded and the molecule showed broad signals due to thermal population of triplet species. These peaks became sharper and extra peaks were observed as the temperature was decreased to 220 K. ESR spectroscopy revealed that, in solution, it behaved as an ordinary benzotriazinyl doublet, while in the solid state as the quintet spin state, due to the interaction of two triplet S = 1 state molecules of a dimer within the crystal lattice, and the triplet induced by all four spins interacting in the dimer. Zheng et al. further elaborated on the nitrogen analogs of Chichibabin's hydrocarbon **88** and Müller's hydrocarbon **89** with open-shell ground state [63]. Large diradical character ($y_0$ = 0.63 for **88** and 0.85 for **89**) was calculated. The spin density distribution dominates in the triazinyl rings leading to a weak spin coupling between two radical centers and small singlet–triplet energy gaps (−1.05 to −1.27 kcal/mol). Diradicaloids based on triphenylamine cations [64] and boron anions [65–68] have also been reported (see Chapter 12), but they are usually sensitive to moisture and oxygen.

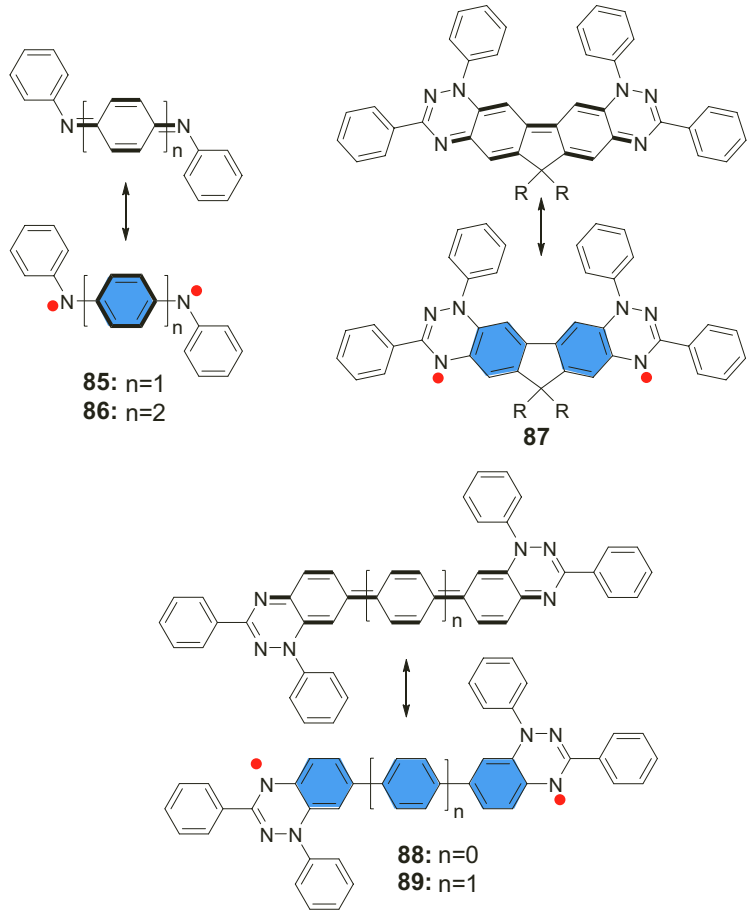


**Figure 7.9** Representative examples of nitrogen-centered analogs of quinoidal hydrocarbons.

## 7.3 Quinoidal Oligothiophenes

Owing to the lower aromatic stabilizing energy of thiophene than that of benzene, the thienoquinoidal structure is expected to exhibit lower diradical character and more stabilized than the benzoquinoidal counterpart. For the reported cases of thienoquinoidal systems, majority of them bear strong electron-withdrawing groups, such as cyano to afford high stability (Figure 7.10).

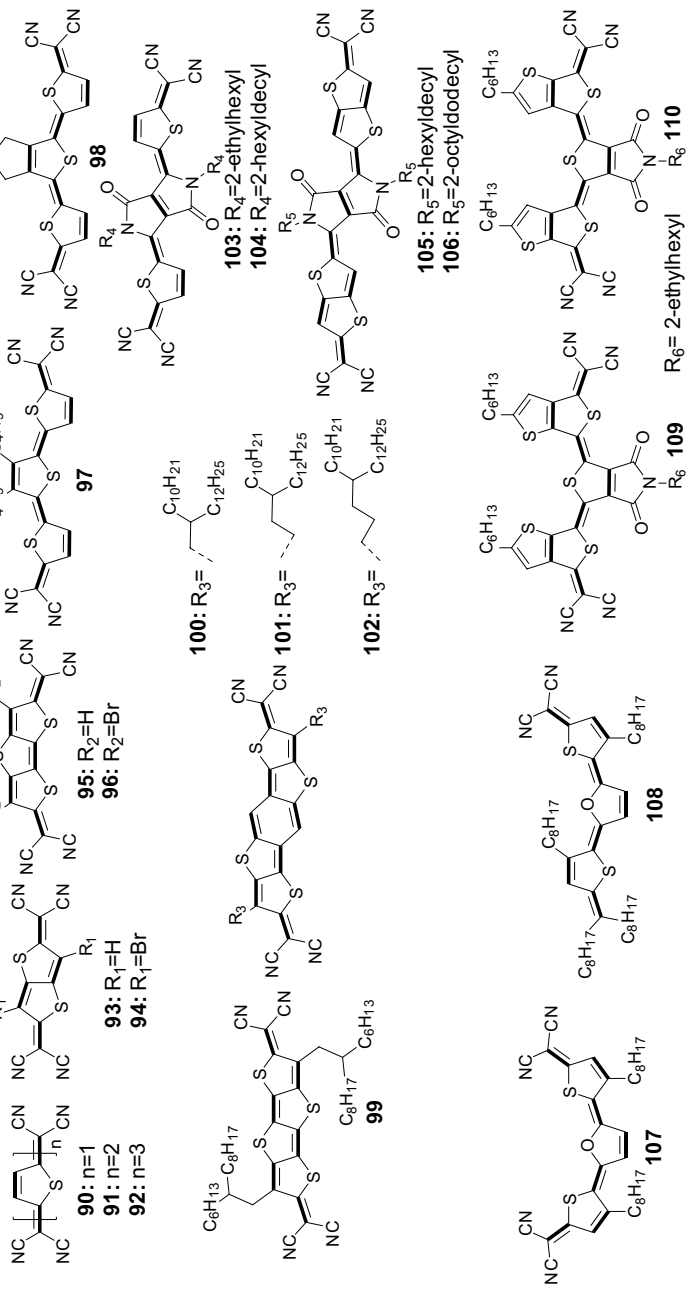


**Figure 7.10** Representative examples of quinoidal oligothiophenes.

The firstly reported quinoidal thiophene, the thiophene-7,7,8,8-TCNQ **90**, was developed as the alternative to TCNQ in 1974 by Gronowitz and Uppström [69]. The compound was synthesized by a pyrolytic reaction of 2,5-dibromothiophene with tetracyanoethylene oxide in dry 1,2-dibromoethane under reflux. The same method was used for the synthesis of extended quinoidal thiophenes such as 5,5′-bis-(dicyanomethylene)-5,5′-dihydro-2,2′-bithiophene **91** and 5,5′′-bis(dicyanomethylene)-5,5′′-dihydro-2,2′:5′,2′′-terthiophene **92,** and both are able to form conductive CT complexes with TTF [70]. Later, Koji et al. reported several condensed homologs of **90**, compounds **93**–**96**, which have been found to be superior electron acceptors with very small on-site Coulomb repulsion [71, 72]. They were synthesized from the dibromo-intermediates through Takahashi coupling followed by oxidation. They formed a variety of molecular complexes with π-electron donors, most of which exhibited very high electrical conductivities up to the metallic region. The solubility of quinoidal oligothiophenes is rapidly reduced when the chain is extended, and the poor solubility limits the applications. Thus, Mann et al. developed a highly soluble quinoidal terthiophene **97** with two butyl side chains, and solution processing for FET devices became possible due to the good solubility [73]. Electron field effect mobility in vapor- and solution-deposited films was measured as 0.005 $cm^2V^{-1}s^{-1}$ and 0.002 $cm^2V^{-1}s^{-1}$, respectively. The solution-processed device performance could be enhanced and reached a saturation electron mobility of 0.2 $cm^2V^{-1}s^{-1}$ at room temperature. It also showed that devices with **97** films grown at higher temperature can be ambipolar [74]. Then, lots of work were focused on improving their performance via structure or device modification. Takimiya et al. reported a quinoidal terthiophene **98** with a bis(butoxymethyl) cyclopentane ring [75]. Organic field-effect transistors (OFETs) fabricated on the as-spun film showed poor FET characteristics with electron mobility of $1.4 \times 10^{-4}$ $cm^2V^{-1}s^{-1}$. The electron mobility of **98** was improved to 0.16 $cm^2V^{-1}s^{-1}$ via annealing at 150 °C. A high electron mobility of 0.9 $cm^2V^{-1}s^{-1}$ was achieved based on the solution-processed thin film of a condensed quinoidal thiophene **99** under ambient condition without post-treatment [76]. Zhu et al. reported the effect of the branching position of alkyl chains (**100**–**102**) to

the performance of OFET device [77]. Compound **100** exhibited *n*-channel behavior, with electron mobility as high as 0.57 $cm^2V^{-1}s^{-1}$ without post-treatment. **102**-based transistors displayed electron-dominated ambipolar transport behavior, with electron mobilities reaching 0.2 $cm^2V^{-1}s^{-1}$ and hole mobilities in the range of $10^{-3}$–$10^{-4}$ $cm^2V^{-1}s^{-1}$. **101** showed solution-concentration-dependent carrier transport characteristics, exhibiting *n*-type behavior at low solution concentrations and ambipolar performance at high solution concentrations with an electron mobility of 0.22 $cm^2V^{-1}s^{-1}$ and a hole mobility of 0.034 $cm^2V^{-1}s^{-1}$. The diketopyrrolopyrrole (DPP)-containing quinoidal thiophenes **103** and **104** were synthesized by Zhu's group [78]. They exhibited maximum electron mobility up to 0.55 $cm^2V^{-1}s^{-1}$ for **103** by vapor evaporation, and 0.35 $cm^2V^{-1}s^{-1}$ for **104** by solution processing in air. Later, their extended analogs **105** and **106** were prepared, and they showed a small HOMO–LUMO energy gap of 1.41 eV, with an absorption onset of 879 nm [79]. Spin-coated OFETs based on **105** and **106** exhibited electron mobility values up to 0.22 and 0.16 $cm^2V^{-1}s^{-1}$, respectively, with $I_{on}/I_{off}$ greater than $10^6$. Their ground states were confirmed to be closed-shell singlet [80]. The good device performance and lower diradical character may be derived from the rigid and planar geometry induced by intramolecular hydrogen bonding between the DPP unit and thiophene ring. Li et al. reported a furan–thiophene-based quinoidal compound, which existed as a mixture of *cis*–*cis* (**107**) and *cis*–*trans* (**108**) isomers in solution and as a dominant *cis*–*cis* (**107**) structure in the solid state [81]. The thin films based on the mixture deposited from non-chlorinated solvent displayed a high electron mobility of 1.11 $cm^2V^{-1}s^{-1}$ and the micro-sized ribbon showed electron mobility as high as 7.7 $cm^2V^{-1}s^{-1}$, which was two orders of magnitude higher than the corresponding thiophene-based compound. Zhu et al. developed 2D π-expanded quinoidal terthiophenes **109** and **110** with outstanding semiconducting properties [82]. They exhibited quite different FET performances, with electron mobility of 0.44 $cm^2V^{-1}s^{-1}$ for **109** and 3.0 $cm^2V^{-1}s^{-1}$ for **110**, which were derived from the different film morphologies due to the minor change of thiophene orientation. The superior electron mobility of **110** was attributed to its higher crystallinity, longer crystalline coherence lengths, and lower orientational disorder, as compared to **109**.

In addition to the semiconducting behavior, magnetic property of extended quinoidal oligothiophenes is also of interest considering their possible open-shell diradical character. Otsubo et al. reported a series of dicyanomethylene-capped quinoidal oligothiophenes **111**–**116** (Figure 7.11), which were highly amphoteric redox systems and showed strong electronic absorption in the visible to NIR region [83]. Interestingly, the NMR spectra of **101** and **102** showed no signals due to the tetracyanothienoquinodimethane and cyclopentane carbons, indicating an open-shell ground state. The ESR measurements suggested about 2.8% and 29% population of triplet biradical species in **101** and **102**, respectively. Ponce Ortiz et al. presented a set of spectroscopic (i.e., Raman spectroscopy) and theoretical evidence that supports the existence of very low energy, thermally accessible excited triplet states, which are responsible for the magnetic activity in long quinoidal thienyl molecules (also see Chapter 4) [84]. Those results also demonstrated a relatively lower driving force to recover aromaticity in quinoidal oligothiophenes compared to the benzoquinoids. Zhu, Casanova, and Casado et al. reported a series of thienoquinoidal oligothiophenes from dimer to pentamer (**117**–**120**) [85]. Going from dimer to pentamer, a progressive change in the diradical character and aggregation mode was observed. Quantum chemical calculations revealed the diradical index $y_0$ increased from 0.00 (**117**) and 0.02 (**118**) to 0.22 (**119**) and 0.46 (**120**). ESR spectra were in accordance with calculations and showed that **117** was silent, while the ESR intensity increased in neutral films from **118** to **120**. More interestingly, *n*-type doped thin films of **119** exhibited an electrical conductivity as high as 14.0 S/cm and extraordinary stability in air, which can attain over 80% of the initial value after exposure for 240 h without encapsulation. Baumgarten et al. discussed a thieno[3,2-b]thiophene-based quinoidal compound **121** and its diradical character was systematically investigated [86]. $^1$H NMR spectra of **121** gave a sharp peak at 298 K, but became broader as the temperature was increased step by step. The peaks further disappeared at 393 K and no new peak was observed, suggesting the existence of thermally populated triplet species. Compound **121** exhibited increasing ESR signal intensities upon warming the sample from 220 K to 320 K,

which was in accordance with the variable-temperature $^1$H NMR measurements. The singlet–triplet energy gap was determined to be −6.88 kcal/mol via DFT calculations on the B3LYP/6-31g(d) level. Wu and Xia et al. reported two benzodithiophene based quinoidal compounds **122** and **123** [87]. VT $^1$H NMR measurements gave conclusive evidence of the closed-shell ground state for **123** and open-shell singlet ground state for **122**. A diradical character value of 0.59 was obtained via DFT calculation. ESR and SQUID further demonstrated the open-shell nature of **122**. A singlet-triplet energy gap of −0.49 kcal/mol was determined by SQUID measurement. The absorption spectrum of **122** in solution dramatically red-shifted to the NIR region with a peak at 816 nm as compared to **123** at 598 nm. Compound **123** exhibited unipolar electron transport characteristic with an optimal electron motility of 0.021 $cm^2V^{-1}s^{-1}$. Compound **122** displayed ambipolar behavior under ambient conditions with a much higher electron mobility of 0.32 $cm^2V^{-1}s^{-1}$ and a balanced hole mobility of 0.16 $cm^2V^{-1}s^{-1}$. This was a decent example that demonstrated an important role of the diradical character in tuning the charge transport property of organic π-functional materials.

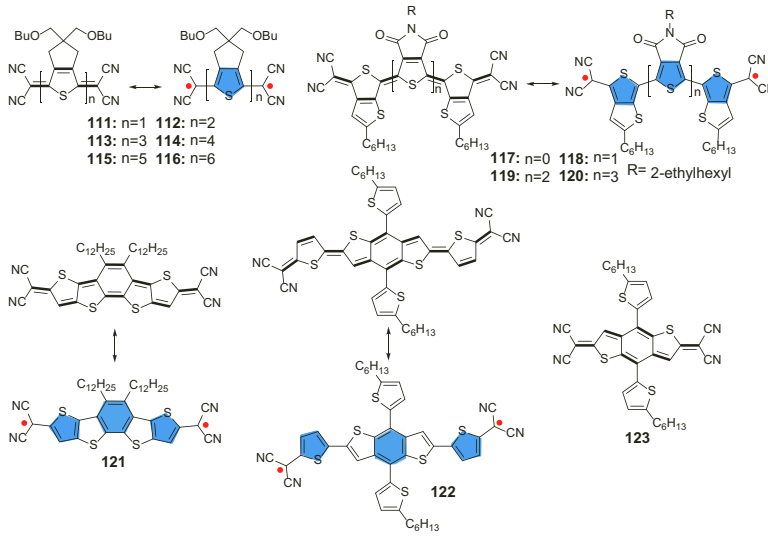


**Figure 7.11** Representative examples of open-shell quinoidal oligothiophenes.

Takimiya et al. developed a series of ((alkyloxy)carbonyl) cyanomethylene-substituted thienoquinoidal compounds **124**–**129** (Figure 7.12) [88]. The newly employed terminal groups play two important roles in those compounds, such as a solubilizing group for solution processability and an electron-withdrawing group to keep LUMO energy levels sufficiently low to ensure *n*-channel character. They all exhibited good solubility and solution-processed OFETs were easily fabricated. The terthienoquinoidal one (**125**) exhibited good *n*-channel FET characteristics with mobilities of up to 0.015 $cm^2V^{-1}s^{-1}$ and $I_{on}/I_{off}$ values of $\sim 10^5$ under ambient condition. Takimiya, Casado et al. reported the quinoidal naphthodithiophene **130**, which could undergo reversible diradical σ-dimerization/σ-polymerization triggered by mild stimuli such as concentration, temperature, and pressure [89]. The quinonoidal molecule has intrinsic tendency to change its structure to an aromatic open-shell diradical species, which can form weak and long intermolecular C–C single bonds. The reaction provoked a giant chromic effect of about 2.5 eV. The two opposite, but complementary quinonoidal and aromatic tautomers provide the Janus faces of the reactants and products, which produced the observed chromic effect. The diradical σ-dimer is the key intermediate, which is formed initially from unstable π-dimer intermediates and is able to either intramolecularly form a closed-shell σ-cyclophane, or represent the initiation step of the propagation mechanism of the oligomerization/polymerization reaction. Zhu et al. successfully developed new fluorophores **131**–**136** based on the rarely emissive quinoidal bithiophenes [90]. **131** shows enhanced fluorescence with a fluorescence quantum yield of 8.5%, 25-fold higher than that of the parent quinoidal (**124**) chromophore with maximum emission at similar wavelengths. Introduction of intramolecular charge transfer (ICT) by attaching aryl groups can further shift the maximum emissions into the NIR region. The ICT can be synthetically enhanced by tuning the substituents on the aryl groups, from the electron-withdrawing trifluoromethyl to the electron-donating methoxy groups. Positively related ICT and fluorescence quantum yield were unexpectedly observed, which gave high quantum yields of up to 53.1% (682 nm, **136**).

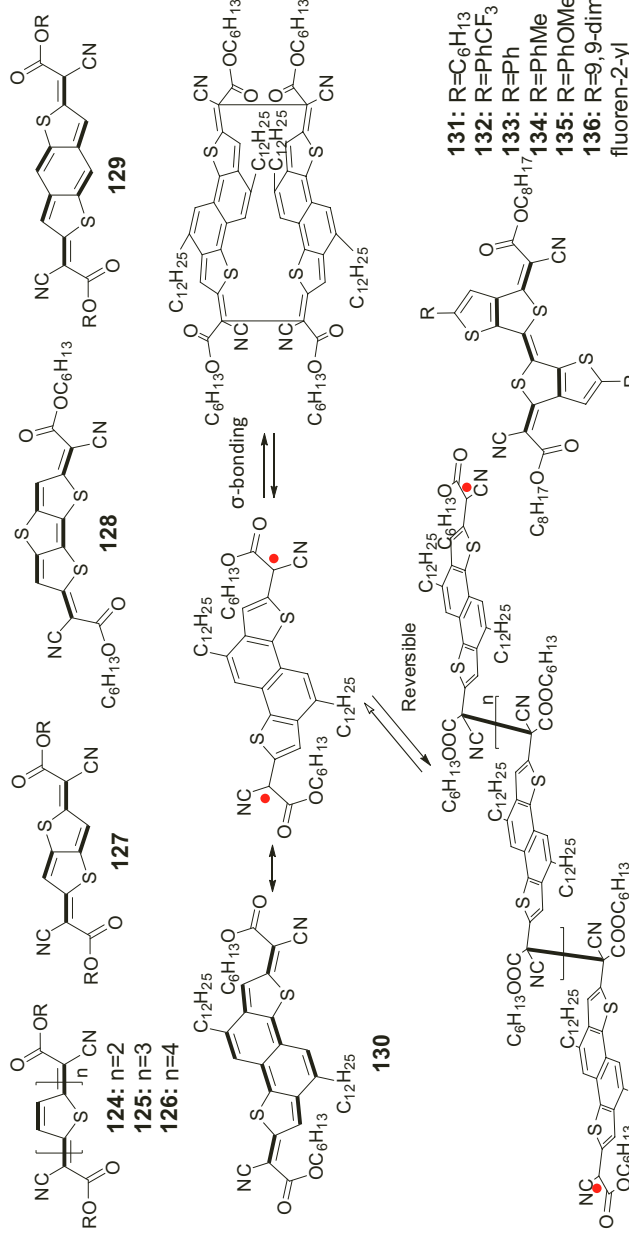


**Figure 7.12** Representative examples of quinoidal oligothiophenes with ((alkyloxy)carbonyl)cyanomethylene capping groups.

## 7.4 Conclusion

In summary, quinoidal conjugated molecules have intrinsic tendency to become open-shell diradicals, and thus, they are good building blocks for the design of open-shell singlet diradicaloids. Over a century, various extended *p*-QDM and quinones have been developed and some of them indeed displayed open-shell diradical character, which is dependent on the chain length and topological structure. Magnetic activity was observed due to the existence of thermally populated triplet species. These quinoidal compounds served as excellent *n*-type or ambipolar semiconductors and exhibited high charge carrier mobilities. In addition, doping of these small-band gap compounds led to high conductivity, which is desirable for thermoelectric applications [91]. Moreover, by taking advantage of both charge transporting property and magnetic activity, one can apply these materials for spintronics such as giant magnetoresistance, which was recently demonstrated by us in hybrid **27**/graphene (or $MoS_2$) monolayer devices [92].

### References


1. Szwarc, M. (1947). Some remarks on the *p*-xylene radical molecule, *Discuss. Faraday Soc.*, **2**, pp. 46–49.
2. Szwarc, M. (1947). The C—H bond energy in toluene and xylenes, *Nature,* **160**, pp. 403–403.
3. Mahaffy, P. G., Wieser, J. D., and Montgomery, L. K. (1977). An electron diffraction study of p-xylylene, *J. Am. Chem. Soc.*, **99**, pp. 4514–4515.
4. Williams, D. J., Pearson, J. M., and Levy, M. (1970). Nuclear magnetic resonance spectra of quinodimethanes, *J. Am. Chem. Soc.*, **92**, pp. 1436–1438.
5. Pearson, J. M., Six, H. A., Williams, D. J., and Levy, M. (1971). Spectroscopic studies of quinodimethanes, *J. Am. Chem. Soc.*, **93**, pp. 5034–5036.
6. Koenig, T., Wielesek, R., Snell, W., and Balle, T. (1975). Helium(I) photoelectron spectrum of *p*-quinodimethane, *J. Am. Chem. Soc.*, **97**, pp. 3225–3226.
7. Flynn, C. R. and Michl, J. (1974). .pi., .pi.-Biradicaloid hydrocarbons. o-Xylylene: Photochemical preparation from 1,4-dihydrophthalazine

in rigid glass, electric spectroscopy, and calculations, *J. Am. Chem. Soc.*, **96**, pp. 3280–3288.

8. Doehnert, D. and Koutecky, J. (1980). Occupation numbers of natural orbitals as a criterion for biradical character: Different kinds of biradicals, *J. Am. Chem. Soc.*, **102**, pp. 1789–1796.
9. Koenig, T. and Southworth, S. (1977). The helium (He I) photoelectron spectrum of 3,7-dimethyl-p-quinodimethane: A non-Koopmans theorem effect, *J. Am. Chem. Soc.*, **99**, pp. 2807–2809.
10. Pollack, S. K., Raine, B. C., and Hehre, W. J. (1981). Determination of the heats of formation of the isomeric xylylenes by ion cyclotron double-resonance spectroscopy, *J. Am. Chem. Soc.*, **103**, pp. 6308–6313.
11. Bryce, M. R. and Murphy, L. C. (1984). Organic metals, *Nature*, **309**, pp. 119–126.
12. Kaplan, M. L., Haddon, R. C., Bramwell, F. B., Wudl, F., Marshall, J. H., Cowan, D. O., and Gronowitz, S. (1980). Cyano-based acceptor molecules: Electrochemistry and electron spin resonance spectroscopy, *J. Phy. Chem.,* **84**, pp. 427–431.
13. Yanagimoto, T., Takimiya, K., Otsubo, T., and Ogura, F. (1993). 11,11,12,12-Tetracyano-2,6-anthraquinodimethane (TANT) as a novel extensive electron acceptor, *J. Chem. Soc. Chem. Commun.*, **6**, pp. 519–520.
14. Yamaguchi, S., Hanafusa, T., Tanaka, T., Sawada, M., Kondo, K., Irie, M., Tatemitsu, H., Sakata, Y., and Misumi, S. (1986). Synthesis of 29,29,30,30-tetracyanobianthraquinodimethane, *Tetrahedron Lett.*, **27**, pp. 2411–2414.
15. Tanaka, K., Aratani, N., Kuzuhara, D., Sakamoto, S., Okujima, T., Ono, N., Uno, H., and Yamada, H. (2013). A soluble bispentacenequinone precursor for creation of directly 6,6'-linked bispentacenes and a tetracyanobipentacenequinodimethane, *RSC Adv.*, **3**, pp. 15310–15315.
16. Maxfield, M., Willi, S. M., Cowan, D. O., Bloch, A. N., and Poehler, T. O. (1980). Synthesis of 13,13,14,14-tetracyanopyreno-2,7-quinodimethane, an electron acceptor for organic metals, *J. Chem. Soc., Chem. Commun.*, pp. 947–948.
17. Maxfield, M., Bloch, A. N., and Cowan, D. O. (1985). Large electron acceptors for molecular metals: 13,13,14,14-tetracyano-4,5,9,10-tetrahydro-2,7-pyrenoquinodimethane (TCNTP) anions of 13,13,14,14-tetracyano-2,7-pyrenoquinodimethane (TCNP), *J. Org. Chem.*, **50**, pp. 1789–1796.

18. Fukushima, T., Okazeri, N., Miyashi, T., Suzuki, K., Yamashita, Y., and Suzuki, T. (1999). First stable tetracyanodiphenoquinodimethane with a completely planar geometry: Preparation, X-ray structure, and highly conductive complexes of bis[1,2,5]thiadiazolo-TCNDQ, *Tetrahedron Lett.*, **40**, pp. 1175–1178.

19. Wang, D., Capel Ferrón, C., Li, J., Gámez-Valenzuela, S., Ponce Ortiz, R., López Navarrete, J. T., Hernández Jolín, V., Yang, X., Peña Álvarez, M., García Baonza, V., Hartl, F., Ruiz Delgado, M. C., and Li, H. (2017). New multiresponsive chromic soft materials: Dynamic interconversion of short 2,7-dicyanomethylenecarbazole-based biradicaloid and the corresponding cyclophane tetramer, *Chem. Eur. J.*, **23**, pp. 13776–13783.

20. Zhu, X., Tsuji, H., Nakabayashi, K., Ohkoshi, S.-i., and Nakamura, E. (2011). Air- and heat-stable planar tri-p-quinodimethane with distinct biradical characteristics, *J. Am. Chem. Soc.*, **133**, pp. 16342–16345.

21. Wu, H., Wang, Y., Qiao, X., Wang, D., Yang, X., and Li, H. (2018). Pyrrolo[3,2-b]pyrrole-based quinoidal compounds for high performance *n*-channel organic field-effect transistor, *Chem. Mater.*, **30**, pp. 6992–6997.

22. Zeng, Z., Ishida, M., Zafra, J. L., Zhu, X., Sung, Y. M., Bao, N., Webster, R. D., Lee, B. S., Li, R.-W., Zeng, W., Li, Y., Chi, C., Navarrete, J. T. L., Ding, J., Casado, J., Kim, D., and Wu, J. (2013). Pushing extended p-quinodimethanes to the limit: Stable tetracyano-oligo(*N*-annulated perylene)quinodimethanes with tunable ground states, *J. Am. Chem. Soc.*, **135**, pp. 6363–6371.

23. Zeng, Z., Lee, S., Zafra, J. L., Ishida, M., Zhu, X., Sun, Z., Ni, Y., Webster, R. D., Li, R.-W., López Navarrete, J. T., Chi, C., Ding, J., Casado, J., Kim, D., and Wu, J. (2013). Tetracyanoquaterrylene and tetracyanohexarylenequinodimethanes with tunable ground states and strong near-infrared absorption, *Angew. Chem. Int. Ed.*, **52**, pp. 8561–8565.

24. Zeng, Z., Lee, S., Zafra, J. L., Ishida, M., Bao, N., Webster, R. D., López Navarrete, J. T., Ding, J., Casado, J., Kim, D., and Wu, J. (2014). Turning on the biradical state of tetracyano-perylene and quaterrylenequinodimethanes by incorporation of additional thiophene rings, *Chem. Sci.*, **5**, pp. 3072–3080.

25. Thiele, J. and Balhorn, H. (1904). Ueber einen chinoïden Kohlenwasserstoff, *Ber. Dtsch. Chem. Ges.*, **37**, pp. 1463–1470.

26. Okamoto, Y., Tanioka, M., Muranaka, A., Miyamoto, K., Aoyama, T. Ouyang, X., Kamino, S., Sawada, D., and Uchiyama, M. (2018). Stable

Thiele's hydrocarbon derivatives exhibiting near-infrared absorption/emission and two-step electrochromism, *J. Am. Chem. Soc.*, **140**, pp. 17857–17861.

27. Tschitschibabin, A. E. (1907). Über einige phenylierte derivate des p, p-Ditolyls, *Ber. Dtsch. Chem. Ges.*, **40**, pp. 1810–1819.
28. Müller, E. and Pfanz, H. (1941). Mer biradikaloide Terphenylderlvate, *Ber. Dtsch. Chem. Ges. B*, **74**, pp. 1051–1074.
29. Montgomery, L. K., Huffman, J. C., Jurczak, E. A., and Grendze, M. P. (1986). The molecular structures of Thiele's and Chichibabin's hydrocarbons, *J. Am. Chem. Soc.*, **108**, pp. 6004–6011.
30. Wang, J., Xu, X., Phan, H., Herng, T. S., Gopalakrishna, T. Y., Li, G., Ding, J., and Wu, J. (2017). Stable oxindolyl-based analogues of Chichibabin's and Müller's hydrocarbons, *Angew. Chem. Int. Ed.*, **56**, pp. 14154–14158.
31. Ghadwal, R. S. (2019). Stable carbon-centered radicals based on *N*-heterocyclic Carbenes, *Synlett*, **30**, pp. 1765–1775.
32. Zeng, Z., Sung, Y. M., Bao, N., Tan, D., Lee, R., Zafra, J. L., Lee, B. S., Ishida, M., Ding, J., López Navarrete, J. T., Li, Y., Zeng, W., Kim, D., Huang, K.-W., Webster, R. D., Casado, J., and Wu, J. (2012). Stable tetrabenzo-Chichibabin's hydrocarbons: Tunable ground state and unusual transition between their closed-shell and open-shell resonance forms, *J. Am. Chem. Soc.*, **134**, pp. 14513–14525.
33. Lim, Z., Zheng, B., Huang, K.-W., Liu, Y., and Wu, J. (2015). Quinoidal oligo(9,10-anthryl)s with chain-length-dependent ground states: A balance between aromatic stabilization and steric strain release, *Chem. Eur. J.*, **21**, pp. 18724–18729.
34. Iwatsuki, S., Itoh, T., Iwai, T., and Sawada, H. (1985). Polymerization behavior of 7,8-bis(butoxycarbonyl)-7,8-dicyanoquinodimethane, *Macromolecules*, **18**, pp. 2726–2732.
35. Shouji, I., Takahito, I., Katsumi, N., and Hidehiko, F. (1982). Syntheses and homopolymerization of 7,8-dialkoxycarbonyl-7,8-dicyanoquinodimethanes, *Chem. Lett.*, **11**, pp. 517–520.
36. Mayer, U., Baumgärtel, H., and Zimmermann, H. (1966). Biradicals, quinones, and semiquinones of the imidazole series, *Angew. Chem. Int. Ed.*, **5**, pp. 311–311.
37. Sakaino, Y. (1983). Structures and chromotropic properties of imidazole derivatives produced from 3,6-bis(4,5-diphenyl-2H-imidazol-2-ylidene)cyclohexa-1,4-diene, *J. Chem. Soc. Perkin Trans. 1*, **1**, pp. 1063–1066.

38. Sakaino, Y., Kakisawa, H., Kusumi, T., and Maeda, K. (1979). Structures and chromotropic properties of 1,4-bis(4,5-diphenylimidazol-2-yl) benzene derivatives, *J. Org. Chem.,* **44**, pp. 1241–1244.
39. Kikuchi, A., Iwahori, F., and Abe, J. (2004). Definitive evidence for the contribution of biradical character in a closed-shell molecule, derivative of 1,4-bis-(4,5-diphenylimidazol-2-ylidene)cyclohexa-2,5-diene, *J. Am. Chem. Soc.*, **126**, pp. 6526–6527.
40. Boldt, P., Bruhnke, D., Gerson, F., Scholz, M., Jones, P. G., and Bär, F. (1993). Synthesis and structure of a p-terphenoquinone and paramagnetic species derived therefrom, *Helv. Chim. Acta*, **76**, pp. 1739–1751.
41. Dimroth, K., Umbach, W., and Blöcher, K. H. (1963). Bis-phenoxy-radicals of the polyphenyl series, *Angew. Chem. Int. Ed.*, **2**, pp. 620–621.
42. West, R., Jorgenson, J. A., Stearley, K. L., and Calabrese, J. C. (1991). Synthesis, structure and semiconductivity of a p-terphenoquinone, *J. Chem. Soc. Chem. Comm.,* **18**, pp. 1234–1235.
43. Zhou, J. and Rieker, A. (1997). Electrochemical and spectroscopic properties of a series of tert-butyl-substituted para-extended quinones, *J. Chem. Soc. Perkin Trans. 2*, **5**, pp. 931–938.
44. Rebmann, A. (1996). Synthesis, EPR spectroscopy and voltammetry of a p-quaterphenyl biradical/quinone, *J. Chem. Res. Synop.,* **7**, pp. 318–319.
45. Takahashi, K. and Suzuki, T. (1989). p-Diphenoquinone analogs extended by dihydrothiophenediylidene insertion: A novel amphoteric multistage redox system, *J. Am. Chem. Soc.*, **111**, pp. 5483–5485.
46. Di Motta, S., Negri, F., Fazzi, D., Castiglioni, C., and Canesi, E. V. (2010). Biradicaloid and polyenic character of quinoidal oligothiophenes revealed by the presence of a low-lying double-exciton state, *J. Phys. Chem. Lett.,* **1**, pp. 3334–3339.
47. Fazzi, D., Canesi, E. V., Negri, F., Bertarelli, C., and Castiglioni, C. (2010). Biradicaloid character of thiophene-based heterophenoquinones: The role of electron–phonon coupling, *ChemPhysChem*, **11**, pp. 3685–3695.
48. Hiroyuki, K., Tomomi, T., and Masaji, O. (1999). Dibenzoannulated 3,5,3′′,5′′-tetra(t-butyl)-p-terphenoquinone: A reversible, photochemical-thermal switching system involving restricted conformational change, *Chem. Lett.,* **28**, pp. 749–750.
49. Zhang, K., Huang, K.-W., Li, J., Luo, J., Chi, C., and Wu, J. (2009). A soluble and stable quinoidal bisanthene with NIR absorption and amphoteric redox behavior, *Org. Lett.*, **11**, pp. 4854–4857.

50. Schmidt, D., Son, M., Lim, J. M., Lin, M.-J., Krummenacher, I., Braunschweig, H., Kim, D., and Würthner, F. (2015). Perylene bisimide radicals and biradicals: Synthesis and molecular properties, *Angew. Chem. Int. Ed.*, **54**, pp. 13980–13984.
51. Naoda, K., Shimizu, D., Kim, J. O., Furukawa, K., Kim, D., and Osuka, A. (2017). Thienylquinonoidal porphyrins and hexaphyrins with singlet diradical ground states, *Chem. Eur. J.,* **23**, pp. 8969–8979.
52. West, R. and Zecher, D. C. (1967). Synthesis of a triquinocyclopropane, *J. Am. Chem. Soc.*, **89**, pp. 152–153.
53. West, R., Zecher, D. C., Koster, S. K., and Eggerding, D. (1975). Diquinocyclopropanones, diquinoethylenes, and the anion-radical and free-radical intermediates in their formation, *J. Org. Chem.,* **40**, pp. 2295–2299.
54. Hagenbruch, B., Hesse, K., Hünig, S., and Klug, G. (1981). Mehrstufige redoxsysteme, XXVIII. Ein butatrien und ein [4]-radialen mit gekreuzt konjugierten doppelbindungen als endgruppen; synthese und voltammetrie, *Liebigs Ann. Chem.*, **2**, pp. 256–263.
55. Feng, J., Gopalakrishna, T. Y., Phan, H., and Wu, J. (2018). Hexakis(3,6-di-tert-butyl-4-oxo-2,5-cyclohexadien-1-ylidene)cyclohexane: Closed-shell [6]radialene or open-shell hexa-radicaloid?, *Chem. Eur. J.,* **24**, pp. 9499–9503.
56. Li, G., Phan, H., Herng, T. S., Gopalakrishna, T. Y., Liu, C., Zeng, W., Ding, J., and Wu, J. (2017). Toward stable superbenzoquinone diradicaloids, *Angew. Chem. Int. Ed.*, **56**, pp. 5012–5016.
57. Li, G., Han, Y., Zou, Y., Lee, J. J. C., Ni, Y., and Wu, J. (2019). Dearomatization spproach toward a superbenzoquinone-based diradicaloid, tetraradicaloid, and hexaradicaloid, *Angew. Chem. Int. Ed.*, **58**, pp. 14319–14326.
58. Macdiarmid, A. G., Chiang, J. C., Richter, A. F., and Epstein, A. J. (1987). Polyaniline: A new concept in conducting polymers, *Synth. Met.,* **18**, pp. 285–290.
59. Baughman, R. H., Wolf, J. F., Eckhardt, H., and Shacklette, L. W. (1988). The structure of a novel polymeric metal: Acceptor-doped polyaniline, *Synth. Met.*, **25**, pp. 121–137.
60. Hammond, G. S., Seidel, B., and Pincock, R. E. (1963). Mechanism of the benzidine rearrangement. V.1 Acid-catalyzed decomposition of tetraphenyltetrazene and related compounds, *J. Org. Chem.,* **28**, pp. 3275–3279.

61. Seidel, B. and Hammond, G. S. (1963). "Polymerization" of *N*,*N*′-Diphenyl-p,p′-diphenoquinonimine, *J. Org. Chem.,* **28**, pp. 3280–3283.

62. Zheng, Y., Miao, M.-s., Dantelle, G., Eisenmenger, N. D., Wu, G., Yavuz, I., Chabinyc, M. L., Houk, K. N., and Wudl, F. (2015). A solid-state effect responsible for an organic quintet state at room temperature and ambient pressure, *Adv. Mater.*, **27**, pp. 1718–1723.

63. Hu, X., Chen, H., Zhao, L., Miao, M., Han, J., Wang, J., Guo, J., Hu, Y., and Zheng, Y. (2019). Nitrogen analogues of Chichibabin's and Müller's hydrocarbons with small singlet–triplet energy gaps, *Chem. Commun.,* **55**, pp. 7812–7815.

64. Tan, G. and Wang, X. (2017). Isolable bis(triarylamine) dications: Analogues of Thiele's, Chichibabin's, and Müller's Hydrocarbons, *Acc. Chem. Res.*, **50**, pp. 1997–2006.

65. Ji, L., Edkins, R. M., Lorbach, A., Krummenacher, I., Brückner, C., Eichhorn, A., Braunschweig, H., Engels, B., Low, P. J., and Marder, T. B. (2015). Electron delocalization in reduced forms of 2-(BMes2)pyrene and 2,7-Bis(BMes2)pyrene, *J. Am. Chem. Soc.*, **137**, pp. 6750–6753.

66. Braunschweig, H., Dyakonov, V., Engels, B., Falk, Z., Hörl, C., Klein, J. H., Kramer, T., Kraus, H., Krummenacher, I., Lambert, C., and Walter, C. (2013). Multiple reduction of 2,5-bis(borolyl)thiophene: Isolation of a negative bipolaron by comproportionation, *Angew. Chem. Int. Ed.*, **52**, pp. 12852–12855.

67. Zheng, Y., Xiong, J., Sun, Y., Pan, X., and Wu, J. (2015). Stepwise reduction of 9,10-bis(dimesitylboryl)anthracene, *Angew. Chem. Int. Ed.*, **54**, pp. 12933–12936.

68. Yuan, N., Wang, W., Fang, Y., Zuo, J., Zhao, Y., Tan, G., and Wang, X. (2017). Bis(boryl anion)-substituted pyrenes: Syntheses, characterizations, and crystal structures, *Organometallics,* **36**, pp. 2498–2501.

69. Gronowitz, S. and Uppström, B. (1974). On the reaction of 2,5-dihalothiophenes with tetracyanoethylene oxide, *Acta Chem. Scand. B,* **28**, pp. 981–985.

70. Yui, K., Aso, Y., Otsubo, T., and Ogura, F. (1987). New electron acceptors for organic metals: Extensively conjugated homologues of thiophene–7,7,8,8-tetracyanoquinodimethane (TCNQ), *J. Chem. Soc., Chem. Commun.,* **24**, pp. 1816–1817.

71. Koji, Y., Hideki, I., Yoshio, A., Tetsuo, O., Fumio, O., Atsushi, K., and Jiro, T. (1989). Novel electron acceptors bearing a heteroquinonoid system. II. Synthesis and conductive complexes of 2,5-bis(dicyanomethylene)-2,5-dihydrothieno[3,2-b]thiophene, 2,6-Bis(dicyanomethylene)-2,6-

dihydrodithieno[3,2-b:2′,3′-d]thiophene, and their derivatives, *Bull. Chem. Soc. Jpn.,* **62**, pp. 1547–1555.

72. Koji, Y., Hideki, I., Yoshio, A., Tetsuo, O., and Fumio, O. (1987). New electron acceptors of condensed-thiophene TCNQ type, *Chem. Lett.,* **16**, pp. 2339–2342.
73. Pappenfus, T. M., Chesterfield, R. J., Frisbie, C. D., Mann, K. R., Casado, J., Raff, J. D., and Miller, L. L. (2002). A π-stacking terthiophene-based quinodimethane is an n-channel conductor in a thin film transistor, *J. Am. Chem. Soc.*, **124**, pp. 4184–4185.
74. Chesterfield, R. J., Newman, C. R., Pappenfus, T. M., Ewbank, P. C., Haukaas, M. H., Mann, K. R., Miller, L. L., and Frisbie, C. D. (2003). High electron mobility and ambipolar transport in organic thin-film transistors based on a π-stacking quinoidal terthiophene, *Adv. Mater.,* **15**, pp. 1278–1282.
75. Handa, S., Miyazaki, E., Takimiya, K., and Kunugi, Y. (2007). Solution-processible n-channel organic field-effect transistors based on dicyanomethylene-substituted terthienoquinoid derivative, *J. Am. Chem. Soc.*, **129**, pp. 11684–11685.
76. Wu, Q., Li, R., Hong, W., Li, H., Gao, X., and Zhu, D. (2011). Dicyanomethylene-substituted fused tetrathienoquinoid for high-performance, ambient-stable, solution-processable n-channel organic thin-film transistors, *Chem. Mater.,* **23**, pp. 3138–3140.
77. Li, J., Qiao, X., Xiong, Y., Li, H., and Zhu, D. (2014). Five-ring fused tetracyanothienoquinoids as high-performance and solution-processable n-channel organic semiconductors: Effect of the branching position of alkyl chains, *Chem. Mater.,* **26**, pp. 5782–5788.
78. Qiao, Y., Guo, Y., Yu, C., Zhang, F., Xu, W., Liu, Y., and Zhu, D. (2012). Diketopyrrolopyrrole-containing quinoidal small molecules for high-performance, air-stable, and solution-processable n-channel organic field-effect transistors, *J. Am. Chem. Soc.*, **134**, pp. 4084–4087.
79. Wang, C., Zang, Y., Qin, Y., Zhang, Q., Sun, Y., Di, C.-a., Xu, W., and Zhu, D. (2014). Thieno[3,2-b]thiophene-diketopyrrolopyrrole-based quinoidal small molecules: Synthesis, characterization, redox behavior, and n-channel organic field-effect transistors, *Chem. Eur. J.,* **20**, pp. 13755–13761.
80. Ray, S., Sharma, S., Salzner, U., and Patil, S. (2017). Synthesis and characterization of quinoidal diketopyrrolopyrrole derivatives with exceptionally high electron affinities, *J. Phys. Chem. C,* **121**, pp. 16088–16097.

81. Xiong, Y., Tao, J., Wang, R., Qiao, X., Yang, X., Wang, D., Wu, H., and Li, H. (2016). A furan–thiophene-based quinoidal compound: A new class of solution-processable high-performance n-type organic semiconductor, *Adv. Mater.,* **28**, pp. 5949–5953.
82. Zhang, C., Zang, Y., Gann, E., McNeill, C. R., Zhu, X., Di, C.-a., and Zhu, D. (2014). Two-dimensional π-expanded quinoidal terthiophenes terminated with dicyanomethylenes as n-type semiconductors for high-performance organic thin-film transistors, *J. Am. Chem. Soc.*, **136**, pp. 16176–16184.
83. Takahashi, T., Matsuoka, K.-i., Takimiya, K., Otsubo, T., and Aso, Y. (2005). Extensive quinoidal oligothiophenes with dicyanomethylene groups at terminal positions as highly amphoteric redox molecules, *J. Am. Chem. Soc.*, **127**, pp. 8928–8929.
84. Ponce Ortiz, R., Casado, J., Hernández, V., López Navarrete, J. T., Viruela, P. M., Ortí, E., Takimiya, K., and Otsubo, T. (2007). On the biradicaloid nature of long quinoidal oligothiophenes: Experimental evidence guided by theoretical studies, *Angew. Chem. Int. Ed.*, **46**, pp. 9057–9061.
85. Yuan, D., Huang, D., Rivero, S. M., Carreras, A., Zhang, C., Zou, Y., Jiao, X., McNeill, C. R., Zhu, X., Di, C.-a., Zhu, D., Casanova, D., and Casado, J. (2019). Cholesteric aggregation at the quinoidal-to-diradical border enabled stable n-doped conductor, *Chem*, **5**, pp. 964–976.
86. Xia, D., Keerthi, A., An, C., and Baumgarten, M. (2017). Synthesis of a quinoidal dithieno[2,3-d;2′,3′-d]benzo[2,1-b;3,4-b′]-dithiophene based open-shell singlet biradicaloid, *Org. Chem. Front.,* **4**, pp. 18–21.
87. Lin, Z., Chen, L., Xu, Q., Shao, G., Zeng, Z., Wu, D., and Xia, J. (2020). Tuning biradical character to enable high and balanced ambipolar charge transport in a quinoidal π-system, *Org. Lett.,* **22**, pp. 2553–2558.
88. Suzuki, Y., Miyazaki, E., and Takimiya, K. (2010). ((Alkyloxy)carbonyl) cyanomethylene-Substituted thienoquinoidal compounds: A new class of soluble n-channel organic semiconductors for air-stable organic field-effect transistors, *J. Am. Chem. Soc.*, **132**, pp. 10453–10466.
89. Zafra, J. L., Qiu, L., Yanai, N., Mori, T., Nakano, M., Alvarez, M. P., Navarrete, J. T. L., Gómez-García, C. J., Kertesz, M., Takimiya, K., and Casado, J. (2016). Reversible dimerization and polymerization of a Janus diradical to produce labile C–C bonds and large chromic effects, *Angew. Chem. Int. Ed.*, **55**, pp. 14563–14568.
90. Ren, L., Liu, F., Shen, X., Zhang, C., Yi, Y., and Zhu, X. (2015). Developing quinoidal fluorophores with unusually strong red/near-infrared emission, *J. Am. Chem. Soc.*, **137**, pp. 11294–11302.

91. Yuan, D., Guo, Y., Zeng, Y., Fan, Q., Wang, J., Yi, Y., and Zhu, X. (2019). Air-stable n-type thermoelectric materials enabled by organic diradicaloids, *Angew. Chem. Int. Ed.*, **58**, 4958–4962.

92. Datta, S., Cai, Y., Yudhistira, I., Zeng, Z., Zhang, Y.-W., Zhang, H., Adam, S., Wu J., and Loh, K. P. (2017). Tuning magnetoresistance in molybdenum disulphide and graphene using a molecular spin transition, *Nat. Commun.,* **8**, pp. 677.

Chapter 8

# Fused Heteropolycyclic Compounds-Based Diradicaloids

**Shaoqiang Dong and Chunyan Chi**
*Department of Chemistry, National University of Singapore, Singapore 117543*
chmcc@nus.edu.sg

In this chapter, we will provide a summary on open-shell singlet diradicaloids based on fused heteropolycyclic compounds (FHCs), namely: (i) quinoidal acene and heteroacene analogs, (ii) extended aza-acenes and aza-quinodimethanes, and (iii) non-classical acenes capped with thiophenes or thiadiazoles. Synthesis, physical characterization, and fundamental structure-diradical character-electronic property relationships will also be discussed.

## 8.1 Introduction

In the previous chapter, the emphasis was placed on quinoidal oligomers of benzenoid or heterocyclic units. In this chapter, the focus will be placed on the FHCs, in which all the rings are fused

*Diradicaloids*
Edited by Jishan Wu

ISBN 978-981-4968-08-9 (Hardcover), 978-1-003-27724-8 (eBook)
www.jennystanford.com

together to form a rigid structure. Specifically designed FHCs could show open-shell diradical character, and indeed, a family of stable singlet diradicaloids based on FHCs has been synthesized in recent years.

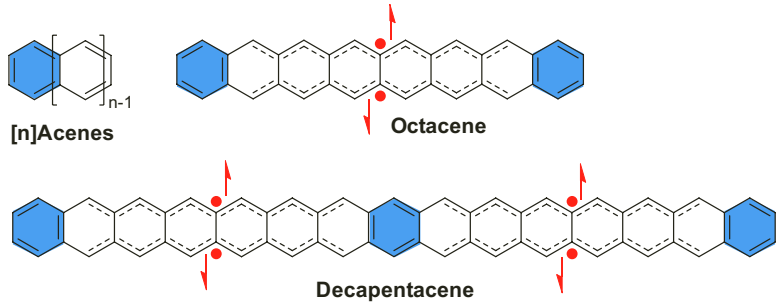


**Figure 8.1** Structures of closed-shell [*n*]acenes, open-shell diradical form of octacene, and open-shell tetraradical form of decapentacene. The hexagons shaded in blue denote Clar's aromatic sextets.

The chemistry of open-shell FHCs was initially derived from the long-term studies on acenes. The [*n*]acenes are a class of polycyclic aromatic hydrocarbons (PAHs) made up of *n* number of linearly fused benzene rings (Figure 8.1). Only one Clar's aromatic sextet can be drawn in the closed-shell resonance form and with extension of molecular length, the molecules show more diene character and thus, higher reactivity. Spin unrestricted density functional theory (UDFT) calculations predicted that higher [*n*]acenes ($n > 6$) would show open-shell diradical character and even polyradical character [1–3]. For example, octacene can be depicted as a structure with two Clar's sextets on the external benzenoid rings and two radicals delocalized along the zigzag edges in the middle. The longer decapentacene can be regarded as a tetraradical with the central ring bearing a Clar sextet and the four unpaired electrons centered at the first and third quarters of the chain (Figure 8.1). With further extension, the polyacenes are supposed to display polyradical character. Solution-phase synthesis of stable long acenes is extremely challenging [4–10], and currently, the longest one is a nonacene derivative reported by Anthony's group [10]. However, there was no clear magnetic evidence on the open-shell character. On-surface synthesis of high order acenes extending up to dodecacene has been

demonstrated, and scanning tunneling spectroscopy measurements on metal surface indeed provided some clues on the open-shell di-(poly-)radical character [11–13]. However, the instability of these long acenes to oxygen hindered detailed studies to be conducted on the magnetic properties.

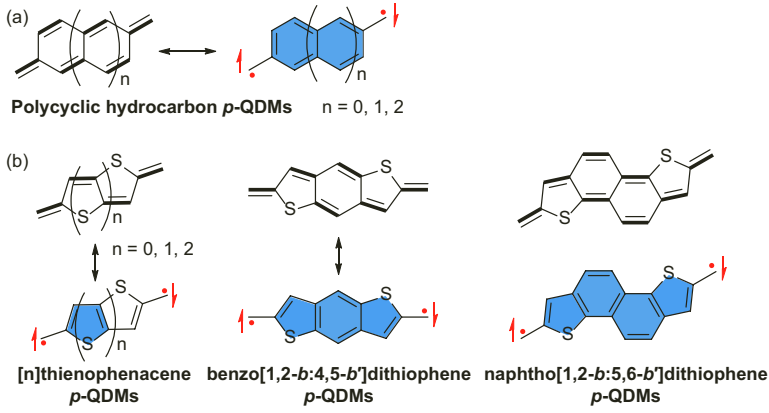


**Figure 8.2** (a) Resonance structures of extended *p*-QDMs. (b) Resonance structures of representative heteropolycyclic *p*-QDMs.

In 2014, our group started to explore alternative approaches accessing long acenes. The main idea was to incorporate one or more quinoidal polycyclic hydrocarbon or heteropolycyclic *para*-quinodimethanes (*p*-QDMs) into the backbone of the acenes (Figure 8.2). Subsequent oxidation or reduction will give isoelectronic structures of acenes, which are expected to show similar electronic properties. These extended *p*-QDMs have intrinsic tendency to become open-shell diradicals and thus, the obtained quinoidal acenene analogs could exhibit open-shell singlet ground state. The diradical character can be tuned by the stability of their resonance form, for example, from the simplest *p*-QDM to its extended structures 2,6-naphthoquinodimethane (*p*-NQDM) and 2,6-anthraquinodimethane (*p*-AQDM). The diradical character would increase due to the gain of more aromatic stabilization energy in the open-shell diradical form (Figure 8.2a). Similarly, heteropolycyclic *p*-QDMs based on [*n*]thienophenacene, benzo[1,2-*b*:4,5-*b*′]dithiophene and *s*-indaceno[1,2-*b*:5,6-*b*′]dithiophene (Figure 8.2b) could be also fused with polycyclic hydrocarbons to

generated quinoidal heteroacene analogs and potentially display open-shell diradical character. In the initial part of this chapter, we will summarize our own research works on the FHC-based diradicaloids.

Incorporating electron-deficient imine *N* atoms to the acene or QDM backbones would generate extended aza-acenes and aza-QDMs, which are expected to show improved stability as compared to all-carbon analogs [14–16]. Indeed, some relatively stable long aza-acenes and aza-QDMs have been synthesized and exhibited diradical-like chemical reactivity. This will be discussed in the second part of this chapter. In addition, non-classical acenes capped with thiophene or thiadiazole rings are also of interest, due to their potential open-shell diradical character, and the attempts to synthesize these reactive species will be discussed at the end of this chapter.

## 8.2 Quinoidal Acene and Heteroacene Analogs

### 8.2.1 General Synthetic Strategies

Two types of FHCs, in which a polycyclic hydrocarbon-based *p*-QDM or a heteropolycyclic *p*-QDM is fused with a conjugated moiety at the two termini, have been synthesized mainly by our group (Scheme 8.1a). Considering the possibility of exhibiting open-shell diradical character, steric bulky groups such as mesityl and triisopropylsilyl (TIPS) ethynyl, or electro-withdrawing phenyl groups such as 2,6-dichlorophenyl, 3,5-bis(trifluoromethyl) phenyl, and 2,3,4,5,6-hexafluorophenyl are attached onto the most reactive sites (the sites with the highest spin density). Two general synthetic strategies have been developed (Scheme 8.1b). In the first synthetic route, the key steps involved the intramolecular Friedel-Crafts (FC) cyclization of diol intermediate compound followed by oxidative dehydrogenation. In the second one, the key steps included nucleophilic addition of diketone compounds by the lithium salt of protecting groups followed by reduction.

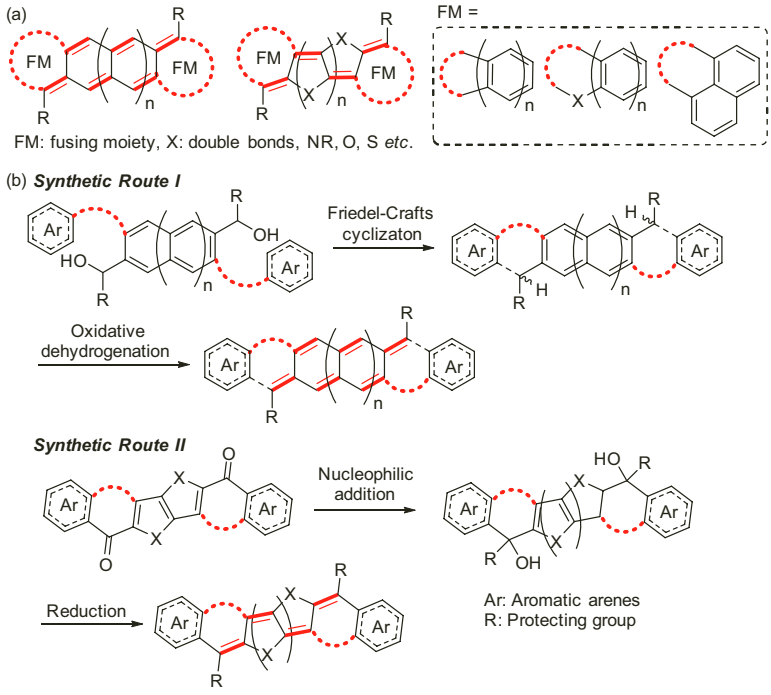


**Scheme 8.1** Strategies toward quinoidal acene and heteroacene analogs: (a) general fusion mode and structures, and (b) two representative synthetic routes.

## 8.2.2 Extended Quinoidal Acene Analogs

We designed a series of bis(arenohetero)quinodimethanes in which both the central QDM and lateral arenes can be extended and bridged by heteroatoms such as S, O, and N (Figure 8.3). These pro-aromatic molecules have tendency to become diradicals. Two-electron oxidation would result in dications, which can be considered as the isoelectronic structures of the respective acenes. These charged species are supposed to show similar properties to acenes, but they are instead more stable due to decreasing HOMO energy level.

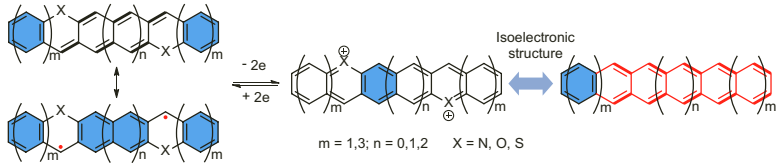


**Figure 8.3** Structures of bis(arenohetero)quinodimethanes, and their dications as isoelectronic structures of acenes.

Over the years, we have developed several stable derivatives of bis(arenohetero)quinodimethanes such as **1**–**8** (Figure 8.4) [17–21]. The ground-state electronic structure, diradical character, optical properties, and electrochemical properties have been investigated in detail. Their charged species were generated, and the electronic properties were compared with the respective acenes.

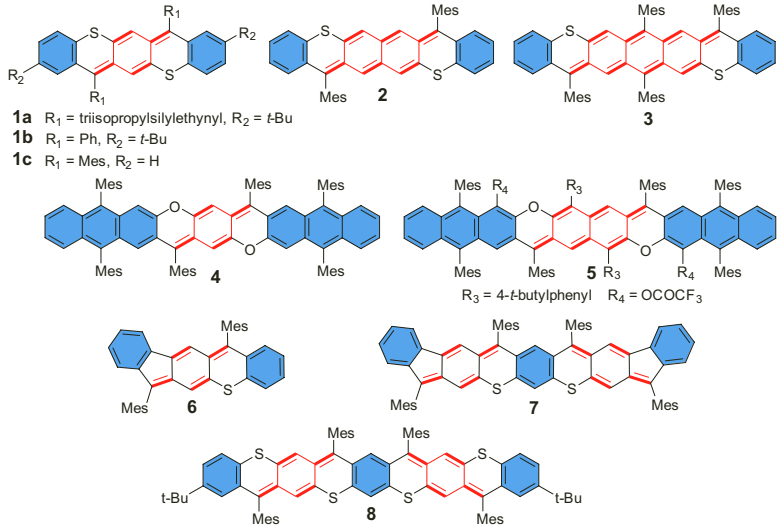


**Figure 8.4** Chemical structures of some derivatives of bis(arenohetero) quinodimethanes.

The shortest in series contains five linearly fused six-membered rings. Its derivatives **1a** and **1b** were prepared via nucleophilic addition of the diketone intermediate compound **10** by the lithium salt of protecting groups followed by reduction with $SnCl_2$ (Scheme 8.2). The diketone was synthesized by intramolecular FC acylation reaction from **9**. X-ray crystallographic analysis of **1a** and

**1b** revealed a typical quinoidal character with a large bond length alternation (BLA) of the central benzenoid ring. Compared to their all-carbon analog pentacene, **1a** and **1b** showed significantly improved stability. Furthermore, **1a** and **1b** showed moderate field effect hole mobility of 0.013 $cm^2\ V^{-1}\ s^{-1}$ and 0.013 $cm^2\ V^{-1}\ s^{-1}$, respectively [17].

The relationship between the extension of the central quinoidal moieties on the ground states of these bis(arenohetero) quinodimethanes was then examined. By changing the central quinoidal *p*-QDM ($n$ = 0) to *p*-NQDM ($n$ = 1) and *p*-AQDM ($n$ = 2), with S atoms as the linkage, compounds **1c**, **2**, and **3** were designed and synthesized (Scheme 8.2) [19]. The synthetic route was mainly focused on intramolecular FC alkylation of the intermediate diols **12a**, **12b**, and **15**, followed by oxidative dehydrogenation by 2,3-dichloro-5,6-dicyano-1,4-benzoquinone (DDQ). Mesityl groups were introduced to protect reactive radical centers and provide enough solubility.

Variable-temperature (VT) NMR measurements indicated that **1c** showed closed-shell ground state, while **2** and **3** showed obvious spectral broadening at elevated temperatures caused by a thermally populated triplet species, indicating their open-shell singlet ground state. UDFT calculations (UCAM-B3LYP/6-31G(d,p)) predicted a closed-shell ground state of **1c**, while **2** and **3** have an open-shell singlet ground state with a diradical character ($y_0$) of 0.195 and 0.384, respectively. The temperature-dependent magnetic susceptibility measurements of **3** (5–380 K) by superconducting quantum interference device (SQUID) confirmed a singlet ground state, and fitting of the data by Bleaney–Bowers equation gave a singlet-triplet energy gap ($\Delta E_{S-T}$) of −5.3 kcal/mol, which was consistent with the theoretical value of −5.49 kcal/mol. X-ray crystallographic analysis (Figure 8.5) of all three compounds further indicated that **2** (1.397 Å) and **3** (1.395 Å) both had a larger C1–C2 bond length than that of compound **1c** (1.384 Å). Nucleus-independent chemical shift ($NICS(1)_{zz}$) values of the central quinoidal units also gradually increased from **1c** to **3**, indicating the increase of aromaticity and diradical character with extension of the molecular length. The absorption spectrum of **3** showed a weak shoulder at the low-energy edge of its main peak, which is associated with a low-lying doubly excited state, further supporting its open-shell singlet diradical character [22].

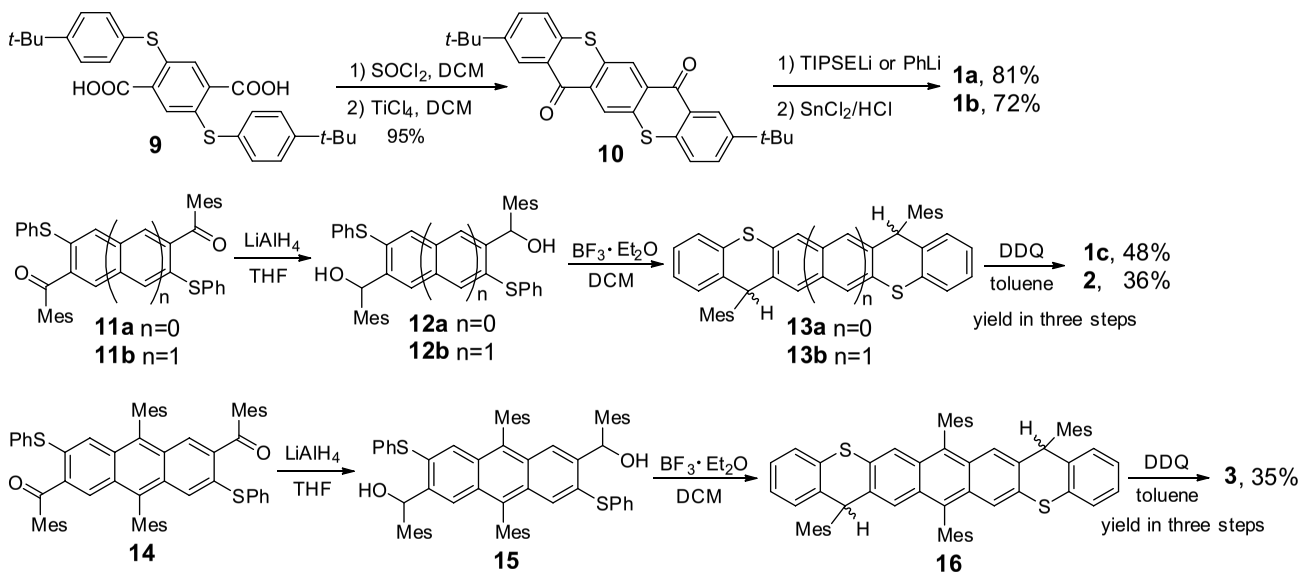


**Scheme 8.2** Synthetic routes to **1a-c**, **2,** and **3**.

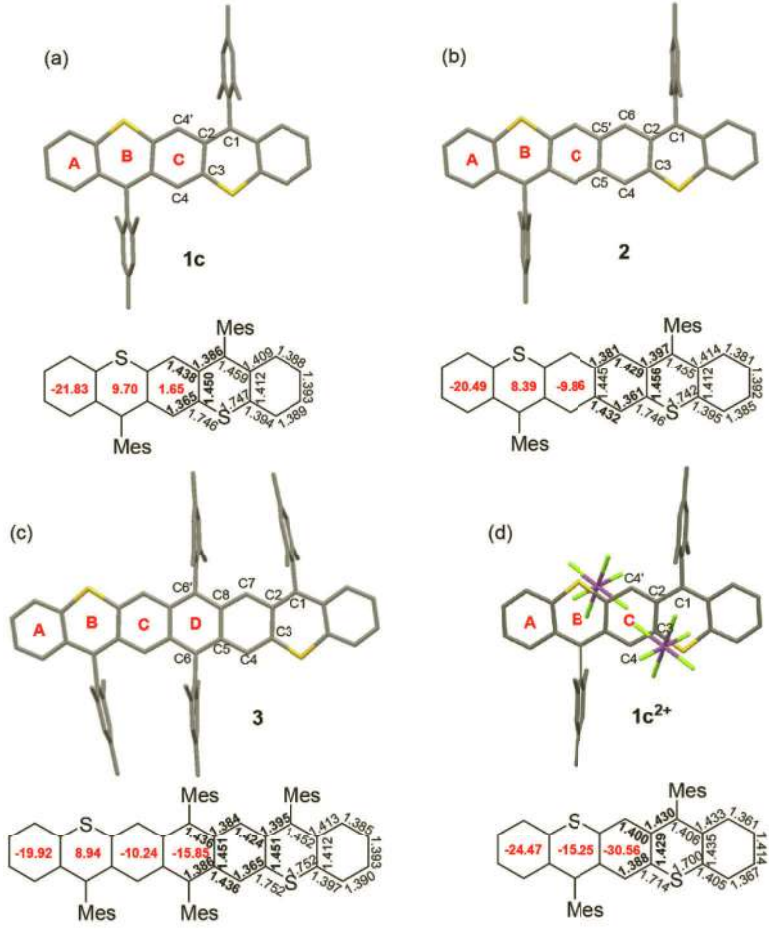


**Figure 8.5** X-ray crystallographic structures, selected bond lengths (Å) from single-crystal structures, and calculated NICS(1)$_{zz}$ values of (a) **1c**, (b) **2**, (c) **3,** and (d) **1c**$^{2+}$. Hydrogen atoms are omitted for clarity. Adapted with permission from Ref. 19. Copyright 2016 Wiley-VCH Verlag GmbH & Co.

Electrochemical measurements showed that **1c**, **2,** and **3** exhibited two reversible oxidative peaks. Chemical oxidation with two equivalent of NO·SbF$_6$ gave their dications. All the above dications were ESR silent and displayed red-shifted absorption compared to the respective neutral compounds. More interestingly, the band shapes of the absorption spectra of the dications are

very similar to their corresponding all-carbon acene analogs, demonstrating their similar electronic structures [23–24]. Taking **1c** as an example, $^1$H NMR spectrum of **1c**$^{2+}$ showed downfield shifted resonances compared to neutral **1c** (Figure 8.6). NICS(1)$_{zz}$ value calculations also showed largely negative values for the framework of **1c**$^{2+}$ (Figure 8.5d). In addition, anisotropy of the induced current-density (ACID) plots of **1c**$^{2+}$ clearly showed clockwise ring currents delocalized along the periphery (Figure 8.6b), which is rather similar to that of pentacene. Single crystals of the dication **1c**$^{2+}$ also indicated its acene-like structure with a clear decrease of the bond length of the two C-S bonds (1.700 Å and 1.714 Å) compared with that of neutral **1c** (1.746 Å and 1.747 Å). These evidences indicated that the dications can be regarded as isoelectronic structures of corresponding all-carbon acenes, and this finding encouraged us to synthesize higher order heteroacenes.

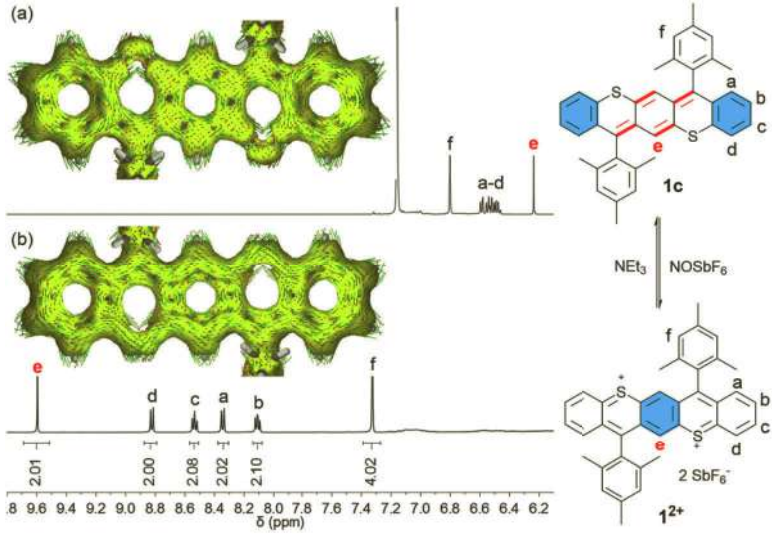


**Figure 8.6** $^1$H NMR spectra (aromatic region) of (a) **1c** and (b) **1c**$^{2+}$. Insets: the corresponding ACID plots and the external magnetic field is applied orthogonal to the plane. Adapted with permission from Ref. 19. Copyright 2016 Wiley-VCH Verlag GmbH & Co.

To explore the limit length of bis(arenohetero)quinodimethane, both the central quinoidal structure and lateral arenes were

extended. O atoms were utilized to link central extended QDMs and two outer anthracene units, and bis(anthraoxa)quinodimethanes containing nine (**4**, $n$ = 0) and ten (**5**, $n$ = 1) consecutively fused six-membered rings were synthesized (Figure 8.4). In contrast to its sulfur analogs **1c**, **2**, and **3**, compounds **4** and **5** exhibited amphoteric redox behavior with two reversible oxidation peaks and two revisable reduction peaks. Therefore, **4** and **5** could be potential candidates to study the ground states and fundamental physical properties of these neutral compounds and their redox forms, which could be regarded as isoelectronic structures of nonacene/decacene and their dianions and tetraanions (Figure 8.7) [20].

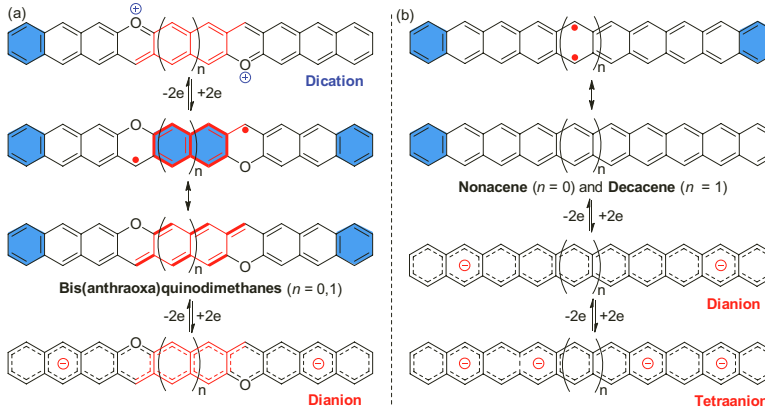


**Figure 8.7** Structures of (a) the bis(anthraoxa)quinodimethanes and their dianion/dication forms, and (b) the nonacene and decacene and their dianion/tetraanion forms. Adapted with permission from Ref. 20. Copyright 2019 American Chemical Society.

Compounds **4** and **5** were synthesized via a "center-to-outer edge" and "outer edge-to-center" intramolecular FC alkylation strategy, respectively (Scheme 8.3). Further oxidative dehydrogenation of **18** by DDQ gave **4** in high yield. However, dehydrogenation of **20** under similar conditions only gave insoluble precipitate, which could probably be due to the formation of charge-transfer complex of **21** with excessive DDQ. The complex dissolved upon addition of trifluoroacetic acid (TFA) and gave monomeric radical cation and dication species, which can undergo nucleophilic substitution with

TFA. Subsequent reduction by $SnCl_2$ gave unexpected trifluoroacetyl substituted compound **5** instead of **21**. The trifluoroacetyl groups were selectively attached onto the anthracene moiety at the $\alpha$ site next to oxygen atoms, presumably due to less steric hindrance at these positions and the electron-donating effect of the oxygen atom.

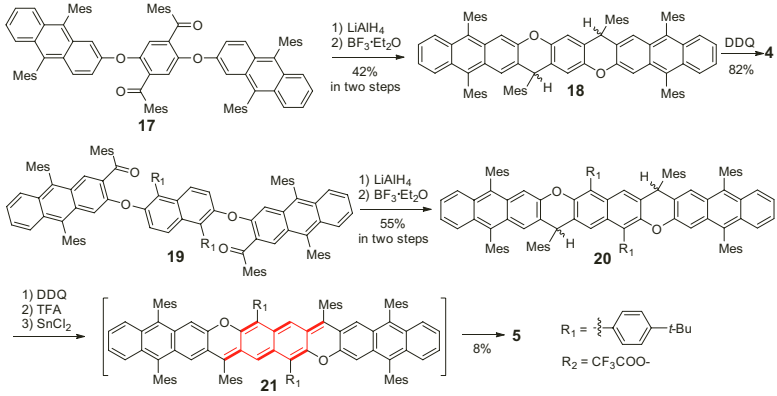


**Scheme 8.3** Synthetic routes to **4** and **5**.

X-ray crystallographic analysis showed that the bond length of the C1–C2 (1.392 Å) bond of **5** was longer than that in **4** (1.375/1.373 Å), indicating a decreased quinoidal character of **5** as compared to **4** (Figure 8.8a,b). No NMR spectral broadening upon heating was observe and the compound was ESR silent, indicating the almost closed-shell nature of **4**. However, compound **5** displayed obvious NMR spectral broadening in toluene-$d_8$ upon heating, suggesting an open-shell singlet ground state. VT ESR measurements gave a $\Delta E_{S-T}$ value of −6.20 kcal/mol. UDFT calculations (UCAM-B3LYP/6-31G(d,p)) well predicted a moderate diradical character ($y_0$ = 25%) for **5**. In addition, the central benzene ring in **4** and the naphthalene ring in **5** showed a calculated $NICS(1)_{zz}$ value of +0.62 ppm and −9.45 ppm, respectively, corresponding to nonaromatic and aromatic character. ACID plots revealed that there was no obvious ring current along the central benzene ring of **4**, but diatropic ring current along the naphthalene ring was observed for **5**. All these calculated results are consistent with experimental results.

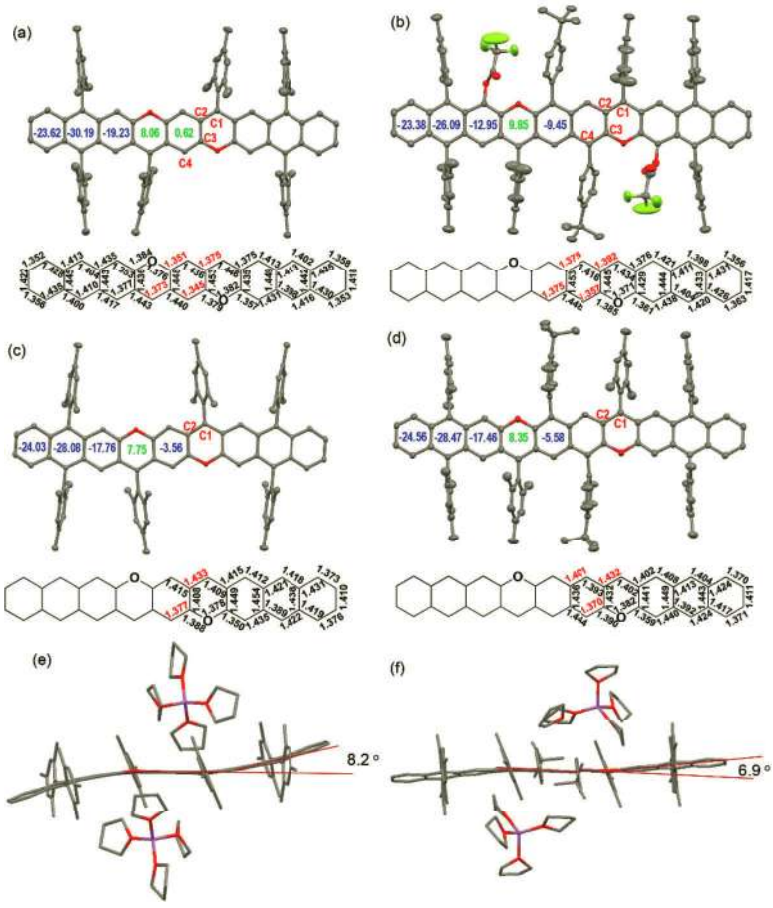


**Figure 8.8** X-ray crystallographic structures, selected bond lengths (in Å) and calculated NICS(1)$_{zz}$ values of (a) **4**, (b) **5**, (c) $\mathbf{4}^{2-}$, and (d) $\mathbf{5}^{2-}$. Side view of the structures of (e) $\mathbf{4}^{2-}$ and (f) $\mathbf{5}^{2-}$, showing the counter ions, distorted backbone, and bending angles. Hydrogen atoms are omitted for clarity. Adapted with permission from Ref. 20. Copyright 2019 American Chemical Society.

To further study the ground states and electronic structure of the charged species, the dications $\mathbf{4}^{2+}$ and $\mathbf{5}^{2+}$ were prepared by oxidation with two equivalents of NO·$SbF_6$. The dianion $\mathbf{4}^{2-}$ was generated by reduction of **4** with two equivalents of lithium anthracenide, while the dianion $\mathbf{21}^{2-}$ (analog of $\mathbf{5}^{2-}$) was obtained by deprotonation of **20** with *n*-BuLi. X-ray crystallographic analysis of

$\mathbf{4}^{2-}$ and $\mathbf{21}^{2-}$ showed that the C1–C2 bond lengths were 1.433 Å and 1.432 Å, respectively, much longer than their neutral compounds. The backbones of both $\mathbf{4}^{2-}$ and $\mathbf{21}^{2-}$ were evidently deviated from planarity, due to the partial $sp^3$ hybridization properties of the C1 anion (Figure 8.8c,d). Interestingly, the $^1$H NMR spectrum of dication $\mathbf{4}^{2+}$ was significantly broadened at room temperature, and the resonances became sharp at lower temperatures in $CD_2Cl_2$. The ESR signal of dication $\mathbf{4}^{2+}$ in solid state increased upon heating, and the $\Delta E_{S\text{-}T}$ value was estimated to be −4.20 kcal/mol. The dication $\mathbf{5}^{2+}$ was ESR silent and displayed sharp NMR signal, implying its closed-shell nature. Similarly, $^1$H NMR spectrum of dianioin $\mathbf{4}^{2-}$ in THF-$d_8$ showed signal broadening upon heating, indicating its open-shell singlet diradical character, while $^1$H NMR spectra of $\mathbf{21}^{2-}$ showed sharp signals even at elevated temperatures, indicating its closed-shell nature. The different ground states for both the dications and dianions of **4** and **5** can be explained by the different intramolecular Coulomb repulsion. Furthermore, the dications of **4** and **5** can be regarded as the isoelectronic structure of the respective nonacene and decacene (Figure 8.7), but they are much more stable. The studies of their dianions also gave insights to the electronic properties of the respective tetraanions, which are not attained.

Although the dications of bis(arenohetero)quinodimethanes could be regarded as isoelectronic structures of their respective all-carbon acenes, the neutral compounds possess $4n$ π electrons, two more than the acenes. Therefore, we designed a novel quinoidal acene analog such as **A**–**C** by removing one sulfur atom (thus 2 πe) per each *p*-QDM unit and the obtained structures can be regarded as the isoelectronic structures of the respective acenes (Figure 8.9) [25, 26]. For example, if a fused moiety of bis(benzothia)quinodimethane is replaced by an indeno group, and the new structure **A** can be considered the isoelectronic structure of pentacene. Similarly, the structures **B** and **C** are isoelectronic structures of nonacene with the same 38 π-electrons. The ground-state geometric and electronic structures of **A**–**C** are of particular interest due to their possible resonance structures of closed-shell quinoidal structure, open-shell diradical form, and dipolar zwitterionic form (Figure 8.9) [18].

Similar to compounds **1**–**5**, an intramolecular FC alkylation followed by oxidative dehydrogenation strategy was utilized to construct the target molecules from the key intermediate diol **22** and

tetrol **24** (Scheme 8.4). Compound **6** was successfully obtained by this strategy in 85% yield. However, implementing the same strategy, the synthesis of mesityl substituted **B** derivative failed, instead, mesityl substituted **C** derivative **7** was obtained. We proposed that the formation of *meta*-dithia compound was due to 1,2-sulfur migration via a spirocyclic cationic intermediate during the ring cyclization reaction in the presence of $BF_3{\cdot}Et_2O$ (Scheme 8.4). Due to their unique structure with one and two more aromatic sextet rings, compounds **6** and **7** were extremely stable in air in contrast to their corresponding reactive pentacene and nonacene derivatives.

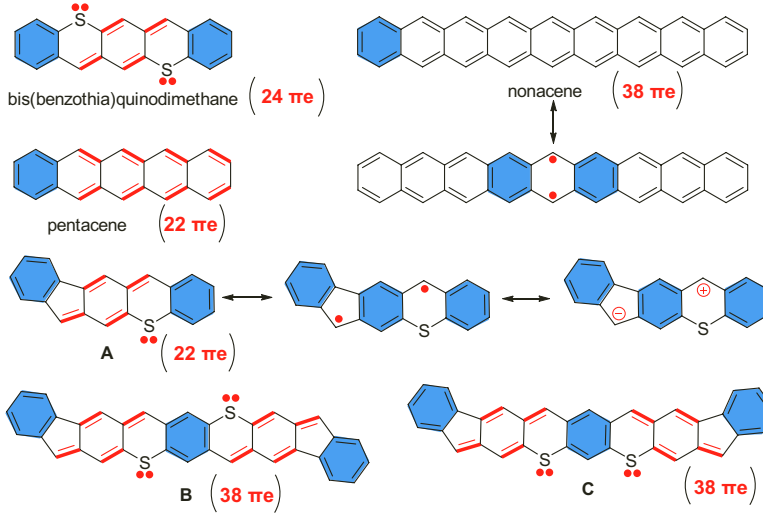


**Figure 8.9** Structures of bis(benzothia)quinodimethane, pentacene, nonacene, and their isoelectronic quinoidal molecules.

Compounds **6** and **7** displayed an intense absorption band at 310–450 nm and a broad band up to 900 nm (for **6**) or 1080 nm (for **7**), which is distinctly different from that of their corresponding analogs **1**–**5**. The unique absorption bands in **6** and **7** could be ascribed to their weak intramolecular donor-acceptor interactions originating from their zwitterionic resonance forms. DFT calculation also confirmed the significant dipole moment of 3.14 D and 2.87 D for **6** and **7**, respectively. Their dipole moments exhibit different structural polarity, which cause the different molecular packing

structure in the solid state. X-ray crystallographic analysis of **6** and **7** revealed their typical quinoidal type conjugation with a large BLA (Figure 8.10). Molecules of **6** packed into a square-like tetrameric structure via intermolecular [C-H···π] interactions between the adjacent molecules for its inherent dipole-dipole interactions. Molecules of **7** packed in a slipped face-to-face manner mainly via [C-H···S] and [C-H···π] interactions between neighboring molecules. Interestingly, the dipole moments of the **7** molecules in crystal pointed to the same direction. Theoretical study of **6** and **7** revealed their negligible diradical character. Therefore, consistent with experimental results, closed-shell quinoidal conjugation with a small dipolar/zwitterionic character dominate their ground-state structure.

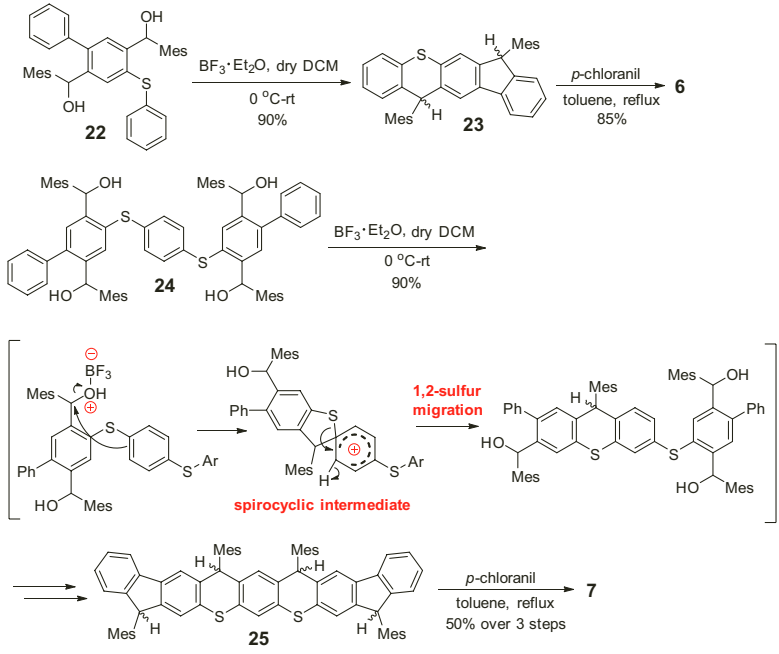


**Scheme 8.4** Synthetic routes to **6** and **7**.

Another strategy to stabilize isoelectronic structures of high-ordered acenes is to incorporate two *p*-QDM units and four electron-rich sulfur atoms into the π-conjugated acene framework

(Figure 8.11), and four-electron oxidation of the quinoidal nonacene analog would result in the isoelectronic structure of nonacene [21].

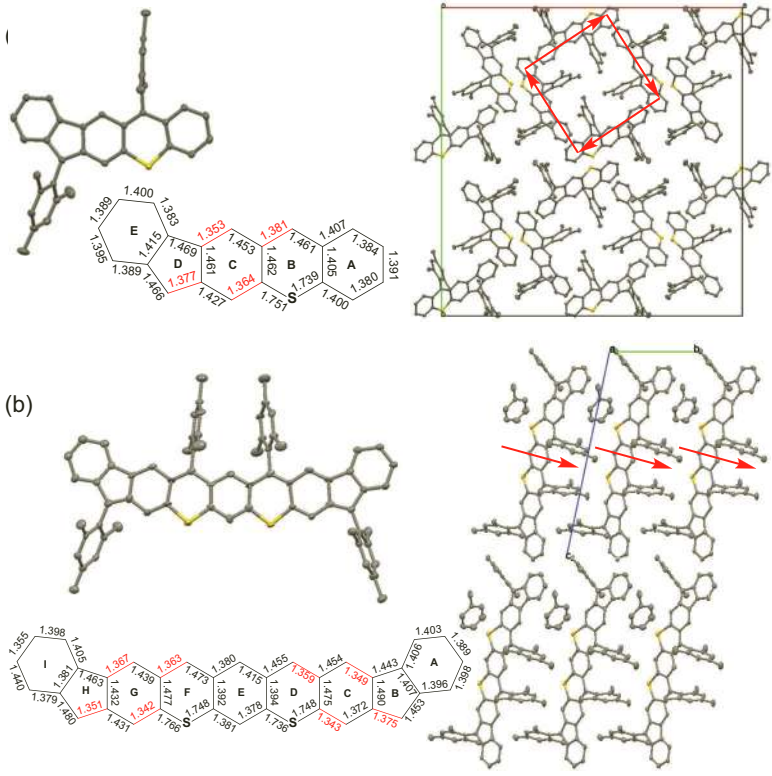


**Figure 8.10** Single crystal structures, 3D packing and bond length analysis of (a) **6** and (b) **7**. The arrows roughly denote the dipole moments. Adapted with permission from Ref. 18. Copyright 2015 Wiley-VCH Verlag GmbH & Co.

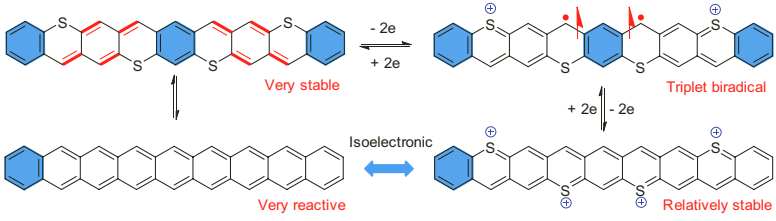


**Figure 8.11** Representative canonical structures of the neutral form, dication, and tetracation of the backbone of **8**.

We also utilized the strategy of intramolecular FC alkylation followed by oxidative dehydrogenation to synthesize the target compound **8** from the key intermediates of diol **26** (Scheme 8.5). Similar to compound **7**, 1,2-sulfur migration took place via a spirocyclic cationic intermediate during the ring cyclization reaction in the presence of $BF_3{\cdot}Et_2O$, and a *meta*-dithia compound **8** was finally obtained. Compound **8** was very stable and no obvious decomposition was observed when the solution was stored for 2 weeks.

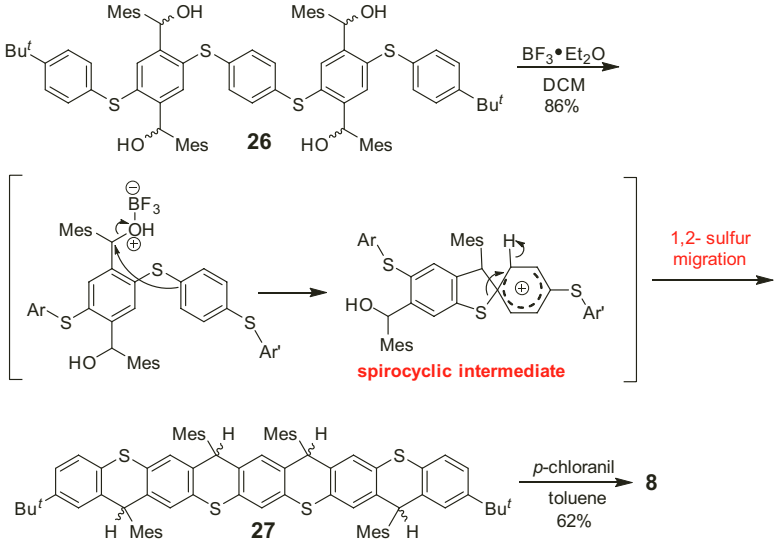


**Scheme 8.5** Synthetic routes to **8**.

X-ray crystallographic analysis showed large BLA for the *p*-QDM units of **8**, indicating its closed-shell quinoidal geometry (Figure 8.12a). Calculated $NICS(1)_{zz}$ values indicate that rings A, E, and I are aromatic, while the two QDM units showed a nearly zero $NICS(1)_{zz}$ value, indicating their nonaromatic character.

Compound **8** exhibited four oxidation waves, and thus, it was oxidized stepwise to four oxidation states by $NO{\cdot}SbF_6$. Both $\mathbf{8}^{\cdot+}$ and $\mathbf{8}^{\cdot 3+}$, showed an intense one-line ESR spectrum with $g_e$ = 2.0042 (Figure 8.12c), indicating that the spin was partially distributed to the sulfur atom. While $\mathbf{8}^{2+}$ showed an intense ESR spectra ($g_e$ =2.0036) with hyperfine structure and the ESR intensity increased

with decreasing temperature. Furthermore, no NMR signal could be observed from room temperature to −80 °C. All these experimental observations revealed that the dication was a triplet diradical. Clear $^1$H NMR spectrum of the $\mathbf{8}^{4+}$ in $CD_2Cl_2$ indicated its closed-shell nature. Similar to the dications of compounds **1**–**5**, the tetracation $\mathbf{8}^{4+}$ showed largely downfield-shifted NMR spectrum as compared to that of neutral **8**, indicating its aromatic character. ACID plots of $\mathbf{8}^{4+}$ clearly displayed clockwise diatropic ring currents delocalized along the periphery of conjugated backbone, similar to nonacene. The absorption spectrum of $\mathbf{8}^{4+}$ also showed a band structure similar to that of Anthony's nonacene derivative [10]. These evidences indicated that $\mathbf{8}^{4+}$ is a genuine isoelectronic structure of nonacene.

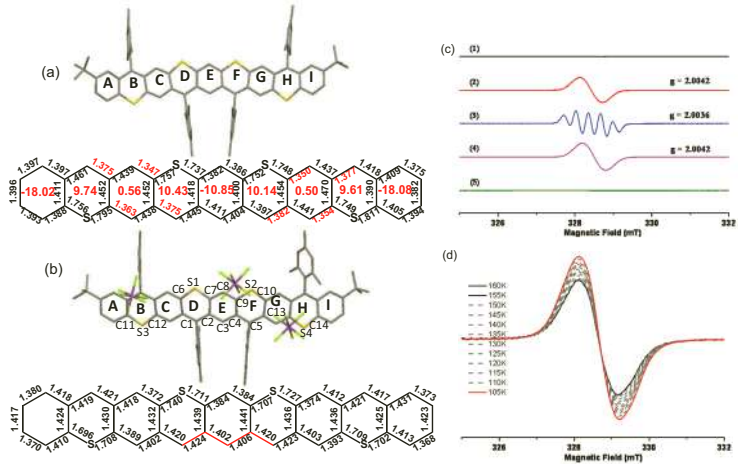


**Figure 8.12** X-ray crystallographic structures, selected bond lengths (Å), and calculated NICS(1)$_{zz}$ values (red and blue numbers in hexagons) of (a) **8** and (b) $\mathbf{8}^{\cdot 3+}$; (c) ESR spectra of (1) **8**, (2) $\mathbf{8}^{\cdot +}$, (3) $\mathbf{8}^{\cdot\cdot 2+}$, (4) $\mathbf{8}^{\cdot 3+}$, and (5) $\mathbf{8}^{4+}$ (0.5 mmol/L) recorded in DCM at room temperature; (d) VT ESR spectra of $\mathbf{8}^{\cdot\cdot 2+}$ in DCM solution from 160 K to 105 K in the frozen state. The ESR spectrum of $\mathbf{8}^{\cdot\cdot 2+}$ becomes broad when the temperature goes below 160 K. Adapted with permission from Ref. 21. Copyright 2019 American Chemical Society.

These series of work provided a potential approach to design and synthesize isoelectronic structures of the highly reactive PAHs such as long acenes, *peri*-acenes, and zigzag-edged graphene nanoribbons.

### 8.2.3 Extended Quinoidal Heteroacene Analogs

Fusion of extended quinoidal heteroacenes such as [*n*] thienophenacene and benzo[1,2-*b*:4,5-*b*′]dithiophene with indeno moiety, heteroatom-linked acene and phenalene would lead to a novel FHCs, which are expected to exhibit open-shell diradical character. Utilizing this concept, our group has synthesized a series of thiophene-containing quinoidal compounds with different fusing moieties to examine their basic ground states and physical properties (**28**–**36**, Figure 8.13) [27–29].

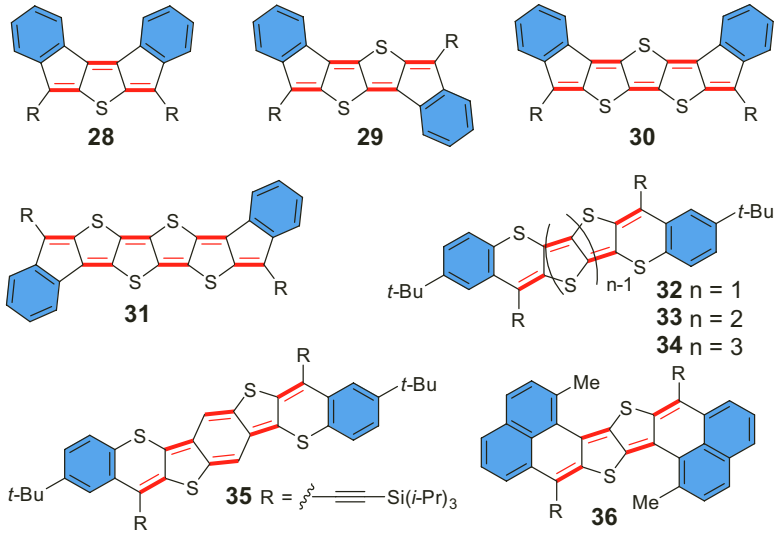


**Figure 8.13** Chemical structures of fused heterocyclic quinoidal thiophene derivatives.

We first targeted bisindeno-[*n*]thienoacenes consisting of a quinoidal thienoacene unit annulated with two indeno moieties. There are different isomers in the bisindeno-[*n*]thienoacenes family. For example, bisindenothiophene has three isomers with different fusion position and orientation of two indeno moieties, as shown in Figure 8.14a. According to a simple resonance structural analysis, different numbers (2 for **A**, 1 for **B,** and 0 for **C**) of aromatic sextet rings could be drawn, implying increased diradical character and decreased stability from **A** to **C**. Therefore, the ground-state electronic structure and aromaticity of this conjugated system are

of great interest. Taking structure **A** as an example, two resonance forms (closed-shell quinoidal form and open-shell diradical form) are believed to contribute to the ground-state structure. Moreover, structure **A** can be regarded as dibenzannulated anti-aromatic system containing $4n$ π electrons including two π electrons of the sulfur atom (Figure 8.14b).

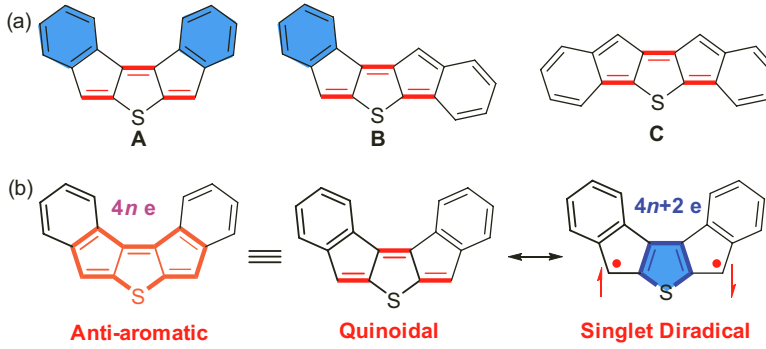


**Figure 8.14** (a) Chemical structures of three isomers of bisindenothiophene and (b) representative resonance forms of bisindenothiophene A.

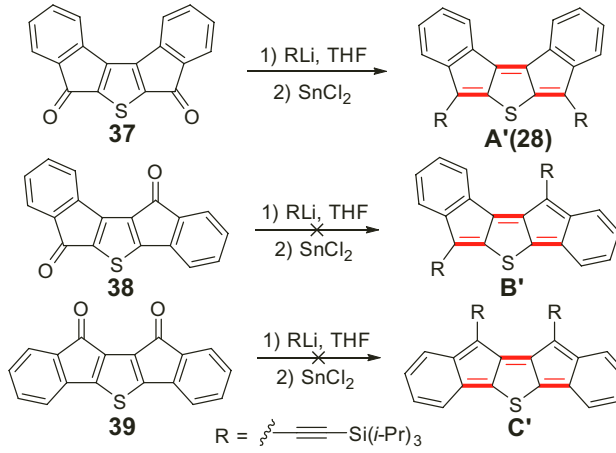


**Scheme 8.6** Synthetic route to compounds **A′(28)**, **B′**, and **C′**.

We further explored strategies to synthesize the derivatives of these isomers (**A′**, **B′,** and **C′**) (Scheme 8.6). The derivative of **A′** (**28**) could be isolated, whereas during the attempted synthesis of

**B′** and **C′**, the final reduction step gave a complicated mixture due to their intrinsic high reactivity, and the mixture could not be isolated. The high reactivity of isomers **B′** and **C′** is likely originated from their inherent singlet diradical character as discussed above. These preliminary results suggested that only isomer **A** of bisindeno-[*n*]thienoacenes could be synthesized in a reasonably stable form. Based on the above work, we began to work on the extended analogs of isomer **A**, namely bisindeno-[*n*]thienoacenes **28**–**31** (Figure 8.13). In 2014, our group [27] and Haley's group [30] independently reported the same system.

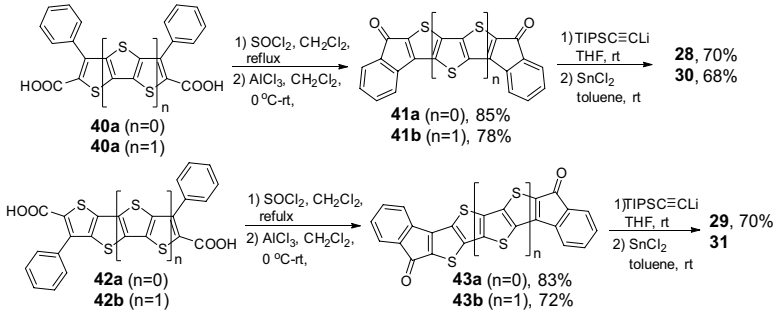


**Scheme 8.7** Synthetic route to bisindeno-[*n*]thienoacenes **28**–**31**.

Different from the oxidative dehydrogenation step of bis(arenohetero)quinodimethane compounds, the synthetic route here involved the nucleophilic addition of diketone compounds by the lithium salt of protecting groups followed by reduction (Scheme 8.7). The dicarboxylic acid compounds **40** and **42** were treated with thionyl chloride to afford dicarbonyl chloride, and subsequent double FC acylation with $AlCl_3$ afforded the diketone precursors **41** and **43**. The target bisindeno-[*n*]thienoacenes **28**–**31** were obtained by nucleophilic addition of the diketones with lithiated triisopropylsilyl ethynylene (TIPSE) followed by reduction of the intermediate diols with $SnCl_2$. Compounds **28**, **29**, and **30** were successfully isolated, however, compound **31** could only be prepared in situ under inert conditions. The reduction reaction was monitored by UV-vis-NIR absorption spectroscopic measurements and the formation of **31** was accompanied by simultaneous decomposition of the product. Attempted separation of **31** by column chromatography or recrystallization failed, due to its high reactivity toward oxygen,

protonated reagents, and silica gel. The high reactivity of **31** was believed to be associated with its anti-aromaticity and open-shell diradical character, which were evidenced by VT ESR measurement and UDFT calculations.

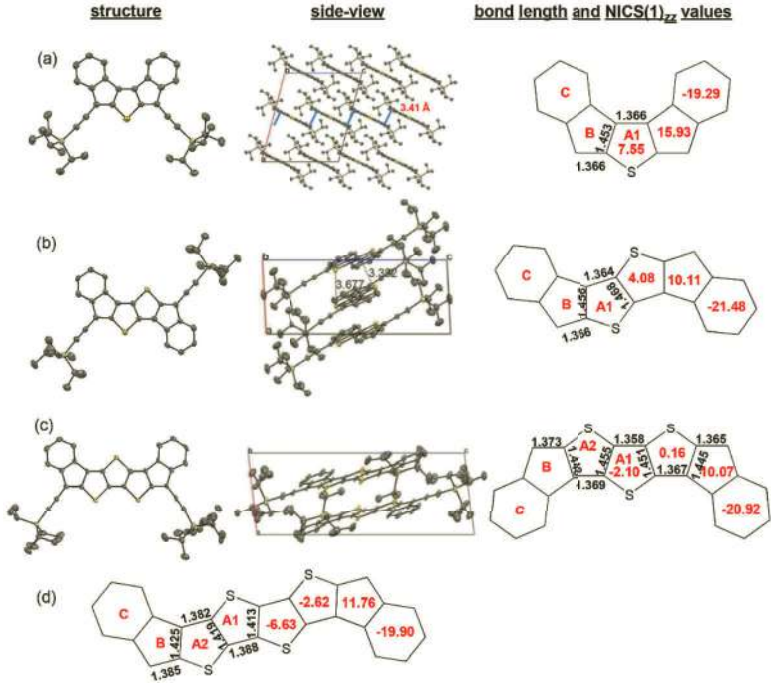


**Figure 8.15** X-ray crystallographic structures, packing structures, and selected bond lengths of (a) **28**, (b) **29,** and (c) **30**, and DFT calculated data of (d) **31**. The red numbers in the rings denote the calculated NICS(1)$_{zz}$ values. Reproduced from Ref. 27 with permission from the Royal Society of Chemistry.

The structures of **28**–**30** were unambiguously confirmed by X-ray crystallographic analysis as shown in Figure 8.15. The π-frameworks (bisindeno[*n*]thienoacene) of all molecules are almost planar and a large BLA was found, indicating that quinoidal resonance forms dominate the ground-state electronic structure. UDFT calculations predicted closed-shell ground states of **28**–**30**, while highly reactive **31** exhibited a diradical character of 0.202. On the other hand, the calculated positive NICS(1)$_{zz}$ values of central quinoidal thienoacene rings (Figure 8.15) implied the anti-aromaticity of this system, which is similar to the reported indenofluorenes. However, from **28**

to **31**, the NICS(1)$_{zz}$ values for the central thiophene ring (ring A1) become more negative, indicating an increase of aromaticity, which is consistent with their increased diradical character. The optical and electronic properties of compounds **28**–**31** were investigated by various experimental techniques, including one-photon absorption, two-photon absorption (TPA), femtosecond transient absorption, Raman spectroscopy, and cyclic voltammetry measurements, further revealing chain length dependent behavior. **28**–**31** showed short singlet excited-state lifetime (7–12 ps), moderate TPA cross-section (340–520 GM) and amphoteric redox behavior, which are related to their anti-aromaticity and diradical character. Their radical cations/anions and dianions are chemically accessible, while dications with two anti-aromatic cyclopentadienyl rings are unstable and difficult to obtain by using electrochemistry. These results fully demonstrated that the bisindeno[*n*]thienoacenes mentioned were anti-aromatic system with quinoidal resonance form dominating their ground states and diradical character increased with extension of the backbone.

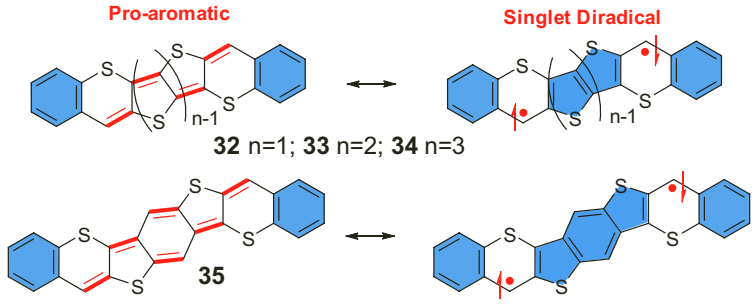


**Figure 8.16** Resonance structures of pro-aromatic benzothia-[*n*]thienoacenequinodimethanes **32**–**35** and their singlet diradical resonance forms (substituents are omitted for clarity).

By changing the fusion moieties of bisindeno[*n*]thienoacenes from indeno to heteroatom-linked benzene (benzothia), the benzothia-[*n*]thienoacenequinodimethanes (**32**–**35**) were designed and synthesized by our group in 2016 (Figure 8.16) [28]. With this fusion mode, only pro-aromatic structures could be drawn instead of anti-aromatic structures in the bisindeno[*n*]thienoacenes (Figure 8.16). Therefore, our aim was to understand how the fusion mode and pro-aromaticity/anti-aromaticity affect their diradical

character and physical properties. The synthetic strategy of **32**–**35** was similar to that of bisindeno[*n*]thienoacenes, mainly via nucleophilic addition of the corresponding diketones with lithiated TIPSE, followed by reduction of the intermediate diols with $SnCl_2$.

UDFT calculation indeed revealed the differences between these two closely related systems in view of aromaticity and singlet diradical character. Bisindeno[*n*]thienoacene is a typical anti-aromatic system, and the $NICS(1)_{zz}$ values of the cyclopenta and the central thiophene rings are significantly positive with small singlet diradical character (Figure 8.15), whereas the benzothia[*n*]thienoacenequinodimethanes are pro-aromatic and $NICS(1)_{zz}$ values of the central thiophene/benzene rings are significantly negative with enhanced singlet diradical character (Figure 8.17). For example, if one compares two compounds with the same central quinoidal moieties, **29** and **33** showed a diradical character of 0 and 0.024, respectively, **30** and **34** exhibited an increased diradical character of 0.03 and 0.184, respectively, and **35** displayed a sharply increased diradical character of 0.384 after incorporation of a benzene ring into the quinoidal structure. Experimental results are also consistent with calculated data. Compound **35** displayed clear temperature-dependent magnetic properties, such as broadened $^1$H NMR spectrum at elevated temperatures and ESR signal at room temperature. In addition, pro-aromatic compounds **32**–**35** showed much longer singlet excited state lifetimes, larger TPA cross-section values, and better redox amphotericity compared with their anti-aromatic counterparts **28**–**31**. This study provided a comprehensive understanding on how the pro-aromaticity/anti-aromaticity affect the ground-state electronic structure, diradical character, and consequently the physical properties of quinoidal compounds.

Another pro-aromatic system based on bisphenaleno-thieno[3,2-*b*]thiophene **36** was also developed by our group (Figure 8.18) [29]. Compound **36** displayed good stability and good solubility in common organic solvents. The X-ray crystallographic analysis revealed a typical quinoidal structure with a surprisingly wave-shaped geometry, presumably due to the strong intermolecular phenalenyl-phenalenyl interaction in crystals (Figure 8.18c). Similar to the above-demonstrated results, **36** also showed larger diradical character, stronger absorption, longer excited-state lifetime, and better redox amphotericity than its anti-aromatic analog **29**. It

is notable that molecules **29**, **33**, and **36** have the same central quinoidal thienoacene unit, but the diradical character of **36** ($y_0$ = 18.6%) is much larger than both **29** ($y_0$ = 0%) and **33** ($y_0$ = 2.4%), predicted using similar calculation method. Comparing with the phenalenyl-containing diradicaloids such as bisphenalenyls [31–32] and extended zethrenes [33–34], the larger diradical charater of **36** likely originated from the thermodynamic stabilizing effect of the delocalized phenalenyl moieties. In addition, organic field-effect transistors (OFETs) based on solution processed thin films of **36** exhibited *p*-type operation with a mobility of 0.26 $cm^2V^{-1}s^{-1}$. The relatively high charge-transport mobility, together with the ordered packing structure, would make this diradicaloid as potential material for spin-dependent charge transport studies in the future.

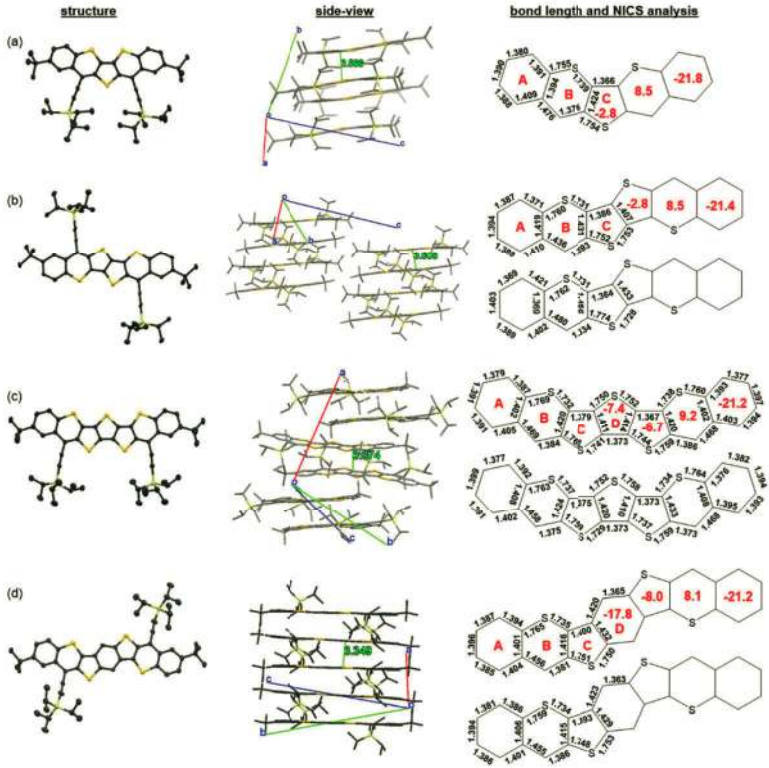


**Figure 8.17** X-ray crystallographic structures, 3D packing structures (side-view), and selected bond lengths of (a) **32**, (b) **33**, (c) **34,** and (d) **35**. The red numbers in the rings denote the calculated NICS(1)$_{zz}$ values. Reproduced from Ref. 28 with permission from the Royal Society of Chemistry.

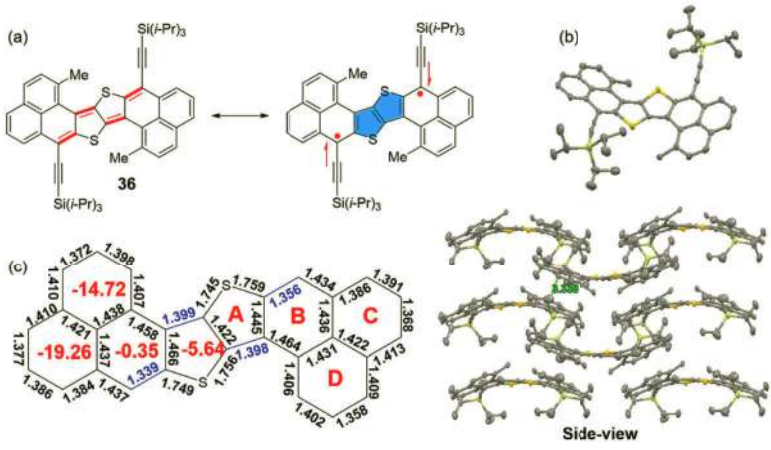


**Figure 8.18** Chemical resonance forms, X-ray crystallographic structures, 3D packing structures (side-view), and bond lengths of bisphenaleno-thieno[3,2-b] thiophene **36**. The red numbers in the rings denote the calculated NICS(1)$_{zz}$ values. Reproduced from Ref. 29 with permission from the Royal Society of Chemistry.

## 8.3 Extended Aza-Acenes and Aza-Quinodimethanes

Incorporation of electron-withdrawing imine *n* atoms to acene backbone would lower their energy levels, and thus, improve their stability toward oxygen and enhance their electron transport properties [14, 15, 35]. However, the intrinsic *cis*-1,3-diene electronic structure remains unchanged. To date, although no direct experimental evidence was reported to support the open-shell diradical character of the extended aza-acenes, it is expected that, like all-carbon acenes, higher order aza-acenes should also show increased diradical character with extension of backbone.

In the recent decade, some photo-reactive aza-hexacenes and heptacenes reported by Bunz's group could give some clues to their ground states (Scheme 8.8). Although the diaza-hexacene **44** could be isolated and the structure could be confirmed by $^{1}$H NMR, Diels-Alder dimerization happened spontaneously when they attempted to grow single crystal [36], which was similar to Anthony's all-carbon hexacene [37]. Oxidation of *N*,*N*-dihydrotetraazahexacene

derivative **46** into the azaacene by using $MnO_2$ also failed. Although six electron-withdrawing fluorine atoms were attached in the monomer **46**, a Diels–Alder adduct dimer **47** could be obtained as the only product indicated by NMR data and UV–vis spectroscopy [38]. Therefore, higher order aza-heptacene **48** was speculated to be unstable during the synthetic procedure and undergo [4+4] dimerization to afford compound **50** in 76% yield. Two highly extended C–C bonds (1.61 Å) link the two backbones [36]. Their further studies demonstrated that the stability of aza-heptacene was largely dependent on the numbers and positions of the substituents. However, even with the aza-heptacene **51** protected using four bulky *s*-butyl silyl acetylene groups, this compound could only be stable for an hour in solution and gradually dimerized to give **52** and **53** as monitored by in situ $^1H$ NMR measurement [39].

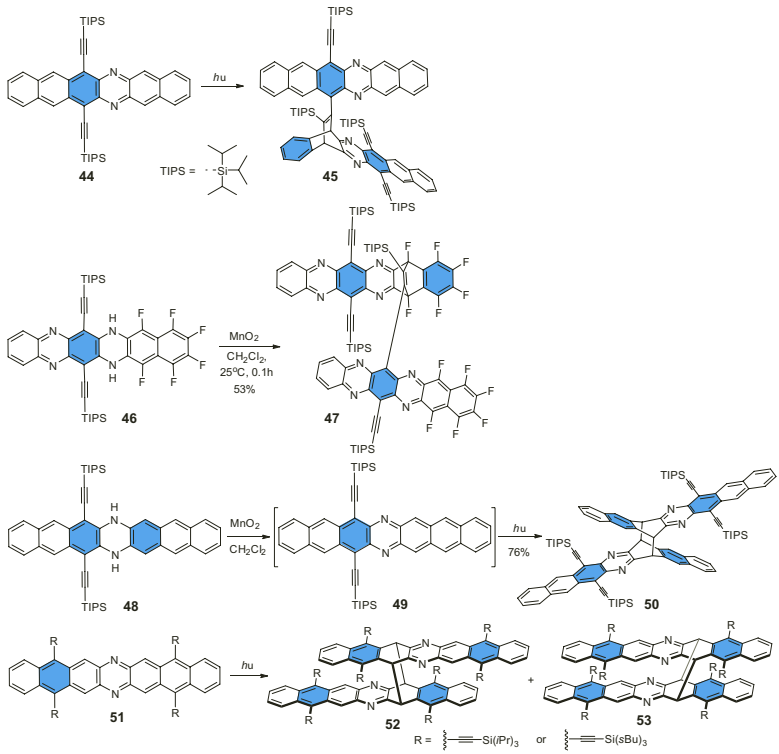


**Scheme 8.8** Photodimerizations of aza-acenes. Adapted with permission from Ref. 36, 38, and 39. Copyright 2013, John Wiley and Sons. Copyright 2013, American Chemical Society. Copyright 2014, American Chemical Society.

Dihydroindolocarbazoles, by fusing an indole unit to a carbazole molecule, represent a family of heterocyclic compounds [40]. Similar to indenofluorene family [41], five isomers could be drawn in indolocarbazole family based on the position and orientation of the indole ring fusion (Figure 8.19). Although dihydroindolocarbazoles and *N*-alkylation indolocarbazoles are well known for their potential biological activity as anti-cancer drugs [42, 43] and semiconductor materials for organic electronics [44–46], indolocarbazole derivatives with imine nitrogen atoms are rarely reported due to their intrinsic instability. Obviously, indolocarbazoles are extremely unstable due to the contribution of open-shell diradical resonance forms (Figure 8.19) and lacking of protecting groups on the most reactive trivalent *N* sites. Furthermore, solubility problem of bare indolocarbazoles is another issue that hinders their synthesis and characterization. Nevertheless, some isomers in indolocarbazole family have been successfully synthesized and their intriguing properties have been disclosed.

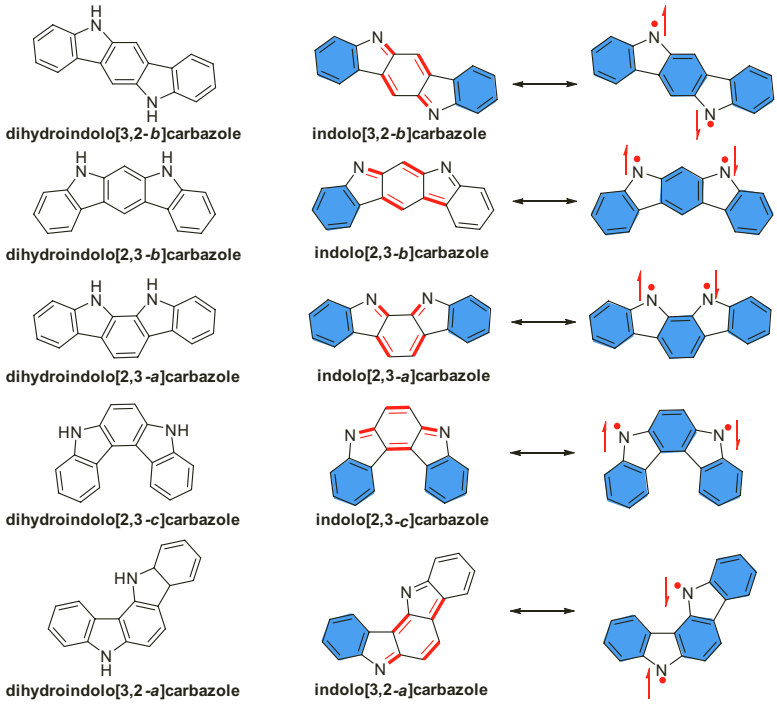


**Figure 8.19** Chemical structures of five isomers of dihydroindolocarbazoles and indolocarbazoles.

In 2000, Yudina et al reported that indolo[3,2-*b*]carbazole could be synthesized via dehydrogenation of dihydroindolo[3,2-*b*] carbazole in the presence of DDQ [47]. Later in 2008, Dehaen and co-workers tried the same condition, but failed to fully convert **54b** to indolo[3,2-*b*]carbazole **55b**. Therefore, they developed an alternative method to synthesize indolo[3,2-*b*]carbazole derivatives **55** via a deprotonation approach with strong bases such as *t*-BuOK and *t*-BuLi, and no need further oxidation with DDQ (Scheme 8.9) [48]. However, compound **55a** could not be synthesized through this method, presumably because it is not sufficiently protected as compared to **55b** and **55c**. This indicated that space shielding of the imine sites by bulky groups is crucial to obtain stable compounds. The authors also found that Michael addition of *n*-BuLi on indolo[3,2-*b*] carbazole generated **56** in good yield. Compound **56** could act as a selective colorimetric sensor in acetonitrile, either for $F^-$ or Brønsted acids. However, except for the basic structural characterization of **55b**, other physical properties such as stability, electrochemical, and optical properties of indolo[3,2-*b*]carbazole derivatives **55** were not mentioned, and their potential diradical character was also not studied.

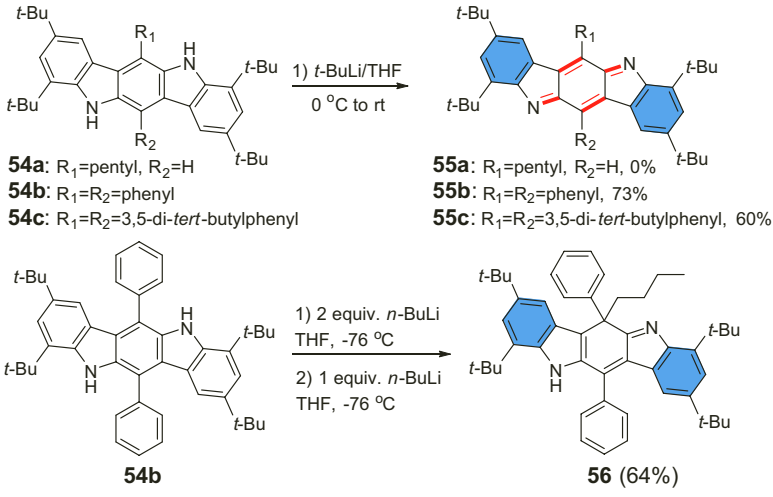


**Scheme 8.9** Synthetic routes to compounds **55a-c** and **56**.

Indolo[2,3-*b*]carbazole was believed to be of higher reactivity and possess larger singlet diradical character than indolo[3,2-*b*]carbazole

based on recent studies of indenofluorene family (Figure 8.20) [41, 49]. Thus, the synthesis of indolo[2,3-*b*]carbazole derivatives will be even more challenging. In 2014, Wu and his co-workers reported the first example of quinoidal indolo[2,3-*b*]carbazole derivatives. They synthesized persistent stable indolo[2,3-*b*]carbazole derivatives **57** and **58** with tunable ground states (Figure 8.20) [50]. The precursors **59** and **60** were obtained by multi-step synthesis and subsequently converted to corresponding **57** and **58** through deprotonation-followed-by-oxidation or by direct oxidative dehydrogenation, respectively (Scheme 8.10). Similar to the design and synthesis of indolo[3,2-*b*]carbazole derivatives **55**, the bulky *tert*-butyl and 4-*tert*-butylphenyl groups were introduced to protect and stabilize such reactive molecules. Consequently, the obtained compounds **57** and **58** were reasonably stable under inert atmosphere. In contrast, the oxidative dehydrogenation of the unblocked precursors **61** and **64** gave the homo-coupled dimers **62** and **65** in good yields. No predicted quinoidal products **63** and **66** or dihydrazine products (via intra-molecular N–N bond formation) were formed with increased reaction time.

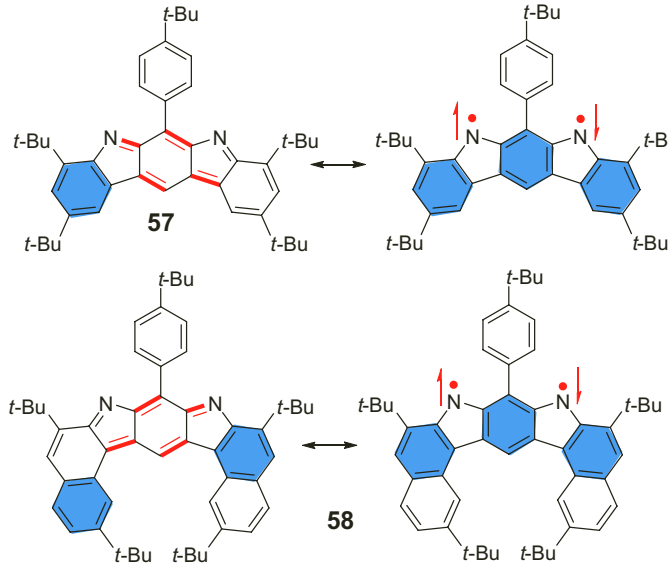


**Figure 8.20** Chemical structures of indolo[2,3-*b*]carbazole derivatives **57** and **58** and their diradical resonance forms.

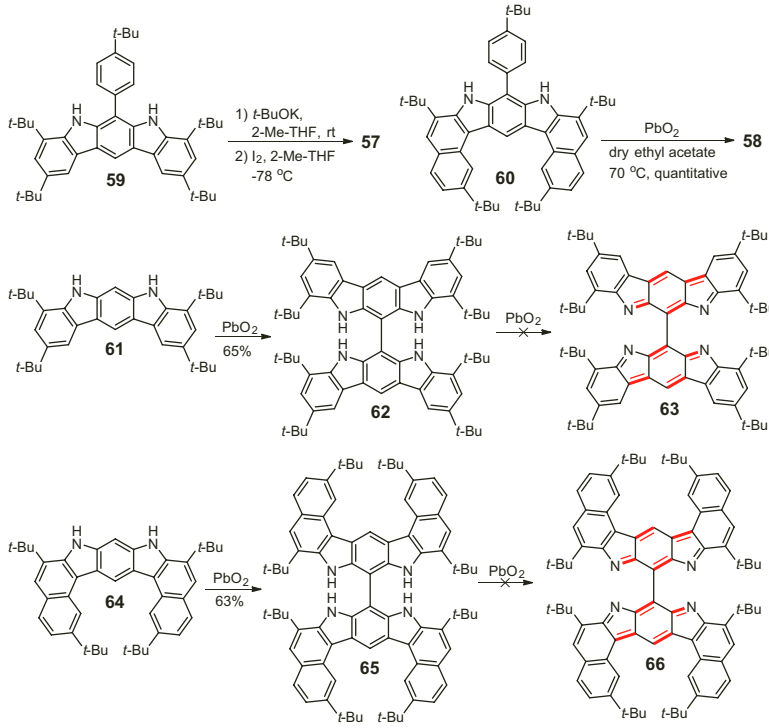


**Scheme 8.10** Synthetic routes to indolo[3,2-*b*]carbazole based compounds **57**, **58**, **62,** and **65**.

The ground states of **57** and **58** were studied by VT NMR and VT ESR measurements, assisted by DFT calculations. It was found that **57** was a persistent singlet diradicaloid in the ground state with a moderate diradical character ($y_0$ = 0.269), while **58** exhibited a quinoidal closed-shell ground state. This difference can be simply explained by Clar's aromatic sextet rule, that is, from closed-shell to open-shell diradical form, **57** gains two while **58** can only gain one aromatic sextet ring. Another notable property of **57** and **58** is that their low-lying LUMO energy levels would make these indolo[3,2-*b*] carbazole derivatives easy to be attacked by active proton either from protic solvents or from silica gel. The high reactivity of indolocarbazoles can be ascribed to their intrinsic singlet diradical character as well as their inherently low-lying LUMO energy level. The study provided insight into the design and synthesis of other indolocarbazole isomers, which are also interesting, but challenging.

1,3-Diaryl-1,2,4-benzotriazinyl based radicals have attracted attention due to their interesting magnetic and electronic properties, and more importantly, their exceptional air and moisture stability. Although the skeleton of tetraphenylhexaazaanthracene (TPHA) was reported in 1908 [51], the ground state of TPHA was not studied until 1998. Wudl and co-workers proposed the singlet zwitterionic ground state of **67B** instead of designed triplet ground state (**67A**), according to X-ray crystallography analysis and DFT calculation (Figure 8.21) [52].

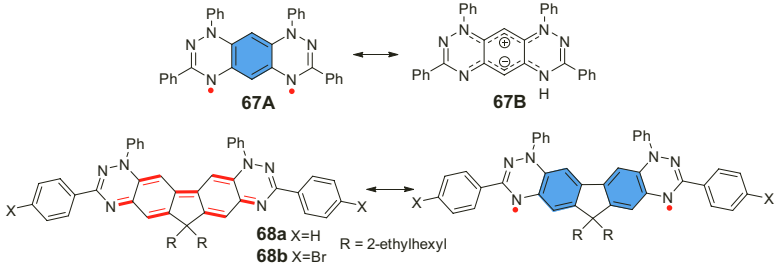


**Figure 8.21** Chemical structures of **67** and **68**.

In 2015, Wudl's group synthesized the benzotriazinyl-based diradicaloid **68a**, which showed a small optical energy gap of around 1.20 eV (Figure 8.21). Sharper and extra peaks observed upon cooling in VT $^1$H NMR spectra indicated its open-shell singlet ground state. However, further ESR studies on the polycrystalline solid demonstrated an intermolecular quintet state at room temperature [53]. In a following work by cooperation of Wudl and Nguyen, they proposed a self-doping mechanism of **68a** and **68b**, involving a radical anion-radical cation pair [54]. Moreover, the amount of the radical ion pair was found to be temperature dependent and reversible, indicating that the phenomenon is not due to oxygen doping. To further confirm the enhanced doping strength with increasing temperature, **68a/68b** was doped with the strong electron acceptor 2,3,5,6-tetrafluoro-7,7,8,8-tetracyanoquino-dimethane (F4TCNQ) to fabricate OFETs. They found that transfer curves were insensitive to the F4TCNQ concentration, with $I_d$ all exhibiting a flat response to $V_g$. Interestingly, transfer curve of the pristine **68a** at 370 K in high $V_g$ region nearly overlapped with that of the F4TCNQ doped OFET at 300 K, which may help to confirm the temperature-enhanced self-doping and electrical conductivity in both systems. The electrical

tenability along with spin properties of diradicaloids may open an avenue for organic optoelectronic applications.

## 8.4 Non-Classical Acenes Capped with Thiophenes or Thiadiazoles

Benzo[*b*]thiophene and benzo[*c*]thiophene could both be regarded as isoelectronic structures of the naphthalene (Figure 8.22a). One benzene aromatic sextet ring can be drawn for benzo[*b*]thiophene, but only one thiophene ring could be drawn for benzo[*c*]thiophene, which renders latter less stable than the former, due to the smaller aromatic stabilization energy of thiophene ring as compared to that of benzene ring. For extended structures of aceno[*c*]thiophene (**AT-n**), aceno[*c*]dithiophene (**ADT-n**), aceno[*c*][1,2,5]thiadiazole (**ATz-n**), and aceno[1,2,5]-dithiadiazole (**ABTz-n**), only one aromatic thiophene or [1,2,5]thiadiazole ring together with extended *cis*-1,3-dienes could be drawn (Figure 8.22b,c). Similar to all-carbon acenes, these extended non-classical acenes could also be drawn in open-shell diradical forms. Therefore, the synthesis of these compounds would be very interesting although challenging, and it is also of great interest to explore their ground states, and basic chemical and physical properties.

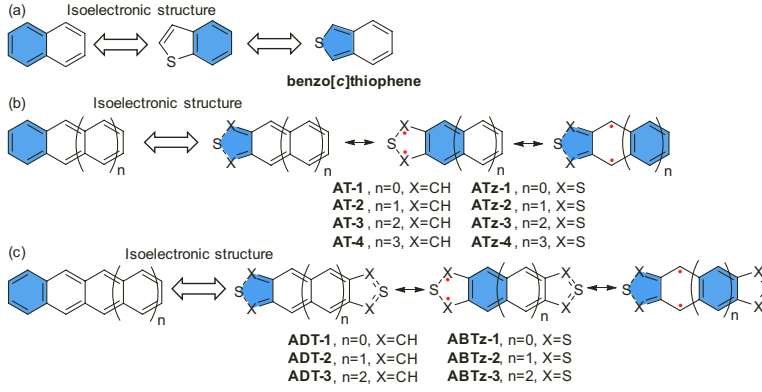


**Figure 8.22** (a) Isoelectronic structures of naphthalene; (b) acenothiophene (**AT-n**) and acenothiadiazole (**ATz-n**) as isoelectronic structures of acenes; and (c) acenodithiophene (**ADT-n**) and acenobisthiadiazole (**ABTz-n**) as isoelectronic structures of acenes.

Before proceeding to the synthetic work, the diradical characters and $\Delta E_{S\text{-}T}$ values of these non-classic acenes were calculated by UDFT method (Table 8.1) [55]. If one compares these molecules with same length, it can be concluded that: (i) one five-membered ring fused compounds, **AT-n** and **ATz-n**, showed smaller diradical character and larger $\Delta E_{S\text{-}T}$ than two five-membered ring fused **ADT-n** and **ABTz-n**; and (ii) thiophene fused compounds showed larger diradical character and smaller $\Delta E_{S\text{-}T}$ than [1,2,5]thiadiazole fused compounds.

**Table 8.1** UDFT calculated diradical characters ($y_0$) and $\Delta E_{S\text{-}T}$ of non-classic acenes

| Name | $y_0$ | $\Delta E_{S\text{-}T}$ (kcal/mol) | Name | $y_0$ | $\Delta E_{S\text{-}T}$ (kcal/mol) |
|---|---|---|---|---|---|
| **AT-1** | 0 | 43.80 | **ATz-1** | 0 | 50.76 |
| **AT-2** | 0 | 25.36 | **ATz-2** | 0 | 28.73 |
| **AT-3** | 0.046 | 13.73 | **ATz-3** | 0.014 | 16.22 |
| **AT-4** | 0.219 | 10.94 | **ATz-4** | 0.149 | 11.05 |
| **ADT-1** | 0.125 | 11.22 | **ABTz-1** | 0.006 | 17.60 |
| **ADT-2** | 0.313 | 8.76 | **ABTz-2** | 0.149 | 10.14 |
| **ADT-3** | 0.490 | 8.72 | **ABTz-3** | 0.353 | 8.52 |

*Note*: $y_0$ and $\Delta E_{S\text{-}T}$ calculated at the UCAM-B3LYP/6-31G(d, p) level.

According to previous experiences on diradiclaoids, we believed that stable non-classical acenes can be isolated if the backbones are strategically protected. Therefore, we conducted experiments to synthesize one or two thiophene-terminated compounds **69**–**73** (Scheme 8.11) [55]. Compounds **69**–**71** with skeleton of **AT-1**, **AT-2,** and **AT-3** could be obtained. However, compound **72**, an isoelectronic structure of TIPS-substituted pentacene, could not be isolated due to its fast decomposition. To prepare the two thiophene rings-capped acene **73**, TIPSE lithium was first added into the quinone followed by reduction of the intermediate diol with $SnCl_2$. However, compound **73** was extremely reactive and quickly dimerized to form a covalently linked dimer **74**, which was confirmed by X-ray crystallographic analysis. The dimerization of **73** happened between the four unblocked carbon centers along

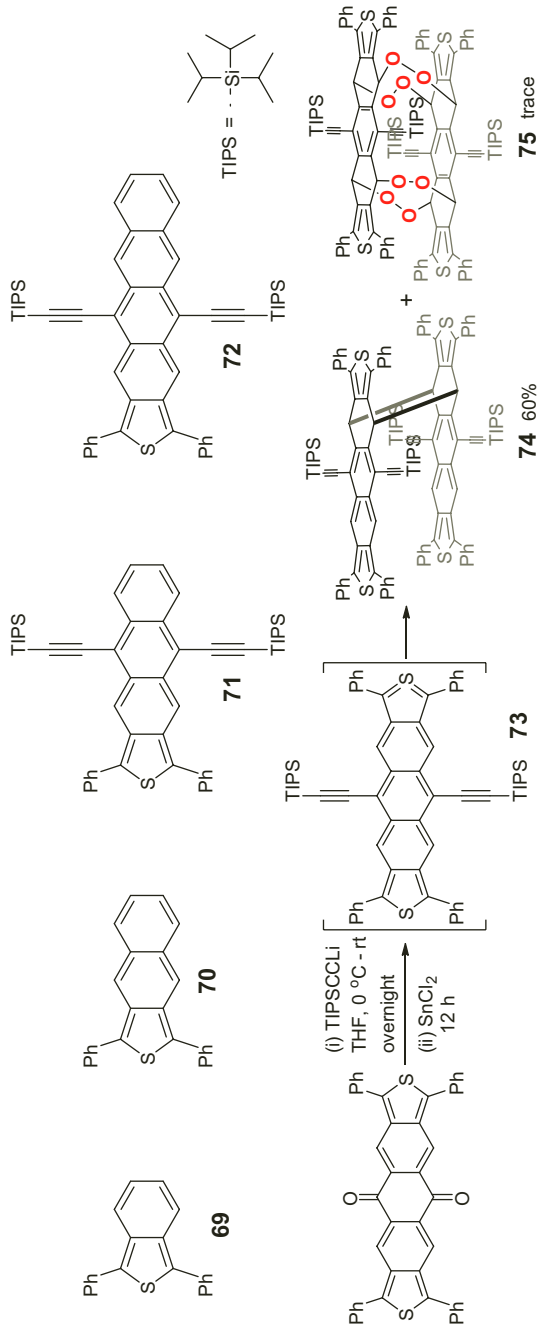


**Scheme 8.11** Chemical structures of some reported acenothiophenes and the attempted synthesis of acenodithiophene derivative **73**.

the zigzag edges in the *cis*-mode. In addition, during the crystal growing process of **73**, a trace amount of peroxy-linked dimer **75** was also identified by X-ray crystallographic analysis. It is a peroxy-bridged dimer with four peroxy groups linked to the unblocked sites. Further photo-stability measurement demonstrated that these non-classical acenes are rather sensitive to light in solution, but they can be stored in the dark for a week without any decomposition. The high reactivity and instability of these compounds could be ascribed to the unique *o*-quinoidal conjugated structure and the open-shell diradical character.

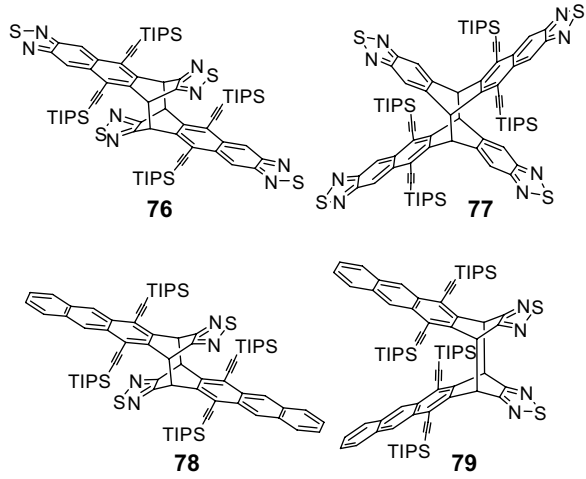


**Figure 8.23** Photodimers of acenes end-capped with 1,2,5-thiadiazoles.

Müllen and co-workers also reported similar dimerization of [1,2,5]thiadiazole terminated acenes [56]. These dimers were isolated without the observation of any monomer (Figure 8.23). It is noteworthy that only the centrosymmetric dimers **76** and **77** were separated, and the centrosymmetric dimer **78** and planosymmetric dimer **79** in the ratio of 5:1 were observed. The molecular structures of these four molecules were determined using single-crystal X-ray diffraction analysis. According to these results, the high reactivity of these [1,2,5]thiadiazole terminated acene monomers could probably originate from their large diradical characters, although the ground states of these monomers were not mentioned in the literature. According to our UDFT calculations (Table 8.1), the monomer

skeleton of **76** is **ABTz-3** with a diradical character 0.353, which is also an isoelectronic structure of **72** and pentacene. Hence, the monomer of **77** with an isoelectronic structure of hexacene should have larger diradical character and higher reactivity. The diradical character of the backbone of dimers **78** and **79** is 0.149 (**ATz-4** in Table 8.1), and dimerization occurred, possibly due to the high reactivity of the monomer. The findings here may provide evidences and a deeper insight into these non-classical acenes.

## 8.5 Summary

We have discussed a class of open-shell diradicaloids based on the fused heteropolycyclic molecules. Like other quinoidal oligomers, the quinoidal FHCs have intrinsic tendency to become open-shell diradical character. They can exhibit anti-aromaticity or pro-aromaticity, depending on the fusion mode. The imine-nitrogen containing aza-acenes or aza-quinodimethanes also displayed diradical-like behavior. The rarely investigated non-classical acenes deserved further attention, due to their unique electronic structure and chemical reactivity. These FHC-based diradicaloids are also promising materials for OFETs, TPA chromophores, photovoltaics, and spintronics.

### References

1. Bendikov, M., Duong, H. M., Starkey, K., Houk, K. N., Carter, E. A., and Wudl, F. (2004). Oligoacenes: Theoretical prediction of open-shell singlet diradical ground states, *J. Am. Chem. Soc.*, **126**, pp. 7416–7417.
2. Trinquier, G., David, G., and Malrieu, J.-P. (2018). Qualitative views on the polyradical character of long acenes, *J. Phys. Chem. A*, **122**, pp. 6926–6933.
3. Qu, Z., Zhang, D., Lium C., and Jiang, Y. (2009). Open-shell ground state of polyacenes: A valence bond study, *J. Phys. Chem. A*, **113**, pp. 7909–7914.
4. Campbell, R. B. and Robertson, J. M. (1962). The crystal structure of hexacene, and a revision of the crystallographic data for tetracene, *Acta Crystallogr.*, **15**, pp. 289–290.

5. Payne, M. M., Parkin, S. R., and Anthony, J. E. (2005). Functionalized higher acenes: Hexacene and heptacene, *J. Am. Chem. Soc.*, **127**, pp. 8028–8029.
6. Chun, D., Cheng, Y., and Wudl, F. (2008). The most stable and fully characterized functionalized heptacene, *Angew. Chem. Int. Ed.*, **47**, pp. 8380–8385.
7. Qu, H. and Chi, C. (2010). A stable heptacene derivative substituted with electron-deficient trifluoromethylphenyl and triisopropylsilylethynyl groups, *Org. Lett.*, **12**, pp. 3360–3363.
8. Kaur, I., Stein, N. N., Kopreski, R. P., and Miller, G. P. (2009). Exploiting substituent effects for the synthesis of a photooxidatively resistant heptacene derivative, *J. Am. Chem. Soc.*, **131**, pp. 3424–3425.
9. Kaur, I., Jazdzyk, M., Stein, N. N., Prusevich, P., and Miller, G. P. (2010). Design, synthesis, and characterization of a persistent nonacene derivative, *J. Am. Chem. Soc.*, **132**, pp. 1261–1263.
10. Purushothaman, B., Bruzek, M., Parkin, S. R., Miller, A.-F., and Anthony, J. E. (2011). Synthesis and structural characterization of crystalline nonacenes, *Angew. Chem. Int. Ed.*, **50**, pp. 7013–7017.
11. Zuzak, R., Dorel, R., Kolmer, M., Szymonski, M., Godlewski, S., and Echavarren, A. M. (2018). Higher acenes by on-surface dehydrogenation: From heptacene to undecacene, *Angew. Chem. Int. Ed.*, **57**, pp. 10500–10505.
12. Krüger, J., García, F., Eisenhut, F., Skidin, D., Alonso, J. M., Guitián, E., Pérez, D., Cuniberti, G., Moresco, F., and Peña, D. (2017). Decacene: On-surface generation, *Angew. Chem. Int. Ed.*, **56**, pp. 11945–11948.
13. Eisenhut, F., Kühne, T., García, F., Fernández, S., Guitián, E., Pérez, D., Trinquier, G., Cuniberti, G., Joachim, C., Peña, D., and Moresco, F. (2020). Dodecacene generated on surface: Reopening of the energy gap, *ACS Nano*, **14**, pp. 1011–1017.
14. Bunz, U. H. F., Engelhart, J. U., Lindner, B. D., and Schaffroth M. (2013). Large N-heteroacenes: New tricks for very old dogs?, *Angew. Chem. Int. Ed.*, **52**, pp. 3810–3821.
15. Bunz, U. H. F. (2015). The larger linear N-heteroacenes, *Acc. Chem. Res.*, **48**, pp. 1676–1686.
16. Müller, M., Ahrens, L., Brosius, V., Freudenberg, J., and Bunz, U. H. F. (2019). Unusual stabilization of larger acenes and heteroacenes, *J. Mater. Chem. C*, **7**, pp. 14011–14034.
17. Ye, Q., Chang, J., Shi, X., Dai, G., Zhang, W., Huang, K., and Chi, C. (2014). Stable 7,14-Disubstituted-5,12-dithiapentacenes with quinoidal conjugation, *Org. Lett.*, **16**, pp. 3966–3969.

18. Shi, X., Kueh, W., Zheng, B., Huang, K., and Chi, C. (2015). Dipolar quinoidal acene analogues as stable isoelectronic structures of pentacene and nonacene, *Angew. Chem. Int. Ed.*, **54**, pp. 14412–14416.
19. Dong, S., Herng, T. S., Gopalakrishna, T. Y., Phan, H., Lim, Z. L., Hu, P., Webster, R. D., Ding, J., and Chi, C. (2016). Extended bis(benzothia) quinodimethanes and their dications: From singlet diradicaloids to isoelectronic structures of long acenes, *Angew. Chem. Int. Ed.*, **55**, pp. 9316–9320.
20. Dong, S., Gopalakrishna, T. Y., Han, Y., Phan, H., Tao, T., Ni, Y., Liu, G., and Chi, C. (2019). Extended bis(anthraoxa)quinodimethanes with nine and ten consecutively fused six-membered rings: Neutral diradicaloids and charged diradical dianions/dications, *J. Am. Chem. Soc*., **141**, pp. 62–66.
21. Chen, Y., Kueh, H., Gopalakrishna, T. Y., Dong, S., Han, Y., and Chi, C. (2019). Sulfur-containing, quinodimethane-embedded acene analogue with nine consecutively fused six-membered rings, *Org. Lett*., **21**, pp. 3127–3130.
22. Motta, S. D., Negri, F., Fazzi, D., Castiglioni, C., and Canesi, E. V. (2010). Biradicaloid and polyenic character of quinoidal oligothiophenes revealed by the presence of a low-lying double-exciton state, *J. Phys. Chem. Lett.*, **1**, pp. 3334–3339.
23. Anthony, J. E., Eaton, D. L., and Parkin, S. R. (2002). A road map to stable, soluble, easily crystallized pentacene derivatives, *Org. Lett*., **4**, pp. 15–18.
24. Payne, M. M., Parkin, S. R., and Anthony, J. E. (2005). Functionalized higher acenes: Hexacene and heptacene, *J. Am. Chem. Soc*., **127**, pp. 8028–8029.
25. Zeng, Z., Lee, S., Son, M., Fukuda, K., Burrezo, P. M., Zhu, X., Qi, Q., Li, R., Navarrete, J. T. L., Ding, J., Casado, J., Nakano. M., Kim, D., and Wu, J. (2015). Push-pull type oligo(*N*-annulated perylene)quinodimethanes: Chain length and solvent-dependent ground states and physical properties, *J. Am. Chem. Soc.*, **137**, pp. 8572–8583.
26. Hu, P., Lee, S., Herng, T. S., Aratani, N., Gonçalves, T. P., Qi, Q., Shi, X., Yamada, H., Huang. K.-W., Ding, J., Kim, D., and Wu, J. (2016). Toward tetraradicaloid: The effect of fusion mode on radical character and chemical reactivity, *J. Am. Chem. Soc.*, **138**, pp. 1065–1077.
27. Shi, X., Burrezo, P. M., Lee, S., Zhang, W., Zheng, B., Dai, G., Chang, J., Navarrete, J. T. L., Huang, K.-W., Kim, D., Casado, J., and Chi, C. (2014). Antiaromatic bisindeno-[*n*]thienoacenes with small singlet biradical

characters: Syntheses, structures and chain length dependent physical properties, *Chem. Sci.,* **5**, pp. 4490–4503.

28. Shi, X., Quintero, E., Lee, S., Jing, L., Herng, T. S., Zheng, B., Huang, K. W., Navarrete, J. T. L., Ding, J., Kim, D., Casado, J., and Chi C (2016). Benzo-thia-fused [*n*]thienoacenequinodimethanes with small to moderate diradical characters: The role of pro-aromaticity versus anti-aromaticity, *Chem. Sci.,* **7**, pp. 3036–3046.
29. Shi, X., Lee, S., Son, M., Zheng, B., Chang, J., Jing, L., Huang, K.-W., Kim, D., and Chi, C. (2015). Pro-aromatic bisphenaleno-thieno[3,2-*b*]thiophene versus anti-aromatic bisindenothieno[3,2-b]thiophene: Different ground-state properties and applications in field-effect transistors, *Chem. Commun*., **51**, pp. 13178–13180.
30. Rudebusch, G. E., Fix, A. G., Henthorn, H. A., Vonnegut, C. L., Zakharov, L. N., and Haley, M. M. (2014). Quinoidal diindenothienoacenes: Synthesis and properties of new functional organic materials, *Chem. Sci.*, **5**, pp. 3627–3633.
31. Kubo, T. (2015). Recent progress in quinoidal singlet biradical molecules, *Chem. Lett*, **44**, pp. 111–122.
32. Konishi, A. and Kubo, T. (2017). Benzenoid quinodimethanes, *Top. Curr. Chem.,* **375**, pp. 69–105.
33. Zeng, Z., Shi, X., Chi, C., Navarrete, J. T. L., Casado, J., and Wu, J. (2015). Pro-aromatic and anti-aromatic p-conjugated molecules: An irresistible wish to be diradicals, *Chem. Soc. Rev.*, **44**, pp. 6578–6596.
34. Gopalakrishna, T. Y., Zeng, W., Lu, X., and Wu, J. (2018). From open-shell singlet diradicaloids to polyradicaloids, *Chem. Commun*., **54**, pp. 2186–2199.
35. Miao, Q. (2014). Ten wears of *N*-heteropentacenes as semiconductors for organic thin-film transistors, *Adv. Mater*., **26**, pp. 5541–5549.
36. Engelhart, J. U., Lindner, B. D., Tverskoy, O., Rominger, F., and Bunz, U. H. F. (2013). Pd-catalyzed coupling of non-activated dibromoarenes to 2,3- diaminoarenes: Formation of *N*,*N*′-dihydropyrazines, *Chem. Eur. J*., **19**, pp. 15089–15092.
37. Purushothaman, B., Parkin, S. R., and Anthony, J. E. (2010). Synthesis and stability of soluble hexacenes, *Org. Lett*., **12**, pp. 2060–2063.
38. Engelhart, J. U., Lindner, B. D., Tverskoy, O., Rominger, F., and Bunz, U. H. F. (2013). Partially fluorinated tetraazaacenes by nucleophilic aromatic substitution, *J. Org. Chem*., **78**, pp. 10832–10839.
39. Engelhart, J. U., Tverskoy, O., and Bunz, U. H. F. (2014). A persistent diazaheptacene derivative, *J. Am. Chem. Soc*., **136**, pp. 15166–15169.

40. Janosik, T., Wahlström, N., and Bergman J. (2008). Recent progress in the chemistry and applications of indolocarbazoles, *Tetrahedron*, **64**, pp. 9159–9180.
41. Frederickson, C. K., Rose, B. D., and Haley, M. M. (2017). Explorations of the indenofluorenes and expanded quinoidal analogues, *Acc. Chem. Res*., **50**, pp. 977–987.
42. Long, B. H., Rose, W. C., Vyas, D. M., Matson, J. A., and Forenza, S. (2002). Discovery of antitumor indolocarbazoles: Rebeccamycin, NSC 655649, and fluoroindolocarbazoles, *Curr. Med. Chem. Anti-Cancer Agents*, **2**, pp. 255–266.
43. Sánchez, C. Méndez, C., and Salas, J. (2006). Indolocarbazole natural products: Occurrence, biosynthesis, and biological activity, *Nat. Prod. Rep*., **23**, pp. 1007–1045.
44. Wakim, S., Bouchard, J., Simard, M., Drolet, N., Tao, Y., and Leclerc, M. (2004). Organic microelectronics: Design, synthesis, and characterization of 6,12-dimethylindolo[3,2-b]carbazoles, *Chem. Mater*., **16**, pp. 4386–4388.
45. Wu, Y., Li, Y., Gardner, S., and Ong, B. S. (2005). Indolo[3,2-b]carbazole-based thin-film transistors with high mobility and stability, *J. Am. Chem. Soc*., **127**, pp. 614–618.
46. Li, Y., Wu. Y., and Ong, B. S. (2006). Polyindolo[3,2-b]carbazoles: A new class of p-channel semiconductor polymers for organic thin-film transistors, *Macromolecules*, **39**, pp. 6521–6527.
47. Yudina, L. N., Preobrazhenskaya, M. N., and Korolev, A. M. (2000). Transformation of 5H,11H-indolo[3,2-*b*]carbazole through 5,11-didehydroindolo[3,2-*b*]carbazole, *Chem. Heterocycl. Com*., **36**, pp. 1112–1113.
48. Gu, R., Robeyns, K., Meervelt, L. V., Toppet, S., and Dehaen, W. (2008). Facile synthesis of novel indolo[3,2-*b*]carbazole derivatives and a chromogenic-sensing 5,12-dihydroindolo[3,2-*b*]carbazole, *Org. Biomol. Chem*., **6**, pp. 2484–2487.
49. Kubo, T. (2015). Recent progress in quinoidal singlet biradical molecules, *Chem. Lett*, **44**, pp. 111–122.
50. Luo, D., Lee, S., Zheng, B., Sun, Z., Zeng, W., Huang, K.-W., Furukawa, K., Kim, D., Webster, R. D., and Wu, J. (2014). Indolo[2,3-*b*]carbazoles with tunable ground states: How Clar's aromatic sextet determines the singlet biradical character, *Chem. Sci*., **5**, pp. 4944–4952.
51. Pierron, P. (1908). *Ann. Chim. Phys*., **15**, pp. 269.

52. Hutchison, K., Srdanov, G., Hicks, R., Yu, H., and Wudl, F. (1998). Tetraphenylhexaazaanthracene: A case for dominance of cyanine ion stabilization overwhelming 16 π antiaromaticity, *J. Am. Chem. Soc*., **120**, pp. 2989–2990.

53. Zheng, Y., Miao, M.-S., Dantelle, G., Eisenmenger, N. D., Wu, G., Yavuz, I., Chabinyc, M. L., Houk, K. N., and Wudl, F. (2015). A solid-state effect responsible for an organic quintet state at room temperature and ambient pressure, *Adv. Mater.,* **27**, pp. 1718–1723.

54. Zhang, Y., Zheng, Y., Zhou, H., Miao, M.-S., Wudl, F., and Nguyen, T.-Q. (2015). Temperature tunable self-doping in stable diradicaloid thin-film devices, *Adv. Mater.,* **27**, pp. 7412–7419.

55. Shi, X., Gopalakrishna, T. Y., Wang, Q., and Chi, C. (2017). Non-classical S-heteroacenes with *o*-quinoidal conjugation and open-shell diradical character, *Chem. Eur. J.*, **23**, pp. 8525–8531.

56. Xia, D., Guo, X., Chen, L., Baumgarten, M., Keerthi, A., and Müllen, K. (2016). Layered electron acceptors by dimerization of acenes end capped with 1,2,5-thiadiazoles, *Angew. Chem. Int. Ed.*, **55**, pp. 941–944.

Chapter 9

# Non-Benzenoid Polycyclic Hydrocarbon-Based Diradicaloids

**Ji Ma and Xinliang Feng**
*Centre for Advancing Electronics Dresden,*
*Faculty of Chemistry and Food Chemistry,*
*Technische Universität Dresden, 01062 Dresden, Germany*
xinliang.feng@tu-dresden.de

## 9.1 Introduction

Nanographenes or extended polycyclic aromatic hydrocarbons (PAHs) have captivated tremendous attention in the past decades for both fundamental understanding of structure-property relationship and their promising organic optoelectronic and spintronic applications [1–4]. As the structurally well-defined finite graphene fragments, nanographenes, in principle, consist solely of the six-membered rings. However, microscopy studies have revealed that graphene also contains non-hexagonal rings, including five-, seven- and/or eight-membered rings, as defects, particularly at the grain boundaries of single-layer graphene sheet [5–8]. This irregularity has been observed to significantly influence the structural

*Diradicaloids*
Edited by Jishan Wu

ISBN 978-981-4968-08-9 (Hardcover), 978-1-003-27724-8 (eBook)
www.jennystanford.com

conformation and physicochemical properties of graphene, arising from local changes in strain and π-conjugation [9–11]. Likewise, the imposition of the non-hexagonal-ring defects into nanographenes can be envisioned as ideal models of the defective graphene [2, 12, 13]. Thanks to the development of modern organic synthetic methodology, the incorporation of non-hexagonal rings into nanographenes can be precisely manipulated by chemists, thus opening up the opportunities to study the relationship between the molecular topology and properties. From the chemistry point of view, nanographenes bearing non-hexagonal rings can be also described as the non-benzenoid PAHs [14]. In comparison to the extensively studied benzenoid PAHs, non-benzenoid PAHs have experienced a remarkable renaissance in view of their unique electronic configurations and molecular orbital distribution, which are never shared by the benzenoid systems [15]. The topology of the π-electron network is a primary concern that determines the geometry and ground state electronic structure of PAHs, as exemplified by [*n*]circulene in Figure 9.1a, where changing the value of *n* has significant implications on the molecular shape [16]. For example, the replacement of the central six-membered ring in coronene with a pentagon or a heptagon results in the bowl-shaped corannulene [17] or the saddle-shaped [7]circulene [18], respectively. These changes reduce the molecular symmetry and endow unusual physical or chemical properties of the non-benzenoid π-systems. On the other hand, our recent studies have revealed that the presence of non-benzenoid topological defect (i.e. pentagon) in a benzenoid framework can alter the bond connectivity in the hexagonal lattice, leading to the non-Kekulé nanographene with an unpaired electron as confirmed by the Kondo effect (Figure 9.1b) [19, 20].

Besides the tunable molecular topology of PAHs, aromaticity is also a fundamental concept to understand their chemical reactivities and physical properties [21–24]. Most PAHs can be characterized by a closed-shell configuration, accommodating their π-electrons only in bonding orbitals. In contrast, polycyclic hydrocarbons (PHs) with open-shell configurations refer to those with unpaired electrons or partially unpaired electrons within the molecular scaffold [25, 26]. In the last decade, significant efforts had been devoted to the synthesis and characterization of open-shell PHs with diradical characters

(namely diradicaloids) because of their attractive optical, electronic, and magnetic properties, which can be desirable for applications in molecular spintronics, electronic devices, and non-linear optics [27, 28]. While a growing number of open-shell diradicaloids has been achieved, most of them possess the benzenoid topology that belongs to benzenoid PHs, such as the higher order acenes, zethrenes, anthenes, *peri*-acenes, triangulenes, etc. [29–34]. The inclusion of non-hexagonal rings in the open-shell diradical π-systems has emerged as an efficient strategy to create new molecules with unusual electronic ground states and magnetic properties, due to their irregular molecular orbital levels and distributions. In this chapter, we will review and highlight the recent synthetic works in the field of non-benzenoid PH-based diradicaloids, including the five-membered ring-containing diradicaloids, seven-membered ring-containing diradicaloids, as well as the less explored four- or eight-membered ring-containing diradicaloids. The synthetic strategies and structural characterizations of the class of open-shell PHs as well as the discussion of their optoelectronic and magnetic properties with an eye for potential materials application will be comprehensively provided.

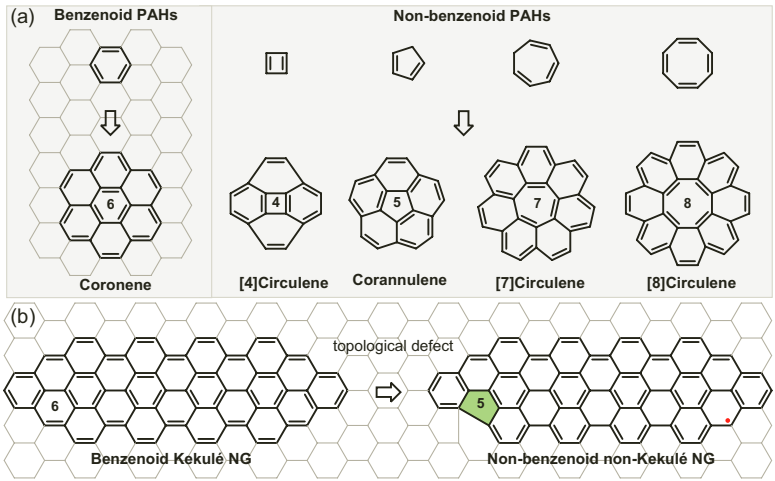


**Figure 9.1** (a) The classification of benzenoid and non-benzenoid PAHs as exemplified by [*n*]circulene (*n* is integer). (b) Topological defect-induced magnetism via a single pentagonal ring in graphene nanostructures.

## 9.2 Five-Membered Ring-Containing Diradicaloids

The introduction of five-membered rings in PAHs has been largely studied as fullerene fragments and endcaps of carbon nanotubes [35, 36]. Apart from the fullerene subunits that mostly have the closed-shell ground state, significant progress had been made in the past decade to constructing the five-membered ring-containing PHs with open-shell diradical characters [37], including pentalene-based diradicaloids, indenofluorenes family, curved diradicaloids with pentagon rings, and other pentagon-based diradicaloids.

### 9.2.1 Pentalene-Based Diradicaloids

Pentalene (**1**, Figure 9.2), composed of two fused cyclopentadiene rings with 8 π-electrons, belongs to the class of antiaromatic PHs [38, 39]. It has been suggested that antiaromatic systems are generally highly reactive and kinetically unstable, due to their small highest occupied molecular orbital (HOMO)–lowest unoccupied molecular orbital (LUMO) energy gaps that tend to increase the diradical character [40, 41]. The unsubstituted pentalene is thermally unstable and dimerizes above −196 °C [42]. Substituents can provide greater stability with electronic or steric stabilization, as observed for hexaphenylpentalene [43], 1,3-bis (dimethylamino) pentalene [44], and 1,3,5-tri-*tert*-butylpentalene [45].

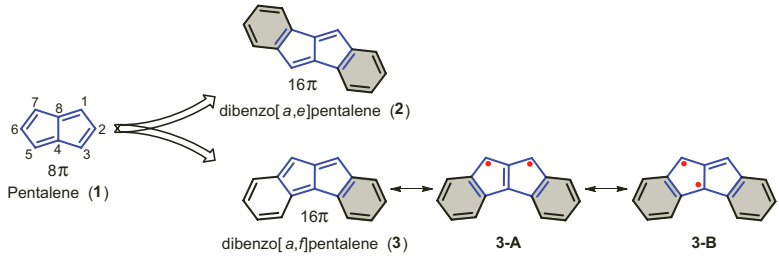


**Figure 9.2** Benzannulation of pentalene.

For antiaromatic compound with non-benzenoid structure, fusion of one or more benzenoid rings to the end of the π-system (i.e., benzannulation) has been used to bestow extra stability,

leading to the possible isolation of stable benzoannulated congeners [46]. Pentalene can be stabilized by the strategy of benzannulation, as the strong tendency to form an aromatic sextet can reduce the antiaromaticity of the parent pentalene. Therefore, major synthetic advances have been focused on benzo-fused pentalene derivatives. By the fusion of two aromatic benzenoid rings to the end of pentalene unit, two structural isomers of dibenzopentalenes can be obtained, that is, dibenzo[*a*,*e*]pentalene (**2**) and dibenzo[*a*,*f*]pentalene (**3**) (Figure 9.2). Since the first isolation of the stable isomer **2** in 1912 by Brand [42], related derivatives have attracted considerable interest due to their potential in optoelectronic applications [47–51]. In isomer **2**, the two fused benzene rings stabilize the pentalene unit through the aromaticity of the outer hexagonal rings, which reduces the antiaromatic character of pentalene and furnishes the inner pentagons with olefinic properties. It is worth to mention that the position of benzannulation also plays a critical role in the electronic structure and chemical stabilization of π-system. In contrast to the stable [*a*,*e*]-type isomer **2**, the [*a*,*f*]-type isomer **3** is expected to provide larger antiaromaticity and thus more reactive [52, 53]. This is because one of the fused benzene rings in **3** adopts an *o*-quinoidal structure in the closed-shell resonance form, which loses the aromatic stabilization and enhances the 4*n* π-electron antiaromatic character [54]. From the resonance structures of **3**, a trimethylenemethane (TMM) diradical subunit (**3-B**) can be drawn, which would provide an open-shell diradical character (Figure 9.2).

Attempts to synthesize the π-extended [*a*,*f*]-type pentalenes with fused naphthyl-ring systems by Diederich's group readily gave Diels–Alder adducts and failed to give fully conjugated products [55]. Recently, the first synthesis and full characterization of the persistent dibenzo[*a*,*f*]pentalene derivatives (**3a** and **3b**) have been reported by Konishi, Yasuda and coworkers (Figure 9.3a) [56]. The synthetic approach involves the nucleophilic addition of dialdehydes **4** with 2-mesitylmagnesium bromide to give diols **5**, followed by the intramolecular cyclization of **5** under acidic condition to afford the dehydrogenated hydrocarbon **6**. Aromatic dianion $\mathbf{7}^{2-}$ was quantitatively generated by treatment of **6** with *n*-BuLi at −35 °C, and subsequent two-electron oxidation of $\mathbf{7}^{2-}$ with *p*-chloranil furnished the mesityl derivatives of dibenzo[*a*,*f*] pentalene **3a** and **3b** as brown solids. However, compounds **3a** and

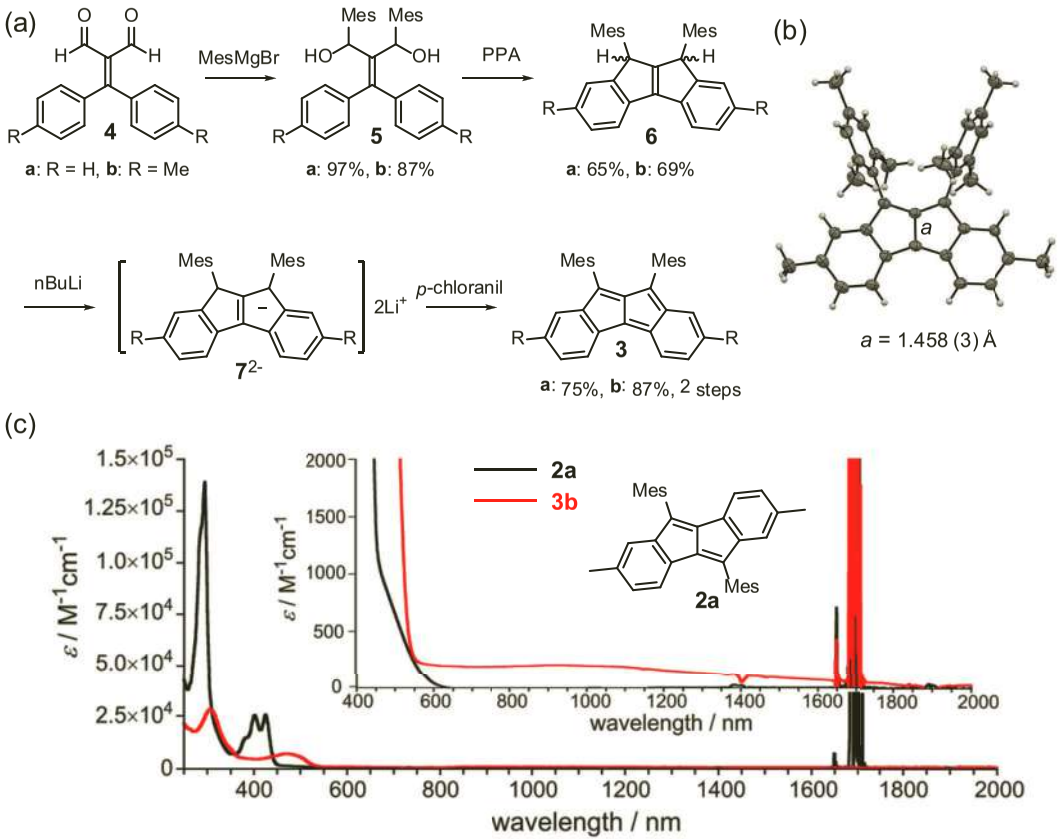


**Figure 9.3** (a) Synthesis of the dibenzo[*a*,*f*]pentalene derivatives (**3a** and **3b**). (b) Single-crystal structure of **3b**. (c) UV-Vis-NIR absorption spectra of **2a** and **3b** in $CH_2Cl_2$. The inset shows a magnified view. Reproduced with permission from Ref. [56]. Copyright 2017 American Chemical Society.

**3b** were immediately oxidized under ambient conditions to give the oxygen-adduct. X-ray crystallographic analysis of **3b** illustrated that the main core of **3b** possessed a planar structure (Figure 9.3b). From the large degree of bond-length alternation in **3b** and the relatively large single bond character of the bond *a*, compound **3b** should be represented as a resonance mixture between the *o*-quinoidal canonical structure and a diradical structure involving the TMM subunit (Figure 9.2). The $^{1}$H nuclear magnetic resonance (NMR) spectrum of **3b** in tetrahydrofuran (THF)-$d_8$ showed severe line broadening at 30 °C, while progressive line sharpening was observed upon cooling, indicating the singlet ground state of **3b** with a small singlet-triplet energy gap ($\Delta E_{S\text{-}T}$). This is also confirmed by the electron-spin resonance (ESR) measurements that the signal intensities increased with rising temperature, and the $\Delta E_{S\text{-}T}$ of −4.30 kcal mol$^{-1}$ was estimated by fitting the ESR curves with Bleaney–Bowers equation. In the UV-Vis absorption spectrum, **3b** displayed a moderate absorption band at 500 nm, together with a weak broad band centered at 965 nm that tailing to 2000 nm (Figure 9.3c). The longest wavelength absorption band was significantly red-shifted, compared to that of the structural isomer **2a**, which leads to a smaller HOMO-LUMO energy gap in **3b**, further supporting the singlet diradical character of **3b**.

## 9.2.2 Indacene-Based Diradicaloids

In addition to the benzannulation of pentalene, the benzinterposition to pentalene unit can gave the antiaromatic indacenes with 12 π-electrons, which have two different structural isomers, including the *s*-indacene (**8**) with linearly fused 5-6-5 membered rings, and *as*-indacene (**9**) with angularly fused 5-6-5 membered rings (Figure 9.4) [57, 58]. Both isomers can be utilized as the useful building blocks to construct open-shell diradicaloids, including the indenofluorenes family and biphenalenyl systems.

### 9.2.2.1 Indenofluorene and its π-extended homologues

Two flanking benzene rings on indacene unit can give indenofluorenes with 20 π-electrons, which can be regarded as a unique anti-aromatic/pro-aromatic system [22] comprising of fully

conjugated array of 6-5-6-5-6-membered rings [59–61]. The fusion pattern of benzene rings to the five-membered rings impacts the stability of the indacene core and produces five structural isomers, consisting of indeno[1,2-*b*]fluorene (**10**), indeno[2,1-*a*]fluorene (**11**), indeno[2,1-*c*]fluorene (**12**), indeno[2,1-*b*]fluorene (**13**), and indeno[1,2-*a*]fluorene (**14**) (Figure 9.5a). These isomers can be characterized by the presence of three types of quinodimethane (QDM) units, that is, *p*-QDM, *o*-QDM, or *m*-QDM, in the hydrocarbon framework, of which the non-Kekulé open-shell resonance form indicates the presence of diradical ground state (Figure 9.5b) [22, 37]. Since compounds **10** and **12** have a *p*-QDM substructure, **13** and **14** possess an *m*-QDM substructure and **11** holds an *o*-QDM substructure, the indenofluorene isomers present different electronic and optical properties from each other. Notably, the five indenofluorene isomers result in a wide range of computed diradical character ($y_0$) values from $y_0$ = 0.25 for indeno[2,1-*c*]fluorene (**12**) to as large as $y_0$ = 0.80 for indeno[1,2-*a*]fluorene (**14**) [62]. The large differences in $y_0$ values for the five isomers can be rationalized by examining the number of Clar's aromatic sextets gained from the open-shell form to closed-shell form. Indenofluorenes with two Clar sextets in the closed-shell form and three in the open-shell form exhibit only a modest gain in stability of one additional Clar sextet in the open-shell form, resulting in indenofluorenes (**10**, **11,** and **12**) with low diradical character. In contrast, two additional aromatic sextets are gained for **13** and **14**, meaning that **13** and **14** receive more resonance stabilization energy in the open-shell form and thus lead to much larger diradical character (Figure 9.5a).

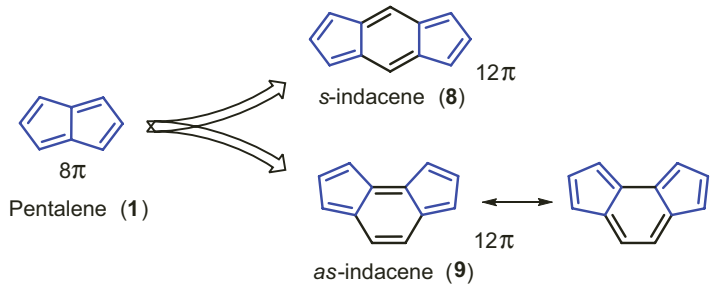


**Figure 9.4** Benzinterposition of pentalene.

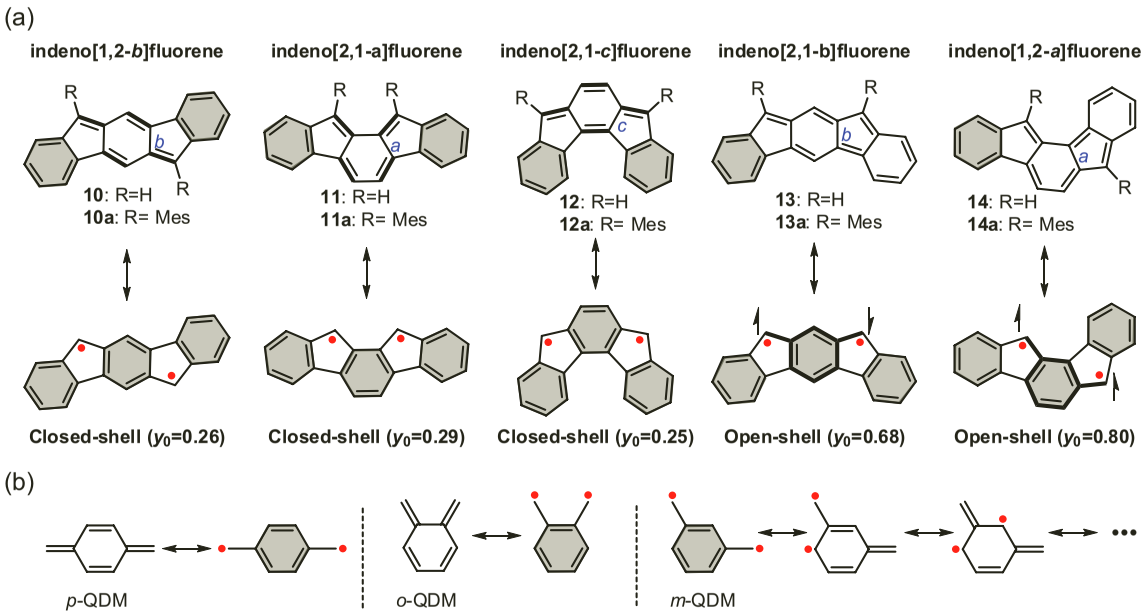


**Figure 9.5** (a) Resonance structure of the five indenofluorenes (**10**–**14**). Diradical character ($y_0$) of the parent hydrocarbon is calculated at PUHF/6–311G*/SF-CL-TDDFT BHandHLYP/6-311G* level of theory. (b) Resonance canonical structures of *p*-QDM, *o*-QDM, and *m*-QDM.

Stabilized derivatives of these five indenofluorene isomers were intensively explored by Haley's group and Tobe's group in the past decade, on account of their small energy gaps associated with the potential diradical character, in which the most reactive sites at the pivotal five-membered ring positions were kinetically stabilized by introducing bulky groups such as mesityl. In 2011, indeno[1,2-*b*] fluorene (**10**) derivatives were synthesized and investigated by Haley's group, with regard to the crystal packing, energy gaps, and charge transport behavior [63, 64]. The stable mesityl substituted isomers **11a** and **12a** were also studied by Tobe's group in 2011 [65] and Haley's group in 2013 [66], respectively, regarding their molecular structures and optical and electrochemical properties. These three indenofluorenes (**10a**, **11a,** and **12a**) mentioned above are better described as antiaromatic closed-shell PHs, owing to the intensive NMR resonance in solution, silent ESR signal, and large bond-length alternation from the single-crystal structure. In 2013, Tobe et al. reported the indeno[2,1-*b*]fluorene derivative **13a** bearing the bulky mesityl substituents [67]. Different from the above three closed-shell indenofluorenes (**10a**–**12a**), compound **13a** turned out to be a singlet diradicaloid in the ground state as indicated by the variable-temperature (VT) NMR, VT ESR, and X-ray single crystal structures. Moreover, compound **13a** exhibited an extremely low-energy light absorption band at 850–2000 nm, despite its small conjugation framework [67]. In 2017, Haley and coworkers reported the synthesis and characterization of the last unknown indenofluorene regioisomer, indeno[1,2-*a*]fluorene derivative (**14a**), as a highly reactive species [62]. X-ray analysis of the dianion of **14a** provided definitive structural proof of the indeno[2,1-*b*]fluorene core. All the experimental and computational results supported **14a** as an open-shell molecule with pronounced diradical character.

In view of the dominant closed-shell character of *p*-QDM, the lateral expansion of the central six-membered ring in **10** is an efficient method to increase the open-shell diradical character, while maintaining the same fused outer rings. In 2016, Haley's group reported the synthesis of sterically protected indenofluorene congeners incorporating higher homologues of *p*-QDMs, that is, the fluoreno[3,2-*b*]fluorene derivative (**15a**) [68] and diindeno[*b*,*i*] anthracene derivative (**16**) [69] with a formal naphthalene or

anthracene core in the center (Figure 9.6a and 9.6b). From the experimental and calculated results, compound **15a** was more regarded as a closed-shell PH with a moderate diradical character ($y_0$ = 0.43). Interestingly, the larger congener **16** exhibited pronounced open-shell character ($y_0$ = 0.62) with remarkable stability (half-life ($t_{1/2}$) = 64 days). Compound **16** was centrosymmetric and planar from the single-crystal X-ray analysis (Figure 9.6c). The bond-length analysis revealed that the solid-state structure of **16** is a resonance hybrid in which both the closed-shell and open-shell forms contribute to the overall ground electronic state. VT $^1$H NMR experiment (Figure 9.6d) in degassed 1,2-dichlorobenzene-$d_4$ showed broadening of the aromatic proton resonances with increasing temperature and the return of the original spectrum when cooled at room temperature, suggesting that a thermally accessible triplet state is populated at higher temperatures. Superconducting quantum interference device (SQUID) measurement of **16** revealed a continuous increase of the whole magnetic molar susceptibility, which gave the $\Delta E_{S\text{-}T}$ of −4.18 kcal mol$^{-1}$ through fitting to the Bleaney–Bowers equation. The deep-blue color of **16** in $CH_2Cl_2$ solution showed higher energy transitions in the 300−500 nm rang with the $\lambda_{max}$ of the lowest energy transitions being at 690 nm (Figure 9.6e). Moreover, organic field-effect transistors (FETs) based on **16** gave ambipolar performance with quite balanced electron and hole mobilities (hole mobility ($\mu_h$) = 2 × 10$^{-3}$ cm$^2$ V$^{-1}$s$^{-1}$; electron mobility ($\mu_e$) = 4 × 10$^{-3}$ cm$^2$ V$^{-1}$s$^{-1}$) (Figure 9.6f).

Contrary to the extended indenofluorenes incorporating a *p*-QDM-type unit, Tobe's group reported the synthesis of the laterally extended fluoreno[2,3-*b*]fluorene derivative (**17**) bearing the larger *m*-QDM-type analog (Figure 9.7a) [70]. Compound **17** exhibited an increased open-shell character ($y_0$ = 0.77) compared with the indeno[2,1-*b*]fluorene (**13a**, $y_0$ = 0.68), due to disconnection of π-conjugation between the central naphthalene and external benzene units, localizing odd electron densities on the apical positions of the five-membered rings. Consequently, **17** turned out to be less stable than **13a** ($t_{1/2}$ = 30 h) and decomposed within 18 h in solution under ambient conditions. As shown in Figure 9.7b, the fluoreno[2,3-*b*]fluorene core of **17** had a major planar geometry with deviations from the mean square plane less than 0.157 Å and its larger diradical character was reflected in

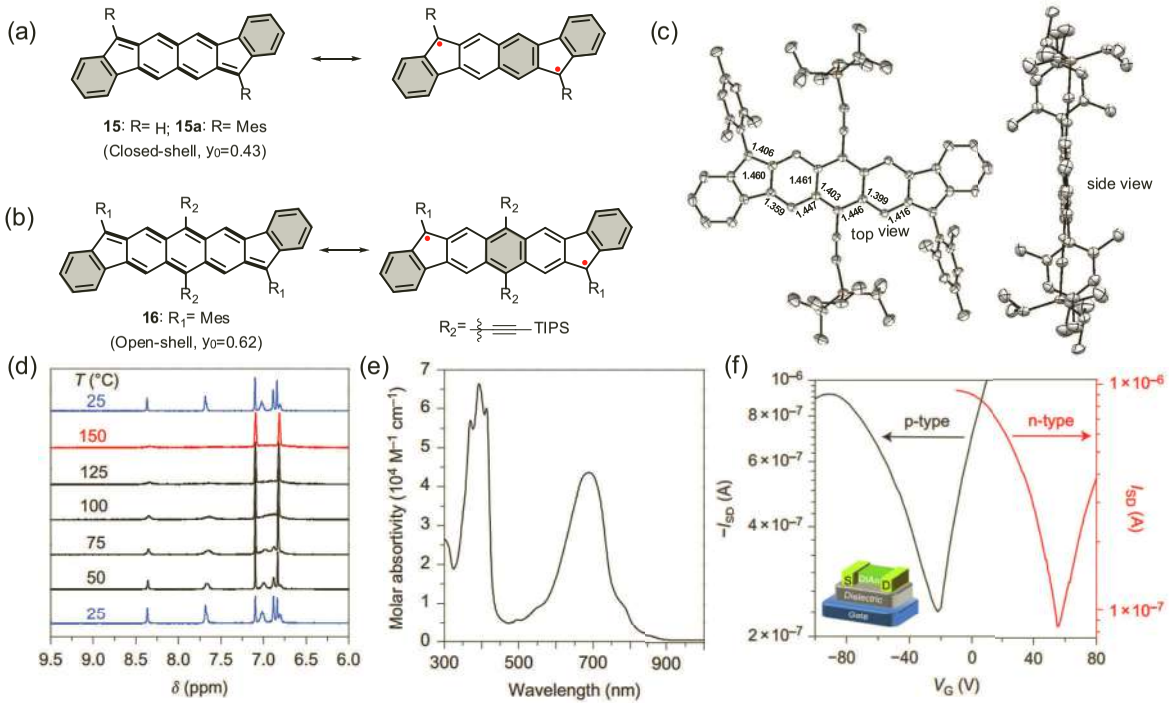


**Figure 9.6** The resonance structures of (a) fluoreno[3,2-*b*]fluorene (**15**) and (b) diindeno[*b*,*i*]anthracene derivative (**16**). (c) Single-crystal structure of **16**. (d) VT $^1$H NMR spectra of **16** in 1,2-dichlorobenzene-$d_4$. (e) Electronic absorption spectrum of **16** in $CH_2Cl_2$. (f) OFET *p*-channel and *n*-channel transfer characteristics of a vapor-deposited film of **16**. Reproduced with permission from Ref. [69]. Copyright 2016 Nature Publishing Group.

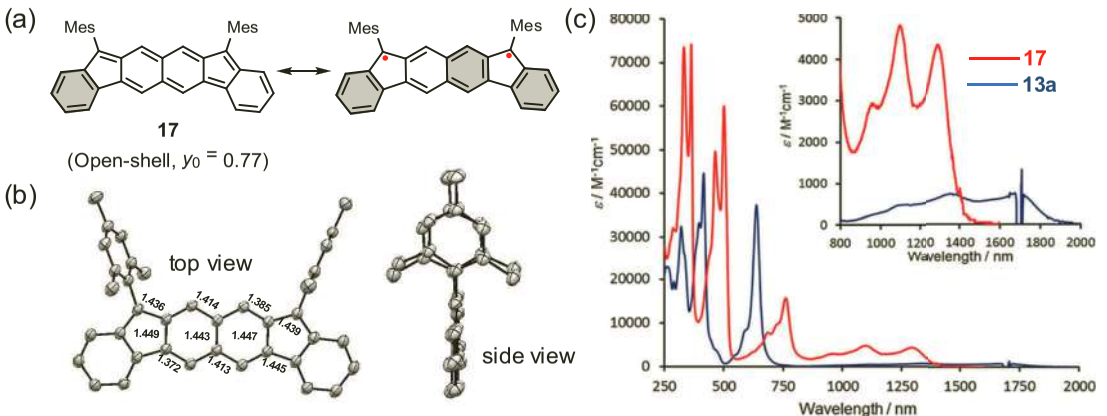


(d)

| | *Comp.* | HOMO (eV) | LUMO (eV) | H-L gap (eV) |
|---|---|---|---|---|
| *p*-QDM type | **10a** | -5.34 | -2.92 | 2.42 |
| | **15**[a] | -5.09 | -3.24 | 1.85 |
| | **16** | -4.97 | -3.52 | 1.45 |
| *m*-QDM type | **13a** | -4.93 | -3.67 | 1.26 |
| | **17** | -4.80 | -3.64 | 1.16 |

**Figure 9.7** (a) Resonance structures of fluoreno[2,3-*b*]fluorene derivative (**17**). (b) The single-crystal structure of **17**. (c) UV-Vis-NIR absorption spectra of **17** (red) and **13a** (blue) in $CH_2Cl_2$ at room temperature. Inset: NIR region with expanded longitudinal axis. (d) HOMO and LUMO energy levels of the reported indeno-based PHs determined by cyclic voltammetry (CV). [a]Calculated at the RB3LYP/6-311+G* level. Reproduced with permission from Ref. [70]. Copyright 2017 American Chemical Society.

the bond-length alternation of the fluoreno[2,3-*b*]fluorene core. Figure 9.7c showed the absorption spectra for **17** together with that of **13a** for comparison in $CH_2Cl_2$. Compound **17** exhibited an intense absorption band located at 761 nm and a weak absorption band located at 1293 nm. Interestingly, the lowest-energy maximum was shifted to shorter wavelength (1293 nm) in the larger 24 π-electron system **17** compared to that of the 20 π-electron system **13a** (1700 nm). This trend is contrary to the commonly observed character in alternant aromatic hydrocarbons such as for acenes [71] and rylenes [72], in which the larger π-system exhibits a lower energy maximum in a homologous series due to the smaller HOMO-LUMO energy gap. Theoretical analysis revealed that the moderate diradical character of **13a**, in addition to its smaller π-conjugation size, is critical for the unusual low-energy light absorption behavior. Moreover, by comparing the energy gap between the *m*-QDM-type and the *p*-QDM-type indeno-based PHs (Figure 9.7d), the HOMO-LUMO energy gap of **13a** and **17** is much smaller than that of **10a**, **15,** and **16,** owing to their increasing open-shell diradical character.

Different with the above lateral extension, the vertical extension of the QDM core can also alter the electronic ground state and diradical character of the PHs. As mentioned above, the indeno[2,1-*a*]fluorene (**11**) containing the *o*-QDM unit possesses a closed-shell ground state. The benz[*c*]indeno[2,1-*a*]fluorene (**18**) obtained by the vertical π-extension of the *o*-QDM core are expected to display larger open-shell character than that of **11**. In 2016, Tobe and coworkers synthesized and isolated the vertically extended *o*-QDM derivative **18a** [73], which was confirmed by the X-ray crystallographic analysis. Theoretical calculations (UB3LYP/6-31G(d) level) indicated that **18** has larger diradical character ($y_0$ = 0.63) and smaller single-triplet energy gap (−7.46 kcal $mol^{-1}$) compared to **11**. Compound **18a** was found to be much more reactive in air than **11a,** due to its increased diradical character. Exposure of **18a** under air condition afforded the endoperoxide **19**, in which the oxygen bridge attached at the naphthalene core because the most reactive sites were kinetically protected by the bulky mesityl groups (Figure 9.8b). Similarly, [4+2] cycloaddition of 2,3-dichloro-5,6-dicyano-1,4-benzoquinone (DDQ) took place at the same position to give adduct **20**. This regioselectivity can be attributed to both electronic and steric reasons. In contrast to **11a**, the relatively large spin densities are located at the inner naphthalene rings of **18a** as shown

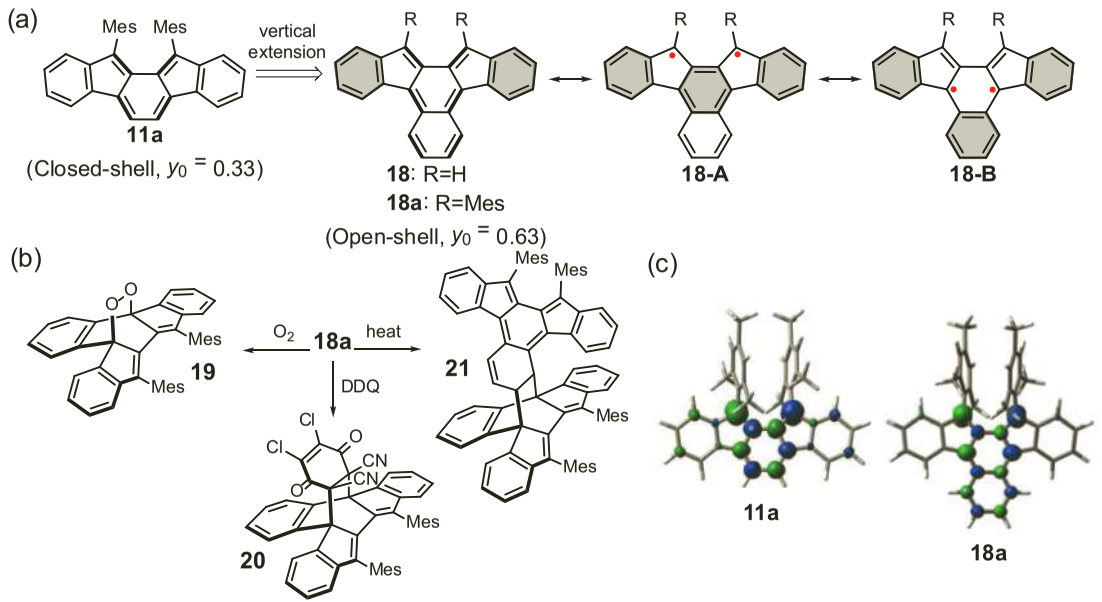


**Figure 9.8** (a) Resonance structures for **18**. (b) The $O_2$ adduct **19**, the DDQ adduct **20**, and the dimer **21** from **18**. (c) Spin-density distribution of **11a** and **18a** calculated at the B3LYP/6-31G(d) level. Reproduced with permission from Ref. [73]. Copyright 2014 The Royal Society of Chemistry.

in Figure 9.8c, indicating the relatively high reactivity at the inner position of the naphthalene ring in **18a**. Furthermore, compound **18a** underwent the [4+2] dimerization at 80 °C in the degassed toluene-$d_8$ solution and gave the σ-dimer **21** in almost quantitative yield.

Among the various types of diindeno-fused ring systems, changing central arene core is found to give rise to either closed-shell or open-shell structures with different diradical characters depending on the nature of the ring fusion patterns and the structure of the central π-system. For example, the diindenopyrenes [74] and diindeno[1,2-*b*:2′,1′-*n*]perylene [75] are reported to show the closed-shell electronic configuration. In contrast, the diindeno-based indeno[2,1-*a*]indene (**22**) [76], diindeno-based dibenzo[*c*,*pqr*] tetraphene (**23**) [77], and diindenophenanthrene (**24**) [78] possess the open-shell ground state with moderate diradical character (Figure 9.9). Interestingly, compound **24** is actually a structural isomer of **16**, where the central anthracene core of **16** is replaced by phenanthrene. Consequently, the number of Clar sextets in the open-shell resonance form of **24** is increased relative to that in **16** (four in the open-shell form of **24** vs. three in **16**), resulting in the slight increase of the diradical character ($y_0$ = 0.69). Moreover, compound **24** has the narrower electronic HOMO-LUMO energy gap (1.39 eV) and the smaller singlet-triplet energy gap ($\Delta E_{S\text{-}T}$ = −1.30 kcal mol$^{-1}$ from ESR) than those of **16**.

Another way to vary the structure and thus property of the indenofluorene-based diradicaloids is the extension of the outer benzenes with other ring system. In 2012, Haley's group reported the synthesis of the fluoreno[4,3-*c*]fluorene derivative (**25**) [79], in which the experimental and computational results proved that the compound **25** has a closed-shell ground state with a small diradical character ($y_0$ = 0.38). By fusion of the pyrene units in **25** leads to the formation of compound **26**, which is supposed to have a lower HOMO-LUMO energy gap and larger diradical character, due to the increase of the π-conjugation size (Figure 9.10a). Recently, our group reported an efficient synthetic route toward the pyrene-fused dicyclopenta[*a*,*f*]naphthalene derivative **26** bearing a 2,6-naphthoquinodimethane bridge [80]. Interestingly, compound

**26** exhibited the increased open-shell diradical character of 0.44 and the lower energy gap of 1.1 eV compared to those of **25**. The broaden NMR signal at high temperatures and intensive ESR signal of **26** suggested its open-shell singlet ground state. In particular, compound **26** showed good stability as proved by the slight decrease in its absorption intensity over the course of one month under ambient conditions (Figure 9.10b). Moreover, the constitutional isomer **27** bearing a 1,5-naphthoquinodimethane unit was prepared by us, which also had the open-shell ground state with a moderate diradical character and small energy gap of 1.0 eV. However, the solution of compound **27** was unstable and displayed a half-life time of about one day as shown in Figure 9.10c, which can be ascribed to the higher diradical character ($y_0$ = 0.48) and larger spin density at the mesityl-shielded carbon atoms originating from the central 1,5-naphthoquinodimethane motif. This result suggests that the bridge unit has significant effect on the diradical character, chemical reactivity, and physical properties of the open-shell PHs.

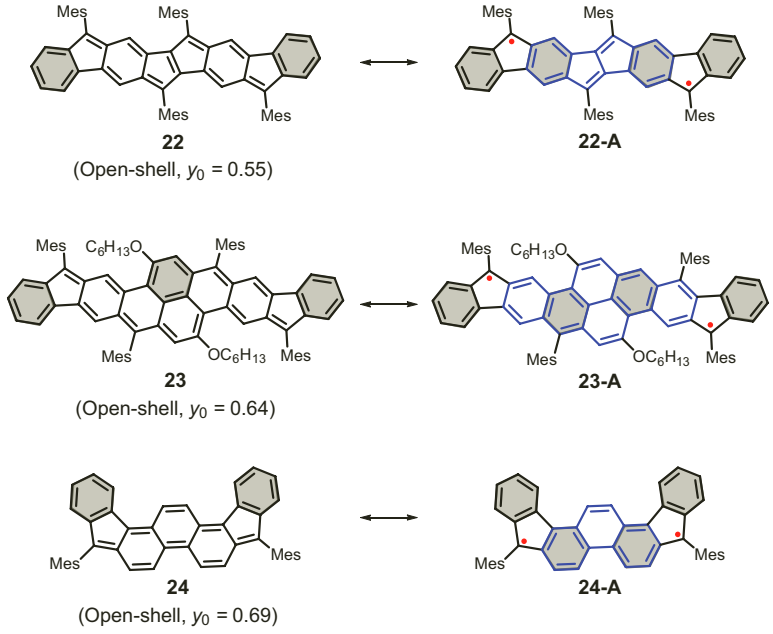


**Figure 9.9** Representative diradicaloids that obtained by varying the inner core of indenofluorenes.

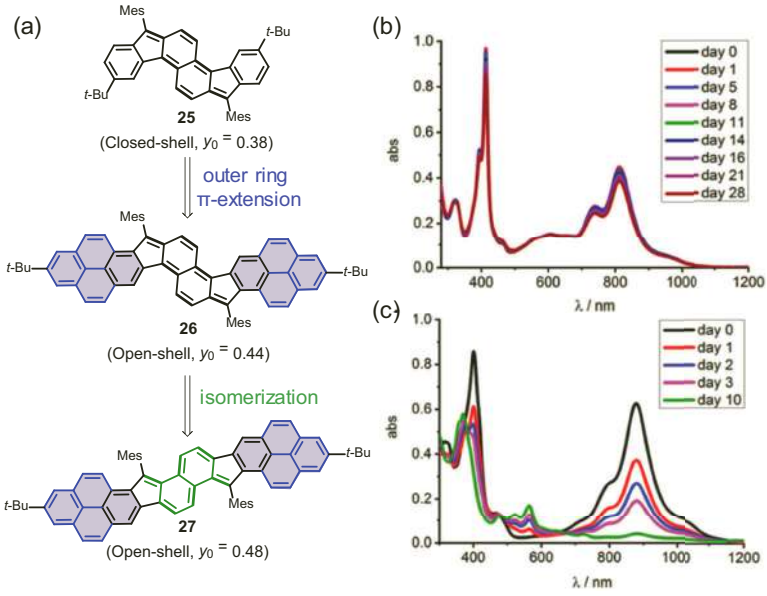


**Figure 9.10** (a) The structures of the dipyrene-fused dicyclopenta[*a*,*f*] naphthalenes that derived from the fluoreno-[4,3-*c*]fluorene. Time-dependent UV-Vis absorption spectra of (b) **26** and (c) **27** in chloroform under ambient air and light conditions. Reproduced with permission from Ref. [80]. Copyright 2020 American Chemical Society.

Very recently, Haley's group synthesized a series of diradicaloids based on the diindenoanthracene framework (Figure 9.11a) through the π-extension of its outer benzene rings, including the dibenzo-fused diindenoanthracene regioisomers (**28**–**30**) and the dibenzothiophene-fused dicyclopentaanthracene derivative **31** (Figure 9.11b) [81]. The diradical behaviors of these four derivatives were well investigated by VT NMR and Raman spectroscopy as well as the bond-length analysis of their single-crystal structures. Unlike the parent compound **16** with a half-life time of 64 days in solution, the half-life time of the π-extended derivatives **28**–**31** in solution range from ~20 days for **28** to as small as 4.5 days for **31**, suggesting that the stability decreases as the diradical character of the molecule increases. Furthermore, SQUID measurements of these molecules showed a clear increase of the magnetic molar susceptibility from low to high temperature, indicating their open-shell singlet ground state (Figure 9.11c). The Bleaney–Bowers fitting of the SQUID data

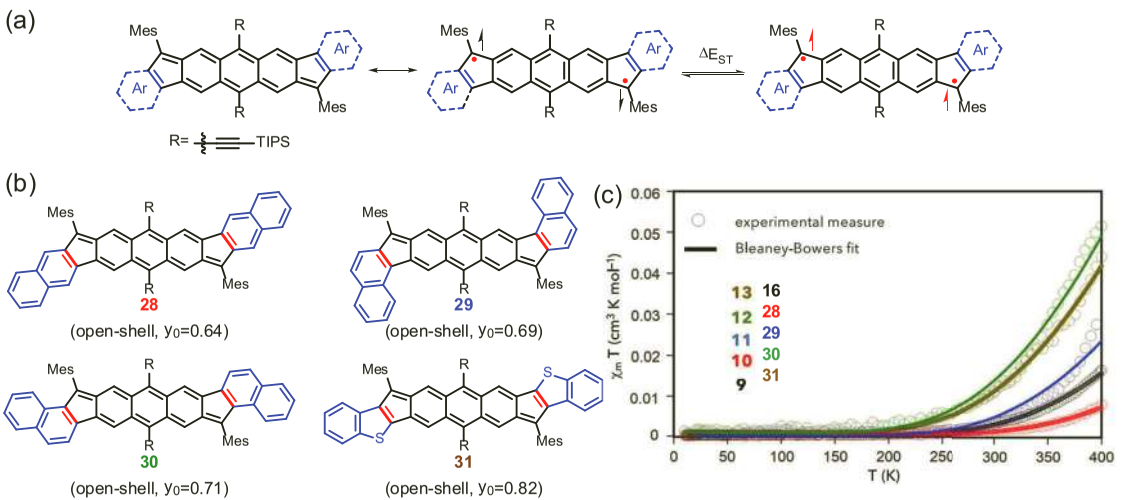


**Figure 9.11** (a) The resonance structures of the diindenoanthracene derivatives with generic fused aryl groups. (b) Diindenoanthracene derivatives **28–31**, where the outer benzene rings have been altered. (c) SQUID magnetometry data of compounds **16** and **28–31** (empty circles) along with the corresponding Bleaney–Bowers fits (solid lines). Reproduced with permission from Ref. [81]. Copyright 2020 Elsevier.

gave their $\Delta E_{S\text{-}T}$ gaps (**28**: −4.83 kcal mol$^{-1}$, **16**: −4.18 kcal mol$^{-1}$, **29**: −3.84 kcal mol$^{-1}$, **30**: −3.24 kcal mol$^{-1}$, and **31**: −3.38 kcal mol$^{-1}$), which agreed well with the calculated values (**28**: −5.09 kcal mol$^{-1}$, **16**: −4.91 kcal mol$^{-1}$, **29**: −4.16 kcal mol$^{-1}$, **30**: −3.45 kcal mol$^{-1}$, and **31**: −3.41 kcal mol$^{-1}$). Therefore, by making the minor changes to the outer rings of the diindenoanthracene, $\Delta E_{S\text{-}T}$ can be rationally tuned over a narrow 1.6 kcal mol$^{-1}$ range within these five derivatives, revealing that the magnetic properties of the diradicaloids can be finely modulated by using a structure refinement strategy.

#### 9.2.2.2 Biphenalenyls

Connection of two phenalenyl moieties with an indacene spacer together can produce a series of compounds called bisphenalenyls [82–83]. By using the *s*-indacene or *as*-indacene as the spacer, the linear isomer **32** or the angular one **33** can be furnished, respectively (Figure 9.12a) [84]. In these systems, the intrinsic delocalization of phenalenyl unit and the aromatic stabilization through the recovery of one additional Clar sextet from the quinoidal resonance form to the open-shell diradical form play a major role in stabilization. Since there are excellent reviews summarizing the bisphenalenyls system [22, 85–87], only a brief discussion will be given here. In short, the derivatives of these two isomers and their higher homologues were well studied by Kubo et al. In 1998, Nakasuji and Kubo synthesized the linear bisphenalenyl derivative with one benzene in the central (**32a**), which behaved as a four-stage amphoteric redox hydrocarbon [88]. X-ray crystallographic analysis shows that **32a** possesses a delocalized structure with a $D_{2h}$ geometry. Later in 2001, the angular bisphenalenyl derivative **33a** with *tert*-butyl substituents was prepared and found that it behaved as a four-stage amphoteric redox compound [84]. Compared to **32a** that was stable for several weeks, compound **33a** was reported to be extremely air-sensitive and decompose in the air. To further elaborate the fundamental structure and physical property relationship in bisphenalenyl-based diradicaloids, a naphthalene-linked bisphenalenyl **34** with larger diradical character ($y_0$ = 0.50) than that of **32** ($y_0$ = 0.30) was further developed in 2007 (Figure 9.12b) [89]. The electrochemical HOMO-LUMO gap of **34** was determined as 1.04 eV, and the $\Delta E_{S\text{–}T}$ was estimated to be −3.78 kcal mol$^{-1}$ by SQUID measurements, both being smaller than those of **32** (1.15 eV and $\Delta E_{S\text{–}T}$ = −4.37 kcal

$mol^{-1}$). In 2012, bisphenalenyl linked by anthracene spacer **35** was synthesized by the same group, which possessed a larger diradical character ($y_0 = 0.68$) in the ground state compared to the naphthalene and benzene counterparts [90]. The enhanced diradical contribution of **35** was ascribed to the high aromatic stabilization energy of the anthracene, which was further supported by X-ray crystallographic analysis, where the bond *a* in **35** was found to be longer (1.467(3) Å) than that of **34** (1.465(7) Å) and **32** (1.457(2) Å) [86]. Remarkably, compound **35** formed a 1D stack with a superimposed phenalenyl overlap in the solid state and showed a prominent intermolecular covalent bonding interaction between molecules (Figure 9.12c).

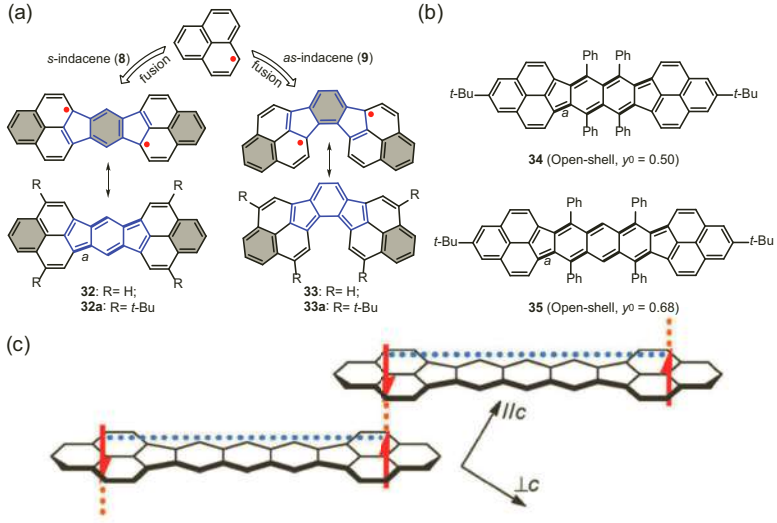


**Figure 9.12** (a) The resonance structures of two isomers of bisphenalenyls (**32** and **33**). (b) Chemical structures of the π-extended bisphenalenyls **34** and **35**. (c) Intra and intermolecular covalent bonding interactions in a schematic 1D stack of **35** (blue and orange dotted lines represent the intra- and intermolecular covalent bonding interactions, respectively). Reproduced with permission from Ref. [90]. Copyright 2012 The Royal Society of Chemistry.

## 9.2.3 Curved Diradicaloids with Pentagons

Recent studies revealed that the diradical character of the diindeno-fused arenes strongly depends on the geometry and π-conjugation of the molecular framework [37, 60]. Note also that the distortion

from planarity caused by the steric strain from atom crowding (e.g. helicenes) or the presence of non-hexagonal rings deeply influences the molecular geometries and consequently the electronic structures of the original PHs [12, 35, 91, 92]. Therefore, the curved diradicaloids might exhibit unique ground-state electronic structures and physical properties that are not shared by the planar diradicaloids. However, most of the thus-far studied diradicaloids are related to the planar structures. In this section, the latest progress on the curved diradicaloids with pentagons will be described.

The efficient strategy to achieve curved diradicaloids containing pentagons is to fuse the indene units onto a twisted π-conjugated spacer because the nonplanar π-bridges with torsional strain could lead to a small singlet-triplet gap as a result of the promotion of magnetic response in a quinoidal structure [93–94]. In 2017, our group for the first time incorporated the nonplanar core, fused bischrysene, into the diindeno-based ring system [95]. Shown in Figure 9.13a is the synthesis of diradicaloid **39** from the key precursor bischrysene **36**, which already has a nonplanar conformation resulting from the two [4]helicene subunits. The Suzuki coupling of **36** with the commercially available (2-formylphenyl)boronic acid gave the dialdehyde **37**. Subsequently, **37** was treated with mesitylmagnesium bromide to give the intermediate diol, which was subjected to a Friedel-Crafts alkylation promoted by $BF_3{\cdot}OEt_2$ to afford the dihydro precursor **38**. Finally, the oxidative dehydrogenation of **38** with DDQ in dry toluene yielded the target compound **39**. X-ray crystallographic analysis showed that **39b** had a saddle-shaped π-conjugated carbon skeleton, due to steric hindrance from the cove and fjord regions (Figure 9.13a). A narrow optical energy gap of 0.92 eV was estimated for **39b** from the onset of its UV-Vis absorption, which is consistent with the value (0.89 eV) that calculated from CV. Temperature-dependent NMR and ESR measurements (Figure 9.13b) revealed that **39b** possesses an open-shell singlet ground state, which is further supported by its moderate diradical character ($y_0$ = 0.69) from DFT calculations at the CASSCF(4,4)/6-311G** level of theory. Remarkably, **39b** displayed excellent stability under ambient conditions with a half-life of 39 days (Figure 9.13c), which could be explained by the fact that the curved geometry of **39b** can largely localize its electron distribution along the saddle-shaped molecular skeleton and the kinetic stabilization by blocking

the most reactive sites with bulky mesityl groups. In view of the highly stable open-shell diradical feature of **39a**, the pulsed ESR measurement was conducted in Bogani's group to investigate its quantum properties [96, 97], in which decoherence mechanisms were clearly unraveled, and the nuclear and environmental effects were quantified. Remarkably, large spin-coherence times were observed for **39a** that outclass most nanomaterials, opening up an unprecedented application of the diradicaloids in the quantum computation.

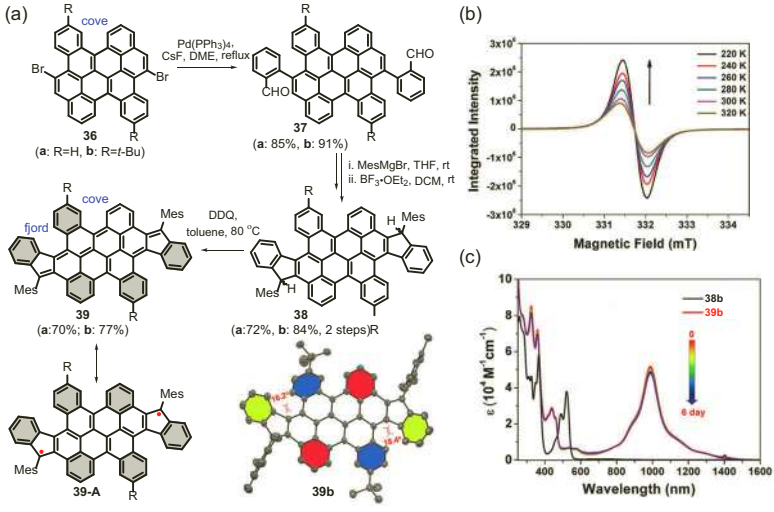


**Figure 9.13** (a) Synthetic route toward **39**. Inset is single-crystal structure of **39b**. (b) VT ESR spectra of **39b** in the solid state. (c) Time-dependent UV-Vis spectra of **39b** in $CH_2Cl_2$ at room temperature under ambient conditions. Reproduced with permission from Ref. [95]. Copyright 2017 John Wiley and Sons Inc.

Lateral extension of the diradicaloid **39** with two indene units is expected to provide open-shell PHs with tetraradical character given the two flanked indenofluorene subunits in the π-systems. In this respect, our group synthesized the constitutional isomers **40** and **41** by controlling the annulated direction of the two indene units into the molecular backbone of **39** (Figure 9.14a) [98]. As a result, two *m*-QDM units are embedded into the carbon skeleton of compound **40**, while **41** contains two *p*-QDM units. Single-crystal X-ray crystallographic analysis revealed that compound **40** adopted

the unprecedented wave-shaped π-conjugated carbon skeleton that induced by steric congestion in the [4]helicene subunits and [7] helicene-like subunits (Figure 9.14b). Theoretical calculations at the CASSCF(4,4)/6-31G** level of theory predicted that **40** possessed remarkable diradical and tetraradical characters ($y_0 = 0.23$; $y_1 = 0.22$) in the ground state and had a small singlet-triplet energy gap($\Delta E_{S\text{-}T}$ = −4.2 kcal mol$^{-1}$). In contrast, compound **41** showed essentially a lower degree of diradical or tetraradical features ($y_0 = 0.08$; $y_1 = 0.08$) and had a large singlet–triplet energy gap ($\Delta E_{S\text{-}T}$ = −9.55 kcal mol$^{-1}$). Indeed, the VT ESR proved the open-shell singlet ground state of **40** (Figure 9.14c), while the isomer **41** exhibited the closed-shell nature due to the silent ESR signal in its solid form. The experimental $\Delta E_{S\text{-}T}$ of compound **40** was determined to be −2.08 kcal mol$^{-1}$ from SQUID measurements (Figure 9.14d). The electrochemical energy gap for **40** was estimated to be 1.02 eV on the basis of the first reduction and oxidation peaks in CV, which was consistent with the optical energy gap (0.96 eV) that was determined from the onset of its UV-Vis absorption. Notably, the wave-shaped tetradicaloid **40** displayed high stability under the ambient air and light conditions ($t_{1/2}$ = 91 days), which seems to be a result of its unusual geometry. Moreover, the tetraradicaloid **40** exhibited unique ambipolar charge transport behavior ($\mu_h = 6.2 \times 10^{-4}$ cm$^2$ V$^{-1}$s$^{-1}$; $\mu_e = 1.3 \times 10^{-4}$ cm$^2$ V$^{-1}$s$^{-1}$) in solution-processed organic thin-film transistors (Figure 9.14e).

In addition to the nonplanar bischrysene unit, corannulene is an alternative candidate to construct curved diradicaloids in view of its bowl-shaped geometry [99–101]. The first example of the corannulene-based diradicaloid **42** was prepared by Morita and coworkers, which has two phenoxyl radical moieties (Figure 9.15a) [102]. Oxidation of the diradical bis-phenol precursor with $PbO_2$ and subsequent recrystallization gave single crystals of **42**, which can survive in air at −30 °C for a few weeks. Moreover, diradicaloid **42** was also stable in degassed solution. X-ray structure analysis revealed that the corannulene-bridged phenoxyl diradicaloid **42** had a curved π-conjugated system and the unit cell contained three crystallographically independent diradical molecules **42i**, **42ii**, and **42iii** that stacked in a convex-concave fashion (Figure 9.15b). Bond-length analysis showed that compound **42** has much larger contributions of the diradical structures with quinoidal character such as **42-A** and **42-B** than closed Kekulé structure **42-C**. Compound

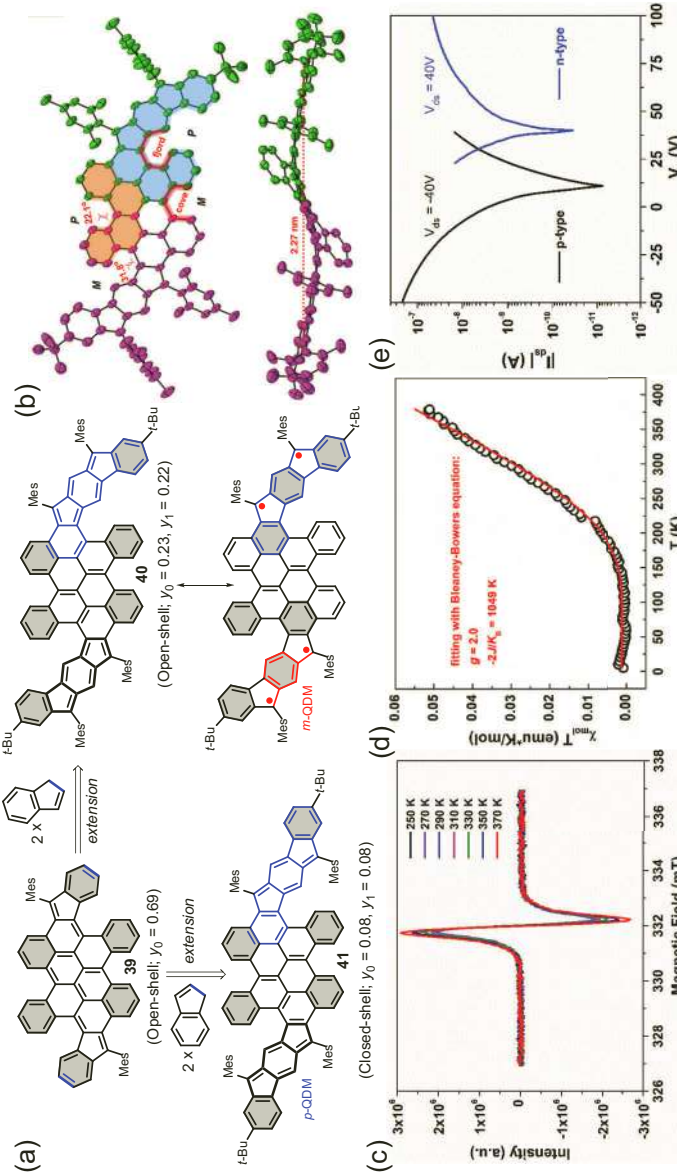


**Figure 9.14** (a) $\pi$-extended stable wave-shaped PHs **40** and **41** (the flanked indeno[1,2-*b*]fluorene and indeno[2,1-*b*]fluorene units in **40** and **41** are highlighted by blue color). (b) Top view and side view of the X-ray crystallographic structure of **40**. (c) ESR spectra of the powder of **40** recorded at 250–370 K. (d) SQUID measurement of **40** from 5 K to 400 K, experimental data plotted as black "○" and fitted curve according to the Bleaney–Bowers equation with $g_e$ = 2.00 as a red line. (e) Transfer characteristics for an ambipolar transistor based on the spin-coated film of **40**. Reproduced with permission from Ref. [98]. Copyright 2019 The Royal Society of Chemistry.

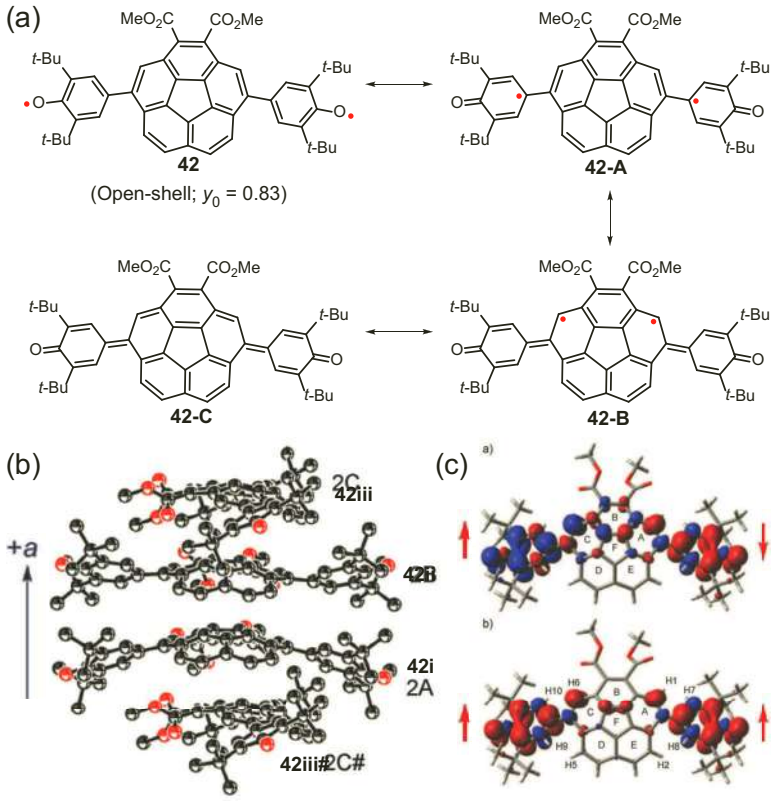


**Figure 9.15** (a) Canonical resonance structures of **42**. (b) Packing structure of **42** along the *a* axis. # denotes the symmetry operation x+1, y, z. The thermal ellipsoids are scaled to the 50% probability level. (c) Calculated spin-density distributions of broken-symmetry singlet state (top) and triplet state (bottom) for **42i** at the UB3LYP/6-31G(d,p) level. Red: positive, blue: negative spin densities. Reproduced with permission from Ref. [102]. Copyright 2010 John Wiley and Sons, Inc.

**42** showed significant intramolecular antiferromagnetic interaction through the curved and nonalternant 3D corannulene π-electron network and the $\Delta E_{S\text{–}T}$ was estimated to be −1.61 kcal mol$^{-1}$ from the SQUID measurements. Calculated spin-density distributions (UB3LYP/6-31G(d,p)) revealed that the unpaired electronic spins in both broken-symmetry singlet and triplet state are extensively delocalized onto the corannulene skeleton from the phenoxyl moieties (Figure 9.15c). Furthermore, the different curvature of the

corannulene skeleton in the three crystallographically independent molecules **42i**-**42iii** also correlates with the magnitude of the intramolecular exchange interactions and singlet diradical character of **42**. The magnitude of the intramolecular exchange interaction is enhanced by decreasing the curvature of the corannulene skeleton.

Similar to the design concept for the diindeno-fused bischrysene **39**, another type of corannulene-based diradicaloids, diindeno-fused corannulene isomers **45** and **46**, in which the central nonplanar bischrysene in **39** was replaced by a bowl-shaped corannulene unit, were synthesized by Cao and coworkers in 2019 [103]. As shown in Figure 9.16a, the twofold regioselective acylations of corannulene at the 1st and 8th positions and 1st and 5th positions, followed by the intramolecular couplings with $Pd(OAc)_2$, afforded the key intermediates **43** and **44**, respectively. Then, the nucleophilic addition of mesityl lithium on **43** and **44** and the subsequent reductive aromatization with $SnCl_2$ yielded the **45** and **46**, respectively. The isomer **45** was stable enough for silica gel column chromatography under ambient conditions, while **46** was unstable on both silica gel and semi-preparative high-performance liquid chromatography. X-ray single-crystal diffraction of **45** revealed its bowl-shaped conformation (Figure 9.16b). The critical length of bond *a* is 1.406 Å, which is similar to that of indenoacenes with open-shell singlet ground state (ca. 1.41 Å), but much longer than those closed-shell indenes (ca. 1.39 Å), indicating the large contribution of the open-shell resonance structure in its ground state. The singlet ground state of **45** and **46** was confirmed by ESR and SQUID measurements. The singlet-triplet energy gap of **45** was determined to be −0.011 kcal $mol^{-1}$ by SQUID, indicating the weak electron exchange interaction (Figure 9.16c). For **46**, two more Clar aromatic sextets can be drawn in the diradical resonance form **46-A** than in the closed-shell form (Figure 9.16a). However, for isomer **45**, the open-shell resonance structure **45-A** had three more aromatic sextets than the closed-shell resonance form, which was expected to show a larger diradical character than **46**, as a result of the more driving force to form the diradical resonance structure. DFT calculation at the UCAM-B3LYP/6-311G(d,p) level of theory revealed that **45** possessed a larger diradical character ($y_0$ = 0.98) compared to isomeric **46** ($y_0$ = 0.89). In addition, the spin-density distributions are highly delocalized over the 3D molecular skeletons

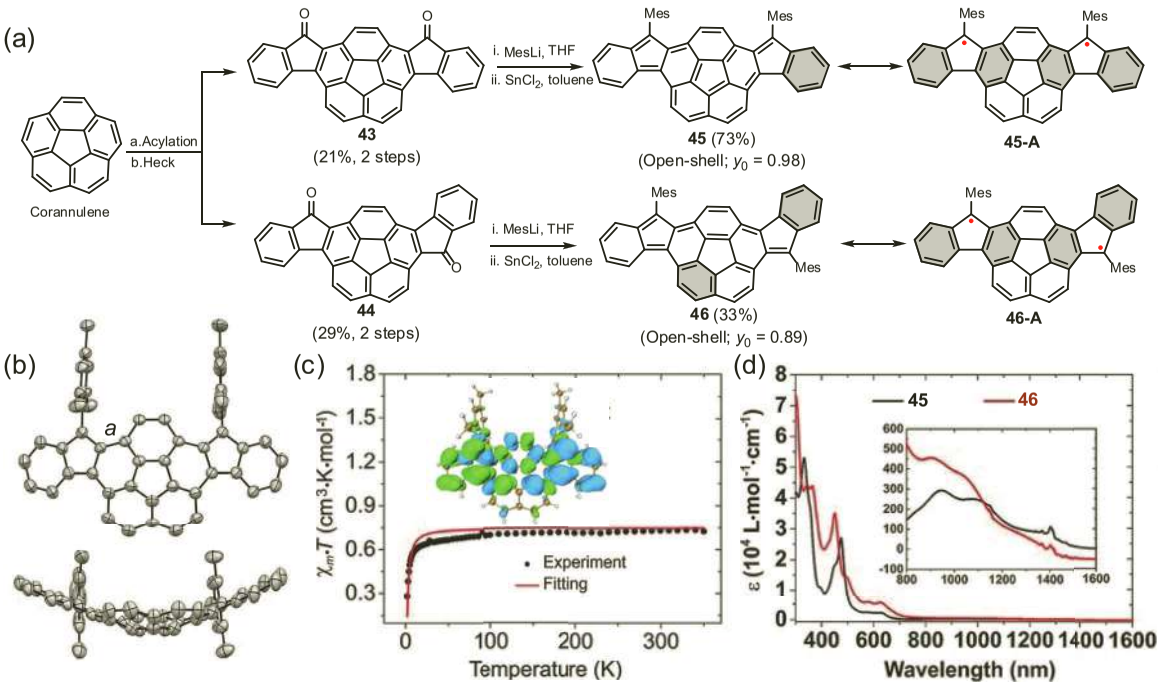


**Figure 9.16** (a) Synthesis of curved diindeno-fused corannulene regioisomers **45** and **46**. (b) Top view and side view of the X-ray crystallographic structure of **45**. (c) Experimental and fitted $\chi_m T$-$T$ plots of powder **46**. Inset is the spin density (isovalue: 0.001) of **46** calculated at the singlet solution (broken-symmetry UB3LYP/6-311G(d,p)). (d) UV-Vis-NIR absorption spectra of **44** and **45** in $CH_2Cl_2$. Reproduced with permission from Ref. [103]. Copyright 2019 John Wiley and Sons Inc.

with the pronounced spin populations on the apical positions of the two cyclopenta rings in the indene units (Figure 9.16c). Although compounds **45** and **46** have significant diradical characters, they exhibited excellent stability under ambient conditions (**45**: $t_{1/2}$ = 37 days; **46**: $t_{1/2}$ = 6.6 days). Moreover, both compounds **45** and **46** showed weak and broad absorption in the near-infrared region (Figure 9.16d) that was also observed in indeno[2,1-*b*]fluorene derivative **13a**, thus giving rise to low HOMO-LUMO gaps (**45**: 0.81 eV; **46**: 0.80 eV).

Apart from the above curved diradicaloid with only one corannulene unit, Wu et al. reported the first stable π-conjugated corannulene dimer diradicaloid **49**, in which two corannulene moieties were annulated with a 2,6-naphthoquinodimethane unit (Figure 9.17a) [104]. The dialdehyde **48** was firstly obtained from compound **47** and 3,7-diformylnaphthalene-2,6-diyl bis(trifluoromethanesulfonate). Then, the nucleophilic attack on the aldehyde groups in **48** and the subsequent intramolecular cyclization of the corresponding diol promoted by $BF_3{\cdot}OEt_2$ gave the dihydro precursor, which was further subjected to a DDQ-mediated oxidative dehydrogenation to afford the final product **49**. Compound **49** was stable and could be purified by normal silica gel column chromatography. From the X-ray crystallographic analysis, compound **49** adopted a dumbbell-shaped geometry with the two outer corannulene bowls bent to opposite directions (Figure 9.17b). The central 2,6-naphthoquinodimethane unit in **49** showed significant bond-length alternation, with the exo-methylene C1-C2 bond being elongated (1.389 Å) that is longer than that of typical olefins (1.33–1.34 Å), suggesting the certain contribution of its diradical form. DFT calculations at UCAM-B3LYP/6-31G(d,p) level based on the X-ray structure suggested that **49** has a diradical character ($y_0$) of 16.9%. In $^1$H NMR spectrum, **49** exhibited the temperature-dependent line broadening in toluene-$d_8$ from 333 K to 373 K. Moreover, the powder of **49** showed an intense one-line ESR signal with $g_e$ = 2.0027 at room temperature, indicating a singlet ground state in **49**. The singlet-triplet energy gap was estimated to be −3.0 kcal mol$^{-1}$ based on the SQUID measurement on the powder sample of **49** (Figure 9.17c). In addition, the calculated spin-density distribution for the triplet diradical of **49** show that the unpaired electronic spin is largely delocalized onto the two

corannulene bowls, with the largest spin density distributed at the zigzag edges (Figure 9.17c). Compound **49** showed two reduction waves in CV, which can be chemically reduced into dianion by sodium anthracenide in anhydrous THF. The dianion of **49** showed prominent global aromaticity with 42 π-electrons delocalized along the periphery from the anisotropy of the induced current-density (ACID) plot and nucleus independent chemical shift (NICS) calculations.

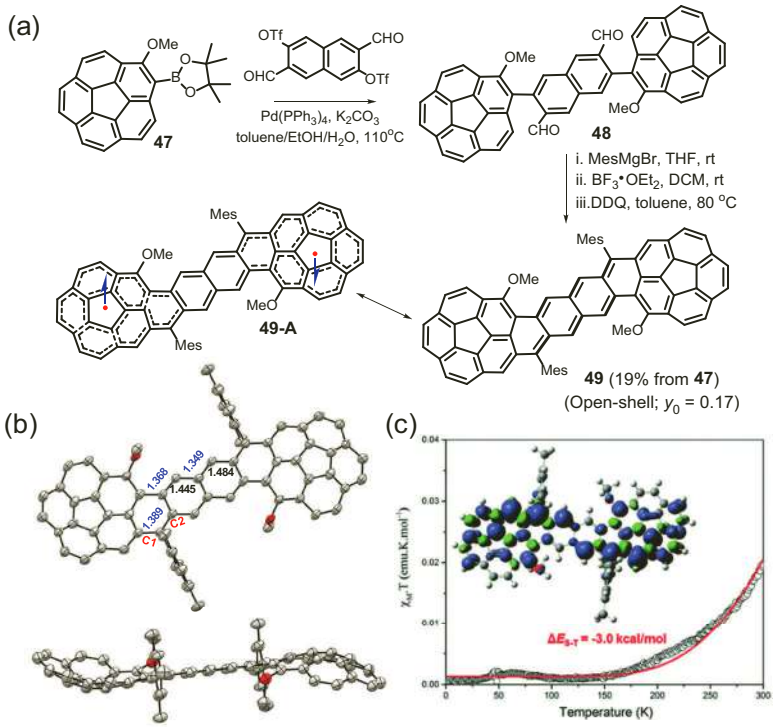


**Figure 9.17** (a) Synthesis of curved open-shell corannulene dimer **49**. (b) Top view and side view of the X-ray crystallographic structure of **49**. (c) $\chi_m T$-$T$ curve in the SQUID measurement for powder **49** and the red line is the fitted curve by Bleaney–Bows equation. Inset is the calculated spin-density distribution map of its triplet diradical form. Reproduced with permission from Ref. [104]. Copyright 2018 The Royal Society of Chemistry.

Different with the incorporation of the known curved aromatics into the diindeno-fused arenes, an alternative strategy is to embed the helicene moiety into the diradicaloids in view of their unique π-conjugated screw-skeleton shaped structural features and excellent

chiroptical properties [105]. Though the open-shell compounds **39** and **40** also contain the helical subunits, the extremities of the helical unit in these examples are separated relatively far away. In 2018, Wu and coworkers synthesized three diindeno[2,1-*f*:1′,2′-*j*] picene derivatives **53a-c** with an open-shell diradical ground state [106]. As illustrated in Figure 9.18a, the treatment of **50** with *n*-BuLi and subsequent with the aryl-aldehyde furnished diol **51**, which underwent the Friedel-Crafts cyclization to afford dihydrohelicene **52** by using with $BF_3{\cdot}OEt_2$. The final oxidative dehydrogenation with a mixture of potassium *tert*-butoxide (*t*-BuOK) and dimethylformamide (DMF) yielded the desired product **53**. Notably, the aerobic solution of **53a** was stable at room temperature for more than two months. The helical backbone, which incorporated an *o*-QDM unit, was verified by X-ray crystallographic analysis of the crystals of **53b** (Figure 9.18b). This structure feature led to a larger racemization barrier (exceeding 50 kcal $mol^{-1}$) than that of [7] helicene (42.5 kcal $mol^{-1}$). Two enantiomers of **53a** were separated by high-performance liquid chromatography (HPLC) and their circular dichroism spectra showed mirror symmetry. Furthermore, the progressive line broadening of the NMR spectra of **53a** and **53b** at temperatures above 323 K indicated the existence of thermally populated paramagnetic species. The ESR spectra of powders **53a-c** recorded at room temperature showed a featureless broad signal, similar to many other PH-based diradicaloids. Fitting of the SQUIDs data of **53b** using the Bleaney−Bowers equation gave the $\Delta E_{S\text{-}T}$ as −4.16 kcal $mol^{-1}$, which is smaller than those of **53a** (−4.75 kcal $mol^{-1}$) and **53c** (−5.14 kcal $mol^{-1}$). The diradical character for **53a**, **53b,** and **53c** were determined as 0.23, 0.26, and 0.09 from DFT calculations (UCAM-B3LYP), respectively. Most of the calculated spin density of **53** was found at positions C-9b/9e and C-5/14, corresponding to its open-shell resonance structure of **53-A** and **53-B** (Figure 9.18c). In addition, all the three derivatives exhibited the two-photon absorption activity. However, although the FET based on compounds **53a** or **53c** showed ambipolar character after being annealed at 200 °C, its electron and hole mobility were relatively low ($\mu_h$ = 3.9 × $10^{-4}$ $cm^2$ $V^{-1}s^{-1}$ and $\mu_e$ = 1.6 × $10^{-4}$ $cm^2$ $V^{-1}s^{-1}$ for **53a**; $\mu_h$ = 1.4 × $10^{-4}$ $cm^2$ $V^{-1}s^{-1}$ and $\mu_e$ = 2.8 × $10^{-4}$ $cm^2$ $V^{-1}s^{-1}$ for **53c**). In contrast, the **53b** FET only exhibited the *p*-type character under the same condition. Moreover, **53a** and **53c**-modified perovskite solar cells could deliver power conversion efficiency (PCE) of over 18%, surpassing the performance (15.6%) of the control device using a

pristine inorganic nickel oxide ($NiO_x$) hole-transporting layer, and the maximum PCE could reach 19% [107].

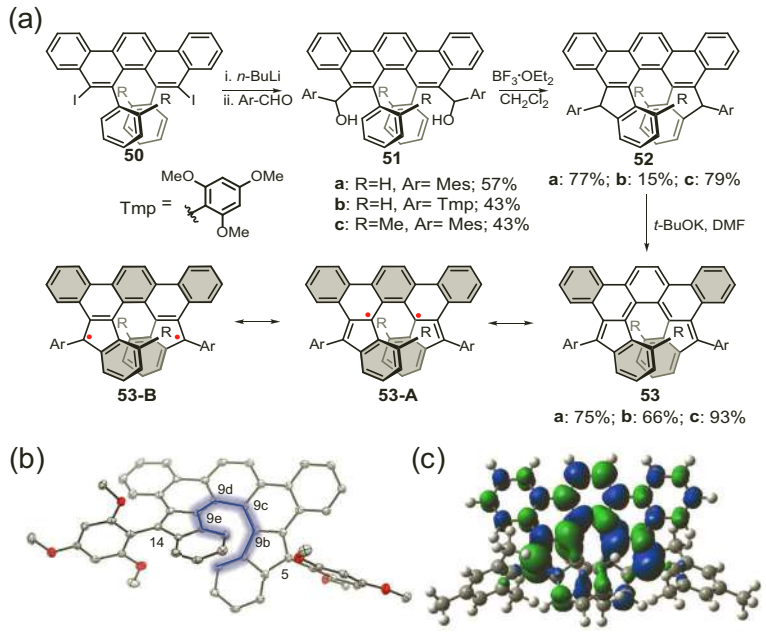


**Figure 9.18** (a) Synthetic route toward the helical open-shell singlet diradicaloid **53**. (b) Oak Ridge Thermal Ellipsoid Plot (ORTEP) drawing of **53b** with 50% thermal ellipsoids. (c) Calculated spin-density distribution of the open-shell singlet ground state of **53a**. Reproduced with permission from Ref. [106]. Copyright 2018 American Chemical Society.

In order to examine the through-space interaction on the properties of diindeno[2,1-*f*:1',2'-*j*]picene **53**, Wu et al. further synthesized the other two curved diradicaloids, diindeno-fused dibenzo[*a*,*h*]anthracene (**54**) and diindeno-fused dibenzo[*c*,*l*]chrysene (**55**) (Figure 9.19a), which contain the key units 1,4-quinodipropene and 2,6-naphthoquinodipropene, respectively [108]. The synthetic method toward **54** and **55** is similar to that of **53**, which is not described here. The half-life time of **55** was estimated to be around 12 days in an aerobic solution at room temperature. The single-crystal structure of **55** exhibited the distorted molecular backbone, due to the presence of two [4]helicene units (Figure 9.19b). The remarkable triplet population of **55** resulted in the gradual increase in ESR signal intensity above 310 K, suggesting that the $\Delta E_{S\text{-}T}$ of **55** was smaller than that of **54**. Indeed, the $\Delta E_{S\text{-}T}$ of **54** and **55** was

determined as −5.26 and −2.44 kcal mol$^{-1}$, respectively, which is also consistent with the DFT calculations at the UCAM-B3LYP/6-311G** level of theory (−5.27 kcal mol$^{-1}$ for **54**, −2.08 kcal mol$^{-1}$ for **55**). In addition, compound **55** has a higher diradical index ($y_0$ = 0.51) than **54** ($y_0$ = 0.22). The $CH_2Cl_2$ solutions of **54** and **55** displayed broad UV-Vis absorption spectra with the maxima at 587 nm and 667 nm (Figure 9.19c), giving the optical energy gap as 1.39 eV and 1.06 eV, respectively. Though **54** and helical **53a** are isoelectronic structure isomers, the through-space interaction of the latter diradicaloid resulted in the lower HOMO-LUMO gap (1.31 eV) and smaller $\Delta E_{S\text{-}T}$ (4.75 kcal mol$^{-1}$).

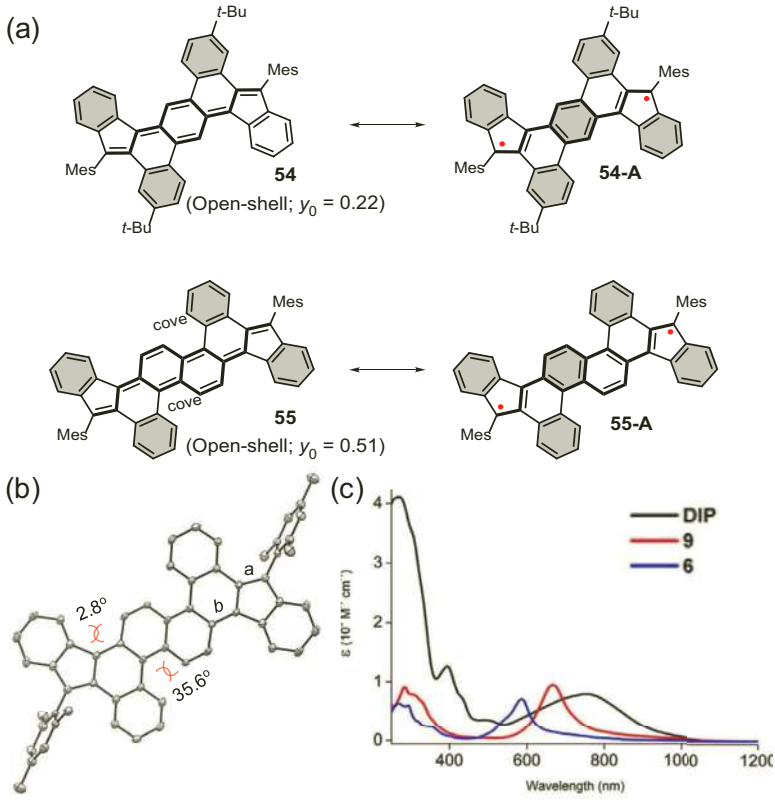


**Figure 9.19** (a) Resonance structure of the curved open-shell singlet diradicaloid **54** and **55**. The structures of 1,4-quinodipropene and 2,6-naphthoquinodipropene are highlighted in bold. (b) ORTEP drawing of **55** with 50% thermal ellipsoids. (c) The photoabsorption spectra of **53a**, **54**, and **55** in $CH_2Cl_2$. Reproduced with permission from Ref. [108]. Copyright 2019 John Wiley and Sons Inc.

### 9.2.4 Other Diradicaloids with Pentagons

Another class of hydrocarbons that is related to dibenzo[*cd*,*gh*] pentalene (**56**) might has the potential of open-shell singlet diradical character (Figure 9.20a). Compound **56** can be regarded as a perturbed [12]annulene, which has the tendency to become diradicaloid, since the outer periphery contains 4n π-electrons [109]. DFT calculations have showed the lowest triplet state that is only 0.32 eV above the singlet ground state. Although several attempts by different synthetic approaches have been done to attain **56**, none of them is successful. However, the properties of dianion of **56** obtained by deprotonation of the dihydro derivative were inspected in detail and the electrochemically generated semiquinone radical anion from the quinone derivative supported the peripheral delocalization of π-electrons [110]. Lateral extension of **56** by replacing the benzene rings with naphthalene or anthracene leads to the larger analogs **57** and **58**, respectively. Wu et al. reported the synthesis of the aryl-substituted dicyclopenta-fused perylene derivative **57a**, which can be regarded as the fragment of $C_{70}$ [111]. The bowl-shaped geometry of **57a** was determined by X-ray diffraction and a fast bowl-to-bowl inversion process with a small inversion energy barrier was observed by VT NMR. No significant NMR spectral broadening was observed for **57a** even after heating up its benzene-$d_6$ solution to 70 °C, indicating its closed-shell ground state, which was also supported by the DFT calculations. Different from many other aromatic buckybowls, **57a** displayed global antiaromaticity, while its dication and dianion were aromatic, as revealed from the NMR measurement and ACID plots. In addition, **57a** did not display an expected an annulene-within-an-annulene (AWA) structure, due to electronic coupling between the inner core and outer rim. Furthermore, the further extended system, dicyclopenta-fused bisanthene derivative **58a**, was synthesized by Chi and coworkers [112]. As shown in Figure 9.20b, the preparation of **58a** started from the key intermediate **60**, which was synthesized by the regioselective formylation of the *meso*-mesityl-substituted bisanthene **59**. By using the common nucleophilic addition/Friedel-Crafts alkylation/oxidative dehydrogenation strategy, the target molecule **58a** was obtained with 60% yield in three steps, which exhibited extremely stable in air due to the kinetic blocking by bulky mesityl groups. Different with **57a**, compound **58a** has a

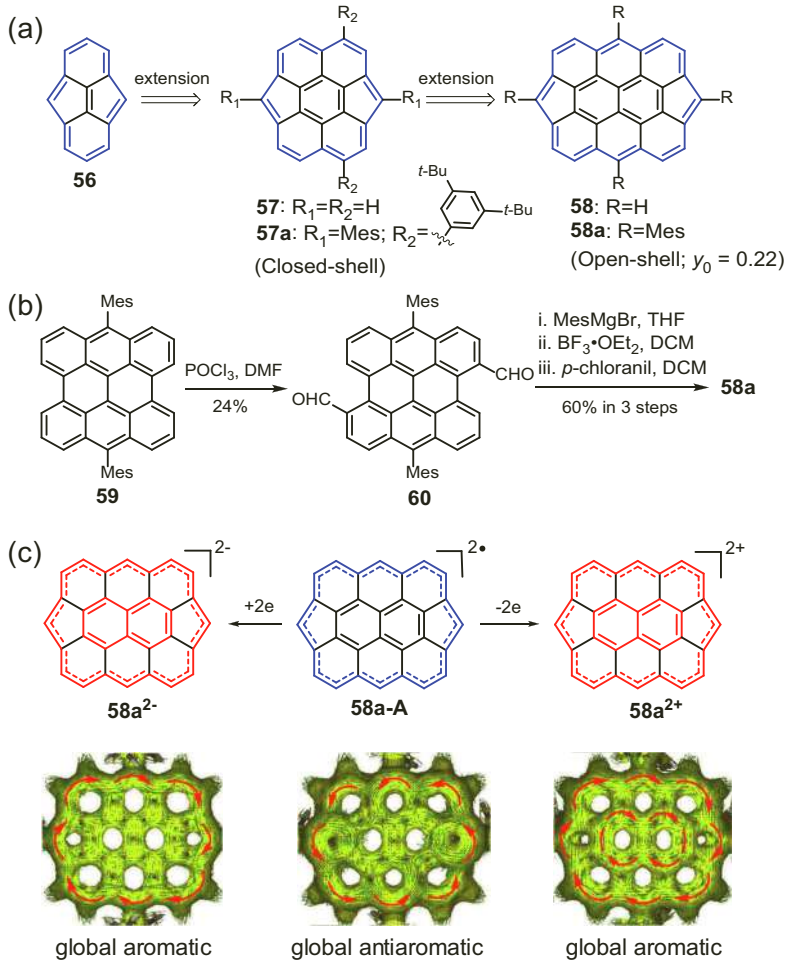


**Figure 9.20** (a) Structures of dibenzo[*cd*,*gh*]pentalene (**56**) and its π-extended analogs (**57** and **58**). (b) Synthetic route to diradicaloid **58a**. (c) Structures of the dianion, neutral state, and dication of **58a,** as well as their corresponding ACID plots (the external magnetic field is applied orthogonal to the plane). Reproduced with permission from Ref. [112]. Copyright 2017 John Wiley and Sons Inc.

rigid and nearly planar molecular skeleton according to the X-ray crystallographic analysis. The large bond-length alternation along the outer rim of **58a** indicated its antiaromatic character of the 4*n* (20) π-electron circuit. The radial bonds (1.409–1.426 Å) connecting

the inner naphthalene unit and the outer circle are shorter than typical single C–C bonds (1.47 Å), indicating that **58a** was not decoupled as in an AWA system. The distinctive NMR spectral broadening of **58a** in tetrachloroethane-$d_2$ was observed along with the elevated temperatures, indicating its open-shell singlet ground state, which was consistent with the moderate diradical character ($y_0$ = 0.22) calculated at UCAM-B3LYP/6-31G(d,p) level of theory. In addition, compound **58a** showed a strong ESR signal in the solid state at room temperature and the $\Delta E_{S\text{-}T}$ of **58a** was estimated to be −3.17 kcal mol$^{-1}$ from the SQUID measurement. Given the excellent amphoteric redox behavior of **58a** in CV, its dication and dianion can be easily generated by oxidation with NO·$SbF_6$ and by reduction with sodium anthracenide, respectively (Figure 9.20c). The $^1$H NMR analysis, NICS(1)$_{zz}$ and ACID calculation disclosed that the dication **58a$^{2+}$** showed open-shell singlet diradical character ($y_0$ = 0.44), but had a unique AWA structure with global aromaticity, while dianion **58a$^{2-}$** exhibited closed-shell ground state with the global aromaticity for which 22 π-electrons were delocalized on the outer rim (Figure 9.20c).

## 9.3 Seven-Membered Ring-Containing Diradicaloids

In contrast to the pentagon-embedded diradicaloids, the field of open-shell PHs containing seven-membered carbocycles is still much less studied, with the known examples mainly limited to a few molecular systems, due to the lack of suitable synthetic strategies and their low stability. This section surveys the heptagon-embedded diradicaloids, with highlights on their chemical reactivity, synthesis, and interesting physicochemical properties.

The representative example here is pleiadene (**61**), which contains one seven-membered ring. It has attracted significant interest for several decades both to experimentalists and theoreticians, because it contains the *o*-QDM substructure with potential diradical feature [113]. After Fieser's early unsuccessful attempts [114], in 1963, Cava et al. firstly reported the generation of **61** by a pyrolysis of sulfone precursor **62** in the molten state [115]. Compound **61** is exceedingly prone to a dimerized form, but could be trapped as a

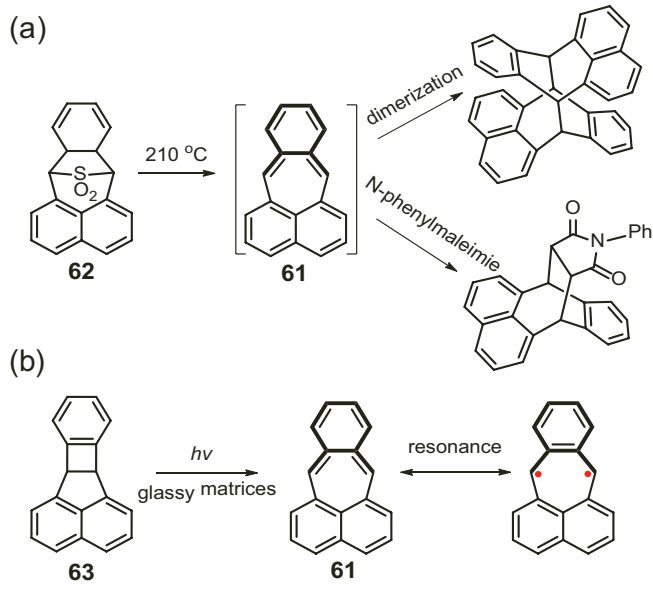


**Figure 9.21** (a) Thermal generation of **61** by Cava et al. (b) Photogeneration of **61** by Michl et al. and its diradical resonance form.

Diels–Alder adduct with *N*-phenylmaleimide (Figure 9.21a). In view of the extreme reactivity of **61**, Michl et al. successfully synthesized **61** through the photochemical generation in a low-temperature matrix (Figure 9.21b) [116]. UV irradiation of a dilute solution of benzocyclobutene precursor **63** in 3-methylpentane glass at 77 K in a quartz cell yielded a stable yellow-green **61**, which disappeared in 10–15 s at the glass melting temperature (110 K). The mechanism of the rapid reaction for the formation of dimer, whether it is a stepwise one involving radical intermediate or a concerted one if the transition state bears diradicaloid character, is not proven. The most important insight from Michl and coworkers is the contribution of doubly excited state in the ground state electronic configuration of **61**, which is closely related to singlet diradical character [117]. On the basis of the Pariser–Parr–Pople (PPP) SCF-CI calculations, the occupation number of the highest occupied natural orbital (HONO) of **61** is 1.90 and that of the lowest unoccupied natural orbital (LUNO) is 0.09, suggesting the diradical nature of its ground state. In addition, the calculations suggested that the singlet to triplet excitation energy of **61** is very small, indicating the potential

occupation of thermally excited triplet states. Indeed, the state dominated by the doubly excited configuration was experimentally observed to be low-lying by using UV-Vis absorption spectroscopy [118].

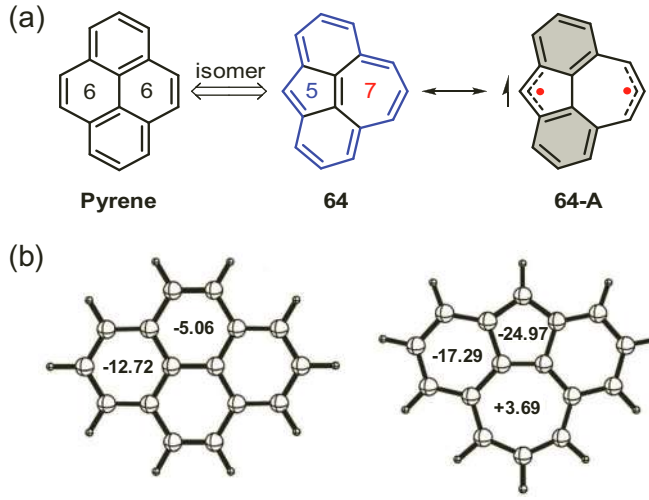


**Figure 9.22** (a) Structures of pyrene and bis-periazulene **64** with resonance structure. (b) NICS values for singlet bis-periazulene **64** ($C_{2v}$) and pyrene ($D_{2h}$) (B3LYP/6-31G*).

Replacement of one or more six-membered rings in benzenoid system with five- and seven-membered rings can trigger large structural and electronic perturbations of the original PHs. For example, the transformation of two hexagons in pyrene with a pair of heptagon and pentagon leads to the cyclohepta[*def*]-fluorene (or bis-periazulene) **64**, which has been attracting continuing interest for a long time due to its potential diradical character. However, attempts to synthesize **64** and its derivatives have been never successful, even when the precursors contain substituents, which are likely to stabilize the diradicals [119, 120]. In 1965, it was predicted by Heilbronner on the basis of PPP calculations that **64** would have either a triplet ground-state or a low lying, thermally excitable triplet state [121]. Later in 1999, Houk and coworkers, on the basis of B3LYP/6-31G* calculations, also predicted a triplet ground state for **64** and its singlet state was 2.3 kcal $mol^{-1}$ in energy above the triplet state with the zero-point energy corrections [122,

123]. Furthermore, the NICS values for singlet states of pyrene and bis-periazulene **64** were compared as shown in Figure 9.22b. The two benzenoid rings of the biphenyl unit in pyrene had the large NICS value of −12.7 ppm, in the same range as benzene itself (−11.5 ppm) and the additional benzenoid rings were weakly aromatic with a small NICS values (−5.1 ppm). In **64**, the NICS values for the five-, six-, and seven-membered rings were −24.97 ppm, −17.29 ppm, and 3.69 ppm, respectively, indicating the highly aromatic five-membered ring and slightly antiaromatic seven-membered ring. The calculations further supported the diradical nature of **64**, which arises from the fact that the most stable form is a biphenyl linked by methyl radical and allyl radical units.

Another important example is the structural isomer of bisanthene **65,** difluoreno-[1,9,8-*alkj*:1‘,9‘,8‘-*gfed*]heptalene **66**, which is deduced by the replacement of the four hexagons in bisanthene **65** with two pairs of pentagons and heptagons (Figure 9.23a). Bisanthene **65**, as the smallest member of the *peri*-acene series, is a benzenoid hydrocarbons with a local aromatic character, which has the closed-shell ground state [124]. However, its structural isomer **66** bearing two *o*-QDM moieties could realize the conversion of the closed-shell feature of **65** into the open-shell character. From the resonance structure of **66**, two more Clar sextets can be drawn in the diradical resonance form (**66-B**) in comparison to the closed-shell form (**66-A**), which can push out the two unpaired electrons on the apical carbons of the heptagons. In 2019, Konishi and Yasuda et al. reported the synthesis of the derivatives of **66** (Figure 9.23b) [125]. Different from the conventional methods such as dehydrogenation or dehydration to construct open-shell PHs, compounds **66a** and **66b** were attained by reduction of the key aromatic dication specie **69**, which was obtained by nucleophilic attack on dione **67** with arylmagnesium bromides and the subsequent treatment of the diol **68** with a tetrafluoroboric acid diethyl ether complex ($HBF_4{\cdot}Et_2O$). Compound **66a** in a $CH_2Cl_2$ solution of gradually decomposed with a half-life of three days under ambient conditions. X-ray crystallographic analysis of **66a** revealed that the main core of **66a** possessed a planar structure with an approximated $D_{2h}$ symmetry (Figure 9.23c). In contrast to the reported heptalene derivatives possessing the twisted geometries with non-aromatic character, the planar geometry of the inner heptalene unit in **66a** should

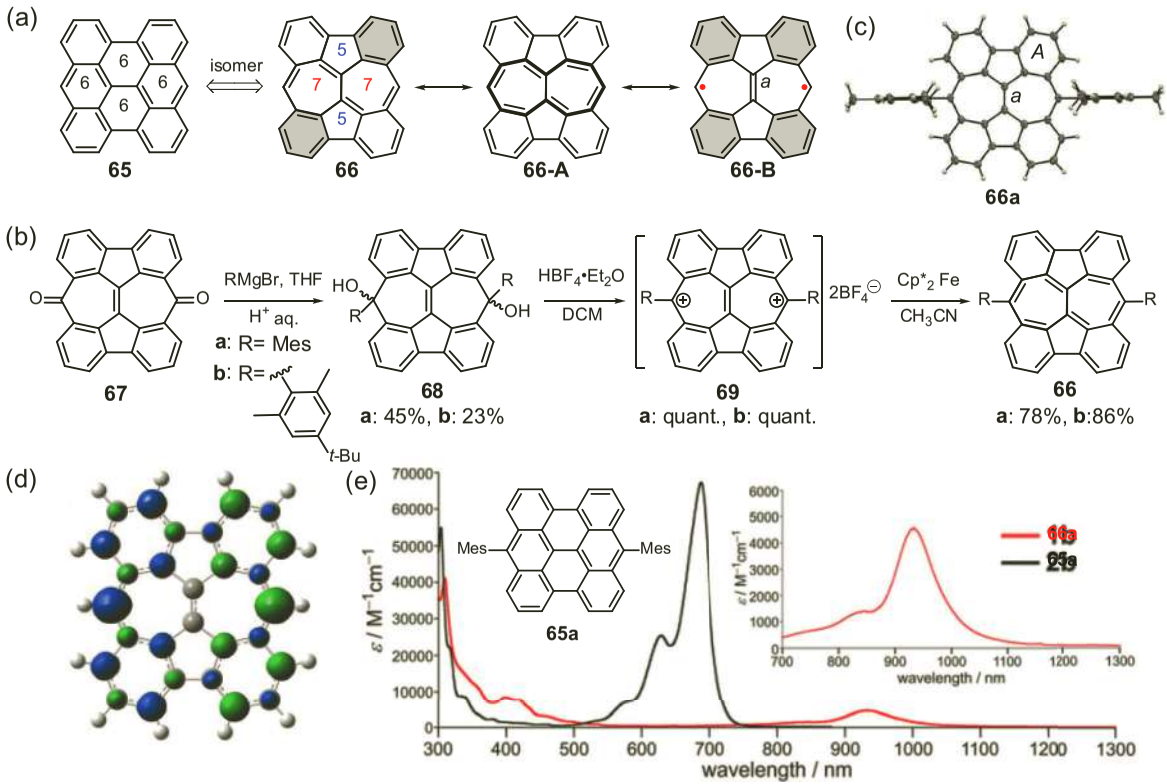


**Figure 9.23** (a) Structures of bisanthene **65** and its structural isomer **66** with resonance forms. (b) Synthetic route toward the kinetically protected derivatives of **66**. (c) Single-crystal structure of **66a**. (d) Spin-density distribution of the open-shell singlet ground state of **66**. (e) UV-Vis absorption spectra of **65a** and **66a** in $CH_2Cl_2$. Reproduced with permission from Ref. [125]. Copyright 2019 American Chemical Society.

enhance the contribution of the 4*n* π-system, which is supported by the large positive NICS(1) value (+11.2 ppm) of the heptagons in **66a**. In addition, the pentagons in **66a** have the small NICS(1) values (−3.90 ppm), indicating the nonaromatic characters of the pentagons. The electrostatic potential map suggested that the contribution of the polarized structure like azulene is negligible. The double-bond character of *a* bond (1.373 Å) in **66a** reflected the diradical resonance contribution to the ground state. Theoretical calculations (CASSCF(2,2)/6-31G*) gave the diradical character of **66** as 0.75 compared to only 0.065 for its benzenoid isomer **65**, and the spin-density distributions are mainly located at the apical carbons on the heptagons (Figure 9.23d). These results indicated that the dominant resonance structure of **66** should be drawn as **66-B**, which has a certain degree of antiaromatic feature derived from **66-A**. The SQUID measurement of **66a** displayed an increasing susceptibility above 150 K and the $\Delta E_{S\text{-}T}$ was estimated to be −2.15 kcal mol$^{-1}$ for **66a** from the Bleaney−Bowers fitting of the observed increase, which is consistent with the theoretical value (−2.72 kcal mol$^{-1}$) using the UB3LYP-D3/6-311G* method. As a result of the small $\Delta E_{S\text{-}T}$ of **66a**, the $^{1}$H NMR signal of the main core in **66a** was absent, even at −100 °C. Furthermore, UV-Vis absorption spectrum of **66a** showed the weak and lowest-energy band at 934 nm, which is significantly red-shifted compared to the intensive absorption at 686 nm of its benzenoid isomer **65a**. The time-dependent DFT calculations suggested that the absorption maximum of **66a** at 934 nm is attributed to the partially allowed HOMO to LUMO+1 transitions and these orbitals exhibit the disjoint feature with the α/β spins localized at the two head carbons on the seven-membered rings.

Further extension of bisanthene **65** leads to the higher homologue *peri*-tetracene **70**, which possesses the open-shell diradical character (see Chapter 5). As shown in Figure 9.24a, the non-benzenoid structural isomer **71** would be obtained by the replacement of the two naphthalene subunits in **70** with two azulene units. In 2018, our group firstly reported the synthesis of pristine *peri*-tetracene **70** and compound **71** on Au(111) surface [126]. The scanning tunneling spectroscopy (STS) measurements revealed that the electronic gap of **71** (180 meV) was largely lower than that for the *peri*-tetracene **70** (350 meV), indicating that the incorporation of non-benzenoid rings in a benzenoid system can provide a route to control over

the electronic structure of PAHs. In the same year, the successful synthesis and isolation of stable *peri*-tetracene derivatives of **70** was independently reported by us and Wu's group [127, 128]. The obtained *peri*-tetracene derivative **70a** possessed a singlet diradical character ($y_0$ = 0.72) from DFT calculations (UHF/6-31G*) and exhibited remarkable persistent stability in $CH_2Cl_2$ with a half-life time ($t_{1/2}$) of ~3 h under ambient conditions. In 2019, our group also depicted the synthetic route toward the derivative of **71** in solution [129]. As shown in Figure 9.24b, the derivative **71a** was obtained from the key dialdehyde intermediate **72** by using the nucleophilic addition or Friedel-Crafts alkylation, or oxidative dehydrogenation procedure. The absence of signal in the $^1$H NMR spectrum of **71a** above −70 °C indicated the population of thermally excited triplet states. A well-resolved ESR spectrum with five lines was observed for compound **71a** in toluene at room temperature and the solid-state ESR signal intensity decreased upon cooling, suggesting the open-shell singlet ground state of **71a**. The magnetic property was further confirmed by the SQUID measurements in the temperature range of 5–400 K, from which the $\Delta E_{S\text{-}T}$ of −2.15 kcal mol$^{-1}$ was estimated, which is close to the theoretical value of −1.14 kcal mol$^{-1}$ using the UB3LPY method. In addition, UV-Vis absorption spectrum of **71a** exhibited a broad peak in the near-infrared region with a maximum at 936 nm, which elucidated the low energy gap of 1.13 eV based on the lowest energy absorption onset. The half-life time of **71a** in $CH_2Cl_2$ was estimated to be ~2 h under ambient conditions from the time-dependent UV-Vis absorption measurement. Because the in-solution synthesis of **71a** suffers from the instability issue, the possibility of surface-assisted dehydrogenation of precursor **73** was also investigated. However, one or two xylenyl groups were lost during the sublimation process of **73** on Au(111) surface, and the cyclopenta-fused nanographene **74** with two embedded azulene units was observed finally after the annealing, whose structure was clearly confirmed by the scanning tunneling microscope (STM) imaging (Figure 9.24c). STS measurements acquired on **74** with a carbon monoxide (CO) functionalized tip exhibited a strong peak at −0.10 V and a shoulder at +0.17 V, which were assigned to the positive and the negative ion resonances (PIR and NIR) deriving from the resonant tunneling of the electrons through the HOMO and LUMO of **74**. Therefore, a remarkably low HOMO-LUMO gap of **74** on Au(111) was elucidated to be 0.27 eV. Moreover, UHF-calculations

gave a large open-shell diradical character of **74** to be 0.92 and the calculated open-shell singlet electronic ground state of **74** was 0.45 eV lower than its open-shell triplet state, confirming the distinct open-shell character of **74**.

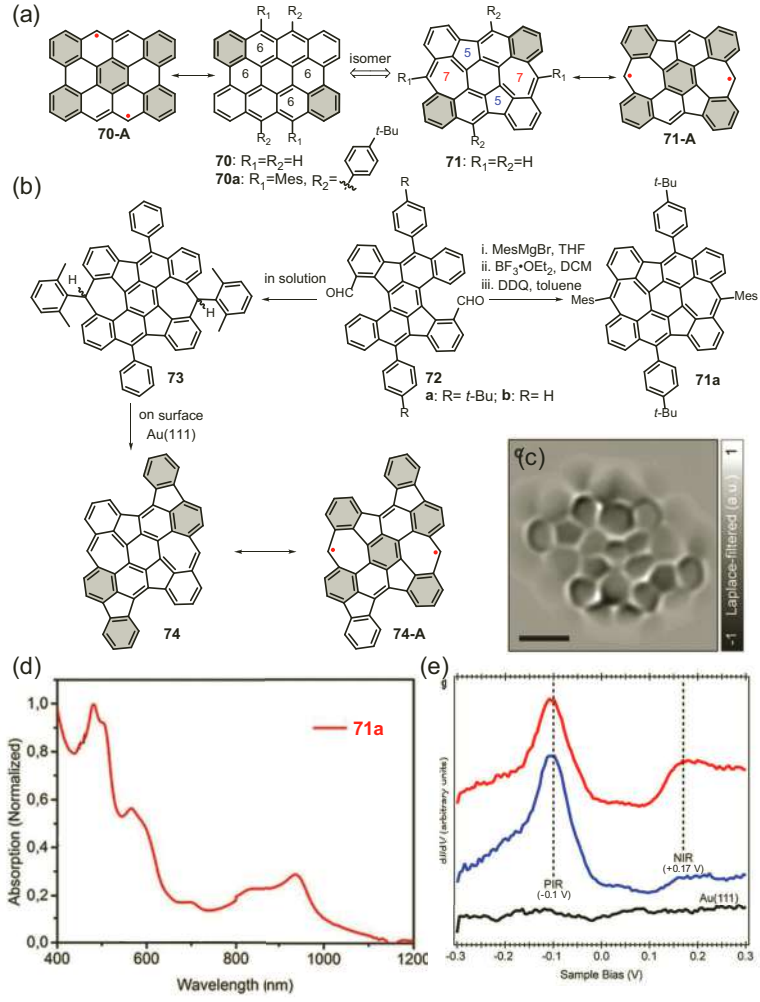


**Figure 9.24** (a) Structures of *peri*-tetracene **70** and its structural isomer **71** as well as their resonance structures. (b) In-solution and on-surface synthesis of heptagon-embedded open-shell PHs **71a** and **74**. (c) Laplace-filtered ultrahigh resolution STM image of **74**. (d) UV-Vis absorption spectrum of **71a** in $CH_2Cl_2$. (e) d*I*/d*V* spectrum of **74** acquired with a CO-functionalized tip. Adapted with permission from Ref. [129]. Copyright 2019 American Chemical Society.

Another strategy to construct the heptagon-embedded open-shell diradicaloids is to directly fuse two aromatic azulene rings to an antiaromatic *s*-indacene unit to form a new 7-5-5-6-5-5-7 fused ring system with 28 π-electrons, which is also related to the 6-5-6-5-6 fused indenofluorene system that the outer benzene rings are replaced by the azulene units [63, 67]. As shown in Figure 9.25a, two structural isomers, the diazuleno[2,1-*a*:2′,1′-*g*]-*s*-indacene (**75**) and diazuleno[2,1-*a*:1′,2′-*h*]-*s*-indacene (**76**), were obtained depending on the fusion pattern of the outer azulene units. From the resonance structures of both isomers, they have a tendency to form open-shell diradicaloids by recovery of the aromaticity from the central benzenoid ring. In 2018, Chi and coworkers synthesized four derivatives (**75a**, **75b**, **76a,** and **76b**) of two bis(azuleno)-s-indacene isomers [130]. The synthesis of **75a** and **76a** was obtained from the dihydro precursors **78a** and **80a**, which was attained by nucleophilic addition on dialdehyde intermediates **77**/**79** with anthryl lithium reagent followed by the $BF_3{\cdot}Et_2O$-mediated Friedel-Crafts alkylation reaction. However, compounds **75a** and **76a** were sensitive to even deactivated silica gel, though they exhibited very good photostability ($t_{1/2}$: 210 days for **75a** and 9 days for **76a**) under ambient conditions. Therefore, **78a** and **80a** were converted to compounds **78b** and **80b** by the treatment with trifluoroacetic anhydride (TFAA) and the subsequent dehydrogenation yielded more stable compounds **75b** and **76b** ($t_{1/2}$: 290 days for **75b** and 240 days for **76b**), which can be purified by the conventional silica gel column chromatography. Compounds **75b** and **76b** have a nearly planar backbone with the anthryl groups almost perpendicular to the core from the single-crystal X-ray structures. Bond-length analysis of **75b** and **76b** revealed that the quinoidal character of the central *p*-QDM unit is diminished by the appearance of the diradical contribution. DFT calculations (LC-UBLYP/6-31G(d)) predicted a diradical character of 0.36, 0.07, 0.52, and 0.35 for **75a**, **75b**, **76a,** and **76b**, respectively. The larger diradical character of **76b** versus **75b** can be ascribed to the recovery of one aromatic benzene ring and one aromatic azulene unit in **76** from the closed-shell form to the open-shell diradical form, while only one aromatic benzene ring is recovered in diradical form of **75** (Figure 9.25a). ACID and NICS $(1)_{ZZ}$ calculations revealed that **75b** and **76b** maintain the aromatic feature of the outer azulene units and the antiaromaticity of the central *s*-indacene moiety. Compound **75a** showed an absorption maximum at 818 nm and a weak long tail till to 1291 nm, while **75b** exhibited a hypochromic shift with the absorption peak at 764

nm as a result of the introduction of strong electron-withdrawing trifluoroacetic (TFA) groups. Compared to **75a** and **75b**, compounds **76a** and **76b** showed a bathochromic shift of their absorption spectra, due to the enhanced diradical character (Figure 9.25c). Moreover, compound **75b** and **76b** can be readily oxidized into stable radical cations and dications by $NO{\cdot}SbF_6$, as shown in Figure 9.25b. The structures of the dications $\mathbf{75b}^{2+}$ and $\mathbf{76b}^{2+}$ were confirmed by the X-ray crystallographic analysis. NICS and ACID calculations of these two dications indicated the aromatic character of the tropylium rings and the weakly antiaromaticity of the nearby five-membered rings, while the other two pentagons are highly antiaromatic with large positive $NICS(1)_{zz}$ value and the central six-membered ring is nearly non-aromatic (Figure 9.25d).

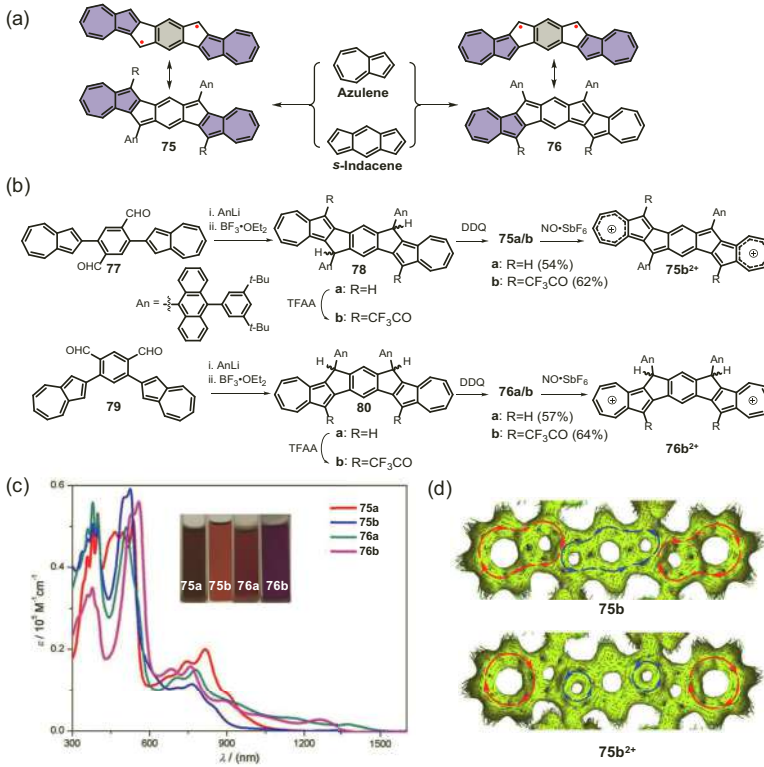


**Figure 9.25** (a) Representative resonance structures of diazuleno-*s*-indacene isomers **75** and **76**. (b) Synthesis of **75a/b** and **76a/b**. (c) UV-Vis absorption spectra of **75a**, **75b**, **76a**, and **76b** in $CH_2Cl_2$. (d) Calculated ACID plots of **75b** and $\mathbf{75b}^{2+}$ (iso-value: 0.04). Reproduced with permission from Ref. [130]. Copyright 2018 John Wiley and Sons Inc.

Apart from the above heptagon-embedded diradicaloids that are synthesized by the extension of the antiaromatic indacenes with azulene units, another synthetic strategy to achieve the non-benzenoid diradicaloids is the replacement of the five-membered rings of indacenes by seven-membered rings [131–133]. For example, replacing the pentagons of *s*-indacene with one or two heptagons leads to the 5-6-7 fused ring system (**81**) and 7-6-7 fused ring system (**82**), which are unknown so far (Figure 9.26a). However, benzannulation on cyclohepta[*f*]indene (**81**) can give 6-5-6-7-6 ring system, in which two different structural isomers (**83** and **84**) can be obtained by changing the fusion direction of the two outer benzene rings (Figure 9.26b). In 2016, Miao and Chi et al. reported the synthesis of the mesityl-substituted derivative of **83** [134]. Besides the closed-shell quinoidal resonance structure, one open-shell diradical form (**83-A**) and one dipolar zwitterion resonance structure (**83-B**) can be drawn for **83a**. Theoretical and experimental results revealed that compound **83a** has a closed-shell ground state with zero diradical character. In comparison to **83a**, its regioisomer **84a** is anticipated to have distinct diradical property because two extra Clar sextets can be gained in **84a** upon changing from the closed-shell to the diradical form (Figure 9.26b) [135]. DFT calculation (UB3LYP/6-311G(d)) showed that **84a** has significant open-shell character with a small $\Delta E_{S\text{-}T}$ (−1.84 kcal mol$^{-1}$), while a closed-shell ground state with a much larger $\Delta E_{S\text{-}T}$ of −18.49 kcal mol$^{-1}$ was obtained for **83a**. In addition, **84a** has a more localized charge distribution on the HOMO and LUMO as well as a larger dipole moment (4.75 D) than that of **83a** (2.76 D), suggesting the more pronounced charge separation feature of **84a**. Zhao and coworkers synthesized and investigated the properties of **84a** [135]. Starting from a double nucleophilic addition to dione **85** with mesityllithium, diol precursor **86** was obtained. However, applying the common reducing procedure to **86** with $SnCl_2$ was not able to isolate **84a**. Then, diol **86** was subjected to reaction with $Et_3SiH$ in the presence of $BF_3{\cdot}Et_2O$, a protonated salt of **87** was attained, whose structure was confirmed by $^1H$ NMR and X-ray crystallographic analysis. As shown in Figure 9.26c, compound **87** possessed a planar molecular backbone composed of linear 6-5-6-7-6 framework isomeric to pentacene. The average bond length of the heptagon was 1.418 Å, which was slightly shorter than that (1.425 Å) of the reported dibenzotropylium cation

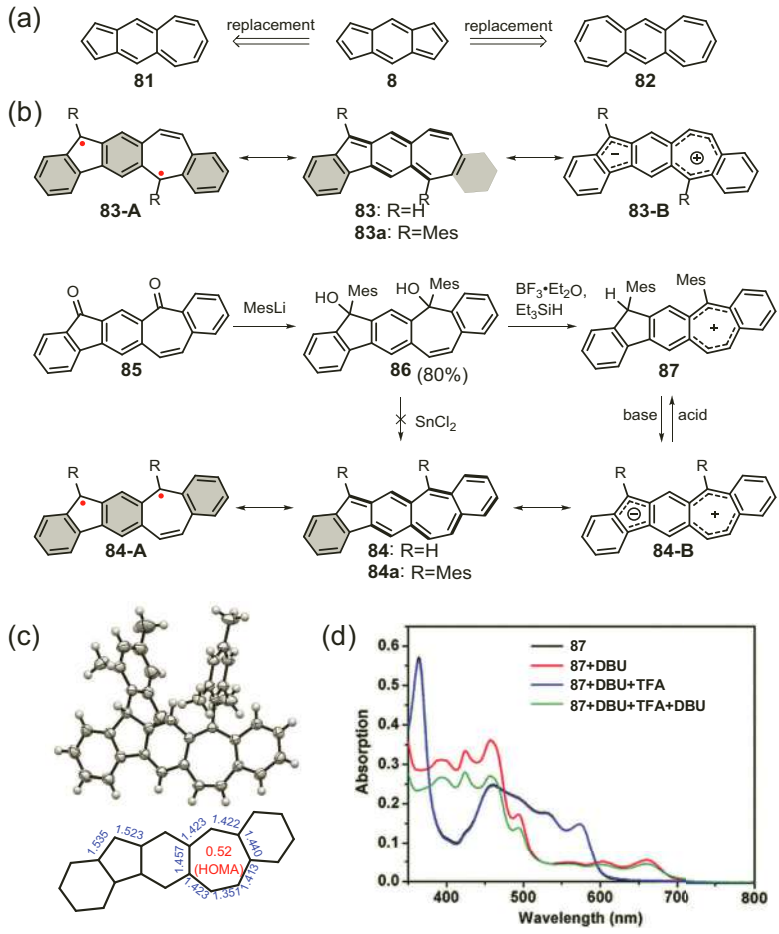


**Figure 9.26** (a) Structures of 5-6-7 and 7-6-7 ring systems (**81** and **82**) based on *s*-indacene (**8**). (b) Synthesis of **83a** and **84a**. (c) X-ray crystallographic structure of **86** (counter ion $BF_4^-$ omitted for clarity), and the selected bond lengths (Å) and the calculated HOMA index of the seven-membered ring of **86**. (d) Absorption spectra of **86** in $CH_2Cl_2$ upon sequential additions of DBU, TFA, and DBU again (the black and blue lines overlap almost completely; spectra were collected from the same sample subjected to repeated acid/base additions). Reproduced with permission from Ref. [135]. Copyright 2020 The Royal Society of Chemistry.

derivative. In addition, the seven-membered ring in **87** had a larger harmonic oscillator model of aromaticity (HOMA) index of 0.52 as compared to that of the dibenzotropylium cation (0.48), indicating

a comparable aromatic character. Furthermore, the protonated salt **87** can be in-situ converted to its neutral form of **84a** by reacting with organic bases, such as 1,8-diazabicyclo[5.4.0]undec-7-ene (DBU). The diradical properties of **84a** were clearly evidenced by the obvious ESR signal detectable around room temperature and a small $\Delta E_{S\text{-}T}$ of −0.95 kcal mol$^{-1}$ was estimated for **84a** from the VT ESR measurements. Interestingly, compound **87** demonstrated a reversible deprotonation and protonation reactions in response to pH changes in solution, which was proved by the monitoring of $^{1}$H NMR, fluorescence emission and UV-Vis absorption spectra (Figure 9.26d). Upon adding ca. 2 equiv. of DBU to a solution of **87** in $CH_2Cl_2$, a clear color change from red to green as well as the obvious absorption spectrum change was observed, indicating the formation of neutral form of **84a**. Fitting the absorption decay of in-situ generated **84a** in $CH_2Cl_2$ under a nitrogen atmosphere gave the half-life time of **84a** to be about 35 h. Importantly, the absorption spectrum of **87** was completely regained when the solution of **84a** was treated with TFA, evidencing the conversion back to **87**. Moreover, the pH-controlled reversible magnetic switching behavior was also revealed by monitoring the on and off cycles of ESR signal in response to repeated addition of acids and bases to a solution or exposing a thin film of **87** to base vapor followed by acid vapor.

## 9.4 Four- or Eight-Membered Ring-Containing Diradicaloids

In addition to the five- or seven-membered ring containing diradicaloids, open-shell PHs bearing four- or eight-membered ring have been rarely explored, due to their challenging synthesis. Cyclobutadiene (CBD) is the smallest four-membered antiaromatic ring containing 4 π-electrons, which is highly unstable [136]. Fusing CBD with appropriate aromatic motifs can give relatively stable π-systems. Additionally, it has been revealed above that non-benzenoid PHs containing antiaromtic rings (i.e. pentalene and indacenes) can decrease the HOMO-LUMO energy gap and lead to interesting π-electron molecular scaffolds, which potentially exhibit the open-shell diradical character. However, most of the reported PHs with four-membered rings, such as [N]phenylenes [137] and

[N]naphthylenes [138, 139], displayed the closed-shell ground state. In 2018, Zeng et al. synthesized the tetraindeno-based non-benzenoid PHs **91a** and **91b** by connecting two indeno[1,2-*b*] fluorene units with a four-membered ring (Figure 9.27a) [140]. Both molecules exhibited an open-shell singlet diradical structure in the ground state, while their quinoidal resonance form will lose two Clar sextets, producing an antiaromatic CBD bridged unit. As shown in Figure 9.27a, the two key stereoisomers **90a** and **90b** were obtained by an intermolecular dimerization [141] of precursor **89**, which was prepared by the nucleophilic attack on **88** with an equimolar mesitylethynyl lithium. The treatment of diones **90a** and **90b** with mesitylmagnesium bromide and the subsequent reduction reaction promoted by $SnCl_2$ yielded the deep solids **91a** and **91b**, respectively. The broadened $^1H$ NMR signals in the aromatic region even at −60 °C indicated the open-shell feature of **91a** and **91b** with significant diradical character. By VT ESR measurements, the $\Delta E_{S\text{-}T}$ of **91a** and **91b** were estimated to be as small as −0.53 kcal mol$^{-1}$ and −0.69 kcal mol$^{-1}$, respectively, which are comparable to the theoretical values (−0.40 kcal mol$^{-1}$ for **91a** and −0.46 kcal mol$^{-1}$ for **91b**). The large diradical characters were predicted to be 0.99 for **91a** and 0.94 for **92a** by DFT calculations (UCAM-B3LYP/6-31G(d,p)). To be noted, the solids of **91a/b** were unstable when exposed to air over a long time, while they were stable for more than two months under a nitrogen atmosphere. In addition, the solutions of **91a/b** under air yielded the oxygen-adduct **92**, whose structure was confirmed by X-ray crystallographic analysis (Figure 9.27b). In contrast to the closed-shell compound **92**, which had an intense absorption maximum at 712 nm, the diradicaloids **91a/b** in $CH_2Cl_2$ exhibited the weak and low-energy absorption band extending into the NIR region (1150 nm), further supporting their open-shell character (Figure 9.27c).

The cyclic fusion of two angle-shaped indeno[2,1-*c*] fuorenes (**12**) can generate the eight-membered ring-containing tetracyclopenta[*def*,*jkl*,*pqr*,*vwx*]tetraphenylene (**93**), which might have potential tetraradical character with a hydrocarbon scaffold. As shown in Figure 9.28a, the closed-shell ($D_{2h}$ symmetric) resonance form **93** and open-shell tetraradical ($D_{4h}$ symmetric) resonance form **93**-B can be drawn in addition to the intermediate diradical form **93-A** with $C_{2v}$ geometry. Therefore, compound **93**

was supposed to be highly instable under air due to its expected antiaromatic feature with 28 ($4n$) π-electrons and the radical character expected at each head of the pentagons. In 1970, Hellwinkel and Reiff reported the generation of dicationic species of **93** with $4n$ (26) π-electrons in a mass spectral chamber [142]; however, the isolation and characterization of **93** or its derivatives are still challenging. In 2015, Tobe et al. disclosed the synthesis of its derivative **93a** substituted with four sterically protected mesityl groups through the dehydrogenation of dihydro precursor **94** with DDQ, which could be stable under air for a few months in the solid state [143]. DFT calculations (SF-TDBHHLYP/6-311G(d,p)) indicated that the diradical character ($y_0$) and tetraradical character ($y_1$) values for the closed-shell $D_{2h}$ geometry (model A) were 0.095 and 0.032. The structure of the experimental model C obtained by the X-ray structure was similar to that of the $D_{2h}$ geometry and showed a relatively small $y_0$ value of 0.258 and $y_1$ value of 0.085. On the other hand, the open-shell $D_{4h}$ structure (model B) had a higher energy (8.3 kcal mol$^{-1}$) than the closed-shell $D_{2h}$ structure (model A), featuring a significantly diradical character ($y_0$ = 1.000) with a slightly tetraradical feature ($y_1$ = 0.166). X-ray crystallographic analysis of **93a** revealed its planar molecular backbone with an approximate $D_{2h}$ geometry. The observed bond length from X-ray analysis agreed well with the theoretical bond lengths for the $D_{2h}$ structure. The $^1$H NMR spectrum of **93a** measured in toluene-$d_8$ at 30 °C exhibited a single peak at 2.85 ppm for the core "aromatic" proton, which can be ascribed to the paramagnetic shielding effect of the outer 20 π-electrons system. NICS(1) calculations of **93a** based on the experimental model C and $D_{2h}$ symmetric model A indicated nonaromatic to weak antiaromatic character in the six-membered rings and significant antiaromatic character in the five- and eight-membered rings (Figure 9.28c). At 50 °C, the NMR signals of **93a** started to broaden, indicating the presence of thermally populated triplet state, although the calculated $\Delta E_{S\text{-}T}$ for model A (−19.3 kcal mol$^{-1}$) and model C (−16.5 kcal mol$^{-1}$) were relatively large. Moreover, compound **93a** showed a strong absorption maximum at 475 nm along with a broad low energy absorption band centered at 909 nm.

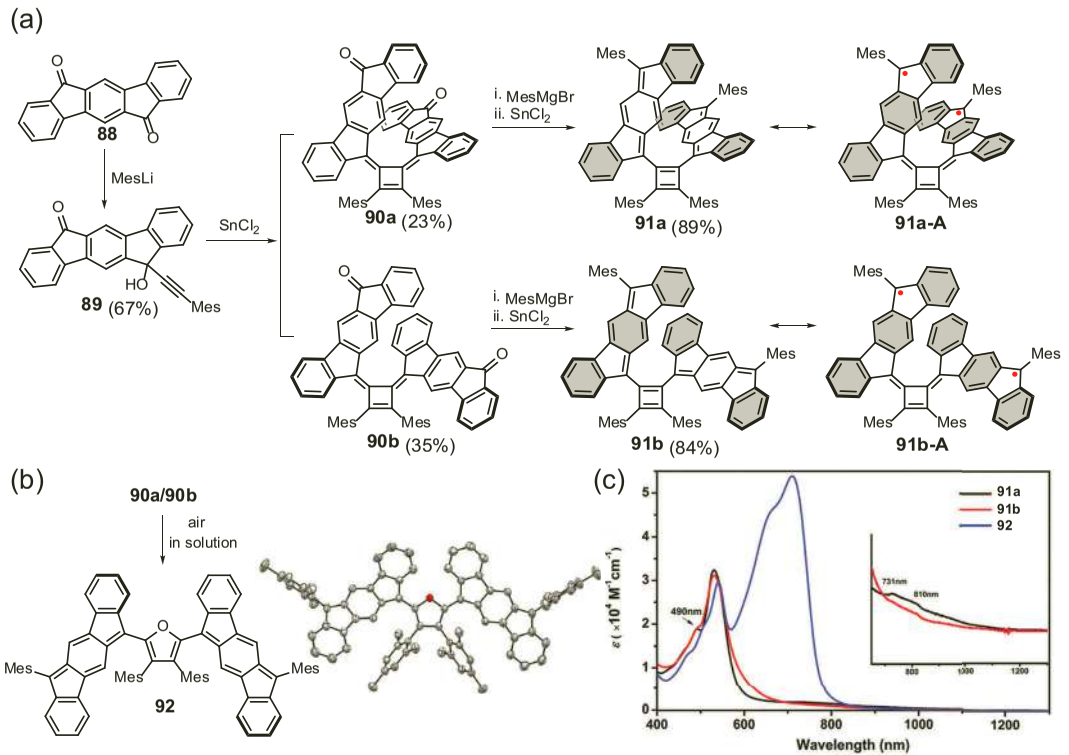


**Figure 9.27** (a) Synthetic route toward helical diradicaloids **91a** and **91b** containing four-membered ring. (b) Oxidized product **92** from diradicaloids **91a/b** when exposed to the air, and its X-ray crystallographic structure. (c) UV-Vis-NIR spectra of **91-a**, **91-b,** and **92** recorded in $CH_2Cl_2$. Inset shows a magnified view in the NIR region. Reproduced with permission from Ref. [140]. Copyright 2018 The Royal Society of Chemistry.

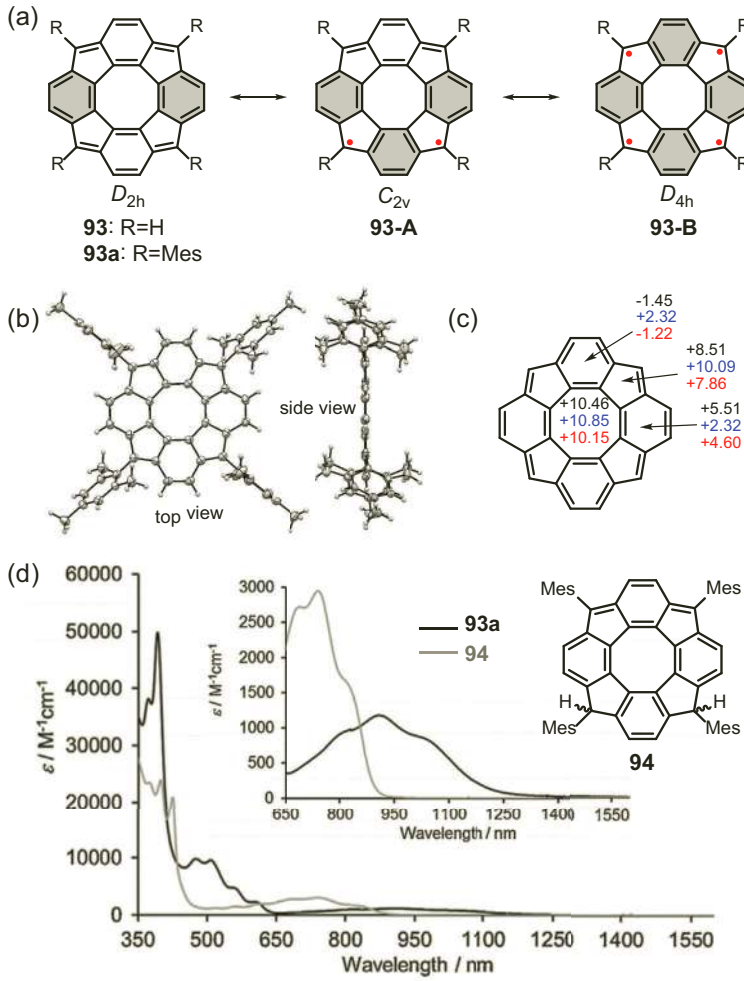


**Figure 9.28** (a) Structures of **93/93a** as well as their resonance structures. (b) Top view and side view of the X-ray crystallographic structure of **93a**. (c) NICS(1) values of **93** in model A (with the structure of **93** optimized under the constraint of $D_{2h}$ symmetry, in black) and model B (with the structure of **93** optimized under the constraint of $D_{4h}$ symmetry, in blue), and model C (with the core structure of **93a** obtained from single-crystal X-ray analysis, in red) calculated at the LC-UBLYP/6-311+G(d,p) level. (d) UV-Vis-NIR spectra of **93a** and its dihydro precursor **94** in $CH_2Cl_2$. Reproduced with permission from Ref. [143]. Copyright 2015 John Wiley and Sons Inc.

## 9.5 Summary

Over the past decade, the synthesis of non-benzenoid open-shell PHs has been widely explored in view of their unusual chemical and physical properties, which are not shared by their benzenoid counterparts. Among these systems, the antiaromatic units, pentalene, indacene, and CBD are the important building blocks to construct non-benzenoid diradicaloids and the structural diversity of these systems allow the investigation of their fundamental structure-property relationships. Particularly, the pentagon-embedded diradicaloids with curved conformation represent a novel class of open-shell PHs, in which the curved geometry plays an important role in determining their stability and electronic structure. Additionally, it has been shown that the incorporation of non-alternant non-benzenoid azulene unit into PHs can be regarded as a powerful strategy to attain the heptagon-embedded diradicaloids and thus tune the electronic structure of the original system, such as the non-benzenoid isomers of bisanthene and *peri*-tetracene. In contrast to solution synthesis, on-surface synthesis in ultrahigh vacuum is also proved to be a promising way to fabricate non-benzenoid open-shell PHs, especially for the highly reactive mono-radical system and high-spin diradicaloids or multiradicaloids with challenging synthesis in solution, leading to the possibility to reveal their intriguing electronic structures and physical properties. Furthermore, the stability issue is an important concern to ensure the integration of this novel class of organic materials for the device application. Thanks to the recently developed strategies (either kinetic or thermodynamic stabilization), the applications of stable open-shell non-benzenoid PHs in the field of organic ambipolar FETs and photovoltaics have been investigated in the last few years. On the other hand, the recently emerging interests in the spintronics and organic quantum computing have accelerated the development of novel non-benzenoid diradicaloids with unique quantum properties. Without doubt, new open-shell systems based on non-benzenoid PHs are waiting us with challenging structures as well as fascinating properties, which overall cover a rich field of research in synthesis, in theory and materials with a bright future.

## References


1. Wu, J., Pisula, W., and Müllen, K. (2007). Graphenes as potential material for electronics, *Chem. Rev.*, **107**, pp. 718–747.
2. Narita, A., Wang, X.-Y., Feng, X., and Müllen, K. (2015). New advances in nanographene chemistry, *Chem. Soc. Rev.*, **44**, pp. 6616–6643.
3. Rieger, R., and Müllen, K. (2010). Forever young: Polycyclic aromatic hydrocarbons as model cases for structural and optical studies, *J. Phys. Org. Chem.*, **23**, pp. 315–325.
4. Wang, X.-Y., Yao, X., and Müllen, K. (2019). Polycyclic aromatic hydrocarbons in the graphene era, *Sci. China Chem.*, **62**, pp. 1099–1144.
5. Huang, P. Y., Ruiz-Vargas, C. S., van der Zande, A. M., Whitney, W. S., Levendorf, M. P., Kevek, J. W., Garg, S., Alden, J. S., Hustedt, C. J., Zhu, Y., Park, J., McEuen, P. L., and Muller, D. A. (2011). Grains and grain boundaries in single-layer graphene atomic patchwork quilts, *Nature*, **469**, pp. 389–392.
6. Kim, K., Lee, Z., Regan, W., Kisielowski, C., Crommie, M. F., and Zettl, A. (2011). Grain boundary mapping in polycrystalline graphene, *ACS Nano*, **5**, pp. 2142–2146.
7. Kurasch, S., Kotakoski, J., Lehtinen, O., Skákalová, V., Smet, J., Krill, C. E., Krasheninnikov, A. V., and Kaiser, U. (2012). Atom-by-atom observation of grain boundary migration in graphene, *Nano Lett.*, **12**, pp. 3168–3173.
8. Lahiri, J., Lin, Y., Bozkurt, P., Oleynik, I. I., and Batzill, M. (2010). An extended defect in graphene as a metallic wire, *Nat. Nanotechnol.*, **5**, pp. 326–329.
9. Banhart, F., Kotakoski, J., and Krasheninnikov, A. V. (2011). Structural defects in graphene, *ACS Nano*, **5**, pp. 26–41.
10. Cretu, O., Krasheninnikov, A. V., Rodríguez-Manzo, J. A., Sun, L., Nieminen, R. M., and Banhart, F. (2010). Migration and localization of metal atoms on strained graphene, *Phys. Rev. Lett.*, **105**, pp. 196102.
11. Terrones, H., Terrones, M., Hernández, E., Grobert, N., Charlier, J. C., and Ajayan, P. M. (2000). New metallic allotropes of planar and tubular carbon, *Phys. Rev. Lett.*, **84**, pp. 1716–1719.
12. Márquez, I. R., Castro-Fernández, S., Millán, A., and Campaña, A. G. (2018). Synthesis of distorted nanographenes containing seven- and eight-membered carbocycles, *Chem. Commun.*, **54**, pp. 6705–6718.
13. Pun, S. H., and Miao, Q. (2018). Toward negatively curved carbons, *Acc. Chem. Res.*, **51**, pp. 1630–1642.

14. Baker, W. (1945). Non-benzenoid aromatic hydrocarbons, *J. Chem. Soc. (Resumed)*, **258**, pp. 258–267.
15. Miyoshi, H., Nobusue, S., Shimizu, A., and Tobe, Y. (2015). Non-alternant non-benzenoid kekulenes: The birth of a new kekulene family, *Chem. Soc. Rev.*, **44**, pp. 6560–6577.
16. Christoph, H., Grunenberg, J., Hopf, H., Dix, I., Jones, P. G., Scholtissek, M., and Maier, G. (2008). MP2 and DFT calculations on circulenes and an attempt to prepare the second lowest benzolog, [4]circulene, *Chem. Eur. J.*, **14**, pp. 5604–5616.
17. Lawton, R. G., and Barth, W. E. (1971). Synthesis of corannulene, *J. Am. Chem. Soc.*, **93**, pp. 1730–1745.
18. Yamamoto, K., Harada, T., Okamoto, Y., Chikamatsu, H., Nakazaki, M., Kai, Y., Nakao, T., Tanaka, M., Harada, S., and Kasai, N. (1988). Synthesis and molecular structure of [7]circulene, *J. Am. Chem. Soc.*, **110**, pp. 3578–3584.
19. Mishra, S., Beyer, D., Berger, R., Liu, J., Gröning, O., Urgel, J. I., Müllen, K., Ruffieux, P., Feng, X., and Fasel, R. (2020). Topological defect-induced magnetism in a nanographene, *J. Am. Chem. Soc.*, **142**, pp. 1147–1152.
20. Zheng, Y., Li, C., Zhao, Y., Beyer, D., Wang, G., Xu, C., Yue, X., Chen, Y., Guan, D.-D., Li, Y.-Y., Zheng, H., Liu, C., Luo, W., Feng, X., Wang, S., and Jia, J. (2020). Engineering of magnetic coupling in nanographene, *Phys. Rev. Lett.*, **124**, pp. 147206.
21. Watson, M. D., Fechtenkötter, A., and Müllen, K. (2001). Big is beautiful – "Aromaticity" revisited from the viewpoint of macromolecular and supramolecular benzene chemistry, *Chem. Rev.*, **101**, pp. 1267–1300.
22. Zeng, Z., Shi, X., Chi, C., López Navarrete, J. T., Casado, J., and Wu, J. (2015). Pro-aromatic and anti-aromatic π-conjugated molecules: An irresistible wish to be diradicals, *Chem. Soc. Rev.*, **44**, pp. 6578–6596.
23. Krygowski, T. M., Cyrañski, M. K., Czarnocki, Z., Häfelinger, G., and Katritzky, A. R. (2000). Aromaticity: A theoretical concept of immense practical importance, *Tetrahedron*, **56**, pp. 1783–1796.
24. Randić, M. (2003). Aromaticity of polycyclic conjugated hydrocarbons, *Chem. Rev.*, **103**, pp. 3449–3606.
25. Sun, Z., and Wu, J. (2012). Open-shell polycyclic aromatic hydrocarbons, *J. Mater. Chem.*, **22**, pp. 4151–4160.
26. Sun, Z., Ye, Q., Chi, C., and Wu, J. (2012). Low band gap polycyclic hydrocarbons: From closed-shell near infrared dyes and semiconductors to open-shell radicals, *Chem. Soc. Rev.*, **41**, pp. 7857–7889.

27. Y. Gopalakrishna, T., Zeng, W., Lu, X., and Wu, J. (2018). From open-shell singlet diradicaloids to polyradicaloids, *Chem. Commun.*, **54**, pp. 2186–2199.
28. Hu, X., Wang, W., Wang, D., and Zheng, Y. (2018). The electronic applications of stable diradicaloids: Present and future, *J. Mater. Chem. C*, **6**, pp. 11232–11242.
29. Sun, Z., Zeng, Z., and Wu, J. (2013). Benzenoid polycyclic hydrocarbons with an open-shell biradical ground state, *Chem. Asian J.*, **8**, pp. 2894–2904.
30. Ye, Q., and Chi, C. (2014). Recent highlights and perspectives on acene based molecules and materials, *Chem. Mater.*, **26**, pp 4046–4056.
31. Sun, Z., Zeng, Z., and Wu, J. (2014). Zethrenes, extended *p*-quinodimethanes, and periacenes with a singlet biradical ground state, *Acc. Chem. Res.*, **47**, pp. 2582–2591.
32. Hu, P., and Wu, J. (2016). Modern zethrene chemistry, *Can. J. Chem.*, **95**, pp. 223–233.
33. Liu, J., and Feng, X. (2020). Synthetic tailoring of graphene nanostructures with zigzag-edged topologies: Progress and perspectives, *Angew. Chem. Int. Ed.*, **59**, pp. 23386–23401
34. Su, J., Telychko, M., Song, S., and Lu, J. (2020). Triangulenes: From precursor design to on-surface synthesis and characterization, *Angew. Chem. Int. Ed.*, **59**, pp. 7658–7668.
35. Wu, Y.-T., and Siegel, J. S. (2006). Aromatic molecular-bowl hydrocarbons: Synthetic derivatives, their structures, and physical properties, *Chem. Rev.*, **106**, pp. 4843–4867.
36. Tsefrikas, V. M., and Scott, L. T. (2006). Geodesic polyarenes by flash vacuum pyrolysis, *Chem. Rev.*, **106**, pp. 4868–4884.
37. Tobe, Y. (2018). Quinodimethanes incorporated in non-benzenoid aromatic or antiaromatic frameworks, *Top. Curr. Chem.*, **376**, pp. 12.
38. Hafner, K. (1980). Pentalen: Die lösung eines alten problems, *Nachr. Chem. Tech. Lab.*, **28**, pp. 222–226.
39. Hopf, H. (2013). Pentalenes-from highly reactive antiaromatics to substrates for material science, *Angew. Chem. Int. Ed.*, **52**, pp. 12224–12226.
40. Breslow, R. (1973). Antiaromaticity, *Acc. Chem. Res.*, **6**, pp. 393–398.
41. Minkin, V. I., Glukhovtsev, M. N., and Simkin, B. I. A. (1994). Aromaticity and antiaromaticity: Electronic and structural aspects, Wiley-Interscience Publication, J. Wiley & Sons.

42. Brand, K. (1912). Über gefärbte kohlenwasserstoffe der diphensuccinden-reihe. I, *Ber. Dtsch. Chem. Ges.*, **45**, pp. 3071–3077.
43. Le Goff, E. (1962). The synthesis of hexaphenylpentalene, *J. Am. Chem. Soc.*, **84**, pp. 3975–3976.
44. Hafner, K., Bangert, K. F., and Orfanos, V. (1967). 1,3-Bis(Dimethylamino) pentalene, *Angew. Chem. Int. Ed.*, **6**, pp. 451–452.
45. Hafner, K., and Süss, H. U. (1973). 1,3,5-Tri-*tert*-butylpentalene: A stabilized planar 8π-electron system, *Angew. Chem. Int. Ed.*, **12**, pp. 575–577.
46. Balaban, A., Banciu, M., and Ciorba, V. (1986). Annulenes, benzo-, hetero-, homo-derivatives and their valence isomers, CRC Press, Boca Raton, FL.
47. Kawase, T., and Nishida, J. (2015). pi-Extended pentalenes: The revival of the old compound from new standpoints, *Chem. Rec.*, **15**, pp. 1045–1059.
48. Saito, M. (2010). Synthesis and reactions of dibenzo[a,e]pentalenes, *Symmetry-Basel*, **2**, pp. 950–969.
49. Frederickson, C. K., Zakharov, L. N., and Haley, M. M. (2016). Modulating paratropicity strength in diareno-fused antiaromatics, *J. Am. Chem. Soc.*, **138**, pp. 16827–16838.
50. Kawase, T., Fujiwara, T., Kitamura, C., Konishi, A., Hirao, Y., Matsumoto, K., Kurata, H., Kubo, T., Shinamura, S., Mori, H., Miyazaki, E., and Takimiya, K. (2010). Dinaphthopentalenes: Pentalene derivatives for organic thin-film transistors, *Angew. Chem. Int. Ed.*, **49**, pp. 7728–7732.
51. Dai, G., Chang, J., Zhang, W., Bai, S., Huang, K.-W., Xu, J., and Chi, C. (2015). Dianthraceno[a,e]pentalenes: Synthesis, crystallographic structures and applications in organic field-effect transistors, *Chem. Commun.*, **51**, pp. 503–506.
52. Cristol, S. J., Whittle, P. R., and Dahl, A. R. (1970). Bridged-polycyclic compounds LXIII: Reductive ring opening of 3,6-dibenzotricyclo[3.3.0.02,8]octadiene, *J. Org. Chem.*, **35**, pp. 3172–3174.
53. Baker, W., McOmie, J. F. W., Parfitt, S. D., and Watkins, D. A. M. (1957). 799. Attempts to prepare new aromatic systems. Part VI. 1 : 2-5 : 6-Dibenzopentalene and derivatives, *J. Chem. Soc. (Resumed)*, pp. 4026–4037.
54. Fowler, P. W., Steiner, E., Havenith, R. W., and Jenneskens, L. W. (2004). Current density, chemical shifts and aromaticity, *Magn. Reson. Chem.*, **42**, pp. S68–S78.

55. London, G., von Wantoch Rekowski, M., Dumele, O., Schweizer, W. B., Gisselbrecht, J.-P., Boudon, C., and Diederich, F. (2014). Pentalenes with novel topologies: Exploiting the cascade carbopalladation reaction between alkynes and gem-dibromoolefins, *Chem. Sci.*, **5**, pp. 965–972.

56. Konishi, A., Okada, Y., Nakano, M., Sugisaki, K., Sato, K., Takui, T., and Yasuda, M. (2017). Synthesis and characterization of dibenzo[a,f] pentalene: Harmonization of the antiaromatic and singlet biradical character, *J. Am. Chem. Soc.*, **139**, pp. 15284–15287.

57. Zahradnik, R. (1965). Electronic structure and properties of non-alternant hydrocarbons, *Angew. Chem. Int. Ed.*, **4**, pp. 1039–1050.

58. Peters, D. (1958). 206. Structure and properties of mesomeric systems, Part II: The chemical reactivity of alternant and non-alternant hydrocarbons, *J. Chem. Soc. (Resumed)*, pp. 1028–1039.

59. Fix, A. G., Chase, D. T., and Haley, M. M. (2012). Indenofluorenes and derivatives: Syntheses and emerging materials applications, Polyarenes I., Springer, Berlin, Heidelberg, pp. 159–195.

60. Frederickson, C. K., Rose, B. D., and Haley, M. M. (2017). Explorations of the indenofluorenes and expanded quinoidal analogues, *Acc. Chem. Res.*, **50**, pp. 977–987.

61. Shimizu, A., Nobusue, S., Miyoshi, H., and Tobe, Y. (2014). Indenofluorene congeners: Biradicaloids and beyond, *Pure Appl. Chem.*, **86**, pp. 517–528.

62. Dressler, J. J., Zhou, Z., Marshall, J. L., Kishi, R., Takamuku, S., Wei, Z., Spisak, S. N., Nakano, M., Petrukhina, M. A., and Haley, M. M. (2017). Synthesis of the unknown indeno[1,2-a]fluorene regioisomer: Crystallographic characterization of its dianion, *Angew. Chem. Int. Ed.* , **56**, pp. 15363–15367.

63. Chase, D. T., Rose, B. D., McClintock, S. P., Zakharov, L. N., and Haley, M. M. (2011). Indeno[1,2-b]fluorenes: Fully conjugated antiaromatic analogues of acenes, *Angew. Chem. Int. Ed.* , **50**, pp. 1127–1130.

64. Chase, D. T., Fix, A. G., Kang, S. J., Rose, B. D., Weber, C. D., Zhong, Y., Zakharov, L. N., Lonergan, M. C., Nuckolls, C., and Haley, M. M. (2012). 6,12-Diarylindeno[1,2-b]fluorenes: Syntheses, photophysics, and ambipolar OFETs, *J. Am. Chem. Soc.* , **134**, pp. 10349–10352.

65. Shimizu, A., and Tobe, Y. (2011). Indeno[2,1-a]fluorene: An air-stable ortho-quinodimethane derivative, *Angew. Chem. Int. Ed.*, **50**, pp. 6906–6910.

66. Fix, A. G., Deal, P. E., Vonnegut, C. L., Rose, B. D., Zakharov, L. N., and Haley, M. M. (2013). Indeno[2,1-c]fluorene: A new electron-accepting scaffold for organic electronics, *Org. Lett.*, **15**, pp. 1362–1365.

67. Shimizu, A., Kishi, R., Nakano, M., Shiomi, D., Sato, K., Takui, T., Hisaki, I., Miyata, M., and Tobe, Y. (2013). Indeno[2,1-b]fluorene: A 20-pi-electron hydrocarbon with very low-energy light absorption*, Angew. Chem. Int. Ed.*, **52**, pp. 6076–6079.

68. Barker, J. E., Frederickson, C. K., Jones, M. H., Zakharov, L. N., and Haley, M. M. (2017). Synthesis and properties of quinoidal fluorenofluorenes*, Org. Lett.*, **19**, pp. 5312–5315.

69. Rudebusch, G. E., Zafra, J. L., Jorner, K., Fukuda, K., Marshall, J. L., Arrechea-Marcos, I., Espejo, G. L., Ortiz, R. P., Gomez-Garcia, C. J., Zakharov, L. N., Nakano, M., Ottosson, H., Casado, J., and Haley, M. M. (2016). Diindeno-fusion of an anthracene as a design strategy for stable organic biradicals*, Nat. Chem.*, **8**, pp. 753–759.

70. Miyoshi, H., Miki, M., Hirano, S., Shimizu, A., Kishi, R., Fukuda, K., Shiomi, D., Sato, K., Takui, T., Hisaki, I., Nakano, M., and Tobe, Y. (2017). Fluoreno[2,3-b]fluorene vs Indeno[2,1-b]fluorene: Unusual relationship between the number of π electrons and excitation energy in *m*-quinodimethane-type singlet diradicaloids*, J. Org. Chem.*, **82**, pp. 1380–1388.

71. Anthony, J. E. (2008). The larger acenes: Versatile organic semiconductors*, Angew. Chem. Int. Ed.*, **47**, pp. 452–483.

72. Bohnen, A., Koch, K.-H., Lüttke, W., and Müllen, K. (1990). Oligorylene as a model for "poly(perinaphthalene)"*, Angew. Chem. Int. Ed.*, **29**, pp. 525–527.

73. Miyoshi, H., Nobusue, S., Shimizu, A., Hisaki, I., Miyata, M., and Tobe, Y. (2014). Benz[c]indeno[2,1-a]fluorene: A 2,3-naphthoquinodimethane incorporated into an indenofluorene frame*, Chem. Sci.*, **5**, pp. 163–168.

74. Hibi, D., Kitabayashi, K., Fujita, K., Takeda, T., and Tobe, Y. (2016). Diindenopyrenes: Extended 1,6- and 1,8-pyrenoquinodimethanes with singlet diradical characters*, J. Org. Chem.*, **81**, pp. 3735–3743.

75. Sbargoud, K., Mamada, M., Marrot, J., Tokito, S., Yassar, A., and Frigoli, M. (2015). Diindeno[1,2-b:2′,1′-n]perylene: A closed shell related Chichibabin's hydrocarbon, the synthesis, molecular packing, electronic and charge transport properties*, Chem. Sci.*, **6**, pp. 3402–3409.

76. Maekawa, T., Ueno, H., Segawa, Y., Haley, M. M., and Itami, K. (2016). Synthesis of open-shell ladder π-systems by catalytic C–H annulation of diarylacetylenes*, Chem. Sci.*, **7**, pp. 650–654.

77. Hu, P., Lee, S., Herng, T. S., Aratani, N., Gonçalves, T. P., Qi, Q., Shi, X., Yamada, H., Huang, K.-W., Ding, J., Kim, D., and Wu, J. (2016). Toward tetraradicaloid: The effect of fusion mode on radical character and chemical reactivity*, J. Am. Chem. Soc.*, **138**, pp. 1065–1077.

78. Majewski, M. A., Chmielewski, P. J., Chien, A., Hong, Y., Lis, T., Witwicki, M., Kim, D., Zimmerman, P. M., and Stępień, M. (2019). 5,10-Dimesityldiindeno[1,2-a:2',1'-i]phenanthrene: A stable biradicaloid derived from Chichibabin's hydrocarbon, *Chem. Sci.*, **10**, pp. 3413–3420.

79. Rose, B. D., Vonnegut, C. L., Zakharov, L. N., and Haley, M. M. (2012). Fluoreno[4,3-c]fluorene: A closed-shell, fully conjugated hydrocarbon, *Org. Lett.*, **14**, pp. 2426–2429.

80. Melidonie, J., Dmitrieva, E., Zhang, K., Fu, Y., Popov, A. A., Pisula, W., Berger, R., Liu, J., and Feng, X. (2020). Dipyrene-fused dicyclopenta[a,f] naphthalenes, *J. Org. Chem.*, **85**, pp. 215–223.

81. Dressler, J. J., Cárdenas Valdivia, A., Kishi, R., Rudebusch, G. E., Ventura, A. M., Chastain, B. E., Gómez-García, C. J., Zakharov, L. N., Nakano, M., Casado, J., and Haley, M. M. (2020). Diindenoanthracene diradicaloids enable rational, incremental tuning of their singlet-triplet energy gaps, *Chem*, **6**, pp. 1353–1368.

82. Wehrmann, C. M., Charlton, R. T., and Chen, M. S. (2019). A concise synthetic strategy for accessing ambient stable bisphenalenyls toward achieving electroactive open-shell π-conjugated materials, *J. Am. Chem. Soc.*, **141**, pp. 3240–3248.

83. Kubo, T., Shimizu, A., Sakamoto, M., Uruichi, M., Yakushi, K., Nakano, M., Shiomi, D., Sato, K., Takui, T., Morita, Y., and Nakasuji, K. (2005). Synthesis, intermolecular interaction, and semiconductive behavior of a delocalized singlet biradical hydrocarbon, *Angew. Chem. Int. Ed.*, **44**, pp. 6564–6568.

84. Kubo, T., Yamamoto, K., Nakasuji, K., and Takui, T. (2001). Tetra-tert-butyl-as-indaceno[1,2,3-cd:6,7,8-c'd']diphenalene: A four-stage amphoteric redox system, *Tetrahedron Lett.*, **42**, pp. 7997–8001.

85. Nakasuji, K., and Kubo, T. (2004). Multi-stage amphoteric redox hydrocarbons based on a phenalenyl radical, *Bull. Chem. Soc. Jpn.*, **77**, pp. 1791–1801.

86. Kubo, T. (2015). Phenalenyl-based open-shell polycyclic aromatic hydrocarbons, *Chem. Rec.*, **15**, pp. 218–232.

87. Kubo, T. (2015). Recent progress in quinoidal singlet biradical molecules, *Chem. Lett.*, **44**, pp. 111–122.

88. Ohashi, K., Kubo, T., Masui, T., Yamamoto, K., Nakasuji, K., Takui, T., Kai, Y., and Murata, I. (1998). 4,8,12,16-Tetra-tert-butyl-s-indaceno[1,2,3-cd:5,6,7-c'd']diphenalene: A four-stage amphoteric redox system, *J. Am. Chem. Soc.*, **120**, pp. 2018–2027.

89. Kubo, T., Shimizu, A., Uruichi, M., Yakushi, K., Nakano, M., Shiomi, D., Sato, K., Takui, T., Morita, Y., and Nakasuji, K. (2007). Singlet biradical character of phenalenyl-based Kekulé hydrocarbon with naphthoquinoid structure*, Org. Lett.*, **9**, pp. 81–84.

90. Shimizu, A., Hirao, Y., Matsumoto, K., Kurata, H., Kubo, T., Uruichi, M., and Yakushi, K. (2012). Aromaticity and π-bond covalency: Prominent intermolecular covalent bonding interaction of a Kekulé hydrocarbon with very significant singlet biradical character*, Chem. Commun.*, **48**, pp. 5629–5631.

91. Ball, M., Zhong, Y., Wu, Y., Schenck, C., Ng, F., Steigerwald, M., Xiao, S., and Nuckolls, C. (2015). Contorted polycyclic aromatics*, Acc. Chem. Res.*, **48**, pp. 267–276.

92. Liu, J., Ma, J., Zhang, K., Ravat, P., Machata, P., Avdoshenko, S., Hennersdorf, F., Komber, H., Pisula, W., Weigand, J. J., Popov, A. A., Berger, R., Müllen, K., and Feng, X. (2017). π-Extended and curved antiaromatic polycyclic hydrocarbons*, J. Am. Chem. Soc.*, **139**, pp. 7513–7521.

93. DeFrancisco, J. R., López-Espejo, G., Zafra, J. L., Yadav, S., Messersmith, R. E., Gómez-García, C. J., Ottosson, H., Casado, J., and Tovar, J. D. (2018). Torsional bias as a strategy to tune singlet–triplet gaps in organic diradicals*, J. Phys. Chem. C*, **122**, pp. 12148–12157.

94. Ravat, P., Solomek, T., Rickhaus, M., Haussinger, D., Neuburger, M., Baumgarten, M., and Juricek, M. (2016). Cethrene: A helically chiral biradicaloid isomer of heptazethrene*, Angew. Chem. Int. Ed.*, **55**, pp. 1183–1186.

95. Ma, J., Liu, J., Baumgarten, M., Fu, Y., Tan, Y. Z., Schellhammer, K. S., Ortmann, F., Cuniberti, G., Komber, H., Berger, R., Müllen, K., and Feng, X. (2017). A stable saddle-shaped polycyclic hydrocarbon with an open-shell singlet ground state*, Angew. Chem. Int. Ed.*, **56**, pp. 3280–3284.

96. Lombardi, F., Lodi, A., Ma, J., Liu, J., Slota, M., Narita, A., Myers, W. K., Müllen, K., Feng, X., and Bogani, L. (2019). Quantum units from the topological engineering of molecular graphenoids*, Science*, **366**, pp. 1107–1110.

97. Lombardi, F., Myers, W. K., Ma, J., Liu, J., Feng, X., and Bogani, L. (2020). Dynamical nuclear decoupling of electron spins in molecular graphenoid radicals and biradicals*, Phys. Rev. B*, **101**, pp. 094406.

98. Ma, J., Zhang, K., Schellhammer, K. S., Fu, Y., Komber, H., Xu, C., Popov, A. A., Hennersdorf, F., Weigand, J. J., Zhou, S., Pisula, W., Ortmann, F., Berger, R., Liu, J., and Feng, X. (2019). Wave-shaped polycyclic hydrocarbons with controlled aromaticity*, Chem. Sci.*, **10**, pp. 4025–4031.

99. Li, X., Kang, F., and Inagaki, M. (2016). Buckybowls: Corannulene and its derivatives, *Small*, **12**, pp. 3206–3223.

100. Morita, Y., Ueda, A., Nishida, S., Fukui, K., Ise, T., Shiomi, D., Sato, K., Takui, T., and Nakasuji, K. (2008). Curved aromaticity of a corannulene-based neutral radical: Crystal structure and 3 D unbalanced delocalization of spin, *Angew. Chem. Int. Ed.*, **47**, pp. 2035–2038.

101. Janata, J., Gendell, J., Ling, C.-Y., Barth, W. E., Backes, L., Mark, H. B., and Lawton, R. G. (1967). Concerning the anion and cation radicals of corannulene, *J. Am. Chem. Soc.*, **89**, pp. 3056–3058.

102. Ueda, A., Nishida, S., Fukui, K., Ise, T., Shiomi, D., Sato, K., Takui, T., Nakasuji, K., and Morita, Y. (2010). Three-dimensional intramolecular exchange interaction in a curved and nonalternant pi-conjugated system: Corannulene with two phenoxyl radicals, *Angew. Chem. Int. Ed.*, **49**, pp. 1678–1682.

103. Lu, R. Q., Wu, S., Yang, L. L., Gao, W. B., Qu, H., Wang, X. Y., Chen, J. B., Tang, C., Shi, H. Y., and Cao, X. Y. (2019). Stable diindeno-fused corannulene regioisomers with open-shell singlet ground states and large diradical characters, *Angew. Chem. Int. Ed.*, **58**, pp. 7600–7605.

104. Wang, Q., Hu, P., Tanaka, T., Gopalakrishna, T. Y., Herng, T. S., Phan, H., Zeng, W., Ding, J., Osuka, A., Chi, C., Siegel, J., and Wu, J. (2018). Curved π-conjugated corannulene dimer diradicaloids, *Chem. Sci.*, **9**, pp. 5100–5105.

105. Li, Y., Jia, Z., Xiao, S., Liu, H., and Li, Y. (2016). A method for controlling the synthesis of stable twisted two-dimensional conjugated molecules, *Nat. Commun.*, **7**, pp. 11637.

106. Hsieh, Y. C., Wu, C. F., Chen, Y. T., Fang, C. T., Wang, C. S., Li, C. H., Chen, L. Y., Cheng, M. J., Chueh, C. C., Chou, P. T., and Wu, Y. T. (2018). 5,14-Diaryldiindeno[2,1-f:1′,2′-j]picene: A new stable [7]helicene with a partial biradical character, *J. Am. Chem. Soc.*, **140**, pp. 14357–14366.

107. Lee, C. C., Chen, C. I., Fang, C. T., Huang, P. Y., Wu, Y. T., and Chueh, C. C. (2019). Improving performance of perovskite solar cells using [7] helicenes with stable partial biradical characters as the hole-extraction layers, *Adv. Funct. Mater.*, **29**, pp 1808625.

108. Boominathan, S. S. K., Chang, K. H., Liu, Y. C., Wang, C. S., Wu, C. F., Chiang, M. H., Chou, P. T., and Wu, Y. T. (2019). Diindeno-fused dibenzo[a,h] anthracene and dibenzo[c,l]chrysene: Syntheses, structural analyses, and properties, *Chem. Eur. J.*, **25**, pp. 7280–7284.

109. Trost, B. M., and Kinson, P. L. (1975). Perturbed [12]annulenes: Derivatives of dibenzo[cd,gh]pentalene, *J. Am. Chem. Soc.*, **97**, pp. 2438–2449.

110. Kinson, P. S., and Trost, B. M. (1971). Dibenzo[cd,gh]pentaleno-4,8-quinone and its semiquinone radical anion: Model planar [12] annulene derivatives*, J. Am. Chem. Soc.*, **93**, pp. 3823–3825.

111. Zou, Y., Zeng, W., Gopalakrishna, T. Y., Han, Y., Jiang, Q., and Wu, J. (2019). Dicyclopenta[4,3,2,1-ghi:4′,3′,2′,1′-pqr]perylene: A bowl-shaped fragment of fullerene C70 with global antiaromaticity*, J. Am. Chem. Soc.*, **141**, pp. 7266–7270.

112. Wang, Q., Gopalakrishna, T. Y., Phan, H., Herng, T. S., Dong, S., Ding, J., and Chi, C. (2017). Cyclopenta ring fused bisanthene and its charged species with open-shell singlet diradical character and global aromaticity/anti-aromaticity*, Angew. Chem. Int. Ed.*, **56**, pp. 11415–11419.

113. Binsch, G., and Tamir, I. (1969). Double-bond fixation in conjugated pi-electron systems V: Self-consistent field calculations for nonalternant hydrocarbons and nitrogen heterocycles*, J. Am. Chem. Soc.*, **91**, pp. 2450–2455.

114. Louis, F., and Fieser, M. (1933). A synthesis of phthaloylnaphthol*, J. Am. Chem. Soc.*, **55**, pp. 3010–3018.

115. Cava, M., and Schlessinger, R. (1963). Reactive *o*-quinonoid aromatic hydrocarbons of the pleiadene series*, J. Am. Chem. Soc.*, **85**, pp. 835–836.

116. Kolc, J., and Michl, J. (1970). Photochemical synthesis of matrix-isolated pleiadene*, J. Am. Chem. Soc.*, **92**, pp. 4147–4148.

117. Downing, J., Dvorak, V., Kolc, J., Manzara, A., and Michl, J. (1972). Direct observation of a doubly excited-state of pleiadene*, Chem. Phys. Lett.*, **17**, pp. 70–73.

118. Kolc, J., and Michl, J. (1973). π, π-Biradicaloid hydrocarbons, Pleiadene family. I, Photochemical preparation from cyclobutene precursors*, J. Am. Chem. Soc.*, **95**, pp. 7391–7401.

119. Das, S., and Wu, J. (2015). Toward singlet–triplet bistable nonalternant Kekulé hydrocarbons: Azulene-to-naphthalene rearrangement*, Org. Lett.*, **17**, pp. 5854–5857.

120. Grieser, U., and Hafner, K. (1994). Synthesis and properties of kinetically stabilized cyclohepta[*def*]fluorene derivatives*, Chem. Ber.*, **127**, pp. 2307–2314.

121. Baumgartner, P., Weltin, E., Wagnière, G., and Heilbronner, E. (1965). Ist die molekel ein biradikal?*, Helv. Chim. Acta,* **48**, pp. 751–764.

122. Nendel, M., Goldfuss, B., Houk, K. N., Hafner, K., and Grieser, U. (1999). Bis-periazulene: A simple Kekulé biradical with a triplet ground state*, Theor. Chem. Acc.*, **102**, pp. 397–400.

123. Nendel, M., Goldfuss, B., Beno, B., Houk, K. N., Hafner, K., and Lindner, H. J. (1999). Theoretical studies of novel aromatic molecules and transition states, *Pure Appl. Chem.*, **71**, pp. 221–229.

124. Clar, E. (1949). Synthesen von benzologen des perylens und bisanthens. (Aromatische Kohlenwasserstoffe, XLVIII. Mitteil.). (Mitbearbeitet von H. Frömmel.), *Chem. Ber.*, **82**, pp 46–60.

125. Konishi, A., Horii, K., Shiomi, D., Sato, K., Takui, T., and Yasuda, M. (2019). Open-shell and antiaromatic character induced by the highly symmetric geometry of the planar heptalene structure: Synthesis and characterization of a nonalternant isomer of bisanthene, *J. Am. Chem. Soc.*, **141**, pp. 10165–10170.

126. Mishra, S., Lohr, T. G., Pignedoli, C. A., Liu, J., Berger, R., Urgel, J. I., Müllen, K., Feng, X., Ruffieux, P., and Fasel, R. (2018). Tailoring bond topologies in open-shell graphene nanostructures, *ACS Nano*, **12**, pp. 11917–11927.

127. Ajayakumar, M. R., Fu, Y., Ma, J., Hennersdorf, F., Komber, H., Weigand, J. J., Alfonsov, A., Popov, A. A., Berger, R., Liu, J., Müllen, K., and Feng, X. (2018). Toward full zigzag-edged nanographenes: peri-Tetracene and its corresponding circumanthracene, *J. Am. Chem. Soc.*, **140**, pp. 6240–6244.

128. Ni, Y., Gopalakrishna, T. Y., Phan, H., Herng, T. S., Wu, S., Han, Y., Ding, J., and Wu, J. (2018). A peri-tetracene diradicaloid: Synthesis and properties, *Angew. Chem. Int. Ed.*, **57**, pp. 9697–9701.

129. Liu, J., Mishra, S., Pignedoli, C. A., Passerone, D., Urgel, J. I., Fabrizio, A., Lohr, T. G., Ma, J., Komber, H., Baumgarten, M., Corminboeuf, C., Berger, R., Ruffieux, P., Müllen, K., Fasel, R., and Feng, X. (2019). Open-shell nonbenzenoid nanographenes containing two pairs of pentagonal and heptagonal rings, *J. Am. Chem. Soc.*, **141**, pp. 12011–12020.

130. Jiang, Q., Tao, T., Phan, H., Han, Y., Gopalakrishna, T. Y., Herng, T. S., Li, G., Yuan, L., Ding, J., and Chi, C. (2018). Diazuleno-s-indacene diradicaloids: Syntheses, properties, and local (anti)aromaticity shift from neutral to dicationic State, *Angew. Chem. Int. Ed.*, **57**, pp. 16737–16741.

131. Nakajima, T. (1971). Bond distortions in nonalternant hydrocarbons, *Pure Appl. Chem.*, **28**, pp. 219.

132. Hess Jr, B. A., and Schaad, L. (1971). Hueckel molecular orbital π resonance energies: Nonalternant hydrocarbons, *J. Org. Chem.*, **36**, pp. 3418–3423.

133. Boehm, M. C., and Schuett, J. (1992). Correlation effects and electron delocalization in nonalternant hydrocarbon π compounds, *J. Phys. Chem.*, **96**, pp. 3674–3683.

134. Yang, X., Shi, X., Aratani, N., Gonçalves, T. P., Huang, K.-W., Yamada, H., Chi, C., and Miao, Q. (2016). Benzo[4,5]cyclohepta[1,2-b]fluorene: An isomeric motif for pentacene containing linearly fused five-, six-, and seven-membered rings, *Chem. Sci.*, **7**, pp. 6176–6181.

135. Fu, X., Han, H., Zhang, D., Yu, H., He, Q., and Zhao, D. (2020). A polycyclic aromatic hydrocarbon diradical with pH-responsive magnetic properties, *Chem. Sci.*, **11**, pp. 5565–5571.

136. Bally, T., and Masamune, S. (1980). Cyclobutadiene, *Tetrahedron*, **36**, pp. 343–370.

137. Berris, B. C., Hovakeemian, G. H., Lai, Y. H., Mestdagh, H., and Vollhardt, K. P. C. (1985). A new approach to the construction of biphenylenes by the cobalt-catalyzed cocyclization of o-diethynylbenzenes with alkynes: Application to an iterative approach to [3]phenylene, the first member of a novel class of benzocyclobutadienoid hydrocarbons, *J. Am. Chem. Soc.*, **107**, pp. 5670–5687.

138. Jin, Z., Teo, Y. C., Teat, S. J., and Xia, Y. (2017). Regioselective synthesis of [3]naphthylenes and tuning of their antiaromaticity, *J. Am. Chem. Soc.*, **139**, pp. 15933–15939.

139. Jin, Z., Teo, Y. C., Teat, S. J., and Xia, Y. (2018). Iterative synthesis of edge-bent [3]naphthylene, *Synlett*, **29**, pp. 2547–2551.

140. Qiu, S., Wang, C., Xie, S., Huang, X., Chen, L., Zhao, Y., and Zeng, Z. (2018). Toward helical-shaped diradicaloids: Cyclobutenyl o-quinodimethane-bridged indeno[1,2-b]fluorenes, *Chem. Commun.*, **54**, pp. 11383–11386.

141. Qiu, S., Zhang, Y., Huang, X., Bao, L., Hong, Y., Zeng, Z., and Wu, J. (2016). 9-Ethynylfluoroenyl radicals: Regioselective dimerization and post ring-cyclization reactions, *Org. Lett.*, **18**, pp. 6018–6021.

142. Hellwinkel, D., and Reiff, G. (1970). Cyclooctatetraene systems flattened by steric constraints, *Angew. Chem. Int. Ed.*, **9**, pp. 527–528.

143. Nobusue, S., Miyoshi, H., Shimizu, A., Hisaki, I., Fukuda, K., Nakano, M., and Tobe, Y. (2015). Tetracyclopenta[def,jkl,pqr,vwx]tetraphenylene: A potential tetraradicaloid hydrocarbon, *Angew. Chem. Int. Ed.*, **54**, pp. 2090–2094.

## Chapter 10

# Photo-Responsive Diradicaloids

**Jiro Abe,[a] Katsuya Mutoh,[a] and Yoichi Kobayashi[b]**
[a]*Department of Chemistry, Aoyama Gakuin University,*
*5-10-1 Fuchinobe, Chuo-ku, Sagamihara, Kanagawa 252-5258, Japan*
[b]*Department of Applied Chemistry, Ritsumeikan University,*
*1-1-1 Nojihigashi, Kusatsu, Shiga 525-8577, Japan*
jiro_abe@chem.aoyama.ac.jp

We have investigated the electronic structures and the reaction kinetics of the transient biradicals generated by photochromic reaction of radical-dissociative photochromic molecules. This photochromic system causes not only a color change, but also a large change in the spin state. Some of them show the valence isomerization from the open-shell biradical to the closed-shell quinoidal form. The valence isomerization effectively tunes the open-shell feature in time and drastically changes the spectral features. Moreover, we found that visible-light excitation to the quinoidal form causes valence photoisomerization to form the biradical.

*Diradicaloids*
Edited by Jishan Wu

ISBN 978-981-4968-08-9 (Hardcover), 978-1-003-27724-8 (eBook)
www.jennystanford.com

## 10.1 Introduction

It is well known that a certain type of polycyclic aromatic hydrocarbons has singlet biradical character in the ground state [1–15]. The strong antiferromagnetic interaction between unpaired electrons in an open-shell singlet biradical eventually makes a covalent bond and stabilizes a closed-shell quinoidal form. The magnitude of the spin–spin interaction of biradical depends on the π-conjugation scaffold connecting the two spin centers, and singlet biradicals can be usually described as a resonance hybrid of biradical and quinoidal forms. Molecules with significant biradical character in the ground state are known as diradicaloids [8]. Due to the contribution of biradical character, quinoidal molecules may have reactivity characteristic of biradicals. The historically representative diradicaloid is Chichibabin's hydrocarbon [16, 17]. The electronic structure of Chichibabin's hydrocarbon has been studied in detail and is accepted to have a large biradical character in the ground state [18]. On the other hand, a large deviation from the planarity weakens the interaction between the two spin centers, resulting in the splitting of the energy levels of biradical and quinoidal forms [19, 20]. Thus, the flexibility of the molecular framework determines whether biradical and quinoidal forms are present as a resonance hybrid or as a thermal equilibrium [3, 6].

One of the examples of which has distinct biradical and quinoidal forms is tetrabenzo-Chichibabin's hydrocarbon. Wu and coworkers reported the irreversible thermal valence isomerization from the unstable biradical to the stable quinoidal form of newly designed tetrabenzo-Chichibabin's hydrocarbon [21]. Unlike the parent Chichibabin's hydrocarbon, tetrabenzo-Chichibabin's hydrocarbon is not a planar molecule, due to the large steric hindrance caused by the two anthracene sites. The freshly generated electron spin resonance (ESR)-active biradical monoexponentially decays to the ESR-silent quinoidal form with a half-life of 495 min at 298 K. Thus, the presence of the two valence isomers was clearly confirmed in tetrabenzo-Chichibabin's hydrocarbon. They also determined the thermodynamic parameters for this decay process. Though this is a one-way chemical reaction, it is noteworthy as the first paper to report the dynamic behavior of the valence isomerization from a biradical to a quinoidal form.

Another example of such a valence isomerization is found in the intramolecular imidazole dimers exhibiting photochromism. Photochromism is defined as a reversible transformation of a chemical species between two isomers having different absorption spectra induced in one or both directions by irradiation of light. Imidazole dimers are radical-dissociation-type photochromic molecules that generate imidazolyl radicals upon UV light irradiation and the photogenerated radicals thermally return to the parent imidazole dimer by the radical coupling reaction [22–28]. On the other hand, the photochromic reaction of the intramolecular imidazole dimers involves the valence isomerization from the biradical to the quinoidal form. While light irradiation to the intramolecular imidazole dimers gives the transient biradical composed of two imidazolyl radical units in the early stage of the photochemical reaction, the spin–spin interaction between the two imidazolyl radical units causes the valence isomerization that leads to the formation of the quinoidal form. That is, the photogenerated biradical thermally equilibrates with the quinoidal form and the equilibrated two forms return to the initial imidazole dimer with a time scale of milliseconds to seconds [29–32]. In this chapter, we describe the details of the kinetics of the biradical–quinoidal equilibrium and the unprecedented photoresponse of the equilibrium, leading to break fresh ground for the photochemistry of singlet biradical.

## 10.2 Pentaarylbiimidazole

Hexaarylbiimidazole (HABI, Scheme 10.1a) generates a radical pair upon UV light irradiation and the radical pair gradually returns to the initial form with a time scale of tens of seconds to minutes when light irradiation is stopped [22, 23]. By connecting two imidazolyl radicals with a molecular linker such as [2.2]paracyclophane ([2.2]PC, Scheme 10.1b) [26] and naphthalene [25], the rates of the radical recombination are greatly accelerated to sub-milliseconds to seconds. These fast and reversible reactions can quickly switch various optical properties, such as color, emission, and refractive index, by shining light. Therefore, these photochromic molecules can be applied to holographic movies [33–35] and fluorescence switching [36–38]. Moreover, these fast-responsive photochromic

molecules are also interesting from the viewpoint of spin chemistry. For example, the imidazolyl radicals of [2.2]PC-bridged imidazole dimers are close enough to interact electronically, and therefore, the optical and spin properties of these radicals are different from individual radicals of HABI. For example, colors of the radical pairs of bridged imidazole dimers are different (such as blue and green) from that of triphenylimidazolyl radical (reddish purple) because of the through-space spin–spin interaction. It is expected that the spin–spin interaction between the radicals becomes stronger when two radicals are covalently connected by σ- and π-bonds. It is interesting to investigate how the optical properties and the open-shell character of a biradical change by the through-bond spin–spin interaction.

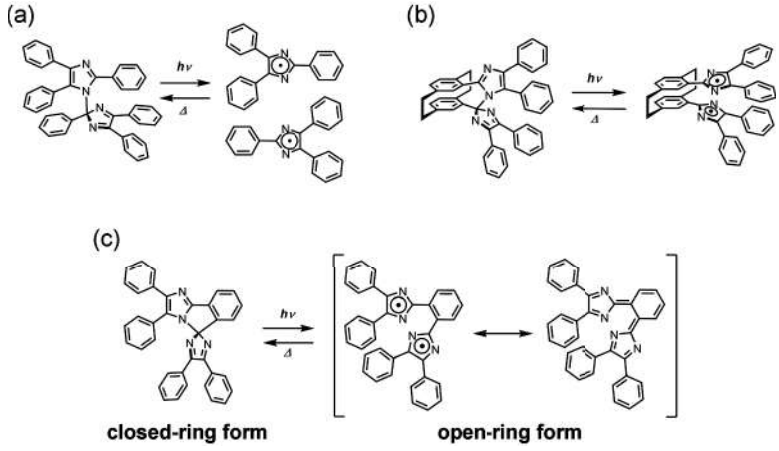


**Scheme 10.1** Photochromism of (a) HABI, (b) [2.2]PC-bridged imidazole dimer, and (c) PABI.

A simple architecture to impart the through-bond spin–spin interaction to a pair of imidazolyl radicals is to connect the two imidazolyl radicals with a phenyl ring as shown in Scheme 10.1c, i.e. pentaarylbiimidazole (PABI) [39]. The π-electronic structure of PABI is considered to be topologically equivalent to that of *o*-quinodimethane [40]. *o*-Quinodimethane has a singlet ground state as predicted by Ovchinnikov's rule and has been studied for a fundamental model of biradical. Moreover, it is expected that the

biradical property of PABI dynamically changes in the process of relaxing from the structure immediately after formation to a stable structure of the biradical. Namely, two imidazole rings of PABI are orthogonally aligned in the closed-ring form. Therefore, there are few spin–spin interactions between the two imidazolyl radicals just after the bond cleavage. However, after the bond breaking by light irradiation, the dihedral angles between imidazole rings and the phenylene linker gradually decrease and the spin–spin interaction becomes stronger, due to the through-bond spin–spin interaction. Dynamic behaviors of biradical properties have been recently reported in several systems, such as tetrabenzo-Chichibabin's hydrocarbon [21] and phenoxyl-imidazolyl radical complex (PIC) derivatives [29] (shown later). These dynamic evolutions of biradical properties are not only important for fundamental radical chemistry, but also for developing advanced photofunctional materials [41].

Figure 10.1a shows the Oak Ridge Thermal Ellipsoid Plot (ORTEP) representation of the molecular structure of PABI. Two imidazole moieties are almost perpendicular to each other. The C–N bond length between the two imidazole rings of PABI (1.459 Å) is shorter than those of HABI derivatives, owing to the spiroconjugation. For example, the C–N bond length of [2.2]PC-bridged imidazole dimer is 1.488 Å [26]. The photochromic behavior of HABI is described by the photoinduced homolytic cleavage of the C–N bond between the imidazole rings and the thermal radical recombination [42, 43]. The ESR measurements under UV light irradiation (365 nm) revealed that the photogenerated transient species of PABI are radicals with unpaired electrons. This result indicates that the homolytic bond cleavage occurs in PABI as similar to HABI. The ESR signal intensities of the open-ring form increase with the increase in temperature from −195 to −73 °C [39]. That is, the open-ring form of PABI has the singlet ground state and the population of the thermally excited triplet state increases with increasing temperature. Therefore, the electron spins of the open-ring form of PABI interact anti-ferromagnetically with each other. On the other hand, the ESR signal intensity begins to decrease sharply, due to the radical recombination to form the closed-shell imidazole dimer by increasing the temperature above −73 °C.

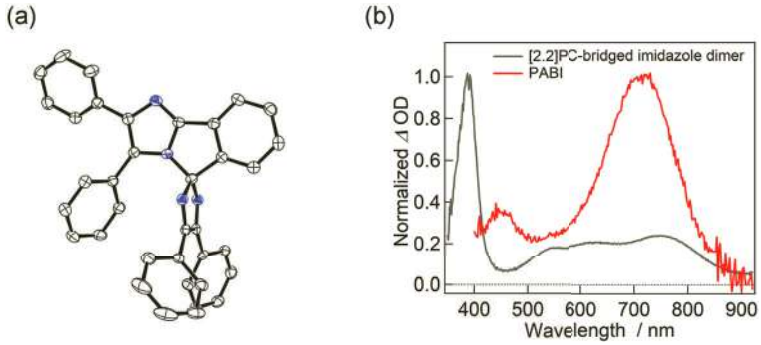


**Figure 10.1** (a) ORTEP representation of the molecular structure of PABI with thermal ellipsoids (50% probability), where nitrogen atoms are highlighted in blue. (b) Normalized transient absorption spectra of PABI and [2.2]PC-bridged imidazole dimer in degassed benzene at 298 K (excitation wavelength, 355 nm; pulse width, 5 ns; and power 4 mJ/pulse).

Figure 10.1b shows the nanosecond-to-millisecond transient absorption spectra of PABI and [2.2]PC-bridged imidazole dimer in degassed benzene. As can be expected from the large difference in the molecular structures, the spectral shape of the open-ring form of PABI is quite different from that of the colored species of [2.2] PC-bridged imidazole dimer. The remarkable feature is the intense absorption band at 715 nm. It is known that the absorption band of the colored species of [2.2]PC-bridged imidazole dimer at 750 nm is due to the through-space radical-radical interaction [44]. The absorption band at the 715 nm region of PABI is also attributable to the radical–radical interaction, which is supported by the TDDFT calculations (UB3LYP/6-31+G(d,p)). This result indicates that the spin–spin interaction of the open-ring form of PABI is stronger than the colored species of bridged imidazole dimers. The α- and β-spins in the colored species of the [2.2]PC-bridged imidazole dimers are localized on each imidazole rings. In that case, the through-space spin–spin interaction is dominant. On the other hand, in the open-ring form of PABI, the through-bond spin–spin interaction is considered to play an important role, due to the spin delocalization from one imidazole ring to another ring via the phenyl group. The generated open-ring form decays monoexponentially with a half-life of 2 μs in benzene at 298 K. The signal amplitude of the open-ring form does not decrease at all even after 13,000 shots of the

355 nm laser pulses (the pulse duration and the power are 5 ns and 4 mJ, respectively), indicating that the photogenerated biradicaloid species of PABI is durable.

The dynamic behavior, including changes in spin state during the biradical formation and recombination process, is important for demonstrating the nature of chemical bonds and applying biradicals to advanced photofunctional materials. To reveal the dynamical process of the biradical of PABI in detail, we conducted ultrafast visible and infrared (IR) absorption measurements and quantum chemical calculations with the multireference wavefunction theory, referred to as the extended multi-state complete active space second-order perturbation (XMS-CASPT2) theory [30]. Figure 10.2a shows the total energies of the singlet ground state ($S_0$) and four lowest-lying singlet excited states ($S_1$ to $S_4$) of PABI obtained by the XMS-CASPT2 method, as a function of the reaction coordinate, i.e. the distance between the C and N atoms, which connect two imidazole rings in the closed-ring form. The potential energy curves were modeled using the density functional theory (DFT) calculations at UCAM-B3LYP/def2-SVP level of the theory [45]. For the formation process of the open-ring form, we considered the singlet states because the extremely fast bond breaking process (~140 fs, as shown later) suggests that the triplet excited state is not involved in the bond breaking process (the intersystem crossing usually takes several hundreds of picoseconds to nanoseconds) [46]. The generation and recombination of the biradical of PABI can be interpreted as follows. After the excitation of the closed-ring form by UV light irradiation, the energy quickly relaxes to the $S_1$ state ((i) in Figure 10.2a). It is noted that the $S_1 \leftarrow S_0$ transition is optically forbidden. The C–N bond between the imidazole rings is homolytically cleaved most probably through the conical intersection between the $S_0$ and $S_1$ potential curves ((ii) in Figure 10.2a). The two radicals generated immediately after the bond cleavage should be a pair of individual radicals. Then, the spin–spin interaction between the radicals gradually becomes stronger with the decrease in the dihedral angles between the imidazole rings and the phenylene linker, and the open-ring isomer is formed ((iii) in Figure 10.2a). The open-ring form thermally reverts to the closed-ring form through the $S_0$ potential curve.

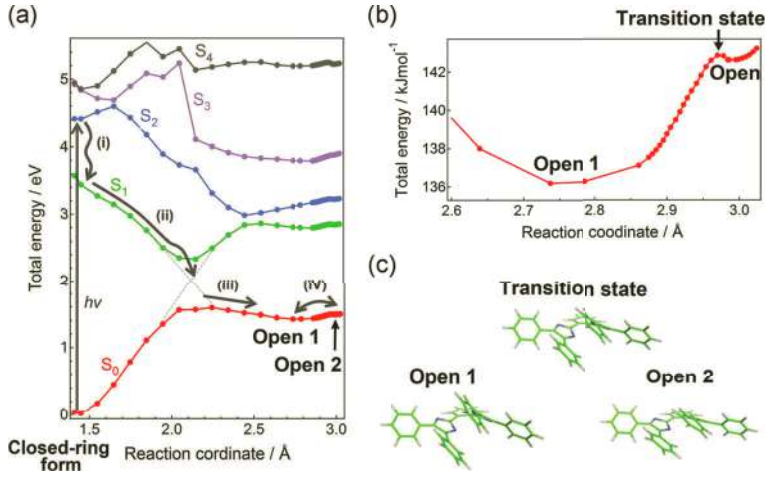


**Figure 10.2** (a) Potential energy curves of the $S_0$ to $S_4$ states obtained by the combinations of DFT calculations (UCAM-B3LYP/def2-SVP level of the theory) and XMS-CASPT2 calculations, (b) magnified potential curve of the $S_0$ state around the open-ring isomer, and (c) optimized molecular structures of the Open 1, Open 2, and transition state of PABI. Dashed lines in (a) indicate a schematically illustrated conical intersection.

Figure 10.2b shows the magnified potential energy curve around the open-ring form. The figure suggests that the open-ring form has two metastable states, namely Open 1 (lower energy) and Open 2 (higher energy). The energy difference between the Open 1 and Open 2 is 4.27 kJ/mol and 5.48 kJ/mol for the DFT-PCM (polarizable continuum model) calculations with the solvents, benzene and dichloromethane, respectively. These values are in the order of the thermal fluctuation energy at room temperature (~2.5 kJ/mol). Therefore, this result suggests that the photogenerated open-ring form is in the thermal equilibrium between Open 1 and Open 2 ((iv) in Figure 10.2a). Figure 10.2c shows the optimized molecular structures of Open 1, Open 2, and the transition state. The main difference between the molecular structures of Open 1 and Open 2 is the dihedral angle between the imidazole rings and the phenylene linker, namely 31.0° and 22.5° for Open 1 and Open 2, respectively. Notably, there is a substantial van der Waals interaction between the phenyl rings substituted at the imidazole rings.

The configuration analysis on the reference CASSCF wavefunctions characterizes the open-ring form mainly as the open-

shell singlet biradical configuration with a weight of ca. 86.3% and 84.8% for Open 1 and Open 2, respectively. The rest of the description arises primarily from the closed-shell configuration, corresponding to the quinoidal structure, with a weight of 8.6% and 9.9% for Open 1 and Open 2, respectively. Overall, the biradical character is slightly more weighted toward Open 1 relative to Open 2, while the quinoidal character is less. This result suggests that Open 1 has a larger amount of open-shell biradical character than Open 2. This result is related to the larger dihedral angle between the imidazole rings and the phenylene linker of Open 1.

To prove the formation process of the biradical of PABI predicted by the quantum chemical calculation, we conducted ultrafast visible and IR transient absorption measurements of PABI. Figure 10.3a shows the visible transient absorption spectra of PABI in benzene excited at 330 nm of a femtosecond laser pulse. At 220 fs after the excitation, broad transient absorption bands were observed over the visible region, which is assigned to the transition from the $S_1$ to $S_n$ states [47, 48]. The absorption band due to the $S_n \leftarrow S_1$ transition quickly decays with a time constant of 140 fs and other transient absorption bands appear at 470 nm and 725 nm within 1 ps. This transient spectrum is similar to that of the open-ring form found in the photochromic reaction of PABI. Therefore, this result shows that the bond cleavage process occurs with the time constant of 140 fs. The transient absorption bands at 470 nm and 725 nm gradually shift to 450 nm and 707 nm, respectively, with a time scale of several picoseconds. Although the initial fast decay with a time scale of hundreds of femtoseconds was observed in similar photochromic imidazole dimers such as HABI and bridged imidazole dimers [47–49], the spectral shift and the large increase in the signal with a time scale of picoseconds have not been observed. The multireference multi-state calculations suggest that the absorption bands appear at 521 nm and 732 nm in Open 1 and 517 nm and 714 nm in Open 2, which are consistent with the observed spectral shift (from 470 nm and 725 nm to 450 nm and 707 nm). Therefore, the spectral shift observed by the visible spectroscopy at a picosecond time scale indicates that the initially generated Open 1 equilibrates to Open 2.

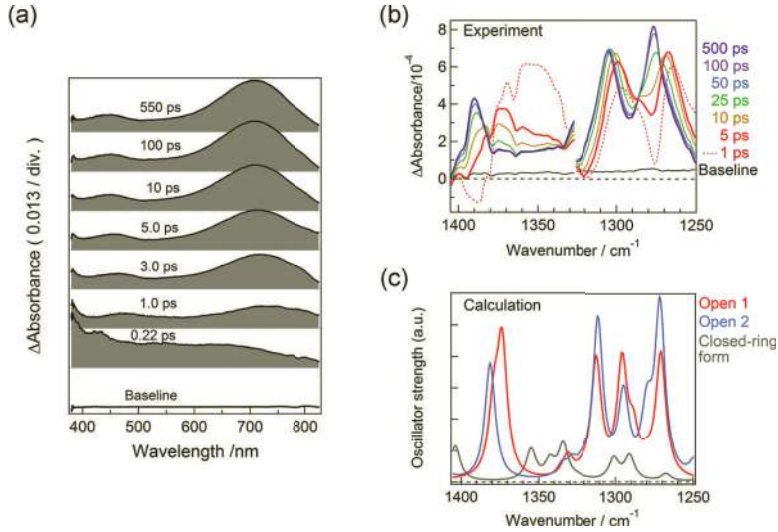


**Figure 10.3** (a) Transient absorption spectra of PABI in benzene ($3.1\times10^{-3}$ M) at the visible region excited at 330 nm of a femtosecond laser pulse (~25 fs, 200 nJ/pulse), (b) time-resolved IR spectra of PABI in $CD_2Cl_2$ ($\sim3\times10^{-2}$ M) excited at 330 nm (~100 fs, 3 μJ /pulse) at room temperature, and (c) calculated IR absorption spectra of Open 1, Open 2, and closed-ring form (UCAM-B3LYP/def2-SVP level of the theory). The scaling factor (0.970) was multiplied to the calculated IR wavenumbers.

Figures 10.3b and 10.3c show the time-resolved IR spectra of PABI in $CD_2Cl_2$ excited at 330 nm at room temperature and the calculated IR spectra of Open 1, Open 2, and the closed-ring form by the broken-symmetry DFT method (UCAM-B3LYP-D3BJ/def2-SVP level of the theory), respectively. At 1 ps after the excitation, several transient absorption bands are observed, namely, the narrow bands at 1267 $cm^{-1}$, 1300 $cm^{-1}$, and 1375 $cm^{-1}$, a shoulder band at 1285 $cm^{-1}$, and a broad band around 1350 $cm^{-1}$. The broad absorption band around 1350 $cm^{-1}$ quickly decays within several picoseconds. The absorption band at 1360 $cm^{-1}$ most probably reflects the transient structures between the $S_1$ state and Open 1 on the potential curve and the vibrational cooling process. The transient absorption spectrum at 5 ps is very similar to those of Open 1 (red curve) and Open 2 (blue curve) obtained by the DFT calculations as shown in Figure 10.3c. The transient absorption bands gradually shift to the higher wavenumber with a time scale of several picoseconds

with an isosbestic point at 1287 $cm^{-1}$. The isosbestic point shows that this process is not due to the vibrational cooling, but due to a reaction between two states. These spectral shifts can be explained by the spectral evolution caused by the interconversion from Open 1 to Open 2. These experimental results are consistent with those by quantum chemical calculations, and these results show that the spin–spin interaction between the radicals is dynamically evolved during the formation of the biradical of PABI.

In conclusion of this section, we developed a new type of photoresponsive radical dimer, PABI, and revealed the ultrafast formation dynamics of the biradical of PABI. Femtosecond visible and IR absorption spectroscopies detect the dynamic equilibrium process between the two states whose biradical contributions are different with a time scale of picoseconds. Photoresponsive dynamic diradicaloid materials will stimulate to explore further flexible and delocalized biradical systems.

## 10.3 Phenoxyl-Imidazolyl Radical Complex

The photochromic dimers generating two radicals via the homolytic bond-breaking reaction of N–N or C–N bonds upon light irradiation have been reported from the 1960s. HABI, PABI, tetraphenylhydrazine, and tetraphenylpyrryl are the typical examples of the photochromic molecules generating two structurally identical radicals [22, 23, 50, 51]. On the other hand, no photochromic molecules generating two structurally and electronically different radicals have been previously reported. Thus, we have reported a novel type of the photochromic molecules, PIC (Scheme 10.2a), which generates two different radicals, a phenoxyl radical and an imidazolyl radical, upon light irradiation [52]. The basic concept of the molecular design of PIC is inspired by the similarities in the reactivity of the oxidation products between phenol and imidazole.

The intramolecular recombination between the phenoxyl and imidazolyl radicals forms the colorless closed-ring isomer. The four different PIC derivatives (**PIC1–4**) were synthesized and the structures of the closed-ring isomers were determined by X-ray diffraction analysis of the single crystals (Scheme 10.2b and Figure 10.4). The results suggest that the thermal intramolecular

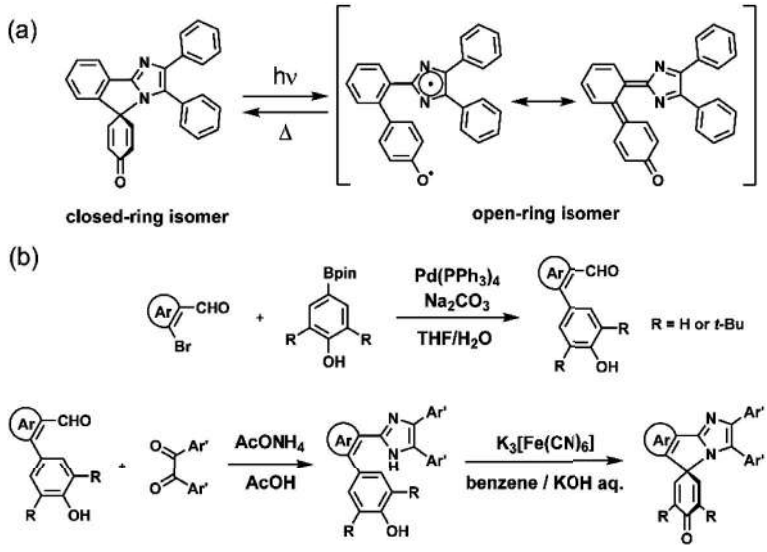


**Scheme 10.2** (a) Photochromism and (b) synthetic scheme of PIC.

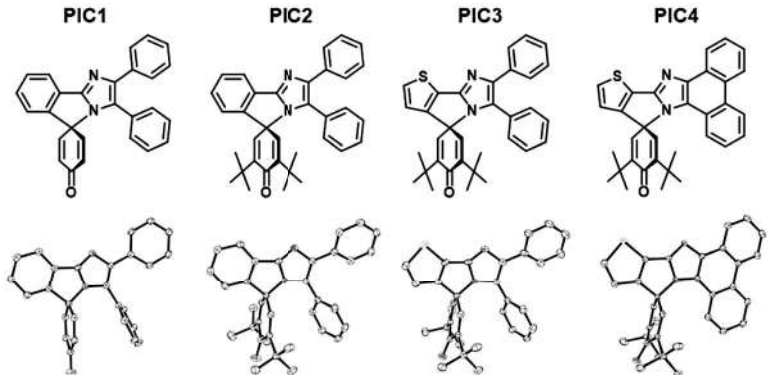


**Figure 10.4** Molecular structures and ORTEP representations of **PIC1–4** with thermal ellipsoids (50% probability), where nitrogen, oxygen, and sulfur atoms are highlighted in blue, red, and green, respectively.

recombination reaction between the phenoxyl and imidazolyl radicals forms the closed-ring isomers possessing the intramolecular C–N bond as similar to the other photochromic imidazole dimers [26, 39]. The PIC derivatives show the photo-induced homolytic breaking of the C–N bond upon UV light irradiation. The DFT calculations of

the PIC derivatives revealed that the frontier molecular orbitals (HOMOs and LUMOs) of the closed-ring isomers of the PIC derivatives are distributed similarly to those of PABI. The ultrafast time-resolved spectroscopy and the electrochemical measurement of the photochromic imidazole dimers have revealed that the anti-bonding characteristic of the C–N bond of the LUMO is the key characteristic to be induced the homolytic C–N bond-breaking reaction caused by light irradiation [44, 47, 49, 53–56]. The DFT calculations indicate that the lowest excited states of the PIC derivatives have similar anti-bonding characters. It suggests the PIC derivatives show the homolytic breaking to produce the open-ring isomer (biradical) upon light irradiation. The laser flash photolysis was performed to investigate the photochromic reactions of the PIC derivatives. Figure 10.5 shows the transient absorption spectra and the time variations of the transient absorbance at the maximum absorption wavelength. The absorption bands of the open-ring isomer cannot be reproduced by a superposition of the absorption spectra of the individual 2,4,5-triphenylimidazolyl radicals and 2,6-di-*tert*-butyl-4-phenylphenoxyl radical because the imidazolyl and the phenoxyl radicals show the absorption bands at around 500–600 nm in addition to the bands at around 400–450 nm [57]. The characteristic large absorption bands in the near-infrared (NIR) light region (600–850 nm) are attributable to the intramolecular radical-radical interaction of the imidazolyl and the phenoxyl radicals. The shape of the absorption spectra and the decay profiles are not affected by the presence of molecular oxygen, indicating no contribution of the triplet biradical to the transient species at room temperature. Because the open-ring form of the PIC derivatives exists as a resonance hybrid of the open-shell biradical and the closed-shell quinoidal structures, the correct electronic structure of the open-ring isomer could not be obtained by a single Slater determinant wavefunction calculated by a simple DFT calculation. That is, the wavefunction of the open-ring isomer cannot be described either by an open-shell biradical state or a closed-shell quinoidal state. Therefore, further discussion by the reactivity of the open-ring isomer will be required to predict the biradical character as discussed later. The photochromic reaction of **PIC1** is highly fatigue resistant because no significant changes were observed in the decay profile of the transient absorbance after irradiation with 13,000 shots of nanosecond laser pulses

(355 nm, 4 mJ). The diphenylimidazolyl radical is kinetically and thermodynamically stabilized by the phenyl rings. On the other hand, although phenoxyl radicals with bulky substituents such as tert-butyl groups are kinetically stabilized, it has been known that a phenoxyl radical unencumbered by bulky substituents is highly reactive [58]. However, **PIC1** shows a highly durable photochromic reaction against the repeated laser irradiation. This means the intramolecular reaction between the phenoxyl radical and the imidazolyl radical preferentially takes precedence over the other intermolecular side reactions. Therefore, both the rapid intramolecular recombination reaction and the thermodynamic stabilization of the radicals by the electron delocalization are important to develop the highly durable photochromic molecules [59]. The half-lives of the colored open-ring isomers of **PIC1**, **PIC2**, **PIC3**, and **PIC4** were estimated to be $2.5 \times 10^{-7}$ s, $2.6 \times 10^{-8}$ s, 1.1 s, and $6.6 \times 10^{-3}$ s, respectively. These results suggest that the replacement of the bridging phenyl ring by the thienyl ring significantly decelerates the thermal back reaction of the open-ring isomer. The deceleration can be explained by the geometric and electronic characteristics of the thienyl ring. The molecular structures of the open-ring isomers of **PIC3** and **PIC4** will be more planar conformations, compared with those of **PIC1** and **PIC2** because the five-membered ring of the thienyl ring reduces the steric repulsion between the phenoxyl and imidazolyl rings compared to the six-membered ring. Besides, the thienyl bridge increases the distance between the reactive carbon and nitrogen atoms making the C–N bond, leading to the deceleration of the rate of the thermal recombination reaction. It has been known that thienyl rings have less aromaticity than phenyl rings. The electronic structure of the open-ring isomer can be described by the resonance hybrid of the open-shell biradical and the closed-shell quinoidal contributing structures by the valence bond theory. The quinoidal contributing structure forming π-bonds between the bridging aromatic ring and the imidazolyl or the phenoxyl ring is stabilized by the bonding energy, whereas it loses the aromatic stabilization energy of the bridging unit. Because the thienyl ring has less aromaticity than the phenyl ring, the contribution of the quinoidal structure to the open-ring isomer is larger than the biradical structure, leading to the deceleration of the thermal back reaction. Meanwhile, the open-ring isomer of **PIC4** shows the thermal back reaction relatively faster

than that of **PIC3**. Because the replacement of the diphenylimidazole by a rigid phenanthroimidazole increases the steric hindrance between the phenanthroimidazole and the *tert*-butyl phenoxyl ring, the open-ring isomer is destabilized, resulting in the acceleration of the thermal back reaction.

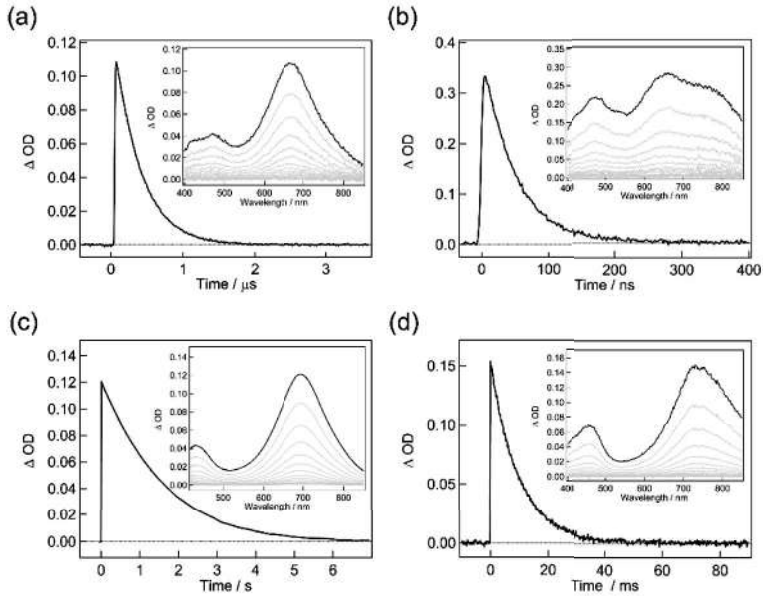


**Figure 10.5** Time profiles of the transient absorbance and transient absorption spectra of (a) **PIC1**, (b) **PIC2**, (c) **PIC3**, and (d) **PIC4** in degassed benzene at 298 K ($\lambda_{ex}$ = 355 nm, pulse width = 5 ns, and energy = 4 mJ/pulse).

We also designed and synthesized a PIC derivative, reversed PIC (**RPIC**), with the flipping imidazole ring [29, 31]. The flipping of the imidazole ring decreases the spin–spin interaction between the imidazolyl radical and the phenoxyl radical. **RPIC** shows the unusual sequential photochromic reaction involving the biradical–quinoidal valence isomerization. Especially, the transient absorption spectroscopy and the time-resolved Fourier transform infrared (FTIR) spectroscopy of 1-pyrene-substituted RPIC (**Py-RPIC**) give definitive evidence of the biradical–quinoidal valence isomerization. The transient absorption spectra of **Py-RPIC** at 298 K in benzene upon 355 nm laser irradiation are shown in Figure 10.6. The two broad transient absorption bands at 530 nm and 850 nm are observed at

100 ns after the laser irradiation. The transient absorption spectrum thermally changes to the other spectrum with an isosbestic point at 425 nm within a microsecond. The isosbestic point suggests the thermal isomerization of the transient species with no side reactions. The time constants of the rise profile at 400 nm and the decay profile at 520 nm are consistent and estimated to be $3.65\times10^{6}$ $s^{-1}$. After the isomerization, the transient species monoexponentially decays with a time constant of $1.98\times10^{2}$ $s^{-1}$. Because these time constants of the fast and slow decay components are not affected by the presence of molecular oxygen, the triplet state is not involved in the decay kinetics after light irradiation. The factor analysis by using a singular value decomposition (SVD) algorithm and the global fitting to the two-state equilibrium model were performed to reveal the pure absorption spectra of the biradical and the quinoidal forms [60–62]. The analyzed absorption spectra corresponding to the biradical and quinoidal forms are shown in Figure 10.7.

The time-resolved FTIR spectroscopy by using a step scan technique was performed to reveal the molecular structures of the transient species in the sequential photochromic reaction of **Py-RPIC**. Figure 10.8 shows the time-resolved FTIR spectra of **Py-RPIC** in $CD_2Cl_2$ ($3\times10^{-2}$ M) upon 355 nm nanosecond laser pulse excitation at room temperature. The three characteristic FTIR peaks at 1305 $cm^{-1}$, 1351 $cm^{-1}$, and 1375 $cm^{-1}$ and the bleach signals of the ground state at 1673 $cm^{-1}$ were observed at 100 ns after laser irradiation. The three peaks can be assigned to the vibrational modes derived from the imidazolyl radical substituted by a pyrene moiety because of the similarity to the FTIR peaks of the individual pyreno-imidazolyl radical. On the other hand, the strong FTIR peak at 1582 $cm^{-1}$, which can be assigned to the vibrational peak of the C–O stretching mode, indicates the generation of the phenoxyl radical [57, 63]. Therefore, it is suggested that the initial transient species generated by irradiation with UV light is the open-shell biradical form. The rise of the new peak at 1630 $cm^{-1}$ was observed along with the decay of the peak at 1582 $cm^{-1}$, indicating the carbonyl bond of the phenoxyl radical is tightened by the thermal isomerization of the biradical form within hundreds of nanoseconds. That is, the photogenerated biradical form thermally equilibrated to the quinoidal form. The equilibrated state reverts to the initial closed form with a time scale of milliseconds.

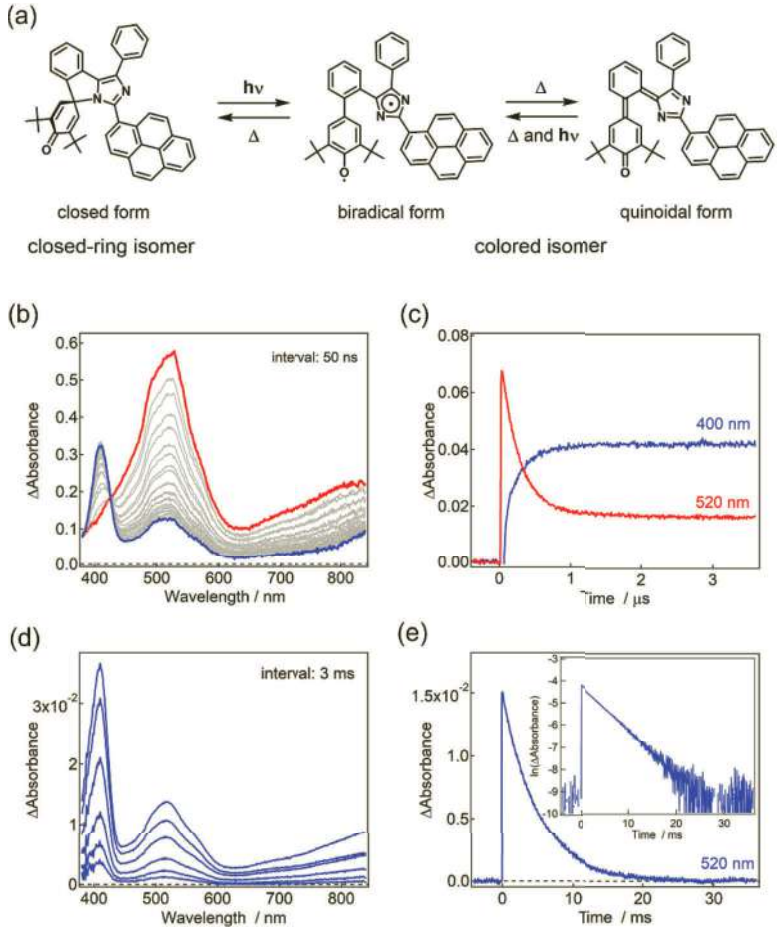


**Figure 10.6** (a) Transient absorption spectra and (b) the dynamics observed at 400 nm and 520 nm of **Py-RPIC** in benzene ($5.7 \times 10^{-5}$ M) at room temperature ($\lambda_{ex}$ = 355 nm, 5 mJ/pulse). (c) Transient absorption spectra and (d) dynamics of **Py-RPIC** observed at 520 nm at millisecond time scales.

We also investigated the temperature dependence of the thermal back reaction to the closed-ring form. The activation parameters, $\Delta H^{\ddagger}$, $\Delta S^{\ddagger}$, and $\Delta G^{\ddagger}$, estimated by the Eyring analysis are 52.6 kJ mol$^{-1}$, −24.9 J K$^{-1}$ mol$^{-1}$, and 60.0 kJ mol$^{-1}$, respectively. The rate constants of the forward reaction ($k_A$) and the backward reaction ($k_B$) for the thermal equilibrium estimated by the global analysis are $2.90 \times 10^6$ and $0.76 \times 10^6$ s$^{-1}$, respectively, at 298 K. Therefore, the equilibrium constant of the biradical–quinoidal equilibrium is estimated to be

3.8. The activation parameters for the forward and the backward reactions were also determined by the Eyring analysis from the temperature dependence of the rate constants. The $\Delta H^{\ddagger}$, $\Delta S^{\ddagger}$, and $\Delta G^{\ddagger}$ at 298 K for the forward reaction were 29.3 kJ mol$^{-1}$, −22.9 J K$^{-1}$ mol$^{-1}$, and 36.1 kJ mol$^{-1}$, respectively. Similarly, those for the backward reaction were 34.7 kJ mol$^{-1}$, −15.3 J K$^{-1}$ mol$^{-1}$, and 39.3 kJ mol$^{-1}$, respectively. The $\Delta G_0$ is determined to be 3.18 kJ mol$^{-1}$ by subtracting the $\Delta G^{\ddagger}$ of the forward reaction from that of the backward reaction. Thus, the thermodynamic parameters for the biradical–quinoidal equilibrium were revealed from the experimental results for the first time.

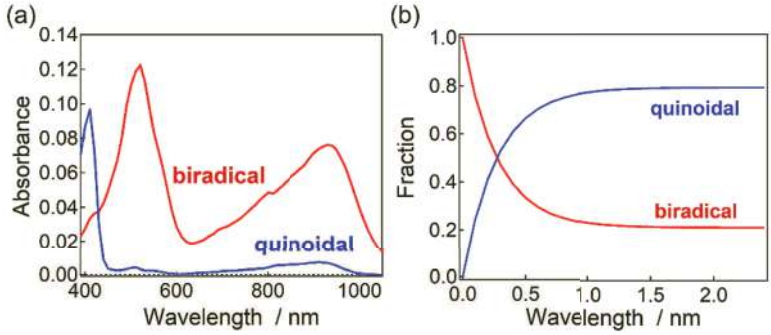


**Figure 10.7** (a) The resolved pure spectra of the biradical and the quinoidal forms obtained by the global analysis. (b) The associated pure fraction profiles for the biradical and quinoidal forms determined by the global analysis.

We demonstrated the photoresponsivity of the quinoidal form of **Py-RPIC**. The photoisomerization from the quinoidal form to the biradical form was observed by using two excitation laser sources. The transient absorption spectra at 243 K recorded by double-pulse laser flash photolysis are shown in Figure 10.9. The time delay between the first and the second laser pulse ($\lambda_{ex1}$ = 355 nm and $\lambda_{ex2}$ = 430 nm, respectively) was set to 40 μs. The photochromic reaction of the closed-ring isomer is not induced by the irradiation with the second laser pulse alone. The concentrations of the biradical and the quinoidal forms reach equilibrium at ~40 μs after 355 nm laser irradiation at 243 K. After reaching the equilibrium state, the excitation with a 430 nm laser pulse induces the valence photoisomerization to the biradical form from the quinoidal form because the absorption spectra at 3.5 μs and 40.6 μs are similar to each other. The valence photoisomerization was investigated in detail

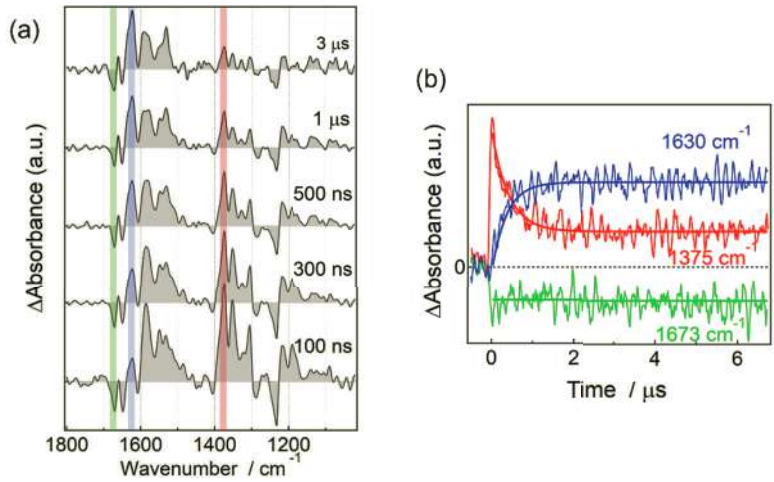


**Figure 10.8** (a) Time-resolved FTIR spectra of **Py-RPIC** in $CD_2Cl_2$ ($\lambda_{ex.}$ = 355 nm) at room temperature, and (b) the time profiles of the transient absorbance of **Py-RPIC**.

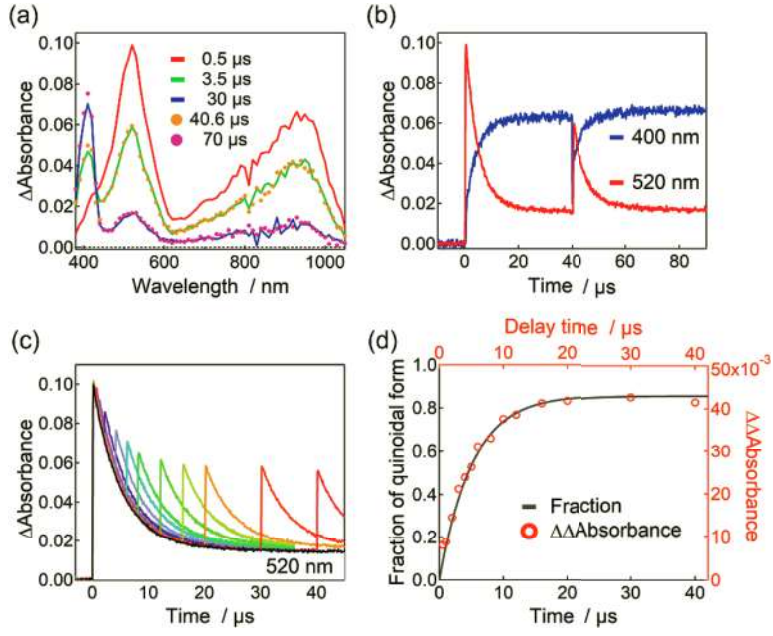


**Figure 10.9** (a) Transient absorption spectra of **Py–RPIC** in toluene ($4.9 \times 10^{-5}$ M) at 243 K obtained by double-pulse laser excitation with 355 nm and 430 nm ($\lambda_{ex1}$ = 355 nm, 3.5 mJ/pulse, $\lambda_{ex2}$ = 430 nm, and 8.0 mJ//pulse. (b) Time profiles of the ΔAbsorbance at 400 nm and 520 nm. (c) Temporal changes of the transient absorbance at 520 nm of **Py–RPIC** after the double laser pulse excitation. (d) The time profile of the fraction of **Q** obtained by global analysis and ΔΔAbsorbance at 520 nm as a function of the delay time.

by changing the delay time between the first and the second laser pulses for the double pulse laser flash photolysis. ΔΔAbsorbance which is defined as the difference between ΔAbsorbance measured after the first 355 nm laser irradiation and that after the second 430 nm laser irradiation corresponds to the amount of the biradical form generated by the photoisomerization. The time profile of the fraction of the quinoidal form shows good agreement with the plots of ΔΔAbsorbance against the delay time between the two excitation laser pulses. The biradical and quinoidal forms recover to the equilibrium state by thermal relaxation after laser irradiation. These results suggest that the biradical character of the open-ring isomer of the RPIC system can be modulated by light irradiation.

## 10.4 Bis(Phenoxyl-Imidazolyl Radical Complex)

The "photosynergetics" is recently termed as a cooperative interaction between multiple photons and molecules to realize photochemical reactions and applications, which cannot be achieved by conventional one-photon absorption process [41]. The establishment of a basic principle to achieve the advanced photoresponse beyond a one-photon reaction is an important proposition in recent photochemical studies. Nonlinear photoresponses to excitation light intensity are especially important in terms of spatiotemporally-controlled photochemical reactions. Although a simultaneous two-photon absorption process has been widely applied to two-photon microscopy [64–66], 3D lithographic fabrication [67, 68], and optical storage [69, 70], a high-energy pulse laser is required as the excitation light source (MW to GW/cm$^2$). Therefore, a molecular design with a large two-photon absorption cross-section and a two-photon absorption process with a stepwise manner have been advocated as efficient strategies to reduce the power threshold of excitation light. The power threshold for the stepwise absorption process can be effectively reduced by using a long-lived intermediate state like triplet states. Because the intermediate state for the stepwise two-photon absorption process is not confined to the excited electronic state, a photochemical product generated by a reversible photochemical reaction is one of the attractive candidates for the intermediated state. A simple kinetic analysis suggests that a lifetime from hundreds of microseconds to

sub-millisecond time scales for the intermediate state is suitable to achieve a clear nonlinear optical response to the excitation light intensity [41].

Therefore, we developed a stepwise two-photon induced photochromic molecule, **bisPIC**, by combining the two photochromic PIC units in a molecule to realize the "photosynergetic" effect [71]. We have recently reported a stepwise two-photon induced photochromic compound, [2.2]PC-bridged bis(imidazole dimer) [72]. The key feature to realize the nonlinear photochromic reaction is the specific spin–spin interaction between the two transient radical units. The tetraradical species generated by the two-photon absorption shows the antiferromagnetic coupling between the two imidazolyl radicals substituted at the 1,4-positions of the central phenylene ring, leading to the formation of closed-shell quinoidal species. The difference in the electronic structures between the one-photon generated biradical and the two-photon generated quinoidal species gives clear alterations in the color and the thermal back reaction speed that depend on the excitation light intensity. Based on this basic principle, it is expected that **bisPIC** shows the stepwise photochromic reaction in the same manner with [2.2]PC-bridged bis(imidazole dimer). We designed three different bisPIC derivatives, ***p*-bisPIC**, ***m*-bisPIC,** and **bisTPIC** (Scheme 10.3), to investigate the relationship between the spin interactions and the photochromic properties.

Figure 10.10 shows the absorption spectra of the bisPIC derivatives in benzene. The efficient conjugation between the two imidazole rings of ***p*-bisPIC** and **bisTPIC** was observed, compared with the absorption spectra of **PIC** and ***m*-bisPIC**, because of the planar geometry between the central aromatic ring and the imidazole rings of ***p*-bisPIC** and **bisTPIC**. We carried out the laser flash photolysis of the bisPIC derivatives to investigate the dependence of the photochromic properties on the excitation light intensity. The time-resolved absorption spectra of bisPIC derivatives are shown in Figure 10.11. The weak laser pulse irradiation generates the biradical species (**BR**) through a C–N bond-breaking reaction by the one-photon absorption process. The biradical species shows the broad absorption spectrum in visible and NIR regions. The differences in the transient absorption spectral shapes of ***p*-bisPIC**, ***m*-bisPIC**, and **bisTPIC** reflect the difference in the conjugation between the

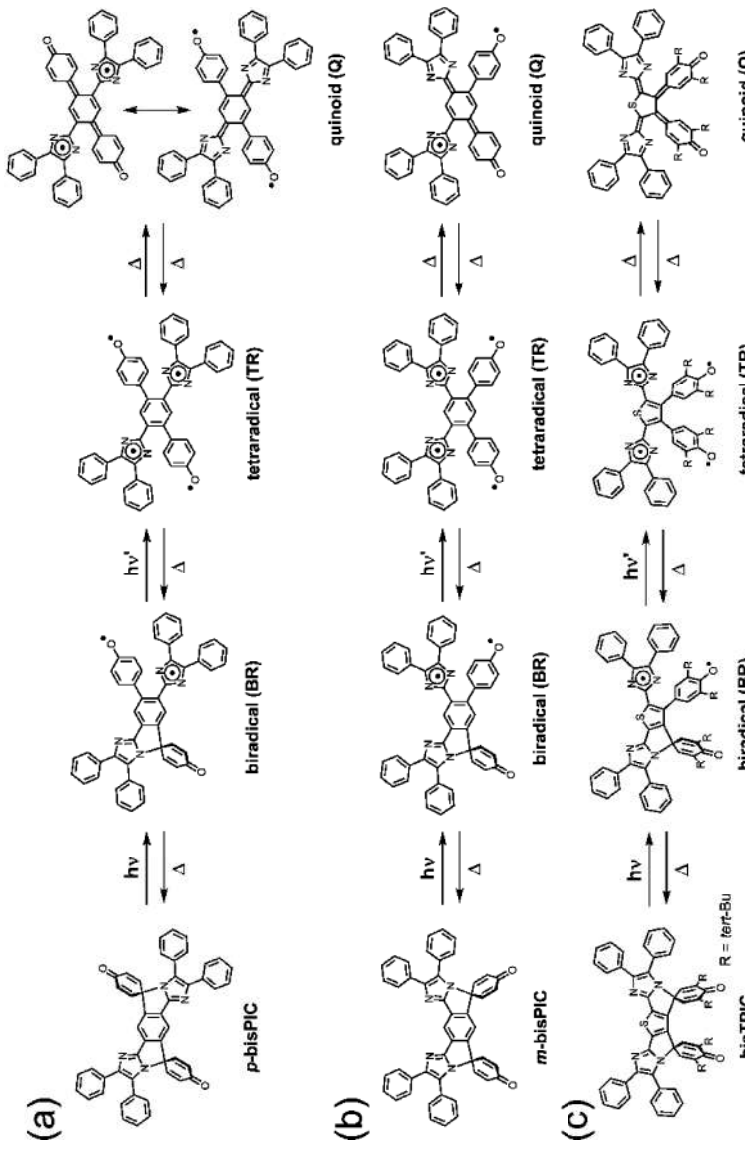


**Scheme 10.3** Stepwise photochromism of (a) ***p*-bisPIC**, (b) ***m*-bisPIC**, and (c) **bisTPIC**.

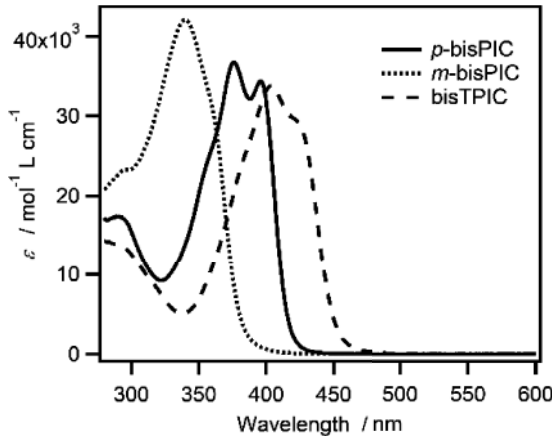


**Figure 10.10** UV–vis absorption spectra of ***p*-bisPIC**, ***m*-bisPIC**, and **bisTPIC** in benzene.

biradical units. On the other hand, intense laser pulse irradiation leads to the generation of the other transient species with different absorption spectra. The new absorption band at 600 nm for ***p*-bisPIC** is consistent to the absorption spectrum of the closed-shell species of 1,4-bis(4,5-diphenyl-2H-imidazol-2-ylidene)-cyclohexa-2,5-diene (BDPI-2Y). This result suggests that ***p*-bisPIC** shows the stepwise two-photon induced photochemical reaction to produce the closed-shell quinoidal species by the further photochemical reaction of **BR** by additional photon absorption. ***m*-BisPIC** and **bisTPIC** also show the excitation light intensity-dependent photochromism, indicating that ***m*-bisPIC** and **bisTPIC** generate the closed-shell quinoidal species (**Q**) by the stepwise photochromic reaction. The decay profiles of the transient absorbance consist of the fast and slow components, which can be assigned to thermal back reactions of **BR** and **Q**, respectively. Especially, the half-life of **Q** of **bisTPIC** is 300 times longer than that of **BR**. The significant deceleration is observed in the thermal back reaction of **bisTPIC**, indicating that the transient biradical species are stabilized by the substitution of the thiophene ring, due to the large contribution of the closed-shell quinoidal character [73]. The slow thermal back reaction of **Q** can be also explained by the stabilization of **Q** by the contribution of the closed-shell character to form the quinoidal structure at the para-

position. It was observed that the ratio of the slow decay component assigned to **Q** increases with the increase in the excitation intensity. The generation amount of **Q** shows a quadratic dependence on the intensity of the 355 nm excitation laser pulse. Thus, the reaction mechanism of the photochromic reactions of bisPIC derivatives can be described as the stepwise two-photon process.

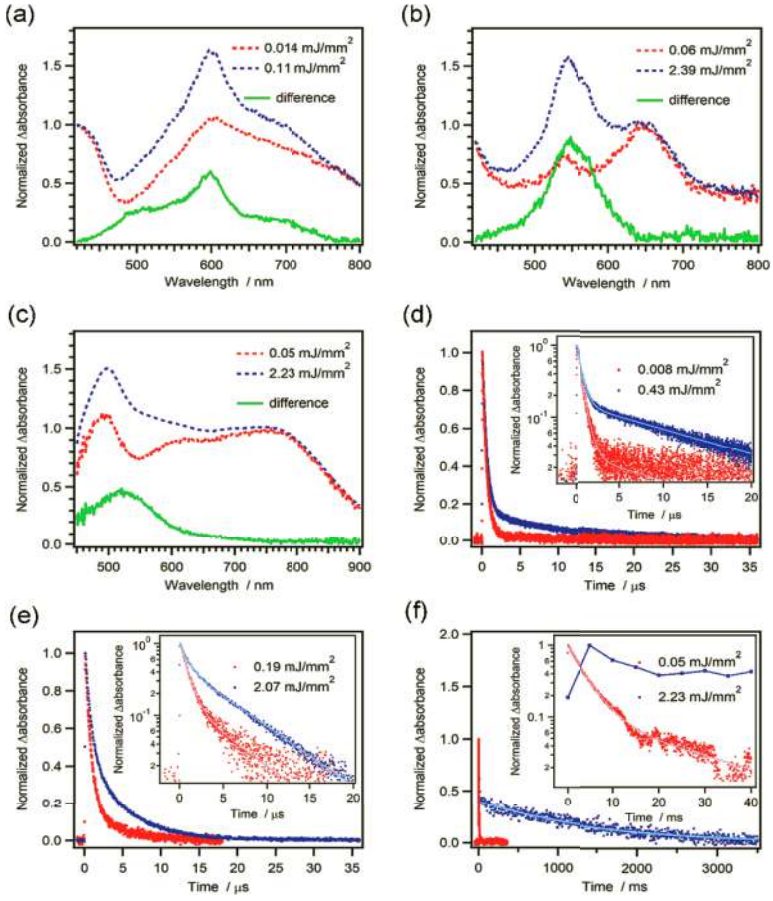


**Figure 10.11** Dependence of the transient vis–NIR absorption spectra of (a) ***p*-bisPIC**, (b) ***m*-bisPIC**, and (c) **bisTPIC** on the excitation laser intensity. Dependence of the decay profiles of the transient species of (a) ***p*-bisPIC**, (b) ***m*-bisPIC**, and (c) **bisTPIC** on the laser excitation intensity.

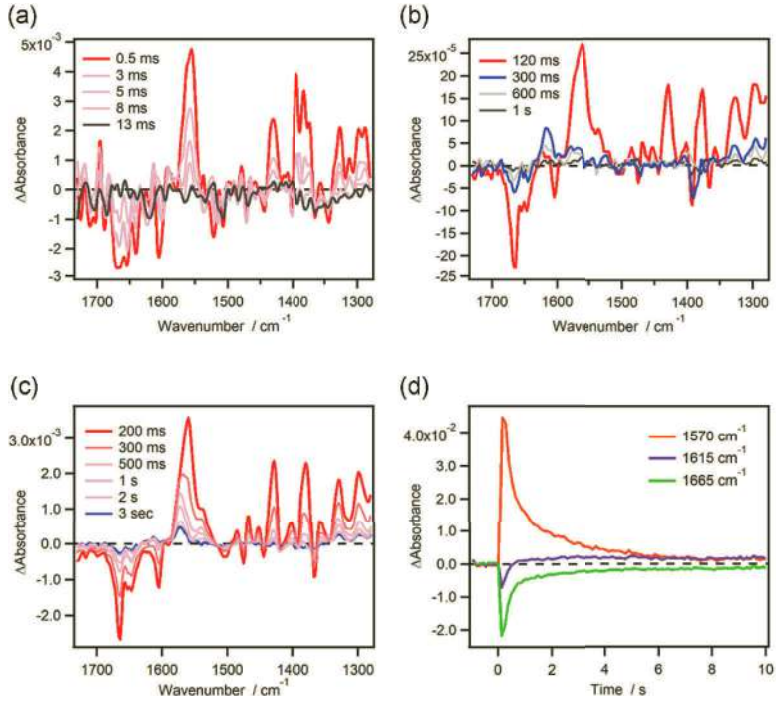


**Figure 10.12** (a, b) Time-resolved FTIR spectra of **bisTPIC** in $CD_2Cl_2$ at room temperature (a) upon weak laser excitation ($\lambda_{ex}$ = 355 nm, 0.5 mJ/pulse), and (b) upon intense laser excitation ($\lambda_{ex}$ = 355 nm, 4.0 mJ/pulse). (c) Time-resolved FTIR spectra of **bisTPIC** in $CD_2Cl_2$ at 253 K ($\lambda_{ex}$ = 355 nm, 8.0 mJ/pulse). (d) The time profiles of transient absorbance at 253 K, probed at 1570 $cm^{-1}$, 1615 $cm^{-1}$, and 1665 $cm^{-1}$.

The molecular structures of **BR** and **Q** were investigated by the time-resolved FTIR spectroscopy. The characteristic FTIR signals of the carbonyl groups of PIC derivatives are the marker bands to distinguish the open-shell biradical and the closed-shell quinoidal forms. Figure 10.12 shows the time-resolved FTIR spectra and the time profiles of **bisTPIC** in $CD_2Cl_2$. The step-scan and the rapid-scan techniques were utilized to measure the FTIR spectra upon weak laser irradiation (355 nm, 0.5 mJ/pulse) and intense laser irradiation (355 nm, 4.0 mJ/pulse), respectively. The time-resolved FTIR spectra in the millisecond time scale upon weak laser irradiation are

shown in Figure 10.12a. The signals monotonically decreased and disappeared at 13 ms after the laser irradiation at room temperature. The FTIR signal at 1560 $cm^{-1}$ is characteristic of the vibrational mode of the C–O stretching, indicating the open-shell electronic structure of **BR**. In contrast, an intense laser excitation generates the slow decay component, which shows the FTIR peak at 1560 $cm^{-1}$ in addition to **BR** (Figure 10.12b). The peak 1560 $cm^{-1}$ shifts to the peak at 1615 $cm^{-1}$ in a few hundreds of millisecond time scale. This higher frequency shift of the carbonyl band indicates the large contribution of the double-bond character of the carbonyl bond. This suggests the generation of the closed-shell quinoidal structure. Furthermore, it can be predicted that the sequential thermal isomerization reaction proceeds in the two-photon generated product. That is the thermal isomerization process from the tetraradical species with an open-shell character (such as **TR** in Scheme 10.3) to the quinoidal species with a large closed-shell character (**Q**). The generation of the signal at 1615 $cm^{-1}$ was inhibited at 253 K, indicating the activation energy barrier for the isomerization from **TR** to **Q** is higher than the thermal recombination reaction to generate the initial **bisTPIC** (Figures 10.12c and 10.12d).

## 10.5 Conclusion

Most of the biradicals investigated so far are characterized by the static electronic states described by resonance structures between the open-shell biradical state and the closed-shell state. In general, it was difficult to control the biradical character by external stimuli. On the other hand, we have developed the novel fast photoswitch system, involving the valence isomerization from the biradical to the quinoidal form. We have investigated the radical-dissociative photochromic molecules that generate colored transient biradicals upon light irradiation. This photochromic system causes not only a color change, but also a large change in the spin state. The photogenerated biradical thermally equilibrates with the quinoidal form with a time scale of hundreds of nanoseconds, while the equilibrated two forms return to the parent colorless molecule with a time scale of milliseconds. It was clarified that by changing the

geometrical arrangement of the two spin centers, the changes in the spin–spin interaction result in drastic changes in the biradical properties. Moreover, we found that the visible-light excitation to the equilibrium state results in the valence photoisomerization from the quinoidal form to the biradical. The dynamic biradical systems are of special interest not only for the singlet biradical chemistry, but also for their applications in future photoswitching materials.

## Acknowledgments

This work was supported in part by JSPS KAKENHI Grant Numbers JP18H05263, JP26107010 in Scientific Research on Innovative Areas "Photosynergetics".

## References

1. Kolc, J., and Michl, J. (1973). π, π-Biradicaloid hydrocarbons. The pleiadene family. I. Photochemical preparation from cyclobutene precursors, *J. Am. Chem. Soc.,* **95**, pp. 7391–7401.
2. Bendikov, M., Duong, H. M., Starkey, K., Houk, K. N., Carter, E. A., and Wudl, F. (2004). Oligoacenes: Theoretical prediction of open-shell singlet diradical ground states, *J. Am. Chem. Soc.,* **126**, pp. 7416–7417.
3. Kikuchi, A., Iwahori, F., and Abe, J. (2004). Definitive evidence for the contribution of biradical character in a closed-shell molecule, derivative of 1,4-bis-(4,5-diphenylimidazol-2-ylidene)-cyclohexa-2,5-diene, *J. Am. Chem. Soc.,* **126**, pp. 6526–6527.
4. Kubo, T., Sakamoto, M., Akabane, M., Fujiwara, Y., Yamamoto, K., Akita, M., Inoue, K., Takui, T., and Nakasuji, K. (2004). Four-stage amphoteric redox properties and biradicaloid character of tetra-*tert*-butyldicyclopenta[*b*;*d*]thieno[1,2,3-*cd*;5,6,7-*c´d´*]diphenalene, *Angew. Chem., Int. Ed.,* **43**, pp. 6474–6479.
5. Norton, J. E., and Houk, K. N. (2005). Electronic structures and properties of twisted polyacenes, *J. Am. Chem. Soc.,* **127**, pp. 4162–4163.
6. Kikuchi, A., and Abe, J. (2005). A new family of π-conjugated delocalized biradicals: Electronic structures of 1,4-bis(2,5-diphenylimidazol-4-ylidene)cyclohexa-2,5-diene, *J. Phys. Chem. B,* **109**, pp. 19448–19453.
7. Kubo, T., Shimizu, A., Uruichi, M., Yakushi, K., Nakano, M., Shiomi, D., Sato, K., Takui, T., Morita, Y., and Nakasuji, K. (2007). Singlet

biradical character of phenalenyl-based Kekulé hydrocarbon with naphthoquinoid structure, *Org. Lett.,* **9**, pp. 81–84.

8. Abe, M. (2013). Diradicals, *Chem. Rev.,* **113**, pp. 7011–7088.
9. Sun, Z., Zeng, Z., and Wu, J. (2014). Zethrenes, extended *p*-quinodimethanes, and periacenes with a singlet biradical ground state, *Acc. Chem. Res.,* **47**, pp. 2582–2591.
10. Yamashita, H., and Abe, J. (2014). Remarkable solvatochromic color change via proton tautomerism of a phenol-linked imidazole derivative, *J. Phys. Chem. A,* **118**, pp. 1430–1438.
11. Kubo, T. (2015). Recent progress in quinoidal singlet biradical molecules, *Chem. Lett.,* **44**, pp. 111–122.
12. Zeng, Z., and Wu, J. (2015). Stable π-extended *p*-quinodimethanes: Synthesis and tunable ground states, *Chem. Rec.,* **15**, pp. 322–328.
13. Rudebusch, G. E., Zafra, J. L., Jorner, K., Fukuda, K., Marshall, J. L., Arrechea-Marcos, I., Espejo, G. L., Ortiz, R. P., Gómez-García, C. J., Zakharov, L. N., Nakano, M., Ottosson, H., Casado, J., and Haley, M. M. (2016). Diindeno-fusion of an anthracene as a design strategy for stable organic biradicals, *Nat. Chem.,* **8**, pp. 753–759.
14. Konishi, A., and Kubo, T. (2017). Benzenoid quinodimethanes, *Top. Curr. Chem.,* **375** *375*: 83.
15. Gopalakrishna, T. Y., Zeng, W., Lu, X., and Wu, J. (2018). From open-shell singlet diradicaloids to polyradicaloids, *Chem. Commun.,* **54**, pp. 2186–2199.
16. Tschitschibabin, A. E. (1907). Über einige phenylierte derivate des *p*, *p*-ditolyls, *Ber. Dtsch. Chem. Ges.,* **40**, pp. 1810–1819.
17. Sloan, G. J., and Vaughan, W. R. (1957). Stable organic biradicals, *J. Org. Chem.,* **22**, pp. 750–761.
18. Montgomery, L. K., Huffman, J. C., Jurczak, E. A., and Grendze, M. P. (1986). The molecular structures of Thiele's and Chichibabin's hydrocarbons, *J. Am. Chem. Soc.,* **108**, pp. 6004–6011.
19. Molins, E., Miravitlles, C., Espinosa, E., and Ballester, M. (2002). 1,1′,3,3′,6,6′,8,8′-Octachloro-9,9′-bifluorenylidene and perchloro-9,9′-bifluorenylidene, two exceedingly twisted ethylenes, *J. Org. Chem.,* **67**, pp. 7175–7178.
20. Zhang, H., Phan, H., Herng, T. S., Gopalakrishna, T. Y., Zheng, W., Ding, J., and Wu, J. (2017). Conformationally flexible bis(9-fluorenylidene) porphyrin diradicaloids, *Angew. Chem. Int. Ed.,* **56**, pp. 13484–13488.
21. Zeng, Z., Sung, Y. M., Bao, N., Tan, D., Lee, R., Zafra, J. L., Lee, B. S., Ishida, M., Ding, J., Lopez Navarrete, J. T., Li, Y., Zeng, W., Kim, D., Huang,

K-W., Webster, R. D., Casado, J., and Wu, J. (2012). Stable tetrabenzo-Chichibabin's hydrocarbons: Tunable ground state and unusual transition between their closed-shell and open-shell resonance forms, *J. Am. Chem. Soc.,* **134**, pp. 14513–14525.

22. Hayashi, T., and Maeda, K. (1960). Preparation of a new phototropic substance, *Bull. Chem. Soc. Jpn.,* **33**, pp. 565–566.
23. Hayashi, T., Maeda, K., and Morinaga, M. (1964). The mechanism of the photochromism and thermochromism of 2,2′,4,4′,5,5′-Hexaphenyl-1,1′-biimidazolyl, *Bull. Chem. Soc. Jpn.,* **37**, pp. 1563–1564.
24. Iwahori, F., Hatano, S., and Abe, J. (2007). Rational design of a new class of diffusion-inhibited HABI with fast back-reaction, *J. Phys. Org. Chem*., **20**, pp. 857–863.
25. Fujita, K., Hatano, S., Kato, D., and Abe, J. (2008). Photochromism of a radical diffusion-inhibited hexaarylbiimidazole derivative with intense coloration and fast decoloration performance, *Org. Lett.,* **10**, pp. 3105–3108.
26. Kishimoto, Y., and Abe, J. (2009). A fast photochromic molecule that colors only under UV light, *J. Am. Chem. Soc.,* **131**, pp. 4227–4229.
27. Harada, Y., Hatano, S., Kimoto, A., and Abe, J. (2010). Remarkable acceleration for back-reaction of a fast photochromic molecule, *J. Phys. Chem. Lett.,* **1**, pp. 1112–1115.
28. Shima, K., Mutoh, K., Kobayashi, Y., and Abe, J. (2014). Enhancing the versatility and functionality of fast photochromic bridged-imidazole dimers by flipping imidazole rings, *J. Am. Chem. Soc.,* **118**, pp. 2288–2297.
29. Kobayashi, Y., Shima, K., Mutoh, K., and Abe, J. (2016). Fast photochromism involving thermally-activated valence isomerization of phenoxyl-imidazolyl radical complex derivatives, *J. Phys. Chem. Lett.,* **7**, pp. 3067–3072.
30. Kobayashi, Y., Okajima, H., Sotome, H., Yanai, T., Mutoh, K., Yoneda, Y., Shigeta, Y., Sakamoto, A., Miyasaka, H., and Abe, J. (2017). Direct observation of the ultrafast evolution of open-shell biradical in photochromic radical dimer, *J. Am. Chem. Soc.,* **139**, pp. 6382–6389.
31. Tokunaga, A., Mutoh, K., Hasegawa, T., and Abe, J. (2018). Reversible valence photoisomerization between closed-shell quinoidal and open-shell biradical forms, *J. Phys. Chem. Lett.,* **9**, pp. 1833–1837.
32. Usui, R., Yamamoto, K., Okajima, H., Mutoh, K., Sakamoto, A., Abe, J., and Kobayashi, Y. (2020). Photochromic radical complexes that show heterolytic bond dissociation, *J. Am. Chem. Soc.,* **142**, pp. 10132–10142.

33. Ishii, N., Kato, T., and Abe, J. (2012). A real-time dynamic holographic material using a fast photochromic molecule, *Sci. Rep.,* **2**, pp. 819.
34. Ishii, N., and Abe, J. (2013). Fast photochromism in polymer matrix with plasticizer and real-time dynamic holographic properties, *Appl. Phys. Lett.,* **102**, pp. 163301.
35. Kobayashi, Y., and Abe, J. (2016). Real-time dynamic hologram of a 3D object with fast photochromic molecules, *Adv. Opt. Mater.,* **4**, pp. 1354–1357.
36. Mutoh, K., Sliwa, M., and Abe, J. (2013). Rapid fluorescence switching by using a fast photochromic [2.2]paracyclophane-bridged imidazole dimer, *J. Phys. Chem. C,* **117**, pp. 4808–4814.
37. Mutoh, K., Sliwa, M., Fron, E., Hofkens, J., and Abe, J. (2018). Fluorescence modulation by fast photochromism of a [2.2]paracyclophane-bridged imidazole dimer possessing a perylene bisimide moiety, *J. Mater. Chem. C,* **6**, pp. 9523–9531.
38. Mutoh, K., Miyashita, N., Arai, K., and Abe, J. (2019). Turn-on mode fluorescence switch by using negative photochromic imidazole dimer, *J. Am. Chem. Soc.*, **141**, pp. 5650–5654.
39. Yamashita, H., and Abe, J. (2014). Pentaarylbiimidazole, PABI: An Easily synthesized fast photochromic molecule with superior durability, *Chem. Commun.,* **50**, pp. 8468–8471.
40. Döhnert, D., and Koutecky, J. (1980). Occupation numbers of natural orbitals as a criterion for biradical character: Different kinds of biradicals, *J. Am. Chem. Soc.,* **102**, pp. 1789–1796.
41. Kobayashi, Y., Mutoh, K., and Abe, J. (2016). Fast photochromic molecules toward realization of photosynergetic effects, *J. Phys. Chem. Lett.,* **7**, pp. 3666–3675.
42. Kawano, M., Sano, T., Abe, J., and Ohashi, Y. (1999). The first in situ direct observation of the light-induced radical pair from a hexaarylbiimidazolyl derivative by x-ray crystallography, *J. Am. Chem. Soc.,* **121**, pp. 8106–8107.
43. Abe, J., Sano, T., Kawano, M., Ohashi, Y., Matsushita, M. M., and Iyoda, T. (2001). EPR and density functional studies of light-induced radical pairs in a single crystal of a hexaarylbiimidazolyl derivative, *Angew. Chem. Int. Ed.,* **40**, pp. 580–582.
44. Mutoh, K., Nakano, E., and Abe, J. (2012). Spectroelectrochemistry of a photochromic [2.2]paracyclophane-bridged imidazole dimer: Clarification of the electrochemical behavior of HABI, *J. Phys. Chem. A,* **116**, pp. 6792–6797.

45. Yanai, T., Tew, D. P., and Handy, N. C. (2004). A new hybrid exchange-correlation functional using the Coulomb-attenuating method (CAM-B3LYP), *Chem. Phys. Lett.,* **393**, pp. 51–57.

46. Tamai, N., and Miyasaka, H. (2000). Ultrafast dynamics of photochromic systems, *Chem. Rev.,* **100**, pp. 1875–1890.

47. Satoh, Y., Ishibashi, Y., Ito, S., Nagasawa, Y., Miyasaka, H., Chosrowjan, H., Taniguchi, S., Mataga, N., Kato, D., Kikuchi, A., and Abe, J. (2007). Ultrafast laser photolysis study on photodissociation dynamics of a hexaarylbiimidazole derivative, *Chem. Phys. Lett.,* **448**, pp. 228–231.

48. Yamaguchi, T., Hilbers, M. F., Reinders, P. P., Kobayashi, Y., Brouwer, A. M., and Abe, J. (2015). Nanosecond photochromic molecular switching of a biphenyl-bridged imidazole dimer revealed by wide range transient absorption spectroscopy, *Chem. Commun.,* **51**, pp. 1375–1378.

49. Miyasaka, H., Satoh, Y., Ishibashi, Y., Ito, S., Nagasawa, Y., Taniguchi, S., Chosrowjan, H., Mataga, N., Kato, D., Kikuchi, A., and Abe, J. (2009). Ultrafast photodissociation dynamics of a hexaarylbiimidazole derivative with pyrenyl groups: Dispersive reaction from femtosecond to 10 ns time regions, *J. Am. Chem. Soc.,* **131**, pp. 7256–7263.

50. Blinder, S. M., Peller, M. L., Lord, N. W., Aamodt, L. C., and Ivanchukov, N. S. J. (1962). Electron spin resonance of tetraphenylpyrryl radical, *Chem. Phys.*, **36**, pp. 540–544.

51. Shida, T., and Kira, A. (1969). Optical and electron spin resonance studies on photolyzed and radiolyzed tetraphenylhydrazine and related compounds, *J. Phys. Chem.*, **73**, pp. 4315–4320.

52. Yamashita, H. Ikezawa, T. Kobayashi Y., and Abe J. (2015). Photochromic phenoxyl-imidazolyl radical complexes with decoloration rates from tens of nanoseconds to seconds, *J. Am. Chem. Soc.*, **137**, pp. 4952–4955.

53. Liu, A., Trifunac, A. D., and Krongauz, V. V. (1992). Photodissociation of hexaarylbllmldazole. 2. Direct and sensitized dissociation, *J. Phys. Chem.*, **96**, pp. 207–211.

54. Lin, Y., Liu, A., Trifunac, A. D., and Krongauz, V. V. (1992). Investigation of electron transfer between hexaarylbiimidazole and visible sensitizer, *Chem. Phys. Lett.*, **198**, pp. 200–206.

55. Nakano, E., Mutoh, K., Kobayashi, Y., and Abe, J. (2014). Electrochemistry of photochromic [2.2]paracyclophane-bridged imidazole dimers: Rational understanding of the electronic structures, *J. Phys. Chem. A*, **118**, pp. 2288–2297.

56. Yamamoto, K., Mutoh, K., and Abe, J. (2019). Photo- and electro-driven molecular switching system of aryl-bridged photochromic radical complexes, *J. Phys. Chem. A*, **123**, pp. 1945–1952.

57. Morita, Y., Ueda, A., Nishida, S., Fukui, K., Ise, T., Shiomi, D., Sato, K., Takui, T., and Nakasuji, K. (2008). Curved aromaticity of a corannulene-based neutral radical: Crystal structure and 3D unbalanced delocalization of spin, *Angew. Chem., Int. Ed.*, **47**, pp. 2035–2038.
58. Foti, M., Ingold, K. U., and Lusztyk, J. (1994). The surprisingly high reactivity of phenoxyl radicals, *J. Am. Chem. Soc.*, **116**, pp. 9440–9447.
59. Kobayashi, Y., Mishima, Y., Mutoh, K., and Abe, J. (2017). Highly durable photochromic radical complexes having no steric protections of radicals, *Chem. Commun.*, **53**, pp. 4315–4318.
60. van Stokkum, I. H. M., Larsen, D. S., and van Grondelle, R. (2004). Global and target analysis of time-resolved spectra, *Biochim. Biophys. Acta, Bioenerg.*, **1657**, pp. 82–104.
61. Matheson, I. B. C. (1990). A critical comparison of least absolute deviation fitting (robust) and least-squares fitting: The importance of error distributions, *Comput. Chem.*, **14**, pp. 49–57.
62. Matheson, I. B. C., Parkhurst, L. J., and DeSa, R. J. (2004). Efficient integration of kinetic differential equation sets using matrix exponentiation, *Methods Enzymol.*, **384**, pp. 18–39.
63. Cook, C. D., Kuhn, D. A., and Fianu, P. (1956). Oxidation of hindered phenols. IV. Stable phenoxy radicals, *J. Am. Chem. Soc.*, **78**, pp. 2002–2005.
64. König, K. J. (2000). Multiphoton microscopy in life sciences, *J. Microsc.*, **200**, 83–104.
65. Zipfel, W. R., Williams, R. M., and Webb, W. W. (2003). Nonlinear magic: Multiphoton microscopy in the biosciences, *Nat. Biotechnol.*, **21**, pp. 1369–1377.
66. Helmchen, F., and Denk, W. (2005). Deep tissue two-photon microscopy, *Nat. Methods*, **2**, pp. 932–940.
67. Cumpston, B. H., Ananthavel, S. P., Barlow, S., Dyer, D. L., Ehrlich, J. E., Erskine, L. L., Heikal, A. A., Kuebler, S. M., Lee, I.-Y. S., McCord-Maughon, D., Qin, J., Rockel, H., Rumi, M., Wu, X., Marder, S. R., and Perry, J. W. (1999). Two-photon polymerization initiators for three-dimensional optical data storage and microfabrication, *Nature*, **398**, pp. 51–54.
68. Kawata, S., Sun, H. B., Tanaka, T., and Takada, K. (2001). Finer features for functional microdevices, *Nature*, **412**, pp. 697–698.
69. Parthenopoulos, D. A., and Rentzepis, P. M. (1989). Three-dimensional optical storage memory, *Science*, **245**, pp. 843–845.
70. Kawata, S., and Kawata, Y. (2000). Three-dimensional optical data storage using photochromic materials, *Chem. Rev.*, **100**, pp. 1777–1788.

71. Mutoh, K., Kobayashi, Y., Yamane, T., Ikezawa, T., and Abe, J. (2017). Rate-tunable stepwise two-photon-gated photoresponsive systems employing a synergetic interaction between transient biradical units, *J. Am. Chem. Soc.*, **139**, pp. 4452-4461.

72. Mutoh, K., Nakagawa, Y., Sakamoto, A., Kobayashi, Y., and Abe, J. (2015). Stepwise two-photon-gated photochemical reaction in photochromic [2.2]paracyclophane-bridged bis(imidazole dimer), *J. Am. Chem. Soc.*, **137**, pp. 5674–5677.

73. Ikezawa, T., Mutoh, K., Kobayashi, Y., and Abe, J. (2016). Thiophene-substituted phenoxyl-imidazolyl radical complexes with high photosensitivity, *Chem. Commun.* **52**, pp. 2465–2468.

## Chapter 11

# Porphyrinoid-Based Diradicaloids

**Kenichi Kato and Atsuhiro Osuka**
*Department of Chemistry, Graduate School of Science, Kyoto University, Kitashirakawa-Oiwake-cho, Sakyo-ku, Kyoto, 606-8502, Japan*
osuka@kuchem.kyoto-u.ac.jp

Porphyrinoids have attracted the increasing attention as an excellent platform for air- and moisture-stable radicals in the last decades. Porphyrinoid-based radical chemistry has a long history of intensive studies on the catabolic processes of hemes, where porphyrin *meso*-oxy radicals were regarded as key intermediates. On the other hand, continuous efforts have been devoted toward the creation of novel radicals and diradicaloids using expanded, core-modified, and peripherally functionalized porphyrins. Some of them have been shown to be highly stable, indicating good radical-stabilizing ability of porphyrins. These porphyrinoid-based radicals have helped our understanding of the electronic structures, spin delocalization, and stability, which has allowed for rational designs and synthesis of air-stable radicals, diradicaloids, and other multi-spin systems. This chapter summarizes the recent advance in porphyrinoid-based diradicaloid chemistry, aiming to provide a comprehensive

*Diradicaloids*
Edited by Jishan Wu

ISBN 978-981-4968-08-9 (Hardcover), 978-1-003-27724-8 (eBook)
www.jennystanford.com

understanding of their stabilities and magnetic properties from the perspective of spin density distribution.

## 11.1 Introduction—Porphyrinoid-Based Mono-Radicals

In this section, we briefly introduce the characteristics of porphyrinoids, focusing on their unique electronic structures derived from the pyrrole-based macrocycles. Then, we overview the relationships between chemical structures and stability, as well as outline the dependence of spin density distribution on the attached radical-center units, using representative examples of air-stable porphyrinoid-based radicals. These general aspects are useful for deeper understanding of their diradicaloids.

### 11.1.1 Electronic Flexibility and Radical-Stabilizing Ability of Porphyrinoids

Porphyrin and related macrocycles play various roles indispensable for living things as Heme, Chlorophyll, and Vitamin $B_{12}$, thereby being called as "pigments of life". In addition to the biological functions, porphyrinoids display outstanding light-harvesting abilities, intriguing electrochemical properties, structural flexibility, and rich coordination chemistry toward diverse metals and elements. These attractive features have made porphyrinoids the key players in biochemistry, catalysis, light-harvesting systems, and also in the materials science field [1–6]. Along this line, synthetic porphyrinoid chemistry has produced many different kinds of expanded porphyrins, which consist of more than four pyrrole units [7–11], core-modified [12–19], and π-extended derivatives [20–24], and their covalently linked arrays [25–31]. Notably, some of these novel compounds exhibit small HOMO–LUMO gaps, large two-photon absorption (TPA) cross-section, sizable nonlinear optical properties, and ambipolar multi-redox behaviors, which are also realized by diradicaloid π-systems, though most of them are closed-shell compounds without explicit diradical characters. These distinctive natures are derived from effective conjugative effects in

porphyrinoid π-systems, which are also crucial for stabilization of radical species.

Porphyrin, the prototype of porphyrinoids, is a non-benzenoid aromatic macrocycle composed of four pyrroles and four methine carbons (Figure 11.1). The coexistence of local pyrrolic and global macrocyclic aromaticity and that of amine- and imine-type pyrroles endow porphyrins with excellent "electronic flexibility" as compared with other normal polycyclic aromatic hydrocarbons (PAHs) [32, 33]. The total aromatic stabilization energies of porphyrins are reported to be largely dependent on the local pyrrolic 6π circuits (ca. 80%) [34–36]. The minor contributions of macrocyclic aromaticity in the energetic criteria cause the non-aromatic resonance contributors (e.g., structures in Figure 11.1c), in which formal radical center is located within the macrocycle, to have stability similar to those with macrocyclic aromaticity because they retain local pyrrolic aromaticity. In addition, amine-imine interconversion allows porphyrin to serve as both electron-donor and acceptor units. Further, cyclic structures themselves prefer well-delocalized frontier orbitals, spin densities, and charge distribution, rather than those localized at some part of the π-systems. For these features, large resonance stabilization is gained in porphyrin and related macrocycles, resulting in their high radical-stabilizing ability.

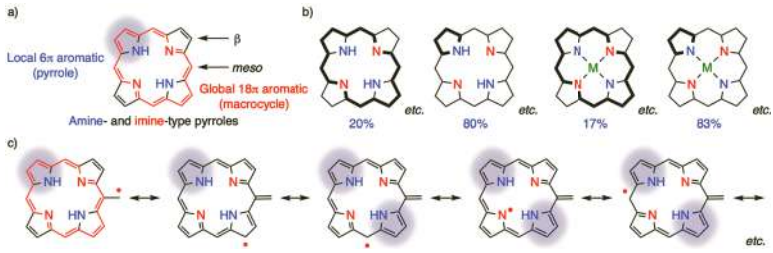


**Figure 11.1** Electronic flexibility of porphyrin. (a) Chemical structure of porphyrin, (b) contributions of macrocyclic and local circuits to aromatic stabilization energies of free-base porphyrin (left) and its metal complex (right), and (c) major resonance contributors of a radical-appended porphyrin.

In general, steric protection, spin delocalization, and electronic tuning are cooperatively employed to endow organic radicals with high stability [33, 37]. Incorporation of bulky substituents

improves the stabilities of the original radical species by hampering intermolecular interactions. On the other hand, extensive spin delocalization allows intermolecular magnetic interactions through π-π stacking, while it makes σ-bond formation less viable via spin density dilution. Electronic tuning offers perturbations on redox potentials, charge distribution, and frontier orbital coefficients of the parent radicals. Porphyrinoid-based radicals are usually fairly stabilized by the effective spin conjugation onto their electronically flexible π-systems, so that they need less bulky substituents. Such natures make porphyrinoid-based radicals promising platforms for appropriately spin-correlated systems via well-conjugated π-electrons and through-space interactions in π-stacked dimers.

### 11.1.2 Examples of Stable Porphyrinoid-Based Radicals

Heme is an iron complex of porphyrin and its catabolism is known to start with *meso*-oxygenation (Figure 11.2a) [38–40]. Hence, porphyrin *meso*-oxy radicals have attracted great interest as important model compounds of reactive intermediate for heme catabolism. When *meso*-hydroxy β-octaethylporphyrins (OEPs, **1M**) were oxidized, the resulting oxy radicals were reported to dimerize with σ-bonds at the 15-positions ($\mathbf{2M_2}$) [41]. Later, Balch et al. found that aerobic oxidation in pyridine produced pyridine-coordinated $Ni^{II}$- and $Zn^{II}$-porphyrin *meso*-oxy radicals **2M**·**2py** with considerable stability caused by steric protection of axial pyridines [42, 43]. In 1997, Smith and coworkers rationally prepared a fairly stable free-base radical, **3**, by introducing a bulky *tert*-butyl group at the 15-position [44]. Figure 11.2d visualizes the spin density distribution of a typical porphyrin *meso*-oxy radical. Large values are observed at the *meso*-positions, which explain the selective dimerization at the 15-position. Using *meso*-aryl-type porphyrinoids, Osuka and coworkers have extensively investigated stable oxy radicals since 2008. In the first report, a dumbbell-shaped 5,10,20,25-tetrakis(pentafluorophenyl)[26]hexaphyrin was found to form its *meso*-oxy radical **4** gradually in an aerated solution [45]. Notably, the radical **4** was unreactive to air, water, and silica gel, despite its free *meso*-position, enabling easy manipulations like usual closed-shell molecules. Air-stable *meso*-oxy radicals based on *meso*-aryl-substituted $B^{III}$-subporphyrin (**5**) and free-base,

$Ni^{II}$-, and $Zn^{II}$-porphyrins (**6M**) were also prepared upon oxidation of the corresponding hydroxy compounds with $PbO_2$ [46, 47]. These compounds clearly exemplified the advantage of using *meso*-aryl porphyrinoids as a stable radical platform.

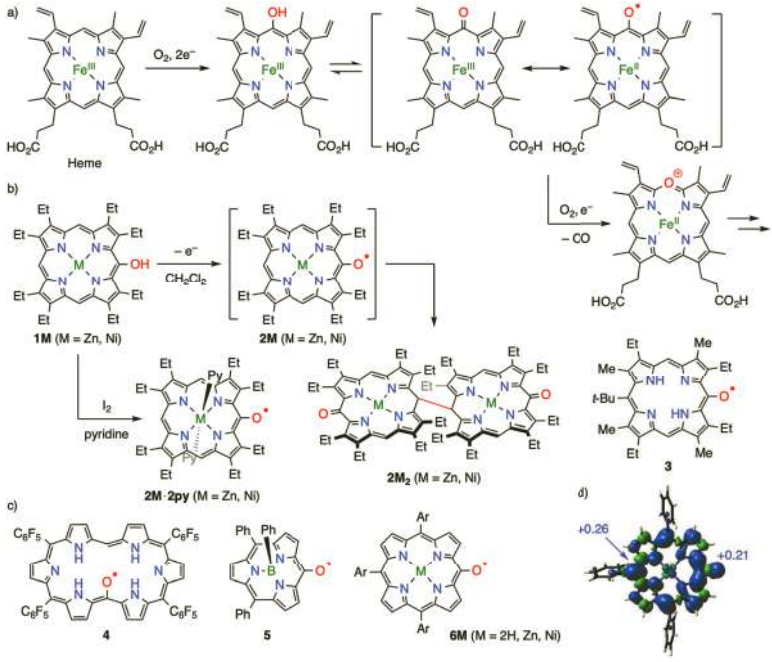


**Figure 11.2** Porphyrin *meso*-oxy radicals. (a) Catabolic pathway of Heme, (b) OEP *meso*-oxy radicals, (c) *meso*-aryl porphyrinoid *meso*-oxy radicals, and (d) spin density distribution plot of *meso*-aryl porphyrinoxyl calculated at the UB3LYP/6-31G(d) level (isovalue: 0.001). Py = pyridine, Ar = 3,5-di-*tert*-butylphenyl.

Porphyrinoids were also effective to stabilize *meso*-aminyl radicals, without an adjoining heteroatom that can stabilize radicals by conjugative resonance effect when the aminyl radical centers were protected by bulky substituents, such as 2,4,6-trichlorophenyl (**7X**), *meso*-subporphyrinyl (**8**), and *meso*-porphyrinyl groups (**9**) (Figure 11.3) [48, 49]. Dicyanomethyl radicals were reported as fairly air-stable monomeric radicals when the dicyanomethyl was attached to the porphyrinoid *meso*-positions (**10X** and **11X**), while they were dynamically stable in equilibrium with the

corresponding σ-dimers when it was attached at the β-positions (**12X**) [50, 51]. A porphyrin β-dicyanomethyl radical displays rather localized spin density distribution with less efficient delocalization (Figure 11.3c), which explains the high propensity toward σ-bond formation. Unfortunately, normal carbon-centered radicals have not been successfully generated as stable species, though porphyrin *meso*-carbocation **13+** and anion **13–** were characterized with spectroscopic methods (Figure 11.4a) [52].

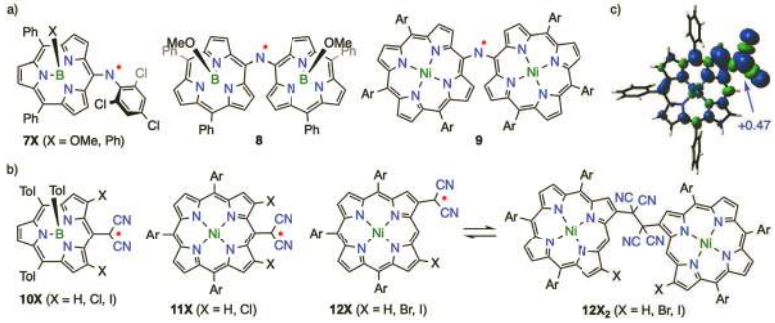


**Figure 11.3** (a) Subporphyrin and porphyrin *meso*-aminyl radicals and (b) dicyanomethyl radicals. (c) Spin density distribution plot of porphyrin β-dicyanomethyl calculated at the UB3LYP/6-31G(d) level (isovalue: 0.001). Ar = 3,5-di-*tert*-butylphenyl, Tol = 4-methylphenyl.

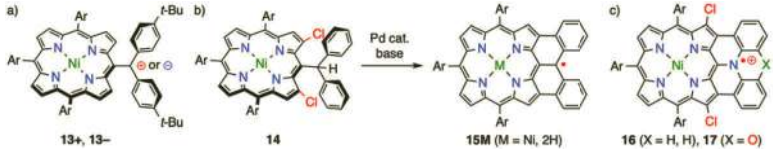


**Figure 11.4** (a) Porphyrin *meso*-carbocation and anion, (b) production of carbon-centered radicals fused with porphyrin, and (c) porphyrin-fused aminium radical cations. Ar = 3,5-di-*tert*-butylphenyl.

Fusion of porphyrinoids with appended π-conjugated units leads to enforced coplanar structures, which increases the electronic perturbation [24]. By applying this strategy to radical stabilization, a diphenylmethane-appended $Ni^{II}$-triarylporphyrin was converted to air-stable carbon-centered radical **15Ni** (Figure 11.4b) [53]. This radical was formed directly via Pd-catalyzed intramolecular C–H

arylation without any additional oxidation step. Radical **15Ni** was shown to be stable also toward reducing reagents, such as ascorbic acid and tin hydride, while such reagents sometimes reduce oxy, aminyl, and dicyanomethyl radicals. Fused $Ni^{II}$-triarylporphyrin skeleton was further utilized for stabilization of electrophilic aminium radical cation centers (**16**, **17**) (Figure 11.4c) [54]. Although the stabilities of these radicals were not perfect and required additional steric protection by β-chlorine atoms, most of these aminium radical cations exhibited high stability toward water, silica gel, atmospheric oxygen, and dimerization.

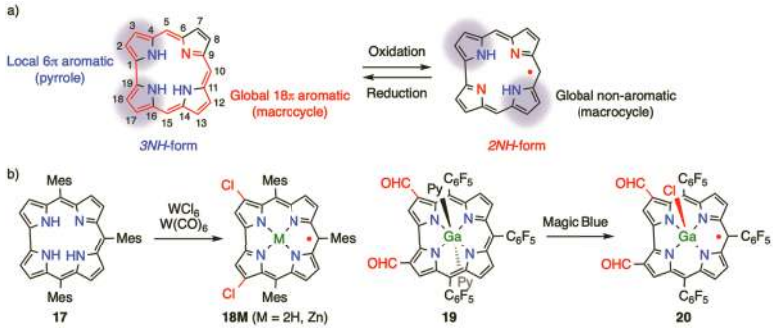


**Figure 11.5** (a) *3NH*- and *2NH*-Corroles and (b) examples of stable *2NH*-corrole radicals. Py = pyridine, Magic Blue = $(4\text{-}BrC_6H_4)_3N{\cdot}SbCl_6$.

Besides appended or fused segment-centered radicals, porphyrinoid macrocycles themselves can be an origin of radical nature [32]. Corrole, a ring-contracted porphyrinoid lacking one methine carbon, takes a slightly distorted conformation due to the steric hindrance between the three NH protons inside the cavity (Figure 11.5). Corrole displays more electron-rich nature than a typical porphyrin because it accommodates 18π electrons in its small π-system. Hence, corrole can take *2NH*-radical states easily, upon oxidation-induced de-protonation or metalation, to furnish a neutral radical that is highly planar, owing to a favorable hydrogen-bond network in the resultant two NHs corrole [55–58]. Along this line, Bröring and coworkers reported that reactions of 5,10,15-trimesitylcorrole **17** with $WCl_6$ and $W(CO)_6$ resulted in the production of air-stable *2NH*-corrole radical $\mathbf{18H_2}$ with concomitant 3,17-dichlorination [59]. In the spin density distribution map of a

free-base corrole and zinc(II) complex (Figure 11.6), relatively large spin densities were computed at the 3,17-positions, in addition to three *meso*-carbons, which were consistent with the observed chlorination.

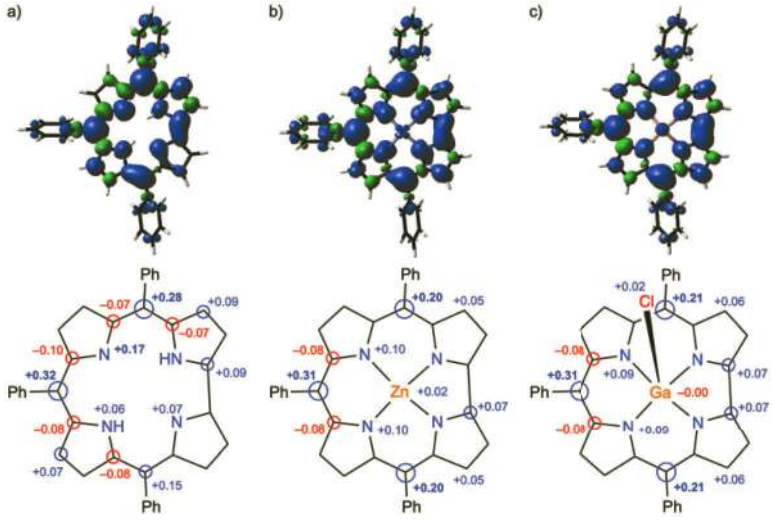


**Figure 11.6** Spin density distribution plots (top) and atomic spin densities (bottom) of (a) free-base *2NH*-corrole radical and its (b) zinc(II), and (c) gallium(III) complexes calculated at the UB3LYP/6-31G(d) level (isovalue: 0.001).

Later, Sankar and coworkers also prepared an air-stable [2,17-diformyl-5,10,15-tris(pentafluorophenyl)corrolato] gallium(III) chloride radical **20** via oxidation of the corresponding $Ga^{III}$-corrole bearing neutral axial ligand(s) using tris(4-bromophenyl)aminium hexachloroantimonate (Magic Blue) [60]. Exchange of porphyrinic methine carbons with *N*-substituted amine-type nitrogen atoms gave a series of azaporphyrinoids [12], which can alter their porphyrinic 18π macrocycles to 19π or 20π electronic systems that are easily oxidized. Matano and coworkers reported highly stable 5,10,15,20-tetraaryl-5,15-diazaporphyrin radical cations **21R** and **22R** [61, 62] and 5,10,20-triaryl-5,15-diazaporphyrin neutral radical **23R** [63] with a 19π circuit (Figure 11.7). As the size of porphyrinoid macrocycles increases, the spin and charge densities are naturally more diluted, so that the reactivity is mitigated. For instance, mild oxidation of a

conformationally rigid figure-of-eight-shaped regular octaphyrin bis-$Si^{IV}$-complex afforded its 37π radical cation **24** as a stable species [64]. For the same reason, other expanded porphyrinoids can yield stable radical states upon oxidation/reduction, protonation, and metalation as well as via "intrinsic non-innocence".

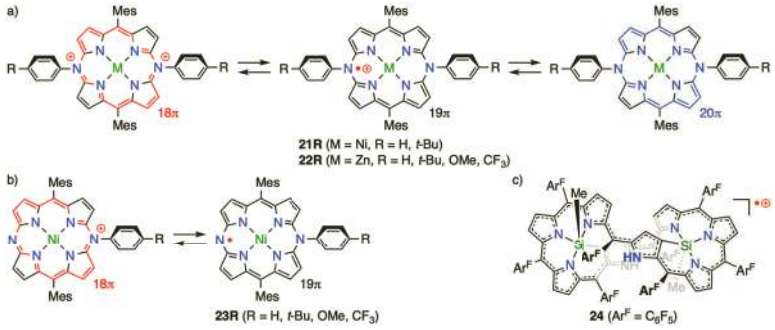


**Figure 11.7** Redox interconversion of (a) tetra- and (b) triaryl-5,15-diazaporphyrins. (c) A stable bis-$Si^{IV}$-octaphyrin radical cation with 37π-electron system.

### 11.1.3 Spin Density Distribution Depending on Incorporated Radical Units

Spin density distribution is of critical importance to understand the magnetic properties of diradicaloids and other multi-spin systems. Figure 11.8 summarizes the calculated atomic spin densities and experimental redox potentials of typical *meso*-aryl-type porphyrinoid-based radicals. Hexaphyrin *meso*-oxy radical **A** [45] displays a highly delocalized spin density distribution with only +0.02 spin at the formal radical center. Instead, larger values are calculated at the five *meso*-carbons (–0.17 and +0.19 to +0.21) and two α-carbons bonded to the free *meso*-carbon (+0.15). This result accords general trends that radicals are electron-deficient species and porphyrinoid precursors are electron-rich macrocycles with flexible π-conjugation. Regular porphyrin and ring-contracted subporphyrin *meso*-oxy radicals **B** and **C** [46, 47] also show the largest spin density at the *meso*-carbons (+0.26), but retain considerable spin densities at their oxygen atoms (+0.19 to +0.21). Notably, the *meso*-carbon at the opposite side (+0.26) has almost a double spin

density than at the other two sites (+0.13). The spin distributions of aminyl radicals **D** and **E** [48, 49] are quite similar to those of oxy radical counterparts (**B** and **C**, respectively), but show slightly increased values at the nitrogen atoms (+0.25 to +0.26), reflecting the decreased electronegativity of nitrogen atom. *meso*-Dicyanomethyl radical **G** [50] exhibits a further increased spin density at the radical center (+0.30) and slightly decreased ones at the *meso*-carbons on the opposite side (+0.22). Importantly, setting of radical segments at *meso*-positions is critical to effective spin conjugation, while only diminished spin delocalization is seen in porphyrins bearing radical centers at the β-positions. For example, porphyrin β-dicyanomethyl radical **F** [51] has dominant spin densities at the radical center (+0.47) and shows spin densities less than 0.10 at the porphyrin carbon atoms, except for the allylic β-position (+0.23). Fused carbon-centered radical **I** [53] exhibits the highest spin density at the formal radical center (+0.32) and a large value at the *meso*-carbon on the opposite side (+0.20). It is noteworthy that the β-carbons next to the fused β-positions have higher spin densities (+0.14 to +0.16) than the remaining *meso*-carbons (+0.08 to +0.09), owing to the additional conjugative circuits including fused β-linkages. On the other hand, in aminium radical cation **H** [54], which is isoelectronic to carbon-centered radical, minor spin density (+0.12) is computed at the nitrogen center due to the positive charge. Large values are distributed mainly to three *meso*-carbons (+0.21 to +0.26) with moderate contribution of the β-carbons next to the β-linkages (+0.09 to +0.14).

Changes in the spin density values at the *meso*-carbons and radical centers accord well with the experimental redox potentials, which are negatively shifted in the order of aminium > oxy > aminyl > carbon-centered radical. These values are critically important to understand the reactivities at specific positions and the overall stabilities of radicals. The spin distribution of these mono-radicals plays a central role also in determining the magnetic properties of the corresponding dimer diradicals. When two mono-radical segments are connected with each other at spin-rich sites, intramolecular magnetic coupling becomes significant. Singlet dimers exhibit small diradical nature with negatively large singlet–triplet energy gaps and triplet ones strongly prefer spin-aligned states due to positively

large values. While oxy and dicyanomethyl radicals are monovalent and have no substituents other than porphyrinoid groups, aminyl radicals are divalent and aminium cations and carbon-centered ones are trivalent. The additional valence can be used for construction of intricately designed multi-radical systems with inter-porphyrinic magnetic interactions.

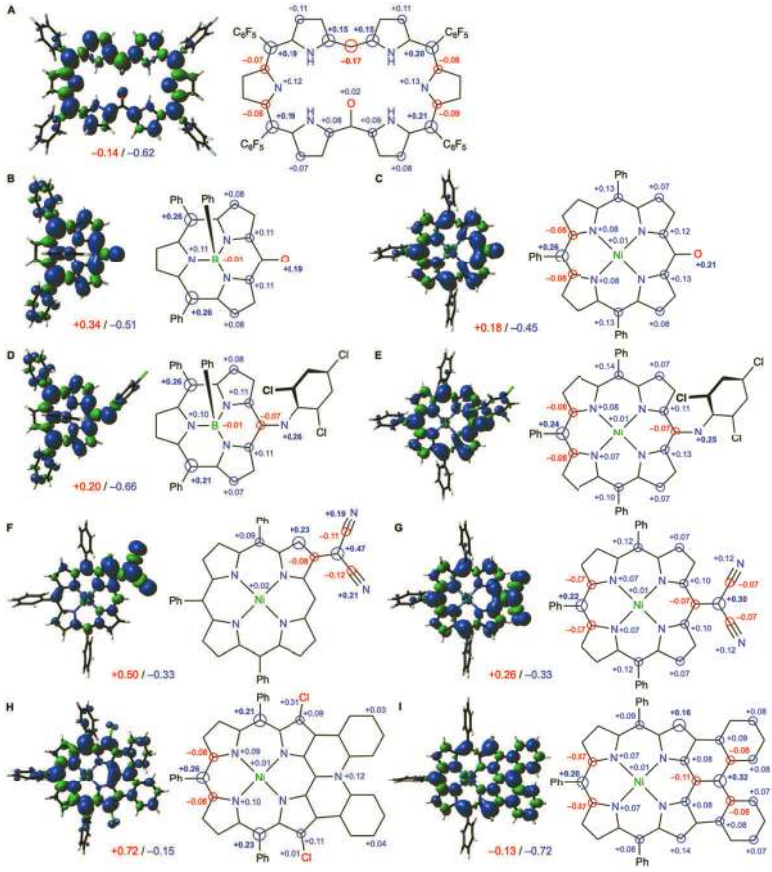


**Figure 11.8** Spin density distribution plots and atomic spin densities of hexaphyrin, subporphyrin, and porphyrin *meso*-oxy radicals (**A**, **B**, and **C**), subporphyrin and porphyrin *meso*-aminyl radicals (**D** and **E**), porphyrin β- and *meso*-dicyanomethyl radicals (**F** and **G**), and porphyrin-fused aminium radical cation and carbon-centered radical (**H** and **I**). The calculations were performed at the UB3LYP/6-31G(d) level (isovalue: 0.001). The first oxidation/reduction potentials (V, vs ferrocene/ferrocenium cation) were also given below the plots.

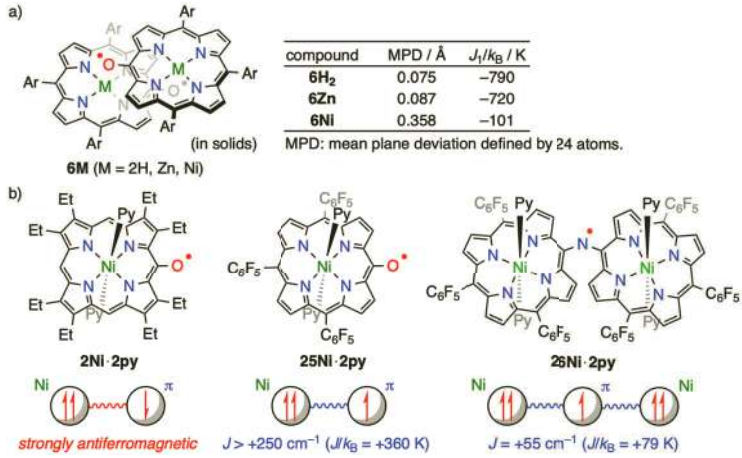


**Figure 11.9** (a) π-Stacked dimers of *meso*-aryl porphyrin *meso*-oxy radicals. (b) Magnetic interactions between paramagnetic metal ions and π-radicals. Ar = 3,5-di-*tert*-butylphenyl, Py = pyridine.

Aside from conjugative interactions, spatial arrangements of two radical segments are also important for control of their magnetic properties. Due to the large π-planes, porphyrinoid radicals can form π-stacked dimers with fairly strong antiferromagnetic coupling. A series of metal complexes of porphyrin oxy-radical **6M** [47] was actually shown to give π-stacked dimers by X-ray structural analysis (Figure 11.9). The superconducting quantum interference device (SQUID) studies revealed that the strength of intermolecular interactions was highly dependent on the effectiveness of π-π stacking and hence planarity of porphyrins. Furthermore, the magnetic coupling with paramagnetic metals in the central cavity is determined by how pairwise planar porphyrinoid π-radicals are interacted. Additional coordination of axial ligands changes a diamagnetic $Ni^{II}$ ion to high-spin one ($S$ = 1), which interacts ferromagnetically with *meso*-aryl porphyrinoxyl to take a quartet ground state (**25Ni·2py**) [65]. On the other hand, the magnetic coupling in high-spin $Ni^{II}$ complex of OEP *meso*-oxy radical was antiferromagnetic to give doublet one (**2Ni·2py**) because the contorted π-plane broke the orthogonality of σ- and π-spin orbitals [43]. As a natural extension, the *meso*-aryl-type di-porphyrin aminyl radical was reported to mediate two high-spin $Ni^{II}$ centers with

ferromagnetic coupling to attained spin-aligned state (**26Ni·2py**) [66]. In this system, the spin density of π-radical was delocalized onto the two porphyrin segments with spin dilution and hence the observed magnetic interaction was fairly weak as compared with that of the oxy radical monomer.

## 11.2 Classification of Porphyrinoid-Based Diradicaloids

In this section, we classify porphyrinoid-based diradicaloids into three groups (Figure 11.10). Type I diradicals and diradicaloids are composed of porphyrins or other aromatic macrocycles in the centers and two radical segments attached to their peripheries. In type I Kekulé compounds, diradical characters are understood as balances between aromatic diradical and closed-shell quinoidal structures. On the other hand, type II diradicals and diradicaloids hold diradical centers fused with porphyrinoid π-frameworks, which improves the stability and perturbs the magnetic properties of the original diradical units via spin delocalization. In type I and II diradicals and diradicaloids, the constituent elements of the external radical centers are critical to their magnetic properties. As introduced in the previous section, carbon-centered radicals tend to retain the spin

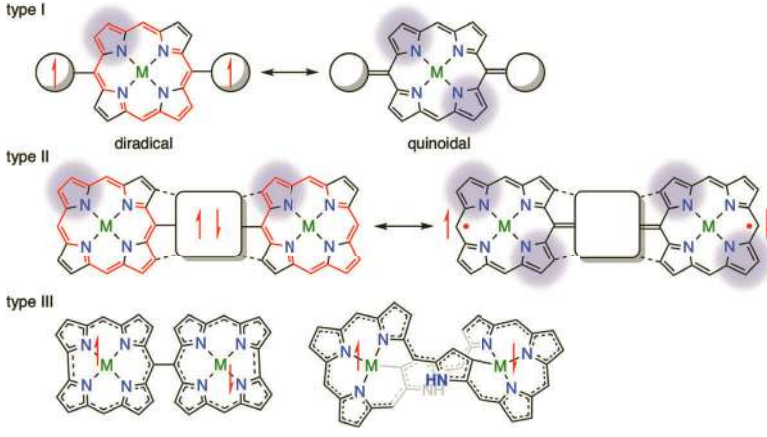


**Figure 11.10** Classification of porphyrinoid-based diradicaloids.

densities at the formal radical carbons and hence the original natures of the incorporated radical segments. In contrast, porphyrinoid-based oxy radicals display more porphyrinoid-centered characters with ketone-like C–O bonds, due to the larger spin densities at the porphyrinoid sides. Type III diradicaloids consist of porphyrinoids possessing radical natures in the macrocycles themselves. Dimers of intrinsically mono-radical porphyrinoids, such as corroles, are attractive platforms for diradicaloids as well as core-modified expanded porphyrins and strongly antiaromatic norcorroles (ring-contracted porphyrinoids without two methine carbons).

## 11.3 Porphyrinoids Bearing Two Radical Units at Their Periphery (Type I)

This section describes porphyrinoid-based diradicaloids with two radical centers at the periphery. Quinoidal diradicaloids display high diradical characters when the porphyrinoid cores favor to retain their aromatic nature rather than take cross-conjugated electronic states or the spin densities are located at around the appended radical units without significant inter-spin interactions across the macrocycles. A few non-Kekulé compounds were also prepared via introduction of radical centers at appropriate substitution sites and their magnetic interactions were evaluated by magnetic measurement.

### 11.3.1 Quinoidal Porphyrinoids

Incorporation of two oxygens at the porphyrinic 5,15-positions provides a quinoidal compound, which can also be drawn as a diradical structure with the retained 18π aromaticity (Figure 11.11). However, such 5,15-dioxoporphyrins **27** were reported as closed-shell quinoidal molecules without any diradical characters [67]. The situations were the same for 5,10,15,20-tetraoxoporphyrin **28a** and those with other diradical-inducing units such as dicyanomethylene and 3,5-di-*tert*-butyl-4-oxo-2,5-cyclohexadienylidene (**28b–33**) [68–72]. The preferred quinoidal natures were rationalized by the small macrocyclic stabilization energy [34–36] as compared with additional bond energies in the quinoidal structures. Quite recently, Osuka and coworkers have reported a series of dynamically stable

bis-dicyanomethyl diradical **34** [73]. Due to rather ineffective spin delocalization through the β-bonds, diradical **34** did not take closed-shell quinoidal structures, but formed dimers that possess σ-bonds between dicyanomethyl centers and allylic β-carbons in *syn*-(**34aNi$_2$**) and *anti*-configurations (**34aZn$_2$**). The σ-bonds dissociated in solution to give equilibrium states with some radical species. The $^1$H NMR signals of **34aNi$_2$** became broader upon heating and those of **34aZn$_2$** were unclear without lowering the temperature. Owing to the two fragile C–C bonds, thermal scrambling was observed for hetero dimer **34aNi**·**34bNi** and homo dimers **34aNi$_2$** and **34bNi$_2$**.

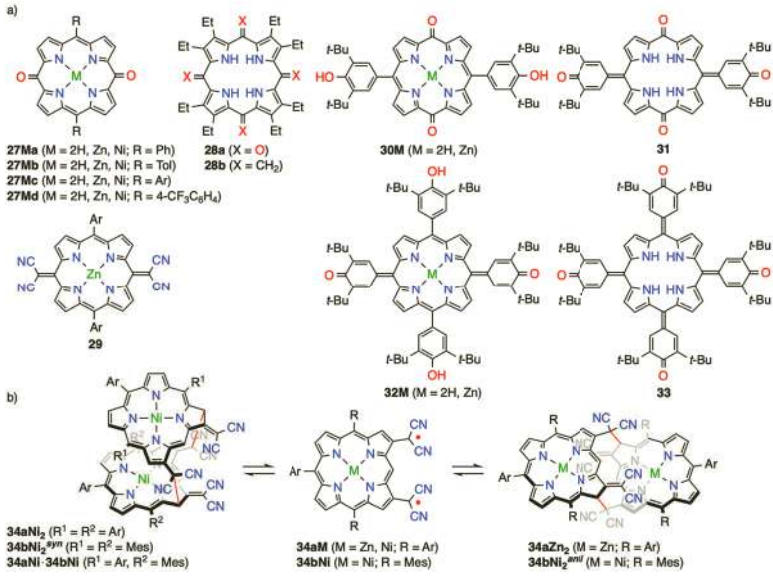


**Figure 11.11** (a) Quinoidal porphyrins with closed-shell natures and (b) porphyrin β,β-bis-dicyanomethyl diradicals and their reversible dimerization. Tol = 4-methylphenyl, Ar = 3,5-di-*tert*-butylphenyl.

With hydrocarbon-based segments, fused quinoidal porphyrins have been prepared and their electronic structures have been examined (Figure 11.12). In 2012, Kim, Wu, and coworkers attained the direct fusion of two diarylated-*exo*-methylene fragments to Ni$^{II}$-5,15-dimesitylporphyrin [74]. The obtained π-extended porphyrin **35** had a closed-shell electronic state despite its elongated *exo*-methylene bonds upon fusion (1.414 Å in the calculated structure).

In 2016, Tanaka, Kim, Osuka, and coworkers synthesized di-*peri*-dinaphthoporphryin **36** via $PtCl_2$-mediated cyclization of alkynes. Owing to the existence of four fused benzo segments, *exo*-methylene bonds were fully conjugated, but the fused porphyrins exhibited certain 24π antiaromaticity instead of explicit diradicaloid natures [75, 76]. Further, Thompson and coworkers reported bis-phenalenyl-fused $Zn^{II}$-porphyrin **37** using *syn*-selective Scholl-type oxidative fusion and subsequent thermal dehydrogenation. This porphyrin also had a dominant quinoidal character, while it displayed broad and intense near-infrared (NIR) absorption [77].


**Figure 11.12** Fused quinoidal porphyrinoids without diradical characters. Ar = 3,5-di-*tert*-butylphenyl.

While effective conjugation in fused π-skeletons was not sufficient to prevent diradicaloid candidates from falling into closed-shell quinoidal states, the assistance of steric congestion realized diradicaloids in twisted conformations (Figure 11.13). In 2017, Wu and coworkers reported the conformation-dependent diradical properties of 5,15-bis(9-fluorenylidene) porphyrin **38M** [78]. The free-base molecule had a closed-shell singlet ground state taking a saddle-shaped geometry with short C–C double bonds of 1.355 Å as revealed by X-ray crystallographic analysis, but it acquired diradical natures upon heating. At 393 K, the $^1$H NMR signals due to the fluorenyl units were significantly broadened and the powder sample showed a single-line EPR signal at $g$ = 2.0029. The variable-temperature magnetic measurement by SQUID gave a singlet–triplet energy gap ($\Delta E_{ST}$) of –3.80 kcal mol$^{-1}$ and unusual broad-range hysteresis upon slow temperature change. Along this line, theoretical calculations suggested three additional local minimum structures besides lowest-energy saddle-shaped one when the dihedral angles between the porphyrin and fluorenylidene segments were varied. Two of them showed significant diradical characters ($y_0$) of

74.4% and 54.0%, reflecting the orthogonal fluorenyl units, one of which was accessible with a relatively small energy barrier of 12.45 kcal $mol^{-1}$. They also prepared the corresponding $Ni^{II}$-complex **38Ni**, which exhibited broad $^1H$ NMR peaks even at room temperature, a triple-line EPR signal at $g$ = 2.0059, and a smaller $\Delta E_{ST}$ of –2.70 kcal $mol^{-1}$. Furthermore, double protonation with two equivalents of trifluoroacetic acid (TFA) was performed. The resulting dicationic specie **39** was confirmed as a closed-shell compound with a drastically contorted tetrapyrrolic core, displaying sharp $^1H$ NMR spectrum even at high temperature. In 2018, Cui, Wang, and coworkers also prepared 5,15-bis(diarylamino)porphyrin diradical dication **40X** as air-insensitive specie by using $[Al(OR_F)_4]^-$ ($R_F$ = $C(CF_3)_3$) as the counter anion [79]. These dications exhibited EPR signal at $g$ = 2.0034 and 2.0036 with those due to the forbidden half-field transitions in the powder states at 87.6 K as well as broad NIR absorption in $CH_2Cl_2$ solution. Although the crystal structures of the diradicals were not obtained, those of charge-neutral molecules indicated large dihedral angles between the diarylamine and porphyrin planes (69.9° and 77.8°).

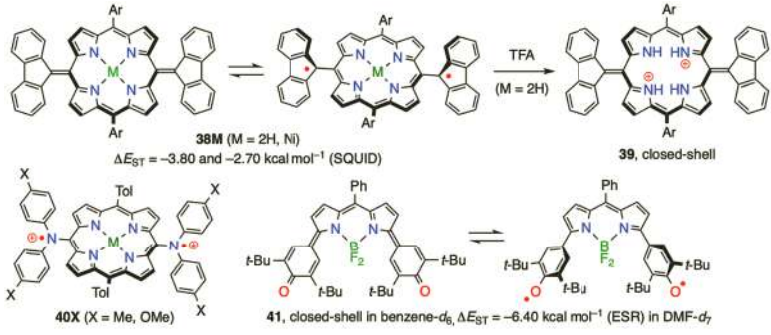


**Figure 11.13** Porphyrinoid-based diradicaloids with twisted conformations. Ar = 3,5-di-*tert*-butylphenyl, Tol = 4-methylphenyl.

Similar conformational flexibility afforded another diradicaloid based on a boron dipyrromethene (BODPY) bearing two phenoxyls (**41**) [80]. In the crystal structure, the two phenoxyl rings were slightly twisted with small dihedral angles of 15.5° and –6.3° and showed significant bond length alternation with large C–O double bond natures (1.238 Å and 1.233 Å). Due to the intermolecular

dipole–dipole interaction, **41** adopted a rigid dimeric structure with an inter-plane distance of 3.862 Å in the antiparallel stacking. Along this line, a set of sharp NMR signals and silent EPR spectrum were observed in benzene-$d_6$ at room temperature, indicating the closed-shell electronic configuration. On the other hand, the NMR peaks were broadened in DMF-$d_7$ above 223 K. A moderate EPR signal was detected at $g$ = 2.0034 in frozen solution and its variable-temperature intensity plot gave a singlet–triplet energy gap ($\Delta E_{ST}$) of –6.40 kcal mol$^{-1}$. According to the DFT calculations, the diradical character ($y_0$) became larger from 26.8% to 83.8% as the dihedral angles between the BODPY core and phenoxyl segments increased from the optimized angle of 17.6° to 77.6°. Wu and coworkers proposed that its large dipole moment prompted the formation of dimeric structures with small dihedral angles both in the solid state and non-polar solvents, while in highly polar solvents such as DMF, **41** was solvated as a single-molecule form to display more free rotation, larger averaged dihedral angles, and thus larger diradical characters.

Insertion of π-spacers between porphyrinoids and appended radical units is another way to realize diradical electronic states in porphyrinoids (Figure 11.14). In 2017, Furukawa, Kim, Osuka, and coworkers studied a series of porphyrin- and hexaphyrin-based singlet diradicals, **42$^n$** and **43$^n$**, bearing two sets of varying (oligo)thiophene linkers and terminal 3,5-di-*tert*-butyl-4-oxo-2,5-cyclohexadienylidenes [81]. A quinoidal porphyrin without any thiophene spacer (**42$^0$**) had a closed-shell electronic structure and displayed clear $^1$H and $^{19}$F NMR peaks. Their chemical shifts, as well as nucleus-independent chemical shift (NICS(1)) values of +0.01 to –1.94 ppm inside the macrocycle, indicated non-aromatic nature of the porphyrinic unit, which was consistent with split and broad electronic absorption bands at 411 nm, 434 nm, and 615 nm. In the crystal structure, two dipyrromethene segments were bent with a dihedral angle of 132.1° and C–C bond lengths of 1.379(2) Å and 1.373(2) Å indicated a double-bond character for the exo-methylene unit. In contrast, a thiophene-inserted counterpart **42$^1$** showed very broad $^1$H NMR spectra in $CD_2Cl_2$ at both room temperature and –90 °C, suggesting its paramagnetic character. The magnetometry measurement gave a quite small singlet–triplet energy gap ($\Delta E_{ST}$)

of –0.13 kcal $mol^{-1}$, indicating a weakly coupled singlet diradical nature. By point dipole approximation, the inter-spin distance was estimated to be 14.2 Å from *D* value obtained by simulation of EPR spectrum in toluene, which was composed of doublet ($g$ = 2.0057) and triplet signals ($g$ = 2.0062, $D$ = 220 MHz, $E$ = 12 MHz). In theoretical calculation, spin densities were mainly localized on the thiophene and phenoxyl units with small distribution on the porphyrin core and the diradical character index ($y_0$) was computed to be 0.99. These results were well consistent with the SQUID and EPR data. The optimized structure was characterized with a small mean plane deviation (MPD) of the porphyrin core (0.077 Å), longer exo-methylene C–C bond lengths (1.48 Å), and large dihedral angles (61.6° and 61.5°) between the porphyrin and thiophene spacers. The NICS (1) values inside the macrocycle were also markedly negative (–12.18 to –15.58 ppm) and the experimental UV-vis absorption spectrum retained the characteristics of typical aromatic porphyrins. Among the hexaphyrin series, directly and mono-thiophene-bridged 3,5-di-*tert*-butyl-4-oxo-2,5-cyclohexadienylidene-substituted ones **43⁰** and **43¹** [82] exhibited quinoidal closed-shell electronic systems with dumbbell-shaped hexaphyrin segments. They showed clear $^1$H NMR signals with non-aromatic pattern in $CDCl_3$ as well as rather short C–O bonds (1.234(3) to 1.238(6) Å) and *exo*-methylene C–C bonds (1.395(3) to 1.408(6) Å) in their X-ray crystal structures. Bithiophene-bridged congener **43²** gave too broad $^1$H NMR spectrum at room temperature, owing to significant diradical character ($y_0$ = 0.85). Different from the open-shell porphyrin analog, **43²** displayed sharper $^1$H NMR peaks at low temperature, sufficient stability against air and moisture, and a simple EPR signal without any fine-structure splitting. The obtained $\Delta E_{ST}$ value (–3.72 kcal $mol^{-1}$) was much larger than that of the porphyrin derivative **42¹** (–0.13 kcal $mol^{-1}$) and calculated spin distribution was well delocalized over the whole π-network including the hexaphyrin core, allowing two spins to couple with each other. The crystallographic analysis also provided longer *exo*-methylene C–C bonds (1.408(8) to 1.430(6) Å) with more single-bond nature and larger harmonic oscillator model of aromaticity (HOMA) values (0.51 and 0.61) than those of other quinoidal hexaphyrins (0.25 and 0.47).

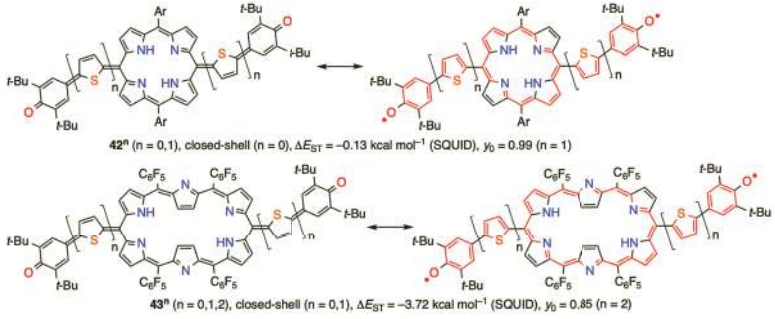


**Figure 11.14** Quinoidal porphyrins and hexaphyrins bearing thiophene-bridged phenoxyl units. Ar = 3,5-di-*tert*-butylphenyl.

### 11.3.2 Diradicaloids Based on Porphyrin Dimers

As seen in the last part of the previous section, increase of aromatic units is an effective method to realize enhanced diradical character in quinoidal compounds. In line with this consideration, *meso-meso* linked dimeric porphyrins have been explored (Figure 11.15). In 2002, Anderson and coworkers developed *meso-meso* linked and fully fused porphyrin dimers, **44** and **45**, with quinoidal π-conjugated systems bearing dicyanomethylene terminals [83]. The *meso-meso* linked one **44** took an *anti*-folded conformation with the central overcrowded C–C double bond (1.38(3) Å), which was significantly elongated to 1.43(4) Å in its fully fused derivative **45** with a planar structure. Both of these dimers showed fairly intense NIR absorption and small electrochemical gaps, but diradical nature was not observed. They also prepared cumulenic dimer **46** as a quinoidal compound with clear $^{1}$H and $^{13}$C NMR signals with non-aromatic characters [84].

In 2016, Arnold and coworkers tested oxidation of $Ni^{II}$-5,15-diphenyl-10-hydroxyporphyrin, leading to generation of a *meso-meso* linked dimer of a quinoidal oxoporphyrin (**47**) via oxidative dehydrogenation at the *meso-meso* bridge [85]. This result was different from those of 10-hydroxylated OEPs, which gave the corresponding singly σ-bonded dimer $\mathbf{2M_2}$ [41]. Quinoidal dimer **47** was calculated to have a parallel-stepped arrangement and indeed exhibited clear $^{1}$H NMR peaks, due to its β-protons in δ = 6.87–6.24

ppm. Later, Osuka and coworkers investigated the effect of central metals on the electronic structures of quinoidal oxoporphyrin dimers bearing mesityl *meso*-substituents (**48M**) [86]. $Ni^{II}$-porphyrin dimer **48Ni** was a closed-shell quinoidal compound showing a set of sharp $^1H$ NMR signals and step-like X-ray structure, in which the two highly distorted porphyrins (MPD: 0.414 Å) were connected by the short *meso*-*meso* bond (1.372(4) Å). In contrast, 1-methylimidazole-coordinated $Zn^{II}$-porphyrin dimer **48Zn**·**Im** displayed explicit open-shell nature as evidenced by silent $^1H$ NMR spectrum and EPR signal at $g$ = 2.0040. The crystal structure was also largely different. The two porphyrin units were highly planar (MPD: 0.0.046 Å and 0.085 Å) and linked together via a long *meso*-*meso* bond (1.492(6) Å) in a twisted conformation with a dihedral angle of 71.23°. The magnetic interaction between the two *meso*-oxy radicals was evaluated by variable-temperature EPR intensity plot and SQUID measurement, affording $J_1/k_B$ values of –94 K in solution and –62.0 K in the solid state, respectively. Intriguingly, free-base porphyrin dimer **48H$_2$** took a quinoidal crystal structure, but showed a weak EPR signal and a clear $^1H$ NMR spectrum in solution at 25 °C, which became broader at higher temperature. These observations suggested that free-base dimer **48H$_2$** was in equilibrium between the folded closed-shell quinoidal form and the perpendicular open-shell diradical one in solution. Theoretical calculations rationalized the central metal-dependence of electronic structures. Namely, decrease of MPD values (Ni: 0.392 > 2H: 0.283 > Zn: 0.243 Å) causes intramolecular steric repulsion around the *meso*-*meso* linkages and destabilize the quinoidal forms. In 2019, Osuka and coworkers also synthesized *meta*- and *para*-phenylene-bridged dimers of porphyrin *meso*-oxy radicals (**49mM** and **49pM**) [87]. These dimers exhibited predominant open-shell characters regardless of the connected positions and the $Zn^{II}$-derivatives formed infinite 1D-chains with Zn–O coordination in the solid states. The intramolecular magnetic interactions of 1-methylimidazole-coordinated $Zn^{II}$-porphyrin dimers were weakly antiferromagnetic not only in *para*-phenylene-bridged dimer **49pZn**·**Im** but also in *meta*-congener **49mZn**·**Im** because large dihedral angles between the phenylene-bridge and porphyrin segments prohibited π-conjugative interactions.

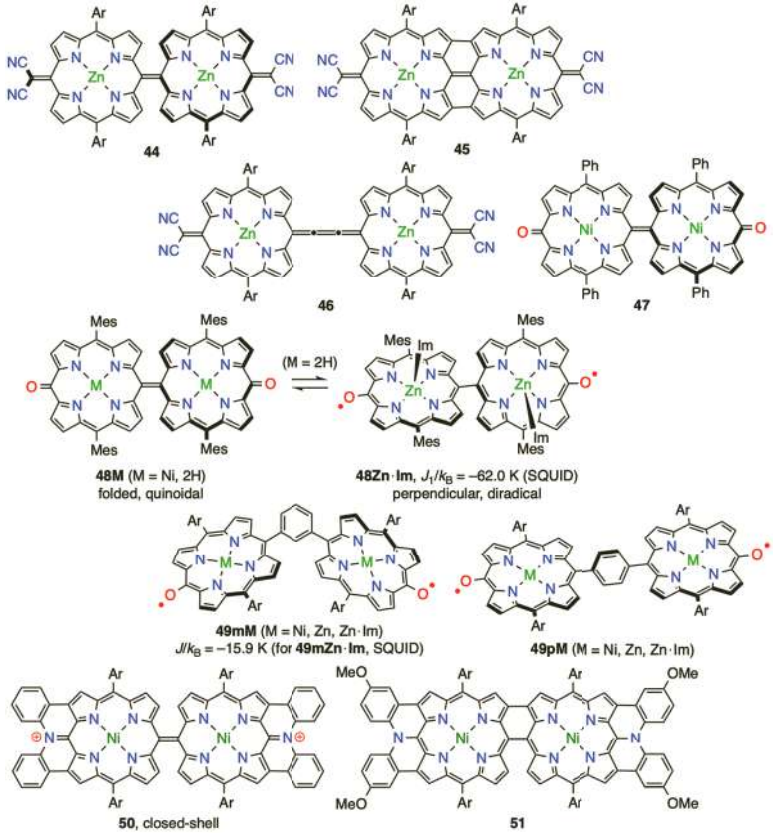


**Figure 11.15** Quinoidal *meso-meso* linked porphyrin dimers. Ar = 3,5-di-*tert*-butylphenyl, Im = 1-methylimidazole.

In 2016, Osuka and coworkers tested oxidation of *meso-meso* linked diarylamine-fused porphyrin dimers [88]. A diphenylamine-fused derivative formed the corresponding closed-shell quinoidal dication **50** with clear $^1$H NMR peaks even at 60 °C upon oxidation with Magic Blue, while dianisylamine-fused one produced a fused dimer with an additional β–β bond (**51**).

### 11.3.3 Non-Kekulé Diradicals Based on Porphyrinoids

In 2010, Osuka, Kim, and coworkers reported that incorporation of two oxygen atoms at 5,15-positions of a hexaphyrin afforded a stable non-Kekulé singlet diradicaloid **52** (Figure 11.16) [89]. The

structure of diradical **52** was confirmed by single-crystal X-ray diffraction analysis. EPR spectroscopy showed a signal at $g$ = 2.003 with temperature-dependent intensities in the solid state. Fitting with Bleaney–Bowers equation gave ($J/k_B$, $\Delta E_{ST}$) values of (–645 K, –2.56 kcal mol$^{-1}$), indicating strong antiferromagnetic coupling. Theoretical calculations were fully consistent with the experiments, displaying similar $\Delta E_{ST}$ value of –2.45 kcal mol$^{-1}$, well delocalized singly occupied molecular orbitals (SOMOs), and considerable diradical character ($y_0$) of 62%. Notably, diradical **52** had a small electrochemical gap (0.84 V) and large TPA cross-section ($\sigma^{(2)}$ = 1600 GM) with excitation at $\lambda_{ex}$ = 1600 nm, which was larger than 28π antiaromatic *meso*-free hexaphyrin (360 GM) and 27π non-aromatic singly *meso*-oxygenated one **4** (600 GM) [90]. The open-shell electronic structures and aromaticity of these hexaphyrins were evaluated in detail by time-resolved spectroscopy and theoretical studies in terms of the second hyperpolarizability, NICS and HOMA values, and anisotropy of the induced current density (ACID) plots.

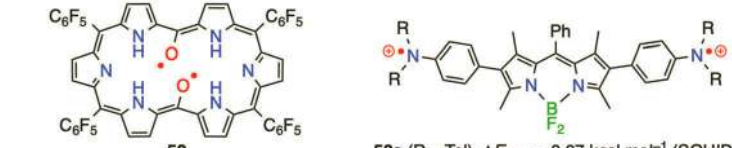


**52**
$\Delta E_{ST}$ = –2.56 kcal mol$^{-1}$ (SQUID), $y_0$ = 0.62

**53a** (R = Tol), $\Delta E_{ST}$ = –0.07 kcal mol$^{-1}$ (SQUID)
**53b** (R = 4-OMeC$_6$H$_4$)

**Figure 11.16** Porphyrinoid-based non-Kekulé diradicals. Tol = 4-methylphenyl.

As another example, Cui, Wang, and coworkers prepared BODPY-based diradicals with two triarylamine radical cations at 2,6-positions (**53**) [79]. Diradicals displayed powder EPR pattern with average $g$ factors of 2.0027 and 2.0011 for **53a** and **53b**, respectively, as well as clear forbidden half-field transitions for $\Delta m_S = \pm 2$. Diradical **53a** was further characterized by X-ray crystallographic analysis and solid-state SQUID magnetometry. The bridging phenyl group showed a small bond-length alteration of 0.026 Å, shorter average N–C bond length of 1.404(5) Å than the peripheral aryl rings (1.422(6) Å), and fairly large dihedral angle of 53.7° from the BODPY plane. $\Delta E_{ST}$ was estimated at a quite small value of –0.07 kcal mol$^{-1}$, which agreed with the computed one (–0.16 kcal mol$^{-1}$).

## 11.4 Porphyrinoid-Fused Diradicals and Diradicaloids (Type II)

This section introduces fused π-conjugated systems with diradical- and diradicaloid-cores stabilized by peripheral porphyrinoids. As compared with type I diradicals that tend to form strong double bonds with porphyrinic carbons, the type II diradicals are more difficult to stabilize especially when radical centers are connected to porphyrinic β-positions or diradicals take triplet ground states. Contrary to the type I diradicaloids, type II Kekulé diradicaloids have strong diradical nature when porphyrinoids favor cross-conjugated non-aromatic states and thereby spin densities are distributed extensively onto the porphyrin segments. In non-Kekulé high-spin systems, the trade-off between strong ferromagnetic coupling and high chemical stability can also be understood in terms of spin density distribution.

### 11.4.1 Kekulé-Type Singlet Diradicaloids

Quinodimethanes, also known as xylylenes, are one of the most representative diradical units and intensive studies have long been devoted to their derivatives, including extended *para*-quinodimethanes [91–93], indenofluorenes [94, 95], and zethrenes [96, 97]. Along this line, porphyrinoid-fused quinodimethanes have been investigated by the group of Wu (Figure 11.17). In 2013, they reported a *para*-quinodimethane-bridged porphyrin dimer **54** with steric protection by bulky mesityl groups, in collaboration with Chi and Kim [98]. Unfortunately, **54** was not very durable on silica gel, but sufficiently stable in the solid state. Although **54** had a Kekulé-type closed-shell electronic structure with positive NICS(1) value of +1.41 ppm on the central benzene, TPA cross-section was fairly large in NIR region ($\sigma^{(2)}$ = 1600 GM at 1800 nm) in addition to strong one-photon absorption at 955 nm and multiple redox behavior with small electrochemical gap of 0.86 V. *para*- and *meta*-Quinodimethanes were also fused with two BODIPY segments by Kim, Wu, and coworkers in 2016 (**55**) [99]. These dimers were very stable under ambient conditions, but found to have small diradical characters ($y_0$ = 6.9% for *para*-isomer and 26.2% for *meta*-one) with

well delocalized spin density distribution according to theoretical calculations. For both *para*- and *meta*-compounds, $NICS(1)_{zz}$ values were computed to be negative at the central benzene rings (–4.16 and –6.3 ppm, respectively) and X-ray diffraction analysis indicated long *exo*-methylene bonds (1.425 and 1.443 Å, respectively), which supported the delocalized diradical natures. Reflecting the excellent absorption and emission properties of BODIPY units, diradicaloid **55** showed sharp and intense NIR absorption, as well as turn-on fluorescence upon addition of hydroxyl radical, probably via their conversion into closed-shell species. The same group reported direct fusion of *meta*-xylylene to one side of single porphyrin (**56**) [100]. In this case, the π-extended porphyrin took a closed-shell structure with a small diradical character ($y_0$ = 0.06) and large singlet–triplet energy gap (calculated $\Delta E_{ST}$ = –4.28 kcal mol$^{-1}$).

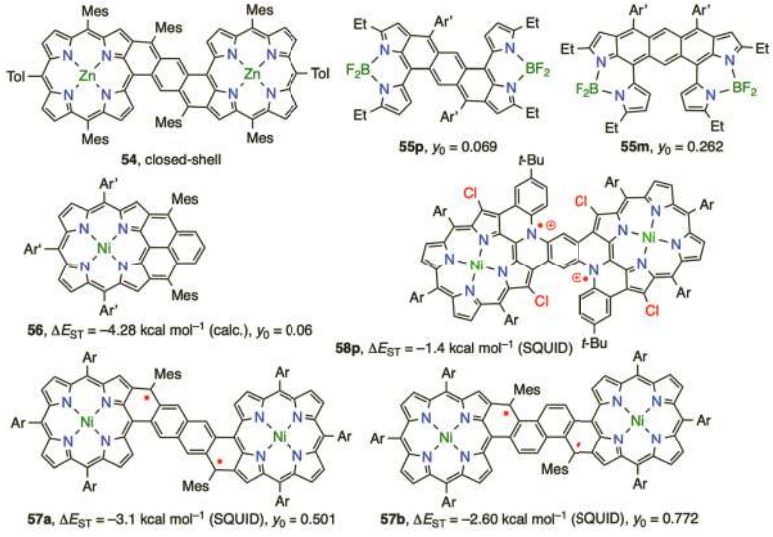


**Figure 11.17** Porphyrinoid-based type II Kekulé diradicaloids. Tol = 4-mehtylphenyl, Ar′ = 4-*tert*-butylphenyl, Ar = 3,5-di-*tert*-butylphenyl.

Further, Kim, Wu, and coworkers synthesized 2,6- and 1,5-naphthoquinodimethane-bridged ones **57** in 2019 [101]. 2,6-Type dimer **57a** was stable enough to be separated on silica gel column and gave a sharp $^1$H NMR signals at 298 K, which got fairly broadened upon heating to 353 K. An EPR signal was also observed

at $g$ = 2.00376 in the solid state at room temperature. $\Delta E_{ST}$ and $y_0$ values were determined to be –3.1 kcal mol$^{-1}$ and 0.501, based on the results of SQUID magnetometry and theoretical calculations, respectively. Notably, **57a** exhibited intense one-electron absorption at 976 nm and large TPA cross-section ($\sigma^{(2)}$ = 3500 GM at 1400 nm). 1,5-Type dimer **57b** was less stable on silica gel column than 2,6-isomer **57a**, requiring rapid elution over silica gel deactivated with triethylamine. While a solid-state EPR peak was observed at $g$ = 2.00314 at room temperature, $^1$H NMR spectrum was significantly broad at 298 K and became relatively sharp at 233 K. Along these behaviors, experimental $\Delta E_{ST}$ and computed $y_0$ values were estimated at –2.60 kcal mol$^{-1}$ and 0.772, indicating easier access to the excited triplet states and larger diradical character, respectively. NIR absorption band of **57b** was red-shifted and broadened with decreased intensities, as compared with **57a**. These differences were consistent with the structural studies, in which the bond length of naphthalene *exo*-methylene was determined to be 1.402(3) Å for 2,6-isomer **57a** by X-ray analysis and that of 1,5-one **57b** was calculated to be 1.410 Å. Shorter bond length in **57a** imply more localized spin nature onto the naphthoquinodimethane core and preferred closed-shell quinoidal state. In line with these results, electrochemical gap of **57a** (1.02 V) was larger than that of **57b** (0.68 V).

Dication of *para*-phenylenediamine, nitrogen analogs of *para*-quinodimethane, was fused with two porphyrin segments to give a highly stable dication **58p** by the Osuka group in 2019 [102]. As mentioned above, aminium radical cations fused with porphyrins let their spin densities spread effectively over the porphyrin π-network with decreased spin densities at the nitrogen atoms. Hence, diradical nature of **58p** was significantly larger than that of the carbon counterpart. $^1$H NMR spectrum was silent even at –60 °C except for broad peaks due to *tert*-butyl groups in the *meso*-substituents, and solid-state SQUID magnetometry revealed its weak antiferromagnetic coupling and the resulting small singlet–triplet energy gap ($J_1/k_B$ = –359 K, $\Delta E_{ST}$ = –1.4 kcal mol$^{-1}$, respectively). Importantly, the $\Delta E_{ST}$ value was smaller than those of other *para*-phenylenediamine dication derivatives [103, 104] except for those of largely twisted ones, indicating the effective spin dilution onto fused porphyrin segments.

### 11.4.2 Non-Kekulé Diradicals with High-Spin Ground States

*meta*-Quinodimethane, or *meta*-xylylene, itself is a non-Kekulé non-disjoint compound and induces strongly favored high-spin states when antiferromagnetic interactions through pyrrolic five-membered rings are not significant or restricted by the geometries of fused π-skeletons. Osuka and a coworker also prepared a *meta*-phenylenediamine-fused porphyrin dimer and its tetra-chlorinated dication as well (Figure 11.18) [102]. Dication **58m** was highly stable under ambient conditions and showed a weak ferromagnetic coupling ($J_1/k_B$ = +27 K, $\Delta E_{ST}$ = –0.11 kcal mol$^{-1}$), reflecting the diminished spin densities at the central phenylenediamine. Osuka group also synthesized a benzene-1,3,5-triaminyl triradical fused with three $Zn^{II}$-porphyrins in 2018 (**59**) [105]. Due to the neutral nitrogen radical centers, ferromagnetic intramolecular coupling ($J/k_B$ = +125 K, $\Delta E_{DQ}$ = +0.74 kcal mol$^{-1}$) was larger than that in the aminium radical cation-based diradical. Its EPR signal in toluene at 120 K appeared as a mixture of quartet and doublet species at ($g_\perp$, $g_{||}$) = (2.0032, 2.0030) and $g$ = 2.0087, respectively. The zero-field splitting parameter ($D$ = 82.5 MHz) was rather small due to the highly delocalized spin natures. Despite the high-spin natures, triradical **59** was very stable under ambient conditions. Triradical **59** took a pseudo-$C_3$-symmetric coplanar structure as revealed by X-ray diffraction analysis and showed reversible redox waves with narrow electrochemical gap of 0.48 V.

Kim, Wu, and coworkers reported that direct fusion of two *meta*-xylylene units led to a porphyrin-based carbon-centered triplet diradical **60** because the second *meta*-xylylene made it impossible to draw any Kekulé structures [100]. Unfortunately, diradical **60** was not able to be isolated as a stable compound, but persistent at room temperature under argon atmosphere. The EPR signal displayed clear split structures at $g$ = 2.00125, which can be interpreted as spin-nucleus coupling with four fused-benzene protons (7.30 MHz) and four pyrrolic β-protons (8.50 MHz). Theoretical calculations supported large spin densities at the fused-benzene carbons (+0.168) and pyrrolic β-positions (+0.305) and afforded a large $\Delta E_{ST}$ value of +6.98 kcal mol$^{-1}$, which was in agreement with the temperature dependence of experimental EPR intensities. Diradical **60** was easily

oxidized by atmospheric oxygen to yield dioxo derivative **61**, since the β-positions possessed large spin densities.

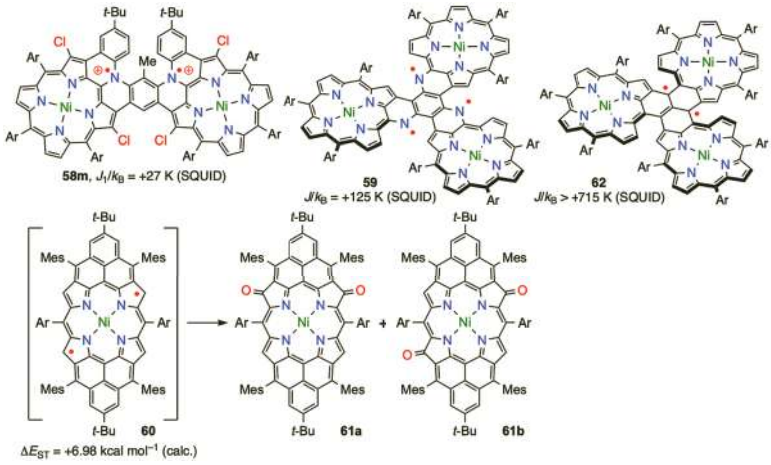


**Figure 11.18** Porphyrinoid-based type II non-Kekulé high-spin radicals. Ar = 3,5-di-*tert*-butylphenyl.

Furukawa, Osuka, and a coworker utilized another non-Kekulé non-disjoint unit, trimethylenemethane (TMM), to synthesize a trimeric porphyrin-fused triplet diradical **62** in 2018 [106]. Diradical **62** was obtained by reduction of the corresponding cation radical with ascorbic acid and stable enough to be handled as a solution open to air, though it slowly decomposed on silica gel. Thermal stability was also confirmed by the negligible change of the electronic absorption spectrum after heating its solution at 80 °C for 10 h. Single-crystal X-ray diffraction analysis revealed its propeller-like π-network, over which spin densities were calculated to be effectively delocalized. The SQUID magnetometry gave a flat $\chi T$-$T$ plot up to 350 K, providing $J_1/k_B$ value of 715 K as a lower limit ($\Delta E_{ST}$ > +2.8 kcal/mol). The observed strong intramolecular ferromagnetic coupling reflected the spin density distribution fairly retained at the TMM moiety and β-positions in the fused pyrroles (0.23–0.29), which can be ascribed to the small TMM structure and carbon-centered radical natures. Diradical **62** underwent reversible redox processes with narrow electrochemical gap of 0.48 V. The resulting dianion and dication species were characterized by electronic

absorption and $^1$H NMR spectroscopy as well as computed NICS(0) values. It was noteworthy that the electronic absorption spectrum of the radical anion was similar to the average of diradical and dianion, although reductive titration experiment gave a two-step spectral change, which supported the highly degenerate features of SOMOs of **62**.

## 11.5 Diradicaloids Based on Intrinsically Radical Porphyrinoids (Type III)

This section discusses diradicaloids in which the radical centers are incorporated into the porphyrinoid macrocycles themselves. For instance, dimers of *2NH*-corrles exhibit variable diradical characters, depending on the positions at which two corroles are connected with each other. Very strong antiaromatic characters of norcorroles result in extremely small HOMO–LUMO gaps, which let a few molecules acquire diradical characters. Large and cyclic π-conjugated systems of ring-expanded porphyrinoids also produce diradical compounds upon core modification.

### 11.5.1 Corrole-Based Diradicaloids

*2NH*-Type corrole radicals display the largest spin densities at 10 positions (+0.31 to +0.32) and the second at 5,15-positions (+0.20 to +0.22 on average) (Figure 11.6). Among the β-carbons, 3,17-positions have higher values (+0.05 to +0.06 on average) than the others and indeed *meso*-triarylcorroles form 3,3′-linked dimers under oxidative coupling conditions. As *2NH*-type corrole dimers, 10-10′ [5]cumulene-bridged dimer **63M** was prepared by Tanaka, Osuka, and coworkers in 2017 (Figure 11.19) [107]. Bis-$Zn^{II}$-dimer **63Zn** showed bond lengths of 1.373(5) Å, 1.239(5) Å, and 1.325(5) Å for the [5]cumulene C–C bonds in the X-ray structure. Although the diradical characters were not discussed in detail, the $^1$H NMR spectra of dimers $\mathbf{63H_2}$ and **63Zn** were broad in $CDCl_3$ at room temperature and recorded at –60 °C as a set of slightly broad peaks. As seen in type I quinoidal diradicaloids, steric congestion around linkages between the porphyrinoids and radical units causes large dihedral angles, decreased propensity toward formation of double

bonds, and large diradical characters. Such effects were also evident in corrole dimers with fairly twisted *meso-meso* linkages. A *meso*-mesityl-substituted 10-10′ linked *3NH*-corrole dimer **64aH$_3$** formed a stable diradical **65H$_2$** upon mild oxidation with an equimolar amount of *p*-chloranil [108]. The SQUID magnetometry revealed strong antiferromagnetic coupling with $J$ of –767 cm$^{-1}$ ($J/k_B$ = –1104 K) and diradical character ($y_0$) was estimated to be 0.82 according to theoretical calculations. In its crystal structure, the dihedral angle between the two *2NH*-corrole planes was 49.7°, being distinctly smaller than that of *3NH*-corroles (87.5°), which can be rationalized by the balance between the steric repulsion and favorable spin-pairing interaction. Bis-Co$^{III}$ diradical **65Co·PyCN** was also prepared by aerobic oxidation of the corresponding pyridine-coordinated closed-shell precursor **64aCo·2Py** with concomitant axial ligand exchange at the Co$^{III}$ centers with cyanide ions. Being similar to the free-base one, Co$^{III}$ diradical **65Co·PyCN** showed smaller dihedral angle around the 10-10′ bond (53.8°) than closed-shell precursor (66.8°) and strong antiferromagnetic coupling with $J$ of –616 cm$^{-1}$ ($J/k_B$ = –887 K). It is noteworthy that oxidation with 2,3-dichloro-5,6-dicyano-*p*-benzoquinone (DDQ) in refluxing $CHCl_3$ produced fused dimer **66** with additional 8-8′ linkage as a minor product.

On the other hand, oxidation of 10-10′ linked *3NH*-corrole dimer **64** with DDQ in refluxing $CHCl_3$ afforded the corresponding triply linked corrole dimer **67** under highly diluted conditions [109]. These fused dimers took both *2NH*- and *3NH*-forms, which interconverted with each other via reduction with $NaBH_4$ and oxidation with air. While dimer **67** exhibited moderate aromaticity in **3NH**-forms, *2NH*-dimer **68** was non-aromatic without explicit diradical nature. $^1$H NMR signals due to the β-protons were observed at 6.63–6.32 ppm for **67b** and 7.51–6.89 ppm for **68c**, being consistent with NICS values of –5.43 ppm and +4.95 ppm calculated at the centers of **67aH$_2$** and **68a**, respectively. Non-aromatic *2NH*-dimer **67aH$_2$** was also characterized by X-ray crystallographic analysis to show bond lengths of 1.395(4) Å, 1.389(4) Å, and 1.395(4) Å for 8-8′, 10-10′, and 12-12′ linkages, respectively. These values were clearly shorter than those of a triply linked Zn$^{II}$-porphyrin dimer (1.43 Å and 1.48 Å) and 10-10′ bond length of non-fused *3NH*-dimer **64aH$_3$** (1.51(1)–1.52(1) Å). The observed closed-shell natures, as well as considerable double bond characters at the fused linkages, were

rationalized by the strong antiferromagnetic interaction due to the large spin densities at 10-positions in monomeric *2NH*-corrle radicals and coplanar structures of **67**. They also prepared another set of fused corrole dimers with 3-3′ and 5-5′ linkages (**69** and **70**) [110]. Similarly to the triply linked ones, doubly linked dimers exhibited redox interconversion between aromatic *3NH*- and non-aromatic *2NH*-forms as evidenced by the $^1$H NMR chemical shifts of their β-proton signals (8.7–7.9 ppm for **70** and 6.43–5.52 ppm for **69**).

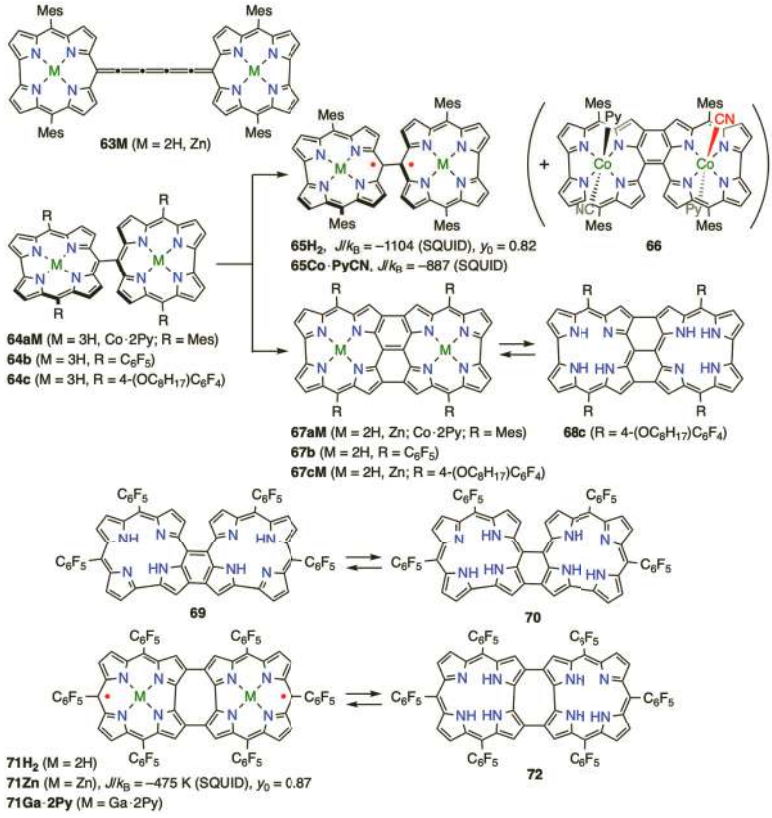


**Figure 11.19** Diradicaloids based on dimeric corroles. Py = pyridine.

Shinokubo, Osuka, and coworkers reported a set of 2-2′ and 18-18′ doubly linked fused corrole dimer $\mathbf{71H_2}$ and its zinc complex **71Zn** in 2006 [111]. Although free-base *3NH*-dimer **72** showed $^1$H

NMR signals, due to the β-protons at 8.91–8.48 ppm, *2NH*-dimer $Zn^{II}$-complex **71Zn** gave virtually no peaks in its $^1$H NMR spectra in $CD_2Cl_2$ and THF-$d_8$ even at −90 °C, owing to severe broadening. The magnetic properties of **71Zn** were evaluated by the solid-state SQUID magnetometry and theoretical calculations, revealing strong antiferromagnetic coupling of −330 cm$^{-1}$ ($J/k_B$ = −475 K) and −178 cm$^{-1}$ ($J/k_B$ = −256 K), respectively. The computed diradical character ($y_0$) value of 87% also supported predominant singlet diradical characters. These results made a sharp contrast with those of *meso-meso* linked fused dimers, **67** and **69**, and were interpreted as weak bonding interactions between β-carbons, where minor spin densities were computed in *2NH*-monomer radicals.

Metalation of the fused corrole dimers have been widely investigated. Gross and coworkers prepared a pyridine-coordinated bis-$Ga^{III}$-complex of a *3NH*-type 2-2′ 18-18′ doubly linked dimer (**71Ga**·**2Py**) and revealed its electrochemistry in 2017 [112]. In both redox processes, two-step spectral changes were observed, leading to appearance of new NIR absorption bands. They also performed computational studies on the reduced and oxidized species, and the dianion of **71Ga**·**2Py** was predicted to be a triplet-ground-state compound stabilized by +1.45 kcal mol$^{-1}$ from its singlet counterpart. In 2018, Tanaka, Osuka, and coworkers tested $Ga^{III}$-metalation of *3NH*-type 8-8′, 10-10′, and 12-12′ triply linked corrole dimers (Figure 11.20) [113]. Interestingly, matrix assisted laser desorption/ionization (MALDI) mass spectrometry (MS) result indicated the formation of doubly μ-hydroxo-bridged dimers of fused dimeric corrole **73**, which were stable during purification by silica gel chromatography. The crystal structure of **73** was revealed to take a fairly curved structure with large MPD of 0.561 Å and a short face-to-face distance of 3.24 Å. The Ga–O bond lengths were 1.874(2) and 1.897(3) Å, confirming the μ-hydroxo bridges, not μ-oxo ones. The bond lengths of 8-8′, 10-10′, and 12-12′ linkages were significantly longer (1.449(4) Å, 1.444(3) Å, and 1.449(4) Å, respectively) than those of free-base fused dimeric corrole **67aH$_2$** (1.395(4) Å, 1.389(4) Å, and 1.395(4) Å, respectively), showing the decreased double bond nature. The $^1$H NMR spectrum was very broad while $^{19}$F NMR signals could be observed at low temperature.

These results suggested considerable π-radical-derived open-shell natures and indeed EPR spectroscopy showed a single peak at $g$ = 2.0025. The SQUID magnetometry revealed a $\chi T$-$T$ plot that could be fitted by the Bleaney–Bowers equation with spin exchange integral of –475 $cm^{-1}$ ($J/k_B$ = –684 K) for **73b** and –447 $cm^{-1}$ ($J/k_B$ = –643 K) for **73c**. These observations concluded that each fused dimeric corrole of **73** was mono-radical formally containing both di- and trivalent corrole ligands and coupled with one another via antiferromagnetic through-space interaction. Theoretical calculations based on this assignment afforded exchange interaction of –454 $cm^{-1}$ ($J/k_B$ = –653 K) and diradical index of 0.88, being well consistent with the experimental values. Furthermore, they converted **73b** into axially aryl-substituted bis-$Ga^{III}$-complex **74b** by the reactions with aryl zinc reagents. Product **74b** was characterized as closed-shell compound with $^1H$ NMR peaks due to β-protons at 6.1–4.9 ppm. The X-ray analysis disclosed less curved structures (MPD: 0.269 Å for **74b**$^{syn}$ and 0.092 Å for **74b**$^{anti}$) and shorter 10-10′ bond lengths (1.416(5) Å for **74b**$^{syn}$ and 1.404(4) Å for **74b**$^{anti}$). In 2019, they investigated a bis-$Cu^{II}$-complex of triply linked corrole dimer **75** and its dication [114]. Although ligand non-innocence behavior was reported for some monomeric Cu-corroles, diradical natures of these dimers were assigned to be predominantly $Cu^{II}$-centered on the basis of EPR patterns and X-ray photoelectron spectroscopy (XPS) analysis. The magnetic coupling between two $Cu^{II}$-centers was revealed to be weakly ferromagnetic ($J$ = +0.90 $cm^{-1}$, $J/k_B$ = +1.30 K) in neutral complex while that of dicationic one was weakly antiferromagnetic ($J$ = –1.83 $cm^{-1}$, $J/k_B$ = –2.63 K).

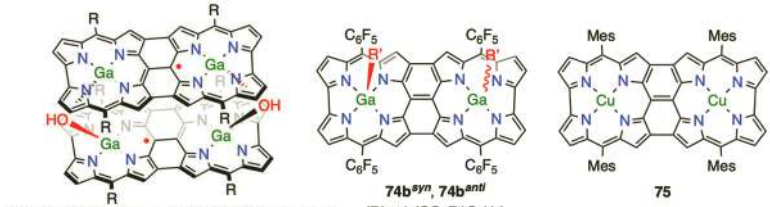


**73b** (R = $C_6F_5$), $J/k_B$ = –684 K (SQUID), $y_0$ = 0.88
**73c** (R = 4-($OC_8H_{17}$)$C_6F_4$), $J/k_B$ = –643 K (SQUID)

**74b**$^{syn}$, **74b**$^{anti}$
(R′ = 4-($CO_2Et$)$C_6H_4$)

**75**

**Figure 11.20** Metal complexes of triply linked corrole dimers.

### 11.5.2 Norcorroles: Strong Antiaromaticity and Singlet Diradical Characters

Norcorrole is a ring-contracted porphyrinoid that lacks two methine carbons and displays very strong antiaromaticity due to its highly planar and 16π-system (Figure 11.21). In 2012, Kobayashi, Shinokubo, and coworkers reported effective synthesis of $Ni^{II}$-norcorrole via reductive homocoupling of a $Ni^{II}$-pre-coordinated 3,5-dibromodipyrrin dimer [115]. Since then, various derivatives have been widely investigated. A ring expansion of norcorrole by one methine carbon leads to production of corrole isomers that possess macrocyclic π-systems involving 17 atoms and can give rise to a radical easily. In 2016, Li, Chmielewski, and coworkers found that amination of norcorrole afforded a pyrimidinenorcorrole radical **76** along with a β-amino norcorrole and 10-azacorrole [116]. The radical was in equilibrium with its $C_2$-symmetric σ-dimer $\mathbf{76_2}$ via C3–C3′ reversible bond formation under inert conditions. The σ-dimer was dehydrogenated in polar solvents or in the presence of catalytic Pd/C, giving another dimer **77** with singlet diradical character. X-ray diffraction analysis of **77** revealed that C3–C3′ bond was fairly short (1.437(5) Å) and two macrocyclic units were twisted with a dihedral angle of 44.0° and a C2-C3-C3′-C2′ torsion of 143.9(4)°. Such a small C3–C3′ double bond character led to weak but distinct paramagnetic properties in the solid-state. EPR spectrum at 77 K was also observed as a typical triplet signal with ($g_\perp$, $g_{||}$, $D$) = (2.0026 $cm^{-1}$, 2.0018 $cm^{-1}$, and 0.0095 $cm^{-1}$). In solution, $^1H$ NMR spectra were evident in lower temperature, but the chemical shifts and peaks widths were fairly temperature-dependent, implying fast chemical exchange between the dominant singlet species and minor triplet one. DFT calculations indicated that the singlet state was more stable than the triplet one by 0.39 kcal $mol^{-1}$, while triplet states were computed to be lower in energy when the C2-C3-C3′-C2′ torsion angles were set close to a perpendicular conformation.

Owing to the extremely strong antiaromaticity, some norcorroles themselves can show open-shell natures. In 2018, Nakano, Shinokubo, and coworkers synthesized benzo-fused norcorroles, **78** and **79**, via cycloreversion of bicyclo[2.2.2]octadiene units [117]. The additional benzannulation disturbed the local pyrrolic 6π circuits and thereby gave an enhanced 16π paratropic ring current of norcorroles. In $^1H$

NMR spectra, **78** and **79** displayed its fused benzo-proton signals at 3.65–0.48 ppm and β-proton ones at –2.79 ppm and –3.91 ppm. The antiaromatic characters were also supported by calculated NICS(1) values (+52 to +68 ppm) and anticlockwise ACID plots. The electrochemical HOMO–LUMO gaps were significantly decreased to 0.75–0.79 eV, giving thermal excitation to triplet states. As a result, paramagnetic contribution was observed in solid-state SQUID study for **79** with $J$ = –616 cm$^{-1}$ ($J/k_B$ = –886 K) and diradical character of **79** was computed to be 0.39.

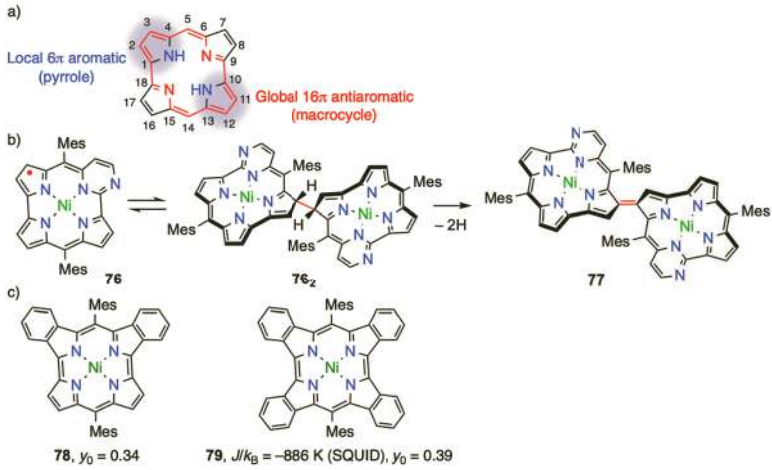


**Figure 11.21** (a) Chemical structure and electron circuits of norcorrole and diradicaloids based on (b) a ring-expanded norcorrole dimer and (c) enhanced antiaromatic contributions.

### 11.5.3 Diradicaloids Based on Core-Modified Expanded Porphyrins

Some open-shell ring-expanded porphyrinoids exhibited high stability because their extensively π-conjugated systems resulted in effective delocalization of spin and charge densities. In 2010, Naruta and coworkers reported a cross-conjugated sapphyrin derivative **80**, which was converted into an open-shell species with a broad NIR absorption spectrum upon protonation with TFA (Figure 11.22) [118]. The $^1$H NMR spectrum of **80** became unclear in $CDCl_3$ containing 1% TFA and the tricationic form **80** · **3HCl** was

revealed by the presence of three chloride anions in X-ray diffraction analysis for a single crystal prepared with concentrated hydrochloric acid. Each of the isolated tricationic salts with TFA (**80**·**3TFA**), trichloroacetic acid (TCA) (**80**·**3TCA**), and HCl (**80**·**3HCl**) showed relatively broad EPR signal at $g$ = 2.0041 in the solid states. The EPR spectrum of **80**·**3TFA** did not change in solution after standing for 24 h, indicating its high stability toward air and moisture. Further, the solid-state magnetic susceptibility was measured for **80**·**3HCl** to reveal a preferred singlet state with $J$ = –470 cm$^{-1}$ ($J/k_B$ = –676 K). Fukuzumi, Kim, Sessler, and coworkers also reported that a set of diradicaloids was generated upon protonation of a rosarin-derived macrocycles **81** and **82** [119, 120]. In the neutral form, **81** displayed 24π antiaromatic character and transformed into the corresponding 25π radical dications (**H$_3$81**·**Cl** and **H$_3$81**·**Br**) and 26π aromatic cation (**H$_3$81**·**2I**) by adding hydrogen halides. While proton-coupled electron transfer (PCET) was promoted by halide anions in these processes, addition of redox-resistant TFA afforded the corresponding tricationic specie **81**·**3TFA** with diradical natures. The EPR signal of **81**·**3TFA** was ascribed to a triplet diradical and its split feature was clearly resolved for a non-benzannulated derivative **82**·**3TFA** in $CH_2Cl_2$ at 4 K. The EPR parameters were determined to be ($g$, $D$, $E$) = (2.003, 577 G, 63 G) and the distance between the two spins was estimated at 3.6 Å from the $D$ value. TFA amount- and temperature-dependent EPR intensity plots indicated the tri-protonated structure and preferred triplet population with ($\Delta H$, $\Delta S$) = (0.02 kcal mol$^{-1}$, 0.2 cal mol$^{-1}$ K$^{-1}$), respectively.

Meyer and coworkers investigated pyrazole-based hexaphyrin **83H$_2$**, which showed significant conformational flexibility and non-aromatic character in NMR and DFT studies despite its 26 π-electrons [121, 122]. Complexation of **83H$_2$** with Cu(OAc)$_2$ yielded the corresponding bis-Cu$^{II}$ complex **83Cu** with complicated and split EPR signals. In the crystal structure, **83Cu** took a helically twisted conformation with Cu–N and Cu–Cu distances of 1.96–2.01 Å and 3.88 Å, respectively. Magnetic susceptibility measurement revealed that two $S$ = 1/2 Cu$^{II}$ centers interacted with each other with sizable ferromagnetic coupling ($J$ = +16.3 cm$^{-1}$, $g$ = 2.17), which was interpreted as the quasi-orthogonality of two Cu$^{II}$ coordination planes. Oxidation of **83Cu** produced the corresponding mono-cationic π-radical complex **83Cu**·**BF$_4$** with overall $S$ = 1/2 ground

state and dicationic one **83Cu·2BF$_4$**. Dication **83Cu·2BF$_4$** was EPR-silent but displayed well-resolved NMR spectrum, indicating $S$ = 0 ground state. The crystal structure of acetone coordinated **83Cu·2BF$_4$** was essentially identical to the neutral one with respect to the core structure and Cu$^{II}$ centers were supported by the X-ray absorption spectroscopy (XAS). On the basis of DFT calculations, it was suggested that two-electron oxidation was ligand-centered and the resulting π-diradical was coupled with Cu$^{II}$ centers antiferromagnetically to give diamagnetic properties.

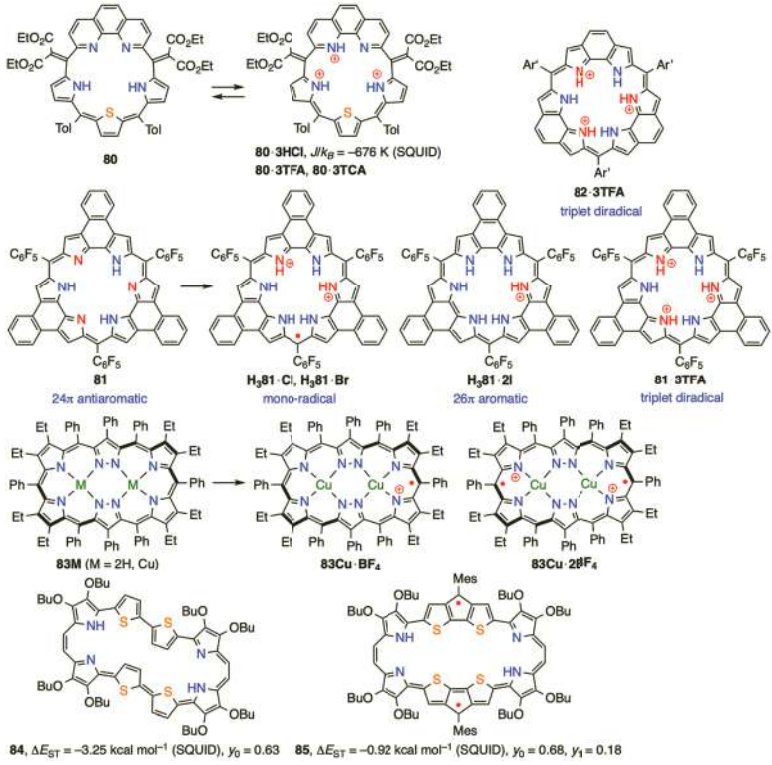


**Figure 11.22** Diradicaloids and multi-spin compounds based on core-modified expanded porphyrins. Ar′ = 4-*tert*-butylphenyl.

In 2018, Kim, Wu, and coworkers reported bithiophene-inserted porphycene derivatives **84** and **85** with considerable diradical nature and high stability [123]. Single-crystal X-ray diffraction analysis was conducted for **84** to take a nearly planar conformation

with *trans* bithiophene linkers, which showed π-π stacking with an interplane distance of 3.44 Å. Owing to the 34π aromatic and 32π antiaromatic conjugation pathways, theoretical calculations of **84** and **85** predicted NICS(0) values of –15.35 ppm and +9.75 ppm, as well as ACID plots of clockwise and anticlockwise ring current, respectively. The $^1$H NMR spectrum of **84** in THF-$d_8$ at 253 K gave a broad signal at 8.81 ppm due to the vinylene protons, which was severely broadened at room temperature. In the case of **85**, the $^1$H NMR spectrum was fully broadened even at –60 °C. These results indicated the contribution of thermally populated triplet species. Indeed, EPR measurement in the solid states and in $CH_2Cl_2$ solution provided featureless peaks at $g$ = 2.0030 for **84** and 2.0035 for **85**, implying fairly delocalized spin densities. The singlet–triplet energy gaps were experimentally evaluated at –3.25 kcal mol$^{-1}$ for **84** and –0.92 kcal mol$^{-1}$ for **85** by the solid-state SQUID measurement, which accorded with the open-shell singlet ground states implied by the NMR studies. Along this line, diradical characters were computed to be moderate (0.63 for **84** and 0.68 for **85**) and tetraradical character was also non-trivial for **85** (0.18). Diradicals **84** and **85** displayed considerably small electrochemical gaps of 0.61 eV and 0.81 eV, respectively, as well as electronic absorption bands ranging to NIR region. Different from a weak tail of antiaromatic **85**, **84** exhibited intense absorption bands at around 1000–1200 nm with a large TPA cross-section of 670 GM at 2000 nm. Furthermore, dications of **84** and **85** were produced by addition of NO·$SbF_6$ and characterized by $^1$H NMR spectroscopy. While dication of **84** was shown to be antiaromatic with a shielded vinylene signal at 5.95 ppm, dication of **85** did not afford well-resolved spectrum because of a large diradical nature ($y_0$ = 0.98).

## 11.6 Summary

Porphyrinoid-based radicals have grown into a promising material field, since various stable radicals with excellent air- and moisture-stabilities have been explored. In the early stage, these species were investigated mainly as reactive intermediates in Heme catabolism or unstable charged species generated by electrochemical or photochemical methods. Recently, a wide range of porphyrinoid-

based radicals have been successfully synthesized as stable compounds. The systematic studies have revealed that the spin-delocalizing abilities of porphyrinoids are a key to stabilize various radicals to the extent to gain sufficient stabilities as usual closed-shell organic molecules. The high radical-stabilizing abilities of porphyrinoids can be mainly ascribed to their electronic flexibilities, which are arisen from the minor energetic contribution of the macrocyclic conjugation. The sign of spin density values where two radicals were joined together is critically important to determine whether combined diradical systems exhibit either ferromagnetic or antiferromagnetic interaction, and the absolute spin densities have a large influence on the strengths of the magnetic coupling.

In this chapter, we describe three types of porphyrinoid-based diradicaloids and high-spin multi-radicals: porphyrinoids bearing two radical segments at the peripheries (type I), diradical and diradicaloids fused with porphyrinoids (type II), and core-modified porphyrinoids with embedded diradical characters (type III). In the early stage, type I diradicaloids were developed as cross-conjugated π-systems with large NIR responses and multi-stage redox properties. Owing to the small macrocyclic aromaticity in energetic criteria, most of these molecules took closed-shell quinoidal states even when the π-systems were well conjugated in fully fused structures. To interrupt strong radical–radical interactions, porphyrinoids and appended radical moieties had to be twisted by steric hindrance. Thus, these systems often showed dihedral angle-dependent magnetic properties. Insertion of aromatic spacers and use of *meso-meso* linked porphyrin dimers were also effective to enhance diradical characters, owing to an additional energy gain associated with aromatic stabilization in diradical forms as well as steric congestion that disfavors planar quinoidal conformation.

Type II diradicaloids have been also extensively explored in the last decade. In this class, effective spin delocalization over the whole fused porphyrinoids played a critical role to attain sufficient chemical stability and enhance open-shell nature. The diradical characters were highly dependent on the topology and constituent elements of the central diradical fragments. Importantly, non-Kekulé high-spin compounds were also fairly stabilized by porphyrin units. Intramolecular ferromagnetic coupling increased in the order of aminium cation < aminyl < carbon-centered radical. This trend was

well correlated to increasing spin densities at the central high-spin units.

A series of *2NH*-corrole dimers and their metal complexes have been investigated as an intriguing redox-responsive π-system. While the simple *meso-meso* linked dimers behaved as diradicaloids, due to the large dihedral angles around the *meso-meso* bonds, non-aromatic closed-shell states were observed in fused derivatives that possess a well conjugated *meso-meso* linkage. On the other hand, the *2NH*-corrole dimer with double β-β connection displayed distinct singlet diradical nature. Benzo-fused norcorroles showed evident singlet diradical properties, owing to the extremely strong antiaromatic characters. Core-modified expanded porphyrins also provided several type III diradicaloids, utilizing their high radical-stabilizing abilities deriving from the large π-conjugated systems. They have also been reported to switch their diradical properties upon protonation and facile redox processes.

As described in this chapter, porphyrinoids can offer excellent stabilization ability toward neighboring (or conjugated) radicals. As a result, porphyrinoid-stabilized radicals need less steric protection as compared with other PAH-based derivatives. In many cases, a few bulky substituents and large π-planes allow for porphyrinoid-based radicals to form π-π stacked dimers or exhibit reversible σ-bonds. Highly spin-delocalized nature also guarantees the effective conjugation between the radical and other functional units in their π-systems. These features are useful for the exploration of intricate multi-spin systems, in which two or more spin centers can be aligned, manipulated, and coupled with other functional groups. Fundamental and systematic studies on porphyrinoid-based radicals would allow for improved design principle of novel radical molecules with sufficient stabilities and aimed magnetic properties. Furthermore, porphyrinoids exhibit attractive optical and electrochemical properties and accommodate many metal ions in their cavities. In particular, most ring-expanded porphyrinoids are conformationally flexible, form multi-metal complexes, and show decreased HOMO–LUMO gaps. These properties of expanded porphyrins are promising for their uses in materials science. We hope that this chapter will be useful for the design of future molecule-based advanced materials

through offering comprehensive understanding about the spin distribution, stability, and magnetic property of porphyrinoid-based radicals.

## Acknowledgments

This work was supported by Grant-in-Aid from JSPS for Scientific Research (A): 18H03910, Challenging Exploratory Research: 16K13952. K.K. appreciates a JSPS Research Fellowship for Young Scientists: 17J09048.

## References

1. Dolphin, D. (1979). *The Porphyrins*, **1**–**2,** Academic Press, New York.
2. Kadish, K. M., Smith, K. M., and Guilard R. (2000). *The Porphyrin Handbook*, **1**–**10**, Academic Press, San Diego.
3. Kadish, K. M., Smith, K. M., and Guilard R. (2003). *The Porphyrin Handbook*, **11**–**20**, Academic Press, San Diego.
4. Kadish, K. M., Smith, K. M., and Guilard R. (2010). *Handbook of Porphyrin Science*, **1**–**10**, World Scientific Publishing, Singapore.
5. Kadish, K. M., Smith, K. M., and Guilard R. (2011). *Handbook of Porphyrin Science*, **11**–**15**, World Scientific Publishing, Singapore.
6. Kadish, K. M., Smith, K. M., and Guilard R. (2012). *Handbook of Porphyrin Science*, **16**–**25**, World Scientific Publishing, Singapore.
7. Sessler, J. L., and Seidel, D. (2003). Synthetic expanded porphyrin chemistry, *Angew. Chem. Int. Ed.*, **42**, pp. 5134–5175.
8. Saito, S., and Osuka, A. (2011). Expanded porphyrins: Intriguing structures, electronic properties, and reactivities, *Angew. Chem. Int. Ed.*, **50**, pp. 4342–4373.
9. Stępień, M., Sprutta, N., and Latos-Grażyński, L. (2011). Figure eights, Möbius bands, and more: Conformation and aromaticity of porphyrinoids, *Angew. Chem. Int. Ed.*, **50**, pp. 4288–4340.
10. Roznyatovskiy, V. V., Lee, C.-H., and Sessler, J. L. (2013). π-Extended isomeric and expanded porphyrins, *Chem. Soc. Rev.*, **42**, pp. 1921–1933.
11. Tanaka, T., and Osuka, A. (2017). Chemistry of *meso*-aryl-substituted expanded porphyrins: Aromaticity and molecular twist, *Chem. Rev.*, **117**, pp. 2584–2640.

12. Matano, Y. (2017). Synthesis of aza-, oxa-, and thia-porphyrins and related compounds, *Chem. Rev.*, **117**, pp. 3138–3191.
13. Chatterjee, T., Shetti, V. S., Sharma, R., and Ravikanth, M. (2017). Heteroatom-containing porphyrin analogues, *Chem. Rev.*, **117**, pp. 3254–3328.
14. Lash T. D. (2017). Carbaporphyrinoid systems, *Chem. Rev.*, **117**, pp. 2313–2446.
15. Furuta, H., Maeda, H., and Osuka, A. (2002). Confusion, inversion, and creation — A new spring from porphyrin chemistry, *Chem. Commun.*, pp. 1795–1804.
16. Srinivassan, A., and Furuta, H. (2005). Confusion approach to porphyrinoid chemistry, *Acc. Chem. Res.*, **38**, pp. 10–20.
17. Toganoh, M., and Furuta, H. (2012). Blooming of confused porphyrinoids—Fusion, expansion, contraction, and more confusion, *Chem. Commun.*, **48**, pp. 937–954.
18. Anguera, G., and Sánchez-García, D. (2017). Porphycenes and related isomers: Synthetic aspects, *Chem. Rev.,* **117**, pp. 2481–2516.
19. Sarma, T., and Panda, P. K. (2017). Annulated isomeric, expanded, and contracted porphyrins, *Chem. Rev.,* **117**, pp. 2785–2838.
20. Fox, S., and Boyle, R. W. (2006). Synthetic routes to porphyrins bearing fused rings, *Tetrahedron*, **62**, pp. 10039–10054.
21. Pereira, A. M. V. M., Richeter, S., Jeandon, C., Gisselbrecht, J.-P., Wytko, J., and Ruppert, R. (2012). Synthesis of extended porphyrins by connection of meso-aryl groups with β-pyrrolic positions, *J. Porphyrins Phthalocyanines*, **16**, pp. 464–478.
22. Lewtak, J. P., and Dryko, D. T. (2012). Synthesis of π-extended porphyrinsvia intramolecular oxidative coupling, *Chem. Commun.*, **48**, pp. 10069–10086.
23. Mori, H., Tanaka, T., and Osuka, A. (2013). Fused porphyrinoids as promising near-infrared absorbing dyes, *J. Mater. Chem. C*, **1**, pp. 2500–2519.
24. Fukui, N., Fujimoto, K., Yorimitsu, H., and Osuka, A. (2017). Embedding heteroatoms: An effective approach to create porphyrin-based functional materials, *Dalton Trans.*, **46**, pp. 13322–13341.
25. Vicente, M. G. H., Jaquinod, L., and Smith, K. M. (1999). Oligomeric porphyrin arrays, *Chem. Commun.*, pp. 1771–1782.
26. Reimers, J. R., Hush, N. S., and Crossley, M. J. (2002). Inter-porphyrin coupling: How strong should it be for molecular electronics applications?, *J. Porphyrins Phthalocyanines*, **6**, pp. 795–805.

27. Aratani, N., and Osuka, A. (2003). Directly linked porphyrin arrays, *Chem Rec.*, **3**, pp. 225–234.

28. Aratani, N., Kim, D., and Osuka, A. (2009). π-Conjugation enlargement toward the creation of multi-porphyrinic systems with large two-photon absorption properties, *Chem. Asian J.*, **4**, pp. 1172–1182.

29. Ikeda, T., Aratani, N., and Osuka, A. (2009). Synthesis of extremely π-extended porphyrin tapes from hybrid *meso-meso* linked porphyrin arrays: An approach towards the conjugation length, *Chem. Asian J.*, **4**, pp. 1248–1256.

30. Tanaka, T., and Osuka, A. (2015). Conjugated porphyrin arrays: Synthesis, properties and applications for functional materials, *Chem. Soc. Rev.*, **44**, pp. 943–969.

31. Tanaka, T., and Osuka, A. (2018). Triply linked porphyrinoids, *Chem. Eur. J.*, **24**, pp. 17188–17200.

32. Shimizu, D., and Osuka, A. (2018). Porphyrinoids as a platform of stable radicals, *Chem. Sci.*, **9**, pp. 1408–1423.

33. Kato, K., and Osuka, A. (2019). Platforms for stable carbon-centered radicals, *Angew. Chem. Int. Ed.*, **58**, pp. 8978–8986.

34. Aihara, J.-i., Kimura, E., and Krygowski, T. M. (2008). Aromatic conjugation pathways in porphyrins, *Bull. Chem. Soc. Jpn.*, **81**, pp. 826–835.

35. Aihara, J.-i. (2008). Macrocyclic conjugation pathways in porphyrins, *J. Phys. Chem. A*, **112**, pp. 5305–5311.

36. Wu, J. I., Fernańdez, I., and Schleyer, P. v. R. (2013). Description of aromaticity in porphyrinoids, *J. Am. Chem. Soc.*, **135**, pp. 315–321.

37. Hicks, R. D. (2007). What's new in stable radical chemistry?, *Org. Biomol. Chem.*, **5**, pp. 1321–1338.

38. Sono, M., Roach, M. P., Coulter, E. D., and Dawson, J. H. (1996). Heme-containing oxygenases, *Chem. Rev.*, **96**, pp. 2841–2888.

39. Unno, M., Matsui, T., and Ikeda-Saito, M. (2007). Structure and catalytic mechanism of heme oxygenase, *Nat. Prod. Rep.,* **24**, pp. 553–570.

40. Matsui, T., Unno, M., and Ikeda-Saito, M. (2010). Heme oxygenase reveals its strategy for catalyzing three successive oxygenation reactions, *Acc. Chem. Res.*, **43**, pp. 240–247.

41. Fuhrhop, J. H., Besecke, S., Subramanian, J., Mengersen, C., and Riesner, D. (1975). Reactions of oxophlorines and their π radicals, *J. Am. Chem. Soc.*, **97**, pp. 7141–7152.

42. Balch, A. L., Noll, B. C., and Zovinka, E. P. (1992). Structural characterization of zinc(II) complexes of octaethyloxophlorin dianion

and octaethyloxophlorin radical anion, *J. Am. Chem. Soc.*, **114**, pp. 3380–3385.

43. Balch, A. L. (2000). Coordination chemistry with *meso*-hydroxylated porphyrins (oxophlorins), intermediates in heme degradation, *Coord. Chem. Rev.*, **200**–**202**, pp. 349–377.
44. Khoury, R. G., Jaquinod, L., Shachter, A. M., Nelson, N. Y., and Smith, K. M. (1997). Stabilization of neutral oxophlorin π-radicals by bulky meso-alkyl groups, *Chem. Commun.*, pp. 215–216.
45. Koide, T., Kashiwazaki, G., Suzuki, M., Furukawa, K., Yoon, M.-C., Cho, S., Kim, D., and Osuka, A. (2008). A stable radical species from facile oxygenation of *meso*-free 5,10,20,25-tetrakis(pentafluorophenyl)-substituted [26]hexaphyrin(1.1.1.1.1.1), *Angew. Chem. Int. Ed.*, **47**, pp. 9961–9965.
46. Shimizu, D., Oh, J., Furukawa, K., Kim, D., and Osuka, A. (2015). meso-Hydroxysubporphyrins: A cyclic trimeric assembly and a stable meso-oxy radical, *Angew. Chem. Int. Ed.*, **54**, pp. 6613–6617.
47. Shimizu, D., Oh, J., Furukawa, K., Kim, D., and Osuka, A. (2015). Triarylporphyrin *meso*-oxy radicals: Remarkable chemical stabilities and oxidation to oxophlorin *π*-cations, *J. Am. Chem. Soc.*, **137**, pp. 15584–15594.
48. Shimizu, D., Furukawa, K., and Osuka, A. (2017). Stable subporphyrin meso-aminyl radicals without resonance stabilization by a neighboring heteroatom, *Angew. Chem. Int. Ed.*, **56**, pp. 7435–7439.
49. Shimizu, D., Fujimoto, K., and Osuka, A. (2018). Stable diporphyrinylaminyl radical and nitrenium ion, *Angew. Chem. Int. Ed.*, **57**, pp. 9434–9438.
50. Adinarayana, B., Shimizu, D., and Osuka, A. (2019). Stable ($B^{III}$-subporphyrin-5-yl)dicyanomethyl radicals, *Chem. Eur. J.*, **25**, pp. 1706–1710.
51. Adinarayana, B., Shimizu, D., Furukawa, K., and Osuka, A. (2019). Stable radical versus reversible σ-bond formation of (porphyrinyl) dicyanomethyl radicals, *Chem. Sci.*, **10**, pp. 6007–6012.
52. Kato, K., Kim, W., Kim, D., Yorimitsu, H., and Osuka, A. (2016). Porphyrin analogues of a trityl cation and anion, *Chem. Eur. J.*, **22**, pp. 7041–7045.
53. Kato, K., Cha, W., Oh, J., Furukawa, K., Yorimitsu, H., Kim, D., and Osuka, A. (2016). Spontaneous formation of an air-stable radical upon the direct fusion of diphenylmethane to a triarylporphyrin, *Angew. Chem. Int. Ed.*, **55**, pp. 8711–8714.

54. Fukui, N., Cha, W., Shimizu, D., Oh, J., Furukawa, K., Yorimitsu, H., Kim, D., and Osuka, A. (2017). Highly planar diarylamine-fused porphyrins and their remarkably stable radical cations, *Chem. Sci.*, **8**, pp. 189–199.
55. Orłowski, R., Gryko, D., and Gryko, D. T. (2017). Synthesis of corroles and their heteroanalogs, *Chem. Rev.*, **117**, pp. 3102–3137.
56. Barata, J. F. B., Neves, M. G. P. M. S., Faustino, M. A. F., Tomé, A. C., and Cavaleiro, J. A. S. (2017). Strategies for corrole functionalization, *Chem. Rev.*, **117**, pp. 3192–3253.
57. Ghosh, A. (2017). Electronic structure of corrole derivatives: Insights from molecular structures, spectroscopy, electrochemistry, and quantum chemical calculations, *Chem. Rev.*, **117**, pp. 3798–3881.
58. Ooi, S., Ueta, K., Tanaka, T., and Osuka, A. (2019). Singly, doubly, and triply linked corrole oligomers: Synthesis, structures, and linking position dependent properties, *ChemPlusChem*, **84**, pp. 578–588.
59. Schweyen, P., Brandhorst, K., Wicht, R., Wolfram, B., and Bröring, M. (2015). The corrole radical, *Angew. Chem. Int. Ed.*, **54**, pp. 8213–8216.
60. Basumatary, B., Rai, J., Reddy, R. V. R., and Sankar, J. (2017). Evidence for a [17]π-electronic full-fledged non-innocent gallium(iii)-corrole radical, *Chem. Eur. J.*, **23**, pp. 17458–17462.
61. Satoh, T., Minoura, M., Nakano, H., Furukawa, K., and Matano, Y. (2016). Redox-switchable 20π-, 19π-, and 18π-electron 5,10,15,20-tetraaryl-5,15-diazaporphyrinoid nickel(II) complexes, *Angew. Chem. Int. Ed.*, **55**, pp. 2235–2238.
62. Sudoh, K., Satoh, T., Amaya, T., Furukawa, K., Minoura, M., Nakano, H., and Matano, Y. (2017). Syntheses, properties, and catalytic activities of metal(II) complexes and free bases of redox-switchable 20π, 19π, and 18π 5,10,15,20-tetraaryl-5,15-diazaporphyrinoids, *Chem. Eur. J.*, **23**, pp. 16364–16373.
63. Sudoh, K., Hatakeyama, T., Furukawa, K., Nakano, H., and Matano, Y. (2018). Redox switchable 19π and 18π 5,10,20-triaryl-5,15-diazaporphyrinoid–nickel(II) complexes, *J. Porphyrins Phthalocyanines*, **22**, pp. 542–551.
64. Ishida, S.-i., Kim, J., Shimizu, D., Kim, D., and Osuka, A. (2018). Synthesis of (bis)silicon complexes of [38], [37], and [36]octaphyrins: Aromaticity switch and stable radical cation, *Angew. Chem. Int. Ed.*, **57**, pp. 5876–5880.
65. Stähler, C., Shimizu, D., Yoshida, K., Furukawa, K., Herges, R., and Osuka, A. (2017). Stable $Ni^{II}$ porphyrin *meso*-oxy radical with a quartet ground state, *Chem. Eur. J.*, **23**, pp. 7217–7220.

66. Shimizu, D., Ide, Y., Ikeue, T., and Osuka, A (2019). Coordination-induced spin-state switching of an aminyl-radical-bridged nickel(II) porphyrin dimer between doublet and sextet states, *Angew. Chem. Int. Ed.*, **58**, pp. 5023–5027.

67. Shen, D.-M., Liu, C., Chen, X.-G., and Chen, Q.-Y. (2009). *meso*-Oxidation of porphyrins: Convenient iron(III)-mediated synthesis of dioxoporphyrins, *Synlett*, **2009**, pp. 945–948.

68. Otto, C., and Breitmaier, E. (1991). Tetra-*meso*-methylenporphyrinogene, *Liebigs Ann. Chem.*, **1991**, pp. 1347–1348.

69. Blake, I. M., Anderson, H. L., Beljonne, D., Brédas, J.-L., and Clegg, W. (1998). Synthesis, crystal structure, and electronic structure of a 5,15-dialkylideneporphyrin: A TCNQ/porphyrin hybrid, *J. Am. Chem. Soc.*, **120**, pp. 10764–10765.

70. Traylor, T. G., Nolan, K. B., and Hildreth, R. (1983). Polyvalent porphyrins: Properties of tetrakis(3,5-di-*tert*-butyl-4-hydroxyphenyl) porphyrin (1-P) and its $Fe^{III}$ and $Zn^{II}$ derivatives, *J. Am. Chem. Soc.*, **105**, pp. 6149–6151.

71. Hill, J. P., Hewitt, I. J., Anson, C. E., Powell, A. K., McCarty, A. L., Karr, P. A., Zandler, M. E., and D'Souza, F. (2004). Highly nonplanar, electron deficient, N-substituted tetra-oxocyclohexadienylidene porphyrinogens: Structural, computational, and electrochemical investigations, *J. Org. Chem.*, **69**, pp. 5861–5869.

72. Ding, Y., Li, X., Hill, J. P., Ariga, K., Ågren, H., Andréasson, J., Zhu, W., Tian, H., and Xie, Y. (2014). Acid/base switching of the tautomerism and conformation of a dioxoporphyrin for integrated binary subtraction, *Chem. Eur. J.*, **20**, pp. 12910–12916.

73. Adinarayana, B., Kato, K., Shimizu, D., Tanaka, T., Furukawa, K., and Osuka, A. (2020). Cyclophane-type chlorin dimers from dynamic covalent chemistry of 2,18-porphyrinyl dicyanomethyl diradicals, *Angew. Chem. Int. Ed.*, **59**, pp. 4320–4323.

74. Zeng, W., Lee, B. S., Sung, Y. M., Huang, K. W., Li, Y., Kim, D., and Wu, J. (2012). Tetrakis(4-*tert*-butylphenyl) substituted and fused quinoidal porphyrins, *Chem. Commun.*, **48**, pp. 7684–7686.

75. Umetani, M., Naoda, K., Tanaka, T., Lee, S.-K., Oh, J., Kim, D., and Osuka, A. (2016). Synthesis of di-*peri*-dinaphthoporphyrins by $PtCl_2$-mediated cyclization of quinodimethane-type porphyrins, *Angew. Chem. Int. Ed.*, **55**, pp. 6305–6309.

76. Umetani, M., Naoda, K., Tanaka, T., and Osuka, A. (2017). Synthesis and antiaromatic character of alkyl-substituted di-peri-

dinaphthoporphyrin Ni(II) complex, *J. Porphyrins Phthalocyanines*, **21**, pp. 850–856.

77. Diev, V. V., Femia, D., Zhong, Q., Djurovich, P. I., Haiges, R., and Thompson, M. E. (2016). A quinoidal bis-phenalenyl-fused porphyrin with supramolecular organization and broad near-infrared absorption, *Chem. Commun.*, **52**, pp. 1949–1952.
78. Zhang, H., Phan, H., Herng, T. S., Gopalakrishna, T. Y., Zeng, W., Ding, J., and Wu, J. (2017). Conformationally flexible bis(9-fluorenylidene) porphyrin diradicaloids, *Angew. Chem. Int. Ed.*, **56**, pp. 13484–13488.
79. Wei, H., Feng, R., Fang, Y., Wang, L., Chen, C., Zhang, L., Cui, H., and Wang, X. (2018). The diradical-dication strategy for BODIPY- and porphyrin-based dyes with near-infrared absorption maxima from 1070 to 2040 nm, *Chem. Eur. J.*, **24**, pp. 19341–19347.
80. Miao, F., Phan, H., and Wu, J. (2019). A BODIPY-bridged bisphenoxyl diradicaloid: Solvent-dependent diradical character and physical properties, *Molecules*, **24**, pp. 1446.
81. Naoda, K., Shimizu, D., Kim, J. O., Furukawa, K., Kim, D., and Osuka, A. (2017). Thienylquinonoidal porphyrins and hexaphyrins with singlet diradical ground states, *Chem. Eur. J.*, **23**, pp. 8969–8979.
82. Naoda, K., Sung, Y. M., Lim, J. M., Kim, D., and Osuka, A. (2014). Cross-conjugated hexaphyrins and their bis-rhodium complexes, *Chem. Eur. J.*, **20**, pp. 7698–7705.
83. Blake, I. M., Rees, L. H., Claridge, T. D. W., and Anderson, H. L. (2000). Synthesis and crystal structure of a cumulenic quinoidal porphyrin dimer with strong electronic absorption in the infrared, *Angew. Chem. Int. Ed.*, **39**, pp. 1818–1821.
84. Blake, I. M., Krivokapic, A., Katterle, M., and Anderson, H. L. (2002). Fusion and planarization of a quinoidal porphyrin dimer, *Chem. Commun.*, pp. 1662–1663.
85. Esdaile, L. J., Rintoul, L., Goh, M. S., Merahi, K., Parizel, N., Wellard, R. M., Choua, S., and Arnold, D. P. (2016). Nickel(II) *meso*-hydroxyporphyrin complexes revisited: Palladium-catalysed synthesis, electronic structures of derived oxy radicals, and oxidative coupling to a dioxoporphodimethene dyad, *Chem. Eur. J.*, **22**, pp. 3430–3446.
86. Jun-i, Y., Fukui, N., Furukawa, K., and Osuka, A. (2018). Metalation control of open-shell character in *meso*-*meso* linked porphyrin *meso*-oxy radical dimers, *Chem. Eur. J.*, **24**, pp. 1528–1532.
87. Yamamoto, T., Kato, K., Shimizu, D., Tanaka, T., and Osuka, A. (2019). Phenylene-bridged porphyrin *meso*-oxy radical dimers, *Chem. Asian J.*, **14**, pp. 4031–4034.

88. Fukui, N., Yorimitsu, H., and Osuka, A. (2016). *meso*–*meso*-Linked diarylamine-fused porphyrin dimers, *Chem. Eur. J.*, **22**, pp. 18476–18483.

89. Koide, T., Furukawa, K., Shinokubo, H., Shin, J.-Y., Kim, K. S., Kim, D., and Osuka, A. (2010). A stable non-Kekulé singlet biradicaloid from *meso*-free 5,10,20,25-tetrakis(Pentafluorophenyl)-substituted [26] hexaphyrin(1.1.1.1.1.1), *J. Am. Chem. Soc.*, **132**, pp. 7246–7247.

90. Ishida, M., Shin, J.-Y., Lim, J. M., Lee, B. S., Yoon, M.-C., Koide, T., Sessler, J. L., Osuka, A., and Kim, D. (2011). Neutral radical and singlet biradical forms of meso-free, -keto, and -diketo hexaphyrins(1.1.1.1.1.1): Effects on aromaticity and photophysical properties, *J. Am. Chem. Soc.*, **133**, pp. 15533–15544.

91. Kubo, T. (2015). Recent progress in quinoidal singlet biradical molecules, *Chem. Lett.*, **44**, pp. 111–122.

92. Zeng, Z., Shi, X., Chi, C., Navarrete, J. T. L., Casado, J., and Wu, J. (2015). Pro-aromatic and anti-aromatic π-conjugated molecules: An irresistible wish to be diradicals, *Chem. Soc. Rev.*, **44**, pp. 6578–6596.

93. Gopalakrishna, T. Y., Zeng, W., Lu, X., and Wu, J. (2018). From open-shell singlet diradicaloids to polyradicaloids, *Chem. Commun.*, **54**, pp. 2186–2199.

94. Shimizu, A., Nobusue, S., Miyoshi, H., and Tobe, Y. (2014). Indenofluorene congeners: Biradicaloids and beyond, *Pure Appl. Chem.*, **86**, pp. 517–528.

95. Frederickson, C. K., Rose, B. D., and Haley, M. M. (2017). Explorations of the indenofluorenes and expanded quinoidal analogues, *Acc. Chem. Res.*, **50**, pp. 977–987.

96. Sun, Z., Zeng, Z., and Wu, J. (2014). Zethrenes, extended *p*-quinodimethanes, and periacenes with a singlet biradical ground state, *Acc. Chem. Res.*, **47**, pp. 2582–2591.

97. Hu, P., and Wu, J. (2017). Modern zethrene chemistry, *Can. J. Chem.*, **95**, pp. 223–233.

98. Zeng, W., Ishida, M., Lee, S., Sung, Y. M., Zeng, Z., Ni, Y., Chi, C., Kim, D., and Wu, J. (2013). A *p*-quinodimethane-bridged porphyrin dimer, *Chem. Eur. J.*, **19**, pp. 16814–16824.

99. Ni, Y., Lee, S., Son, M., Aratani, N., Ishida, M., Samanta, A., Yamada, H., Chang, Y.-T., Furuta, H., Kim, D., and Wu, J. (2016). A diradical approach towards BODIPY-based dyes with intense near-infrared absorption around $\lambda$ = 1100 nm, *Angew. Chem. Int. Ed.*, **55**, pp. 2815–2819.

100. Zeng, W., Lee, S., Son, M., Ishida, M., Furukawa, K., Hu, P., Sun, Z., Kim, D., and Wu, J. (2015). Phenalenyl-fused porphyrins with different ground states, *Chem. Sci.*, **6**, pp. 2427–2433.

101. Zhang, H., Kim, J., Phan, H., Herng, T. S., Gopalakrishna, T. Y., Zeng, W., Ding, J., Kim, D., and Wu, J. (2019). 2,6-/1,5-Naphthoquinodimethane bridged porphyrin dimer diradicaloids, *J. Porphyrins Phthalocyanines*, ***23***, pp. 1–10.

102. Kato, K., and Osuka, A. (2019). *meta*- and *para*-Phenylenediamine-fused porphyrin dimers: Synthesis and magnetic interactions of their dication diradicals, *Angew. Chem. Int. Ed.*, **58**, pp. 8546–8550.

103. Tan, G., and Wang, X. (2017). Isolable bis(triarylamine) dications: Analogues of Thiele's, Chichibabin's, and Müller's hydrocarbons, *Acc. Chem. Res.*, **50**, pp. 1997–2006.

104. Suzuki, S., Tanaka, N., Kozaki, M., Shiomi, D., Sato, K., Takui, T., and Okada, K. (2017). Synthesis and magnetic properties of trioxytriphenylamine dimers in their di(radical cationic) states, *Chem. Eur. J.*, **23**, pp. 16014–16-25.

105. Shimizu, D., and Osuka, A. (2018). A benzene-1,3,5-triaminyl radical fused with $Zn^{II}$-porphyrins: Remarkable stability and a high-spin quartet ground state, *Angew. Chem. Int. Ed.*, **57**, pp. 3733–3736.

106. Kato, K., Furukawa, K., and Osuka, A. (2018). A stable trimethylenemethane triplet diradical based on a trimeric porphyrin fused π-system, *Angew. Chem. Int. Ed.*, **57**, pp. 9491–9494.

107. Ueta, K., Naoda, K., Ooi, S., Tanaka, T., and Osuka, A. (2017). *meso*-Cumulenic *2H*-corroles from *meso*-ethynyl-*3H*-corroles, *Angew. Chem. Int. Ed.*, **56**, pp. 7223–7226.

108. Ooi, S., Adinarayana, B., Shimizu, D., Tanaka, T., and Osuka, A. (2020). Stable *meso*–*meso*-linked *2NH*-corrole radical dimers as a key intermediate to corrole tape, *Angew. Chem. Int. Ed.*, **59**, pp. 9423–9427.

109. Ooi, S., Tanaka, T., Park, K. H., Kim, D., and Osuka, A. (2016). Triply linked corrole dimers, *Angew. Chem. Int. Ed.*, **55**, pp. 6535–6539.

110. Ooi, S., Tanaka, T., Park, K. H., Lee, S., Kim, D., and Osuka, A. (2015). Fused corrole dimers interconvert between nonaromatic and aromatic states through two-electron redox reactions, *Angew. Chem. Int. Ed.*, **54**, pp. 3107–3111.

111. Hiroto, S., Furukawa, K., Shinokubo, H., and Osuka, A. (2006). Synthesis and biradicaloid character of doubly linked corrole dimers, *J. Am. Chem. Soc.*, **128**, pp. 12380–12381.

112. Bhowmik, S., Kosa, M., Mizrahi, A., Fridman, N., Saphier, M., Stanger, A., and Gross, Z. (2017). The planar cyclooctatetraene bridge in bis-metallic macrocycles: Isolating or conjugating?, *Inorg. Chem.*, **56**, pp. 2287–2296.

113. Ooi, S., Shimizu, D., Furukawa, K., Tanaka, T., and Osuka, A. (2018). Stable face-to-face singlet diradicaloids: Triply linked corrole dimer gallium(III) complexes with two $\mu$-hydroxo-bridges, *Angew. Chem. Int. Ed.*, **57**, pp. 14916–14920.

114. Ooi, S., Tanaka, T., Ikeue, T., Yamasumi, K., Ueta, K., Shimizu, D., Ishida, M., Furuta, H., and Osuka, A. (2019). Bis-copper(II) complex of triply-linked corrole dimer and its dication, *Chem. Asian J.*, **14**, pp. 1771–1776.

115. Ito, T., Hayashi, Y., Shimizu, S., Shin, J.-Y., Kobayashi, N., and Shinokubo, H. (2012). Gram-scale synthesis of nickel(II) norcorrole: The smallest antiaromatic porphyrinoid, *Angew. Chem. Int. Ed.*, **51**, pp. 8542–8545.

116. Liu, B., Yoshida, T., Li, X., Stępień, M., Shinokubo, H., and Chmielewski, P. J. (2016). Reversible carbon–carbon bond breaking and spin equilibria in bis(pyrimidinenorcorrole), *Angew. Chem. Int. Ed.*, **55**, pp. 13142–13146.

117. Yoshida, T., Takahashi, K., Ide, Y., Kishi, R., Fujiyoshi, J.-y., Lee, S., Hiraoka, Y., Kim, D., Nakano, M., Ikeue, T., Yamada, H., and Shinokubo, H. (2018). Benzonorcorrole $Ni^{II}$ complexes: Enhancement of paratropic ring current and singlet diradical character by benzo-fusion, *Angew. Chem. Int. Ed.*, **57**, pp. 2209–2213.

118. Ishida, M., Karasawa, S., Uno, H., Tani, F., and Naruta, Y. (2010). Protonation-induced formation of a stable singlet biradicaloid derived from a modified sapphyrin analogue, *Angew. Chem. Int. Ed.*, **49**, pp. 5906–5909.

119. Ishida, M., Kim, S.-J., Preihs, C., Ohkubo, K., Lim, J. M., Lee, B. S., Park, J. S., Lynch, V. M., Roznyatovskiy, V. V., Sarma, T., Panda, P. K., Lee, C.-L., Fukuzumi, S., Kim, D., and Sessler, J. L. (2013). Protonation-coupled redox reactions in planar antiaromatic *meso*-pentafluorophenyl-substituted *o*-phenylene-bridged annulated rosarins, *Nat. Chem.*, **5**, pp. 15–20.

120. Fukuzumi, S., Ohkubo, K., Ishida, M., Preihs, C., Chen, B., Borden, W. T., Kim, D., and Sessler, J. L. (2015). Formation of ground state triplet diradicals from annulated rosarin derivatives by triprotonation, *J. Am. Chem. Soc.*, **137**, pp. 9780–9783.

121. Frensch, L. K., Pröpper, K., John, M., Demeshko, S., Brückner, C., and Meyer, F. (2011). Siamese-twin porphyrin: A pyrazole-based expanded

porphyrin providing a bimetallic cavity, *Angew. Chem. Int. Ed.*, **50**, pp. 1420–1424.

122. Blusch, L. K., Craigo, K. E., Martin-Diaconescu, V., McQuarters, A. B., Bill, E., Dechert, S., DcBeer, S., Lehnert, N., and Meyer, F. (2013). Hidden non-innocence in an expanded porphyrin: Electronic structure of the siamese-twin porphyrin's dicopper complex in different oxidation states, *J. Am. Chem. Soc.*, **135**, pp. 13892–13899.
123. Rana, A., Hong, Y., Gopalakrishna, T. Y., Phan, H., Herng, T. S., Yadav, P., Ding, J., Kim, D., and Wu J. (2018). Stable expanded porphycene-based diradicaloid and tetraradicaloid, *Angew. Chem. Int. Ed.*, **57**, pp. 12534–12537.

## Chapter 12

# Heteroatom (N, P, B, S, etc.) Centered Monoradicals and Diradicals

**Gengwen Tan[a] and Xinping Wang[b]**
[a]*College of Chemistry, Chemical Engineering and Materials Science, Soochow University, Suzhou 215123, China*
[b]*State Key Laboratory of Coordination Chemistry, School of Chemistry and Chemical Engineering, Nanjing University, Nanjing 210023, China*
gwtan@suda.edu.cn, xpwang@nju.edu.cn

Synthesis of stable main-group element-based radicals represents one of the most interesting topics in contemporary organometallic chemistry because of their vital roles in organic, inorganic, and biological chemistry as well as materials science. However, the access of stable main-group element-based radicals is highly challenging, owing to the lack of energetically accessible orbitals in the main-group elements. In this chapter, we summarize our contribution in the synthesis and characterization of stable heteroatom (N, P, B, S, etc.) centered radical and diradical salts.

*Diradicaloids*
Edited by Jishan Wu

ISBN 978-981-4968-08-9 (Hardcover), 978-1-003-27724-8 (eBook)
www.jennystanford.com

## 12.1 Introduction

Radicals are species containing unpaired valence electrons. Since the isolation of the first stable organic radical, triphenymethyl radical, by Gomberg in 1900 [1], the radical chemistry has been developed rapidly during the last decades, and it becomes one of the hottest topics in contemporary scientific research because of the vital roles of radicals in theoretical, organic, inorganic, and biological chemistry, as well as materials science [2–18].

Main-group element-centered radicals are usually highly reactive in nature, due to the limited energetically accessible orbitals to stabilize the unpaired electrons. Due to persistent efforts devoted to radical chemistry, a variety of stable main-group radicals have been isolated by utilizing sterically encumbering and/or π-conjugated ligands. Based on the number of the unpaired electrons, they can be categorized into monoradicals, diradicals, and polyradicals. The ground state of diradicals can be open-shell singlet or triplet state, due to the different spin alignments of the unpaired electrons. Monoradicals and diradicals are the most intensively investigated in the radical chemistry. The research of our group has been focused on the synthesis of stable radical ions of *p*-block elements. We found that the weakly coordinating anions (WCAs) [19, 20] are exceptionally useful in the stabilization and crystallization of radical cations. The synthetic method utilized to synthesize radical cations was chemical oxidation of the neutral precursors with $Ag^+$ or $NO^+$ salts bearing WCAs, including $[Al(OR_F)_4]^-$, $[BAr^F{}_4]^-$ ($Ar^F$ = 3,5-$(CF_3)_2C_6H_3$), and $[SbF_6]^-$. To access stable radical anions, we applied the reducing agents, such as alkali metals and $KC_8$, to reduce the precursors bearing sterically encumbered and π-conjugated ligands, which are crucial to stabilize the radical centers. Herein, we give a summary of our work on isolable monoradicals and diradicals of heteroatoms.

## 12.2 Group 13 Element-Centered Radicals

### 12.2.1 Boron-Centered Radical Anions

Boranes bearing a three coordinate boron atom are electron deficient, rendering them elegant precursors to synthesize radical

anions [21–24]. For instance, Kaim and coworkers demonstrated that 1,4-phenylene and 4,4′-diphenylene linked diboranes could undergo one-electron reduction affording their radical anions as detected in situ by electron paramagnetic resonance (EPR) spectroscopy [23]. Since the first isolation of the trimesityl borane radical anion [25], several stable boron-based monoradicals [26–30] and diradicals [31, 32], with boranes as the spin carriers have been synthesized.

The novel dimesitylpyridine borane **1** exhibits a reversible one-electron reduction peak, and its reduction with elemental potassium in the presence of 18-c-6 afforded the stable blue radical product **1K** (Scheme 12.1) [33]. The crystal structure shows that it is a contact ion-pair. The boron atom has a trigonal planar geometry. The B–C bond distance (1.554(3) Å) to the pyridine group shortens in comparison to that in **1** (1.594(3) Å). The pyridinyl ring in **1K** becomes quinoidal and is slightly puckered.

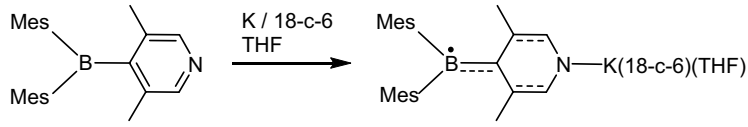


**1** **1K**

**Scheme 12.1** Synthesis of radical **1K**.

The solution EPR spectrum of **1K** at 298 K affords the isotropic hyperfine coupling (HFC) constants: $a(^{11}B)$ = 7.90 G, $a(^{10}B)$ = 3.8 G, $a(^{14}N)$ = 1.6 G, and $a(^{1}H)$ = 1.2–1.5 G. The $a(^{11}B)$ is slightly smaller than those of triarylborane radical anions [26–30], but larger than those of stable neutral boron-based radicals [34–36], indicating considerable localization of the unpaired electron on the boron atom. Density functional theory (DFT) calculations demonstrate that the spin density largely resides on the boron atom (0.53) with a significant contribution from the nitrogen atom (0.18).

The dimesitylpyridylboranes **1** and **2** could also activate the B–B bond in diborane 4,4,4′,4′,6,6,6′,6′-octamethyl-2,2′-bi(1,3,2-oxaborinane) ($B_2mpd_2$) affording the stable diboryl radicals **3** and **4** in moderate yields, respectively (Scheme 12.2) [37]. EPR and theoretical calculations reveal that the spin density mainly resides at the boron atom of the $Mes_2B$ moiety and the pyridine group. The diboryl radicals could react with the substrates *p*-benzoquinone,

2,2,6,6-tetramethyl-1-piperidinyloxy (TEMPO) and its derivative to form useful boron-containing reagents. Moreover, much higher yield was achieved in the catalytic reaction of *p*-benzoquinone and diborane with **1** or **2** in comparison to 4-cyanopyridine as the catalyst, in which the diboryl radicals act as reaction intermediates, highlighting the importance of the stability of the boryl radicals in improving the reaction efficiency [38–44].

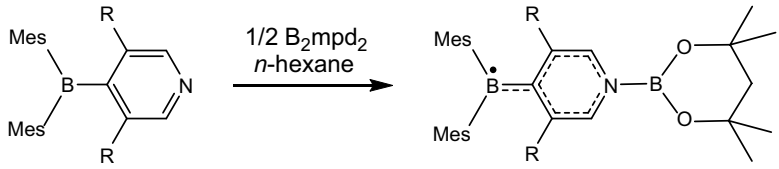


**1**: R = Me
**2**: R = H

**3**: R = Me
**4**: R = H

**Scheme 12.2** Synthesis of diboryl radicals **3** and **4**.

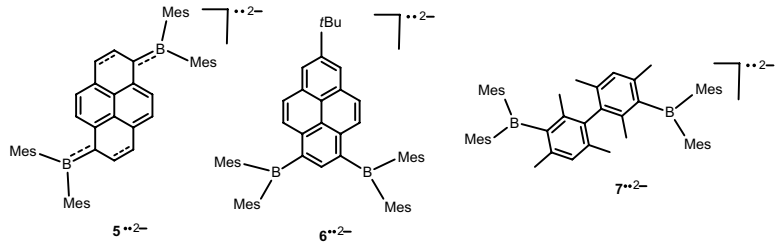


**Scheme 12.3** Structurally characterized borane-based diradical dianions.

In order to access boron-based diradicals, especially those featuring triplet ground states, we designed the diboranes bridged by pyrene [45] and diphenyl groups [46], which show two reversible one-electron reduction peaks. They readily underwent two-electron reductions to the diradical dianions $\mathbf{5}^{\bullet\bullet 2-}$–$\mathbf{7}^{\bullet\bullet 2-}$ (Scheme 12.3). All the boron centers in these dianions feature a trigonal planar geometry. In $\mathbf{5}^{\bullet\bullet 2-}$, the B–C(pyrene) bonds reflect some double bond characters, and the C–C bonds of the central naphthalene moiety have the property of aromatic C–C bonds, thus the dianion is best described as a naphthalene substituted by two boron analogs of butadiene at the 1,8- and 4,6-positions. In contrast, the C–C bonds of the pyrene group in $\mathbf{6}^{\bullet\bullet 2-}$ and the diphenyl group in $\mathbf{7}^{\bullet\bullet 2-}$ exhibit an aromatic

C–C bond property, showing limited electron delocalization over the central linkers.

The solid sample of $\mathbf{5}^{\bullet\bullet 2-}$ is EPR silent at both room temperature and low temperatures, and the results from theoretical calculations indicate that it has an open-shell singlet ground state with a relatively high singlet–triplet gap $\Delta E_{ST}$ (–6.6 kcal mol$^{-1}$). In contrast, $\mathbf{6}^{\bullet\bullet 2-}$ is EPR active, and a weak half-field signal was observed, suggesting its spin-triplet state at the measurement conditions. Theoretical calculations and variable temperature EPR spectroscopy revealed that $\mathbf{6}^{\bullet\bullet 2-}$ features an open-shell singlet ground state with a singlet–triplet energy gap of –4.8 kcal mol$^{-1}$. It is noteworthy that the singlet–triplet energy gaps of $\mathbf{5}^{\bullet\bullet 2-}$ and $\mathbf{6}^{\bullet\bullet 2-}$ are much smaller than that of 2,7-bis(boryl anion)pyrene (–13 kcal mol$^{-1}$) [30].

The EPR spectrum of the solid sample of $\mathbf{7}^{\bullet\bullet 2-}$ at 100 K showed two broad peaks and a weak half-field signal. The superconducting quantum interference device (SQUID) measurements indicated that it has a triplet ground state, but the singlet–triplet energy gap is quite small (8.82 cal mol$^{-1}$), suggesting its singlet and triplet states are almost degenerated (Figure 12.1a). The dianion $\mathbf{7}^{\bullet\bullet 2-}$ is the first boron-centered diradical with a triplet ground state.

Except linking two borane radical centers with organic groups, we found coordination of borane radicals to metal ions is also a practical approach to access radical species. Reduction of the dimesitylpyridylborane **8** with sodium and potassium in tetrahydrofuran (THF) gave different products (Scheme 12.4) [47]. The former reaction afforded the monoradical **8Na**, while the latter produced the diradical **8K-8K**. Interestingly, when **8Na** was recrystallized in toluene, the diradical **8Na-8Na** was obtained. Moreover, the diradical **8K-8K** could also be converted to the monoradical **8K(crown)** by adding 18-c-6 to the reaction mixture. Both of the diradicals **8Na-8Na** and **8K-8K** have an open-shell singlet ground state as shown by SQUID measurements and DFT calculations.

The reduction of the borane **9** with potassium in the presence of 18-c-6 led to the formation of the stable radical **9K(crown)** (Scheme 12.5) [48]. Strikingly, when 18-c-6 was not used, the radical species crystallized as a one-dimensional radical chain, which is the first example of radical polymers based on main-group element. Magnetic studies and theoretical calculations reveal that

the radical centers feature an antiferromagnetic interaction in the chain. Compound **9** could also be doubly reduced to the diamagnetic dianions, existing as a monomer or a polymer depending on whether 18-c-6 was added.

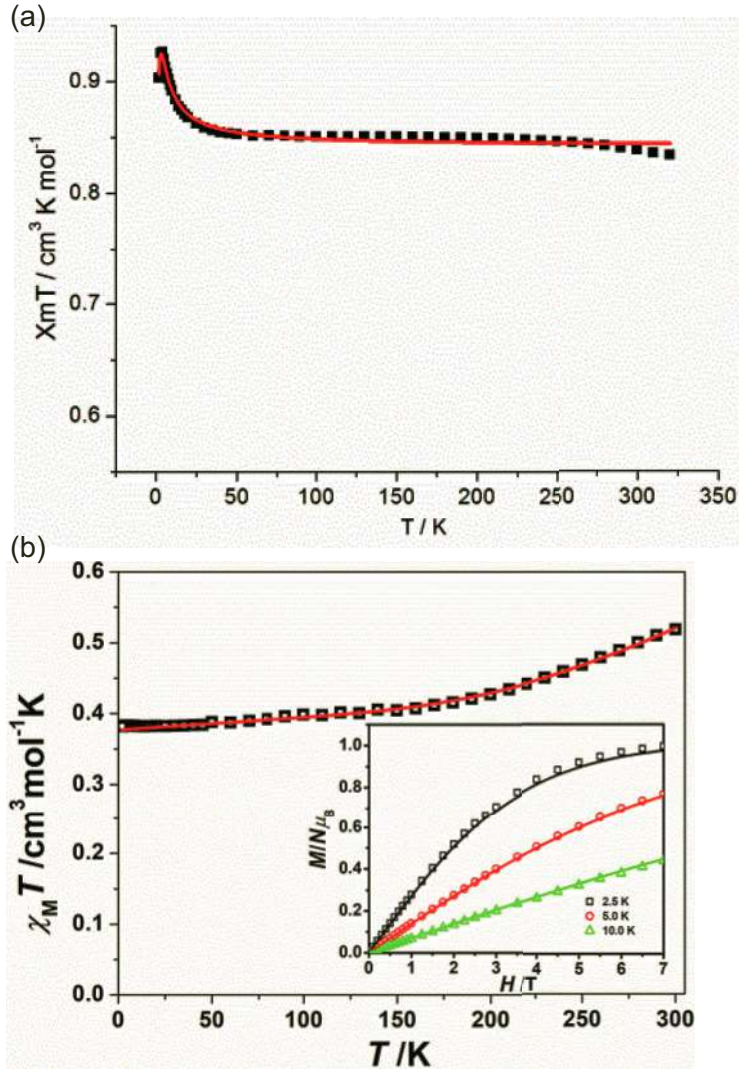


**Figure 12.1** Temperature dependence of $\chi_M T$ under a 1.0 kOe field at 1.8–300 K of $\mathbf{7}^{\bullet\bullet 2-}$ (a) and **11** (b).

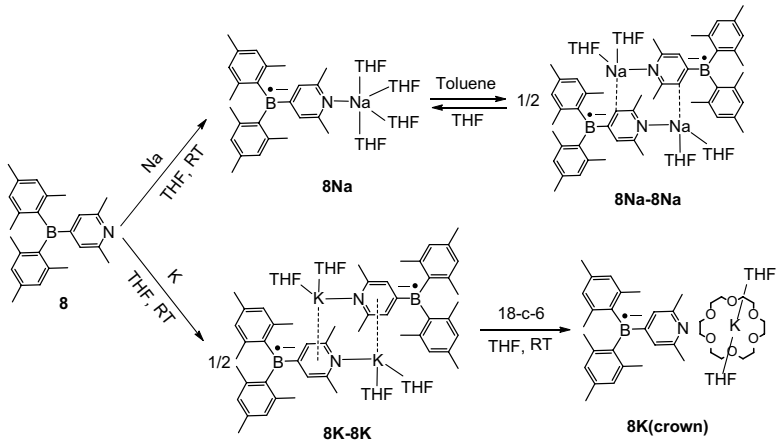


**Scheme 12.4** Synthesis of alkaline metal-containing radical species.

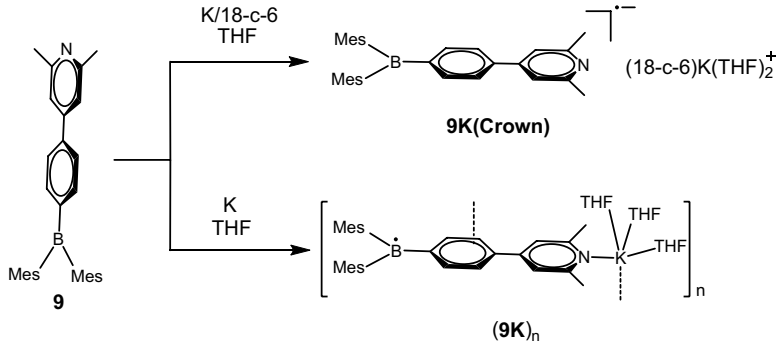


**Scheme 12.5** Synthesis of alkaline metal-containing radical species.

Although several boron-based diradicals have been reported, only one example of its polyradical (i.e. tetraradical) was reported by Bertrand and coworkers [49]. We found that the $Fe^{II}$ ion could facilely coordinate three 5,5′-bis(dimesitylboranyl)-2,2′-bipyridine ($bpy^B$) molecules affording the complex **10** (Scheme 12.6) [50]. The solid state structural parameters, EPR spectroscopy and SQUID measurements showed that **10** is an open-shell singlet diradical, in which two $bpy^B$ ligands are in the radical anion state. Complex **10** could further undergo one-electron reduction to the anion salt **11**. The solid state structural parameters suggested that all the three

bpy$^{B}$ ligands are in the radical forms, making it the first example of boron-based triradical. The SQUID measurements demonstrated that the anion **11** has a doublet ground state, and the doublet-quartet energy gap is 502.7 cm$^{-1}$ (1.4 kcal mol$^{-1}$) (Figure 12.1b).

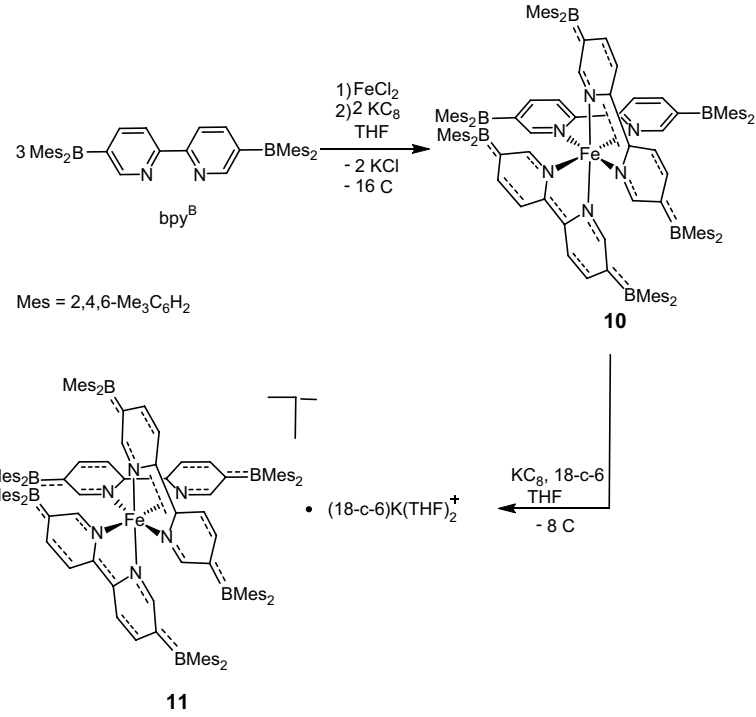


**Scheme 12.6** Synthesis of borane-based diradical and triradical fused by a Fe$^{II}$ ion.

## 12.2.2 Gallium-Centered Radical Cation

The chemistry of heavy group 13 element-based radicals is much less explored in comparison to boron-centered radicals, and only anionic and neutral radicals have been isolated [51–60]. The groups of Power, Uhl, and Pörschke independently reported the dialane(4) and digallane(4) radical anions, which were formed by populating the empty p orbitals of the $E_2$ (E = Al or Ga) unit to generate a one-electron E–E π bond [53–57]. In 2005, Sekiguchi and

coworkers obtained the first mononuclear tricoordinate aluminum- and gallium-centered radical anions [58]. Strikingly, Aldridge, and coworkers reported the first neutral radicals featuring five-valence electrons at the E centers [59]. Klopper et al. isolated the first aluminum-centered $Al_2P_2$-cyclic singlet diradical [60]. However, no radical cations of heavy group 13 elements have been isolated.

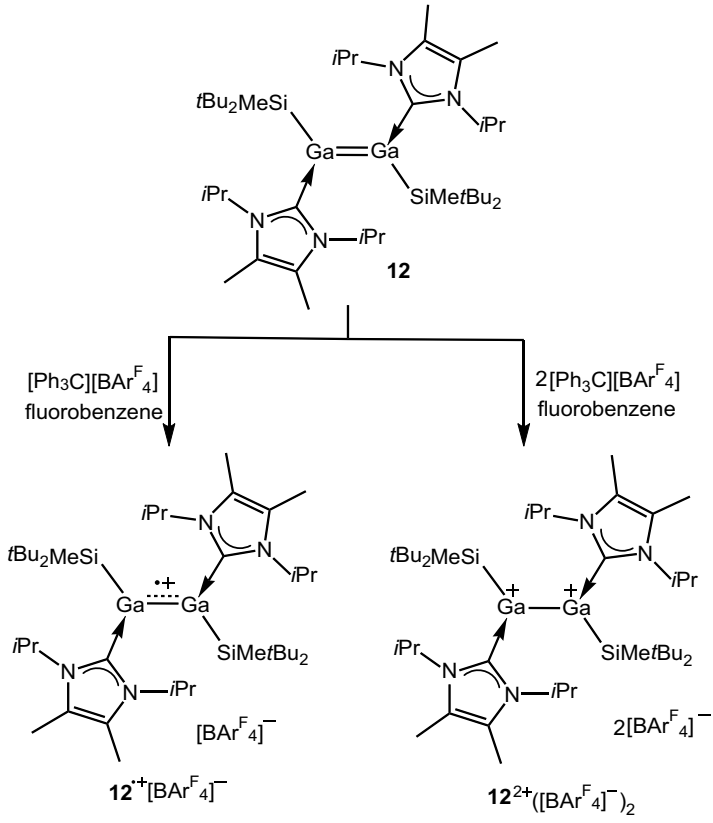


**Scheme 12.7** Synthesis of radical cation and dication of digallene.

Reduction of the NHC-coordinated silyl-substituted gallium dichloride with $KC_8$ resulted in the digallene **12**, which is isoelectronic to alkenes. Natural bond analysis of **12** shows the double bond nature of the Ga=Ga bond. One- and two-electron oxidation of **12** with $[Ph_3C][BAr^F_4]$ ($Ar^F$ = 3,5-$(CF_3)_2C_6H_3$) afforded the corresponding radical cation and dication salts (Scheme 12.7). Structural analysis shows

that upon oxidation the Ga–Ga distance increases, consistent with removal of the Ga–Ga π-bonding electron. Theoretical calculations indicate that the bond order is also decreasing from **12**, $\mathbf{12}^{\bullet+}$ to $\mathbf{12}^{2+}$, and the spin density of the radical cation mainly resides at the two gallium centers. The radical reacted instantly with $n$Bu$_3$SnH at room temperature, and the hydride abstraction product [**12**-H]$^+$[BAr$^F{}_4$]$^-$ was isolated in moderate yield, exhibiting the reactivity of gallium-centered radical. Interestingly, the reaction of $\mathbf{1}^{2\bullet+}$[BAr$^F{}_4$]$^-$ with cyclo-S$_8$ afforded a dication salt bearing an unprecedented ladder-like structure Ga$_4$S$_4$ core. The product may serve as a molecular precursor to access gallium sulfides, which are an important class of semiconducting materials [61–63].

## 12.3 Group 15 Element-Based Radicals

### 12.3.1 Nitrogen-Based Diradicals and Dications

Since the pioneer work by Thiele [64], Chichibabin [65], and Müller [66], who synthesized the first triarylmethyl-based diradicals (Scheme 12.8), tremendous efforts have been devoted to synthesize stable diradicals in the last decades [2–12]. When the carbinyl centers are replaced by the isoelectronic aminium centers, the nitrogen analogs of Thiele's, Chichibabin's and Müller's hydrocarbons can be achieved. We found that these bis(triarylamine) dications are much more stable than their hydrocarbon analogs, and the WCAs are exceptionally useful in isolating bis(triarylamine) dications. By using the salts of WCAs as the oxidizing reagents, we have successfully isolated a variety of bis(triarylamine) dications in the crystalline forms. The highly stable nature of these dications allowed us to have a deep investigation of their solid state and electronic structures, as well as physical properties.

Before 2013, only three stable bis(triarylamine) dications having been reported (Scheme 12.9). In 2006, Barlow and coworkers isolated two bis(triarylamine) dications $\mathbf{13}^{2+}$ and $\mathbf{14}^{2+}$, both of them possess closed-shell singlet ground states, and their structures were determined by single crystal X-ray diffraction, which were proven to be the first solid state structures of bis(triarylamine) dications [67]. In 2003, Tanaka and coworkers obtained the first stable

bis(triarylamine) diradical dication **15**$^{2+}$ fused by a spiro structural motif, which showed a triplet ground state, while its crystal structure was not gained [68, 69].

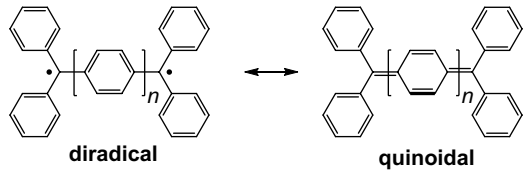


*n* = 1,Thiele's hydrocarbon
*n* = 2, Chichibabin's hydrocarbon
*n* = 3, Müller's hydrocarbon

**Scheme 12.8** Thiele's, Chichibabin's, and Müller's hydrocarbons.

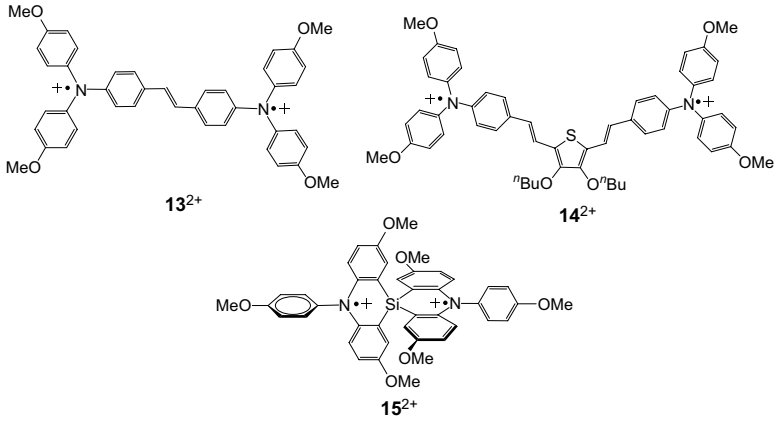


**Scheme 12.9** Structurally characterized bis(triarylamine) dications **13**$^{2+}$**–15**$^{2+}$.

### 12.3.1.1 Nitrogen analogs of Thiele's hydrocarbon

The electrochemical studies of the neutral compounds **16**–**22** revealed two reversible one-electron oxidation waves, indicating their doubly oxidized species might be stable [70, 71]. The dications **16**$^{2+}$–**22**$^{2+}$ were isolated as crystalline solids through two-electron oxidation of the corresponding neutral precursors with two-molar equivalent of $Ag[Al(OR_F)_4]$ ($OR_F$ = $OC(CF_3)_3$)[72] or $AgSbF_6$ and $Li[Al(OR_{Me})_4]$ ($OR_{Me}$ = $OC(CF_3)_2Me$)[72] in $CH_2Cl_2$ at room temperature (Scheme 12.10) [73, 74].

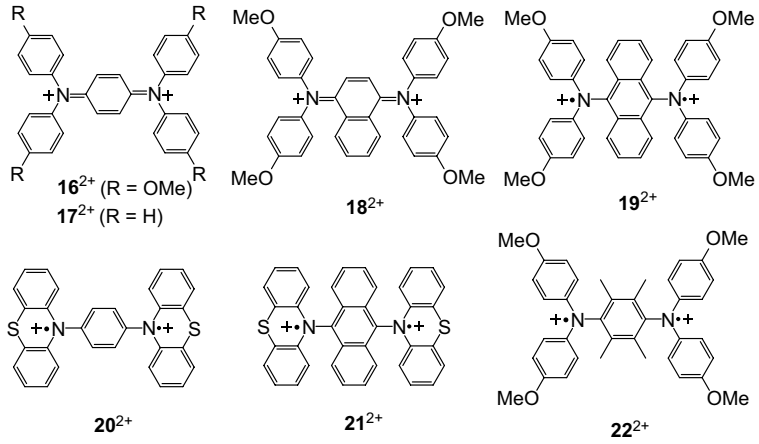


**Scheme 12.10** Structurally characterized examples of nitrogen analogs of Thiele's hydrocarbons.

The molecular structures of $\mathbf{17}^{2+}$–$\mathbf{22}^{2+}$ were determined by single crystal X-ray diffraction, the important structural parameters as well as the corresponding theoretical calculation results are listed in Table 12.1. The nitrogen atoms in the dications exhibit a trigonal planar geometry, and the two $C_3N$ planes are nearly coplanar ($\alpha$, Table 12.1). The angle ($\theta$, Table 12.1) between the $\alpha$ plane and the plane made up of the central bridge ($\beta$ plane) increases from $\mathbf{17}^{2+}$, $\mathbf{18}^{2+}$ to $\mathbf{19}^{2+}$ (21.6°, 33.0°, 56.2°, respectively), mainly attributing from the increasing steric repulsion from the central linking unit. Interestingly, for both $\mathbf{20}^{2+}$ and $\mathbf{21}^{2+}$, the two phenothiazine moieties are almost perpendicular to the central aromatic bridges (86.4° and 89.6° for $\mathbf{20}^{2+}$ and $\mathbf{21}^{2+}$, respectively).

Furthermore, the average N–C bond lengths to the $\pi$-linker in $\mathbf{17}^{2+}$ (1.346(3) Å) and $\mathbf{18}^{2+}$ (1.354(3) Å) are distinctly shorter relative to that in $\mathbf{19}^{2+}$ (1.405(4) Å). The bond-length alternation (BLA) values of the central benzene ring in $\mathbf{17}^{2+}$ (0.092 Å) and $\mathbf{6}^{2+}$ (0.087 Å) are comparable with that of the Thiele's hydrocarbon (0.103 Å) [75], demonstrating their quasi-quinoidal structures. The BLA values of the central bridge in $\mathbf{19}^{2+}$ (0.002 Å), $\mathbf{20}^{2+}$ (0.008 Å), and $\mathbf{21}^{2+}$ (0.040 Å) are much smaller than that of the Thiele's hydrocarbon [75], indicating the diradical nature of $\mathbf{19}^{2+}$–$\mathbf{21}^{2+}$.

**Table 12.1** Selected experimental and calculated results for $\mathbf{17}^{2+}$–$\mathbf{22}^{2+}$

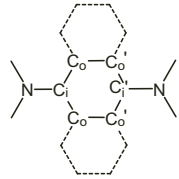


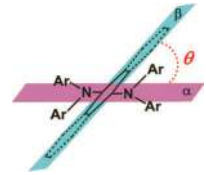


| | | $\Delta E_{X\text{-}OS}$[a] (kcal/mol) | Avg. N–$C_i$ | Avg. $C_o$–$C_o'$ | BLA[b] | $\theta$ | $y$[c] |
|---|---|---|---|---|---|---|---|
| | X-ray | | 1.346 | 1.344(2) | 0.092 | 21.6° | |
| $\mathbf{17}^{2+}$ | CS [a,d] | 0 | 1.362 | 1.365 | 0.071 | | |
| | OS [a,d] | — | — | — | — | | — |
| | T [a,d] | 6.0 | 1.429 | 1.390 | 0.015 | | |
| | X-ray | | 1.354(3) | 1.356(3) | 0.087 | 33.0° | |
| $\mathbf{18}^{2+}$ | CS | 1.82 | 1.380 | 1.372 | 0.066 | | |
| | OS | 0 | 1.400 | 1.384 | 0.043 | | 0.60 |
| | T | 3.26 | 1.439 | 1.406 | 0.002 | | |
| | X-ray | | 1.405(4) | 1.432(5) | 0.002 | 56.2° | |
| $\mathbf{19}^{2+}$ | CS | 3.64 | 1.394 | 1.435 | 0.009 | | |
| | OS | 0 | 1.437 | 1.445 | 0.027 | | 0.85 |
| | T | 1.47 | 1.445 | 1.447 | 0.034 | | |
| | X-ray | | 1.456(2) | 1.390(2) | 0.008 | 86.4° | |
| $\mathbf{20}^{2+}$ | CS | 14.8 | 1.454 | 1.398 | 0.002 | | |
| | OS | 0 | 1.455 | 1.396 | 0.001 | | 0.993 |
| | T | 0.0038 | 1.455 | 1.396 | 0.001 | | |
| | X-ray | | 1.454(10) | 1.436(3) | 0.040 | 89.6° | |
| $\mathbf{21}^{2+}$ | CS | 16.4 | 1.457 | 1.446 | 0.037 | | |
| | OS | 0 | 1.459 | 1.449 | 0.041 | | 0.995 |
| | T | 0.0013 | 1.459 | 1.449 | 0.041 | | |
| | X-ray (100 K) | | 1.433(3) | 1.394(4) | 0.016 | 58.1° | |
| | X-ray (200 K) | | 1.443(4) | 1.397(5) | 0.006 | 61.5° | — |
| $\mathbf{22}^{2+}$ | CS | 8.1 | 1.420 | 1.399 | 0.027 | | |
| | OS | 0 | 1.451 | 1.410 | 0 | | — |
| | T | 0.4 | 1.453 | 1.411 | 0.002 | | |

[a]X = CS (closed-shell singlet), OS (open-shell singlet), or T (triplet). [b]BLA is defined as the difference between the average of all $C_i$–$C_o$ and $C_i'$–$C_o'$ bond lengths and the average of $C_o$–$C_o'$ bond lengths. [c]Diradical character, $y$ values were calculated at the UBHandHLYP/6-31G(d) level. [d]Optimized at the level of (U)B3LYP/6-31G(d).

The singlet–triplet energy gaps of $\mathbf{16}^{2+}$–$\mathbf{21}^{2+}$ were determined by SQUID magnetometry. The measurements indicated that the dications $\mathbf{16}^{2+}$–$\mathbf{18}^{2+}$ featured a closed-shell singlet ground state. In contrast, $\mathbf{19}^{2+}$–$\mathbf{21}^{2+}$ exhibited an open-shell singlet ground state, and the singlet–triplet energy gaps are –489.98 $cm^{-1}$ (–1.40 kcal $mol^{-1}$), –6.07 $cm^{-1}$ (–0.017 kcal $mol^{-1}$), and –0.75 $cm^{-1}$ (–0.0021 kcal $mol^{-1}$), respectively, obtained by fitting the curves using the Bleaney–Bowers equation with Hamiltonian $H = -2JS_1S_2$ ($S_1 = S_2 = 1/2$) [76]. The experimental results agree well with the singlet–triplet energy gaps obtained by DFT calculations (Table 12.1). In addition, the calculated $y$ values increase from $\mathbf{17}^{2+}$ to $\mathbf{21}^{2+}$, suggesting the increased diradical character (Table 12.1).

The SQUID measurements of $\mathbf{22}^{2+}$ exhibited a thermal hysteresis loop at the temperature range from 118 K to 131 K (Figure 12.2a). Moreover, the powder EPR spectra display typical broad triplet-state signals (Figure 12.2b). The two phases in the loop correspond to two different singlet states of the diradical dications, and the singlet–triplet energy gaps are estimated to be $2J$ = –1.06 kcal $mol^{-1}$ and –0.54 kcal $mol^{-1}$ for the low-temperature and high-temperature phases, respectively, according to the SQUID measurements.

In order to have a further insight into the cause of the hysteresis loop for $\mathbf{22}^{2+}$, we measured the crystal structures at 100 K and 200 K, respectively. The structures reveal that the molecular packing modes at 100 K and 200 K are almost identical, and there is no significant difference for the anion–cation interaction. However, some structural parameters differ significantly at 100 K and 200 K. For example, the angles ($\theta$) between the $\alpha$ and $\beta$ planes are 58.1° and 61.5° at 100 K and 200 K, respectively (Table 12.1). In addition, there is a crucial difference between the BLAs of the central phenyl groups at 100 K (0.016 Å) and 200 K (0.006 Å). They are much less than that of the Thiele's hydrocarbon (0.052 Å), suggesting strong diradical character at both temperatures. The N–C bond lengths to the central bridge at 100 K and 200 K are similar (1.433(3) and 1.443(4) Å, respectively), which are much larger in comparison with those in $\mathbf{17}^{2+}$–$\mathbf{19}^{2+}$. Compound $\mathbf{22}^{2+}$ represents the first example of the magnetic bistability mainly induced by intramolecular electron–exchange interaction, in contrast to those of previously reported organic radicals, which are caused by the intermolecular interaction, such as radical stacks or dimers [77–91].

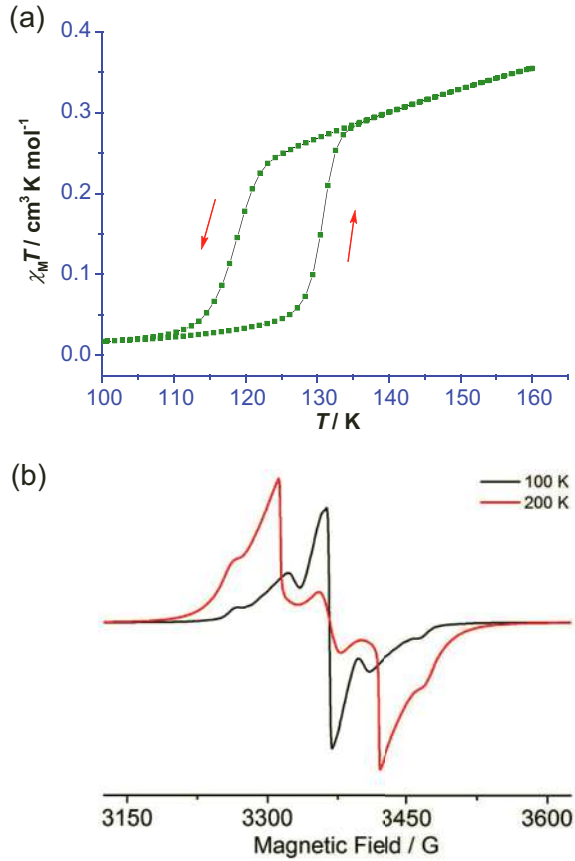


**Figure 12.2** (a) Temperature-dependent of $\chi_M T$ for $\mathbf{22}^{2+}$ measured in the sweep mode at the scan rate of 1 K min$^{-1}$ from 100–150 K. (b) Powder EPR spectra of $\mathbf{22}^{2+}$ at 100 (in black) and 200 K (in red).

The EPR silence of $\mathbf{16}^{2+}$–$\mathbf{18}^{2+}$ in solution and in the solid state, as well as their diamagnetism in the SQUID measurements of the crystalline samples demonstrate that they exhibit a singlet ground state with a relatively large single–triplet energy gap. In contrast, the powder samples of $\mathbf{19}^{2+}$–$\mathbf{22}^{2+}$ are EPR active, and the characteristic half-field resonance signals were observed, indicating the spin-triplet state is thermally accessible. Through the simulated EPR spectrum, the zero field parameters $D$ = 13.4 mT (12.5 × 10$^{-3}$ cm$^{-1}$) and $E$ = 1.28 mT (1.19 × 10$^{-3}$ cm$^{-1}$) for $\mathbf{19}^{2+}$ are obtained. The average spin-spin distance (5.9 Å) is estimated according to the $D$

value, which is slightly longer than the intramolecular N…N distance (5.6 Å) determined in the crystal structure, such an outcome should be ascribing to the delocalization of the two unpaired electrons over the peripheral aromatic groups. The powder EPR spectra of $\mathbf{22}^{2+}$ display typically broad triplet-state signals (Figure 12.1b). The temperature-dependent spin susceptibility determined by solid state EPR spectroscopy shows a similar hysteresis loop in comparison to that observed in SQUID measurements.

### 12.3.1.2 Nitrogen analogs of Chichibabin's hydrocarbon

Chichibabin's hydrocarbon is a diradical with a diphenylene group served as a π-linker. Its stable nitrogen analogs $\mathbf{24}^{2+}$–$\mathbf{28}^{2+}$ bearing different substituents, $\mathbf{29}^{2+}$ and $\mathbf{30}^{2+}$, with a bisanthrancene as linker, have been synthesized and fully characterized (Scheme 12.11).

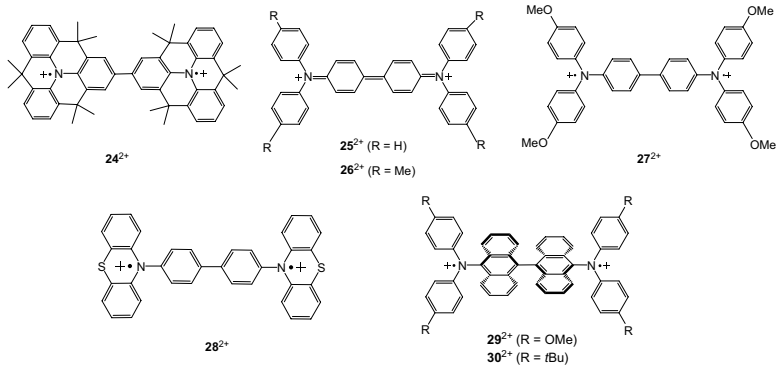


**Scheme 12.11** Structurally characterized examples of nitrogen analogs of Chichibabin's hydrocarbon.

The bis(triarylamine) diradical dication $\mathbf{24}^{2+}$ was obtained by the reaction of **23** with half-molar equivalent of $Ag[Al(OR_F)_4]$ (Scheme 12.12) [92]. $\mathbf{24}^{2+}$ could also be straightforwardly prepared by two-electron oxidation of the neutral compound **23** with two-molar equivalent of $Ag[Al(OR_F)_4]$.

The configuration of the diradical dication $\mathbf{24}^{2+}$ is not completely flat, but slightly curved. The average N–C bond length to the biphenyl moiety (1.404(5) Å) is shorter than those to the peripheral aryl ring systems (1.442(5) Å). The bond length (1.467(8) Å) between the two triarylamine moieties is slightly shorter than a typical biphenyl single bond, but longer than a typical double bond, reflecting that

$\mathbf{24}^{2+}$ has an open-shell singlet ground state, which is further verified by theoretical calculations. The calculations give a small singlet–triplet energy gap $\Delta E_{OS-T}$ (–1.0 kcal mol$^{-1}$) and a moderate $y$ value (0.77).

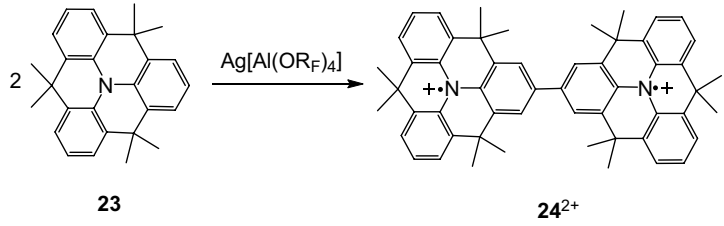


**23** $\mathbf{24}^{2+}$

**Scheme 12.12** Synthesis of diradical dication $\mathbf{24}^{2+}$.

The cyclic voltammograms of **25–28** show two reversible oxidation peaks [71], suggesting that they are readily to undergo two-electron oxidation reactions. The dications $\mathbf{25}^{2+}$–$\mathbf{28}^{2+}$ were synthesized by the oxidation reactions of the neutral bis-triarylamines with two-molar equivalent of silver salts bearing WCAs [73, 93, 94]. The dication $\mathbf{25}^{2+}$ has a bent geometry, whereas $\mathbf{26}^{2+}$ and $\mathbf{27}^{2+}$ have planar structures [93]. The average N–C bond lengths to the diphenyl units increase from $\mathbf{25}^{2+}$ to $\mathbf{28}^{2+}$, while the BLA values decrease (Table 12.2). The BLA values of $\mathbf{27}^{2+}$ and $\mathbf{28}^{2+}$ are less than that of Chichibabin's hydrocarbon (0.052) [75], suggesting their diradical character. The comparison of the experimental and calculated structural parameters clearly reveals that $\mathbf{25}^{2+}$ and $\mathbf{26}^{2+}$ possess closed-shell singlet structures, whereas $\mathbf{27}^{2+}$ and $\mathbf{28}^{2+}$ exhibit open-shell singlet ground states.

The dications $\mathbf{25}^{2+}$ and $\mathbf{26}^{2+}$ are EPR silent both in solution and solid state, and their SQUID measurements in the powder form only show diamagnetism, consistent with their closed-shell structures [93]. The powder sample of $\mathbf{27}^{2+}$ is EPR active and a $\Delta m_s$ = 2 resonance singly attributed to the spin-triplet state is observed at 320 K. The zero-field splitting parameters of $D$ = 9.45 mT (8.84 × 10$^{-3}$ cm$^{-1}$) and $E$ = 0.92 mT (8.60 × 10$^{-4}$ cm$^{-1}$) were determined by spectral simulation of the $\Delta m_s$ = 1 resonance for $\mathbf{27}^{2+}$ [93]. From the $D$ value, the average spin-spin distance is estimated to be 6.6 Å, which is much smaller than the distance (9.8 Å) between the two N atoms in the solid state structure. Moreover, the singlet–triplet energy gap ($2J$ = –2.8 kcal mol$^{-1}$) was estimated from the SQUID measurements.

**Table 12.2** Selected experimental and calculated bond lengths (Å) and diradical character ($y$) for the nitrogen analogs of Chichibabin's hydrocarbon

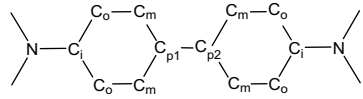


| | | Avg. $N–C_i$ | Avg. $C_{p1}–C_{p2}$ | Avg. $C_i–C_o$ and $C_m$-$C_p$ | Avg. $C_o–C_m$ | BLA[b] | $y$[c] |
|---|---|---|---|---|---|---|---|
| | X-ray | 1.404(5) | 1.467(8) | 1.422(6) | 1.380(6) | 0.042 | 0.77 |
| **24**$^{2+}$ | CS | 1.378 | 1.441 | 1.428 | 1.375 | 0.053 | |
| | OS | 1.412 | 1.472 | 1.413 | 1.388 | 0.025 | |
| | T | 1.423 | 1.482 | 1.409 | 1.392 | 0.017 | |
| | X-ray | 1.339(4) | 1.414(4) | 1.431(4) | 1.357(4) | 0.074 | 0.47 |
| **25**$^{2+}$ | CS | 1.368 | 1.434 | 1.432 | 1.369 | 0.063 | |
| | OS | 1.403 | 1.470 | 1.414 | 1.383 | 0.031 | 0.81 |
| | T | 1.418 | 1.482 | 1.409 | 1.387 | 0.022 | |
| | X-ray | 1.365(6) | 1.422(9) | 1.426(7) | 1.363(6) | 0.063 | 0.61 |
| **26**$^{2+}$ | CS | 1.374 | 1.439 | 1.428 | 1.371 | 0.057 | |
| | OS | 1.411 | 1.474 | 1.411 | 1.385 | 0.026 | 0.85 |
| | T | 1.421 | 1.482 | 1.408 | 1.388 | 0.020 | |
| | X-ray | 1.383(7) | 1.457(7) | 1.407(7) | 1.370(7) | 0.037 | 0.79 |
| **27**$^{2+}$ | CS | 1.386 | 1.448 | 1.423 | 1.375 | 0.048 | |
| | OS | 1.419 | 1.477 | 1.408 | 1.387 | 0.021 | 0.88 |
| | T | 1.425 | 1.483 | 1.406 | 1.389 | 0.017 | |
| | X-ray | 1.459(5) | 1.47(3) | 1.392 | 1.390 | 0.002 | — |
| **28**$^{2+}$ | CS | 1.455 | | 1.401 | 1.394 | 0.002 | |
| | OS | 1.456 | | 1.401 | 1.394 | 0.002 | 0.999 |
| | T | 1.456 | | 1.401 | 1.394 | 0.007 | |
| | X-ray | 1.400 | 1.502 | 1.407 | 1.437 | 0.030 | |
| **29**$^{2+}$ | CS | 1.447 | 1.371 | 1.481 | 1.423 | 0.058 | 0.998 |
| | OS | 1.406 | 1.504 | 1.415 | 1.466 | 0.031 | |
| | T | 1.406 | 1.504 | 1.415 | 1.466 | 0.031 | |
| | X-ray | 1.441 | 1.497 | 1.406 | 1.438 | 0.032 | |
| **30**$^{2+}$ | CS | 1.330 | 1.370 | 1.482 | 1.422 | 0.060 | 0.985 |
| | OS | 1.430 | 1.504 | 1.419 | 1.445 | 0.026 | |
| | T | 1.430 | 1.504 | 1.419 | 1.445 | 0.027 | |

[a]X = CS (closed-shell singlet), OS (open-shell singlet), or T (triplet). [b]BLA is defined as the difference between the average of all $C_i–C_o$ and $C_m–C_p$ bond lengths and the average of $C_o–C_m$ bond lengths. [c]diradical character, $y$ values were calculated at the UBHandHLYP/6-31G(d) level. [d]Optimized at the level of (U)B3LYP/6-31G(d).

The two phenothiazine moieties in $\mathbf{28}^{2+}$ are almost coplanar, and they are nearly orthogonal with the biphenyl bridge (83.5°) [73]. The C–C bond (1.47(3) Å) between the diphenyl group is quite close to that of a typical biphenyl single bond (1.48 Å). Moreover, the BLA of the central biphenyl bridge is 0.002 Å, substantially smaller than that of Chichibabin's hydrocarbon [75]. In addition, a very small singlet–triplet gap (–0.019 kcal $mol^{-1}$) was afforded from the SQUID measurements, suggesting that the open-shell singlet state is nearly degenerated with the triplet state.

Bisanthrancene motif features an almost orthogonal configuration due to steric hindrance, thus electron delocalization over the bisanthrancene group is very small. When the bisanthrancene motif is applied as a linker, the bis(triarylamine) diradical dication salts of $\mathbf{29}^{2+}$ and $\mathbf{30}^{2+}$ feature an almost degenerated singlet–triplet state, although the singlet is the ground state structure.

#### 12.3.1.3 Nitrogen analogs of Müller's hydrocarbon

The diradical dication $\mathbf{31}^{2+}$ is the only reported stable nitrogen analog of Müller's hydrocarbon (Scheme 12.13) [95]. The magnetic susceptibility measurements showed that its singlet–triplet energy gap could be tunable by temperature, making it the first example of a thermally controllable singlet–triplet gap for a diradical in the solid state. The $\chi_m T$ value slowly decreases from 300 K to 170 K, then suddenly increases to a maximum at 130 K, followed by a gradual decrease to zero at 50 K (Figure 12.2a), indicating that there are two singlet states occurred at low temperature (LT) and high temperature (HT), respectively, and the singlet–triplet gaps are estimated to be –400.6 $cm^{-1}$ (–1.14 kcal $mol^{-1}$) and 872.8 $cm^{-1}$ (–2.49 kcal $mol^{-1}$) for LT and HT phases, respectively. The EPR spectra at 123 K and 290 K also display two different broad signals with $g$ factors of 2.0026 and 2.0021, respectively (Figure 12.2b).

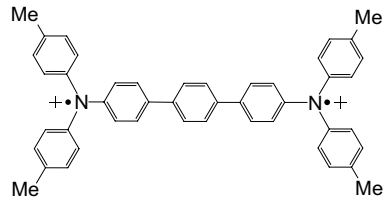


$\mathbf{31}^{2+}$

**Scheme 12.13** The nitrogen analog of Müller's hydrocarbon.

In order to figure out the properties of $\mathbf{31}^{2+}$, we measured the crystal structures by single crystal X-ray diffraction at 123 K and 200 K, respectively. For the structure determined at 200 K, the central terphenyl backbone is nearly planar, while at 123 K, it is turned out to be a large torsion angle (26.76°). Besides, there are obvious difference of the N–$C_{terphenyl}$ bond lengths between the crystal structures at 200 K (1.366(4) Å) and 123 K (1.392(3) Å). In addition, the calculated *y* values of the two structures are 0.89 and 0.79 at 123 K and 200 K, respectively, showing larger diradical character at LT phase than that of at HT phase (Figure 12.3).

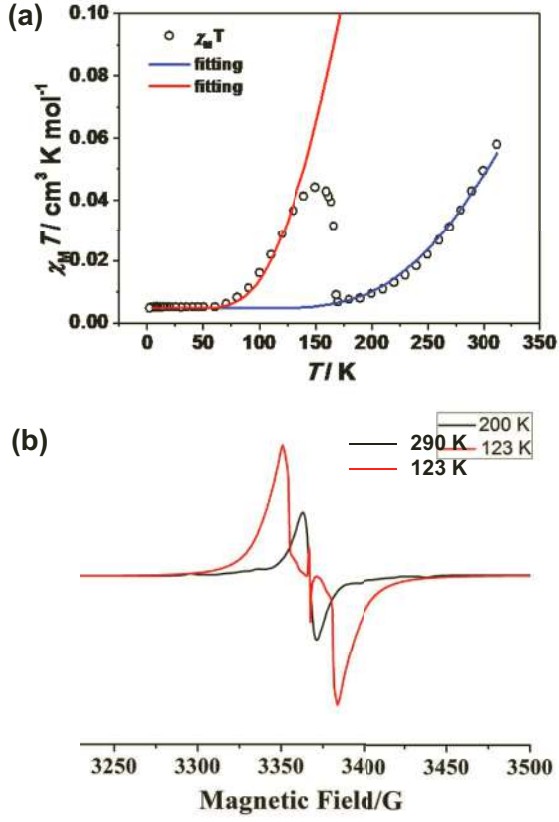


**Figure 12.3** (a) The $\chi_m T$ versus *T* plot for the crystals of $\mathbf{31}^{2+}$, and the fitting plots via the Bleaney−Bowers equation. (b) The powder EPR spectra of $\mathbf{31}^{2+}$ at 123 K and 290 K.

### 12.3.1.4 Other amine-based diradical dications

Except the isolation of the nitrogen analogs of Thiele's, Chichibabin's, and Müller's hydrocarbons, we have also successfully synthesized the nitrogen analogs of *o*-quinodimethane $\mathbf{32}^{2+}$–$\mathbf{34}^{2+}$ [96], the tetraazacyclophane diradical dications $\mathbf{35}^{2+}$–$\mathbf{37}^{2+}$ [97, 98], and stable alkylate-bridged Würster's blue-based diradical dications $\mathbf{38}^{2+}$ and $\mathbf{39}^{2+}$ (Scheme 12.14) [99].

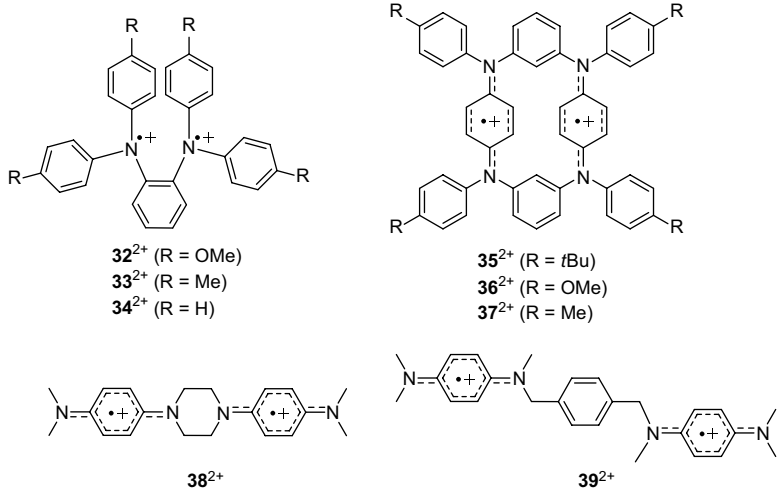


**Scheme 12.14** Other amine-based diradical dications.

All the neutral compounds exhibit reversible two-electron oxidation peaks in the cyclic voltammograms. They were obtained as crystalline samples by two-electron oxidation of the corresponding neutral precursors with two-molar equivalent of silver salts bearing WCAs. Structural, magnetic, and theoretical investigations show that $\mathbf{32}^{2+}$–$\mathbf{34}^{2+}$ have open-shell singlet ground states with thermally accessible triplet states, and feature unexpected non-Kekulé diradical character, sharply different from *o*-quinodimethane. $\mathbf{35}^{2+}$–$\mathbf{37}^{2+}$ feature triplet ground states with quite large singlet–triplet gaps (484 K, 400 K, and 240 K, respectively), which exceed the thermal energy at room temperature. Interestingly, the solid-state packing structures of $\mathbf{35}^{2+}$–$\mathbf{37}^{2+}$ were tunable by substituent effect, e.g. $\mathbf{35}^{2+}$ exists as a monomer and $\mathbf{36}^{2+}$ as a dimer, while $\mathbf{37}^{2+}$ features a one-dimensional chain structure. Moreover, the diradical

dication salt of $\mathbf{37}^{2+}$ possesses extraordinary stability with onset of decomposition at temperature of about 180 °C (~450 K), based on thermogravimetric analysis and EPR spectroscopy. The SQUID measurements demonstrate that $\mathbf{38}^{2+}$ has an open-shell singlet ground state with a singlet–triplet energy gap of $2J$ = –186.38 $cm^{-1}$ (–0.54 kcal $mol^{-1}$), whereas the singlet and triplet states of $\mathbf{39}^{2+}$ are almost degenerated and it can be basically viewed as a pure diradical.

#### 12.3.1.5 Nitrogen-based radical anions

Azaacenes have received great attention, owing to their novel structures, tunable properties, and potential applications in organic electronic devices, such as organic field-effect transistors (OFETs), organic photovoltaic devices (OPVs), and organic light-emitting diodes (OLEDs) [100–106]. Intrigued by the high *n*-channel charge mobility of a silylethynylated tetraazapentacene by Miao and coworkers [107], the anionic azaacene species have attracted great attention. There are several reports of structurally characterized radical anions and dianions, however all the dianions have a closed-shell singlet ground state [108–111]. We carried out one- and two-electron reductions of pyrene-fused azaacenes **40** and **41**, and obtained the corresponding radical anions and diradical dianions (Scheme 12.15) [112]. The diradical dianions feature open-shell singlet ground states with thermally accessible triplet states ascribed to the small singlet–triplet gaps. The spin density of the radical species delocalizes over the whole π-system.

### 12.3.2 Heavy Pnictogen-Centered Radical Ions

#### 12.3.2.1 Heavy pnictogen-centered radical cations

Triarylphosphines are widely used as ligands for transition metal mediated organic catalysis [113], and they also serve as potential candidates for redox centers in functional materials [114]. Triarylphosphine radical cations have been investigated by EPR spectroscopy in solution and were proposed to adopt a pyramidal geometry, but no X-ray structures have been obtained. The sterically encumbered triarylphosphines **42** and **43** feature reversible one-electron oxidation peaks in the cyclic voltammograms, suggesting that their radical cations might be stable. By utilizing the bulky aromatic

substituents and the WCAs as the counterions, we successfully isolated the stable triarylphosphine radical cations in the crystalline form through one-electron oxidation of triarylphosphines with silver salts (Scheme 12.16) [115].

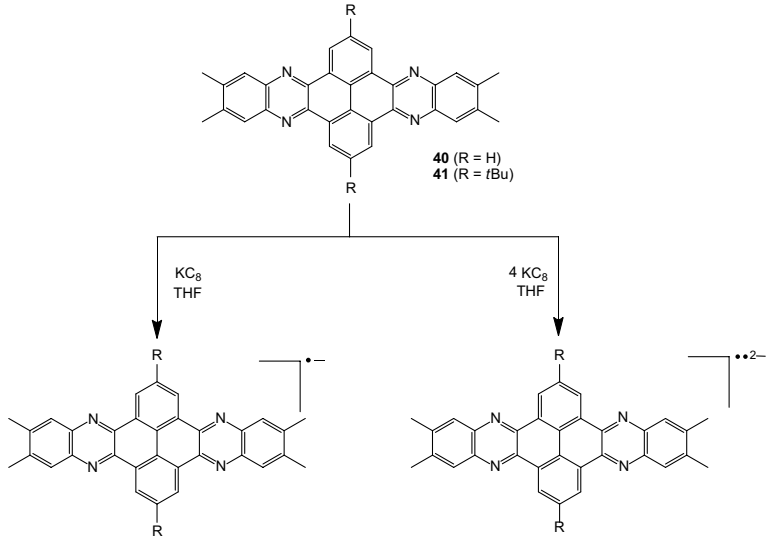


**Scheme 12.15** Synthesis of pyrene-fused azaacene radical anions and dianions.

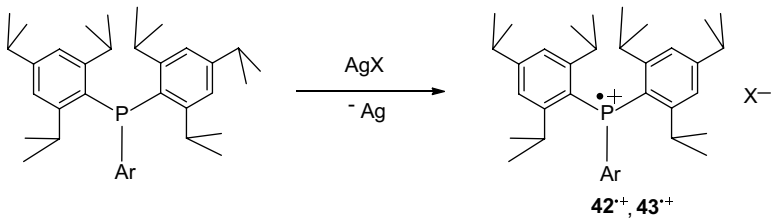


**42**$^{\bullet+}$ : Ar = 2,4,6-$Me_3C_6H_2$; X = $Al(O(C(CF_3)_3)_4$

**43**$^{\bullet+}$ : Ar = 2,4,6-*i*$Pr_3C_6H_2$; X = $SbF_6$, $Al(OCMe(CF_3)_2)_4$, $Al(O(C(CF_3)_3)_4$

**Scheme 12.16** Synthesis of triarylphosphine radical cations.

The EPR spectra of **42**$^{\bullet+}$ and **43**$^{\bullet+}$ recorded at 273 K afforded the isotropic coupling constants of 236 G and 233 G, respectively. The anisotropic HFC constants of $g_{||}$ = 2.004, $a_{||}$ = 409 G, $g_{\perp}$ = 2.012, $a_{\perp}$ = 159 G and $g_{||}$ = 2.003, $a_{||}$ = 417 G, $g_{\perp}$ = 2.011, $a_{\perp}$ = 114 G for **42**$^{\bullet+}$

and **43**$^{\bullet+}$ were extracted from the EPR spectra obtained at 77 K. The ratios of the isotropic and anisotropic hyperfine constants suggest that ~64 and 5% of the unpaired electron are localized on the 3p and 3s orbitals of the phosphorus nucleus in **42**$^{\bullet+}$, respectively (~77 and 5%, respectively, in **43**$^{\bullet+}$) [116].

The crystal structures of **42**$^{\bullet+}$ and **43**$^{\bullet+}$ reveal that the C–P bond lengths are shorter and the C–P–C angles are larger than those in the corresponding neutral phosphines. The phosphorus center in **42**$^{\bullet+}$ becomes less pyramidalized, and strikingly, the phosphorus center in **43**$^{\bullet+}$ has a trigonal planar geometry. These data demonstrate that the removal of one electron from triarylphosphine has significant effects on its molecular structure. The DFT calculations show that the 3p character of the singly occupied molecular orbital (SOMO) increases with sterically bulkier substituents, and the SOMO of $Dipp_3P^{\bullet+}$ (Dipp = 2,6-*i*$Pr_2C_6H_3$) has an almost pure P 3p character, which can explain the planar configuration of **43**$^{\bullet+}$. It is noteworthy that Stephan and coworkers reported the $Mes_3P^{\bullet+}$ generated through the frustrated Lewis pair approach [117].

By employing the same stabilization strategy, we were able to synthesize and fully characterize the triarylarsine [118] and triarylstibine [119] radical cation salts, although the $[BAr^F]^-$ anion was used. In contrast to the trigonal planar geometry of the bulky triarylphosphine radical cations, all the triarylarsine and triarylstibine radical cations have trigonal pyramidal structures. The unpaired electron almost entirely locates at the pnictogen atom center.

Encouraged by the isolation of triarylphosphine radical cations, we further investigated the oxidation reaction of tetraaryldiphosphine **44**, which shows two one-electron oxidation peaks in the electrochemical studies. The one-electron oxidation of **44** with stoichiometric amount of $Ag[Al(OCMe(CF_3)_2)_4]$ afforded the radical cation **44**$^{\bullet+}$ in high yield as green crystals (Scheme 12.17). Upon two-electron oxidation with two-molar equivalent of $Ag[Al(OCMe(CF_3)_2)_4]$, **44** could be converted to the red dication **44**$^{2+}$ [120].

The EPR spectrum of **44**$^{\bullet+}$ at 273 K reveals a triplet signal with an isotropic coupling constant of 176 G at $g$ = 2.009 due to the coupling with two phosphorus nuclei. The EPR spectrum of the frozen solution at 77 K gives $g$ factors and HFC tensors as follows: $g_{||}$ = 2.004, $a_{||}$ =

287 G, $g_{\perp}$ = 2.014, $a_{\perp}$ = 140 G. The localization of ~38 and 4% of the unpaired electron at the P 3p and 3s orbitals of each phosphorus center is calculated [116].

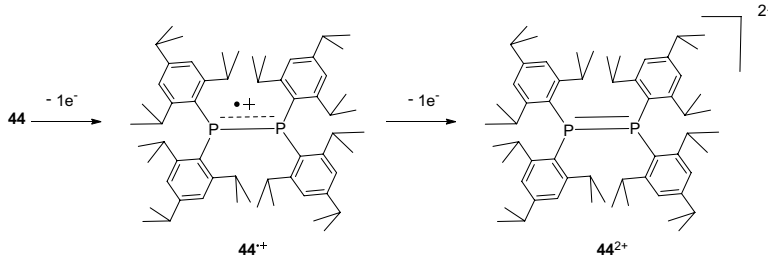


**Scheme 12.17** Synthesis of tetraaryldiphosphine radical cation and dication.

The crystal structures of $\mathbf{44}^{\bullet+}$ and $\mathbf{44}^{2+}$ were determined by single crystal X-ray crystallography. It is shown that the phosphorus centers become less pyramidal upon one-electron oxidation, and they are completely flat upon loss of the second electron. Moreover, the P–P bond length shortens from **44**, $\mathbf{44}^{\bullet+}$ to $\mathbf{44}^{2+}$, suggesting an increasing bond order upon oxidation. The P–P length (2.136(5) Å) in $\mathbf{44}^{\bullet+}$ is between a P–P double bond (~2.02 Å) [121–123] and a P–P single bond (~2.20 Å), while in dication $\mathbf{44}^{2+}$, it unambiguously shows a P–P double bond character (2.021(2) Å).

The calculations on the model diphosphine $(Dipp)_2PP(Dipp)_2$ (**45**, Dipp = 2,6-*i*$Pr_2C_6H_3$) and its oxidized species $\mathbf{45}^{\bullet+}$ and $\mathbf{45}^{2+}$ suggest that the highest occupied molecular orbital (HOMO) of **45** is mainly $\pi^*(P_2)$, which is singly occupied in $\mathbf{45}^{\bullet+}$ and unoccupied in $\mathbf{45}^{2+}$. This can explain the shortening of the P–P bond length upon oxidation. In addition, the calculated spin density of $\mathbf{45}^{\bullet+}$ is mainly localized on two phosphorus atoms (0.43e × 2), which agrees well with the experimental EPR spectra.

Phosphaalkenes, $RP{=}CR'_2$, a class of low-coordinate organophosphorus compounds, have been extensively investigated and their redox behaviors in solution suggest that they can be oxidized as well as reduced to the corresponding radical cations and anions, respectively. There are several reports of radical cations derived from the oxidation of the P=C or As=C bond containing precursors [124–128]. We carried out the one-electron oxidation reactions of the phosphaalkenes **46** and **47** with one-molar

equivalent of $Ag[Al(OC(CF_3)_3)_4]$ and $NO[Al(OC(CF_3)_3)_4]$, respectively, and purple and green solutions of the radical cations **46**$^{\bullet+}$ and **47**$^{\bullet+}$ were obtained (Scheme 12.18) [129].

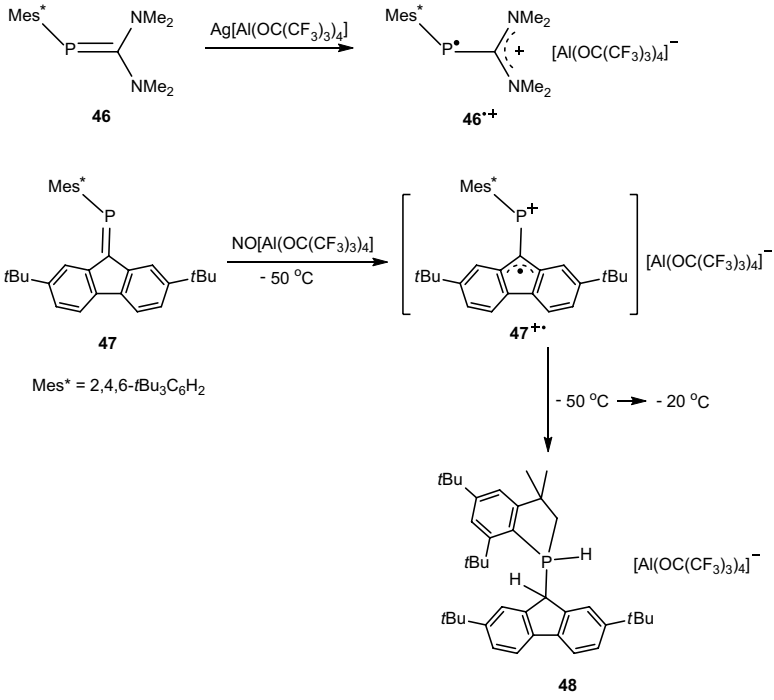


**Scheme 12.18** Synthesis of phosphaalkene radical cations.

The EPR spectra of **46**$^{\bullet+}$ and **47**$^{\bullet+}$ are obviously different, the former shows a doublet signal due to the coupling with one phosphorus nucleus ($a(^{31}P)$ = 101.6 G), whereas the latter reveals two sets of septet signals because of the coupling with one phosphorus nucleus and six hydrogen atoms ($a(^{31}P)$ = 23.9 G and $a(^{1}H)$ = 4.2 G) (Figure 12.4). This suggests that **46**$^{\bullet+}$ and **47**$^{\bullet+}$ have quite different electronic structures. Indeed, the spin density distributions demonstrate that it mainly locates at the phosphorus center in **46**$^{\bullet+}$ (80.9%), while it spreads over the phosphorus center (9.7%) and the fluorenyl moiety in **47**$^{\bullet+}$.

The radical cation **46**$^{\bullet+}$ is stable at ambient temperature, and its structure was determined by X-ray crystallography. It features

a V-shaped geometry. The structural alternations in comparison to the neutral compound suggest a phosphinyl radical bearing a cationic substituent. In contrast, **47**$^{\bullet+}$ is only persistent in solution below –50 °C, the green solution gradually turned to yellow and the intramolecular cyclization product **48** was isolated. The additional hydrogen atom at the carbon center is most likely from the solvent due to the hydrogen abstraction by the carbon radical.

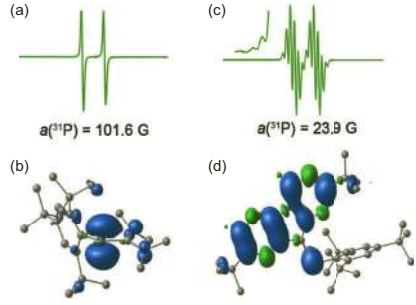


**Figure 12.4** (a) Experimental EPR spectrum of **46**$^{\bullet+}$, (b) spin density distribution of **46**$^{\bullet+}$, (c) experimental EPR spectrum of **47**$^{\bullet+}$, and (d) spin density distribution of **47**$^{\bullet+}$.

Similar to phosphaalkenes, diphosphenes can also undergo one-electron oxidation to the radical cations. Bertrand et al. [130] and Robinson et al. [131] reported carbene-substituted diphosphorus and diarsenic radical cations, respectively. However, the species [ArP=PAr]$^{\bullet+}$ and [ArAs=AsAr]$^{\bullet+}$ are still elusive. We found that one-electron oxidation of Mes*P=PMes* with various oxidants did not led to the formation of the expected radical cations. Therefore, we turned to diphosphene-chromium complexes **49** and **50**. The radical cation salts of **51** and **52** were isolated from the one-electron oxidation reactions (Scheme 12.19) [132]. The P–P bond is coordinated to the Cr center in an end-on mode in **51**, whereas it is in a side-on fashion in **52**. The spin density is delocalized over the Cr atom and the two P atoms in **51**, while it is mainly localized on the Cr atom in **52**. Very recently, Ghadwal and coworkers reported the stable devinyldiphosphene [125] and divinyldiarsene radical cations [126].

**Scheme 12.19** Synthesis of diphosphene-chromium radical cations.

Although cyclotetraphosphine radical cations and their lighter analog tetrazetidine radical cation have been investigated by EPR spectroscopy [133, 134], no stable species has been isolated. We studied the one-electron reduction of two phosphorus-containing four-membered ring compounds **53** and **54**. The reaction of **53** with a mixture of $NOSbF_6$ and $Li[Al(OC(CF_3)_3)_4]$ led to the formation of intensely violet radical cation salt $\mathbf{53}^{\bullet+}\bullet[Al(OC(CF_3)_3)_4]^-$ (Scheme 12.20). The red radical cation salt $\mathbf{54}^{\bullet+}\bullet SbF_6^-$ was synthesized by one-electron oxidation of **54** with $NOSbF_6$ (Scheme 12.20) [135].

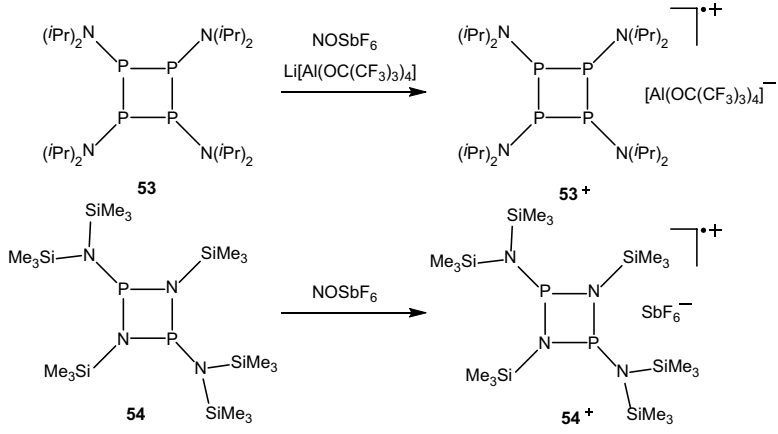


**Scheme 12.20** Synthesis of four-membered ring radical cations $\mathbf{53}^{\bullet+}$ and $\mathbf{54}^{\bullet+}$.

The solution EPR spectrum of $\mathbf{53}^{\bullet+}$ displays a 13-line signal, which is attributed to the coupling to four phosphorus atoms ($a(^{31}P)$ = 5.11 G) and four nitrogen atoms ($a(^{14}N)$ = 4.94 G) (Figure 12.5). The quite small $^{31}P$ HFC constant in comparison to those observed in phosphinyl (63–108 G) [130, 136–138], phosphonyl (300–700 G) [136], and phosphoniumyl radicals (176–800 G) [115, 117, 120, 136, 139] suggests a small amount of spin density at the phosphorus atoms. In contrast, the solution EPR spectrum of $\mathbf{54}^{\bullet+}$ exhibits two almost overlapping doublets ($a(^{31}P)$ = 263 and 244 G), owing to the coupling to two nonequivalent phosphorus nuclei. The large $^{31}P$ coupling constants indicate substantial amount of the unpaired electron localizing at the phosphorus centers, strikingly different from $\mathbf{53}^{\bullet+}$. Moreover, the signals are further split by two nitrogen

atoms of the $P_2N_2$ ring ($a(^{14}N)$ = 5.90 G). The inverse spin density distributions of **53**$^{\bullet+}$ and **54**$^{\bullet+}$ were unambiguously confirmed by theoretical calculations.

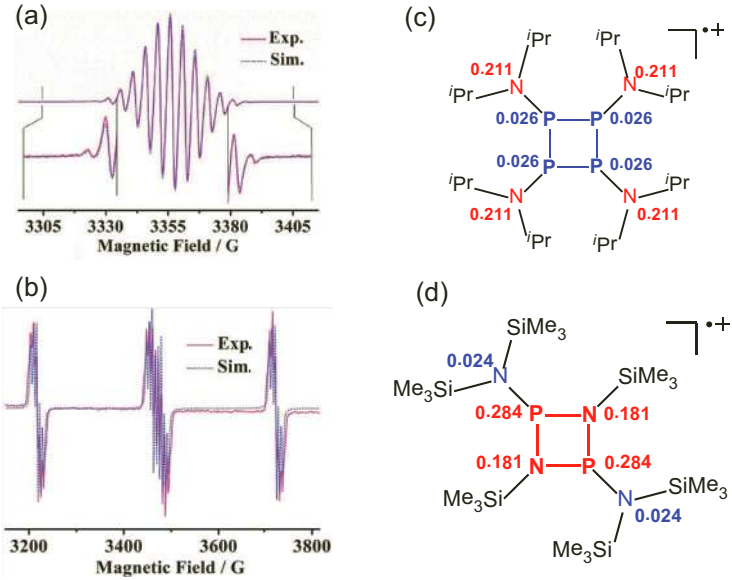


**Figure 12.5** Experimental (pink solid lines) and simulated (blue dot lines) EPR spectrum of **53**$^{\bullet+}$ (a) and **54**$^{\bullet+}$ (b) measured in $CH_2Cl_2$ solution at 243 K and 298 K, respectively. Mulliken spin density distributions of **53**$^{\bullet+}$ (c) and **54**$^{\bullet+}$ (d).

The single-crystal X-ray diffraction analysis reveals that the $P_4$ ring in **53**$^{\bullet+}$ is composed of four pyramidal phosphorus atoms, and the exocyclic amino groups are all-*trans* orientated to each other. In contrast, **54**$^{\bullet+}$ features an essentially square $P_2N_2$ core with pyramidalized phosphorus atoms. It is worth mentioning that after our report of the radical cations **53**$^{\bullet+}$ and **54**$^{\bullet+}$, several four-membered ring radical cations with the central rings comprising heavy pnictogen, nitrogen, or carbon were reported [140, 141].

Although there are several examples of heavy pnictogen-bearing ring radicals, there are no cyclic radical cations containing both heavy groups 14 and 15 elements. Recently, several 4π electron resonance-stabilized heavy congeners of cyclobutadiene bearing polarized Si=E or Ge=E (E = N, P, As) double bonds have been realized

in attempts to achieve triply bonded compounds between groups 14 and 15 elements [142–148]. We found that one-electron oxidation of the 2,4-digerma-1,3-dipnictacyclobutadienes **55** and **56** with silver salt afforded the corresponding radical cations (Scheme 12.21) [149]. EPR spectroscopy and theoretical calculations show that the unpaired electron mainly resides at the two heavy pnictogen atom centers.

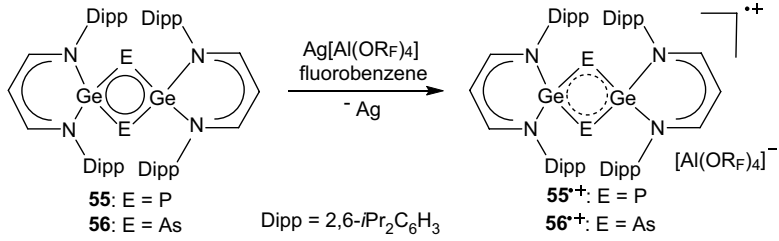


**55**: E = P
**56**: E = As

Dipp = 2,6-*i*Pr$_2$C$_6$H$_3$

**55**$^{\bullet+}$: E = P
**56**$^{\bullet+}$: E = As

**Scheme 12.21** Synthesis of radical cation salts **55**$^{\bullet+}$•[Al(OR$_F$)$_4$]$^-$ and **56**$^{\bullet+}$•[Al(OR$_F$)$_4$]$^-$.

### 12.3.2.2 Heavy pnictogen-centered radical anions

As mentioned above, phosphaalkenes can also be reduced to the radical anions. We found that the phosphaalkene **47** bearing the fluorene substituent shows a reversible one-electron oxidation peak in the cyclic voltammogram, and it is readily reduced by elemental potassium and lithium in THF and dimethoxyethane (DME), respectively, affording the purple radical anion salts [K(THF)$_3$]$^+$•**47**$^{\bullet-}$ and [Li(DME)$_3$]$^+$•**47**$^{\bullet-}$ (Scheme 12.22) [150]. In the radical [K(THF)$_3$]$^+$•**47**$^{\bullet-}$, the solvated K$^+$ cation interacts with the fluorene moiety in a $\eta^4$ mode, whereas [Li(DME)$_3$]$^+$•**47**$^{\bullet-}$ is a discrete salt without a direct cation–anion interaction. The P–C bond lengths to the fluorene moiety in the radical anions are comparable (1.757(3) Å and 1.754(2) Å), and they are longer than that of the neutral precursor (1.681(5) Å), indicating that the unpaired electron localizes at the $\pi^*$(P=C). Moreover, the spin density distribution shows that it mainly resides at the phosphorus center (0.594) with a small contribution from the adjacent carbon atom of the fluorene group (0.108).

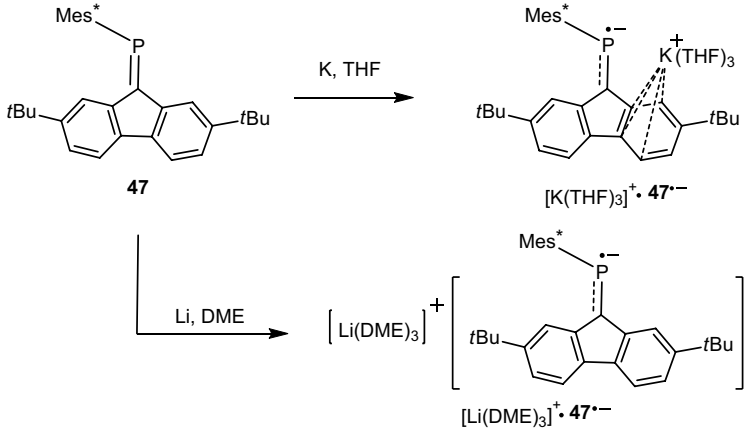


**Scheme 12.22** Synthesis of phosphaalkene radical anions.

The THF solution EPR spectrum of $[K(THF)_3]^+$•**47**$^{\bullet-}$ at 273 K displays a doublet signal arising from the coupling with one phosphorus atom ($a(^{31}P)$ = 80.4 G), which is within the range of persistent phosphorus radical anions (21.0–118.7 G) [151–160]. The frozen EPR spectrum in THF solution at 110 K afforded the $g$ factors and HFC tensors: $g_{||}$ = 2.0045, $a_{||}$ = 211 G, $g_{\perp}$ = 2.0087, $a_{\perp}$ = 10.2 G. From these data, the localization of 51.09% and 1.62% spins on the 3p and 3s orbitals of the phosphorus atom was calculated [116], consistent with the theoretical calculation results.

Inspired by the isolation of stable phosphaalkene radical anions bearing the fluorene fragment, we were interested in utilizing it as a building block to construct phosphorus- and arsenic-based diradical dianions. Therefore, we first designed and synthesized the diphosphaalkene **57** bearing an indenofluorene group, which shows two one-electron oxidation peaks. The one-electron and two-electron reductions of **57** afforded the deep-green and brown crystals of the radical anion salt $[(18\text{-c-6})K(THF)_2]^+$•**57**$^{\bullet-}$ and the diradical dianion $[(18\text{-c-6})K(THF)_2]_2^{2+}$•**57**$^{\bullet\bullet2-}$, respectively (Scheme 12.23) [161].

The P–C bond lengths to the indenofluorene moiety in **57**$^{\bullet-}$ (1.741(5) Å) are larger than those in the neutral compound **57** (av. 1.689 Å), and they further elongate in **57**$^{\bullet\bullet2-}$, consistent with the results that the unpaired electrons locate at the $\pi^*$(P=C) orbitals. Moreover, the P–C bonds are almost coplanar with the

indenofluorene group, indicating a π-conjugation of the P–C bonds with the indenofluorene fragment.

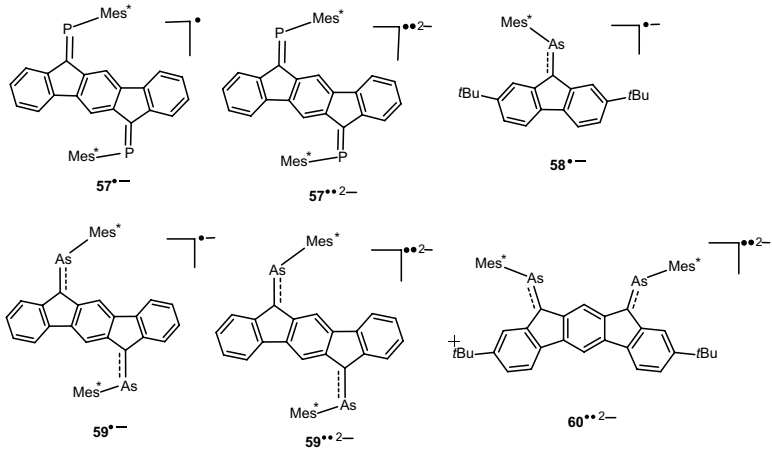


**Scheme 12.23** Phosphorus- and arsenic-centered radical anions and diradical dianions.

The solution EPR spectrum of $\mathbf{57}^{\bullet-}$ at room temperature exhibits a triplet signal, owing to the coupling to two phosphorus nuclei ($a(^{31}P)$ = 53.3 G). The coupling constant is within the range of persistent phosphorus radical anions (21.0–118.7 G) [151–160]. The EPR spectrum of the frozen THF solution at 110 K shows high-resolution anisotropic HFC, and afforded the $g$ factors and HFC tensors: $g_{||}$ = 2.0020, $a_{||}$ = 135 G, $g_{\perp}$ = 2.0086, $a_{\perp}$ = 20 G. The spin density distribution reveals that it mainly resides on the two phosphorus centers, consistent with the results from EPR spectroscopy.

The diradical dianion $\mathbf{57}^{\bullet\bullet 2-}$ is EPR silent both in solid state and in solution. The DFT calculations suggest that its ground state is open-shell singlet state, and a singlet–triplet energy gap of –6.7 kcal $mol^{-1}$ is obtained. $\mathbf{57}^{\bullet\bullet 2-}$ is the first example of phosphorus-centered diradical dianion.

The arsenic analogs of the phosphorus radical anions and diradical danion were also isolated (Scheme 12.23) [162]. In addition, the diradical dianion $\mathbf{60}^{\bullet\bullet 2-}$ with the As=C moieties at the *meta* position was obtained. The major difference of the phosphorus diradical $\mathbf{57}^{\bullet\bullet 2-}$ and the arsenic diradicals $\mathbf{59}^{\bullet\bullet 2-}$ and $\mathbf{60}^{\bullet\bullet 2-}$ is that

the arsenic diradicals have much smaller singlet–triplet energy gaps, and the triplet states are thermally accessible at room temperature.

## 12.4 Group 16 Element-Based Radicals

Thiophene-containing molecules, oligomers and polymers have been widely investigated as functional materials [163]. For instance, polythiophenes become electrically conductive upon partial oxidation. In order to understand the structure-property relationships, we synthesized three thiophene-bearing radical cations **61**$^{\bullet+}$–**63**$^{\bullet+}$ with different chain lengths (Scheme 12.24) [164]. They were prepared by one-electron oxidation with $Ag[Al(OC(CF_3)_3)_4]$. In the crystal structure of **62**$^{\bullet+}$, the cations are infinitely stacked along the *c*-axis with channels occupied by $[Al(OC(CF_3)_3)_4]^-$ anions. One stack is neighboring to four others by π–π interactions, forming an achiral chain with helical conformers of opposite chirality alternating around the inversion center. Moreover, the studies show that the conductivity is gradually enhanced as the increase in number of thiophene groups in the molecules.

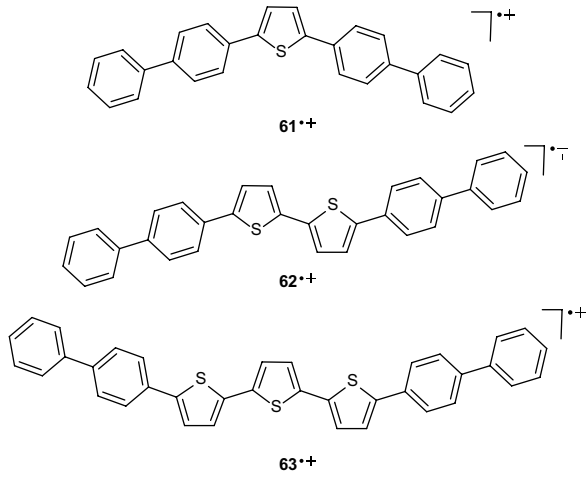


**Scheme 12.24** Thiophene-bearing radical cations.

Dithienylethenes are a well-studied class of molecular photochromic and electrochromic switches, due to the equilibrium between the ring-open isomers and ring-closing isomers [165,

166]. DFT calculations have shown that in the switching processes the dithienylethene dications are evolved [167]. Two-electron oxidation of the dithienylethene **64o** in the ring-open state afforded the dication $\mathbf{64c}^{2+}$ in the ring-closing form as violet crystals (Scheme 12.25) [168]. The UV-vis absorption spectroscopy at variable temperatures suggests that there is a reversible process between $\mathbf{64c}^{2+}$ and $\mathbf{64o}^{2+}$. Cooling the solution favors the formation of $\mathbf{64c}^{2+}$. The equilibrium was also confirmed by NMR spectroscopy, and the reduction reactions at different temperatures with zinc dust, which mainly afforded the ring-open isomer **64o** at 313 K and the ring-closing isomer **64c** at 193 K.

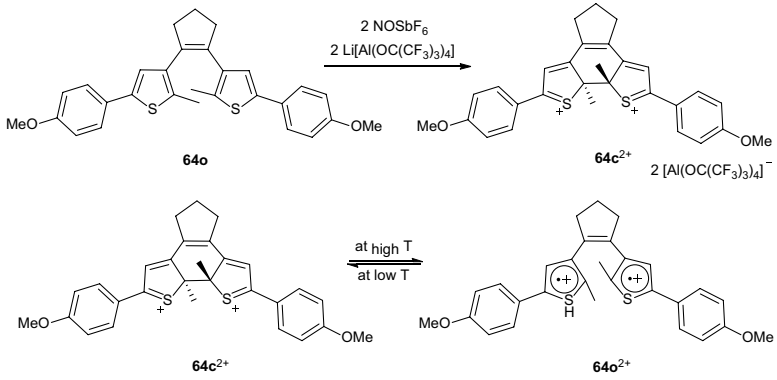


**Scheme 12.25** Two-electron oxidation of dithienylethene **64o** affording $\mathbf{64c}^{2+}$ and the reversible process between $\mathbf{64o}^{2+}$ and $\mathbf{64c}^{2+}$.

Tetrathiafulvalene (TTF) and its derivatives, sulfur-rich organic molecules, have been widely applied as organic conductors and molecular optoelectronic materials, owing to their unique donor properties. When treated with organic or inorganic acceptors, these redox-active molecules are inclined to form charge transfer compounds, in which some species possess unpaired electrons [169–171]. However, two-electron oxidation of TTF derivatives and their stable dications in the solid state are rarely investigated. We found that the tetrakis(methylthio)-tetrathiafulvalene (**65**) could be one-electron and two-electron oxidized to the stable radical cation $\mathbf{65}^{\bullet+}$ and dication $\mathbf{65}^{2+}$. The salt of the radical cation $\mathbf{65}^{\bullet+}$ was synthesized by the reaction of **65** and $Ag[Al(O(C(CF_3)_3)_4]$, whereas $\mathbf{65}^{2+}\bullet[Al(O(C(CF_3)_3)_4]$ was obtained by the reaction **65**

with two-molar equivalent of a stronger oxidant ($NOSbF_6$ and $Li[Al(O(C(CF_3)_3)_4])$ (Scheme 12.26) [172]. As elucidated by the crystal structure, the extended structure of $\mathbf{65}^{\bullet+}$ constructed by the head-to-tail stacking of two $\mathbf{65}^{\bullet+}$ cations forms the π-dimer with short [S···S] contacts. In contrast, no intermolecular π-π and [S···S] interactions were observed in $\mathbf{65}^{2+}$.

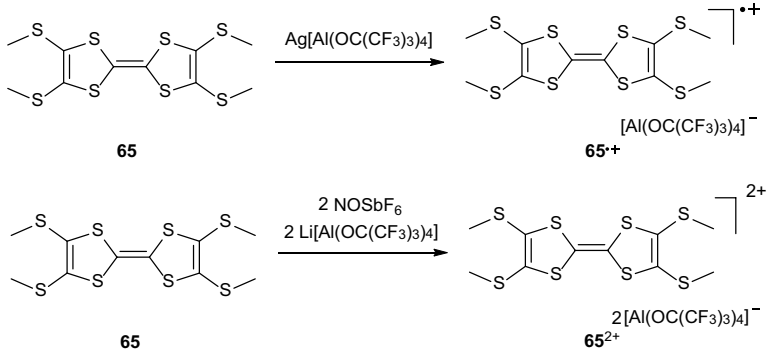


**Scheme 12.26** Synthesis of $\mathbf{65}^{\bullet+}$ and $\mathbf{65}^{2+}$.

Three-electron σ-bonds, firstly described by Pauling in the 1930s, have attracted significant attention in the experimental and theoretical perspectives [173]. Although several three-electron σ-bonding systems X∴X and X∴Y (X, Y = He, N, S, P, halogen and so on) have been studied in the gas phase, solution, and solid matrix, few of them are stable at room temperature because of their high reactive and dimerization in the solid state [174–182]. Gerson et al. [183] and Alder et al. [184] reported the N∴N three-electron σ-bonds constrained in cyclic frameworks. Drews and Seppelt isolated and structurally characterized the $Xe_2^+$ ion bearing a Xe∴Xe three-electron σ-bond in 1997 [185].

One-electron oxidations of **66** and **67** afforded the isolable radical cations $\mathbf{66}^{\bullet+}$ and $\mathbf{67}^{\bullet+}$ as crystalline solids bearing S∴S and Se∴Se three-electron σ-bonds, respectively (Scheme 12.27) [186, 187]. The two phenyl groups in $\mathbf{66}^{\bullet+}$ and $\mathbf{67}^{\bullet+}$ overlap in a face-to-face offset arrangement with centroid-centroid distance (3.592(1) Å and 3.651(1) Å, respectively) within the range for typical π-π stacking (3.3–3.8 Å). The E···E distances are shorter than those in the corresponding neutral precursors. DFT calculations indicate that both E atoms are main contributors to the SOMO, and occupy

considerable spin density, suggesting the formation of a hemi bond between the E atoms. Moreover, the calculated bond order for E–E bond further supports the hemi bond character.

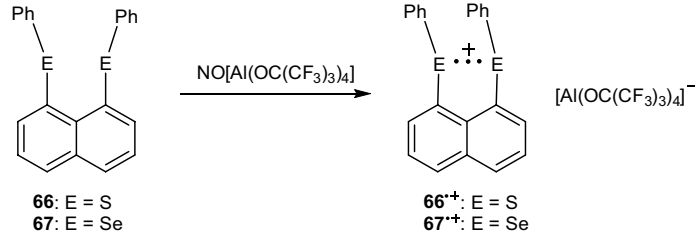


**Scheme 12.27** Synthesis of S∴S and Se∴Se three-electron σ-bond bearing radical cation salts.

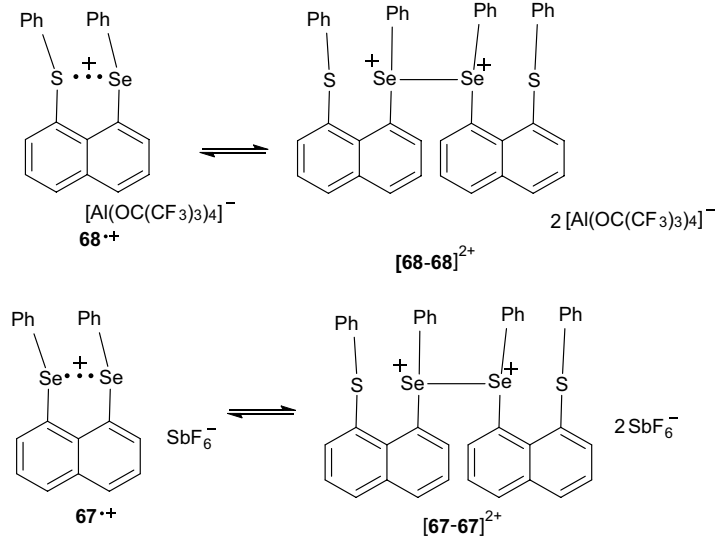


**Scheme 12.28** Reversible dimerization by the formation and dissociation of a Se–Se bond.

Interestingly, the radical **68**$^{\bullet+}$•$[Al(O(C(CF_3)_3)_4]^-$ containing a S∴Se three-electron σ-bond crystallizes out as a dimer **[68-68]**$^{2+}$•2$[Al(O(C(CF_3)_3)_4]$ through the formation of an intermolecular Se–Se bond, but becomes back to monomer upon redissolving in $CH_2Cl_2$ solution (Scheme 12.28) [186]. The radical **67**$^{\bullet+}$•$[SbF_6]^-$ bearing a smaller counterion also has an equilibrium

between the monomer and dimer through the formation and dissociation of an intermolecular Se–Se bond in solution and solid state, respectively [187].

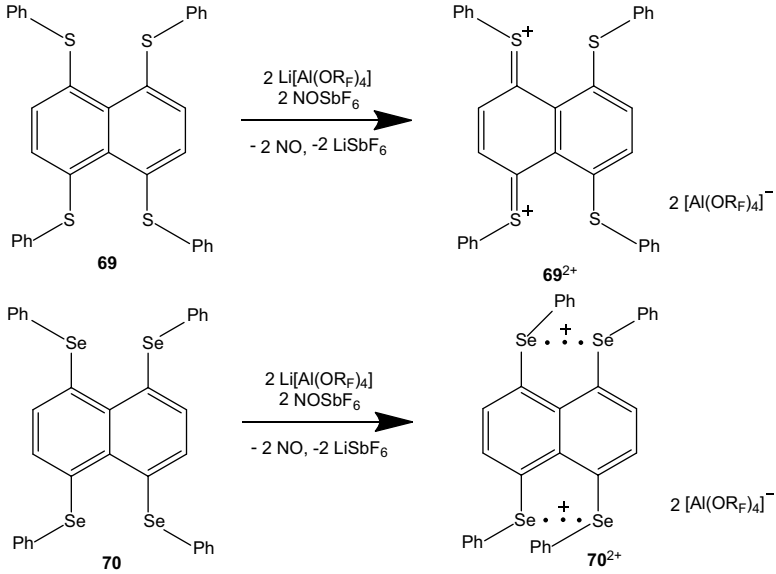


**Scheme 12.29** Two-electron oxidation of **69** and **70** to their dications.

Inspired by the isolation of the stable three-electron radical cations, we targeted the synthesis of diradical dications based on three-electron σ-bonds. For this purpose, we synthesized tetrachalcogenides **69** and **70**, which showed two reversible one-electron oxidation peaks in the cyclic voltammetry measurements. When they were treated with two-molar equivalent of Li[Ar(ORF)] and $NOSbF_6$ in $CH_2Cl_2$, the dications $\mathbf{69}^{2+}$ and $\mathbf{70}^{2+}$ were isolated, respectively (Scheme 12.29) [188]. In $\mathbf{69}^{2+}$, the two S–$C_{Ph}$ bonds at the same side of the naphthalene moiety are nearly linear and all four S–$C_{Ph}$ bonds are coplanar to the naphthyl plane, whereas the corresponding Se–$C_{Ph}$ bonds are parallel and are nearly perpendicular to the naphthyl group in $\mathbf{70}^{2+}$. The average Se–$C_{nap}$ bond distance is slightly shorter than that in the neutral compound, while the mean S–$C_{nap}$ bond distance is notably shorter in comparison to that in the neutral precursor. Moreover, the naphthalene skeleton of $\mathbf{69}^{2+}$ becomes quinoidal, but this is not the case in $\mathbf{70}^{2+}$, suggesting

significantly different electronic structure between them. Indeed, the EPR analysis shows that $\mathbf{69}^{2+}$ is EPR silent, while typical triplet state signals are observed for $\mathbf{70}^{2+}$, indicating $\mathbf{69}^{2+}$ is a diamagnetic dication and $\mathbf{70}^{2+}$ is diradical dication. This is also confirmed by SQUID measurements and theoretical calculations, which reveal that $\mathbf{70}^{2+}$ is the first example of open-shell singlet diradicals based on odd-electron σ-bonds (Figure 12.6).

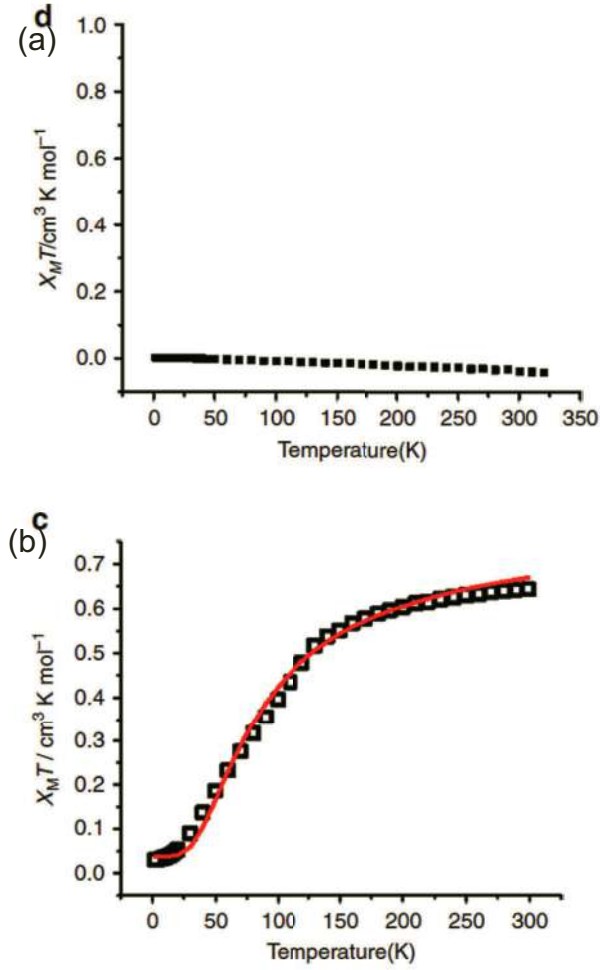


**Figure 12.6** The $\chi_m T$ vs $T$ plot for the crystals of the dication salts of $\mathbf{69}^{2+}$ (a) and $\mathbf{70}^{2+}$ (b).

Although the C/N/O-based high-spin diradicals have been widely studied, sulfur-containing triplet diradicals are much less reported and restricted to species containing sulfur and nitrogen comprised rings, in which the electronegative nitrogen atoms play a crucial role in stabilization of the diradicals [189–193]. In order to access sulfur-based triplet diradicals without nitrogen atoms, we designed tetrathiolated di-*tert*-butylpyrene compound **71**, which shows two reversible oxidation peaks at 1.26 V and 1.42 V vs Ag/AgCl. Successive oxidation of **71** with $[NO][Al(OR_F)_4]$ afforded the monoradical cation $\mathbf{71}^{\bullet+}$ and diradical dication $\mathbf{71}^{\bullet\bullet 2+}$ (Scheme 12.30) [194].

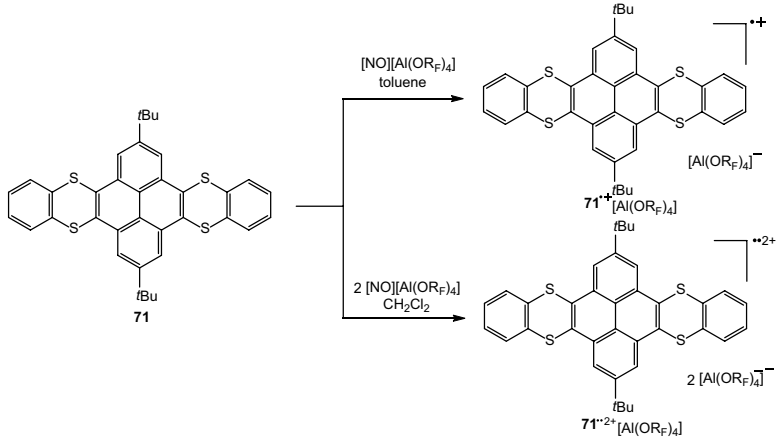


**Scheme 12.30** Oxidation of **71** to its radical cation and diradical dication salts.

The sulfur-doped rings in **71** are bent away to the central pyrene moiety in a *trans* fashion. Upon removal of one-electron, one of the sulfur-doped rings becomes nearly planar to the central pyrene group, while the whole dication becomes almost planar. This indicates that the oxidation happens at the sulfur-doped rings. Consequently, the C–S bond lengths of the planarized ring decrease in the oxidized products in comparison to the precursor **71**.

EPR spectroscopic studies of $\mathbf{71}^{\bullet+}$ show that the coupling of the unpaired electron with two sulfur and eight hydrogen atoms. The smaller isotropic coupling constant to the sulfur atoms ($a(^{33}S)$ = 3.25 G) than that of the thianthrene radical cation ($a(^{33}S)$ = 9.15 G) suggests the unpaired electron is partially delocalized in the molecule [195]. Due to the intermolecular interaction, a half-field

signal was also observed for the power sample of the radical cation salt. Moreover, the antiferromagnetic intermolecular interaction with a singlet–triplet energy gap of −373 K (−741 cal $mol^{-1}$) was determined by variable temperature EPR spectroscopy.

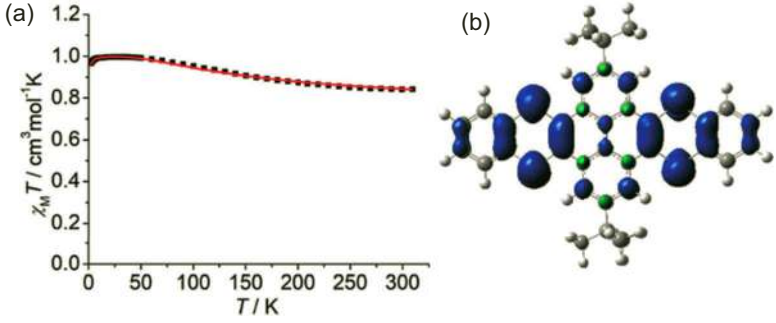


**Figure 12.7** $\chi_M T$ vs $T$ curve for the powder of **71**$^{\bullet\bullet 2+}$ in the SQUID measurement and the fit using the Bleaney–Bowers equation. (b) Spin density distribution of **71**$^{\bullet\bullet 2+}$ calculated at the (U)WB97XD/6-31G(d) level (isovalue = 0.002).

The EPR spectra of the dication salt of **71**$^{\bullet\bullet 2+}$ show a clear half-field signal at room temperature and 87 K, indicating the strong intramolecular interaction between the two unpaired electrons. The SQUID measurements on a powder sample of the diradical dication reveal that it has a triplet ground state with the singlet–triplet energy gap $2J$ = 174 K (346 cal $mol^{-1}$) (Figure 12.7a). Theoretical calculations also confirm its triplet ground, and show that the spin density mainly delocalizes over the two sulfur-doped rings (Figure 12.7b). **71**$^{\bullet\bullet 2+}$ is the first example of a pure sulfur-hydrocarbon (i.e., no nitrogen incorporated) diradical featuring a triplet ground state.

## 12.5 Conclusion

We have summarized our recent work on stable radical ions of *p*-block elements. We found that the WCAs are quite versatile in stabilizing and crystallizing the radical cations. In order to stabilize the radical ions, sterically demanding and conjugated ligands are needed to prevent unwanted side reactions. With these radicals in hand, we have studied their properties in detail, and the phenomena of magnetic bistability caused by intramolecular electron–exchange

interaction and thermally controlling the singlet–triplet energy gap were observed for the diradical dications. Moreover, we have also used the boron- and phosphorus-centered radical anions to synthesize *d*- and *f*-block metal complexes, some of which exhibit single-molecule magnetic properties [196–198]. These results highlight the potential of main-group element-based radicals in constructing functional materials.

## Acknowledgment

We thank the National Key R&D Program of China (Grants 2016YFA0300404 and 2018YFA0306004, X.W.), the National Natural Science Foundation of China (Grants 21525102 and 21690062, X.W., 21601082, G.T.).

## References

1. Gomberg, M. (1900). An instance of trivalent carbon: Triphenylmethyl, *J. Am. Chem. Soc.*, **22**, pp. 757–771.
2. Benelli, C. and Gatteschi, D. (2002). Magnestism of lanthnides in molecular materials with transition-metal ions and organic radicals, *Chem. Rev.*, **102**, pp. 2369–2387.
3. Abe, M. (2013). Diradicals, *Chem. Rev.*, **113**, pp. 7011–7088.
4. Himo, F. and Siegbahn, P. E. M. (2003). Quantum chemical studies of radical-containing enzymes, *Chem. Rev.*, **103**, pp. 2421–2456.
5. Power, P. P. (2003). Persistent and stable radicals of the heavier main group elements and related species, *Chem. Rev.*, **103**, pp. 789–809.
6. Rajca, A. (1994). Organic diradicals and polyradicals: From spin coupling to magnetism?, *Chem. Rev.*, **94**, pp. 871–893.
7. Abe, M., Ye, J., and Mishima, M. (2012). The chemistry of localized singlet 1,3-diradicals (biradicals): From putative intermediates to persistent species and unusual molecules with a π-single bonded character, *Chem. Soc. Rev.*, **41**, pp. 3808–3820.
8. Chandra Mondal, K., Roy, S., and Roesky, H. W. (2016). Silicon based radicals, radical ions, diradicals and diradicaloids, *Chem. Soc. Rev.*, **45**, pp. 1080–1111.
9. Ratera, I. and Veciana, J. (2012). Playing with organic radicals as building blocks for functional molecular materials, *Chem. Soc. Rev.*, **41**, pp. 303–349.

10. Zeng, Z., Shi, X., Chi, C., Lopez Navarrete, J. T., Casado, J., and Wu, J. (2015). Pro-aromatic and anti-aromatic π-conjugated molecules: An irresistible wish to be diradicals, *Chem. Soc. Rev.*, **44**, pp. 6578–6596.
11. Breher, F. (2007). Stretching bonds in main group element compounds—Borderlines between biradicals and closed-shell species, *Coord. Chem. Rev.*, **251**, pp. 1007–1043.
12. Demir, S., Jeon, I.-R., Long, J. R., and Harris, T. D. (2015). Radical ligand-containing single-molecule magnets, *Coord. Chem. Rev.*, **289–290**, pp. 149–176.
13. Zhou, W., Zhang, Y., Cao, G., Liu, H., and Yu, D. (2017). Palladium-catalyzed radical-type transformations of alkyl halides, *Chin. J. Org. Chem.*, **37**, pp. 1322–1337.
14. Yuan, S., Wang, Y., Qiu, G., and Liu, J. (2017). Recent advances in radical initiated C–N bond formation under transition metal-free conditions, *Chin. J. Org. Chem.*, **37**, pp. 566–576.
15. Song, H., Liu, X., and Qin Y. (2017). Advances on nitrogen-centered radical chemistry: A photocatalytic N–H bond activation approach., *Acta Chim. Sinica*, **75**, pp. 1137–1149.
16. Sun, X., Wang, W., Ma, J., and Yu, S. (2017). Halogen-bond-promoted radical isocyanide insertion of o-diisocyanoarenes with perfluoroalkyl bromides under visible light irradiation, *Acta Chim. Sinica*, **75**, pp. 115.
17. Zhang, J. R., Xu, L., Liao, Y. Y., Deng, J. C., and Tang, R. Y. (2017). Advances in radical oxidative C—H alkylation of n-heteroarenes, *Chin. J. Chem.*, **35**, pp. 271–279.
18. Mao, L., Li, Y., and Yang, S. (2017). Silver-catalyzed cascade radical cyclization for stereoselective synthesis of exocyclic phosphine oxides, *Chin. J. Chem.*, **35**, pp. 316–322.
19. Engesser, T. A., Lichtenthaler, M. R., Schleep, M., and Krossing, I. (2016). Reactive p-block cations stabilized by weakly coordinating anions, *Chem. Soc. Rev.*, **45**, pp. 789–899.
20. Krossing, I. and Raabe, I. (2004). Noncoordinating anions—Fact or fiction? A survey of likely candidates, *Angew. Chem., Int. Ed.*, **43**, pp. 2066–2090.
21. Kaim, W., Hosmane, N. S., Záliš, S., Maguire, J. A., and Lipscomb, W. N. (2009). Boron atoms as spin carriers in two- and three-dimensional systems, *Angew. Chem., Int. Ed.*, **48**, pp. 5082–5091.
22. Ji, L., Griesbeck, S., and Marder, T. B. (2017). Recent developments in and perspectives on three-coordinate boron materials: A bright future, *Chem. Sci.*, **8**, pp. 846–863.

23. Kaim, W. and Schulz, A. (1984). p-Phenylenediboranes: Mirror images of p-phenylenediamines?, *Angew. Chem., Int. Ed.*, **23**, pp. 615–616.
24. Fiedler, J., Zališ, S., Klein, A., Hornung, F. M., and Kaim, W. (1996). Electronic structure of π-conjugated redox systems with borane/borataalkene end groups, *Inorg. Chem.*, **35**, pp. 3039–3043.
25. Olmstead, M. M. and Power, P. P. (1986). First structural characterization of a boron-centered radical: X-ray crystal structure of $[Li(12\text{-crown-}4)_2]^+[BMes_3]^{-\bullet}$, *J. Am. Chem. Soc.*, **108**, pp. 4235–4236.
26. Braunschweig, H., Dyakonov, V., Jimenez-Halla, J. O. C., Kraft, K., Krummenacher, I., Radacki, K., Sperlich, A., and Wahler, J. (2012). An isolable radical anion based on the borole framework, *Angew. Chem., Int. Ed.*, **51**, pp. 2977–2980.
27. Kushida, T. and Yamaguchi, S. (2013). A radical anion of structurally constrained triphenylborane, *Organometallics*, **32**, pp. 6654–6657.
28. Bissinger, P., Braunschweig, H., Damme, A., Hörl, C., Krummenacher, I., and Kupfer, T. (2015). Boron as a powerful reductant: Synthesis of a stable boron-centered radical-anion radical-cation pair, *Angew. Chem., Int. Ed.*, **54**, pp. 359–362.
29. Zheng, Y., Xiong, J., Sun, Y., Pan, X., and Wu, J. (2015). Stepwise reduction of 9,10-bis(dimesitylboryl)anthracene, *Angew. Chem., Int. Ed.*, **54**, pp. 12933–12936.
30. Ji, L., Edkins, R. M., Lorbach, A., Krummenacher, I., Brückner, C., Eichhorn, A., Braunschweig, H., Engels, B., Low, P. J., and Marder, T. B. (2015). Electron delocalization in reduced forms of 2-($BMes_2$)pyrene and 2,7-bis($BMes_2$)pyrene, *J. Am. Chem. Soc.*, **137**, pp. 6750–6753.
31. Braunschweig, H., Dyakonov, V., Engels, B., Falk, Z., Hörl, C., Klein, J. H., Kramer, T., Kraus, H., Krummenacher, I., Lambert, C., and Walter, C. (2013). Multiple reduction of 2,5-bis(borolyl)thiophene: Isolation of a negative bipolaron by comproportionation, *Angew. Chem., Int. Ed.*, **52**, pp. 12852–12855.
32. Scheschkewitz, D., Amii, H., Gornitzka, H., Schoeller, W. W., Bourissou, D., and Bertrand, G. (2002). Singlet diradicals: From transition states to crystalline compounds, *Science*, **295**, pp. 1880–1881.
33. Yuan, N., Wang, W., Wu, Z., Chen, S., Tan, G., Sui, Y., Wang, X., Jiang, J., and Power, P. P. (2016). A boron-centered radical: A potassium-crown ether stabilized boryl radical anion, *Chem. Commun.*, **52**, pp. 12714–12716.
34. Chiu, C.-W. and Gabbaï, F. P. (2007). A 9-borylated acridinyl radical, *Angew. Chem., Int. Ed.*, **46**, pp. 1723–1725.

35. Bissinger, P., Braunschweig, H., Damme, A., Krummenacher, I., Phukan, A. K., Radacki, K., and Sugawara, S. (2014). Isolation of a neutral boron-containing radical stabilized by a cyclic (alkyl)(amino)carbene, *Angew. Chem., Int. Ed.*, **53**, pp. 7360–7363.

36. Aramaki, Y., Omiya, H., Yamashita, M., Nakabayashi, K., Ohkoshi, S.-i., and Nozaki, K. (2012). Synthesis and characterization of B-heterocyclic π-radical and its reactivity as a boryl radical, *J. Am. Chem. Soc.*, **134**, pp. 19989–19992.

37. Feng, R., Yang, W., Wang, W., Zhao, Y., Tan, G., Zhang, L., and Wang, X. (2019). Isolable diboryl radicals acting as highly efficient reaction intermediates under mild conditions, *Chem. Commun.*, **55**, pp. 12908–12911.

38. Hioe, J., Karton, A., Martin, J. M. L., and Zipse, H. (2010). Borane–Lewis base complexes as homolytic hydrogen atom donors, *Chem. Eur. J.*, **16**, pp. 6861–6865.

39. Lalevée, J., Blanchard, N., Tehfe, M. A., Chany, A. C., and Fouassier, J. P. (2010). New boryl radicals derived from N-heteroaryl boranes: Generation and reactivity, *Chem. Eur. J.*, **16**, pp. 12920–12927.

40. Wang, G., Zhang, H., Zhao, J., Li, W., Cao, J., Zhu, C., and Li, S. (2016). Homolytic cleavage of a B–B bond by the cooperative catalysis of two lewis bases: Computational design and experimental verification, *Angew. Chem., Int. Ed.*, **55**, pp. 5985–5989.

41. Wang, G., Cao, J., Gao, L., Chen, W., Huang, W., Cheng, X., and Li, S. (2017). Metal-free synthesis of C-4 substituted pyridine derivatives using pyridine-boryl radicals via a radical addition/coupling mechanism: A combined computational and experimental study, *J. Am. Chem. Soc.*, **139**, pp. 3904–3910.

42. Gao, L., Wang, G., Cao, J., Yuan, D., Xu, C., Guo, X., and Li, S. (2018). Organocatalytic decarboxylative alkylation of N-hydroxy-phthalimide esters enabled by pyridine-boryl radicals, *Chem. Commun.*, **54**, pp. 11534–11537.

43. Cao, J., Wang, G., Gao, L., Cheng, X., and Li, S. (2018). Organocatalytic reductive coupling of aldehydes with 1,1-diarylethylenes using an in situ generated pyridine-boryl radical, *Chem. Sci.*, **9**, pp. 3664–3671.

44. Cao, J., Wang, G., Gao, L., Chen, H., Liu, X., Cheng, X., and Li, S. (2019). Perfluoroalkylative pyridylation of alkenes via 4-cyanopyridine-boryl radicals, *Chem. Sci.*, **10**, pp. 2767–2772.

45. Yuan, N., Wang, W., Fang, Y., Zuo, J., Zhao, Y., Tan, G., and Wang, X. (2017). Bis(boryl anion)-substituted pyrenes: Syntheses, characterizations, and crystal structures, *Organometallics*, **36**, pp. 2498–2501.

46. Wang, L., Fang, Y., Mao, H., Qu, Y., Zuo, J., Zhang, Z., Tan, G., and Wang, X. (2017). An isolable diboron-centered diradical with a triplet ground state, *Chem. Eur. J.*, **23**, pp. 6930–6936.
47. Feng, R., Zhang, L., Chen, C., Fang, Y., Zhao, Y., Tan, G., and Wang, X. (2019). Reversible self-assembling of boryl radical anions to their diradicals with tunable singlet ground states, *Chem. Eur. J.*, **25**, pp. 4031–4035.
48. Feng, R., Zhang, L., Ruan, H., Zhao, Y., Tan, G., and Wang, X. (2019). A main-group element radical based one-dimensional magnetic chain, *Angew. Chem., Int. Ed.*, **58**, pp. 6084–6088.
49. Rodriguez, A., Tham, F. S., Schoeller, W. W., and Bertrand, G. (2004). Catenation of two singlet diradicals: Synthesis of a stable tetraradical (tetraradicaloid), *Angew. Chem., Int. Ed.*, **43**, pp. 4876–4880.
50. Wang, L., Li, J., Zhang, L., Fang, Y., Chen, C., Zhao, Y., Song, Y., Deng, L., Tan, G., Wang, X., and Power, P. P. (2017). Isolable borane-based diradical and triradical fused by a diamagnetic transition metal ion, *J. Am. Chem. Soc.*, **139**, pp. 17723–17726.
51. Wiberg, N., Blank, T., Amelunxen, K., Nöth, H., Knizek, J., Habereder, T., Kaim, W., and Wanner, M. (2001). On the gallanyls $R^*_3Ga_2^{\cdot}$ and $R^*_4Ga_3^{\cdot}$ as well as gallanides $R^*_3Ga_2^{-}$ and $R^*_4Ga_3^{-}$ ($R^*$ = $SitBu_3$)– syntheses, characterization, structures, *Eur. J. Inorg. Chem.*, **2001**, pp. 1719–1727.
52. Wiberg, N., Blank, T., Kaim, W., Schwederski, B., and Linti, G. (2000). Tri(supersilyl)dialanyl $(tBu_3Si)_3Al_2^{\bullet}$ and tetra(supersilyl) cyclotrialanyl $(tBu_3Si)_4Al_3^{\bullet}$- new stable radicals of a group 13 element from thermolysis of $(tBu_3Si)_4Al_2$, *Eur. J. Inorg. Chem.*, **2000**, pp. 1475–1481.
53. He, X., Bartlett, R. A., Olmstead, M. M., Ruhlandt-Senge, K., Sturgeon, B. E., and Power, P. P. (1993). Reduction of a tetraaryldigallane to afford a radical anion with Ga-Ga multiple bonding character, *Angew. Chem., Int. Ed.*, **32**, pp. 717–719.
54. Uhl, W., Vester, A., Kaim, W., and Poppe, J. (1993). Dialan-radikalanionen $[R_2Al\text{-}AlR_2]^{\bullet-}$, *J. Organomet. Chem.*, **454**, pp. 9–13.
55. Pluta, C., Pörschke, K.-R., Krüger, C., and Hildenbrand, K. (1993). An Al-Al one-electron π bond, *Angew. Chem., Int. Ed.*, **32**, pp. 388–390.
56. Wehmschulte, R. J., Ruhlandt-Senge, K., Olmstead, M. M., Hope, H., Sturgeon, B. E., and Power, P. P. (1993). Reduction of a tetraaryldialane to generate aluminum-aluminum π-bonding, *Inorg. Chem.*, **32**, pp. 2983–2984.

57. Uhl, W., Schütz, U., Kaim, W., and Waldhör, E. (1995). Das tetraalkyldigallan-radikalanion $[R_2Ga–GaR_2]^-$ [R = $CH(SiMe_3)_2$] mit langer einelektron-π-bindung, *J. Organomet. Chem.*, **501**, pp. 79–85.
58. Nakamoto, M., Yamasaki, T., and Sekiguchi, A. (2005). Stable mononuclear radical anions of heavier group 13 elements: $[(tBu_2MeSi)_3E^{\bullet-}]\cdot[K^+(2.2.2\text{-cryptand})]$ (E = Al, Ga), *J. Am. Chem. Soc.*, **127**, pp. 6954–6955.
59. Protchenko, A. V., Dange, D., Harmer, J. R., Tang, C. Y., Schwarz, A. D., Kelly, M. J., Phillips, N., Tirfoin, R., Birjkumar, K. H., Jones, C., Kaltsoyannis, N., Mountford, P., and Aldridge, S. (2014). Stable $GaX_2$, $InX_2$ and $TlX_2$ radicals, *Nat. Chem.*, **6**, pp. 315–319.
60. Henke, P., Pankewitz, T., Klopper, W., Breher, F., and Schnöckel, H. (2009). Snapshots of the Al-Al σ-bond formation starting from $\{AlR_2\}$ units: Experimental and computational observations, *Angew. Chem., Int. Ed.*, **48**, pp. 8141–8145.
61. Wuttig, M., Bhaskaran, H., and Taubner, T. (2017). Phase-change materials for non-volatile photonic applications, *Nat. Photonics*, **11**, pp. 465–476.
62. Gillan, E. G. and Barron, A. R. (1997). Chemical vapor deposition of hexagonal gallium selenide and telluride films from cubane precursors: Understanding the envelope of molecular control, *Chem. Mater.*, **9**, pp. 3037–3048.
63. Řičica, T., Milasheuskaya, Y., Růžičková, Z., Němec, P., Švanda, P., Zmrhalová, Z. O., Jambor, R., and Bouška, M. (2019). Synthesis and application of monomeric chalcogenolates of 13 group elements, *Chem. Asian J.*, **14**, pp. 4229–4235.
64. Thiele, J. and Balhorn, H. (1904). Ueber einen chinoïden kohlenwasserstoff, *Ber. Dtsch. Chem. Ges.*, **37**, pp. 1463–1470.
65. Tschitschibabin, A. E. (1907). Über einige phenylierte derivate des p, p-ditolyls, *Ber. Dtsch. Chem. Ges.*, **40**, pp. 1810–1819.
66. Müller, E. and Pfanz, H. (1941). Über biradikaloide terphenylderivate, *Ber. Dtsch. Chem. Ges.*, **74**, pp. 1051–1074.
67. Zheng, S., Barlow, S., Risko, C., Kinnibrugh, T. L., Khrustalev, V. N., Jones, S. C., Antipin, M. Y., Tucker, N. M., Timofeeva, T. V., Coropceanu, V., Brédas, J.-L., and Marder, S. R. (2006). Isolation and crystal structures of two singlet bis(triarylamine) dications with nonquinoidal geometries, *J. Am. Chem. Soc.*, **128**, pp. 1812–1817.

68. Ito, A., Urabe, M., and Tanaka, K. (2003). A spiro-fused triarylaminium radical cation with a triplet ground state, *Angew. Chem., Int. Ed.*, **42**, pp. 921–924.
69. Ito, A., Urabe, M., and Tanaka, K. (2009). A spiro-fused triarylaminium radical cation with a triplet ground state, *Angew. Chem., Int. Ed.*, **48**, pp. 5785–5785.
70. Lambert, C., Risko, C., Coropceanu, V., Schelter, J., Amthor, S., Gruhn, N. E., Durivage, J. C., and Brédas, J.-L. (2005). Electronic coupling in tetraanisylarylenediamine mixed-valence systems: The interplay between bridge energy and geometric factors, *J. Am. Chem. Soc.*, **127**, pp. 8508–8516.
71. Lambert, C. and Nöll, G. (1999). The class II/III transition in triarylamine redox systems, *J. Am. Chem. Soc.*, **121**, pp. 8434–8442.
72. Krossing, I. (2001). The facile preparation of weakly coordinating anions: Structure and characterisation of silverpolyfluoroalkoxyaluminates $GaI(OR_F)_4$, calculation of the alkoxide ion affinity, *Chem. Eur. J.*, **7**, pp. 490–502.
73. Wang, X., Zhang, Z., Song, Y., Su, Y., and Wang, X. (2015). Bis(phenothiazine)arene diradicaloids: Isolation, characterization and crystal structures, *Chem. Commun.*, **51**, pp. 11822–11825.
74. Su, Y., Wang, X., Li, Y., Song, Y., Sui, Y., and Wang, X. (2015). Nitrogen analogues of thiele's hydrocarbon, *Angew. Chem., Int. Ed.*, **54**, pp. 1634–1637.
75. Montgomery, L. K., Huffman, J. C., Jurczak, E. A., and Grendze, M. P. (1986). The molecular structures of Thiele's and Chichibabin's hydrocarbons, *J. Am. Chem. Soc.*, **108**, pp. 6004–6011.
76. Bleaney, B. and Bowers, K. D. (1952). Anomalous paramagnetism of copper acetate, *Proc. R. Soc. London Ser. A*, **214**, pp. 451–465.
77. Lekin, K., Phan, H., Winter, S. M., Wong, J. W. L., Leitch, A. A., Laniel, D., Yong, W., Secco, R. A., Tse, J. S., Desgreniers, S., Dube, P. A., Shatruk, M., and Oakley, R. T. (2014). Heat, pressure and light-induced interconversion of bisdithiazolyl radicals and dimers, *J. Am. Chem. Soc.*, **136**, pp. 8050–8062.
78. Alberola, A., Eisler, D. J., Harvey, L., and Rawson, J. M. (2011). Molecular tailoring of spin-transition materials: Preparation, crystal structure and magnetism of trifluoromethyl-pyridyl-1,3,2-dithiazolyl, *CrystEngComm.*, **13**, pp. 1794–1796.
79. Lekin, K., Winter, S. M., Downie, L. E., Bao, X., Tse, J. S., Desgreniers, S., Secco, R. A., Dube, P. A., and Oakley, R. T. (2010). Hysteretic spin

crossover between a bisdithiazolyl radical and its hypervalent σ-dimer, *J. Am. Chem. Soc.*, **132**, pp. 16212–16224.

80. Robertson, C. M., Leitch, A. A., Cvrkalj, K., Reed, R. W., Myles, D. J. T., Dube, P. A., and Oakley, R. T. (2008). Enhanced conductivity and magnetic ordering in isostructural heavy atom radicals, *J. Am. Chem. Soc.*, **130**, pp. 8414–8425.
81. Alberola, A., Collis, R. J., Humphrey, S. M., Less, R. J., and Rawson, J. M. (2006). Spin transitions in a dithiazolyl radical: Preparation, crystal structures, and magnetic properties of 3-cyanobenzo-1,3,2-dithiazolyl, $C_7H_3S_2N_2^{\bullet}$, *Inorg. Chem.*, **45**, pp. 1903–1905.
82. Brusso, J. L., Clements, O. P., Haddon, R. C., Itkis, M. E., Leitch, A. A., Oakley, R. T., Reed, R. W., and Richardson, J. F. (2004). Bistability and the phase transition in 1,3,2-dithiazolo[4,5-b]pyrazin-2-yl, *J. Am. Chem. Soc.*, **126**, pp. 14692–14693.
83. Brusso, J. L., Clements, O. P., Haddon, R. C., Itkis, M. E., Leitch, A. A., Oakley, R. T., Reed, R. W., and Richardson, J. F. (2004). Bistabilities in 1,3,2-dithiazolyl radicals, *J. Am. Chem. Soc.*, **126**, pp. 8256–8265.
84. Itkis, M. E., Chi, X., Cordes, A. W., and Haddon, R. C. (2002). Magneto-opto-electronic bistability in a phenalenyl-based neutral radical, *Science*, **296**, pp. 1443–1445.
85. Shultz, D. A., Fico, R. M., Boyle, P. D., and Kampf, J. W. (2001). Observation of a hysteretic phase transition in a crystalline dinitroxide biradical that leads to magnetic bistability, *J. Am. Chem. Soc.*, **123**, pp. 10403–10404.
86. McManus, G. D., Rawson, J. M., Feeder, N., van Duijn, J., McInnes, E. J. L., Novoa, J. J., Burriel, R., Palacio, F., and Oliete, P. (2001). Synthesis, crystal structures, electronic structure and magnetic behaviour of the trithiatriazapentalenyl radical, C2S3N3, *J. Mater. Chem.*, **11**, pp. 1992–2003.
87. Fujita, W. and Awaga, K. (1999). Room-temperature magnetic bistability in organic radical crystals, *Science*, **286**, pp. 261–262.
88. Barclay, T. M., Cordes, A. W., George, N. A., Haddon, R. C., Itkis, M. E., Mashuta, M. S., Oakley, R. T., Patenaude, G. W., Reed, R. W., Richardson, J. F., and Zhang, H. (1998). Redox, magnetic, and structural properties of 1,3,2-dithiazolyl radicals: A case study on the ternary heterocycle $S_3N_5C_4$, *J. Am. Chem. Soc.*, **120**, pp. 352–360.
89. Shultz, D. A., Fico, R. M., Lee, H., Kampf, J. W., Kirschbaum, K., Pinkerton, A. A., and Boyle, P. D. (2003). Mechanisms of exchange modulation in trimethylenemethane-type biradicals: The roles of conformation and spin density, *J. Am. Chem. Soc.*, **125**, pp. 15426–15432.

90. Vela, S., Mota, F., Deumal, M., Suizu, R., Shuku, Y., Mizuno, A., Awaga, K., Shiga, M., Novoa, J. J., and Ribas-Arino, J. (2014). The key role of vibrational entropy in the phase transitions of dithiazolyl-based bistable magnetic materials, *Nat. Commun.*, **5**, pp. 4411.

91. Fujita, W., Awaga, K., Matsuzaki, H., and Okamoto, H. (2002). Room-temperature magnetic bistability in organic radical crystals: Paramagnetic-diamagnetic phase transition in 1,3,5-trithia-2,4,6-triazapentalenyl, *Phys. Rev. B*, **65**, pp. 064434.

92. Zheng, X., Wang, X., Qiu, Y., Li, Y., Zhou, C., Sui, Y., Li, Y., Ma, J., and Wang, X. (2013). One-electron oxidation of an organic molecule by $B(C_6F_5)_3$: Isolation and structures of stable non-para-substituted triarylamine cation radical and bis(triarylamine) dication diradicaloid, *J. Am. Chem. Soc.*, **135**, pp. 14912–14915.

93. Su, Y., Wang, X., Zheng, X., Zhang, Z., Song, Y., Sui, Y., Li, Y., and Wang, X. (2014). Tuning ground states of bis(triarylamine) dications: From a closed-shell singlet to a diradicaloid with an excited triplet state, *Angew. Chem., Int. Ed.*, **53**, pp. 2857–2861.

94. Kurata, R., Tanaka, K., and Ito, A. (2016). Isolation and characterization of persistent radical cation and dication of 2,7-bis(dianisylamino) pyrene, *J. Org. Chem.*, **81**, pp. 137–145.

95. Su, Y., Wang, X., Wang, L., Zhang, Z., Wang, X., Song, Y., and Power, P. P. (2016). Thermally controlling the singlet-triplet energy gap of a diradical in the solid state, *Chem. Sci.*, **7**, pp. 6514–6518.

96. Li, T., Cheng, C., Yuan, N., Wang, L., Chen, C., Tan, G., and Wang, X. (2018). Nitrogen analogues of o-quinodimethane with unexpected non-kekulé diradical character, *Chin. J. Chem.*, **36**, pp. 487–490.

97. Wang, W., Wang, L., Chen, S., Yang, W., Zhang, Z., and Wang, X. (2018). Air-stable diradical dications with ferromagnetic interaction exceeding the thermal energy at room temperature: From a monomer to a dimer, *Sci. China Chem.*, **61**, pp. 300–305.

98. Wang, W., Chen, C., Shu, C., Rajca, S., Wang, X., and Rajca, A. (2018). *S* = 1 tetraazacyclophane diradical dication with robust stability: A case of low-temperature one-dimensional antiferromagnetic chain, *J. Am. Chem. Soc.*, **140**, pp. 7820–7826.

99. Li, T., Wei, H., Zhang, Z., Zhao, Y., Sui, Y., and Wang, X. (2017). One-dimensional alkylate-bridged Würster's blue-based diradical dications, *Sci. China Chem.*, **60**, pp. 602–606.

100. Bunz, U. H. F. (2009). N-heteroacenes, *Chem. Eur. J.*, **15**, pp. 6780–6789.

101. Richards, G. J., Hill, J. P., Mori, T., and Ariga, K. (2011). Putting the 'N' in acene: Pyrazinacenes and their structural relatives, *Org. Biomol. Chem.*, **9**, pp. 5005–5017.
102. Bunz, U. H. F., Engelhart, J. U., Lindner, B. D., and Schaffroth, M. (2013). Large N-heteroacenes: New tricks for very old dogs?, *Angew. Chem., Int. Ed.*, **52**, pp. 3810–3821.
103. Li, J. and Zhang, Q. (2015). Linearly fused azaacenes: Novel approaches and new applications beyond field-effect transistors (fets), *ACS Appl. Mater. Interfaces*, **7**, pp. 28049–28062.
104. Bunz, U. H. F. and Engelhart, J. U. (2016). The palladium way to N-heteroacenes, *Chem. Eur. J.*, **22**, pp. 4680–4689.
105. Bunz, U. H. F. and Freudenberg, J. (2019). N-heteroacenes and N-heteroarenes as N-nanocarbon segments, *Acc. Chem. Res.*, **52**, pp. 1575–1587.
106. Stępień, M., Gońka, E., Żyła, M., and Sprutta, N. (2017). Heterocyclic nanographenes and other polycyclic heteroaromatic compounds: Synthetic routes, properties, and applications, *Chem. Rev.*, **117**, pp. 3479–3716.
107. Liang, Z., Tang, Q., Xu, J., and Miao, Q. (2011). Soluble and stable N-heteropentacenes with high field-effect mobility, *Adv. Mater.*, **23**, pp. 1535–1539.
108. Ji, L., Haehnel, M., Krummenacher, I., Biegger, P., Geyer, F. L., Tverskoy, O., Schaffroth, M., Han, J., Dreuw, A., Marder, T. B., and Bunz, U. H. F. (2016). The radical anion and dianion of tetraazapentacene, *Angew. Chem., Int. Ed.*, **55**, pp. 10498–10501.
109. Ji, L., Friedrich, A., Krummenacher, I., Eichhorn, A., Braunschweig, H., Moos, M., Hahn, S., Geyer, F. L., Tverskoy, O., Han, J., Lambert, C., Dreuw, A., Marder, T. B., and Bunz, U. H. F. (2017). Preparation, properties, and structures of the radical anions and dianions of azapentacenes, *J. Am. Chem. Soc.*, **139**, pp. 15968–15976.
110. Reiss, H., Ji, L., Han, J., Koser, S., Tverskoy, O., Freudenberg, J., Hinkel, F., Moos, M., Friedrich, A., Krummenacher, I., Lambert, C., Braunschweig, H., Dreuw, A., Marder, T. B., and Bunz, U. H. F. (2018). Bromination improves the electron mobility of tetraazapentacene, *Angew. Chem., Int. Ed.*, **57**, pp. 9543–9547.
111. Ji, L., Hahn, S., Biegger, P., Reiss, H., Han, J., Friedrich, A., Krummenacher, I., Braunschweig, H., Moos, M., Freudenberg, J., Lambert, C., Dreuw, A., Marder, T. B., and Bunz, U. H. F. (2019). Mono- and dianion of a bis(benzobuta)tetraazapentacene derivative, *Chem. Eur. J.*, **25**, pp. 9840–9845.

112. Chen, C., Ruan, H., Feng, Z., Fang, Y., Tang, S., Zhao, Y., Tan, G., Su, Y., and Wang, X. (2020). Crystalline diradical dianions of pyrene-fused azaacenes, *Angew. Chem., Int. Ed.*, **59**, pp. 11794–11799.

113. Tolman, C. A. (1977). Steric effects of phosphorus ligands in organometallic chemistry and homogeneous catalysis, *Chem. Rev.*, **77**, pp. 313–348.

114. Baumgartner, T. and Réau, R. (2006). Organophosphorus π-conjugated materials, *Chem. Rev.*, **106**, pp. 4681–4727.

115. Pan, X., Chen, X., Li, T., Li, Y., and Wang, X. (2013). Isolation and X-ray crystal structures of triarylphosphine radical cations, *J. Am. Chem. Soc.*, **135**, pp. 3414–3417.

116. Morton, J. R. and Preston, K. F. (1978). Atomic parameters for paramagnetic resonance data, *J. Magn. Reson.*, **30**, pp. 577–582.

117. Ménard, G., Hatnean, J. A., Cowley, H. J., Lough, A. J., Rawson, J. M., and Stephan, D. W. (2013). C–H bond activation by radical ion pairs derived from $R_3P/Al(C_6F_5)_3$ frustrated lewis pairs and $N_2O$, *J. Am. Chem. Soc.*, **135**, pp. 6446–6449.

118. Li, T., Tan, G., Cheng, C., Zhao, Y., Zhang, L., and Wang, X. (2018). Syntheses, structures and theoretical calculations of stable triarylarsine radical cations, *Chem. Commun.*, **54**, pp. 1493–1496.

119. Li, T., Wei, H., Fang, Y., Wang, L., Chen, S., Zhang, Z., Zhao, Y., Tan, G., and Wang, X. (2017). Elusive antimony-centered radical cations: Isolation, characterization, crystal structures, and reactivity studies, *Angew. Chem., Int. Ed.*, **56**, pp. 632–636.

120. Pan, X., Su, Y., Chen, X., Zhao, Y., Li, Y., Zuo, J., and Wang, X. (2013). Stable tetraaryldiphosphine radical cation and dication, *J. Am. Chem. Soc.*, **135**, pp. 5561–5564.

121. Power, P. P. (1999). π-Bonding and the lone pair effect in multiple bonds between heavier main group elements, *Chem. Rev.*, **99**, pp. 3463–3504.

122. Fischer, R. C. and Power, P. P. (2010). π-bonding and the lone pair effect in multiple bonds involving heavier main group elements: Developments in the new millennium, *Chem. Rev.*, **110**, pp. 3877–3923.

123. Sasamori, T. and Tokitoh, N. (2008). Doubly bonded systems between heavier group 15 elements, *Dalton Trans.*, pp. 1395–1408.

124. Back, O., Celik, M. A., Frenking, G., Melaimi, M., Donnadieu, B., and Bertrand, G. (2010). A crystalline phosphinyl radical cation, *J. Am. Chem. Soc.*, **132**, pp. 10262–10263.

125. Sharma, M. K., Rottschäfer, D., Blomeyer, S., Neumann, B., Stammler, H.-G., van Gastel, M., Hinz, A., and Ghadwal, R. S. (2019). Diphosphene

radical cations and dications with a π-conjugated c2p2c2-framework, *Chem. Commun.*, **55**, pp. 10408–10411.

126. Sharma, M. K., Blomeyer, S., Neumann, B., Stammler, H.-G., van Gastel, M., Hinz, A., and Ghadwal, R. S. (2019). Crystalline divinyldiarsene radical cations and dications, *Angew. Chem., Int. Ed.*, **58**, pp. 17599–17603.
127. Sharma, M. K., Blomeyer, S., Neumann, B., Stammler, H.-G., Hinz, A., van Gastel, M., and Ghadwal, R. S. (2020). Isolation of singlet carbene derived 2-arsa-1,3-butadiene radical cations and dications, *Chem. Commun.*, **56**, pp. 3575–3578.
128. Sharma, M. K., Blomeyer, S., Glodde, T., Neumann, B., Stammler, H.-G., Hinz, A., van Gastel, M., and Ghadwal, R. S. (2020). Isolation of singlet carbene derived 2-phospha-1,3-butadienes and their sequential one-electron oxidation to radical cations and dications, *Chem. Sci.*, **11**, pp. 1975–1984.
129. Pan, X., Wang, X., Zhang, Z., and Wang, X. (2015). Two phosphaalkene radical cations with inverse spin density distributions, *Dalton Trans.*, **44**, pp. 15099–15102.
130. Back, O., Donnadieu, B., Parameswaran, P., Frenking, G., and Bertrand, G. (2010). Isolation of crystalline carbene-stabilized $P_2$-radical cations and $P_2$-dications, *Nat. Chem.*, **2**, pp. 369–373.
131. Abraham, M. Y., Wang, Y., Xie, Y., Gilliard, R. J., Wei, P., Vaccaro, B. J., Johnson, M. K., Schaefer, H. F., Schleyer, P. v. R., and Robinson, G. H. (2013). Oxidation of carbene-stabilized diarsenic: Diarsene dications and diarsenic radical cations, *J. Am. Chem. Soc.*, **135**, pp. 2486–2488.
132. Wang, W., Xu, C.-Q., Fang, Y., Zhao, Y., Li, J., and Wang, X. (2018). An isolable diphosphene radical cation stabilized by three-center three-electron π-bonding with chromium: End-on versus side-on coordination, *Angew. Chem., Int. Ed.*, **57**, pp. 9419–9424.
133. Schaefer, H. G., Schoeller, W. W., Niemann, J., Haug, W., Dabisch, T., and Niecke, E. (1986). On the redox properties of cyclotetraphosphines: A novel dication rearrangement, *J. Am. Chem. Soc.*, **108**, pp. 7481–7484.
134. Camp, D., Campitelli, M., Hanson, G. R., and Jenkins, I. D. (2012). Formation of an unusual four-membered nitrogen ring (tetrazetidine) radical cation, *J. Am. Chem. Soc.*, **134**, pp. 16188–16196.
135. Su, Y., Zheng, X., Wang, X., Zhang, X., Sui, Y., and Wang, X. (2014). Two stable phosphorus-containing four-membered ring radical cations with inverse spin density distributions, *J. Am. Chem. Soc.*, **136**, pp. 6251–6254.

136. Marque, S. and Tordo, P. (2005). Reactivity of phosphorus centered radicals. In *New aspects in phosphorus chemistry V*, Majoral, J.-P. (ed.), Springer Berlin Heidelberg: Berlin, Heidelberg, pp 43–76.

137. Back, O., Donnadieu, B., von Hopffgarten, M., Klein, S., Tonner, R., Frenking, G., and Bertrand, G. (2011). N-heterocyclic carbenes versus transition metals for stabilizing phosphinyl radicals, *Chem. Sci.*, **2**, pp. 858–861.

138. Ishida, S., Hirakawa, F., and Iwamoto, T. (2011). A stable dialkylphosphinyl radical, *J. Am. Chem. Soc.*, **133**, pp. 12968–12971.

139. Bullock, J. P., Bond, A. M., Boeré, R. T., Gietz, T. M., Roemmele, T. L., Seagrave, S. D., Masuda, J. D., and Parvez, M. (2013). Synthesis, characterization, and electrochemical studies of $PPh_3$–N(dipp) N (dipp = 2,6-diisopropylphenyl): Steric and electronic effects on the chemical and electrochemical oxidation of a homologous series of triarylphosphines and the reactivities of the corresponding phosphoniumyl radical cations, *J. Am. Chem. Soc.*, **135**, pp. 11205–11215.

140. Brückner, A., Hinz, A., Priebe, J. B., Schulz, A., and Villinger, A. (2015). Cyclic group 15 radical cations, *Angew. Chem., Int. Ed.*, **54**, pp. 7426–7430.

141. Li, Z., Chen, X., Andrada, D. M., Frenking, G., Benkö, Z., Li, Y., Harmer, J. R., Su, C.-Y., and Grützmacher, H. (2017). $(L)_2C_2P_2$: Dicarbondiphosphide stabilized by N-heterocyclic carbenes or cyclic diamido carbenes, *Angew. Chem., Int. Ed.*, **56**, pp. 5744–5749.

142. Sen, S. S., Khan, S., Roesky, H. W., Kratzert, D., Meindl, K., Henn, J., Stalke, D., Demers, J.-P., and Lange, A. (2011). Zwitterionic Si-C-Si-P and Si-P-Si-P four-membered rings with two-coordinate phosphorus atoms, *Angew. Chem., Int. Ed.*, **50**, pp. 2322–2325.

143. Inoue, S., Wang, W., Präsang, C., Asay, M., Irran, E., and Driess, M. (2011). An ylide-like phosphasilene and striking formation of a 4π-electron, resonance-stabilized 2,4-disila-1,3-diphosphacyclobutadiene, *J. Am. Chem. Soc.*, **133**, pp. 2868–2871.

144. Yao, S., Xiong, Y., Szilvási, T., Grützmacher, H., and Driess, M. (2016). From a phosphaketenyl-functionalized germylene to 1,3-digerma-2,4-diphosphacyclobutadiene, *Angew. Chem., Int. Ed.*, **55**, pp. 4781–4785.

145. Yao, S., Grossheim, Y., Kostenko, A., Ballestero–Martínez, E., Schutte, S., Bispinghoff, M., Grützmacher, H., and Driess, M. (2017). Facile access to NaOC≡As and its use as an arsenic source to form germylidenylarsinidene complexes, *Angew. Chem., Int. Ed.*, **56**, pp. 7465–7469.

146. Xiong, Y., Yao, S., Szilvási, T., Ballestero-Martínez, E., Grützmacher, H., and Driess, M. (2017). Unexpected photodegradation of a phosphaketenyl-substituted germyliumylidene borate complex, *Angew. Chem., Int. Ed.*, **56**, pp. 4333–4336.

147. Gau, D., Nougué, R., Saffon-Merceron, N., Baceiredo, A., De Cózar, A., Cossío, F. P., Hashizume, D., and Kato, T. (2016). Donor-stabilized 1,3-disila-2,4-diazacyclobutadiene with a nonbonded Si···Si distance compressed to a Si=Si double bond length, *Angew. Chem., Int. Ed.*, **55**, pp. 14673–14677.

148. Seitz, A. E., Eckhardt, M., Erlebach, A., Peresypkina, E. V., Sierka, M., and Scheer, M. (2016). Pnictogen–silicon analogues of benzene, *J. Am. Chem. Soc.*, **138**, pp. 10433–10436.

149. Cui, H., Xiao, D., Zhang, L., Ruan, H., Fang, Y., Zhao, Y., Tan, G., Zhao, L., Frenking, G., Driess, M., and Wang, X. (2020). Isolable cyclic radical cations of heavy main-group elements, *Chem. Commun.*, **56**, pp. 2167–2170.

150. Pan, X., Wang, X., Zhao, Y., Sui, Y., and Wang, X. (2014). A crystalline phosphaalkene radical anion, *J. Am. Chem. Soc.*, **136**, pp. 9834–9837.

151. Badri, A. A., Jouaiti, A., and Geoffroy, M. (1999). Spin delocalization in radical anions containing two phosphaalkene groups: An EPR study, *Magn. Reson. Chem.*, **37**, pp. 735–742.

152. Dutan, C., Shah, S., Smith, R. C., Choua, S., Berclaz, T., Geoffroy, M., and Protasiewicz, J. D. (2003). Sterically encumbered diphosphaalkenes and a bis(diphosphene) as potential multiredox-active molecular switches: Epr and dft investigations, *Inorg. Chem.*, **42**, pp. 6241–6251.

153. Lejeune, M., Grosshans, P., Berclaz, T., Sidorenkova, H., Besnard, C., Pattison, P., and Geoffroy, M. (2011). Role of the aromatic bridge on radical ions formation during reduction of diphosphaalkenes, *New J. Chem.*, **35**, pp. 2510–2520.

154. Sasamori, T., Mieda, E., Nagahora, N., Sato, K., Shiomi, D., Takui, T., Hosoi, Y., Furukawa, Y., Takagi, N., Nagase, S., and Tokitoh, N. (2006). One-electron reduction of kinetically stabilized dipnictenes: Synthesis of dipnictene anion radicals, *J. Am. Chem. Soc.*, **128**, pp. 12582–12588.

155. Gouverd, C., Brynda, M., Berclaz, T., and Geoffroy, M. (2006). Chromium tricarbonyl complex of phosphaalkene: Crystal structure and electrochemistry of the $Cr(CO)_3$ complex of PhC(H)PMes*, EPR and DFT studies of its radical anion, *J. Organomet. Chem.*, **691**, pp. 72–78.

156. Murakami, F., Sasaki, S., and Yoshifuji, M. (2005). Phosphaquinomethane and phosphathienoquinomethanes, and their anion radicals, *J. Am. Chem. Soc.*, **127**, pp. 8926–8927.

157. Geier, J., Harmer, J., and Grützmacher, H. (2004). "Naked" phosphanediide chains and their fragmentation into diphosphene radical anions, *Angew. Chem., Int. Ed.*, **43**, pp. 4093–4097.

158. Al Badri, A., Chentit, M., Geoffroy, M., and Jouaiti, A. (1997). EPR study of phosphafulvene radical anions, *J. Chem. Soc., Faraday Trans.*, **93**, pp. 3631–3635.

159. Alekseiko, L. N., Pen'kovskii, V. V., and Kharchenko, V. I. Structure of ionic and free-radical phosphaalkene derivatives, *Theor. Exp. Chem.*, **28**, pp. 257–261.

160. Geoffroy, M., Jouaiti, A., Terron, G., Cattani-Lorente, M., and Ellinger, Y. (1992). Phosphaalkene radical anions: Electrochemical generation, ab initio predictions, and esr study, *J. Phys. Chem.*, **96**, pp. 8241–8245.

161. Tan, G., Li, S., Chen, S., Sui, Y., Zhao, Y., and Wang, X. (2016). Isolable diphosphorus-centered radical anion and diradical dianion, *J. Am. Chem. Soc.*, **138**, pp. 6735–6738.

162. Fang, Y., Zhang, L., Cheng, C., Zhao, Y., Abe, M., Tan, G., and Wang, X. (2018). Experimental observation of thermally excited triplet states of heavier group 15 element centered diradical dianions, *Chem. Eur. J.*, **24**, pp. 3156–3160.

163. Roncali, J. (1992). Conjugated poly(thiophenes): Synthesis, functionalization, and applications, *Chem. Rev.*, **92**, pp. 711–738.

164. Chen, X., Ma, B., Chen, S., Li, Y., Huang, W., Ma, J., and Wang, X. (2013). Synthesis, crystal structure, and physical property of sterically unprotected thiophene/phenylene co-oligomer radical cations: A conductive π-π bonded supermolecular meso-helix, *Chem. Asia. J.*, **8**, pp. 238–243.

165. Irie, M., Fukaminato, T., Matsuda, K., and Kobatake, S. (2014). Photochromism of diarylethene molecules and crystals: Memories, switches, and actuators, *Chem. Rev.*, **114**, pp. 12174–12277.

166. Tian, H. and Yang, S. (2004). Recent progresses on diarylethene based photochromic switches, *Chem. Soc. Rev.*, **33**, pp. 85–97.

167. Staykov, A., Areephong, J., R. Browne, W., L. Feringa, B., and Yoshizawa, K. (2011). Electrochemical and photochemical cyclization and cycloreversion of diarylethenes and diarylethene-capped sexithiophene wires, *ACS Nano*, **5**, pp. 1165–1178.

168. Yuan, N., Zhang, Z., Wang, X., and Wang, X. (2015). Isolation and crystal structure of a dithiophene dication: Controlling covalent connection and disconnection with temperature and phase, *Chem. Commun.*, **51**, pp. 16714–16717.

169. Ferraris, J., Cowan, D. O., Walatka, V., and Perlstein, J. H. (1973). Electron transfer in a new highly conducting donor-acceptor complex, *J. Am. Chem. Soc.*, **95**, pp. 948–949.

170. Pop, F., Auban-Senzier, P., Frąckowiak, A., Ptaszyński, K., Olejniczak, I., Wallis, J. D., Canadell, E., and Avarvari, N. (2013). Chirality driven metallic versus semiconducting behavior in a complete series of radical cation salts based on dimethyl-ethylenedithio-tetrathiafulvalene (DM-EDT-TTF), *J. Am. Chem. Soc.*, **135**, pp. 17176–17186.

171. Lorcy, D., Bellec, N., Fourmigué, M., and Avarvari, N. (2009). Tetrathiafulvalene-based group XV ligands: Synthesis, coordination chemistry and radical cation salts, *Coord. Chem. Rev.*, **253**, pp. 1398–1438.

172. Gao, F., Zhu, F. F., Wang, X. Y., Xu, Y., Wang, X. P., and Zuo, J. L. (2014). Stabilizing radical cation and dication of a tetrathiafulvalene derivative by a weakly coordinating anion, *Inorg. Chem.*, **53**, pp. 5321–5327.

173. Pauling, L. (1931). The nature of the chemical bond. II. The one-electron bond and the three-electron bond, *J. Am. Chem. Soc.*, **53**, pp. 3225–3237.

174. Drewello, T., Lebrilla, C. B., Asmus, K.-D., and Schwarz, H. (1989). Dithia dications from cyclic and acyclic precursors by gas-phase oxidation (charge stripping) of 3e/2c-radical cations, *Angew. Chem., Int. Ed.*, **28**, pp. 1275–1276.

175. Maity, D. K. (2002). Structure, bonding, and spectra of cyclic dithia radical cations: A theoretical study, *J. Am. Chem. Soc.*, **124**, pp. 8321–8328.

176. Livant, P. and Illies, A. (1991). Estimate of the iodine-iodine two-center three-electron bond energy in $[CH_3\text{-}I\text{-}I\text{-}CH_3]^+$, *J. Am. Chem. Soc.*, **113**, pp. 1510–1513.

177. Braïda, B., Hazebroucq, S., and Hiberty, P. C. (2002). Methyl substituent effects in $[HN_n\therefore XH_n]$+ three-electron-bonded radical cations (X = F, O, N, Cl, S, P; n = 1–3): An ab initio theoretical study, *J. Am. Chem. Soc.*, **124**, pp. 2371–2378.

178. Ekern, S., Illies, A., McKee, M. L., and Peschke, M. (1993). A novel mechanism for reactions of thiirane with the thiirane radical cation: An experimental and ab initio study, *J. Am. Chem. Soc.*, **115**, pp. 12510–12518.

179. Deng, Y., Illies, A. J., James, M. A., McKee, M. L., and Peschke, M. (1995). A definitive investigation of the gas-phase two-center three-electron bond in $[H_2S\text{-}SH_2]^+$, $[Me_2S\text{-}SMe_2]^+$, and $[Et_2S\text{-}SEt_2]^+$: Theory and experiment, *J. Am. Chem. Soc.*, **117**, pp. 420–428.

180. de Visser, S. P., de Koning, L. J., and Nibbering, N. M. M. (1998). Chemical and thermodynamic properties of methyl chloride dimer radical cations in the gas phase, *J. Am. Chem. Soc.*, **120**, pp. 1517–1522.

181. Nichols, L. S., McKee, M. L., and Illies, A. J. (1998). An experimental and theoretical investigation of ion–molecule reactions involving methyl halide radical cations with methyl halides, *J. Am. Chem. Soc.*, **120**, pp. 1538–1544.

182. Dinnocenzo, J. P. and Banach, T. E. (1988). Quinuclidine dimer cation radical, *J. Am. Chem. Soc.*, **110**, pp. 971–973.

183. Gerson, F., Knoebel, J., Buser, U., Vogel, E., and Zehnder, M. (1986). An n-n three-electron .Sigma.-bond. Structure of the radical cation of n,n'-trimethylene-syn-1,6:8,13-diimino[14]annulene as studied by esr spectroscopy and x-ray crystallographic analysis, *J. Am. Chem. Soc.*, **108**, pp. 3781–3783.

184. Alder, R. W., Orpen, A. G., and White, J. M. (1985). Structures of the radical cation and dication from oxidation of 1,6-diazabicyclo[4.4.4] tetradecane, *J. Chem. Soc., Chem. Commun.*, pp. 949–951.

185. Drews, T. and Seppelt, K. (1997). The $Xe^{2+}$ ion—preparation and structure, *Angew. Chem., Int. Ed.*, **36**, pp. 273–274.

186. Zhang, S., Wang, X., Sui, Y. and Wang, X. (2014). Odd-electron-bonded sulfur radical cations: X-ray structural evidence of a sulfur-sulfur three-electron σ-bond, *J. Am. Chem. Soc.*, **136**, pp. 14666–14669.

187. Zhang, S., Wang, X., Su, Y., Qiu, Y., Zhang, Z., and Wang, X. (2014). Isolation and reversible dimerization of a selenium–selenium three-electron σ-bond, *Nat. Commun.*, **5**, pp. 4127.

188. Yang, W., Zhang, L., Xiao, D., Feng, R., Wang, W., Pan, S., Zhao, Y., Zhao, L., Frenking, G., and Wang, X. (2020). A diradical based on odd-electron σ-bonds, *Nat. Commun.*, **11**, pp. 3441.

189. Bryan, C. D., Cordes, A. W., Goddard, J. D., Haddon, R. C., Hicks, R. G., MacKinnon, C. D., Mawhinney, R. C., Oakley, R. T., Palstra, T. T. M., and Perel, A. S. (1996). Preparation and characterization of the disjoint diradical 4,4'-bis(1,2,3,5-dithiadiazolyl) [$S_2N_2C$–$CN_2S_2$] and its iodine charge transfer salt [$S_2N_2C$–$CN_2S_2$][I], *J. Am. Chem. Soc.*, **118**, pp. 330–338.

190. Barclay, T. M., Cordes, A. W., de Laat, R. H., Goddard, J. D., Haddon, R. C., Jeter, D. Y., Mawhinney, R. C., Oakley, R. T., Palstra, T. T. M., Patenaude, G. W., Reed, R. W., and Westwood, N. P. C. (1997). The heterocyclic diradical benzo-1,2:4,5-bis(1,3,2-dithiazolyl): Electronic, molecular and solid state structure, *J. Am. Chem. Soc.*, **119**, pp. 2633–2641.

191. Fatila, E. M., Clérac, R., Rouzières, M., Soldatov, D. V., Jennings, M., and Preuss, K. E. (2013). High-spin ribbons and antiferromagnetic ordering of a mnii-biradical-mnii complex, *J. Am. Chem. Soc.*, **135**, pp. 13298–13301.

192. Cameron, T. S., Decken, A., Grein, F., Knapp, C., Passmore, J., Rautiainen, J. M., Shuvaev, K. V., Thompson, R. C., and Wood, D. J. (2010). Preparation and characterization of $(CNSSS)_2(A)_2$ (A = $AsF_6^-$, $SbF_6^-$, $Sb_2F_{11}^-$) containing the $O_2$-like 5,5′-bis(1,2,3,4-trithiazolium) dication: The second example of a simple nonsterically hindered main-group diradical that retains its paramagnetism in the solid state, *Inorg. Chem.*, **49**, pp. 7861–7879.

193. Tahara, T., Suzuki, S., Kozaki, M., Shiomi, D., Sugisaki, K., Sato, K., Takui, T., Miyake, Y., Hosokoshi, Y., Nojiri, H., and Okada, K. (2019). Triplet diradical-cation salts consisting of the phenothiazine radical cation and a nitronyl nitroxide, *Chem. Eur. J.*, **25**, pp. 7201–7209.

194. Tang, S., Zhang, L., Ruan, H., Zhao, Y., and Wang, X. (2020). A magnetically robust triplet ground state sulfur-hydrocarbon diradical dication, *J. Am. Chem. Soc.*, **142**, pp. 7340–7344.

195. Bock, H., Rauschenbach, A., Näther, C., Kleine, M., and Havlas, Z. (1994). Thianthren-radikalkation-tetrachloroaluminat, *Chem. Ber.*, **127**, pp. 2043–2049.

196. Chen, C., Hu, Z.-B., Ruan, H., Zhao, Y., Zhang, Y.-Q., Tan, G., Song, Y., and Wang, X. (2020). Tuning the single-molecule magnetism of dysprosium complexes by a redox-noninnocent diborane ligand, *Organometallics*, **39**, pp. 4143–4148. DOI: 10.1021/acs.organomet.9b00819.

197. Chen, C., Hu, Z., Li, J., Ruan, H., Zhao, Y., Tan, G., Song, Y., and Wang, X. (2020). Isolable lanthanide metal complexes of a phosphorus-centered radical, *Inorg. Chem.*, **59**, pp. 2111–2115.

198. Tan, G., Li, J., Zhang, L., Chen, C., Zhao, Y., Wang, X., Song, Y., Zhang, Y.-Q., and Driess, M. (2017). The charge transfer approach to heavier main-group element radicals in transition metal complexes, *Angew. Chem., Int. Ed.*, **56**, pp. 12741–12745.

## Chapter 13

# Polyradicaloids and 2D/3D Global Aromaticity

**Yong Ni and Jishan Wu**
*Department of Chemistry, National University of Singapore,*
*3 Science Drive 3, 117543, Singapore*
chmwuj@nus.edu.sg

In this chapter, the synthesis and electronic properties of open-shell singlet polyradicaloids ranging from one-dimensional (1D) polymeric chains, two-dimensional (2D) macrocycles, and three-dimensional (3D) fully conjugated molecular cages to 2D covalent organic radical frameworks (CORFs) will be discussed. Particularly, the moderate anti-ferromagnetic (AFM) coupling between the spins in the macrocycles facilitates electron delocalization in a circuit, thus allowing access to 2D global aromaticity, which can abide to either Hückel's rule or Baird's rule, depending on the spin state. Furthermore, 3D global aromaticity in a fully conjugated diradicaloid cage was discovered, and a [6$N$+2] aromaticity rule was proposed for the specific $D_3$ symmetry molecular cages.

*Diradicaloids*
Edited by Jishan Wu

ISBN 978-981-4968-08-9 (Hardcover), 978-1-003-27724-8 (eBook)
www.jennystanford.com

## 13.1 Introduction

Open-shell polyradicaloids refer to π-conjugated molecules with multiple diradical character $y_i$ (defined by the occupation number of the lowest unoccupied natural orbitals LUNO + $i$ ($i$ = 0, 1, 2,...)) beyond $y_0$ [1]. Due to the polyradcial character, these molecules are expected to be even more reactive than the normal diradicaloids. In addition, it is also essential to engineer the AFM coupling between individual spins in the polyradicaloids, since interactions that are too strong or too weak would generate zero or too large radical character. A balanced intramolecular spin-spin coupling is also desirable to ensure reasonable stability and to attain optimal physical properties. In the past five years, our group has put a lot of efforts to synthesize stable polyradicaloids with desirable electronic structure. Our initial works were focused on linear polyradicaloids in which multiple (more than two) organic radicals are connected by different spacers, and our studies revealed that moderate spin-spin coupling is important for achieving multiple diradical character. This will be discussed in the first part of this chapter. We also synthesized a series of π-conjugated macrocyclic polyradicaloids and disclosed 2D global aromaticity, which can follow either Hückel's rule or Baird's rule, depending on the spin state [2]. This will be discussed in the second part of this chapter. Our very recent effort was to synthesize 3D fully conjugated diradicaloid/polyradicaloid molecular cages and to exploit possible 3D global aromaticity. This will be discussed in the third part of this chapter. Finally, some initial efforts toward 2D CORFs will be introduced at the last part of the chapter. Since the focus of this chapter will be the unique 2D/3D global aromaticity in macrocyclic polyradicaloids and π-conjugated molecular cages, we will firstly provide a brief introduction to various aromaticity rules.

Aromaticity is a virtual concept that governs the electronic properties of a wide range of π-conjugated organic molecules. Combining the distinct points of view among theoretical and experimental chemists, it has been established that a planar, monocyclic, fully conjugated π-electron system is aromatic if it fulfills three main criteria: (i) energetic, (ii) geometric, and (iii) magnetic [3]. Thus, various conceptual extensions of aromaticity have been proposed regarding to the electronic spin states, molecular

topologies, and number of delocalized π electrons. The conventional form of aromaticity complies with Hückel's rule [4], in which [4*N*+2] delocalized π electrons would induce unusual stability for a near-planar conjugated system in its singlet state, whereas those with [4*N*] π electrons are destabilized (Figure 13.1a) [5]. The initial test beds for Hückel's rule have been homoannulenes [6–8], where the aromaticity was proved to be ring-size dependent and vanished with more than 30π-electrons circuit. Latter efforts allowed continued refinement of Hückel's aromaticity in larger π-conjugated systems with conformation-restricted architectures such as porphyrinoids [9–10] and even porphyrin-based nanorings [11–13], if there is a dominant annulene-like conjugation pathway. Topological change from a planar to Möbius strip with [2*n*+1] twists leads to an inverse of aromaticity (Figure 13.1a). In 1964, Heilbronner proposed that cyclic molecules with Möbius topology [14] should be aromatic with [4*N*], rather than [4*N*+2] π electrons [15], and the prediction has been validated experimentally within porphyrinoid systems [16–18].

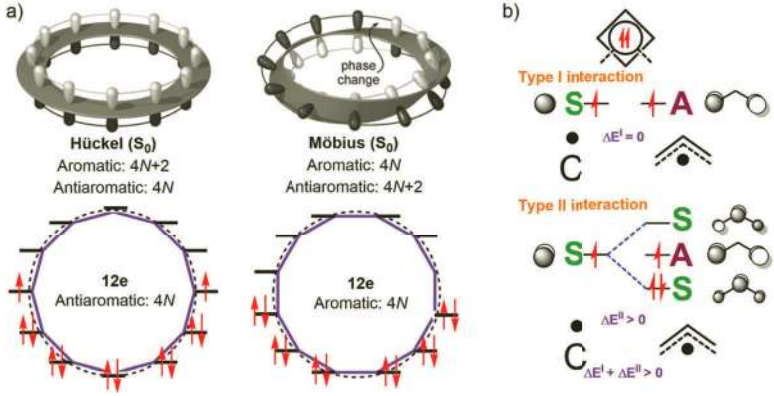


**Figure 13.1** (a) Comparison of theoretical models for Hückel and Möbius (anti) aromaticity applied to the example of [12]annulene. (b) Schematic drawing that displays the types I and II interactions ($\Delta E^I$ and $\Delta E^{II}$, respectively) between the π-orbitals of suitable polyenyl radical fragments, which when combined yield triplet biradical cyclobutadiene. Reproduced with permission from ref 16. Copyright 2007 WILEY-VCH Verlag Gmbh & Co. KGaA, Weinheim.

Hückel's aromaticity rule deals with the singlet ground state ($S_0$) of molecules, which would be reversed in the lowest triplet state

($T_1$), as predicted by N. Collin Baird in 1972 [19]. Baird's approach was to decompose the annulenes into two polyenyl monoradical fragments with odd numbers of π electrons, and then deduce the energy change on fusion of these fragments to give a triplet diradical annulene (Figure 13.1b). Two types of π-orbital interactions were considered: those between the two singly occupied π-MOs (SOMOs), labeled Type I, and those between the SOMO of one fragment with the doubly occupied and vacant π-MOs of the other, labeled Type II. The stabilization or destabilization on fusion to the triplet annulene depends on the symmetries of the π-orbitals of the two monoradical fragments. Neutral monoradical chains with [4$k$+1] ($k$ = 0, 1, 2, …) carbon atoms have SOMOs that are symmetric (S) with regards to a bisecting mirror plane, whereas those with [4$k$+3] carbon atoms have antisymmetric (A) SOMOs. Accordingly, fusion of a [4$k$+1] carbon-atom chain with a [4$k$+3] carbon-atom chain, such as for cyclobutadiene, leads to no Type I interaction because the two SOMOs are of different symmetries ($\Delta E^{\mathrm{I}} = 0$). Therefore, a net stabilization is found on fusion to a triplet [4$N$] π-electron annulene. This pioneering hypothesis has been subsequently supported by many theoretical analyses [20] and spectroscopically validated recently. Ottosson et al. observed the aromatic chameleon spectroscopic features of fulvene based on sensitization [21], in which the Baird's rule was well elaborated. In addition, Osuka and Kim's team presented the absorption spectroscopic features of hexaphyrin analogs in their respective $T_1$ states to concretely characterize Baird-type aromaticity [22]. It is also worth noting that Baird's rule can also be applied to π-conjugated molecules with a triplet ground state [23].

Conceptual extension of aromaticity could extend toward 3D π-conjugated systems, and one notable example is Hirsch's $2(N+1)^2$ spherical aromaticity rule upon correlating the symmetry and energy degeneracy of frontier π-orbitals in fullerenes to that of atomic orbitals (Figure 13.2a) [24, 25]. Such unique form of aromaticity is applicable to molecules with extremely high symmetry, which can be approximate to a super-atom, e.g. some metal-, boron-based clusters and carbon-based polyhedrons [26]. Another type of 3D aromaticity can be achieved through close π-π stacking of antiaromatic systems with strong interactions between the frontier π orbitals [27, 28],

which has been recently validated by Shinokubo and Kim's team in an antiaromatic norcorrole-based cyclophane (Figure 13.2b) [29], and subsequently extended to face-to-face stacked π-dimers of monoradicals, as demonstrated by Iyoda's group [30] and Sun's group [31].

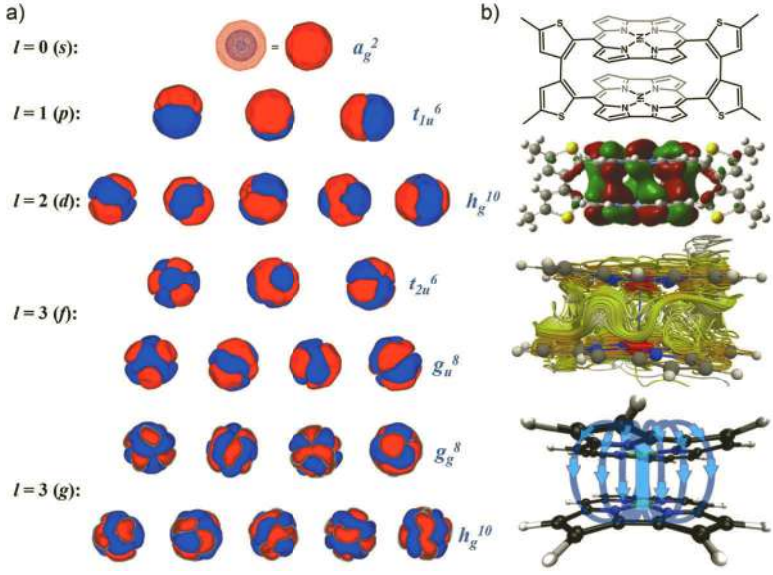


**Figure 13.2** Two types of 3D aromaticity: (a) Hirsch's $2(N+1)^2$ spherical aromaticity upon molecular orbital analysis, and the calculated frontier π orbitals of $C_{60}^{10+}$ are presented with symmetries and energy degeneracy comparable to corresponding atomic orbitals; and (b) representative examples of 3D aromaticity stemmed from frontier orbital stacking of antiaromatic porphyrins, and the calculated magnetically induced current are shown with the schematic visualization of the through-space current channels. Reproduced with permission from ref 24. Copyright 2000 WILEY-VCH Verlag Gmbh & Co. KGaA, Weinheim.

In macrocyclic polyradicaloids with moderately coupled frontier π electrons, the small singlet-triplet energy gap would allow possible spin flipping to relevant electronic states, and thus exhibiting different types aromaticity, complied with the aforementioned Hückel's rule or Baird's rule [2]. This is different from the traditional closed-shell π-conjugated macrocycles. In addition, studies on a fully π-conjugated diradicaloid/polyradicaloid cage can provide insights into the underlying principles of 3D global aromaticity,

which is of great interest, but remains largely unexplored. The aromaticity can be examined by a combination of experimental methods (e.g., NMR, X-ray crystallographic analysis) and theoretical approaches (e.g., anisotropy of the induced current density (ACID) [32], nucleus independent chemical shift (NICS) [33, 34], and isochemical shielding surface (ICSS) [35, 36] calculations). Notably, 3D global aromaticity in a hexacation of a π-conjugated diradicaloid cage was successfully observed for the first time, and a new [6*N*+2] aromaticity rule was proposed for molecular cages with specific $D_3$ symmetry.

## 13.2 Linear Polyradicaloids

With regards to some of our work on zethrenes (see Chapter 6), a fused heptazehrene dimer **1** was designed and synthesized, in hope to achieve tetraradical character ($y_1$) (Figure 13.3) [37]. In addition, its analogs **2**–**4** containing five-membered rings were also prepared for comparison studies. It turned out that the fusion mode had dramatic effect on their ground-state electronic structures, diradical/tetraradical character, and chemical reactivity. Compound **1** has a large diradical character ($y_0$ = 0.713) and thus its derivative is highly reactive. Upon introducing two five-membered rings in **2** and **3**, the diradical character decreased to 0.635 and 0.351, respectively. The kinetically blocked derivative of **2** is a reasonably stable singlet diradicaloid, but the derivative of **3** remains reactive. Compound **4** with four five-membered rings has a very low diradical character and its derivative is very stable and behaves as a closed-shell compound. These differences can be explained by the pro-aromatic/antiaromatic character of the molecules and the intramolecular charge transfer effect. In particular, the introduction of five-membered ring results in the significant contribution of zwitterionic resonance form to the ground-state structure. Due to strong intramolecular radical-radical coupling, these compounds exhibited very low tetraradical character ($y_1$ < 0.04). This work emphasizes the importance of controlling intramolecular spin-spin interactions in attaining significant polyradical character, as strong coupling would lead to low radical character.

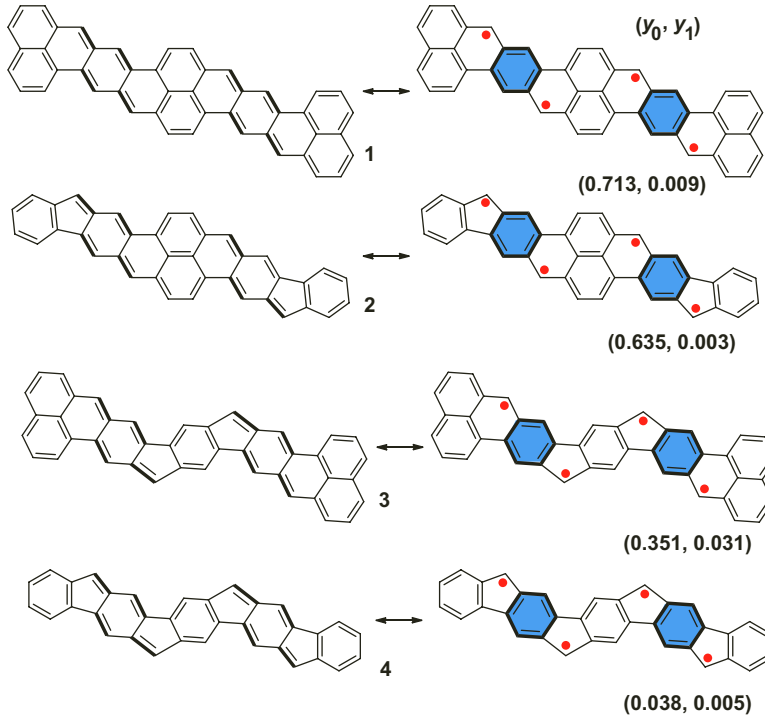


**Figure 13.3** Potential tetraradicaloids **1**–**4** by fusion of *p*-QDM units with naphthalene or benzene rings in different modes. Reproduced with permission from ref 37. Copyright 2016 American Chemical Society.

To fine tune the intramolecular spin-spin coupling, a series of 3,6-linked fluorenyl radical oligomers **5**–**10** were designed and synthesized (Figure 13.4a) [38]. Previous studies by Kubo's group [39] and our group [40] demonstrated that fluorenyl radical could be effectively stabilized by appropriate kinetic blocking with bulky groups such as 9-anthryl (An). Indeed, the oligomers **5**–**10** were also reasonably stable and could be purified by normal silica gel column chromatography. The coupling between the neighboring spins would lead to loss of two Clar's aromatic sextet rings, and thus the interaction was weaker compared that in **1** (with only one sextet lost). As a result, the tetramer (**8**) and pentamer (**9**) were calculated to possess a moderate tetraradical character ($y_1$), and the hexamer (**10**) displayed a hexaradical character ($y_2$) (Figure 13.4b). A clear chain length dependence of their optical, electrochemical, and magnetic properties was found for these oligomers, that is, the HOMO energy

level increases and the LUMO energy level decreases with extension of the molecular size for the even and odd series of oligomers, respectively, leading to a convergence of the electrochemical energy gap ($E_g^{EC}$). In both series, linear correlations between $E_g^{EC} \sim 1/n$ were plotted, and the extrapolation of the two plots to $n = \infty$ implied that the corresponding infinite polymers with even and odd number of fluorenyl radicals might have an approximate $E_g^{EC}$ of 0.84 eV and 0.59 eV (Figure 13.4c), accordingly.

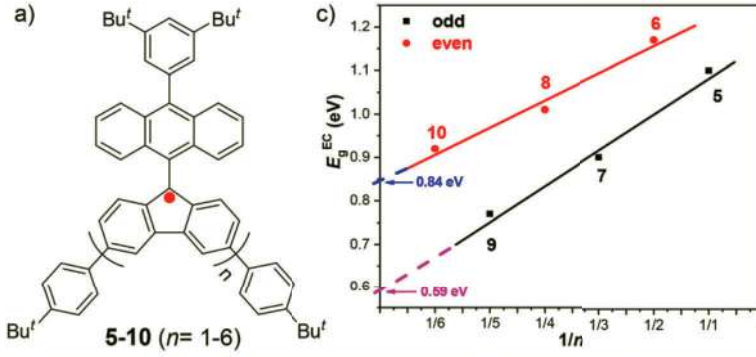


b)

| Molecule | $N_U$ | $y_0$ | $y_1$ | $y_2$ |
|---|---|---|---|---|
| **6** | 1.65 | 0.66 | 0 | 0 |
| **7** | 1.95 | 0.18 | 0 | 0 |
| **8** | 3.32 | 0.75 | 0.59 | 0 |
| **9** | 3.23 | 0.28 | 0.24 | 0 |
| **10** | 5.05 | 0.80 | 0.68 | 0.59 |

**Figure 13.4** (a) Chemical structures the 3,6-linked fluorenyl radical oligomers **5**–**10**, (b) calculated (RAS-SF/6-31G*) number of unpaired electrons (*N*u) and multiple diradical characters ($y_i$, $i$ = 0–2) of **6**–**10**, and (c) chain-length dependence of the electrochemical energy gaps ($E_g^{EC}$) for **5**–**10**. Reproduced with permission from ref 38. Copyright 2016 American Chemical Society.

## 13.3 2D Macrocyclic Diradicaloids and Polyradicaloids

### 13.3.1 Expanded Porphyrinoids with Radical Character

Besides linear polyradicaloids, species with cyclic π-conjugated arrays would be of great interest regarding to their topological

significance as well as the diversity of electronic structures. The most efficient approach toward macrocyclic open-shell systems would be by constructing expanded porphyrinoids with radical character. Over the years, contracted and expanded porphyrins have emerged as novel π-conjugated molecules, due to their unique structural and electronic features, as such heteroannulenes consisting of regularly arranged pyrroles, furans, thiophenes, or other heterocyclic subunits linked by $sp^2$ methine carbons would allow effective π-electron delocalization throughout the conjugated periphery to facilitate global (anti)aromaticity [41]. From another point of view, porphyrinoids have turned out to be a good platform to stabilize radicals through effective spin delocalization. To date, several porphyrinoid-based monoradicals have been developed, including pentaphyrin radical **11** [42], corrole radicals **12** and **13** [43], and tetraazaporphyrin radical **14** (Figure 13.5a) [44]. In addition, diradicaloids based on porphyrinoid have also been synthesized (also see Chapter 11), such as the antiaromatic corrole dimer **15** [45], diketo-hexaphyrin **16** [46, 47], and face-to-face stacked π-dimers **17** [48] and **18** (Figure 13.5b) [30].

Porphyrinoid-based radical species with an overall even number of delocalized π electrons are ideal platforms to investigate the fundamental correlations between aromaticity, radical character, and electronic properties. In this context, our group synthesized a bithiophene bridged expanded porphycene **19** and a cyclopentabithiophene bridged expanded porphycene **20** (Figure 13.6a) [49]. The appearance of diradical/tetraradical characters can be rationalized by recovery of two/four aromatic thiophene rings from closed-shell to open-shell forms for **19** and **20**, respectively. Indeed, theoretical calculations predicted an open-shell singlet ground state with significant radical character for both species ($y_0$ = 0.63 for **19**; $y_0$ = 0.68, $y_1$ = 0.18 for **20**). It is noteworthy that both compounds display unexpected stability under ambient conditions, attributing to effective delocalization of unpaired electrons throughout the π-conjugated periphery. X-ray crystallographic analysis and NMR measurements suggest that **19** is globally aromatic, coinciding with the calculated ACID plot containing a clockwise diatropic ring current in a 34π ([4*N*+2]) circuit (Figure 13.6a). In contrast, **20** was proved to be globally antiaromatic, as the calculated ACID plot revealed a counter-clockwise paratropic

ring current circuit along a 32π ([4*N*]) electronic pathway. These results are further supported by the significantly negative NICS(0) value in **19** (−15.35 ppm) and the moderately positive NICS(0) value in **20** (+9.75 ppm). Moreover, the optical absorption spectrum of **19** exhibited an intense Soret band along with a distinct Q-like band, whereas compound **20** only displayed a weakly broad band tailing up to 2000 nm, consistent with their aromatic/antiaromatic character, respectively.

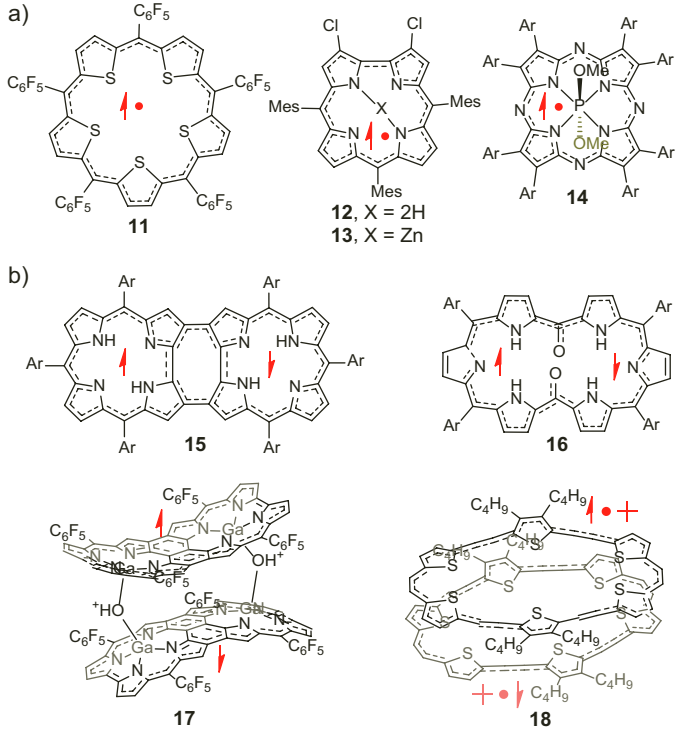


**Figure 13.5** Representative examples of stable porphyrinoid-based (a) monoradicals, and (b) diradicals.

A more extended macrocyclic diradicaloid **21** based on core-modified [38]octaphyrin(1.1.1.0.1.1.1.0) was also synthesized [50] by replacing all the pyrrole rings with thiophene units, which could avoid intramolecular hydrogen bonding and facilitate an unlocked conformation (Figure 13.6b). The diradical character

can also be qualitatively predicted by the recovery of two more aromatic thiophene rings in the diradical resonance form. X-ray crystallographic analysis on the single crystal of **21** revealed a nearly planar rectangular backbone, in which two bithiophene subunits adopt a *trans*-configuration to release the strain along the conjugated periphery (Figure 13.6b). Overall six thiophene units orient inwardly with the sulfur atom pointing toward the macrocyclic center. The C–C bonds linking the methine bridges are somehow equal in length (within 1.394–1.408 Å), with a HOMA value of 0.913 along the all-carbon 38π circuit, thus indicating global aromaticity of **21**.

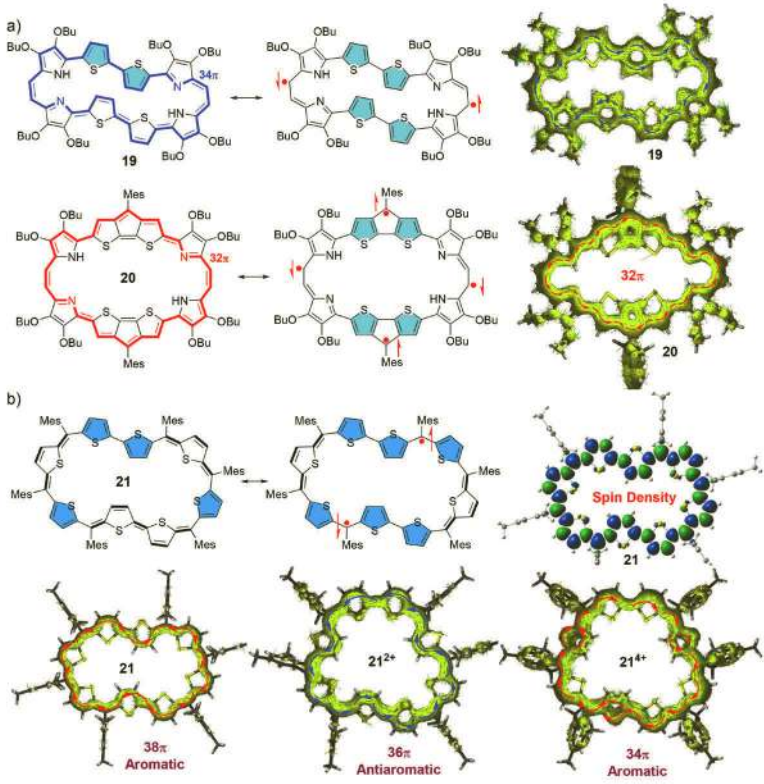


**Figure 13.6** (a) Resonance forms and calculated ACID plots of the expanded porphycenes **19** and **20**, Reproduced with permission from ref 49. Copyright 2018 WILEY-VCH Verlag Gmbh & Co. KGaA, Weinheim. (b) resonance forms of core-modified octaphyrin **21** with spin density map of the singlet diradical, and the calculated ACID plots **21**, $\mathbf{21}^{2+}$, and $\mathbf{21}^{4+}$. Reproduced with permission from ref 50. Copyright 2020 WILEY-VCH Verlag Gmbh & Co. KGaA, Weinheim.

The single-crystal structure of $\mathbf{21}^{2+}$ achieved by two-electron chemical oxidation adopts a distorted geometry with half of the backbone remaining co-planarity, while the other half bent up and deviated by 2.74 Å from the mean plane. Notably, one of the bithiophene units now adopts a *cis*-configuration, and overall there are three inverted thiophene rings (Figure 13.6b). Significant bond length alternation (BLA) was observed for the linking bonds at the methine bridges and an estimated HOMA value of 0.744 in a 36π ([4*N*]) conjugation pathway, indicating global antiaromatic character. Both the neutral and dicationic compounds demonstrated open-shell diradical character with a small singlet-triplet energy gap ($\Delta E_{S-T}$ = −2.70 kcal/mol for **21**, and −3.78 kcal/mol for $\mathbf{21}^{2+}$) as estimated from magnetic measurements. Single-crystal analyses on $\mathbf{21}^{4+}$ obtained by four-electron oxidation revealed similar orientation of thiophene units as that in the dication $\mathbf{21}^{2+}$, whereas the central periphery now adopts a shallow bowl-shaped configuration with a much smaller BLA, leading to efficient electron delocalization along a 34π ([4*N*+2]) conjugation pathway. Indeed, the global aromaticity of neutral compound **21** and tetracation $\mathbf{21}^{4+}$ were confirmed by the $^1$H NMR measurement with the observation of shielding/de-shielding effects at the regions inside/outside the macrocyclic backbone, whereas the antiaromatic dication $\mathbf{21}^{2+}$ showed inverse shielding/de-shielding chemical environments. The conclusion was further supported by NICS(0), ACID, and 2D ICSS calculations. This study demonstrated that stable open-shell diradicaloids could be attained in core-modified expanded porphyrins, and such geometrically flexible system would reach the minimal energy state by adapting their conformation at different oxidation states.

### 13.3.2 Polycyclic Hydrocarbon-Based Macrocyclic Polyradicaloids Showing Hückel (Anti) Aromaticity

In addition to the porphyrinoid-based open-shell systems, polycyclic hydrocarbon-based macrocyclic polyradicaloids could also display global (anti)aromaticity if the frontier radicals are moderately coupled in an AFM mode and the π electrons are effectively delocalized. In 2014, Tobe's group synthesized a non-benzenoid non-alternant

polycyclic hydrocarbon by the arrangement of two indeno[2,1-*c*] fluorene units in a cyclic form, the tetracyclopenta[*def*,*jkl*,*pqr*,*vwx*] tetraphenylene **22** (Figure 13.7a) [51]. Such hydrocarbon was initially proposed by Hellwinkel in 1970 as a doubly annulenoid configuration, in which the internal circuit has 8π electrons, whereas the external ring has 20π electrons. Single crystal structure of **22** revealed a $D_{2h}$ symmetry rather than a $C_{2v}$ symmetry for the open-shell diradical form or $D_{4h}$ symmetry for the double annulenoid form. Theoretical calculations (SF-TDBHHLYP/6-311G(d,p)) based on the X-ray structure gave a diradical character ($y_0$) of 0.095 and a tetraradical character ($y_1$) of 0.032, indicating that the frontier four π-electrons are strongly bonded and the molecule behaves more toward a closed-shell species. Indeed, a sharp NMR spectrum at room temperature was observed. A primary analysis upon Clar's aromatic sextet shows that only one aromatic sextet is gained subsequently from closed-shell to open-shell diradical form, then to tetraradical form, and thus, like the fused heptazethrene dimer **1**, the obtained aromatic stabilization energy is not sufficient to compensate the energy required to break a π-bond. The calculated NICS(1) values of **22** revealed a nonaromatic to weak antiaromatic character in the six-membered rings (−1.45 and +5.51 ppm), whereas significant antiaromatic character in the five-membered (+8.51 ppm) and eight-membered (+10.46 ppm) rings.

In order to amplify the open-shell radical character, our group prepared two fully-fused macrocycles **23** and **24**, consisting of alternating aromatic/quinoidal carbazole units (Figure 13.7b) [52]. In both cases, the resonance analysis shows the gain of two aromatic sextets at each transition stage, that is, from closed-shell form to open-shell diradical form, and then to tetraradical form and finally to hexaradical form, suggesting moderate coupling between the frontier π electrons. Calculations by restricted active space spin-flip (RAS-SF/6-31G(d)) method gave a moderate tetraradical character ($y_1$ = 0.19) and hexaradical character ($y_2$ = 0.27) for **23** and **24**, respectively. VT $^1$H NMR spectra of **23** in $CD_2Cl_2$ showed severely broadened signals at room temperature, due to thermally populated paramagnetic species, and partially resolved spectrum at 0 °C. The NMR signals at −3.2 ppm and 10.62 ppm can be assigned to outer (c,c′) and inner (d,d′) protons of the macrocycle core (Figure 13.7b),

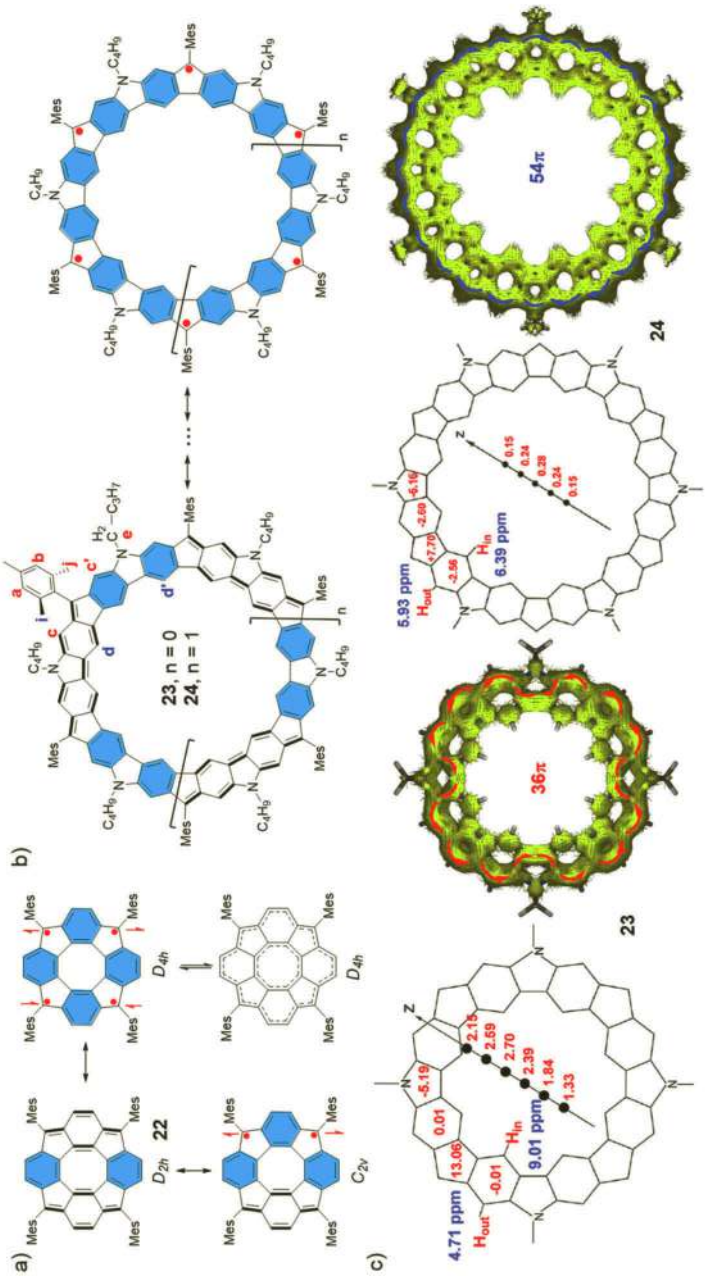


**Figure 13.7** (a) Chemical and resonance structures of **22** with different symmetries, (b) resonance structures of two fully-fused carbazole-based macrocycles, and (c) calculated NICS(0) values (red numbers), chemical shifts (blue numbers), and ACID plots for **23** ($C_{2v}$) and **24** ($C_1$) in the single states. Reproduced with permission from ref 52. Copyright 2016 American Chemical Society.

respectively, in accordance with respective de-shielding and shielding effect from the paratropic ring current. Indeed, the calculated ACID plot of **23** clearly displays a counter-clockwise ring current circuit along the periphery with 36 ([4*N*]) π electrons (Figure 13.7c), further supporting the Hückel's global antiaromaticity. Severely broadened signals were observed for the $^{1}$H NMR spectrum of **24** in full temperature range (213–298 K), due to its larger radical character, which limited the detailed NMR analysis. Nevertheless, the ACID plot of **24** reveals a weakly clockwise ring current circuit containing 54 ([4*N*+2]) π electrons (Figure 13.7c), suggesting a diatropicity similar to the aromatic benzene counterpart. The global antiaromatic/aromatic nature of **23**/**24** was further supported by the NICS and NMR chemical shift calculations (Figure 13.7c). Both **23** and **24** exhibited a small optical energy gap (0.52 eV for both) and small excitation energies from the singlet ground state to higher-spin excited states.

These nitrogen-doped macrocycles are too electron-rich and decomposed under ambient conditions. Considering the good stability of kinetically blocked fluorenyl radicals and its oligomers **5**–**10**, several stable fluorenyl radical-based macrocycles were designed and synthesized by us, including directly linked macrocycles **25**–**26** and the ethynylene bridged macrocycle **27** (Figure 13.8a) [53]. The tetraradical characters ($y_1$) of 0.59 and 0.71 were calculated for the macrocyclic tetramers **25** and **27**, respectively, at RAS-SF/6-31G(d) level of theory, while a hexaradical character ($y_2$) of 0.59 was predicted for the hexamer **26**. X-ray crystallographic analysis on **25** revealed a saddle-shaped geometry with the torsion angles of 26.5° and 28.9° between neighboring fluorenyl units. In contrast, the optimized geometry of **27** adopts a nearly planar conformation. ACID plots of **25** and **27** show a paratropic ring current circuit along a dominant π-conjugation pathway with 36 and 44 ([4*N*]) π electrons, respectively (Figure 13.8b), indicating global antiaromaticity. In addition, large positive NICS(0) values at the centers of macrocycles **25** (+11.7 ppm) and **27** (+14.26 ppm) are further indicative to their global antiaromaticity.

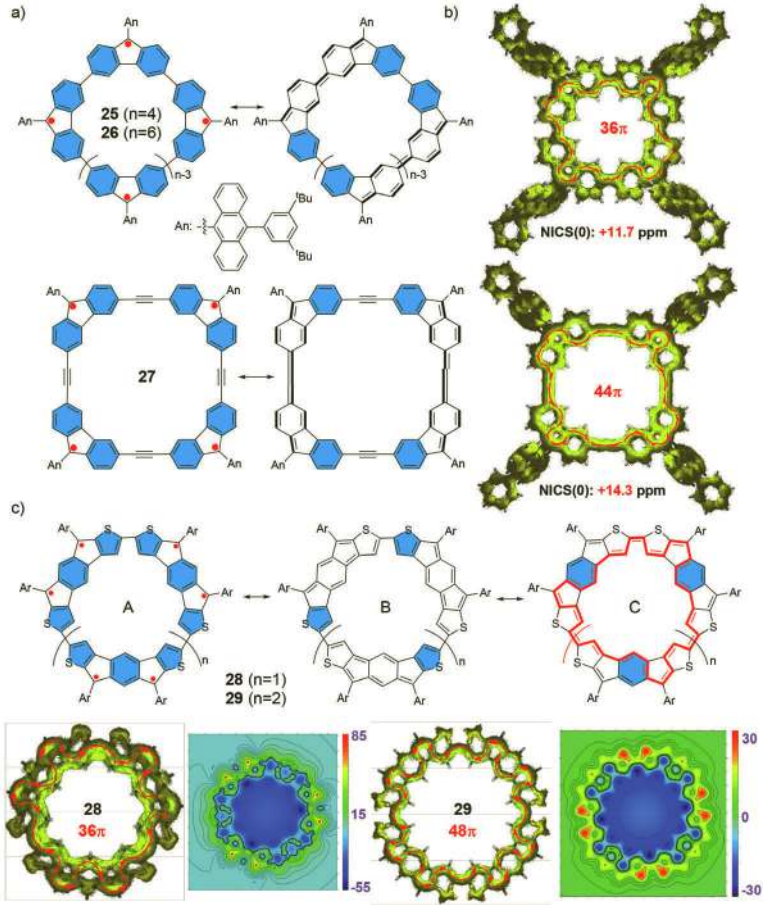


**Figure 13.8** (a) Resonance structures two types of fluorenyl radical-based macrocyclic polyradicaloids **25**–**27**, (b) calculated ACID plots and NICS(0) values of **25** and **27**, Reproduced with permission from ref 53 Copyright 2016 American Chemical Society and (c) representative resonance forms (A–C) of the macrocycles **28** and **29** with the calculated ACID plots and 2D-ICSS maps. Reproduced with permission from ref 54 Copyright 2018 WILEY-VCH Verlag Gmbh & Co. KGaA, Weinheim.

The macrocyclic hexamer **26** adopts a largely distorted figure-eight geometry with no coherent ring current along the periphery of the macrocycle in the ACID plot, even though 54 ([4*N*+2]) π electrons can be counted along the conjugation pathway, suggesting that global aromaticity is diminished in a largely distorted configuration. The moderate AFM coupling between the radicals and the antiaromatic characters of **25** and **27** led to smaller energy gaps

and slightly larger two-photon absorption (TPA) cross sections as compared to the linearly linked tetrameric counterpart **8**. However, **26** exhibited a larger energy gap and smaller TPA cross section than the liner hexamer, due to the highly distorted configuration and the consequently less effective π-conjugation.

Another approach to construct macrocycles with potentially polyradical character and global (anti)aromaticity is by cyclic assembly of open-shell diradicaloid subunits. This concept was validated in two macrocycles **28** and **29** based on dithieno[*a*,*h*]-*s*-indacene diradicaloid (Figure 13.8c) [54]. Different resonance forms can be drawn for both cases, that is, an open-shell hexa-/octa-radical form with all benzene and thiophene rings being aromatic (form A), a closed-shell form in which only three/four thiophene rings are aromatic (form B), and a closed-shell form in which only three/four benzenoid rings are aromatic (form C). Single-crystal structure of **28** adopts a bowl-shaped geometry with a distance of 1.649 Å between the internal and external rims, indicating a large strain within the macrocycle. The bond length analysis revealed quiniodal dithiophene subunits consistent with resonance form C, which can be reasonably explained by the gain of more resonance energy from three aromatic benzene rings in form C than three thiophene rings in form B. The optimized geometry of **29** suggests a similar linking mode as the trimeric analog **28**. The VT $^{1}$H NMR spectra of **28** and **29** clearly demonstrated a closed-shell nature and global antiaromatic character for both species, in which the inner/outer proton on the backbone is de-shielded/shielded, as coincidentally supported by the calculated 2D ICSS maps. In addition, the ACID plots show paratropic ring current circuits with a dominant 36 (for **28**) and 48 (for **29**) π-electron delocalization pathway, and significantly positive NICS(0) values at the geometric center of the macrocycle (+7.02 ppm for **28** and +4.88 ppm for **29**) are calculated, consistent with their global antiaromaticity. On the other hand, the evenly charged species, $\mathbf{28}^{2+}$ and $\mathbf{29}^{2+}$, both turned out to be open-shell singlet diradical dications. A switch from antiaromaticity to aromaticity upon two-electron oxidation was confirmed by $^{1}$H NMR measurements, the calculated 2D ICSS maps, the clockwise diatropic ring current circuit in ACID plots, as well as the negative NICS(0) values (−12.48/−12.55 ppm for $\mathbf{28}^{2+}$/$\mathbf{29}^{2+}$) (Figure 13.8c). Indeed, a 34π/46π conjugation pathway can be drawn for the dicationic state of **28**/**29**, satisfying [4*N*+2] Hückel's aromaticity rule.

### 13.3.3 Macrocyclic Diradicaloids/Polyradicaloids Showing Baird Aromaticity

Cyclic π-conjugated molecules with open-shell electronic structure may allow the access of Baird-type aromaticity, if stable triplet species with [4*N*] π electrons can be afforded. This concept was discussed in a report from Sessler's group, in which several 24π antiaromatic rosarin derivatives were synthesized and the electronic properties of the neutral and protonated species were investigated [55]. The triprotonated rosarins, achieved by using trifluoroacetic acid (TFA), primarily featured as ground-state triplet diradicals confirmed using VT ESR analysis, which should fulfill Baird-type aromaticity. To further test the concept of Baird aromaticity, Kim and Sessler's team reported a purely organic non-planar bicyclic system, the dithienothiophene-bridged [34]octaphyrin **30** [56], which has permitted access to two different limiting aromatic forms as a function of the oxidation state (Figure 13.9a). In the neutral state, spectroscopic and solid-state structural analyses revealed a flattened bicyclic system with the existence of two competing 26 and 34 π-electron diatropic ring current circuits. After two-electron oxidation, an electronically mixed [4*N*+1]/[4*N*+1] triplet diradical species with an overall 40([4*N*]) π electrons in the ground state was obtained, which was supported by low-temperature ESR measurements (Figure 13.9b,c). The dication with [4*N*] delocalized π electrons and a triplet state thus satisfies Baird's rule and is aromatic.

In 2018, our group reported two stable macrocyclic octaradicaloid **31** and decaradicaloid **32** with alternating fused cyclopenta-ring and *m*-phenylene [57] (Figure 13.10a). The magnetic measurements suggested a singlet ground state for **31**, whereas a triplet ground state for higher homolog **32**. RAS-SF calculations predicted that **31** has a moderate octaradical character ($y_3$ = 0.45) and **32** has a moderate decaradical character ($y_4$ = 0.46). A partially resolved $^1$H NMR spectrum of **31** in THF-$d_8$ was recorded at 233 K, in which signals at +11.37 ppm and −12.08 ppm were assigned to the outer and inner protons, indicating a strong aromatic character. Indeed, the 2D ICSS map demonstrated a strongly shielded chemical environment inside the macrocycle (with positive ICSS values), while the outside region is highly de-shielded (Figure 13.10c). The calculated ACID plot of **31**

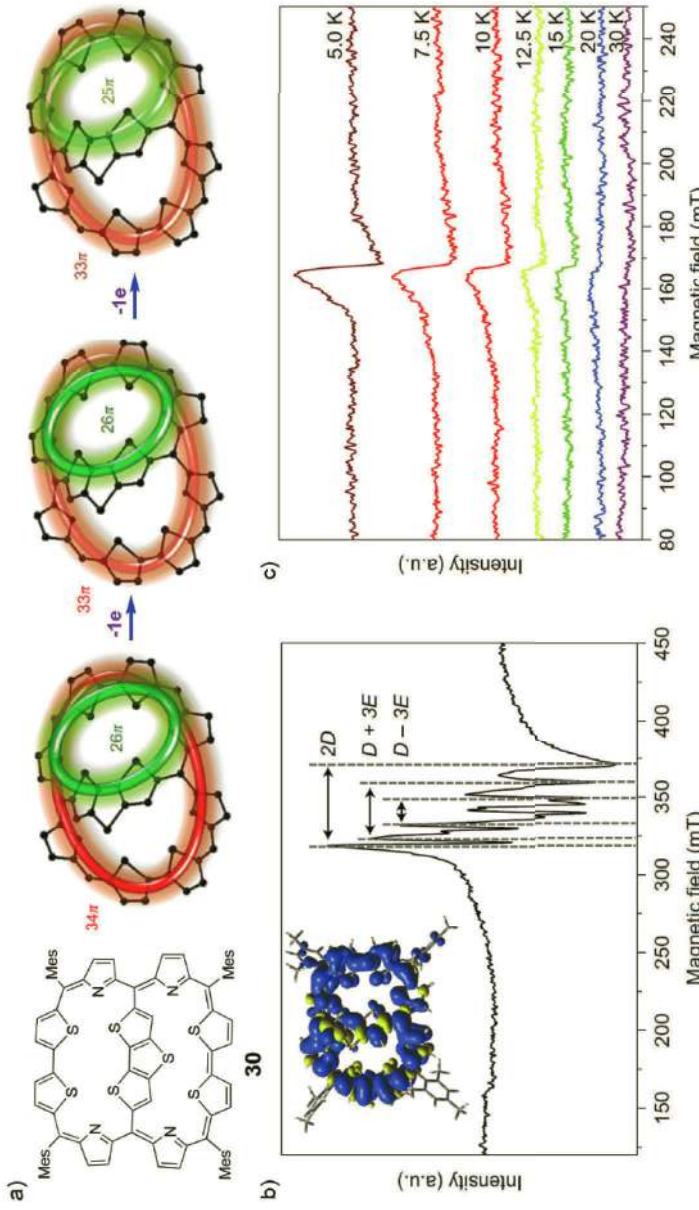


**Figure 13.9** (a) Molecular structure of **30** and schematic dual conjugation pathways in the neutral, one-electron, and two-electron oxidized forms, (b) ESR spectrum of two-electron oxidized form of **30** at 5 K (inset is the spin density distribution map of the triplet biradical), and (c) temperature-dependent ESR spectra of $\mathbf{30}^{2+}$ in the half-field region (30–5 K). Reproduced with permission from ref 56. Copyright © 2017, Nature Publishing Group.

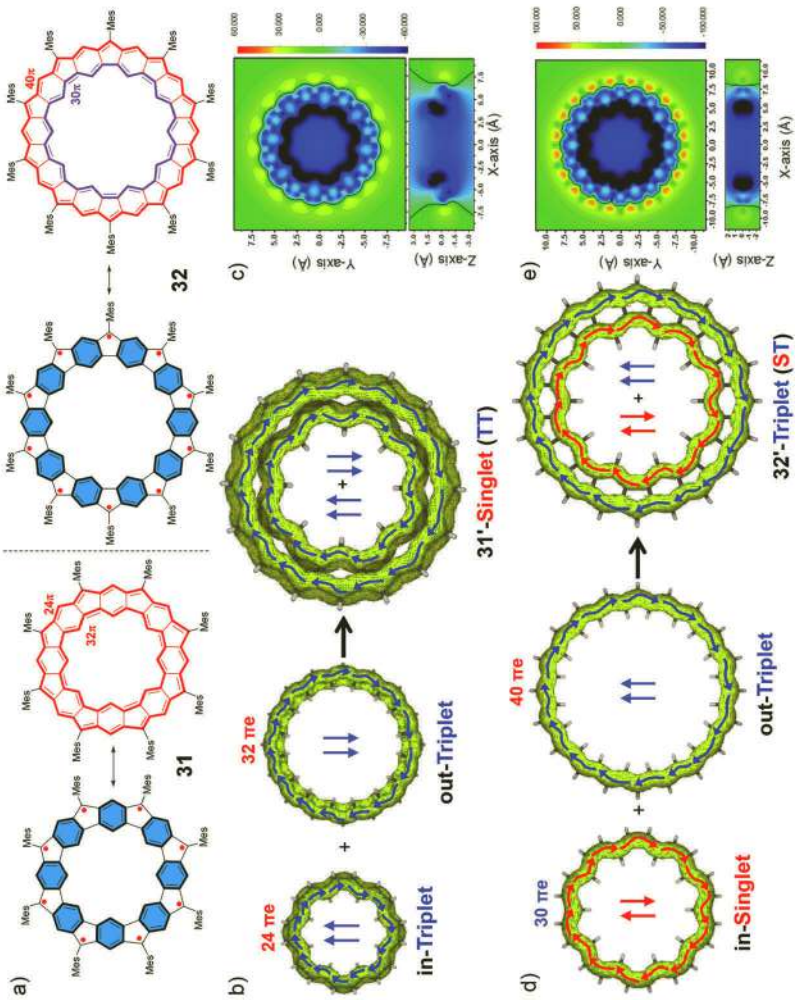


**Figure 13.10** (a) Representative open-shell and closed-shell resonance forms of the macrocycles **31** and **32**, (b) ACID plots of the individual inner/outer rings and the backbone of **31** in the open-shell singlet ground state, (c) 2D $NICS_{zz}$ map of the backbone of **31** (**31′**) in the open-shell singlet ground state, (d) ACID plots of the individual inner/outer rings and the backbone of **32** in the triplet ground state, and (e) 2D $NICS_{zz}$ map of the backbone of **32** (**32′**) in the triplet ground state. Reproduced with permission from ref 57. Copyright 2018, Elsevier Inc.

in ground singlet state unprecedentedly displays a unique annulene-within-an annulene (AWA) super-ring structure with two fully decoupled diatropic ring current circuits formally containing 24π and 32π electrons, respectively, which is contradictory to Hückel's rule (Figure 13.10b). Explanation on such unusual 'anti-Hückel' global aromaticity is thus attempted by two alternative electronic structures: (i) one annulene gives two electrons to the other one ($2^-/2^+$ or $2^+/2^-$ for inner/outer rings), and (ii) each annulene holds a "triplet" diradical character. Constrained DFT calculations predicted that both the $2^-/2^+$ and $2^+/2^-$ states are in much higher energy than the triplet/triplet (TT) state and hence the global aromaticity can be eventually ascribed to the "triplet(in)-triplet(out)" character of the singlet ground state, that is, two triplets coupled as a singlet. These results can be rationalized from the large radical character of **31**. ACID plots of individual inner/outer annulenes also suggest that these [4*N*]annulenes show a clockwise diamagnetic current circuit in the triplet state (Figure 13.10b). Therefore, Baird's rule should be applied to both the inner and outer annulenes, and as a result, the whole molecule exhibits [4*N*] global aromaticity. Similarly, the lowest energy contribution in the triplet ground state of **32** is the singlet/triplet (ST) state, and ACID plots (Figure 13.10d) and 2D NICS map (Figure 13.10e) again reveal a super-aromatic AWA structure, with the inner ring being singlet and aromatic (Hückel's rule) and the outer ring being triplet and aromatic (Baird's rule). Due to the polyradical character and effective conjugation, both compounds showed an optical energy gap smaller than 0.5 eV, and amphoteric redox behavior with at least 12 accessible redox waves.

The unusual AWA super-ring structure observed in **31** and **32** deserves further investigation. It was realized that only four Kekulé structures can be drawn for the backbone of **31** (denoted as **31′**) and **32** in closed-shell form, with all radial bonds being single bonds (A–D, Figure 13.11a). It also suggests that the inner rim and outer rim are almost electronically decoupled, leading to a decoupled AWA structure. To test this concept, another macrocyclic tetraradicaloid **33** (Figure 13.11b) was prepared and systematically investigated [58]. The backbone of **33** can be formally drawn in an AWA resonance form, with a 24π-electron inner rim and a 36π-electron outer rim (A′). However, a closed-shell resonance form with four radial C–C double bonds can also be drawn (B′), suggesting the existence of

electronic coupling between the inner rim and outer rim. Indeed, the ACID plot of **33** shows only one counter-clockwise ring current flow along the periphery with a 36π ([4*N*]) conjugation pathway and no decoupled AWA structure is found. A positive NICS(0) value of +19.8 ppm is calculated, indicating its antiaromatic character, which is also supported by NMR measurements. In addition, two fully conjugated carbon nanobelts **34** and **35** [59], in which six/eight cyclopenta-rings are fused onto a macrocycle, containing three/four alternately linked 2,7-pyrenyl and 2,7-phenanthryl units were synthesized (Figure 13.11c). They both show local aromaticity in the neutral state, but their dications are globally aromatic with a 94π/126π ([4*N*+2]) conjugation pathway, as supported by both NMR measurements and ACID/NICS calculations (Figure 13.11c).

### 13.3.4 Global Antiaromaticity in Transition State of Macrocyclic Polyradicaloid

In 2018, our group reported another series of macrocyclic polyradicaloids, the [*n*]cyclo-*para*-biphenylmethines ([*n*]CPBMs, *n*=3–8; **36**–**40**) (Figure 13.12a) [60], which are similar to the well-studied [*n*]cyclo-*para*-phenylenes ([*n*]CPPs) [61], but with one additional methine site inserted between the neighboring biphenyl units. These molecules contain alternate aromatic biphenyl and quinoidal diphenylquinodimethane. They were calculated (RAS-SF/6-31G(d)) to have significant radical character, with the number of unpaired electrons (*N*u) of 1.70, 2.95, 3.94, 4.61, 5.42, and 5.93 for **36**, **37**, **38**, **39**, **40**, and **41**, respectively (Figure 13.12b,c). Remarkably, the entire series of macrocyclic polyradicaloids were stable under ambient conditions for several days, which can be rationalized by the moderate AFM coupling between neighboring methine-radicals and the kinetic protection by bulky anthryl groups. In addition, the polyradicaloids with odd numbers of repeating unit (*n* = 3, 5, 7) have a doublet ground state, whereas the others with even number of repeating units (*n* = 4, 6, 8) show an open-shell singlet ground state. In all cases, the excitation energies from low-spin ground states (LS) to the lowest high-spin (HS) excited states ($\Delta E_{\mathrm{LS-HS}}$) decreases in larger macrocycles (Figure 13.12c).

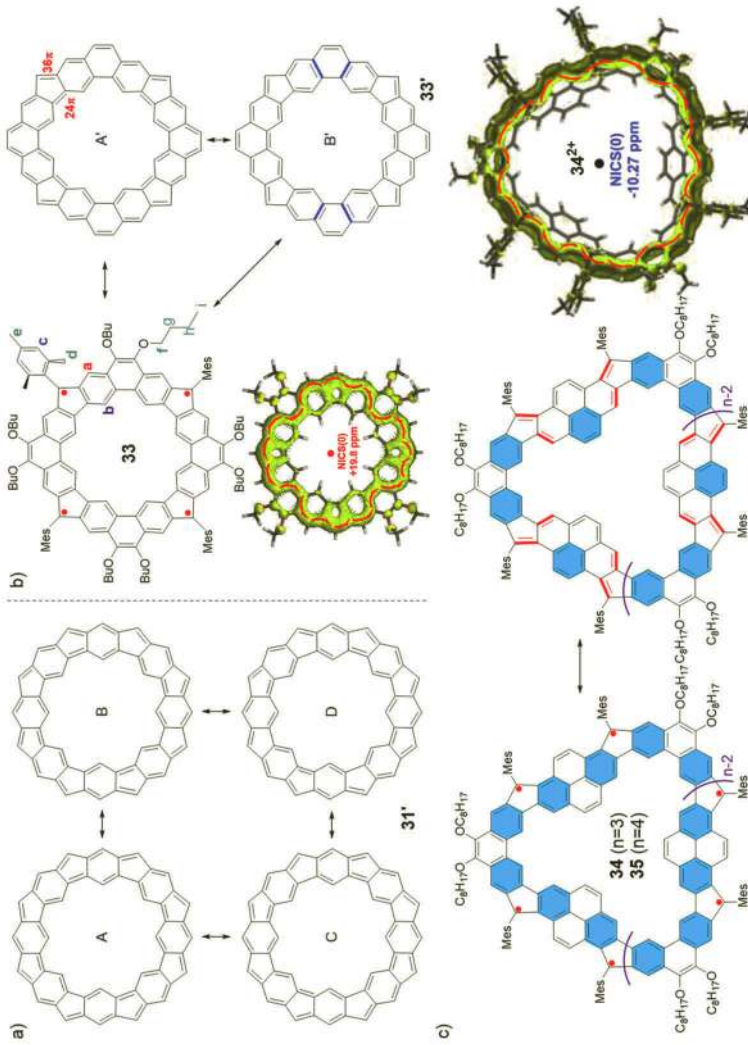


**Figure 13.11** (a) Four possible resonance structures of **31′** (backbone of **31**) in the closed-shell form, (b) open-shell and two representative closed-shell resonance forms (A′ and B′) of **33′** (the backbone of **33**) together with the calculated ACID plot, Reproduced with permission from ref 58. Copyright 2018 WILEY-VCH Verlag Gmbh & Co. KGaA, Weinheim. and (c) structures of **34** and **35**, and the calculated ACID plot of $\mathbf{34}^{2+}$. Reproduced with permission from ref 59. Copyright 2018 American Chemical Society.

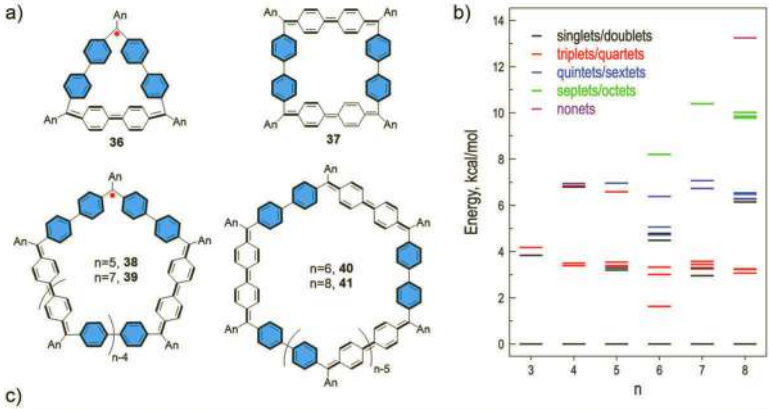


c)

| Molecules | Ground States | Lowest excited states | $N_U$ | $\Delta E_{LS\text{-}HS}$ (kcal/mol) | $E_g^{EC}$ (eV) |
|---|---|---|---|---|---|
| **36** | Doublet | Quartet | 1.7 | -3.5 | 1.75 |
| **37** | Singlet | Triplet | 2.95 | -2.8 | 1.44 |
| **38** | Doublet | Quartet | 3.94 | -2.4 | 1.08 |
| **39** | Singlet | Triplet | 4.61 | -2.2 | 1.07 |
| **40** | Doublet | Quartet | 5.42 | -1.6 | 1.05 |
| **41** | Singlet | Triplet | 5.93 | -2.1 | 1.11 |

**Figure 13.12** (a) Ground-state resonance structures of [*n*]CPBMs **36**–**41** (*n* = 3–8), (b) calculated (RAS-SF/6-31G) energies of [*n*]CPBMs at different spin states, and (c) summary of the electrochemical and magnetic data of [*n*]CPBMs. Reproduced with permission from ref 60. Copyright 2019 Elsevier Inc.

From another point of view, the [*n*]CPBM series can be characterized as 'super-sized' analogs of [*n*]annulenes. According to Hückel's rule, annulenes with [4*N*] π electrons tend to have localized double bonds in the ground state, leading to two potentially interconvertible valence isomers (Figure 13.13a). However, such valence tautomerism is too fast to be monitored by existing equipment, due to the smaller energy barrier [62]. The AFM coupling between neighboring methine radicals results in an alternate aromatic/quinoidal configuration, mimicking the alternating single/double bonds in annulene motifs. In particular, X-ray crystallography of [4]CPBM (**37**) revealed a distinct structural distortion from the idealized square to a rectangular shape. This elongated structure results from quinoidal character of the biphenyl units along two opposite sides of the molecule and aromatic character for those on the other two sides (Figure 13.13b). Interestingly, as a π-extended

analog of cyclobutadiene, **37** undergoes a similar but much slower valence tautomerization, as the process involves rupture and then reformation of aromatic benzene rings via a possible polyradicaloid transition state. This specific molecular dynamics of **37** can be monitored using VT NMR technique (Figure 13.14a), which provided a clear illustration of how bond-shift tautomerization can be reconciled with resonance.

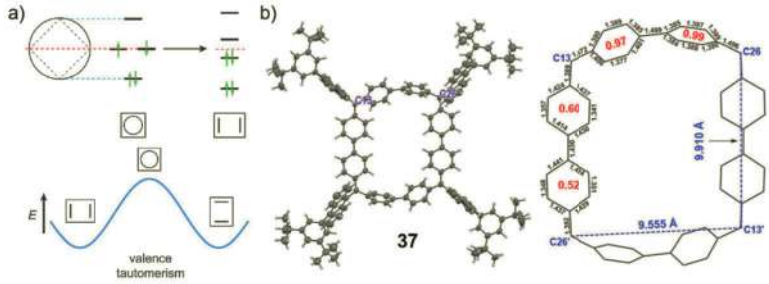


**Figure 13.13** (a) Frost-Musulin diagrams and potential energy surface for the valence tautomerism of cyclobutadiene, (b) X-ray crystallographic structure of [4]CPBM (**37**) with selected bond lengths (in Å, black numbers), HOMA values (red numbers) and distances between the neighboring methyl sites. Reproduced with permission from ref 60. Copyright 2019 Elsevier Inc.

At room temperature, the resonances of the quinoidal and aromatic benzene rings are in fast exchange relative to NMR timescale, and thus only one set of signal was observed for the central biphenyl subunits of **37**. As the temperature was gradually lowered, these resonance peaks were gradually broadened and became fully coalescent at about 263 K. Further lowering the temperature led to distinct resonances for the quinoidal and aromatic benzene protons, and the initial one doublet split into three. Careful line-shape analysis and fitting of the temperature dependent exchange rate constants ($k$) by Eyring equation gave a moderate interconversion barrier (11.22 kcal/mol at 263 K, Figure 13.14b).

Theoretical calculations suggested that the valence tautomerization process between the two ground-state valence isomers need go through a $C_4$ symmetric tetraradicaloid transition state, and the calculated ACID plots based on the optimized transition-state geometry showed a counter-clockwise paratropic ring current circuit along the backbone, indicating global antiaromaticity of the transition state. In addition, NICS(0) values of +0.56/+10.06 ppm

were calculated at the geometric center of ground state/transition state configurations, respectively, further supporting the global antiaromatic character of the transition state (Figure 13.14c), which was believed to have raised the interconversion barrier and led to an unusually slow valence tautomerization process.

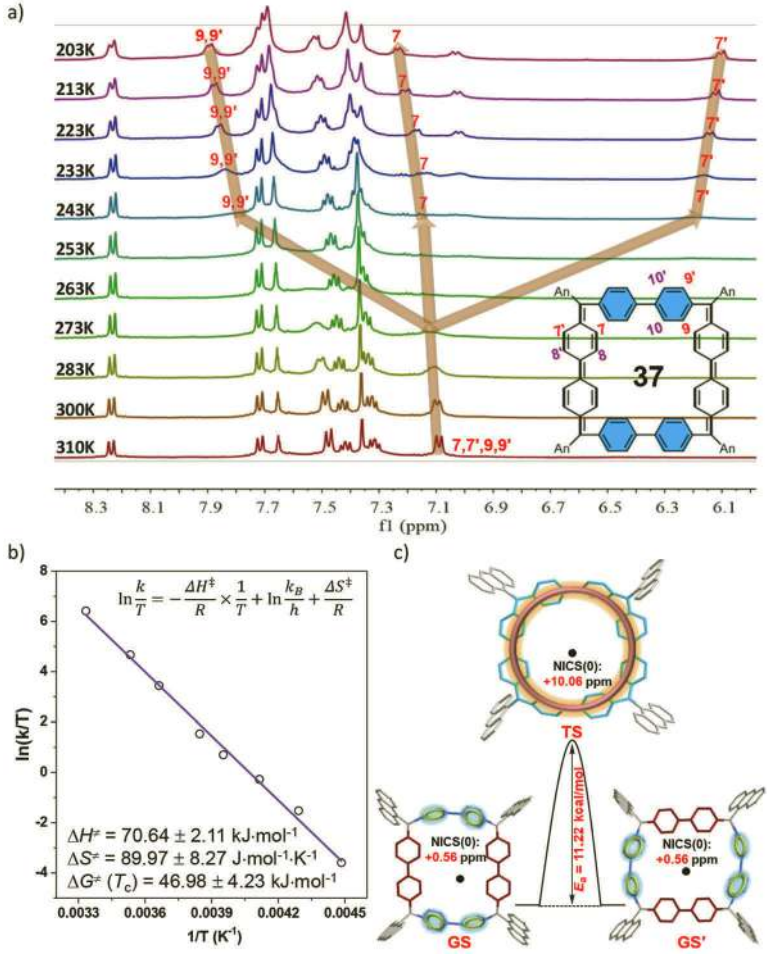


**Figure 13.14** (a) VT $^1$HNMR spectra of **37** (310–203 K) in $d_8$-THF, and the arrows show the splitting of signals corresponding to protons at the central periphery; (b) kinetic analysis of the exchange rates between two valence isomers at different temperatures by Eyring equation, and (c) schematic representation of valence tautomerization process between two ground-state valence isomers via a transition state. Reproduced with permission from ref 60. Copyright 2019 Elsevier Inc.

## 13.4 3D Fully Conjugated Diradicaloid Cages and 3D Global Aromaticity

The concept of global aromaticity in 2D macrocyclic diradicaloids/polyradicaloids can be further extended to 3D π-conjugated molecular cages. A simple example of a three-fold symmetry diradicaloid cage with two bridgehead radicals linked by three conjugated arms is shown in Figure 13.15a. It is interesting to investigate the interaction of π electrons with each other either through bond or space. Synthesis of such type of 3D fully conjugated, open-shell molecular cage is very challenging. In 2017, our group reported the first example of such diradicaloid molecular cage **42**, in which two polychlorotriphenylmethyl (PTM) radicals are linked by three bis(3,6-carbazolyl) bridge arms (Figure 13.15b) [63]. The PTM radical was chosen for its high stability. Electronic coupling between the PTM radicals and the bridges would result in three typical resonance forms (A–C). In general, such resonance transformation can be exhibited in each bridge, and π electrons and spins thus are delocalized throughout the cage framework, which was confirmed by ACID calculation. However, the two PTM radicals in this molecule are proved to be weakly coupled as deduced from magnetic measurements, single-crystal analysis, and the calculated spin-density distribution map (Figure 13.15c,d).

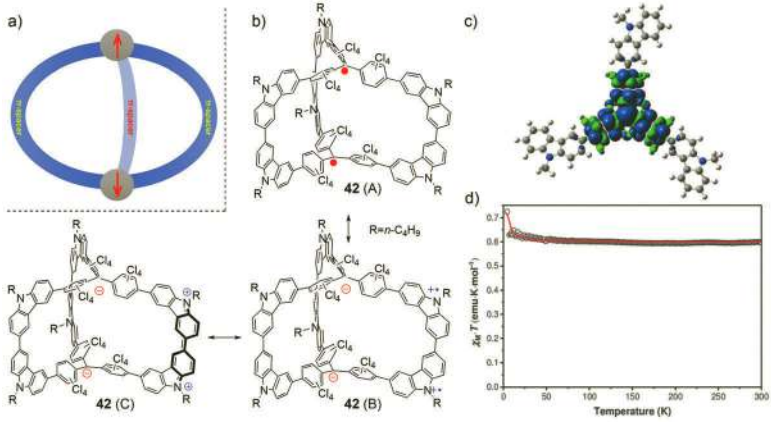


**Figure 13.15** (a) Schemetic presentation of a 3D π-conjugated diradical molecular cage, (b) a new 3D π-conjugated PTM diradical cage (**42**) and its three representative resonance forms (A–C), (c) calculated spin density distribution map of **42**, and (d) SQUID analysis of **42** in solid state. Reproduced with permission from ref 63. Copyright 2017 WILEY-VCH Verlag Gmbh & Co. KGaA, Weinheim.

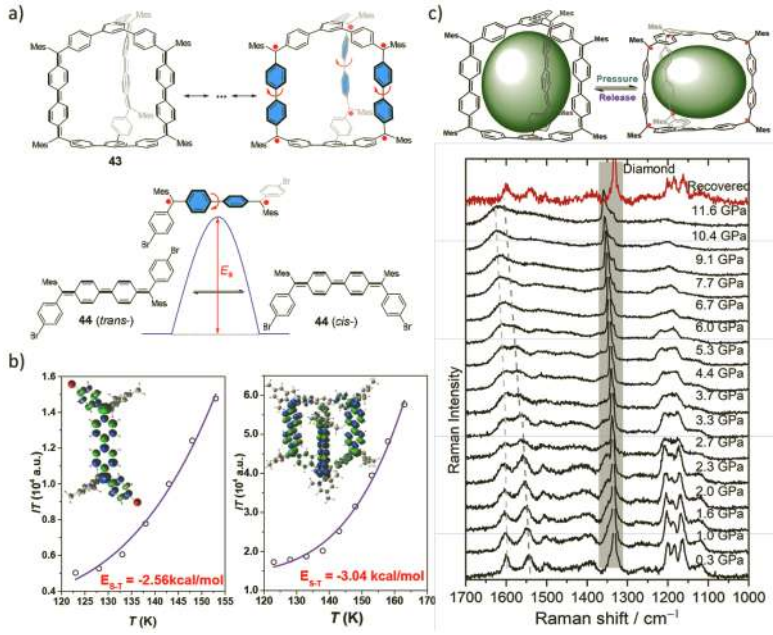


**Figure 13.16** (a) Representative resonance structures of CH-based hexradicaloid cage **43** and the model compound **44** with possible *cis*-/*trans*-dynamics via a diradical transition state, (b) *IT*-*T* plots of **43** and **44** based on VT-ESR data, and (c) proposed quinoidal to aromatic transformation upon pressure at a molecular level supported by pressure-dependent Raman spectra of **43**. Reproduced with permission from ref 64. Copyright 2020 American Chemical Society.

To obtain the 3D polyradicaloids with moderate intramolecular spin-spin coupling, the well-known Chichibabin's hydrocarbon (CH) was chosen as the building block, and a rigid molecular cage **43** with three 'CH' units linked through two benzene-1,3,5-triyl bridgeheads was designed and synthesized by our group (Figure 13.16a) [64]. The individual CH units in **43** have the tendency to become open-shell diradicals as similar to the parent CH, and thus the cage is supposed to display multiple diradical characters. Indeed, natural orbital occupation number calculations based on the optimized geometry of **43** suggest a diradical character ($y_0$) of 0.67, a tetraradical character ($y1$) of 0.66, and a hexaradical character ($y_2$) of 0.51. A restricted rotation process was found for the quinoidal biphenyl unit in the rigid molecular cage **43** as well as the linear model compound **44** by dynamic NMR measurements, but a higher rotation energy barrier

was determined in **43** (15.64 kcal/mol) than that of **44** (11.40 kcal/mol), leading to improved stability, a smaller diradical character, and an increased singlet–triplet energy gap (Figure 13.16b). The pressure-dependent Raman spectroscopic studies on the rigid cage **43** revealed a quinoidal-to-aromatic transformation along the biphenyl bridges (Figure 13.16c). In addition, the ellipsoidal cavity in the cage allowed selective encapsulation of fullerene $C_{70}$ over $C_{60}$, with an associate constant of about $1.43\times10^4$ $M^{-1}$. Moreover, **43** and **44** exhibited similar redox behavior and their cationic species ($\mathbf{43^{6+}}$ and $\mathbf{44^{2+}}$) were obtained by chemical oxidation, and the structures were identified by X-ray crystallographic analysis. The biphenyl unit showed a twisted conformation in $\mathbf{44^{2+}}$ and remained coplanarity in $\mathbf{43^{6+}}$. Notably, molecules of $\mathbf{43^{6+}}$ form a 1D columnar structure via close π–π stacking between the bridgehead benzene rings. This study demonstrated how the structural rigidity in 3D π-conjugated molecular cages affected the dynamics, stability, and electronic properties of diradicaloids/polyradicaloids. However, due to the benzene-1,3,5-triyl linkage, the three CH arms are not really coupled to each other.

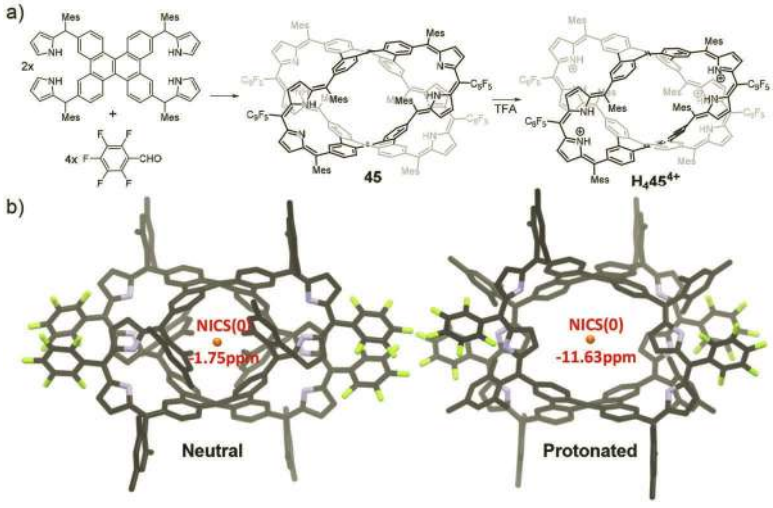


**Figure 13.17** (a) Schematic synthesis of carbaporphyrin cage **45** and subsequent protonation by TFA, and (b) X-ray crystallographic structures of **45** and $\mathbf{H_4 45^{4+}}$ with calculated NICS(0) values. Reproduced with permission from ref 65. Copyright 2018 American Chemical Society.

Sessler and Kim's team reported a 3D expanded carbaporphyrin cage **45** (Figure 13.17) [65], which was proved to be nonaromatic as inferred from UV–vis-NIR, $^1$H NMR spectra, and a near-zero NICS(0) value (−1.75 ppm). The gain of aromatic character was observed upon protonation with TFA, which was evident from a largely negative NICS(0) value (−11.63 ppm), two diatropic ring current circuits in the ACID plot, and eight-fold increase in the excited state lifetime. However, due to the strongly localized aromatic character of the two dibenzo[*g*,*p*]chrysene bridgeheads and the low molecular symmetry, the coherent ring current circuit only dominates in two nearly parallel macrocyclic conjugation pathways and the protonated carbaporphyrin cage, thus cannot be regarded as true 3D globally aromatic system.

As demonstrated in 2D macrocyclic diradicaloids/polyradicaloids, moderate AFM coupling between frontier radicals could facilitate π-electron delocalization and thus lead to global (anti)aromaticity. Therefore, for 3D π-conjugated molecular cages, moderate AFM intramolecular spin-spin interaction is critical for achieving 3D global aromaticity. Considering that thiophene ring has smaller aromatic stabilization energy than benzene ring, we decided to choose thiophene ring as building block to construct the diradicaloid cage. This would allow effective electron delocalization among any macrocycles formed by the two arms and two bridgehead radicals, or throughout the entire cage framework (Figure 13.18a). In view of this, a fully conjugated diradicaloid cage **46** containing twelve thiophene units and eight methine linkages (Figure 13.18b) was designed and synthesized [66]. The compound **46** has an open-shell singlet ground state with moderate diradical character ($y_0$ = 0.549 by UCAM-B3LYP/6-31G(d,p) or $y_0$ = 0.687 by RAS-SF/6-31G(d)). The amphoteric redox behavior of **46** allowed the access to evenly charged species $\mathbf{46^{2+}}$, $\mathbf{46^{4+}}$, and $\mathbf{46^{6+}}$ through sequentially two-, four-, and six-electron oxidation, and all the neutral and charged species can be isolated in single-crystal form (Figure 13.18c).

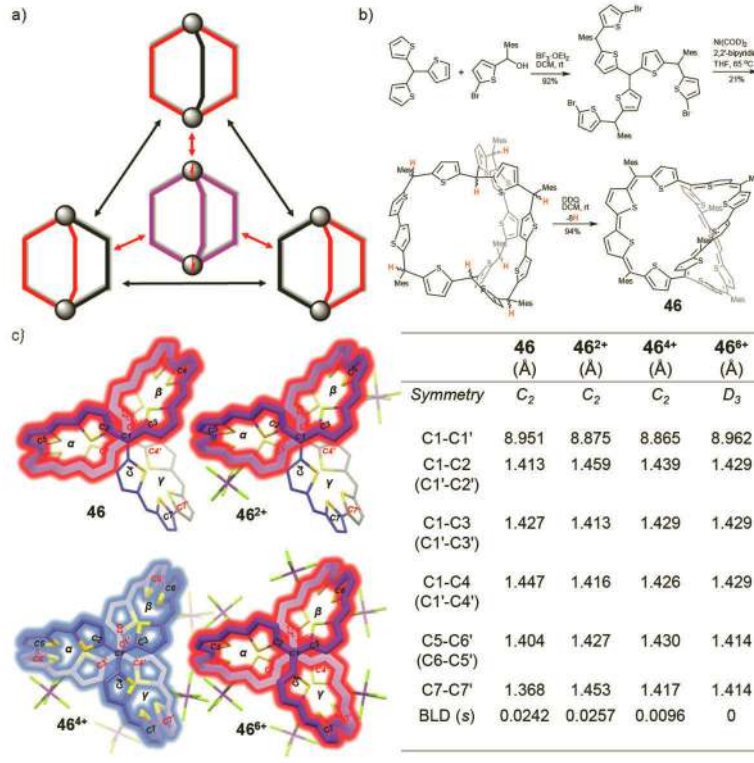


| | 46 (Å) | 46²⁺ (Å) | 46⁴⁺ (Å) | 46⁶⁺ (Å) |
|---|---|---|---|---|
| *Symmetry* | $C_2$ | $C_2$ | $C_2$ | $D_3$ |
| C1-C1' | 8.951 | 8.875 | 8.865 | 8.962 |
| C1-C2 (C1'-C2') | 1.413 | 1.459 | 1.439 | 1.429 |
| C1-C3 (C1'-C3') | 1.427 | 1.413 | 1.429 | 1.429 |
| C1-C4 (C1'-C4') | 1.447 | 1.416 | 1.426 | 1.429 |
| C5-C6' (C6-C5') | 1.404 | 1.427 | 1.430 | 1.414 |
| C7-C7' | 1.368 | 1.453 | 1.417 | 1.414 |
| BLD (*s*) | 0.0242 | 0.0257 | 0.0096 | 0 |

**Figure 13.18** (a) Schematic design of a 3D π-conjugated diradical cage, in which the resonance equilibrium between the open-shell diradical form with three-fold symmetry and the closed-shell form with lowered symmetry is presented, (b) synthesis of **46**, and (c) crystal structure of **46** and the diverse oxidation states **46²⁺**, **46⁴⁺**, and **46⁶⁺** from the top view, mesityl substituents and hydrogen atoms are omitted for clarity, the dominant conjugation pathways are highlighted in purple and blue for aromatic and antiaromatic systems, respectively, and the table includes the symmetry and bond length of all the neutral and oxidized states at specific positions. Reproduced with permission from ref 66. Copyright © 2020, Nature Publishing Group.

X-ray crystallographic analysis of **46** revealed a spiral cage structure with a pair of *P*- and *M*-enantiomers adopting $C_2$ symmetry rather than three-fold symmetry. One of the arms (γ) exhibits typical quinoidal character (large BLA), whereas the macrocycle through α and β arms (denoted as α/β macrocycle) features bond equalization (small BLA, HOMA value: 0.904), suggesting an aromatic character. The ACID plot shows an interrupted current flow along γ arm and a

clockwise diatropic ring current circuit along α/β macrocycle with a formally 38π conjugation pathway, satisfying Hückel's [4*N*+2] aromaticity rule (Figure 13.19a). A NICS(0) value of −11.95 ppm at the geometric center and generally negative NICS values for other coordination sites inside the cage are calculated. In addition, 3D ICSS map also reveals a strongly shielded chemical environment in the cavity of the molecular cage (Figure 13.19b). All these suggest an overall aromatic character of **46**. In contrast, the dication $\mathbf{46}^{2+}$ is a ground-state triplet diradical as concluded from the electronic absorption, ESR, and SQUID measurements, and further supported by calculations. Similar analyses as the neutral structure demonstrated that the triplet ground state of $\mathbf{46}^{2+}$ is aromatic with a 36π conjugation pathway satisfying Baird's [4*N*] aromaticity rule (Figure 13.19c).

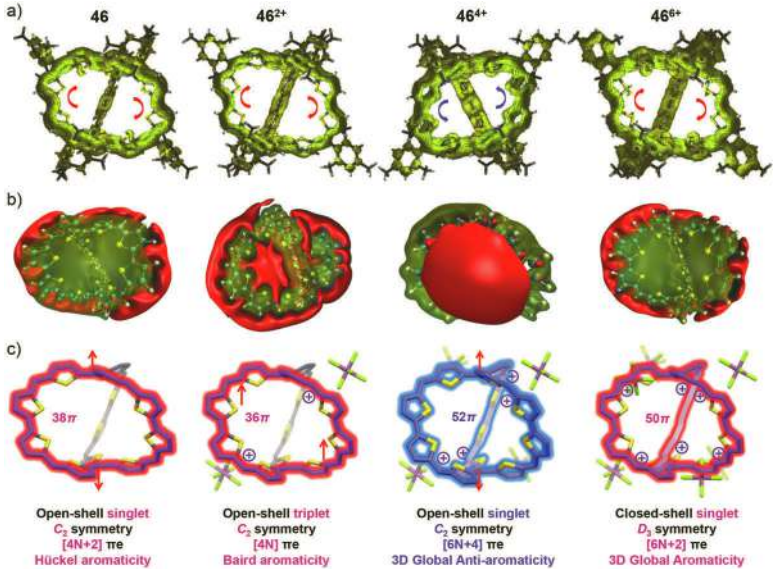


**Figure 13.19** (a) Calculated ACID plots of **46** and its charged forms with magnetic field along the Z-axis; the red and blue arrows indicate the diatropic and paratropic ring current flow, respectively, (b) calculated 3D ICSS maps; the red color represents NICS positive and the transparent space indicates area with negative NICS value, and (c) schematic π-electron delocalization pathways and the applied aromaticity rules; the dominant conjugation pathways are highlighted in purple and blue color for aromatic and anti-aromatic systems, respectively. Reproduced with permission from ref 66. Copyright © 2020, Nature Publishing Group.

The tetracation $\mathbf{46^{4+}}$ possesses an open-shell singlet ground state, as evident from VT $^1$H NMR analysis and ESR measurements, which is also in agreement with theoretical calculations. In the $^1$H NMR spectrum at 203 K, the protons on the bridged bithiophene units are significantly shielded despite the existence of four positive charges, suggesting that $\mathbf{46^{4+}}$ is a strongly antiaromatic system. In addition, the mesityl protons pointing outside the cage are highly shielded, while the inside counterparts appear at the low field. The strongly antiaromatic character was further supported by ACID, NICS (NICS(0) = +18.74 ppm), and 3D ICSS (Figure 13.19b) calculations. In particular, unlike the neutral compound and dication, the ACID plot suggests coherent ring current flow throughout the entire conjugation framework (Figure 13.19a), suggesting 3D antiaromaticity. X-ray analysis on $\mathbf{46^{4+}}$ revealed a $C_2$ symmetry with much smaller bond length differences for C1–C2, C1–C3, and C1–C4 (standard deviation of the three bonds *s:* 0.0096) as compared to the neutral state (**46**, *s:* 0.0242) (Figure 13.18c), further supporting 3D π-electron delocalization, which could be attributed to the enhanced structural rigidity induced by Coulomb repulsion among the four delocalized positive charges within the 3D framework. All these results suggest 3D global antiaromaticity for $\mathbf{46^{4+}}$ with an overall 52 π-electron delocalization.

Remarkably, the hexacation $\mathbf{46^{6+}}$ possesses a rigid structure with an essentially closed-shell nature. $^1$H NMR analysis gave a largely inversed chemical shift difference comparing to $\mathbf{46^{4+}}$, suggesting a strong global aromatic character. In particular, X-ray crystallographic analysis revealed a higher $D_3$ symmetry for $\mathbf{46^{6+}}$ with bond equalization among C1–C2, C1–C3, and C1–C4 (1.429 Å) (Figure 13.18c). The 3D global aromaticity was clearly demonstrated by ACID, NICS (NICS(0) = −8.76 ppm), and 3D ICSS calculations (Figure 13.19a,b). Moreover, in line with the aromatic character, $\mathbf{46^{6+}}$ in $CH_2Cl_2$ showed intense and well-resolved absorption peaks with $\lambda_{max}$ at 647, 815, 991, and 1130 nm.

A [6*N*+2] aromaticity rule was proposed to explain the observed 3D global aromaticity in a simplified D3 symmetrical model (Figure 13.20a). Considering the two-fold symmetry of the conjugated arms, even number of π electrons (2*N*) can be assigned. The number of π electrons at each bridgehead $sp^2$ carbon atom

could be assigned as 0, 1, or 2 for the neutral and evenly charged states. Thereby, the overall number of π electrons is formulated as [6*N*], [6*N*+2], and [6*N*+4], accordingly (Figure 13.20a). The 3D aromaticity can thus be explained by the 2D aromaticity of the three individual macrocycles formed by the neighboring two arms and the two bridgehead carbon atoms. That is, the cage with total [6*N*+2] π electrons will be aromatic in the singlet ground state because each macrocycle has [4*N*+2] π electrons, satisfying the Hückel's rule. On the other hand, the cage with overall [6*N*]/[6*N*+4] π electrons would be antiaromatic because each individual macrocycle has [4*N*]/[4(*N*+1)] π electrons. In addition, the 3D molecules are able to change their geometry and spin state to switch into non-aromatic or 2D aromatic as detailed below (Figure 13.20b,c):

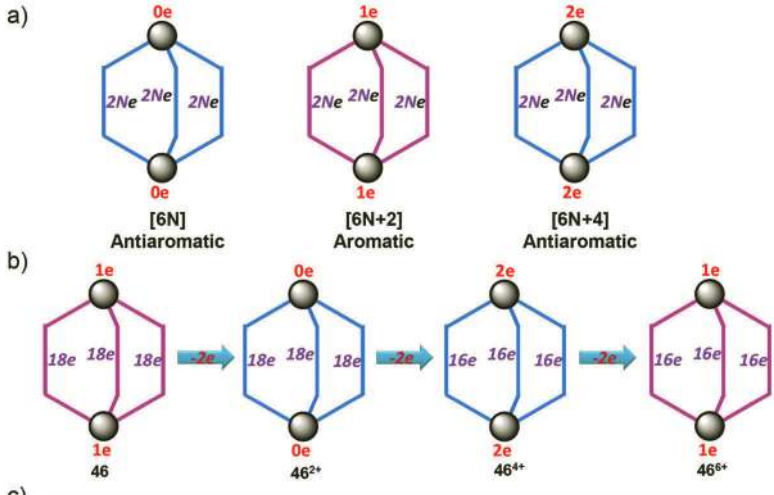


c)

| | **46** | **46²⁺** | **46⁴⁺** | **46⁶⁺** |
|---|---|---|---|---|
| **Total number of π electrons** | 56 | 54 | 52 | 50 |
| **Model of π electrons distribution** | 18×3+2 | 18×3 | 16×3+4 | 16×3+2 |
| **Formula** | 6N+2 | 6N | 6N+4 | 6N+2 |
| **Number of π electrons on each macrocycle** | 38 | 36 | 36 | 34 |
| **Aromaticity** | Aromatic | Aromatic | Antiaromatic | Aromatic |

**Figure 13.20** (a) A general formula for the 3D global (anti)aromaticity rule in a $D_3$ symmetric molecular cage, (b) simplified schematic electron distribution of **46**, **46²⁺**, **46⁴⁺**, and **46⁶⁺** in $D_3$ symmetry, and (c) brief summary of the total number of electrons, model of electron distribution, number of π electrons on each macrocycle, and aromaticity of **46** in different redox states in $D_3$ symmetry.

1. For **46**$^{6+}$, each arm can be assigned to possess 16π electrons together with 1 electron at each bridgehead carbon, that is, 34 ([4×8+2]) π electrons can be observed for each individual macrocycles, satisfying Hückel's rule. Therefore, the hexacation with $D_3$ symmetry and overall 50π electrons ([6×8+2]) is aromatic, following the above proposed 3D [6*N*+2] aromaticity rule.
2. For **46**$^{4+}$, overall the molecule has 52π electrons, which can be formulated as [6(*N*−1)+4], *N* = 9), and the Coulomb repulsion between the four positive charges along the backbone leads to a rigid structure. This results in 52π electrons being enforced to delocalize in three dimension and the molecule follows above mentioned [6*N*+4] anti-aromaticity rule, with 36 ([4×9]) π electrons delocalized along each individual macrocycle. At the same time, **46**$^{4+}$ adopts a slightly distorted conformation ($C_2$) to minimize energy arsing form antiaromaticity.
3. For **46**$^{2+}$, the molecule has overall ([6×9]) 54π electrons and each individual macrocycle has 36 ([4×9]) π electrons, following the above proposed [6*N*] antiaromaticity rule. However, the backbone has larger flexibility than the tetracation and hexacation, and thus the molecule adopts a triplet ground state and a distorted geometry with only one aromatic macrocycle (38π electrons), satisfying the Baird's [4*N*] aromaticity rule (although it is weak).
4. For **46**, overall, the molecule has 56 ([6×9+2]) π electrons and it should be 3D globally aromatic if the molecule adopts a $D_3$ symmetry, since each individual macrocycle has 38 ([4×9+2]) π electrons and overall it satisfies the above proposed [6*N*+2] aromaticity rule. Indeed, the calculated ACID plots and NICS values of **46** with a restricted $D_3$ symmetry suggest 3D global aromaticity. However, the calculated energy of this $D_3$ symmetric 3D aromatic molecule is about 11.5 kcal/mol, higher in energy as compared to $C_2$ symmetric 2D aromatic molecule. Considering the structural flexibility of this neutral molecule, it adopts a lower $C_2$ symmetry, with only one macrocycle being aromatic following Hückel's rule.

Overall, this is a good example showing how 2D and 3D global aromaticity can be achieved in a 3D fully conjugated molecular cage at different oxidation states. It also revealed a universal aromaticity rule: π-conjugated molecules, no matter with a 2D or 3D topological structure, always have a tendency to reach the lowest energy state (aromatic) by adjusting their geometry and spin state. It is also noteworthy that **46**$^{6+}$ with a high symmetry and a spiral-space structure, in which all $sp^2$-carbons distributed symmetrically over the spherical surface, could be considered as a pseudo-spherical geometry. Therefore, it may also be aromatic by following Hirsch's $2(N+1)^2$ spherical aromaticity rule (50π electrons, $N$ = 4). A simple analysis on the 25 frontier MO symmetry and energy level degeneracy of **46**$^{6+}$ implies some correlations with spherical aromaticity. However, since the symmetry of $D_3$ point group is far lower than the $I_h$ group of $C_{60}{}^{10+}$, current evidences are not sufficient to convince spherical aromaticity. To clarify the potentially spherical aromaticity in 3D π-conjugated organic molecules, molecular cages and polyhedrons with higher symmetry are desirable for the future studies.

## 13.5 2D CORFs

The next natural extension of polyradicaloids would be 2D CORFs. Based on the linkage mode, the radicals can be AFM coupled or ferromagnetically (FM) coupled. Different topological structures can be built up, with different electronic properties and diverse material applications (Figure 13.21). For example, the AFM coupled honeycomb-like CORFs (Figure 13.21a) are expected to show Dirac cone band structure, due to its six-fold symmetry like graphene [67], but with finite band gap. The FM coupled honeycomb network (Figure 13.21b) would be good candidates for plastic magnets. The Kagome-type CORFs (Figure 13.21c) could display interesting spin frustration phenomenon and thus are potentially spin liquids [68]. Synthesis of 2D CORFs is a big challenge considering the generally high reactivity of organic radicals and the difficulty to construct covalently linked crystalline frameworks.

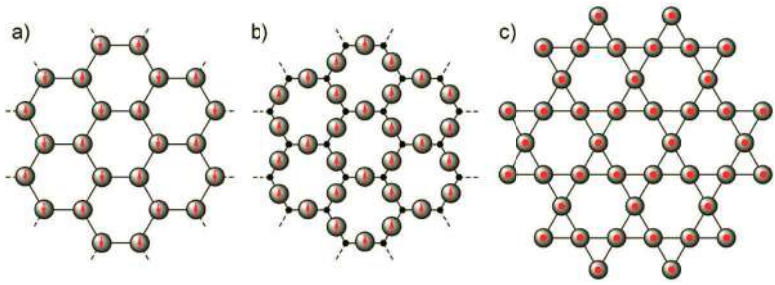


**Figure 13.21** 2D CORFs with different topological structures and intramolecular magnetic couplings.

In 2018, our group reported the synthesis, characterization, and material properties of the first π-conjugated 2D CORF **47** based on the stable PTM radical (Figure 13.22a) [69]. The covalent organic framework precursor was first synthesized via liquid/liquid interfacial acetylenic homo-coupling of a triethynylpolychlorotriphenylmethane monomer **48**. The framework showed crystalline feature with a hexagonal diffraction pattern matching that of A-B-C stacking. Subsequent deprotonation and oxidation of the polychlorotriphenylmethane units in the precursor gave the PTM radical-based π-conjugated CORF **47**. Magnetic measurements revealed that the neighboring PTM radicals in **47** are AFM coupled with each other, with a moderate exchange interaction ($J$ = −375 $cm^{-1}$). Due to the moderate spin-spin interactions, **47** has a small energy gap (ca. 0.88 eV) and a low-lying LUMO energy level (−4.72 eV), and exhibited high electro-catalytic activity and durability toward oxygen reduction reaction.

We also managed to synthesize a 3D porous organic radical network **49,** in which the organic radicals are FM coupled (Figure 13.22b) [70]. In our approach, stable hexacyanotrimethylenecyclopropanide radical anions ([CN6CP]M, M = $K^+$ (**50a**), *n*-$Bu_4N^+$ (**50b**)) were found to undergo either thermal polymerization in solid state at a relatively low temperature (300 °C) or trifluoromethanesulfonic acid-mediated polymerization at 60 °C (for **50b**) to give 1,3,5-triazine linked porous organic radical frameworks **49a** and **49b**, respectively. The resulting material **49a** exhibited spontaneous magnetization at room temperature (RT) with

typical hysteresis of ferromagnets, and the ordering temperature was estimated to be 465 K. While magnetic behavior of **49b** is more like superparamagnetism, the magnetisation is weak mainly due to existence of defects, and thus further optimization is necessary to attain highly crystalline FM coupled CORFs with minimal defects.

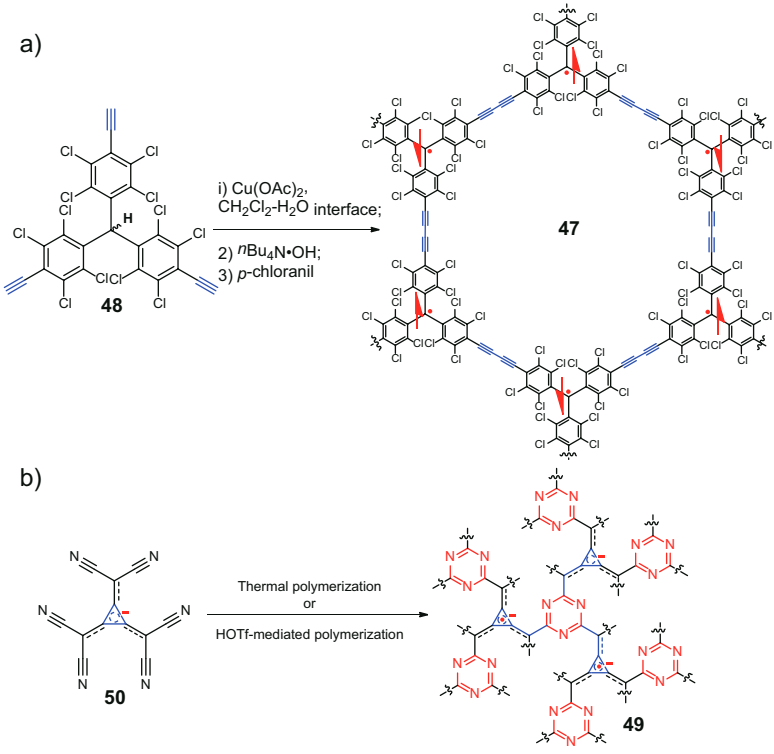


**Figure 13.22** Synthesis of (a) AFM coupled 2D CORF **47**, and (b) FM coupled porous organic radical network **49**.

## 13.6 Conclusion

In summary, in recent years, a number of open-shell polyradicaloids with multiple diradical characters have been successfully synthesized by careful tuning the intramolecular spin-spin interactions. It was found that open-shell macrocyclic polyradicaloids exhibited interesting 2D global aromaticity. In contrast to the traditional

closed-shell systems, both Hückel's rule and Baird's rule can be applicable for these ground-state open-shell molecules by adjusting the geometry and spin state, since the frontier π electrons are moderately coupled and spin flip is allowed. The successful synthesis of a fully conjugated diradicaloid molecular cage also allowed us to investigate 3D global aromaticity, and a novel [6*N*+2] aromaticity rule was proposed for the $D_3$ symmetry molecular cages. The studies can further extend into 2D CORFs with different topological structures and coupling modes, thus opening the opportunities for such as plastic magnets and quantum information processing.

## References


1. Minami T. and Nakano, M. (2012). Diradical character view of singlet fission, *J. Phys. Chem. Lett.,* **3**, pp. 145150.
2. Liu, C., Ni, Y., Lu, X., Li, G., and Wu, J. (2019). Global aromaticity in macrocyclic polyradicaloids: Hückel's rule or Baird's rule?, *Acc. Chem. Res.*, **52**, pp. 2309–2321.
3. Sondheimer, F. (1963). Recent advances in the chemistry of large-ring conjugated systems, *Pure Appl. Chem.*, **7**, pp. 363–388.
4. Hückel, E. (1931). Quantentheoretische Beiträge zum Benzolproblem, *Z. Phys.*, **70**, pp. 204–286.
5. Breslow, R., Brown, J., and Gajewski, J. J. (1967). Antiaromaticity of cyclopropenyl anions, *J. Am. Chem. Soc.*, **89**, pp. 4383–4390.
6. Sondheimer, F. (1972). The annulenes, *Acc. Chem. Res.*, **5**, pp. 81–91.
7. Wiberg, K. B. (2001). Antiaromaticity in monocyclic conjugated carbon rings, *Chem. Rev.*, **101**, pp. 1317–1331.
8. Spitler, E. L., Johnson, C. A., and Haley, M. M. (2006). Renaissance of annulene chemistry, *Chem. Rev.*, **106**, pp. 5344–5386.
9. Tanaka, T. and Osuka, A. (2017). Chemistry of *meso*-aryl-substituted expanded porphyrins: Aromaticity and molecular twist, *Chem. Rev.*, **117**, pp. 2584–2640.
10. Stępień, M. and Latos-Grażyński, L. (2008). Aromaticity and tautomerism in porphyrins and porphyrinoids, *Top. Heterocycl. Chem.*, **19**, pp. 82–153.
11. Peeks, M. D., Claridge, T. D. W., and Anderson, H. L. (2017). Aromatic and antiaromatic ring currents in a molecular nanoring, *Nature*, **541**, pp. 200–203.

12. Peeks, M. D., Jirasek, M., Claridge, T. D. W., and Anderson, H. L. (2019). Global aromaticity and antiaromaticity in porphyrin nanoring anions, *Angew. Chem. Int. Ed.*, **58**, pp. 15717–15720.
13. Rickhaus, M., Jirasek, M., Tejerina, L., Gotfredsen, H., Peeks, M. D., Haver, R., Jiang, H.-W., Claridge, T. D. W., and Anderson, H. L. (2020). Global aromaticity at the nanoscale, *Nat. Chem.*, **12**, pp. 236–241.
14. Heilbronner, E. (1964). Hückel molecular orbitals of Möbius-type conformations of annulenes, *Tetrahedron Lett.*, **5**, pp. 1923–1928.
15. Zimmerman, H. E. (1966). On molecular orbital correlation diagrams, the occurrence of Mobius systems in cyclization reactions, and factors controlling ground- and excited-states reactions I, *J. Am. Chem. Soc.*, **88**, pp. 1564–1565.
16. Stępień, M., Latos-Grażyński, L., Sprutta, N., Chwalisz, P., and Szterenberg, L. (2007). Expanded porphyrin with a split personality: A Hückel-Möbius aromaticity switch, *Angew. Chem. Int. Ed.*, **46**, pp. 7869–7873.
17. Tanaka, Y., Saito, S., Mori, S., Aratani, N., Shinokubo, H., Shinata, N., Higuchi, Y., Yoon, Z. S., Kim, K. S., and Noh, S. B. (2008). Metalation of expanded porphyrins: A chemical trigger used to produce molecular twisting and Möbius aromaticity, *Angew. Chem. Int. Ed.*, **47**, pp. 681–684.
18. Yoon, Z. S., Osuka, A., and Kim, D. (2009). Möbius aromaticity and antiaromaticity in expanded porphyrins, *Nat. Chem.*, **1**, pp. 113–122.
19. Baird, N. C. (1972). Quantum organic photochemistry. II. Resonance and aromaticity in the lowest $^3\pi\pi^*$ state of cyclic hydrocarbons, *J. Am. Chem. Soc.*, **94**, pp. 4941–4948.
20. Martin, M., Dahlstrand, C., Kilså, K., and Ottosson, H. (2014). Excited state aromaticity and antiaromaticity: Opportunities for photophysical and photochemical rationalizations, *Chem. Rev.*, **114**, pp. 5379–5425.
21. Möllerstedt, H., Piqueras, M. C., Crespo, R., and Ottosson, H. (2004). Fulvenes, fulvalenes, and azulene: Are they aromatic chameleons?, *J. Am. Chem. Soc.*, **126**, pp. 13938–13939.
22. Sung, Y. M., Yoon, M.-C., Lim, J. M., Rath, H., Naoda, K., Osuka, A., and Kim, D. (2015). Reversal of Hückel (anti)aromaticity in the lowest triplet states of hexaphyrins and spectroscopic evidence for Baird's rule, *Nat. Chem.*, **7**, pp. 418–422.
23. Saunders, M., Berger, R., Jaffe, A., McBride, J. M., O'Neill, J., Breslow, R., Hoffman, J. M. Jr., Perchonock, C., Wasserman, E., Hutton, R. S., and

Kuck, V. J. (1973). Unsubstituted cyclopentadienyl cation, a ground-state triplet, *J. Am. Chem. Soc.*, **95**, pp. 3017–3018.

24. Hirsch, A., Chen, Z., and Jiao, H. (2000). Spherical aromaticity in $I_h$ symmetrical fullerenes: The $2(N+1)^2$ rule, *Angew. Chem. Int. Ed.*, **39**, pp. 3915–3917.
25. Bühl, M. and Hirsch, A. (2001). Spherical aromaticity of fullerenes, *Chem. Rev.*, **101**, pp. 1153–1183.
26. Chen, Z. and King, R. B. (2005). Spherical aromaticity: Recent work on fullerenes, polyhedral boranes, and related structures, *Chem. Rev.*, **105**, pp. 3613–3642.
27. Bean, D. E. and Fowler, P. W. (2008). Stacked-ring aromaticity: An orbital model, *Org. Lett.*, **10**, pp. 5573–5576.
28. Aihara, J. (2009). Origin of stacked-ring aromaticity, *J. Phys. Chem. A*, **113**, pp. 7945–7952.
29. Nozawa, R., Kim, J., Oh, J., Lamping, A., Wang, Y., Shimizu, S., Hisaki, I., Kowalczyk, T., Fliegl, H., Kim, D., and Shinokubo, H. (2019). Three-dimensional aromaticity in an antiaromatic cyclophane, *Nat. Commun.*, **10**, pp. 3576.
30. Fujiwara, T., Muranaka, A., Nishinaga, T., Aoyagi, S., Kobayashi, N., Uchiyama, M., Otani, H., and Iyoda, M. (2020). Preparation, spectroscopic characterization and theoretical study of a three-dimensional conjugated 70 π-electron thiophene π-mer radical cation π-dimer, *J. Am. Chem. Soc.*, **142**, pp. 5933–5937.
31. Xiang, Q., Guo, J., Xu, J., Ding, S., Li, Z., Li, G., Gu, Y., Dang, Y., Xu, Z., Gong, Z., Hu, W., Zeng, Z., Wu, J., and Sun, Z. (2020). Stable olympicenyl radicals and their π-dimers, *J. Am. Chem. Soc.*, **142**, pp. 11022–11031.
32. Geuenich, D., Hess, K., Köhler, F., and Herges, R. (2005). Anisotropy of the induced current density (ACID), a general method to quantify and visualize electronic delocalization, *Chem. Rev.*, **105**, pp. 3758–3772.
33. Schleyer, P. v. R., Maerker, C., Dransfed, A., Jiao, H., and Hommes, N. J. R. v. E. (1996). Nucleus-independent chemical shifts: A simple and efficient aromaticity probe, *J. Am. Chem. Soc.*, **118**, pp. 6317–6318.
34. Chen, Z., Wannere, C. S., Corminboeuf, C., Puchta, R., and Schleyer, P. v. R. (2005). Nucleus-independent chemical shifts (NICS) as an aromaticity criterion, *Chem. Rev.*, **105**, pp. 3842–3888.
35. Klod, S. and Kleinpeter, E. (2001). Ab initio calculation of the anisotropy effect of multiple bonds and the ring current effect of arenes: Application in conformational and configurational analysis, *J. Chem. Soc., Perkin Trans.*, **2**, pp. 1893–1898.

36. Lu, T. and Chen, F. (2012). Multiwfn: A multifunctional wavefunction analyzer, *J. Comp. Chem.*, **33**, pp. 580–592.
37. Hu, P., Lee, S., Herng, S. T., Aratani, N., Goncalves, T. P., Qi, Q., Si, X., Yamada, H., Huang, K.-W., Ding, J., Kim, D., and Wu, J. (2016). Toward tetraradicaloid: The effect of fusion mode on radical character and chemical reactivity, *J. Am. Chem. Soc.*, **138**, pp. 1065–1077.
38. Lu, X., Lee, S., Kim, J. O., Gopalakrishna, T. Y., Phan, H., Herng, T. S., Lim, Z. L., Zeng, Z., Ding, J., Kim, D., and Wu, J. (2016). Stable 3,6-linked fluorenyl radical oligomers with intramolecular anti-ferromagnetic coupling and polyradical characters, *J. Am. Chem. Soc.*, **138**, pp. 13048–13058.
39. Tian, Y., Uchida, K., Kurata, H., Hirao, Y., Nishiuchi, T., and Kubo, T. (2014). Design and synthesis of new stable fluorenyl-based radicals, *J. Am. Chem. Soc.*, **136**, pp. 12784–12793.
40. Zeng, Z., Sung, Y. M., Bao, N., Tan, D., Lee, R., Zafra, J. L., Lee, B. S., Ishida, M., Ding, J., López Navarrete, J. T., Li, Y., Zeng, W., Kim, D., Huang, K.-W., Webster, R. D., Casado, J., and Wu, J. (2012). Stable tetrabenzo-Chichibabin's hydrocarbons: Tunable ground state and unusual transition between their closed-shell and open-shell resonance forms, *J. Am. Chem. Soc.*, **134**, pp. 14513–14525.
41. Mack, J. (2017). Expanded, contracted, and isomeric porphyrins: Theoretical aspects, *Chem. Rev.*, 117, pp. 3444–3478.
42. Gopalakrishna, T. Y., Reddy, J. S., and Anand, V. G. (2014). An amphoteric switch to aromatic and antiaromatic states of a neutral air-stable 25p radical, *Angew. Chem. Int. Ed.*, **53**, pp. 170–189.
43. Schweyen, P., Brandhorst, K., Wicht, R., Wolfram, B., and Bröring, M. (2015). The corrole radical, *Angew. Chem. Int. Ed.*, **54**, pp. 8213–8216.
44. Yoshida, T., Zhou, W., Furuyama, T., Leznoff, D. B., and Kobayashi, N. (2015). An extremely air-stable 19π porphyrinoid, *J. Am. Chem. Soc.*, **137**, pp. 9258–9261.
45. Hiroto, S., Furukawa, K., Shinokubo, H., and Osuka, A. (2006). Synthesis and biradicaloid character of doubly linked corrole dimers, *J. Am. Chem. Soc.*, **128**, pp. 12380–12381.
46. Koide, T., Furukawa, K., Shinokubo, H., Shin, J.-Y., Kim, K. S., Kim, D., and Osuka, A. (2010). A stable non-Kekulé singlet biradicaloid from *meso*-free 5,10,20,25-tetrakis(pentafluorophenyl)-substituted [26] hexaphyrin(1.1.1.1.1.1), *J. Am. Chem. Soc.*, **132**, pp. 7246–7247.
47. Ishida, M., Shin, J.-Y., Lim, J. M., Lee, B. S., Yoon, M.-C., Koide, T., Sessler, J. L., Osuka, A., and Kim, D. (2011). Neutral radical and singlet biradical

forms of *meso*-free, -keto, and -diketo hexaphyrins(1.1.1.1.1.1): Effects on aromaticity and photophysical properties, *J. Am. Chem. Soc.*, **133**, pp. 15533–15544.

48. Ooi, S., Shimizu, D., Furukawa, K., Tanaka, T., and Osuka, A. (2018). Stable face-to-face singlet diradicaloids: Triply linked corrole dimer Gallium(III) complexes with two $\mu$-hydroxo-bridges, *Angew. Chem. Int. Ed.*, **57**, pp. 14916–14920.
49. Rana, A., Hong, Y., Gopalakrishna, T. Y., Phan, H., Herng, T. S., Yadav, P., Ding, J., Kim, D., and Wu, J. (2018). Stable expanded porphycene-based diradicaloid and tetraradicaloid, *Angew. Chem. Int. Ed.*, **57**, pp. 12534–12537.
50. Ni, Y., Gopalakrishna, T. Y., Wu, S., and Wu, J. (2020). A stable all-thiophene-based core-modified [38]octaphyrin diradicaloid: Conformation and aromaticity switch at different oxidation states, *Angew. Chem. Int. Ed.*, **59**, pp. 7414–7418.
51. Nobusue, S., Miyoshi, H., Shimizu, A., Hisaki, I., Fukuda, K., Nakano, M., and Tobe, Y. (2015). Tetracyclopenta[def,jkl,pqr,vwx]tetraphenylene: A potential tetraradicaloid hydrocarbon, *Angew. Chem. Int. Ed.*, **54**, pp. 2090–2094.
52. Das, S., Herng, T. S., Zafra, J. L., Burrezo, P. M., Kitano, M., Ishida, M., Gopalakrishna, T. Y., Hu, P., Osuka, A., Casado, J., Ding, J., Casanova, D., and Wu, J. (2016). Fully fused quinoidal/aromatic carbazole macrocycles with poly-radical characters, *J. Am. Chem. Soc.*, **138**, pp. 7782–7790.
53. Lu, X., Lee, S., Hong, Y., Phan, H., Gopalakrishna, T. Y., Herng, T. S., Tanaka, T., Sandoval-Salinas, M. E., Zeng, W., Ding, J., Casanova, D., Osuka, A., Kim, D., and Wu, J. (2017). Fluorenyl based macrocyclic polyradicaloids, *J. Am. Chem. Soc.*, **139**, pp. 13173–13183.
54. Li, G., Gopalakrishna, T. Y., Phan, H., Herng, T. S., Ding, J., and Wu, J. (2018). From open-shell singlet diradicaloid to closed-shell global antiaromatic macrocycles, *Angew. Chem. Int. Ed.*, **57**, pp. 7166–7170.
55. Fukuzumi, S., Ohkubo, K., Ishida, M., Preihs, C., Chen, B., Borden, W. T., Kim, D., and Sessler, J. L. (2015). Formation of ground state triplet diradicals from annulated Rosarin derivatives by triprotonation, *J. Am. Chem. Soc.*, **137**, pp. 9780–9783.
56. Cha, W.-Y., Kim, T., Ghosh, A., Zhang, Z., Ke, X.-S., Ali, R., Lynch, V. M., Jung, J., Kim, W., Lee, S., Fukuzumi, S., Park, J. S., Sessler, J. L., Chandrashekar, T. K., and Kim, D. (2017). Bicyclic Baird-type aromaticity, *Nat. Chem.*, **9**, pp. 1243–1248.

57. Liu, C., Sandoval-Salinas, M. E., Hong, Y., Gopalakrishna, T. Y., Phan, H., Aratani, N., Herng, T. S., Ding, J., Yamada, H., Kim, D., Casanova, D., and Wu, J. (2018). Macrocyclic polyradicaloids with unusual super-ring structure and global aromaticity, *Chem*, **4**, pp. 1586–1595.

58. Lu, X., Gopalakrishna, T. Y., Phan, H., Herng, T. S., Jiang, Q., Liu, C., Li, G., Ding, J., and Wu, J. (2018). Global aromaticity in macrocyclic cyclopenta-fused tetraphenanthrenylene tetraradicaloid and its charged species, *Angew. Chem. Int. Ed.*, **57**, pp. 13052–13056.

59. Lu, X., Gopalakrishna, T. Y., Han, Y., Ni, Y., Zou, Y., and Wu, J. (2019). Bowl-shaped carbon nanobelts showing size dependent properties and selective encapsulation of $C_{70}$, *J. Am. Chem. Soc.*, **141**, pp. 5934–5941.

60. Ni, Y., Sandoval-Salinas, M. E., Tanaka, T., Phan, H., Herng, T. S., Gopalakrishna, T. Y., Ding, J., Osuka, A., Casanova, D., and Wu, J. (2019). [*n*]Cyclo-*para*-biphenylmethine polyradicaloids: [*n*]Annulene analogs and unusual valence tautomerization, *Chem*, **5**, pp. 108–121.

61. Lewis, S. E. (2015). Cycloparaphenylenes and related nanohoops, *Chem. Soc. Rev.*, **44**, pp. 2221–2304.

62. Orendt, A. M., Arnold, B. R., Radziszewski, J. G., Facelli, J. C., Malsch, K. D., Strub, H., Grant, D. M., and Michl, J. (1988). $^{13}$C NMR and polarized IR spectra of vicinally labeled [$^{13}$C2]cyclobutadiene in an argon matrix: Interconversion of valence tautomers, *J. Am. Chem. Soc.*, **110**, pp. 2648–2650.

63. Gu, X., Gopalakrishna, T. Y., Phan, H., Ni, Y., Herng, T. S., Ding, J., and Wu, J. (2017). Three-dimensionally π-conjugated diradical molecular cage, *Angew. Chem. Int. Ed.*, **56**, pp. 15383–15387.

64. Ni, Y., Gordillo-Gámez, F., Alvarez, M. P., Nan, Z., Li, Z., Wu, S., Han, Y., Casado, J., and Wu, J. (2020). A Chichibabin's hydrocarbon-based molecular cage: The impact of structural rigidity on dynamics, stability, and electronic properties, *J. Am. Chem. Soc.*, **142**, pp. 12730–12742.

65. Ke, X.-S., Kim, T., He, Q., Lynch, V. M.; Kim, D., and Sessler, J. L. (2018). Three-dimensional fully conjugated carbaporphyrin Cage, *J. Am. Chem. Soc.*, **140**, pp. 16455–16459.

66. Ni, Y., Gopalakrishna, T. Y., Phan, H., Kim, T., Herng, T. S., Han, Y., Tao, T., Ding, J., Kim, D., and Wu, J. (2020). 3D Global aromaticity in a fully conjugated diradicaloid cage at different oxidation states, *Nat. Chem.*, **12**, pp. 242–248.

67. Wallace, P. R. (1947). The band theory of graphite, *Phys. Rev.*, **71**, pp. 622–634.

68. Savary, L. and Balents, L. (2017). Quantum spin liquids: A review, *Rep. Prog. Phys.*, **80**, pp. 016502.

69. Wu, S., Li, M., Phan, H., Wang, D., Herng, T. S., Ding, J., Lu, Z., and Wu, J. (2018). Toward π-conjugated 2D covalent organic radical frameworks, *Angew. Chem. Int. Ed.*, **57**, pp. 8007–8011.

70. Phan, H., Herng, T. S., Wang, D., Li, X., Zeng, W., Ding, J., Loh, K. P., Wee, A. T. S., and Wu, J. (2019). Room-temperature magnets based on 1,3,5-triazine linked porous organic radical frameworks, *Chem*, **5**, pp. 1223–1234.

# Index